

**Synthesis, structure elucidation, and exploration of
potential anti-cancer activity of newly designed
palladium(II) Schiff base complexes**

Thesis
Submitted for the degree of
Doctor of Philosophy (Science)

by

RAHUL NASKAR



DEPARTMENT OF CHEMISTRY
JADAVPUR UNIVERSITY, KOLKATA - 700 032
INDIA

MARCH-2023



Date: 06.03.2023

CERTIFICATE FROM THE SUPERVISOR(S)

This is to certify that the thesis entitled "Synthesis, structure elucidation, and exploration of potential anti-cancer activity of newly designed palladium(II) Schiff base complexes" submitted by Mr. Rahul Naskar, M.Sc., who got his name registered on 01.10.2018 for the award of Ph.D. (Science) degree of Jadavpur University, is absolutely based upon his own work under the joint supervision of Prof. Tapan Kumar Mondal, Department of Chemistry, Jadavpur University, Kolkata-700032, and Dr. Nabendu Murmu, Department of STBA, Chittaranjan National Cancer Institute, Kolkata-700026 and that neither this thesis nor any part of it has been submitted for either any degree / diploma or any other academic award anywhere before.

It is also certified that he has fulfilled all the requirements of the regulations relating to the nature and period of research.

Tapan K. Mondal
06/03/23

Dr. Tapan Kumar Mondal (Supervisor)

Dr. TAPAN KUMAR MONDAL
Professor
Department of Chemistry
Jadavpur University
Kolkata-700032

Nabendu Murmu
6.3.23

Dr. Nabendu Murmu (Co-supervisor)

डॉ० नबेंदु मुरुमु / Dr. Nabendu Murmu Ph.D
वरिष्ठ वैज्ञानिक अधिकारी, सहायक संचालक ग्रेड
Sr. Scientific Officer, Assistant Director Grade
विभाग प्रमुख सिगनाल ट्रांसडक्शन और बायोजेनिक एमाइंस/
Head Department of Signal Transduction and Biogenic Amines
चित्तरेञ्जन राष्ट्रीय कैंसर संस्थान
Chittaranjan National Cancer Institute
स्वास्थ्य और परिवार कल्याण मंत्रालय
Ministry of Health & Family Welfare
कलकत्ता-700 026 / Kolkata-700 026

Signature of the Supervisors and date with official seal

“Believe you can and you’re halfway there.”

~ Theodore Roosevelt

Dedicated to

My parents and Girlfriend...

ACKNOWLEDGEMENTS

At the end of my five-year research journey, now that I glance back, I understand that there are so many people without whose help and guidance, either in a direct or indirect way, I would not have been able to complete this tough journey so successfully. So I will gladly take this opportunity to express my deep sense of reverence and gratitude to my supervisor, Prof. Tapan Kumar Mondal, Department of Chemistry, Jadavpur University, Kolkata, 700032, and also to my co-supervisor, Dr. Nabendu Murmu, Department of STBA, Chittaranjan National Cancer Institute, Kolkata, 700026, for allowing me to pursue research freely in his group. I am really grateful to him for his valuable suggestions during the tenure of my work and for pursuing the entire thesis.

I express my sincere thanks to the faculty members of the Department of Chemistry at Jadavpur University: Prof. Subratanath Koner, Head, Department of Chemistry; Prof. Subenoy Chakraborty, Dean of Science at JU; Prof. Saurabh Das, Section-in-Charge, Inorganic Chemistry Section; and all other faculty members of the Department of Chemistry at Jadavpur University. I express my indebtedness to all the teaching as well as non-teaching staff members of this department and university for their help in various aspects.

Financial assistance received from University Grant Commission, New Delhi is gratefully acknowledged.

I also express my appreciation as well as gratefulness to all my present and former labmates viz., Dr. Krishnendu Aich, Dr. Sangita Das, Dr. Saswati Gharami, Dr. Lakshman Patra, Dr. Chandan Kumar Manna, Mr. Biswajit Bera, Mr. Akash Das, Mr. Amitav Biswas, Mr. Subrata Mandal, Mr. Atanu Maji, Mr. Sandipan Mandal, Mr. Arpan Halder, Ms. Moumita Ghosh, Mr. Chandrasekhar Mandi, Mr. Samik Acharyya, Mrs. Paramita Ghosh, Mr. Debarpan Mitra, Mrs. Depanwita Saha and Mrs. Rimi Mukherjee for their constant help and support throughout my research journey. I would also like to thank all my project students, viz., Ms. Monisha Chawlay, Surabhi Chakraborty, and Sourav Sinha, for helping me carry out reactions. The memories I make with them will be the most valuable asset of my research period. The journey was made much easier and full of enthusiasm by the mere presence of all of them.

I express my deepest gratitude to my M.Sc. project supervisor, Dr. Sukanta Mandal, IIT Kharagpur for initializing the spirit of research through me during my masters which ultimately led me to begin this research journey.

I'm very grateful to my girlfriend, Ms. Tulika Pradhan, for her constant love, support, and understanding while I was getting my Ph.D., which made it possible for me to finish my thesis. Friends and some other well-wishers for their pleasant friendships, which helped me in both academic and non-academic ways directly or indirectly. Last but not least, I owe a lot to my parents, Late Nirmal Kumar Naskar and Mrs. Uma Naskar, and I feel very lucky to have them as my parents. Their love, support, teachings, and blessings have helped me get this far. I'd also like to thank my loving older sister Mrs. Rakhi Naskar, my brother-in-law Mr. Shyamal Kumar Halder, my elder brother Rajat Naskar, and my sister-in-law Vadla Chandurani for their blessings, encouragement, and moral support during my research work. I express my appreciation to all of the people mentioned above for their continuous alliance, support and immense love which made me tough and persistent enough to complete this journey successfully.

I express my appreciation to all of the people mentioned above for their continuous alliance, support and immense love which made me tough and persistent enough to complete this journey successfully.

(Rahul Naskar)

Department of Chemistry
Jadavpur University

CONTENTS		Page no.
PREFACE		i-iii
CHAPTER-I	<i>Introduction</i>	1-49
CHAPTER-II	<i>Palladium(II) complex bearing benzothiazole based O,N,S donor pincer ligand: Study of in-vitro cytotoxicity, interaction with CT-DNA and BSA protein</i>	50-84
CHAPTER-III	<i>Palladium(II) complexes with thioether based ONS donor ligand: Synthesis, characterization, X-ray structure, DFT study and anti-cancer activity</i>	85-115
CHAPTER-IV	<i>Palladium(II) complexes with morpholine based ONN pincers: Synthesis, X-ray structure, protein (CT-DNA/BSA) binding study and in-vitro cytotoxicity</i>	116-157
CHAPTER-V	<i>Synthesis, spectral characterization, DFT investigation, and in vitro anti proliferative activity of new ONN donor morpholine-based ligands and their Pd(II) complexes</i>	158-203
CHAPTER-VI	<i>New coumarin-morpholine O,N,N donor pincer ligand appended Palladium(II) complex : in-situ Synthesis, spectral characterization, in-vitro anti-cancer activity and interaction with protein</i>	204-238
CHAPTER-VII	<i>New Palladium(II) complexes appended with coumarin based Schiff base O,N,S pincers: X-ray structure, protein binding study, DFT study and anti-cancer activity in breast cancer cell lines</i>	239-281
CHAPTER-VIII	<i>A new chromone based fluorescence probe for ratiometric detection of Pd²⁺</i>	282-312
LIST OF PUBLICATION		313-315

PREFACE

My thesis work entitled, “**Synthesis, structure elucidation, and exploration of potential anti-cancer activity of newly designed palladium(II) Schiff base complexes**” contains new design as well as the synthesis of several palladium(II) complexes with different ONS donor Schiff-base ligands. The complexes have been thoroughly studied by UV-Vis, fluorescence and ^1H as well as ^{13}C NMR and HRMS methods. In addition, anti-cancer activity of the palladium(II) complexes were studied in different cancer cell line and theoretical studies will have also been undertaken to probe the electronic structures of the complexes. Interaction with DNA and BSA with the newly synthesized palladium(II) complexes has also been explored. Along with these selective and sensitive analytical method has been designed and developed for the recognition of palladium in environment. This thesis consists of eight chapters based on the synthesis, structure elucidation and potential anti-cancer activity of palladium(II) complexes.

Chapter 1 represents a brief introduction on the a review of the ligands containing ONS and ONN donor site and different complex of Palladium(II). The anti-cancer activities of the complexes and their interactions with DNA and BSA have been described.

Chapter 2 describes the synthesis of a new palladium(II) complex, $[\text{Pd}(\text{LS}^{\text{Et}})\text{Cl}]$ (**C1**) with benzothiazole based ONS donor pincer ligand (HLS^{Et}). The interaction of **C1** with CT DNA was investigated and the proficiency of displacement of ethidium bromide (EB) from its EB-CTDNA complex by **C1** was performed by fluorescence quenching method. Similarly, the interaction of **C1** with BSA protein was investigated by UV-Vis and fluorescence methods. In vitro cytotoxicity of the complex towards human gastric cancer cell lines (AGS) was assessed by MTT assay method.

Chapter 3 deals with the synthesis and characterization of new palladium(II) complexes, $[\text{Pd}(\text{L})\text{Cl}]$ (**C1**) and $[\text{Pd}(\text{L})\text{PPh}_3](\text{ClO}_4)$ (**C2**), with ONS donor thioether ligand (HL). All the complexes were thoroughly characterized by using numerous spectroscopic techniques like FT-IR, NMR and UV-visible spectroscopy and so forth. Moreover, DFT and TDDFT calculations were performed to interpret the electronic structure, redox and spectral properties of the complexes.

Cytotoxicity of the complexes was evaluated *in vitro* using MTT assay on human gastric cancer cell lines (AGS).

Chapter 4 presents the synthesis and characterization of new ONN donor pincer ligands, (HL¹ and HL²) and their palladium complexes [Pd(L¹)Cl] (**C1**) and [Pd(L²)Cl] (**C2**). The ability of the Pd(II) complexes to bind with CT DNA are investigated by UV–Vis method. Moreover, the interactions of Pd(II) complexes (**C1/C2**) with bovine serum albumin (BSA) are also studied. The antiproliferative activity of the complexes are investigated with AGS, MDA-MB 231 and HepG2 cancer cell line. Electronic structure of the complexes are interpreted by DFT/ TDDFT computations.

Chapter 5 deals with the synthesis and characterization of new ONN donor pincer ligands (HL¹ and HL²) and their palladium complexes [Pd(L¹)Cl] and [Pd(L²)Cl]. The ability of the Pd(II) complexes to bind with CT DNA are investigated by UV–Vis method and Competitive binding study with ethidium bromide (EB) by fluorescence method suggests that the Pd(II) complexes efficiently displace EB from EB-DNA complex. Moreover, the interactions of Pd(II) complexes (**C1/C2**) with bovine serum albumin (BSA) are also studied. The antiproliferative activity of the complexes are investigated with different cancer cell line.

Chapter 6 introduces the synthesis and thoroughly characterization of a new coumarin-morpholine O,N,N donor pincer ligand appended palladium(II) complex. Electronic structure and solution spectrum of the complexes are interpreted by DFT/TDDFT studies. The *in vitro* cytotoxic activity of the palladium complexes was carried out against human gastric cancer (AGS) cell lines and breast cancer cell lines (MDA MB 231 and MCF-7) by MTT assay. Intercalation of the complex with DNA was evaluated by performing agarose gel electrophoresis of various concentrations of the complex. The understanding of the complexes to bind with CT DNA investigated carefully through UV-Vis method and fluorescence method. The interaction of the complex with BSA protein was investigated by UV-Vis and fluorescence methods.

Chapter 7 presents the synthesis and characterization of new coumarin based ONS donor ligands containing palladium(II) complexes. Electronic structure, solution spectrum and redox properties of the complexes are interpreted by DFT/TDDFT studies. The *in vitro* cytotoxic activity of the palladium complexes was carried out against breast cancer (MCF 7 and MDA MB 231) cell lines

by MTT assay. The understanding of the complexes to bind with CT DNA investigated carefully through UV-Vis method and fluorescence method. Moreover, the interactions of Pd(II) complexes with bovine serum albumin (BSA) are also studied.

Lastly, **Chapter 8** reports a novel fluorescent probe (HMPM) based on chromone. The selective ratiometric amplification of HMPM fluorescence in the presence of Pd²⁺ can be attributed to the ESIPT and/or ICT processes. In addition, HMPM is able to detect Pd²⁺ in the presence of other metal ions in the nM range. Interaction of HMPM with Pd²⁺ is determined by a variety of spectroscopic approaches. In addition, the square planar geometry of the HMPM-Pd²⁺ complex is validated by the single crystal X-ray diffraction technique. Density Functional Theory (DFT) is used to examine the electronic structures of HMPM and HMPM-Pd²⁺. Importantly, the probe can effectively detect Pd²⁺ using the dip-stick method.

In brief, this thesis deals with the chemistry of Palladium(II) complexes with Schiff base ligands containing O, N, S donors and selective and sensitive analytical method has been designed and developed for the recognition of palladium in environment. I am happy to note that these works have been published in several reputed international journals.

In keeping with the general practice of reporting scientific observation, due acknowledgement has been made whenever the work described as based on the findings of other investigators. I must take the responsibility of any unintentional oversights and errors which might have crept in spite of due precautions.

(Rahul Naskar)

Department of Chemistry

Jadavpur University

CHAPTER-I

INTRODUCTION

*Synthesis, structure elucidation, and
exploration of potential anti-cancer
activity of newly designed palladium(II)
Schiff base complexes*

I.1. General Introduction

The field of inorganic chemistry known as "coordination chemistry" is quite extensive. Chemists from all around the world have found great interest and inspiration in the study of metal complex chemistry. The metal complexes of organic chelating ligands are becoming increasingly popular in research laboratories, in the marketplace, and in the biological sciences. To establish the reactive sites accessible at a metal centre and to modify their reactivity, modern coordination chemists rely on ligands which bond with the transition metal ions in a predictable manner. The role of ligands in coordination chemistry and Schiff bases in particular is one that has not diminished over time. Schiff bases are an important class of ligands because of their structural resemblance to naturally occurring biological molecules and their selectivity and sensitivity towards the central metal atom.

This area of study has been reported to have excellent diuretic, anticancer, antibacterial, and antifungal properties. Schiff bases are advantageous in a variety of industries, including the food industry, the dye industry, analytical chemistry, catalysis, fungicidal, agrochemical, and biological activity [1-10]. Several catalytic organic transformations in which ligands govern the chemical processes are also conceivable [11-13].

Palladium (Pd) is one of the transition metals that caught our attention because of its interesting molecular and electronic structure, redox properties [14-17], various biological activities that show the close connection between inorganic chemistry and biology, and various analytical applications [18-20], as well as its usefulness in various homogeneous catalytic applications [21-23]. Not only the science of catalysis is a fascinating utilization for metal complexes, but so are many other fields, such as biology and medicine. The ancient Greek physician Hippocrates is credited as being the first person to use inorganic substances in medical practice. He suggested employing the use of metallic salts in the treatment of medical conditions. Both diagnostic and therapeutic medicines have been derived from metal

complexes in the past. In the field of bio-inorganic chemistry, some of the most recent active research subjects include investigations into metal-based anticancer medicines and arthritic agents. Numerous palladium-based metal complexes, particularly Schiff bases, have been investigated for their potential use as antibacterial and anticancer medications. Many of these complexes have been found as a result of this area of investigation. This chapter examines the Schiff bases, their metal complexes, and general uses for them.

I.2. Schiff base ligands

Hugo Schiff, a German chemist, came up with a new group of organic compounds in 1864. In his honour, these groups of compounds, called imines, are often called Schiff bases. Most Schiff bases are produced when a primary amine and an aldehyde or ketone join together. Schiff base ligands with an azomethine group ($-\text{HC}=\text{N}-$) are considered "privileged ligands" [24]. They are made when a primary amine and a carbonyl compound join together. The lone pair on N atom is a good way for the azomethine group to bind to metal ions. Schiff bases act as macrocycles or polydentate chelating ligands when they contain one or more donor atoms in addition to the $-\text{C}=\text{N}-$ group. Schiff bases can be made from both aldehydes and ketones, but ketones are less likely to do so than aldehydes. Because Schiff bases can be used in a variety of ways, many complexes with unique structures are being built right now. Schiff bases derived from aliphatic aldehydes are unstable and easily chained [25], whereas Schiff bases derived from aromatic aldehydes are more stable. The majority of Schiff bases are crystalline with a weak base. Schiff bases are typically formed through acid or base catalysis or through the application of heat. A chelating Schiff base is formed when two equivalents of salicylaldehyde are combined with a diamine. Salen ligands are very similar to porphyrins, but they are easier to synthesize. They have four coordinating ligand sites and two open sites along the axis for other ligands. The term "Salen" was only applied to ethylenediamine-based

4 / Chapter I

tetradentate Schiff bases. Salicylaldehyde and diamine can be made in a lab, and when they come together, they usually make the salen ligand in a way that is very close to 100% [26].

Schiff bases have been widely used in many fields, including biology, chemistry, analysis, and drug development. Many Schiff bases and their complexes have been studied for their intriguing and important properties, such as their ability to act as a catalyst and transfer the amino group [27], photochromic behaviour [28], and ability to form complexes with some toxic metals [29]. Spectrofluorimetric monitoring of small changes in pH [30] uses Schiff bases (Fig.I.1) as fluorescent indicators.

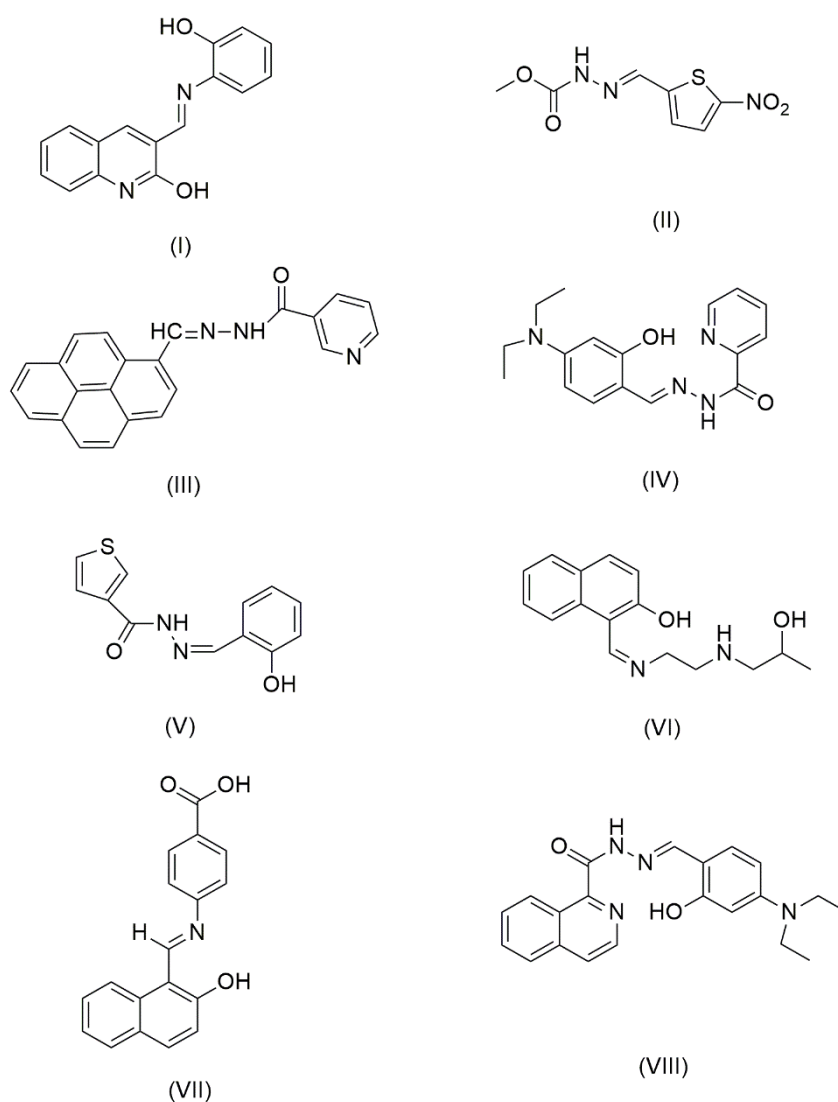


Fig.I.1. Some fluorescent Schiff bases' structures (Adopted from Ref. 30)

I.3. Metal complexes of Schiff base ligands

The discovery and use of Schiff bases has been crucial to the advancement of coordination chemistry. It turns out that Schiff bases can stable a wide range of metals in different oxidation states, allowing one to modulate the metal's activity in a wide range of useful catalytic reactions. Because of their usefulness in a variety of fields, including organic synthesis [31], liquid crystals [32], molecular switches in logic or memory circuits [33], UV stabilizers [34] and laser dyes [35], etc., Schiff base metal complexes have been the subject of substantial research. Each of these ligand types can vary in size and charge, making them ideal for use in a combinatorial library [36]. High homogeneity, repeatability, selectivity, and activity to catalyze reactions under mild circumstances have been demonstrated by Schiff base complexes of numerous transition metal ions complexes, which have been discovered as homogeneous catalysts for diverse processes. Coordination polymers, double helices, and triple helicates are only some examples of the types of supramolecular architecture that can be built with the help of Schiff base ligands [38]. As a result of their versatility, Schiff base ligands can be used to successfully synthesize homo- and hetero-metallic complexes with a wide range of stereochemistry [39]. Biological system active site modelling depends on this property [40]. donor oxygen and nitrogen-containing transition metal complexes Because of their unique conformations, structural instability, and sensitivity to molecular environments [42], Schiff bases are of great interest. Many important biological processes rely on Schiff base complexes, including photosynthesis and oxygen transport in mammalian and animal respiratory systems [43]. It has also been demonstrated [44] that Schiff bases play a critical role in the biological activity of bacteriorhodopsin. A protonated Schiff bases are responsible for the covalent bond between the protein and the retinal chromophore [45]. Additionally, dioxygen absorption [46] and oxidative catalysis [47] of Schiff base complexes have been investigated. By strategically choosing between bulky and/or electron withdrawing or

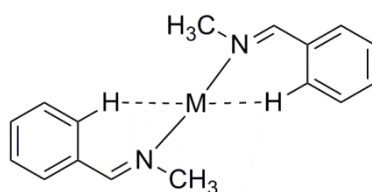
electron donating substitutes, the steric and electrical effects around the metal core can be finely adjusted. The oxygen in phenolates is a hard donor that is known to stabilize the metal atom in its higher oxidation state, whereas the nitrogen in imines is a soft donor that will stabilize the metal atom in its lower oxidation state [48]. When ligands containing donor atoms like N, P, S, or O are present in the coordination sphere of palladium (II) complexes, the resulting complexes have been found to be extremely stable. The theoretical and practical components of producing Schiff base metal complexes are dispersed across numerous sources.

I.4. Different bonding modes of Schiff bases

Coordination of the Schiff bases to the metal ion looks like:

(i) Monodentate

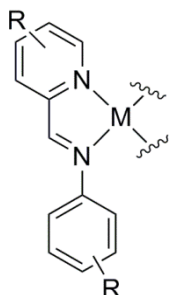
Stable imino-metal complexes cannot be formed because the C=N group is too weak. The metal-nitrogen connection can be stabilized by forming chelate rings, which requires at least one additional donor atom to be present near the nitrogen atom.



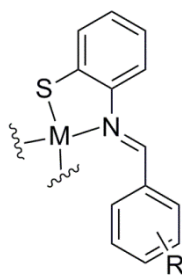
(ii) Bidentate

The Schiff bases can coordinate to the metal atom through Bidentate N, O donor Schiff bases have been investigated extensively.

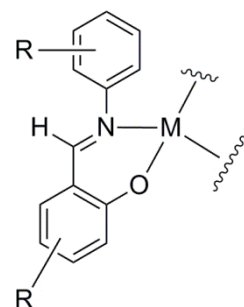
(a) N, N donor atom



(b) N, S donor atom



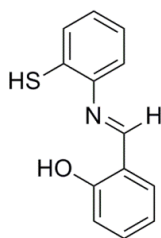
(c) N, O donor atom



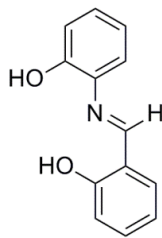
(iii) Tridentate

Many tridentate Schiff bases are used as anionic ligands.

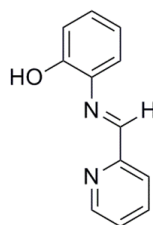
(a) ONS donor



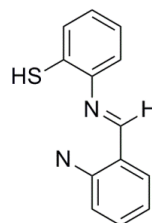
(b) ONO donor



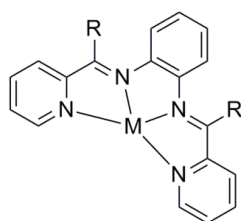
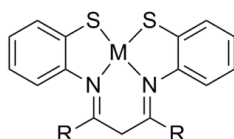
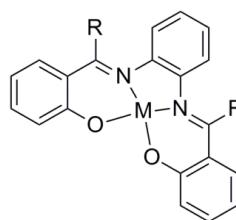
(b) ONN donor



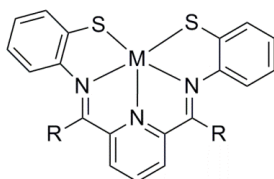
(d) NNS donor

**(iv) Tetradentate**

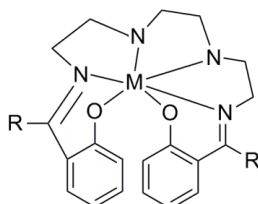
Schiff bases that can coordinate metal ions as N₄, N₂S₂, and N₂O₂ donor sets have been studied a lot for their ability to do this.

(a) N₄ donor(b) N₂S₂ donor(b) N₂O₂ donor**(v) Pentadentate**

Metal complexes of the potentially pentadentate ligands have also been studied.

**(vi) Hexadentate**

In many metal complexes, the Schiff base dianion is a hexa-dentate ligand, causing the octahedral geometry of the complex to be deformed.



I.5. Polydentate ligands

Since the beginning, commercial, pharmaceutical, and academic laboratories have worked to synthesize new and inventive ligand systems for a variety of uses. The ligands that form complexes with transition metal ions can regulate the metals' coordination number, shape, and oxidation state [49]. Polydentate ligands are gaining popularity because they stabilize metal-ligand complexes. The resulting metal-chelate complexes are more stable than monodentate ligands [50]. The synthesis of unsymmetrical polydentate ligands including a number of electrically distinct donor sites is of great interest [51]. Combining hard and soft donor moieties in a ligand can provide a 'masked' empty coordination site at the metal [52]. This event has catalytic potential since the ligand is not lost from the metal's coordination sphere throughout catalytic cycles.

By modifying the ligand structure and donor locations, metal centre coordination can be regulated. Different donor fragments in the same metal scaffold that are different on an electronic level should change how the metal complex reacts. Pearson's "hard-soft-acid-base" (HSAB) theorem says that soft late transition metals should bind more strongly to soft, more polarizable donor moieties, while harder, less polarizable donor segments should bind to earlier metals [53]. Because of this, it is best to add a number of donors with different electronic states to a single ligand framework. For example, adding soft thiols and phosphines to oxygen and amine donors is a good idea. When different donor atoms are put together, their different trans effects can be used to make complexes. Organochalcogen ligands have stronger trans effects than nitrogen donors, which have weaker trans effects than tertiary phosphines [54]. By changing the way the donor works in a planned way, a series of ligands that are very similar to each other can be made. These can be studied in depth using metal centres. The C=N group is not strong enough on its own to make stable imino-metal

complexes. By making chelate rings, at least one more donor atom near the nitrogen atom should stabilize the metal-nitrogen bond.

I.6. Nitrogen donor ligands

Metal-heteroatom complexes, known as Classical or Werner's complex, have been studied since the early 19th century. Some of the simplest ligands and metal-ligand linkages occur in these complexes. Coordination chemistry grew out of studies of complexes like this. Although amine ligands are commonly used in coordination chemistry, they are less prevalent in organometallic chemistry. In this case, there are two primary causes: Most organometallic chemistry focuses on class B metals, which tend to coordinate only weakly, and amines favour class A metals, therefore there is a discrepancy between the two. When amines are used in organometallic chemistry, it is typically with transition metals, where the hard/soft mismatch is less pronounced. Ethylenediamine and other polydentate ligands can be used in place of monodentate amines to improve coordination through the chelate effect [55].

Simple amines like ethylenediamine are just one type of nitrogen donor ligand; others include pyridine ligands like 2,2'-bipyridine (bipy) and phenanthroline (phen), as well as oxazolines, porphyrins, and imines. Since they are easier to work with, organometallic chemistry typically employs ligands based on pyridine, imine, or oxazoline rather than amines [56, 57]. Many ligands feature multiple heteroatoms, such as phosphorus and oxygen. The salen's are an illustrious group of N, O donor ligands that have found use in both catalysis and coordination chemistry. Asymmetric catalysis, such as the Jacobsen epoxidation, is enabled by the use of chiral amines, which in turn generate chiral salen's [58].

I.7. Oxygen/Sulphur containing ligands

Sulphur- and oxygen-based ligands come in a variety of forms, and the literature is full with references to their uses. Oxo-ethers in particular, which are tougher oxygen donors, interact

more strongly with the s-block and the earlier metals. Unquestionably, the best illustration of these donor ligands is the crown ether. An intriguing area of coordination chemistry is the synthesis of the ligand with the thioether donor centre in a chelated environment with additional N and O donors in acyclic/macrocyclic backbone to create good working models to account for the function of metal ions in biological systems.

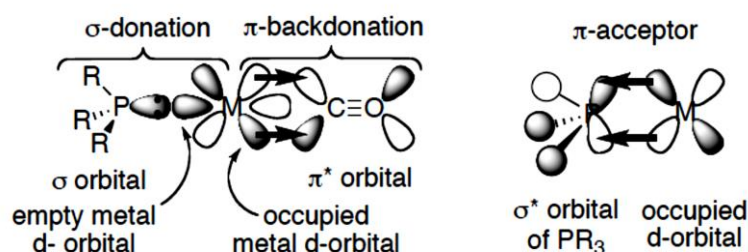
Many research teams are working on the synthesis of various ligands with N, S donor sites to investigate the function of metal ions in biological systems and to extract ecologically hazardous heavy metal ions from everyday products. With N belonging to aromatic nitrogenous systems including pyridine, imidazole, pyrazole, and benzimidazole, a number of N_xS_y donor ligands have been developed, and their reactivity with various transition and non-transition metals has been studied [59-69]. Making chemical analogues of the metalloprotein active site has attracted a lot of research attention, and some of the bioactive compounds carry N and S donor centres. Coordination chemistry requires the synthesis of ligands with thioether donor centres in chelated environments with extra N and O donors in acyclic/macrocyclic platforms [70-72]. Regarding their capacity for soft-hard donation, excited state and photophysical characteristics, production of anticancer platinum medicines with decreased nephrotoxicity, etc. Different fields of research are becoming interested in N_xS_y systems.

I.8. Phosphorus donor ligands

Phosphines are thought of as " σ -donors" since the metal can accept the lone pair on the phosphorus atom. Increased electron density on phosphorus, achieved by adding electron-donating substituents on R, results in a more potent σ -donation. The σ^* -orbital of the P-R bonds is able to play the role of acceptor, allowing these molecules to function as π -acceptors (also known as π -acids) (Scheme I.1). The weakest π -acceptors are alkyl phosphines, next

aryl phosphines, phosphites, and finally PF_3 , which is quite close to CO [73]. Substituents on R that take electrons away from the atom make π -back donation more likely. Although it is difficult to disentangle the phosphine's σ -donor and π -acceptor features using experiments alone, many computational methods have been developed to achieve just that [74]. These investigations demonstrate that phosphines are both σ -donors and π -acceptors, with the majority of the σ -bonding coming from the lone pair of phosphorus and the π -bonding coming from the metal's donation of electron density into an empty orbital of the ligand with phosphorus 3p character.

Triethyl phosphine platinum trichloride was the first phosphorus-metal compound described, by Hofmann in 1857 [75]. For transition metal complexes, phosphines (PR_3) have established themselves as a reliable and flexible ligand class since that time. To access a variety of ligand reactivity profiles, PR_3 allows for the systematic and predictable modification of steric and electrical characteristics by altering R (R = aryl, alkyl) [76].



Scheme I.1. Phosphines as σ -donor and π -acceptor

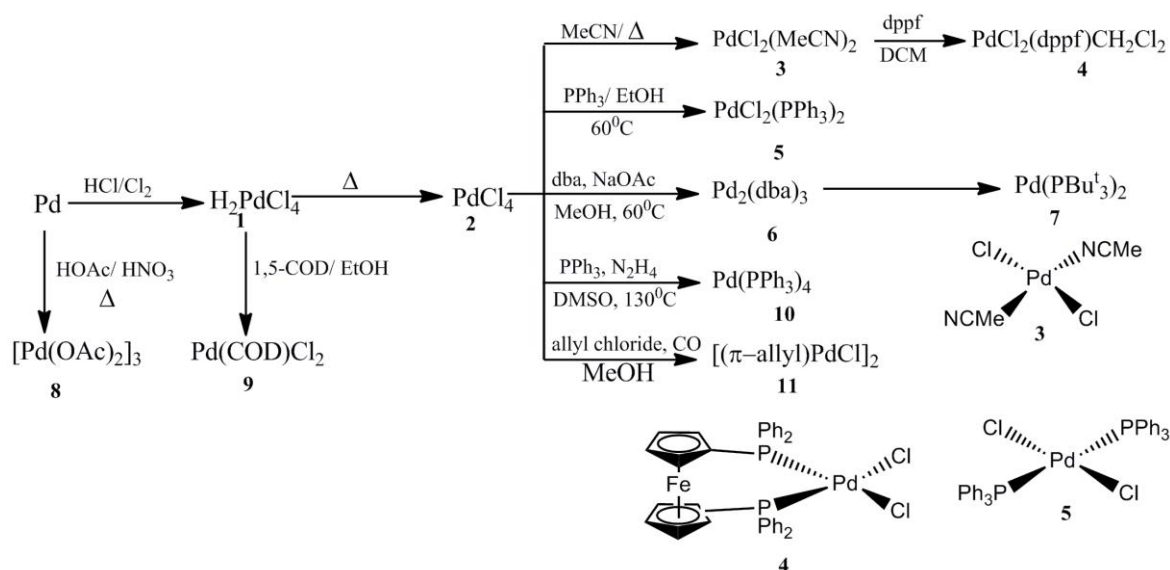
I.9. Palladium

In the modern periodic table, palladium is located in group 10th and the 5th period. It has the symbol Pd and the atomic number 46, and it is a very uncommon chemical element. William Hyde Wollaston made the discovery of the beautiful palladium metal in 1803. Palladium is characterized by its silvery-white colour. He had given it the name palladium, which is derived from the name of the Greek goddess Pallas, which represented wisdom.

Catalytic converters are able to convert up to ninety percent of the dangerous gases that are produced by automobile exhaust (hydrocarbons, carbon monoxide, and nitrogen dioxide) into less toxic chemicals, and they utilize more than half of the world's supply of palladium and its congener platinum (nitrogen, carbon dioxide and water vapor). 0, +1, +2, +4, and +6 are the states of oxidation that palladium can be in. 0, +2, and +4 are the oxidation states that occur most frequently and steadily. There is no indication that palladium occurs in the +3-oxidation state. This has been explored using X-ray diffraction for a number of compounds, and the results indicate that palladium is actually present as a dimer of palladium (II) and palladium (IV) rather than in the +3 state. There are seven naturally occurring isotopes of palladium, although only six of them are stable. The stable isotopes of palladium are ^{102}Pd , ^{104}Pd , ^{105}Pd , ^{106}Pd , ^{108}Pd , and ^{110}Pd . Palladium also has an unstable isotope that is ^{111}Pd . ^{106}Pd has an abundance of 27.33% and is the most stable of the isotopes. The catalytic preparation and utilization of palladium complexes, along with several other features, are detailed in scheme I.2.

Palladium complexes have been used extensively in catalytic processes with a wide variety of environments that engaged in C-C bond making reactions such as carbon-hetero atom reactions, carbonylation, and allylic alkylation. The scheme I.2 presents an overview of some of the most useful catalysts in their generic form. When palladium metal is exposed to an environment containing chlorine and then submerged in a concentrated solution of hydrochloric acid, the resulting reaction produces a solution of chloropalladic acid (**1**). The reddish-brown solution is next subjected to evaporation, which results in the formation of palladium(II) chloride (**2**) in the form of a brown polymeric solid [77]. It is utilized in the huge chemical manufacturing industry as a carbonylation catalyst (Wacker-Hoechst process), which is used for the transformation of ethylene to acetaldehyde, the creation of acetone from propene, and the synthesis of glycol derivatives [78-81]. An orange/yellow crystalline solid is

produced through the synthesis of dichlorobis(acetonitrile)palladium(II), **3**, which involves the reaction of utilizing **2** in an acetonitrile solution while the reaction is carried out under refluxing conditions. It has a role as a catalyst in cross-coupling processes such as Heck, Negishi, and Grignard, and it is also employed in hydro carboxylation reactions [82-87]. By reacting (**3**) with bis(diphenylphosphino)ferrocene in dichloromethane, the dichloro(bis(diphenylphosphino)ferrocene)palladium(II) dichloromethane (**4**) complex can be manufactured. Grignard coupling processes, Buchwald-Hartwig coupling reactions, and Stille coupling reactions all make use of it as a catalyst [88-91]. It is possible to produce dichlorobis(triphenylphosphine)palladium(II), (**5**) by reacting triphenylphosphine with dichlorobis(triphenylphosphine)palladium(II) in ethanol at a temperature of 60 °C. This results in the production of a crystal powder that is light yellow in colour [92, 93]. It plays a role as a catalyst in the Sonogashira coupling of terminal alkynes with aryl halides and as a carbonylation catalyst in the production of certain lactones [94, 95]. Tris(dibenzylideneacetone)dipalladium(0) was generated through the reaction of (**2**) with dibenzylideneacetone and sodium acetate in methanol at a temperature of 60 °C (**6**).



Scheme I.2. Preparation of palladium chemical products and their application

As a catalyst, it is highly useful for a wide variety of carbon-carbon and carbon-heteroatom coupling processes. It is also used in Suzuki coupling of aryl chlorides with an Arduengo imidazolium salt to produce biphenyls by targeted catalysis. By reacting (6) with tri-tert-butylphosphine in dimethylformamide solution, two sterically hindered phosphines (PBu^t_3) are generated, which are then linearly coordinated to palladium metal in the centre to form the essential complex bis(tri-tert-butylphosphine)palladium(0) (7). The Negishi cross coupling of aryl and vinyl chlorides utilizes this zero valent complex catalyst [96-98]. By reacting palladium powder dissolved in acetic acid with nitric acid under refluxing conditions, the palladium(II) acetate salt, 8, can be produced. To create substituted 1,6- and 1,7-dienes from butadiene, it is used as a catalyst [99]. The reaction of (1) with 1,5-COD in ethanol yields the dichloro(1,5-cyclooctadiene)palladium(II) (9) complex, which is used as a catalyst to protect hydroxyl groups and in different organometallic coupling processes [100]. In addition to its fascinating application in catalyzing [3,3] sigmatropic rearrangements [101], tetrakis(triphenylphosphine)-palladium(0) (10) is utilized in catalysis for coupling reactions, most notably the Sonogashira reaction. By reacting (2) with allyl chloride in methanol solvent in the presence of carbon monoxide, the crucial catalyst-allylpalladium(II), (11) can be synthesized. In asymmetric alkylation, where sphingosines, an antifungal drug, are produced, the synthesis of a quaternary centre by alkylation of azlactone has given way to a new approach [102–104].

I.10. Importance of Pd complexes

Albert and coworkers [114,115] reported two interesting contributions regarding the synthesis and a comprehensive analysis of the biological activity of mono- and dinuclear endo cyclopalladated benzophenone imines, which demonstrated potent antiproliferative activity against MCF-7 and MDA-MB-231 cancer cells. Samiee et al. [116] reported in 2019

the catalytic and anticancer activity of a palladium complex that exhibits potent cytotoxicity against HT-29 and A549 cell lines ($IC_{50}(72h) = 9$ and $10 \mu M$, respectively). Fluorescence tests (dual acridine orange/ethidium bromide [AO/EB] double labelling) and morphological analysis of cancer cells treated with complex demonstrated its capacity to trigger apoptosis-mediated cell death. Prabhakaran [117] reported the production of tetranuclear palladacyclic complexes that demonstrated cytotoxicity in the range of $5-7 \mu M$ (48 hours) against HepG2 and HT-29 cancer cells. Che published [118] in 2016 a category of palladacyclic complexes containing several NHCs. In vitro tests on six distinct tumour cell lines (NCI-H1650, NCI-H460, MDA-MB-231, HeLa, A2780, and A2780cis) revealed that these derivatives are significantly more active than compounds containing the same palladacyclic fragment combined with weaker ligands such as chloride, triphenylphosphine, and tert-butyl isocyanate. Klein [119] developed some bis-aryl palladium complexes with 1,2-bis(diphenylphosphino)ethane or 1,5-cyclooctadiene as auxiliary ligands in 2018. Against HT-29 and MCF-7 cell lines, their antiproliferative efficacy was evaluated. As a consequence of this, there is a great deal of published material on the topic, including a number of very good evaluations [120-129].

I.11. Theoretical calculations

❖ Basic ideas behind DFT

With the aid of density functional theory, the quantum state of atoms, molecules, and solids as well as molecular dynamics may be calculated (DFT). Electronic structure of matter-wave functions with density functional and quantum chemical systems [130] are merely a few areas in which it has proven to be a vital tool for achieving precise and thorough simulations of atomic-scale processes in condensed matter phases. Increased development of density functional theory approaches has substantially aided the theoretical description of charge

distribution and related features, such as chemical reactivity descriptors of chemical compounds [131]. However, DFT has allowed theoretical chemistry to reliably predict cluster and molecule structures and energies over the past decade. As a result, these DFT-derived reactivity descriptors are now worthy of increased focus.

❖ **Significance of Density Functional Theory (DFT)**

- To compute the electronic structure of matter as well as chemical reactivity, the density functional theory (also known as DFT) is currently the method that has been the most successful (and most promising).
- It is applicable to atoms, molecules, solids, nuclei, and quantum and classical fluids.
- In the original formulation of the density functional theory, which describes the ground state features of a system, the electron density plays a vital role.
- Molecular features, such as structure, vibrational frequency, atomization energy, ionization energy, electric and magnetic properties, reaction pathways, and so on, may all be reliably predicted by the density-functional theory.
- Spin polarized systems, multicomponent systems such as nuclei and electron hole droplets, free energy, superconductors with electronic pairing mechanisms, relativistic electrons, time-dependent phenomena and excited states, bosons, molecular dynamics, and so on have all been incorporated into the original density functional theory.

❖ **General Application Density Functional Theory (DFT)**

- Total molecular energy calculation and tautomerization
- Molecular geometry optimization and electronic structure assignment
- Frequency calculations are performed for thermochemical analysis and vibrational mode
- Calculating spin density and describing EPR, magnetic, and redox properties

- To follow the reaction pathways, IRC (Intrinsic Reaction Coordinate) is used.
- Potential energy surface scanning.
- Potential energy surface
- Testing wave function stability
- Predicting and interpreting additional chemical characteristics as well as some typical spectra

❖ Time-dependent density function theory (TDDFT)

Overview

The time-dependent density functional theory (TD-DFT) is a quantum mechanical theory used to investigate the properties and dynamics of many-body systems in the presence of time-dependent potentials such as electric or magnetic fields. This theory was developed in the 1970s by physicists and chemists. TDDFT can be utilized to derive excitation energies, frequency-dependent response characteristics, and light absorption spectra when investigating the influence of such fields on molecules and materials.

Time-dependent density function theory (abbreviated as TDDFT) is formally based on the Runge-Gross (RG) theorem (1984) [132], the time-dependent version of the Hohenberg-Kohn (HK) theorem (1964) [133]. The RG theorem shows that there is just one mapping between a system's time-varying external potential and its time-varying density for a given beginning wavefunction. The knowledge of the original wavefunction is required for this. That the density, which depends on only three factors, is identical to the many-body wave function, which depends on $3N$ variables, suggests that all characteristics of a system can be determined from knowledge of the density alone. There is no equivalent to DFT's general minimization principle in time-dependent quantum mechanics. A direct result of this is that proving the RG theorem is far more laborious than demonstrating the HK theorem.

Based on the RG theorem, the next step in developing a computationally practical method is to identify the hypothetical non-interacting system with the same density as the real (interacting) system of interest. To create a technique that can be used in calculation, this is the next stage. This system, like DFT, is time-dependent; it is called the Kohn-Sham system. To put it formally, this system is identified as the fixed point of an action functional defined using the Keldysh formalism [134].

TDDFT is mostly used to estimate excited state energy of isolated systems and solids. Most applications use this. These calculations use the linear response function's poles at a system's specific excitation energy. The linear response function shows how external potential changes affect electron density. The exchange-correlation kernel, which is the functional derivative of the exchange-correlation potential with respect to density [135-139], is also needed for such computations.

❖ **Utility of Time-dependent density functional theory**

The conceptual and computational foundations of TDDFT, which is an extension of density functional theory, are theoretical density functionals that change over time to demonstrate that the (time-dependent) wave function is equivalent to the (time-dependent) electronic density, and then to derive the effective potential of a fictitious non-interacting system that returns the same density as any given interacting system (DFT). Due to the fact that the time-dependent effective potential at each instant is reliant on the value of the density at all previous instants, the task of designing such a system is more challenging for TDDFT. Thus, the implementation of time-dependent approximations for TDDFT has trailed behind the development of DFT.

❖ **Basis set**

In theoretical and computational chemistry, molecular orbitals are constructed from a basis set, which is a collection of functions (called basis functions) that are coupled in linear combinations (often as part of a quantum chemical calculation). Quantum chemical computations in current computational chemistry are often performed with a limited number of fundamental functions. Vectors are utilized to represent the wave functions of the system under consideration; their components are the coefficients in a linear combination of the fundamental functions of the basis set.

❖ **Popular Software**

- Gaussian Software Package (chemistry, Hartree-Fock, correlated approaches. current version: Gaussian09)
- Amsterdam Density Functional (ADF)
- Gamess-UK (chemistry, Hartree-Fock, DFT, correlated approaches)
- VASP (DFT, planewave, ultrasoft, PAW)
- ORCA
- Jaguar
- Turbomole
- Spartan

I.12. Physical measurements

- (i) **Elemental analysis:** Using the pure solid sample, microanalytical data (C, H, and N) were gathered on a Series-II CHN-2400 CHNS/O elemental analyzer, Perkin Elmer, USA.
- (ii) **FTIR spectra:** Samples were prepared as KBr pellets, and FTIR spectra were taken using a Perkin Elmer FT-IR spectrophotometer model RX-1 (KBr disc, 4000-400

cm⁻¹).

- (iii) **UV-Vis spectra:** A solution of the necessary concentration in acetonitrile was used to study the absorption spectra on a Perkin Elmer Lambda 750 spectrophotometer. The solution will be stored in a quartz cell, and absorption spectra from the visible to UV area will be recorded.
- (iv) **¹H and ¹³C NMR spectra:** The Bruker (AC) 300 MHz and 75 MHz FTNMR spectrometer were used to capture ¹H and ¹³C NMR spectra respectively.
- (v) **Single crystal X-ray diffraction study:** Single crystals of the compounds were obtained through slow evaporation of solvent from solutions or diffusion of another solvent into a solution of the compounds. Data were collected using a graphite monochromated Mo-K α radiation ($\lambda = 0.71073 \text{ \AA}$) and an automated Bruker AXS Kappa equipped with an Apex-III diffractometer with area detector. SHELXS-97 and SHELXL-97 programmes will be used for X-ray data reduction, structure solution, and refinement. The structures were solved directly.
- (vi) **Mass Spectroscopic study:** Waters quadruple time-of-flight mass spectrometer (Xevo G2 Q-TOF) was used to get mass spectra.
- (vii) **Electrochemical investigations:** Studies in electrochemistry included the use of a computer-controlled CH-Instrument, an Electrochemical workstation with a Pt-disk milli electrode, and other equipment for conducting electrochemical tests. All of the measurements were performed in a solution of acetonitrile, in a dinitrogen atmosphere, at a temperature of 298 K, with a reference to vs. Ag/AgCl at a scan rate of 100 millivolts per second. The working electrode was a platinum bead, and the supporting electrolyte was [nBu₄N]ClO₄. The junction potential has not been taken into account in the quoted potentials.

(viii) **Emission Measurements:** At room temperature (298 K), emission properties were determined with the assistance of a Perkin Elmer LS 55 fluorescence spectrophotometer. We measured the fluorescence quantum yield of the complexes by comparing them to a reference substance called Coumarin-120 laser dye, which has a known R value of 0.63 when dissolved in MeCN. After retaining a nearly identical absorbance (0.1), the complex as well as the reference dye were stimulated at the same wavelength, and the resulting emission spectra were recorded. Using the software that was provided on the device, the area of the emission spectrum was integrated, and the quantum yield was determined using the following equation:

$$\phi_S/\phi_R = [A_S / A_R] \times [(Abs)_R / (Abs)_S] \times [\eta_S^2/\eta_R^2] \quad (1)$$

In this context, the fluorescence quantum yield of the sample and the reference are denoted by S and R, respectively. A_S and A_R stand for the area under the fluorescence spectra of the sample and the reference, respectively. $(Abs)_S$ and $(Abs)_R$ stand for the respective optical densities of the sample solution and the reference solution at the wavelength of excitation, and S and R stand for the values of the refractive index for the solvent that was used for the sample and the reference.

(ix) **Fluorescence Lifetime:** Fluorescence lifetimes were measured with a time-resolved spectrofluorometer from IBH in the United Kingdom. The excitation source is a picosecond diode laser (NanoLed-07, 370 nm), and the instrument operates on the time-correlated single photon counting principle (TSPC). At FWHM, the instrument response function is 230 ps. To eliminate depolarization effects on fluorescence decays, the excitation and emission polarizers were measured using magic angle geometry (54.7). The following equation, where τ is the fluorescence lifespan and A is the pre-exponential component, illustrates how compound decays fit with a single exponential decay or a bi-exponential decay. The weighted residuals were distributed randomly throughout the data

channels, and the reduced χ^2 values for the fits ranged from 0.97 to 1.1. τ_f stands for the average fluorescence lifetime (meaning of the symbols are usual).

$$I(t) = [\alpha_1 \exp(-t/\tau_1) - \alpha_2 \exp(-t/\tau_2)] \quad (2)$$

$$\tau_f = \alpha_1\tau_1 + \alpha_2\tau_2 \quad (3)$$

I.13. Biological Activities

I.13.1. Antitumor and Cytotoxic activities

Transition metal complexes have been used as probes to figure out the structure of DNA and as chemotherapeutic agents, according to many literature reviews [140-150]. DNA and proteins are the main targets of cytotoxicity because of how small molecules interact with DNA. This interaction can cause DNA damage in cancer cells by stopping them from dividing, which leads to cell death. The next section includes a brief explanation of DNA structure, nucleic acid and heredity, DNA binding modalities, and DNA cleavage in order to better comprehend how DNA binds to Schiff base metal complexes [151-156].

I.13.2. Structure of DNA

Genomic information is stored in DNA, or deoxyribonucleic acid, which is present in all living things. All the cells in a person's body share the same DNA. Nuclear DNA refers to the DNA found in the nucleus of a cell, while mitochondrial DNA (mtDNA) refers to the DNA found in the mitochondria. Adenine (A), Guanine (G), Cytosine (C), and Thymine (T) are the four chemical bases that make up the coding used to store information in DNA (T). An estimated 3 billion bases make up human DNA. A staggering 99.9% of these bases are shared between all human beings. Watson and Crick's 1953 proposal for the structure of the DNA molecule is the most widely recognized one, and it earned them the Nobel Prize in Medicine in 1962. The DNA molecule, he says, is shaped like a double helix (Fig.I.2). The molecule is made up of two polynucleotide strands that are antiparallel to one other and coiled in a right-

handed helix around each other. Hydrogen bonds unite the two strands. The major and minor grooves of the double-helix molecule are arranged in an alternating pattern. Long polymers of deoxyribonucleotides make up each strand. The bases in each strand are arranged differently, making them complimentary to one another. Thus, purines and pyrimidines occur in the double helix as base pairs, i.e., (A and T) and (G and C). Consequently, knowing the base sequence of one strand of DNA makes it trivial to figure out the base sequence of the strand's complementary strand. Deoxyribose sugar and phosphate molecules, linked with phosphodiester connections, comprise the strand's backbone in an alternating order.

Watson and Crick described a B-form DNA molecule. While this is true, there are other kinds of DNA as well. For example, the helix in the A, B, and C forms is right-handed, whereas in the Z form it is left-handed. Form B predominates in the cellular environment.

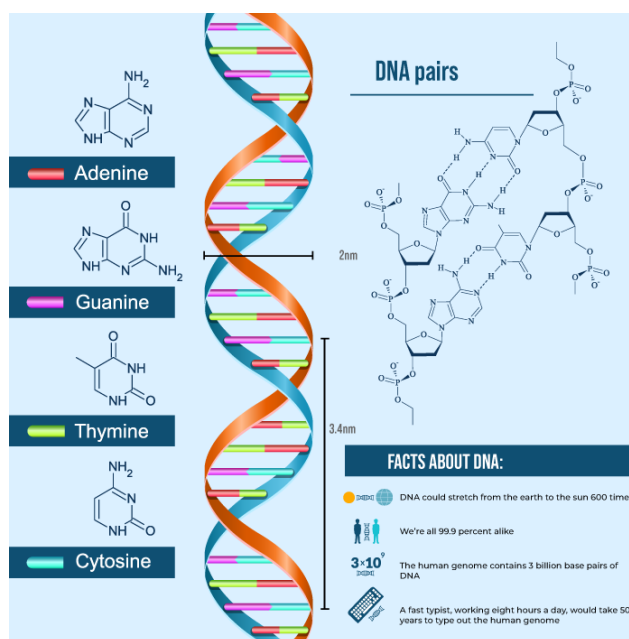


Fig.I.2. Structure of DNA.

I.13.3. DNA Binding Modes

DNA is a fundamental component of all living creatures and the material upon which gene expression depends. Intercalative binding, groove binding, electrostatic/external binding, and

small-molecule electrostatic binding are among ways that DNA might interact [157-160]. (Fig.I.3). Intercalation into the DNA helix's non-polar interior by tiny molecules or the medication leads to intercalative binding. An aromatic group is deposited in the space between DNA base pairs when ligands of the appropriate size and chemical composition are able to squeeze themselves in between DNA base pairs. The majority of polycyclic, aromatic, and planar ligands that are amenable to intercalation also happen to be excellent nucleic acid stains. Since DNA strand molecules could serve as chemotherapeutic agents, there is considerable interest in developing and producing DNA strand. Groove binding interactions occur when the attached molecule meets base pair edges in nucleic acids' major (G-C) or minor (A-T) grooves. A prototypical example of a groove binder, netropsin, is an antibiotic in which intercalation is prevented by methyl groups [161]. Small molecules hardly ever bind in the double helix's main groove. If a molecule is positively charged, then it will interact with other positively charged molecules via electrostatic repulsion. They have an electrical attraction for the DNA's negatively charged phosphates. In a physiological setting, electrostatic attraction is rather weak. This is the typical mode of interaction between cations like Mg^{2+} [162]. The two most common binding mechanisms are intercalation into the central base pair stack of the double helix and insertion into the minor groove. Cationic compounds with plane aromatic rings are particularly prone to intercalation. The positive charge could be on a substituent rather than the ring structure itself. In this method of binding, two base pairs next to each other must be split apart so that a binding pocket can be made for the ligand [163]. Minor groove binders are flexible [164,165], allowing the molecule to follow the groove around the helix's central axis. When compared to intercalative binding, minor groove binding significantly reduces the amount of DNA deformation that is necessary. For elucidating the binding modes of tiny compounds, spectroscopy, UV-Vis spectroscopy,

fluorescence spectroscopy, circular dichroism (CD), and linear dichroism (LD) are all widely used techniques.

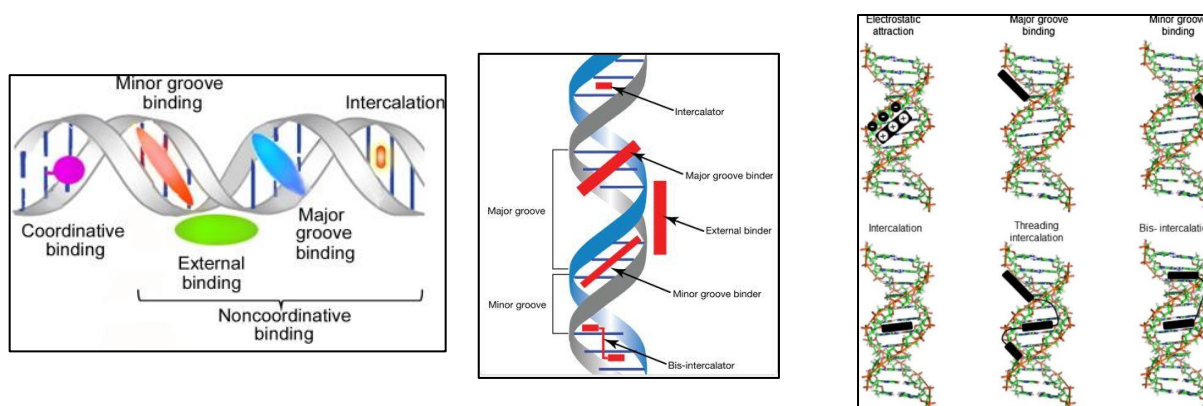


Fig.I.3. Binding modes of DNA

The peak extinction coefficient or absorption maximum will often shift as a result of DNA binding. Although equilibrium binding constants can be determined from the concentration-dependence of any observable changes, this is inadequate to define a binding mode. When attached, fluorescent small molecules frequently behave as energy acceptors from the DNA bases and fluctuate in wavelength or quantum yield. In these tests, ultraviolet (UV) light is used to excite the DNA, and the resulting ligand fluorescence is then observed. Differential absorption of circularly polarized light of different directions (right and left) is quantified by the circular dichroism technique. The method of circular dichroism (CD) can be utilized for an evaluation of DNA-binding mode. Chiral DNA (CD) induction [166, 167] occurs when a ligand has been attached to the DNA strand. The exact sign and magnitude of the generated CD signal are influenced by the DNA sequence, binding mode, and ligand transition dipole orientation. Since a groove binder touches about 4-6 base pairs more of the helix than an intercalator, its CD spectrum is usually brighter than that of an intercalator. A basic intercalator, on the other hand, only affects two base pairs that are next to each other.

I.13.4. Transition metal complexes as DNA chemical probes

The development of compounds with high DNA-binding affinities is a complex area of study. These molecular interactions with DNA make them promising chemotherapeutic reagents [168-173]. The biological activity of these molecules is not only determined by their interactions with DNA, but their method of binding to DNA is generally connected with their reactivity and selectivity. Therefore, a more in-depth understanding of the mechanisms that govern the interactions of small molecules with DNA is necessary for the rational design of a variety of DNA-targeted chemotherapeutic drugs and molecular probes for DNA. As time has gone on, it has become abundantly evident that stable inert compounds that contain active metal centres are very effective as probes of biological systems. Palladium complexes [174-178] are among the most often employed transition metal complexes for studying metal complex-DNA interactions currently.

In recent years, research into the specificity and selectivity of metal complexes' binding to DNA has gained significant momentum. Clinical applications for these investigations in chemotherapy and biotechnology tool development are possible. Numerous efforts have been made to learn about the metal complexes' non-covalent interactions with DNA. Using absorption spectroscopy and electrochemical methods, we have investigated the palladium complexes' interaction with DNA. One of the most potent methods for exploring metal ion DNA interactions [179, 180] is electronic absorption spectroscopy. Spectral properties of DNA's double helix structure include the 'hyperchromic' effect and 'hypochromic' impact. "Hypochromism" is caused by DNA concentration along the helix axis and a change in DNA conformation, while "hyperchromism" is caused by structural damage to DNA [181,182]. Strength of intercalative binding is reflected in the degree of hyperchromism; metal complexes that bind non-intercalatively or electrostatically to DNA can produce either hyperchromism or hypochromism [183, 184]. The interaction of palladium(II) complexes

with DNA cannot be tracked because they do not produce a strong d-d or charge transfer band. Consequently, the shifts are tracked using the absorption band. In order to carry out the electronic absorption titration, the concentration of the complexes was held steady at 100 M in DMSO at a temperature of 25 °C throughout the process. At the same time, the DNA concentration was varied. The 290-370 nm bands observed for palladium complexes in DMSO-buffer solutions are attributed to LMCT transitions. As DNA concentration varies, the charge transfer band's intensity shifts from hypochromism to hyperchromism. The intrinsic binding constant, K_b , was calculated by regressing $[DNA]/(\epsilon_a - \epsilon_f)$ against the $[DNA]$ equation [185], which allowed for direct comparison of the binding strengths of different metal complexes.

$$[DNA]/(\epsilon_a - \epsilon_f) = [DNA]/(\epsilon_b - \epsilon_f) + 1/K_b (\epsilon_b - \epsilon_f),$$

Where, $[DNA]$ stands for the concentration of DNA measured in base pairs and ϵ_a stands for the apparent extinction coefficient which is equal to $(A_{obsd}/[Complex])$. The extinction coefficient for free metal complex is denoted by ϵ_f and ϵ_b represents the extinction coefficient for the fully-bound version of the free metal complex.

K_b was calculated by dividing the slope of the plot ($[DNA]/\epsilon_a - \epsilon_f$) by the intercept ($[DNA]$).

The high K_b values indicate a robust interaction between the complexes and DNA from Calf thymus (CT-DNA).

I.13.5. Albumin-binding properties of the compounds

Due to their participation in the transport of medications and other bioactive small molecules through the bloodstream, serum albumins are among the most essential proteins of the circulatory system. BSA is the albumin that has been studied the most and is structurally similar to HSA (Fig.I.4).

The binding interaction between BSA and metal (II) complexes have been deciphered employing absorption and fluorescence measurements. A stock solution of BSA was prepared

using 500 mM phosphate buffer saline (PBS) at pH 7.4 and stored in the dark at 4°C for further use. The concentration of BSA was determined by calculating the absorbance of UV-Vis spectra taken at 280 nm [186]. The stock solution of the metal (II) complex was produced in a medium containing DMSO, and it was diluted with PBS as appropriate whenever it was required to do so. For recording UV-Vis spectra, BSA-concentration was kept constant while varying the concentration of metal (II) complex added to it. In fluorescence experiment, tryptophan fluorescence of BSA was recorded in the range 290–500 nm at an excitation wavelength of 280 nm using a slit width of 5 nm. With the subsequent addition of metal, the extinction of BSA emission at 336 nm was observed.

In the presence of various concentrations of the complex, the electronic absorption spectrum of BSA (in PBS at pH 7.4) was measured between 200 and 500 nm. At 280 nm, BSA displays a characteristic absorption band. The addition of complex to the BSA solution causes a gradual increase in absorbance at 280 nm and a slight blue shift. This hypsochromic shift correlates to the complex's ground-state connection with the protein [187.(a)-(b)]. Using the following equation, the apparent association constant (K_a) was determined from the plot of $1/(A_{obs}-A_0)$ vs $1/[complex]$: [188.(a)-(b)]

$$\frac{1}{A_{obs} - A_0} = \frac{1}{A_c - A_0} + \frac{1}{K_a(A_c - A_0)[complex]}$$

Where A_{obs} is the observed absorbance (at 280 nm) of the solution having various concentrations of the complex, A_0 and A_c are the absorbance of BSA only and of serum albumin with the complex [189.(a)-(e)].

The fluorescence spectral titration technique was also utilized in order to investigate the BSA-compound interactions. In DMSO solution, complex does not emit any fluorescent light. An aqueous solution of BSA (10.2 M, pH 7.4 PBS buffer) shows a significant amount of fluorescence at 336 nm when excited at 280 nm. Now, by gradually adding complex to the

BSA solution, the fluorescence intensity of the BSA solution was significantly reduced at a wavelength of 336 nm. The interaction of the complex with the protein is primarily thought to be the cause of the hypochromicity seen in the spectra. It was determined how to calculate the Stern-Volmer quenching constant values (K_{sv}) for the complex [190.(a)]. The fact that the complex has a high K_{sv} value suggests that it is capable of effectively dampening fluorescence.

To gain a thorough understanding of the quenching phenomena, the equilibrium binding constant (K_b) and number of binding sites (n) available for the complex were calculated using the Scatchard equation from the plot of $\log [(F_0-F)/F]$ vs $\log [\text{complex}]$ [191.(a)-(c)]:

$$\log \frac{(F_0 - F)}{F} = \log K_b + n \log [\text{complex}]$$

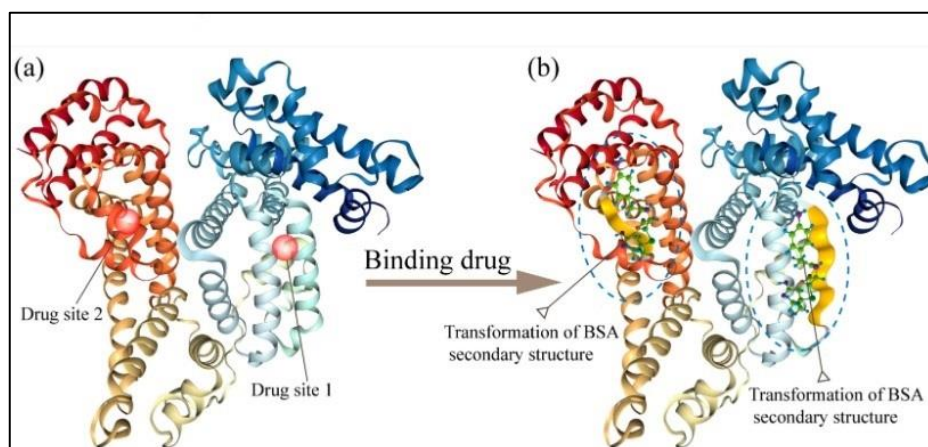


Fig.I.4. (a) Bovine serum albumin (BSA) crystal structure (PDB ID: 3V03). (b) A diagram depicting the structure and conformational variation of BSA in complex with a drug.

I.13.6. Clonogenic assay of cells in vitro

The ability to clone or form colonies from single mammalian cells placed in culture dishes with the right media was first documented in a seminal work published in 1956 by Puck and Marcus [192]. A large number of intensely irradiated "feeder" cells were added to the

specified medium to shape the microenvironment of the significantly smaller number of cells being examined for clone creation. Experiments performed by the authors provided the first radiation-dose survival curve for X-ray-irradiated HeLa cells in culture. They demonstrated that these mammalian cells were extremely radiosensitive, with mean lethal doses in the range of 1-2 Gy, significantly higher than those previously expected for cells in tissues. Over the succeeding decades, this clonogenic assay has been utilized for a wide range of research using a wide range of cell types, with the necessity for feeder cells being largely phased out thanks to advancements in complicated culture media. After treatments that can cause cell reproductive death (due to chromosome damage, apoptosis, etc.) [193], the assays detect all cells that have preserved the capacity to produce a high number of progenies.

The ability of a single cell to divide and form a colony is evaluated in a clonogenic experiment performed in culture. A colony is considered to be at least 50 cells in size. The assay is designed to check whether every cell in the population has the potential for "unlimited" division [194]. After ionizing radiation treatment, the clonogenic assay is the gold standard for measuring cell reproductive mortality, but it can also be used to evaluate the efficacy of other cytotoxic agents. Not all cells that are planted can develop into colonies. The cells are diluted and seeded out either before or after treatment, and within a week to three weeks, colonies have formed [195]. Colonies are counted using a stereomicroscope after being fixed in glutaraldehyde (6.0% v/v), stained with crystal violet (0.5% w/v), and examined under a microscope. This package includes a methodology for analyzing dose-survival curves in relation to radiation exposure.

I.13.7. In vitro scratch assay

Using an in vitro scratch assay to study cell migration is a quick and cheap technique to do so [196]. This strategy is based on the observation that when an artificial gap (or "scratch") is introduced into a monolayer of confluent cells, the cells at the gap's edge migrate toward the

opening to seal it while simultaneously generating new cell-cell connections. Creating a "scratch" on monolayer cells, capturing photos at the beginning and regular intervals during cell movement to close the scratch, and comparing the images to measure cell migration rate are the main processes. This simple approach simulates cell movement *in vivo*. When part of the endothelium in blood arteries is removed, endothelial cells migrate to repair the wound [197]. Migration as a loosely connected population (e.g., fibroblasts) or as sheets of cells (e.g., epithelium and ECs) mimics *in vivo* migration. The *in vitro* scratch experiment is also useful for studying cell migration regulation by ECM and cell-cell interactions. Preparing cells in suspension affects cell-cell and cell-ECM interactions in Boyden chamber studies. Cell migration can be observed in real time via live cell imaging in the *in vitro* scratch assay (for example, by visualizing GFP-tagged proteins for subcellular localization or fluorescence resonance energy transfer for protein-protein interactions). It's also the simplest way to investigate cell migration *in vitro*, using only standard, affordable supplies present in most cell-culturing labs.

In vitro scratch assay has drawbacks compared to other approaches. No chemical gradient is created; therefore, it does not replace well-established chemotaxis methods like the Boyden chamber assay. It is a slow approach. Cell monolayer development takes 1-2 days, and cell migration closes the scratch in 8-18 h. Assays are commonly performed in a tissue culture dish, which requires a lot of cells and chemicals. If the supply of cells (e.g., specialized primary cells) or chemicals (e.g., pricey reagents) is limited, this procedure is not recommended. Despite these limitations, *in vitro* scratch test is often used to study cell migration in a lab since it is straightforward to set up, requires no specialist equipment, and all materials are available in any cell culture facility.

I.13.8. Dual AO/EB Staining to Detect Apoptosis

Apoptosis, a type of genetically regulated programmed cell death, governs the elimination of superfluous, damaged, or diseased cells during the development of multicellular organisms and tissues [198]. Basic oncology research has benefited greatly from studies examining the genes and processes that control apoptosis. Malignant tumours in pre- and post-operative cancer patients must be treated with radiotherapy and chemotherapy. In order to kill tumour cells and slow their development, chemotherapeutics use a process called apoptosis [199]. It is the ability of anticancer medications to specifically target cancer cells and induce their apoptosis that serves as the gold standard for measuring their success. Tumor drug sensitivity testing (DST) is a technique for pinpointing the best medicine for treating tumours. Malignant tumours consist of a cell population that is polymorphous, heterogeneous, and multi-differentiated due to the wide range of underlying genotype and aetiology. Unfortunately for patients, previous chemotherapies only served to increase tumour drug resistance [200]. Malignant tumours might either be sensitive to several medicines or resistant to certain [201, 202]. More effective personalized treatments can be produced by decreasing medication resistance and enhancing the efficacy of DSTs [203, 204]. It is crucial that apoptosis in tumour cells caused by a medication be identified in DSTs. Several different techniques have been developed to identify apoptosis by identifying changes in cell shape and surface markers. However, it's possible for these flaws to manifest at the same time [205]. This can muddy the results of DSTs and reduce confidence in the medications they choose. Apoptotic cell membrane alterations can be detected by fluorescence microscopy visualization of acridine orange (AO) and ethidium bromide (EB) fluorescent stains [207]. Apoptosis can be detected at various stages with this approach [206-208]. Since this is the case, AO/EB staining is a viable option for use in DSTs.

The use of fluorescence microscopy allowed the analysis of normal tumour cells, early and late apoptotic cells, and necrotic cells. Crescent- or granular yellow-green acridine orange nuclear staining was characteristic of apoptotic cells in their first stages. Ethidium bromide staining, an orange nuclear dye, was used to highlight cells that had already undergone late-stage apoptosis. The necrotic cells grew in size and fluoresced orange-red unevenly around their periphery. Some cells even seemed to be dissolving. Flow cytometry and dual acridine orange/ethidium bromide (AO/EB) labelling for apoptotic osteosarcoma cells yielded statistically indistinguishable results ($P > 0.05$).

I.13.9. Analysis of Cell Death Using Hoechst 33342 Nuclear Staining

Staining cells with Hoechst 33342 is an appropriate technique for identifying apoptotic from healthy or necrotic cells [209] because apoptotic cells have condensed DNA and fragmented nuclei [210, 211]. Condensed DNA can also be found in healthy mitotic cells, and some cells can die through apoptosis without nuclear fragmentation [212]. Cells with caspase 3 activation abnormalities are one example [213]. Nuclear fragmentation alone cannot suggest apoptosis. Fluorescence microscopy can identify Hoechst 33342 from fluorescein isothiocyanate and Texas Red. Fluorochrome-conjugated antibodies can be used with Hoechst 33342 to detect caspase activation or cytochrome c release.

I.14. Goals and the scope of the current work

The applications of Schiff base metal complexes in medicine, materials research, and catalysis are fascinating. Thus, the synthesis of novel Schiff bases and their complexes continues to be of interest. Therefore, it was thought desirable to synthesize a few new Schiff base complexes, examine their physicochemical characteristics, and apply them as anticancer agent along with DNA and BSA binding properties. The study in this thesis focuses mostly on Schiff bases in metal complexes with ONS and ONN donor ligands. For this reason, it

might be worthwhile to use an electron-withdrawing heterocyclic system to investigate these Schiff bases, as their projected ligand field strengths are lower than those of the salicylaldehyde-derived Schiff bases. In addition, these ligand complexes are predicted to behave considerably differently from Salen complexes in terms of their ability to cleave DNA. The majority of Pd(II) complexes were synthesized in order to research DNA cleaving characteristics, and they were found to have effective DNA cleaving and BSA binding characteristics. Despite all of these uses, palladium metal's negative impact on human health has given rise to serious worries since its ions can attach to DNA, thiol-containing proteins, such as casein and silk fibroin, and other biomolecules due to their strong nucleophilicity [214, 215]. Palladium residues in environmental or medicinal chemicals pose a significant risk, particularly for emissions of pollutants into water and soil [216]. As a result, less than 1.5–15 μg of palladium per person per day is the recommended maximum nutritional intake by the government [217]. Therefore, it is crucial to design and develop a sensitive and selective analytical method for the detection of palladium in the environment in order to evaluate any potential negative health impacts brought on by this specific metal residue.

Thus, the work presented in this dissertation was conducted with the following goals in mind:

- To synthesize and study the characteristics and activities of novel palladium(II) complexes containing N, S, and O donor imine functional ligands by a facile and inexpensive synthetic method.
- Anticancer activity of Synthesized Pd(II) complexes and their protein (DNA/BSA) binding studies.
- Design and development of a selective and sensitive analytical approach for the detection of palladium in the environment.

I.15. References

1. E. Basaran, H. G. Sogukomerogullari, R. Cakmak, S. Akkoc, T. Taskin-Tok and A. Köse, *Bioorg. Chem.*, 2022, **129**, 106176.
2. S. Bjelogrić, T. Todorović, M. Kojić, M. Senćanski, M. Nikolić, A. Višnjevac, J. Araškov, M. Miljković, C. Muller and N. Filipović, *J. Inorg. Biochem.*, 2019, **199**, 110758.
3. S. Kumar, G. Krishnamurthy, Y. D. Bodke, V. H. Malojirao, T. R. Ravikumar Naik, S. Kandagalla and B. T. Prabhakar, *New J. Chem.*, 2019, **43**, 790.
4. A. M. S. Hossain, J. M. Méndez-Arriaga, C. Xia, J. Xie and S. Gómez-Ruiz, *Polyhedron*, 2022, **217**, 115692.
5. E. M. Zayed, G. G. Mohamed, W. M.I. Hassan A. K. Elkholy and H. Moustafa, *Appl Organometal Chem.*, 2018, **32**, 4375.
6. L. H. A. Rahman, A. M. A. Dief, M. O. Aboelez and A. A. H. A. Mawgoud, *J. Photochem. Photobiol. B.*, 2017, **170**, 271.
7. H. E. Salama, G. R. Saad and M. W. Sabaa, *Int. J. Biol. Macromol.*, 2015, **79**, 996.
8. A. A. Abou-Hussein and W. Linert, *Spectrochim. Acta. Part A*, 2014, **117**, 763.
9. A. W. Jeevadason, K. K. Murugavel and M.A. Neelakantan, *Renewable Sustainable Energy Rev.*, 2014, **36**, 220.
10. S. Omid and A. Kakanejadifard, *RSC Adv.*, 2020, **10**, 30186.
11. B. Li, H. Xie, C. Yang, C. Shi, C. He, N. Zhao and E. Liu, *Appl. Sur. Sci.*, 2022, **595**, 153526.
12. A. Das, C. Hessin, Y. Ren and M. D. E. Murr, *Chem. Soc. Rev.*, 2020, **49**, 8840.
13. J. A. Stubbe and W. A. van der Donk, *Chem. Rev.*, 1998, **98**, 705.
14. D. L. J. Broere, B. Bruin, J. N. H. Reek, M. Lutz, S. Dechert, and J. I. Vlug, *J. Am. Chem. Soc.*, 2014, **136**, 11574.

15. C. H. Yu, C. Zhu, X. Ji, W. H. Xie, N. Bhuvanesh, L. Fang and O. V. Ozerov, *Inorg. Chem. Front.*, 2020, **7**, 4357.
16. B. N. Nguyen, L. A. Adrio, T. Albrecht, A. J. P. White, M. A. Newton, M. Nachtegaal, S. J. A. Figueroa and K. K. Hii, *Dalton Trans.*, 2015, **44**, 16586.
17. A.K. Singh and R. Mukherjee, *Dalton Trans.*, 2008, **2**, 260.
18. M. Tuncel, H. Kahyaoglu and M. Cakir, *Trans. Met. Chem.*, 2008, **33**, 605.
19. J. Wang, L. Kong, W. Shen, X. Hu, Y. Shena and S. Liu, *Anal. Methods.*, 2014, **6**, 4343.
20. Z. Han, L. Dong, J. Zhang, T. Cui, S. Chen, G. Ma, X. Guoa and L. Wang, *RSC Adv.*, 2019, **9**, 38265.
21. J. K. Anjali and K. Sreekumar, *Catal. Lett.*, 2019, **149**, 1952.
22. J. Su, W. Li, X. Li, J. Xu and Q. Song, *ChemCatChem*, 2020, **12**, 5664.
23. C. Santiago, N. Sotomayor and E. Lete, *Molecules*, 2020, **25**, 3247.
24. P. G. Cozzi, *Chem. Soc. Rev.*, 2004, **33**, 410.
25. Z. Li, K.R. Conser and E.N. Jacobsen, *J. Am. Chem. Soc.*, 1993, **115**, 5326.
26. J. F. Larrow and E. N. Jacobsen, *Organometallics in Process Chemistry*, 2004, **6**, 123.
27. G. Henrici-Olive and S. Olive, *Springer, Berlin*, 1984, p.152.
28. H. Dugas and C. Penney, *Bioorganic Chemistry*, Springer, New York, 1981, p.435.
29. K. Sancak, Mustafa. U. Yasemin, M. Yildirim and I. Degirmencioglu, *Transition Met. Chem.*, 2007, **32**, 16.
30. D. Udhayakumari and V. Inbaraj, *Journal of Fluorescence*, 2020, **30**, 1203.
31. W. A. Zoubi and Y. G. Ko, *Appl. Organometal. Chem.*, 2017, **31**, 3574.
32. S. T. Tsantis, A. Lagou-Rekka, K. F. Konidaris, C. P. Raptopoulou, V. Bekiari, V. Psycharis and S.P. Perlepes, *Dalton Trans.*, 2019, **48**, 15668.
33. S. Pu, Z. Tong, G. Liu and R. Wang, *J. Mater. Chem. C.*, 2013, **1**, 4726.

34. N. Shaalan, N. Laftah, G. A. El-Hiti, M. H. Alotaibi, R. Muslih, D. S. Ahmed and E. Yousif, *Molecules*, 2018, **23**, 913.
35. Y. Dong, R. Fan, P. Wang, L. Wei, X. Wang, H. Zhang, S. Gao, Y. Yang and Y. Wang, *Dalton Trans.*, 2015, **44**, 5306.
36. C. Gennari and U. Piarulli, *Chem. Rev.*, 2003, **103**, 3071.
37. W. J. Evans, C. H. Ziller and J. W. Ziller, *Polyhedron*, 2002, **21**, 1683.
38. (a) R. Ziessel, *Coord. Chem. Rev.*, 2001, **195**, 216; (b) M. Albrect, *Chem. Rev.*, 2001, **101**, 3457.
39. C. R. Choudhury, S. K. Dey, N. Mondal, S. Mitra, S. O. G. Mahali and K. M. A. Malik, *J. Chem. Crystallogr.*, 2002, **31**, 57.
40. (a) A. F. Kolodziej, *Prog. Inorg. Chem.*, 1994, **41**, 493; (b) R. K. Parashar, R. C. Sharma, A. Kumar and G. Mohan, *Inorg. Chim. Acta.*, 1998, **151**, 201.
41. C. T. Prabhakara, S. A. Patil, S. S. Toragalmath, S. M. Kinnal and P. S. Badami, *J. Photochem. Photobiol., B*, 2016, **157**, 1.
42. L. Rigamonti, A. Forni, S. Righetto and A. Pasinic, *Dalton Trans.*, 2019, **48**, 11217.
43. W. Zoubia, A. S. Al-Hamdanib and M. Kaseema, *Appl. Organometal. Chem.*, 2016, **30**, 810.
44. L. Rousso, N. Friedman, M. Sheves and O. Ottolenghi, *Biochemistry*, 1995, **34**, 12059.
45. J. K. Lanyi, *Biophys. Acta.*, 1993, **1183**, 241.
46. (a) R. Ramesh and S. Maheswaran, *J. Inorg. Biochem.*, 2003, **96**, 457; (b) G. Givaja, M. Volpe, M. A. Edwards, A. J. Blake, C. Wilson, M. Schroder and J. B. Love, *Angew. Chem. Int. Ed.*, 2007, **46**, 584.
47. W.A. Zoubi and Y. G. Ko, *J. Organomet. Chem.*, 2016, **822**, 173.
48. (a) P. Gueerriero, S. Tamburin and P. A. Vigato, *Coord. Chem. Rev.*, 1995, **139**, 17; (b) P. A. Vigato and S. Tamburini, *Coord. Chem. Rev.*, 2004, **248**, 1717.

49. (a) G. J. P. Britovsek, V. C. Gibson and D. F. Wass, *Angew. Chem. Int. Ed Engl.*, 1999, **38**, 428. (b) R. E. Morris and L. Brammer, *Chem. Soc. Rev.*, 2017, **46**, 5444.
50. (a) Inorganic Chemistry, P. Atkins, T. Overton, J. Rourke, M. Weller and F. Armstrong, 4th Ed. OUP, Oxford, 2006, 494. (b) A.E. Martell, R. D. Hancock and R. J. Motekaitis, *Coord. Chem. Rev.*, 1994, **133**, 39.
51. X. Liu and J. Hamon, *Coord. Chem. Rev.*, 2019, **389**, 94.
52. P. Braunstein and F. Naud, *Angew. Chem. Int. Ed.*, 2001, **40**, 680.
53. R. G. Pearson, *J. Am. Chem. Soc.*, 1963, **85**, 3533.
54. T. G. Appleton, H. C. Clark and L. E. Manzer, *Coord Chem. Rev.*, 1973, **10**, 335.
55. M. G. Gardiner and C. C. Ho, *Coord Chem. Rev.*, 2018, **375**, 373.
56. (a) K. Buldurun and M. Ozdemir, *J. Mol. Struct.*, 2020, **1202**, 127266. (b) M. Ramesh and G. Venkatachalam, *J. Organomet. Chem.*, 2019, **880**, 47.
57. H. A. McManus and P. J. Guiry, *Chem. Rev.*, 2004, **104**, 4151.
58. E. M. McGarrigle and D. G. Gilheany, *Chem. Rev.*, 2005, **105**, 1563.
59. A. M. E. Geary, J. L. Yellowlees, A. L. Jack, D. H. I. Oswald, S. Parsons, N. Hirata, R. J. Durrant and N. Robertson, *Inorg. Chem.*, 2005, **44**, 242.
60. X. Yang, F. Drepper, B. Wu, W. Sun, W. Haehnelb and C. Janiak, *Dalton Trans.*, 2005, **2**, 256.
61. X. Chen, P. Sun, B. Mo, C. Chen and J. Peng, *J. Org. Chem.*, 2021, **86**, 352.
62. J. Yu, J. Li, P. Wang, and J. Yu, *Angew. Chem.*, 2019, **131**, 18309.
63. M. R. Malachonsk, M. Adams, N. Elia, A. L. Rheingold and R. S. Kelly, *J. Chem. Soc., Dalton Trans.*, 1999, 2177.
64. G. Cheng, Y. Weng, X. Yang and X. Cui, *Org. Lett.*, 2015, **17**, 3790.
65. P. Chakraborty, S. K. Chandra and A. Chakravorty, *Organometallics*, 1993, **12**, 4726.
66. S. Budagumpi and S. Endud, *Organometallics*, 2013, **32**, 1537.

67. K. E. Prosser, S. W. Chang, F. Saraci, P. H. Le and C. J. Walsby, *J. Inorg. Biochem.*, 2017, **167**, 89.
68. A. K. Mahapatra, S. N. Dutta, S. Goswami, M. Mukherjee, A. K. Mukherjee and A. Mahapatra, *Inorg. Chem.*, 1986, **25**, 1715.
69. N. Anbu and A. Dhakshinamoorthy, *J. Ind. Eng. Chem.*, 2018, **65**, 120.
70. A. Bhanja, R. Herchel, Z. Travnicek and D. Ray, *Inorg. Chem.*, 2019, **58**, 12184.
71. R. Balamurugan, M. Palaniandaver and R. S. Gopalan, *Inorg. Chem.*, 2001, **40**, 2246.
72. M. Kalita, P. Gogoi, P. Barman, B. Sarma, A. K. Buragohain and R. D. Kalita, *Polyhedron*, 2014, **74**, 93.
73. R. H. Crabtree, *The Organometallic Chemistry of the Transition Metals*, 2nd ed.; Wiley: New York, 1994, Chapter 4.
74. M. P. Mitoraj and A. Michalak, *Inorg. Chem.*, 2010, **49**, 578.; D. Woska, A. Prock and W. P. Giering, *Organometallics*, 2000, **19**, 4629.
75. (a) A. W. Hofmann, *Ann. Chem. Pharm.*, 1857, **104**, 1.; (b) B. W. Malerbi, *Platinum Metal Rev.*, 1965, **9**, 47.
76. (a) J. Jover, N. Fey, J. N. Harvey, G. C. Lloyd-Jones, A. G. Orpen, G. J. J. Owen-Smith, P. Murray, D. R. J. Hose, R. Osborne, M. Purdie, *Organometallics*, 2010, **29**, 6245. (b) T. Sawano, Z. Lin, D. Boures, B. An, C. Wang, and W. Lin, *J. Am. Chem. Soc.*, 2016, **138**, 9783. (c) M. E. van der Boom and D. Milstein, *Chem. Rev.*, 2003, **103**, 1759.
77. J. P. Wolfe, S. Wagaw, J. F. Marcoux and S. L. Buchwald, *Acc. Chem. Res.*, 1998, **31**, 805.
78. P. H. Espeel, G. D. Peuter, M. C. Tielen and P. A. Jacobs, *J. Phys. Chem.*, 1994, **98**, 11588.
79. M. Watanabe, T. Yamamoto and M. Nishiyama, *Angew. chemie.*, 2000, **112**, 2620.

80. M. Opanasenko, P. Stepnicka and J. Cejka, *RSC Adv.*, 2014, **4**, 65137.
81. S. Paul, M. Islamc and M. Islam, *RSC Adv.*, 2015, **5**, 42193.
82. G. Ferguson, R. McCrindle, A. J. McAlees and M. Parvez, *Acta Cryst.*, 1982, **B38**, 2679.
83. R. F. Heck, *J. Am. Chem. Soc.*, 1963, **85**, 657.
84. R. F. Heck, *J. Am. Chem. Soc.*, 1968, **90**, 313.
85. E. Negishi and L. Anastasia, *Chem. Rev.*, 2003, **103**, 1979.
86. E. Negishi, *Acc. Chem. Res.*, 1982, **15**, 340.
87. V. Grignard, *J. Ind. Eng. Chem.*, 1917, **9**, 1142.
88. J. F. Hartwig, *Acc. Chem. Res.*, 1998, **31**, 852.
89. J. F. Hartwig, *Inorg. Chem.*, 2007, **46**, 1936.
90. J. K. Stille, *Organometallics*, 1990, **9**, 3007.
91. J. K. Stille and R. Divakaruni, *J. Am. Chem. Soc.*, 1978, **100**, 1303.
92. J. Tsuji, I. Shimizu, I. Minami, Y. Ohashi and T. Sugiura, *J. Org. Chem.*, 1985, **50**, 1523.
93. B. M. Trost and Z. Shi, *J. Am. Chem. Soc.*, 1996, **118**, 3037.
94. K. Sonogashira, S. Takahashi and N. Hagihara, *Macromolecules*, 1977, **10**, 879.
95. A. C. Skapski and M. L. Smart, *Chem. Commun.*, 1970, **8**, 658.
96. R. Martin and S. L. Buchwald, *Acc. Chem. Res.*, 2008, **41**, 1461.
97. B. M. Trost and M. Lautens, *J. Am. Chem. Soc.*, 1985, **107**, 1781.
98. R. B. Bedford, C. S.J. Cazin and D. Holder, *Coord. Chem. Rev.*, 2004, **248**, 2283.
99. R. Jackstell, A. Grotevendt, D. Michalik, L. E. Firdoussi and M. Beller, *J. Organometal. Chem.*, 2007, **692**, 4737.
100. J. K. Stille and D. E. James, *J. Organometal. Chem.*, 1976, **108**, 401.
101. P. Fitton and E. A. Rick, *J. Organometal. Chem.*, 1971, **28**, 287.

102. T. R. Hoye, C. J. Dinsmore, D. S. Johnson and P. F. Korkowski, *J. Org.Chem.*, 1990, **55**, 4518.
103. Y. Tatsuno, T. Yoshida and S. Otsuka, *Inorg. Synth.*, 1990, **28**, 342.
104. B. M. Trost and C. B. Lee, *J. Am. Chem. Soc.*, 1998, **120**, 6818.
105. S. E. Sherman, D. Gibson, A. H. J. Wang and S. J. Lippard, *J. Am. Chem. Soc.*, 1998, **110**, 7368.
106. M. K. Amir, S. Z. Khan, F. Hayat, A. Hassan and I. S. Butler, *Inorg. Chim. Acta*, 2016, **451**, 31.
107. Y. Gou, G. Huang, J. Li, F. Yang and H. Liang, *Coord. Che. Rev.*, 2021, **441**, 213975.
108. J. Zhang, L. Li, L. Wang, F. Zhang and X. Li., *Eur. J. Med. Chem.*, 2010, **45**, 5337.
109. A. Shoukry, T. Rau, M. Shoukry and R. Van Eldik, *J. Chem. Soc. Dalton Trans.*, 1998, 3105.
110. M. Saeidifar, H. Mirzaei, N. A. Nasab, H. Mansouri-Torshizi, *J. Mol. Struct.*, 2017, **1148**, 339.
111. Md N. Alam and F. Huq, *Coord. Chem. Rev.*, 2016, **316**, 36.
112. T. Thirunavukkarasu, H. A. Sparkes and K. Natarajan, *Inorg. Chim. Acta*, 2018, **482**, 229.
113. M. C. Zhu, X. Cui, S. Zhang, L. Liu, Z. Han and E. Gao, *J. Inorg. Biochem.*, 2016, **157**, 34.
114. J. Albert, L. D'Andrea^a, J. Granell, P. Pla-Vilanova, J. Quirante, M. K. Khosa, C. Calvis, R. Messeguer, J. Badía, L. Baldomà, M. Font-Bardia and T. Calvet, *J. Inorg. Biochem.*, 2014, **140**, 80.
115. J. Albert, J. Granell, R. Qadir, J. Quirante, C. Calvis, R. Messeguer, J. Badia, L. Baldoma, M. Font-Bardia and T. Calvet, *Organometallics*, 2014, **33**, 7284.

116. S. Samiee, A. Shiralinia, E. Hoveizi and R. W. Gable, *Journal of Organometallic Chemistry*, 2019, **900**, 120927.
117. G. Kalaiarasi, S. Dharani, V. M. Lynch and R. Prabhakaran, *Dalton Trans.*, 2019, **48**, 12496.
118. T. T. H. Fong, C. N. Lok, C. Y. S. Chung, Y. M. E. Fung, P. K. Chow, P. K. Wan and C. M. Che, *Angewandte Chemie International Edition*, 2016, **55**, 11935.
119. C. Cullinane, G. B. Deacon, P. R. Drago, A. P. Erven, P. C. Junk, J. Luu, G. Meyer, S. Schmitz, I. Ott, J. Schur and L. K. Webster, *Dalton Trans.*, 2018, **47**, 1918.
120. O. D. Al-Mouqdady, A. S. Al-Janabi, M. R. Hatshan, S. A. Al-Jibori, A. S. Fiahan and C. Wagner, *J. Mol. Struct.*, 2022, **1264**, 133219.
121. K. Karami, F. Mehvari, V. Ramezanzade, M. Zakariazadeh, M. Kharaziha, and A. Ramezanpour, *J. Mol. Liq.*, 2022, **362**, 119493.
122. M. Al-Noaimi, F. F. Awwadi, I. A. Mansi, M. Sawwan, B. Abu-Irmaileh and N. Dege, *Polyhedron*, 2022, **211**, 115541.
123. R. Naskar, P. Ghosh, C. K. Manna, N. Murmu and T. K. Mondal, *Inorganica Chim. Acta*, 2022, **534**, 120802.
124. B. B. Zmejkovski, N. D. Pantelić and G. N. Kaluđerović, *Inorganica Chim. Acta*, 2022, **534**, 120797.
125. T. Scattolin, G. Moro, A. Serena, A. Guadagnin Pattaro, F. Rizzolio, V. Canzonieri, N. Demitri, E. Bortolamiol, L. M. Moretto and F. Visentin, *Appl. Organomet. Chem.*, 2022, **36**, e6629.
126. R. Naskar, P. Ghosh, S. Mandal, S. Jana, N. Murmu and T. K. Mondal, *J. Chem. Sci.*, 2022, **134**, 1.

127. M. Luo, J. C. Zhang, H. Yin, C. M. Wang, L. Xie, K. P. Li, M. Goto, S. L. Morris-Natschke, K. H. Lee, J. H. Zhang and Y. M. Zhang, *J. Inorg. Biochem.*, 2022, p.112048.
128. L. Cheng, Y. Wang, J. Wang, H. Qin, G. Zhu and L. Tao, *J. Healthc. Eng.*, **2022**, 2022.
129. S. M. Hassona, E. A. Saad, H. A. Kiwan and M. M. Hassanien, *Investigational New Drugs*, 2022, **40**, 681.
130. W. Kohn, *Rev. Mod. Phys.*, 1998, **71**, 1253.
131. John Wiley and Sons, Inc. *J Comput Chem.*, 1999, **20**, 129.
132. E. Runge and E. K. U. Gross, *Phys. Rev. Lett.*, 1984, **52**, 997.
133. P. Hohenberg and W. Kohn, *Phys. Rev.*, 1964, **136**, B864.
134. R.V. Leeuwen, *Phys. Rev. Lett.*, 1998, **80**, 1280.
135. M. E. Casida, C. Jamorski, F. Bohr, J. Guan and D. R. Salahub Washington, D.C.: ACS Press. 1996, 145.
136. M. Petersilka, U. J. Gossmann and E. K. U. Gross, *Phys. Rev. Lett.*, 1996, **76**, 1212.
137. E.R. Davidson, *Chem. Rev.*, 1986, **86**, 681.
138. R. Ditchfield, W. J. Hehre, J. A. Pople, *J. Chem. Phys.*, 1971, **54**, 724.
139. Thorn H. Dunning, Jr., *J. Chem. Phys.*, 1989, **90**, 1007.
140. A. Carella, V. Roviello, R. Iannitti, R. Palumbo, S. La Manna, D. Marasco, M. Trifuoggi, R. Diana and G. N. Roviello, *J. Biol. Macromol.*, 2019, **121**, 77.
141. 14 S. Y. Ebrahimipour, I. Sheikhshoae, J. Castro, M. Dušek, Z. Tohidyan, V. Eigner and M. Khaleghi, *RSC Adv.*, 2015, **5**, 95104.
142. M. K. M. Subarkhan and R. Ramesh, *Inorg. Chem. Front.*, 2016, **3**, 1245.
143. M. S. Mohamed Kasim, S. Sundar and R. Rengan, *Inorg. Chem. Front.*, 2018, **5**, 585.
144. P. R. Reddy, A. Shilpa, N. Raju and P. Raghavaiah, *J. Inorg. Biochem.*, 2011, **105**, 1603.

145. K. Nagaraj, K. S. Murugan, P. Thangamuniyandi and S. Sakthinathan, *RSC Adv.*, 2014, **4**, 56084.
146. A. C. Komor and J. K. Barton, *Chem. Commun.*, 2013, **49**, 3617.
147. Q. X. Wang, W. Li, F. Gao, S. Li, J. Ni and Z. Zheng, *Polyhedron*, 2010, **29**, 539.
148. C. Metcalfe and J. A. Thomas, *Chem. Soc. Rev.*, 2003, **32**, 215.
149. K. Karami, Z. Mehri Lighvan, H. Farrokhpour, M. Dehdashti Jahromi and A. A. Momtazi-Borojeni, *J. Biomol. Structure and Dynamics*, 2018, **36**, 3324.
150. K. Divya, V. Smitha and M. S. Jisha, *Int. j. biol. Macromol.*, 2018, **114**, 572.
151. R. L. Siegel, L. A. Torre, I. Soerjomataram, R. B. Hayes, F. Bray, T. K. Weber and A. Jemal, *Gut*, 2019, **68**, 2179.
152. H. W. Liu, L. Chen, C. Xu, Z. Li, H. Zhang, X. B. Zhang and W. Tan, *Chemical Society Reviews*, 2018, **47**, 7140.
153. M. Afzal, A. Alarifi, M. S. Hasnain and M. Muddassir, *Environmental Science and Pollution Research*, 2021, **28**, 44039.
154. C. J. Dhanaraj, I. Ul Hassan, J. Johnson, J. Joseph and R. S. Joseyphus, *J. Photochem. Photobiol. B.*, 2016, **162**, 115.
155. Q. X. Wang, W. Li, F. Gao, S. Li, J. Ni and Z. Zheng, *Polyhedron*, 2010, **29**, 539.
156. A. C. Komor and J. K. Barton, *Chem. Commun.*, 2013, **49**, 3617.
157. W. D. Wilson In: G. M. Blackburn, M. J. Gait (eds) *Nucleic acids in chemistry and biology*. Oxford University Press, Oxford, 1996, 329.
158. J. A. Mountzouris and L. H. Hurley In: S. M. Hecht Ed, *Bioorganic chemistry: nucleic acids*. Oxford University Press, New York, 1996, 288.
159. J. A. Cowan, *Curr. Opin. Chem. Biol.*, 2001, **5**, 634.
160. L. N. Ji, X. H. Zou and J. G. Liu, *Coord. Chem. Rev.*, 2001, **216**, 513.
161. H. Mei and J. Barton, *J. Am. Chem. Soc.*, 1986, **108**, 7414.

162. J. Kelly, A. Tossi and D. McComell, *Nucl. Acids. Res.*, 1985, **13**, 6017.
163. L. S. Lerman, *J. Mol. Biol*, 1961, **3**, 18.
164. B. H. Geierstanger, D. E. Wemmer and R. Annu, *Biophys. Biomol. Struct.*, 1995, **24**, 463.
165. B. A. Armitage, *Top Curr Chem.*, 2005, **253**, 55.
166. R. Lyng, A. Rodger and B. Nordén, *Biopolymers*, 1991, **31**, 1709.
167. R. Lyng, A. Rodger and B. Nordén, *Biopolymers*, 1992, **32**, 1201.
168. B. J. Pages, D. L. Ang, E. P. Wright, J. R. Aldrich-Wright, *Dalton Trans.*, 2015, **44**, 3505.
169. H. Liu and P. J. Sadler, *Acc. Chem. Res.*, 2011, **44**, 349.
170. M. Lazoua, A. Tarushia, P. Gritzapisb, and G. Psomas, *J. Inorg. Biochem.*, 2020, **206**, 111019.
171. E. Moradinia, M. Mansournia, Z. Aramesh-Boroujeni and A. Bordba, *Appl Organometal Chem.*, 2019, **33**, 4893.
172. N. Vamsikrishna, S. Daravath, N. Ganji and N. Pasha, *Inorg. Chem. Commun.*, 2020, **113**, 107767.
173. M. Lazoua, A. Tarushia, P. Gritzapisb and G. Psomasa, *J. Inorg. Biochem.*, 2020, **206**, 111019.
174. D. Cocica, S. Jovanovica, S. Radisavljevica, J. Korzekwab, A. Scheurerb, R. Puchtab, D. Baskice, D. Todorovicf, S. Popovice, S. Maticg and B. Petrovic, *J. Inorg. Biochem.*, 2018, **189**, 91.
175. E. A. Popova, A. V. Protas, A. V. Mukhametshina, G. K. Ovsepyan, R. V. Suezov, A. V. Eremin, E.I. Stepchenkova, E. R. Tarakhovskaya, A. V. Fonin, G. L. Starova, O. V. Mikolaichuk, Y. B. Porozov, M. A. Gureev and R. E. Trifonov, *Polyhedron*, 2019, **158**, 36.

176. G. Onar, C. Gürses, M. O. Karatas, S. Balcıoğlu, N. Akbay, N. Ozdemir, B. Ates and B. Alıcı, *J. Organomet. Chem.*, 2019, **886**, 48.
177. A. Ziannaa, G. D. Geromichalosa, A. G. Hatzidimitrioua, E. Coutouli-Argyropouloub, M. Lalia-Kantouria and G. Psomas, *J. Inorg. Biochem.*, 2019, **194**, 85.
178. A. Querino, J. Silva, J. Teixeira Silva, G. M. Alvarenga, C. H. Silveira, M. T. Q. Magalhaes, O. A. Chaves, B. A. Iglesias, R. Diniz and H. Silva, *J. Biol. Inorg. Chem.*, 2019, **24**, 1087.
179. Q. Wang, Z. Y. Yang, G. F. Qi and D. D. Qin, *Eur. J. Med. Chem.*, 2009, **44**, 2425.
180. X. H. Zou, B. H. Ye, H. Li, J. G. Liu, Y. Xiong and L. N. Ji, *J. Chem. Soc. Dalton Trans.*, 1999, 1423.
181. F. Q. Liu, Q. X. Wang, K. Jiao, F. F. Jian, G. Y. Liu and R. X. Li, *Inorg. Chim. Acta.*, 2006, **359**, 1524.
182. D. Lawrence, V. G. Vaidyanathan and B. Unni Nair, *J. Inorg. Biochem.*, 2006, **100**, 1244.
183. E. C. Long and J. K. Barton, *Acc. Chem. Res.*, 1990, **23**, 271.
184. S. Tabassum and I. U. H. Bhat, *Chem. Pharm. Bull.*, 2010, **58**, 318.
185. A. Wolfe, G. H. Shimer, T. Meehan, *Biochemistry.*, 1987, **26**, 6392.
186. N. S. Quiming, R. B. Vergel, M. G. Nicolas, J. A. Villanueva, *J. Health Sci.*, 2005, **51**, 8.
187. (a) E. Ramachandran, D. S. Raja, N. P. Rath, K. Natarajan, *Inorg. Chem.*, 2013, **52**, 1504. (b) D. Senthil Raja, N. S. P. Bhuvanesh, K. Natarajan, *Inorg. Chem.*, 2011, **50**, 12852.
188. (a) A. Paul, S. Mistri, A. Bhunia, S. Manna, H. Puschmann, S. C. Manna, *RSC Adv.*, 2016, **6**, 60487. (b) A. Wolfe, G. H. Shimer, T. Mechan, *Biochemistry*, 1987, **26**, 6392.

189. a) A. Paul, A. Figuerola, V. Bertolasi, S. C. Manna, *Polyhedron*, 2016, **119**, 460; (b) X.-Q. Zhou, Q. Sun, L. Jiang, S.-T. Li, W. Gu, J.-L. Tian, X. Liu, S.-P. Yan, *Dalton Trans.*, 2015, **44**, 9516; (c) W.-J. Lian, X.-T. Wang, C.-Z. Xie, H. Tian, X.-Q. Song, H.-T. Pan, X. Qiao, J.Y. Xu, *Dalton Trans.*, 2016, **45**, 9073; (d) K. M. Vyas, R. N. Jadeja, D. Patel, R. V. Devkar, V. K. Gupta, *Polyhedron*, 2014, **80**, 20; (e) K. Jeyalakshmi, Y. Arun, N. S. P. Bhuvanesh, P. T. Perumal, A. Sreekanth, R. Karvembu, *Inorg. Chem. Front.*, 2015, **2**, 780.
190. J. R. Lakowicz, Principles of Fluorescence Spectroscopy, Third Edition., *Springer, New York, USA*, 2006
191. (a) X. -Z. Feng, Z. Lin, L. -J. Yang, C. Wang, C. -L. Bai, *Talanta*, 1998, **47**, 1223. (b) J. R. Lakowicz, Fluorescence Quenching: Theory and applications, Principles of Fluorescence Spectroscopy, Kluwer Academic/Plenum Publishers, New York, 1999, p. 53; c) L. M. Surhone, M. T. Tennoe, S. F. Henssonow, Betascript Publishing, 2010.
192. T. T. Puck and P. I. Markus, *J. Exp. Med.*, 1956, **103**, 653.
193. J. M. Brown and L. D. Attardi, *Nat. Rev. Cancer*, 2005, **5**, 231.
194. E. J. Hall, JB Lippincott Company, Philadelphia, 2000.
195. J. E. Till and E. A. McCulloch, *Radiat. Res.*, 1961, **14**, 213.
196. G. J. Todaro, G. K. Lazar and H. Green, *J. Cell Physiol.*, 1965, **66**, 325.
197. C. C. Haudenschild and S. M. Schwartz, *Lab. Invest.*, 1979, **41**, 407.
198. A. K. Taraphdar, M. Roy, R. Bhattacharya, *Curr Sci.*, 2001, **80**, 1387.
199. M. Yamamoto, Y. Maehara, S. Oda, Y. Ichiyoshi, T. Kusumoto and K. Sugimachi, *Cancer Chemother Pharmacol.*, 1999, **43**, 43.
200. N. P. Bown, M. M. Reid, A. J. Malcolm, E. V. Davison, A. W. Craft and A. D. J. Pearson, *Medical and pediatric oncology*, 1994, **23**, 124.

201. T. Efferth, V. B. Konkimalla, Y. F. Wang, A. Sauerbrey, S. Meinhardt, F. Zintl, J. Mattern and M. Volm, *Clinical cancer research*, 2008, **14**, 2405.
202. D. J. Samson, J. Seidenfeld, K. Ziegler and N. Aronson, *Journal of clinical oncology*, 2004, **22**, 3618.
203. R. M. Hoffman, *J Clin Lab Anal.*, 1991, **5**, 133.
204. J. Hatok, E. Babusikova, T. Matakova, D. Mistuna, D. Dobrota and P. Racay, *Clinical and experimental medicine*, 2009, **9**, 1.
205. H. Lecoeur, *Exp Cell Res.*, 2002, **277**, 1.
206. I. C. Gherghi, S. T. Girousi, A. N. Voulgaropoulos and R. Tzimou-Tsitouridou, *Talanta*, 2003, **61**, 103.
207. M. Leite, M. Quinta-Costa, P. S. Leite and J. E. Guimarães, *Analytical Cellular Pathology*, 1999, **19**, 139.
208. D. Baskić, S. Popović, P. Ristić and N. N. Arsenijević, *Cell biology international*, 2006, **30**, 924.
209. B. Zhivotosky and S. Orrenius, *Current protocols in cell biology*, 2001, **12**, 18.
210. D. Matassov, T. Kagan, J. Leblanc, M. Sikorska and Z. Zakeri, *In Apoptosis Methods and Protocols*, 2004, 1.
211. J. M. van de Kamp, O. T. Betsalel, S. Mercimek-Mahmutoglu, L. Abulhoul, S. Grünewald, I. Anselm, H. Azzouz, D. Bratkovic, A. de Brouwer, B. Hamel, T. Kleefstra, *Journal of medical genetics*, 2013, **50**, 463.
212. L. Zhang, W. R. Dawes and G. R. Walker, *Water resources research*, 2001, **37**, 701.
213. W. R. Briggs, C. F. Beck, A. R. Cashmore, J. M. Christie, J. Hughes, J. A. Jarillo, T. Kagawa, H. Kanegae, E. Liscum, A. Nagatani and K. Okada, *The Plant Cell*, 2001, **13**, 993.

214. J. Kielhorn, C. Melber, D. Keller and I. Mangelsdorf, *Int. J. Hyg. Environ. Health.*, 2002, **205**, 417.
215. L. Cui, W. Zhu, Y. Xu and X. Qian, *Anal. Chim. Acta.*, 2013, **786**, 139.
216. (a) International Programme on Chemical Safety, Palladium, Environmental Health Criteria Series 226, World Health Organization, Geneva, 2002; (b) J. Kielhorn, C. Melber, D. Keller and I. Mangelsdorf, *Int. J. Hyg. Environ. Health*, 2002, **205**, 417; (c) C. L. Wiseman and F. Zereini, *Sci. Total Environ.*, 2009, **407**, 2493.
217. C. E. Garrett and K. Prasad, *Adv. Synth. Catal.*, 2004, **346**, 889.

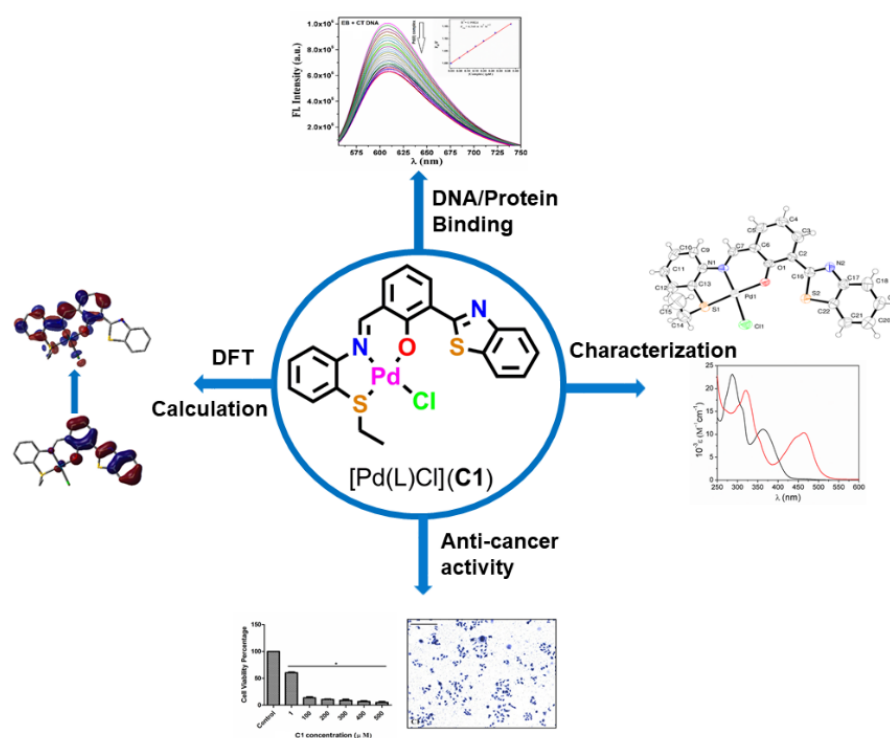
CHAPTER-II

**Palladium(II) complex bearing
benzothiazole based O,N,S donor
pincer ligand: Study of in-vitro
cytotoxicity, interaction with CT-
DNA and BSA protein**

Palladium(II) complex bearing benzothiazole based O,N,S donor pincer ligand: Study of in-vitro cytotoxicity, interaction with CT-DNA and BSA protein

Abstract

A new palladium(II) complex, $[\text{Pd}(\text{LS}^{\text{Et}})\text{Cl}]$ (**C1**) with benzothiazole based ONS donor pincer ligand (HLS^{Et}) was synthesized (where, $\text{HLS}^{\text{Et}} = 2\text{-(benzothiazol-2-yl)-6-(((2\text{-(ethylthio)phenyl)imino)methyl)phenol)}$). Interaction of **C1** with CT DNA was investigated and its binding constant was found to be $4.0 \times 10^5 \text{ M}^{-1}$. The proficiency of displacement of ethidium bromide (EB) from its EB-CTDNA complex by **C1** was performed by fluorescence quenching method and Stern-Volmer quenching constant (K_{sv}) was found to be $4.3 \times 10^5 \text{ M}^{-1}$. Similarly, the interaction of **C1** with BSA protein was investigated by UV-Vis and fluorescence methods. The apparent association constant (K_{a}) and K_{sv} were determined ($K_{\text{a}} = 2.8 \times 10^4 \text{ M}^{-1}$ and $K_{\text{sv}} = 5.5 \times 10^4 \text{ M}^{-1}$). In vitro cytotoxicity of the complex, $[\text{Pd}(\text{LS}^{\text{Et}})\text{Cl}]$ (**C1**) towards human gastric cancer cell lines (AGS) was assessed by MTT assay method. The half maximal inhibitory concentration (IC_{50}) of **C1** ($9.55 \pm 1.23 \mu\text{M}$) towards AGS cancer lines was found to be lower than cisplatin ($23.13 \pm 1.03 \mu\text{M}$).



II.1. Introduction

Among noninfectious diseases causing 72% of death worldwide, cancer is considered the second leading according to mortality [1]. Most anticancer drugs target DNA molecules and modify the DNA structure by forming an irreversible covalent bond and the non-covalent bond, which ultimately affects DNA replication and transcription because cancer cells proliferate more than non-neoplastic cells [2,3]. The ligands around the metal-based anticancer drugs play a pivotal role in showing anticancer activity because of their modifying ability and lipophilicity [4]. There is a considerable interest in Schiff bases containing ONS donor ligand chelated with different 3d- or 4d- metals owing to their chelation mode, structural, spectral features as well as several biological aspects such as anticancer, antibacterial, antiviral, antifungal, and anti-inflammatory activity [5,6]. Schiff base ligands are also important because they can stabilize the uncommon oxidation states of the transition metals [7,8].

Heterocyclic aromatic ligands such as pyridine, phenanthroline and their derivatives are reported to be DNA intercalators in palladium and ruthenium complexes [9]. Moreover, a thioether ligand containing an S atom chelated to metal may replicate the active site structures of several metalloproteins [10-12]. N and S containing metal complexes show promising anticancer, antifungal, and antibacterial activities [13-17]. After the remarkable discovery in medicinal chemistry, cisplatin is used as a chemotherapeutic drug worldwide. Only six platinum-based drugs have been approved so far, including three globally (cisplatin, carboplatin, and oxaliplatin) and three locally (nedaplatin, lobaplatin, and heptaplatin) [18,19]. One of the leading antitumor drugs, cisplatin, may target DNA molecules by pairing platinum metal with adjacent purine bases via its N7 positions [20]. Moreover, these drugs have severe side effects observed in cancer patients during chemotherapy, including nephrotoxicity, ototoxicity, haemolysis, bone marrow suppression, neurotoxicity, and

vomiting [21], which motivate scientists to search for alternate treatment strategies. Currently, the development of new anticancer drugs with improved potency and minimum side effects has drawn much more attention from scientists. Due to structural similarity, coordination ability, and thermodynamic stability, palladium metal can be a viable anticancer substitute for platinum [22]. The palladium complexes show nearly 10^4 - 10^5 times greater ligand exchange activities than their platinum counterparts [23]. Furthermore, serum albumins act as transporters in the circulatory system by binding non-covalently to nutrients and drugs [24]. The binding sites of serum albumins are critical for absorption, metabolism, distribution, excretion [25]. Considering the fact that bovine serum albumin (BSA) and human serum albumin (HSA) are of similar structure [26], investigation of the interactions of palladium metal complexes with DNA and BSA would be more important for developing a new therapeutic drug.

In continuation of research works on the coordination chemistry of transition metals with thioether based azo and imine functional ligands [27-31], herein we have synthesized palladium(II) complex, $[\text{Pd}(\text{LS}^{\text{Et}})\text{Cl}]$ (**C1**) with N,O,S donor benzothiazole based pincer ligand (HLS^{Et}). The compounds are thoroughly characterized by various spectroscopic techniques. Structures of both HLS^{Et} and $[\text{Pd}(\text{LS}^{\text{Et}})\text{Cl}]$ (**C1**) are confirmed by X-ray structure analysis. Interaction with CT DNA is studied by UV-Vis method. In contrast, the fluorescence method helps to evaluate the capability of $[\text{Pd}(\text{LS}^{\text{Et}})\text{Cl}]$ (**C1**) to displace EB from its EB-CTDNA complex. Again, fluorescence and UV-Vis methods are used to study the interactions of BSA with **C1**. In-vitro cytotoxicity of the compounds is evaluated through MTT and colony formation assays on AGS cell lines.

II.2. Experimental section

II.2.1. Material and characterization methods

All the necessary reagents and solvents were purchased commercially and used as it is. Na_2PdCl_4 was bought from Sigma-Aldrich. 3-(2-Benzothiazolyl)-2-hydroxybenzaldehyde was synthesized from 2-(2-hydroxyphenyl)benzothiazole following the reported method [32]. Cisplatin was obtained from calbiochem (sigma Aldrich, 232120-50MG) and dissolved in sodium chloride solution in water (154 mM NaCl) for culture treatment.

Elemental analyses (C, H and N) were performed using a PerkinElmer Series-II CHN-2400 CHNS/O elemental analyzer. UV-Vis spectra were taken on Shimadzu UV-1900i spectrophotometer. IR spectra were recorded on PerkinElmer Spectrum 2 FT-IR Spectrometer. Emission spectra were taken on a Shimadzu spectrofluorometer (Model: RF 6000). NMR spectra were recorded on a Bruker (300 MHz) NMR spectrometer. Waters quadruple time-of-flight mass spectrometer (Xevo G2 Q-TOF) was used to get mass spectra.

II.2.2. Preparation of HLS^{Et} and $[\text{Pd}(\text{LS}^{\text{Et}})\text{Cl}]$ (C1)

II.2.2.1. Preparation of HLS^{Et}

The mixture of 0.116 g (0.5 mmol) 3-(2-benzothiazolyl)-2-hydroxybenzaldehyde and 0.077 g (0.5 mmol) 2-(ethylthio)aniline in 50 mL dry methanol was refluxed for 6 h. The solution was then cooled to room temperature and kept for slow evaporation. The yellow crude product of HLS^{Et} was further crystallized from methanol. Yield was 0.161 g (82%).

Anal. Calc. for $\text{C}_{22}\text{H}_{18}\text{N}_2\text{OS}_2$ (HLS^{Et}): C, 65.87; H, 3.55; N, 5.49. Found: C, 65.61; H, 3.49; N, 5.44. IR (KBr, cm^{-1}): 2972 $\nu(\text{C-H})$, 1608 $\nu(\text{C=N})$, 751 $\nu(\text{C-S})$. ^1H NMR (300 MHz, CDCl_3): δ , 10.54(1H, s), 8.72 (1H, s), 6.68-8.10 (11H, ArH, m), 3.00 (2H, q, $J=7.4$), 1.41 (3H, t, $J=7.2$). λ_{max} , (nm) in acetonitrile (ϵ , $\text{M}^{-1}\text{cm}^{-1}$): 288 (23251); 312 (15567); 363 (11174). HRMS, m/z : Calculated, 391.0939; found, 391.1097 $[\text{M} + \text{H}]^+$.

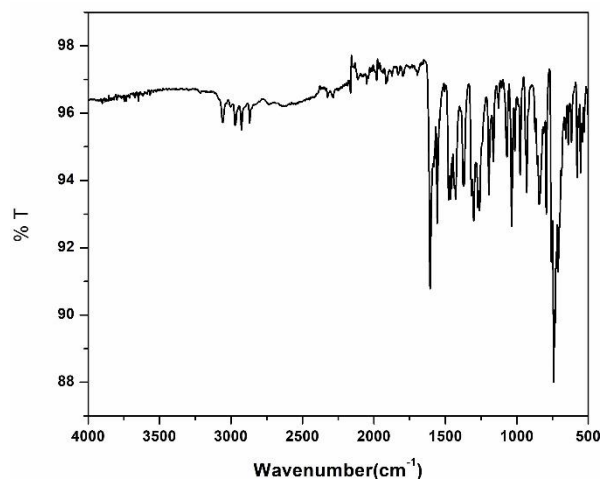


Fig.II.1. IR spectrum of HLS^{Et}(KBr disk)

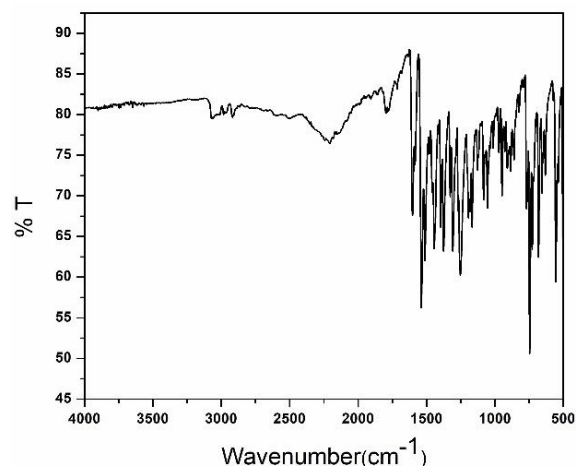


Fig.II.2. IR spectrum of [Pd(LS^{Et})Cl] (KBr disk)

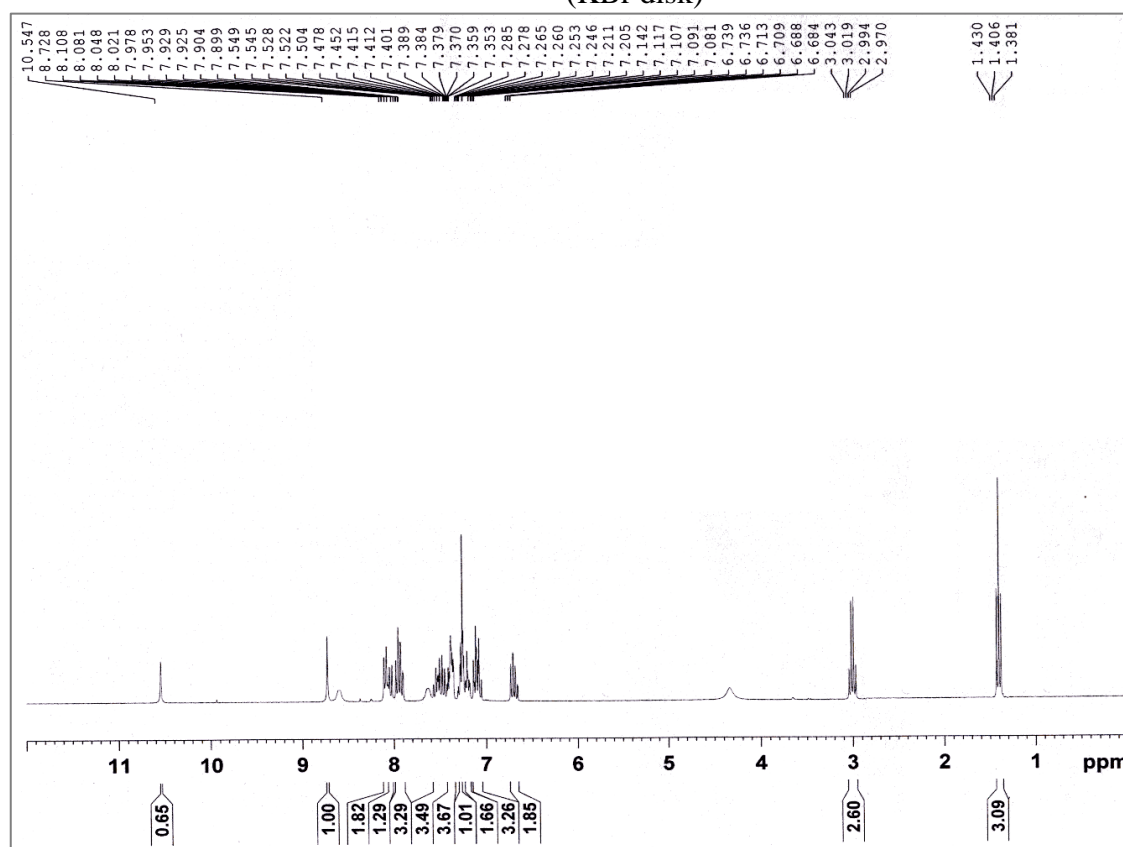


Fig.II.3. ¹H NMR spectrum of HLS^{Et} in CDCl₃

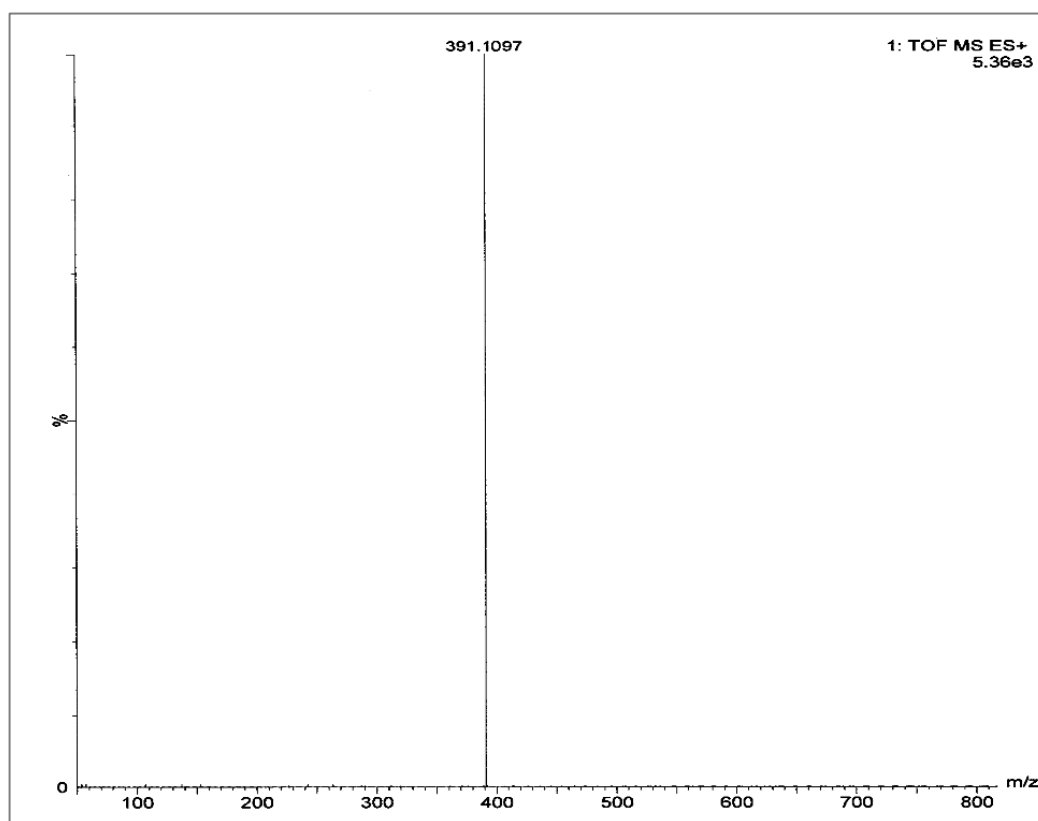


Fig.II.4. HRMS spectrum of HLS^{Et} in acetonitrile

II.2.2.2. Preparation of $[\text{Pd}(\text{LS}^{\text{Et}})\text{Cl}]$ (**C1**)

At first, 0.059 g (0.2 mmol) Na_2PdCl_4 and 0.080 g (0.2 mmol) HLS^{Et} were dissolved in 25 mL acetonitrile. The reaction mixture was then refluxed for 7 h to yield a deep red solution. The solution was then cooled, filtered and allowed to evaporate slowly to give brown crystals of $[\text{Pd}(\text{LS}^{\text{Et}})\text{Cl}]$ (**C1**). Yield was 0.072 g (66%).

Anal. Calc. for $\text{C}_{22}\text{H}_{17}\text{ClN}_2\text{OPdS}_2$ (**C1**): Anal. Calc. (%): C, 49.73; H, 3.22; N, 5.27. Found (%): C, 49.65; H, 3.18; N, 5.25. IR data (KBr disc) (cm^{-1}): 2917 $\nu(\text{C-H})$, 1596 $\nu(\text{C=N})$, 749 $\nu(\text{C-S})$. ^1H NMR data in CDCl_3 (δ , ppm): 9.33 (s, 1H, HC=N); 7.01-8.79 (11H, ArH, m); 3.30 (q, $J = 7.2$ Hz, 2H); 1.37 (t, $J = 6.9$ Hz, 3H). λ_{max} (nm) (ϵ , $\text{M}^{-1}\text{cm}^{-1}$) in acetonitrile: 298 (16064), 321 (19156), 465 (10371). HRMS, m/z: Calc., 494.9817; found, 494.9756 $[\text{M-Cl}]^+$.

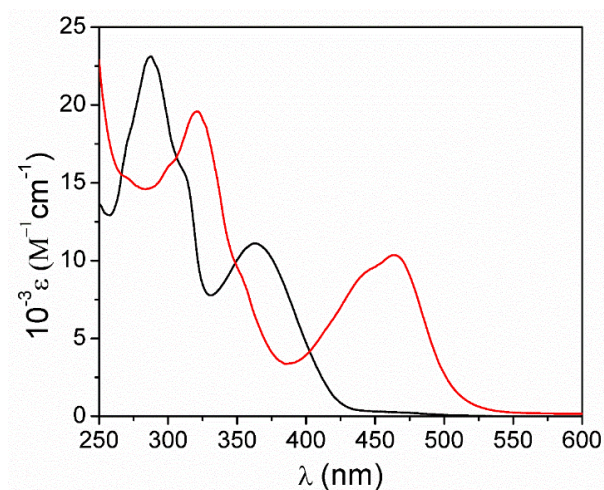


Fig.II.5. UV-Vis spectrum of HLS^{Et} and [Pd(LS^{Et})Cl] in acetonitrile

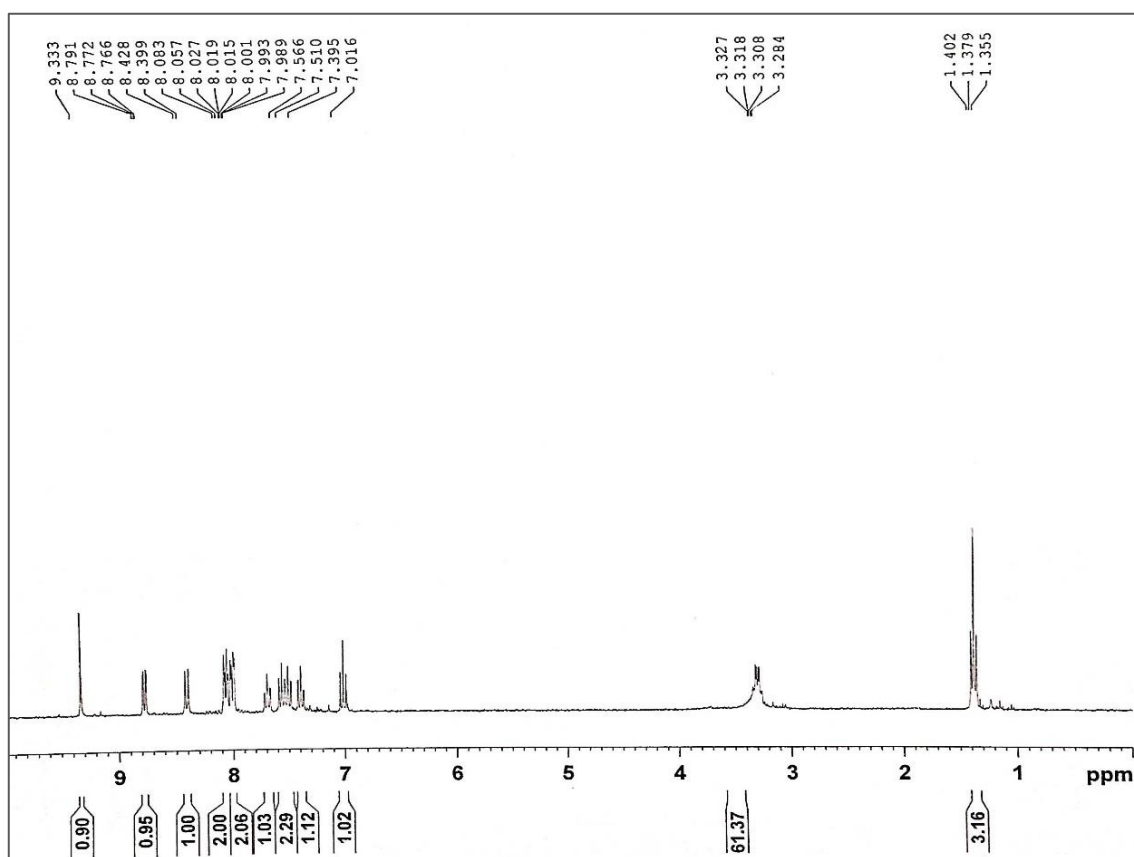


Fig.II.6. ¹H NMR spectrum of [Pd(LS^{Et})Cl] in CDCl₃

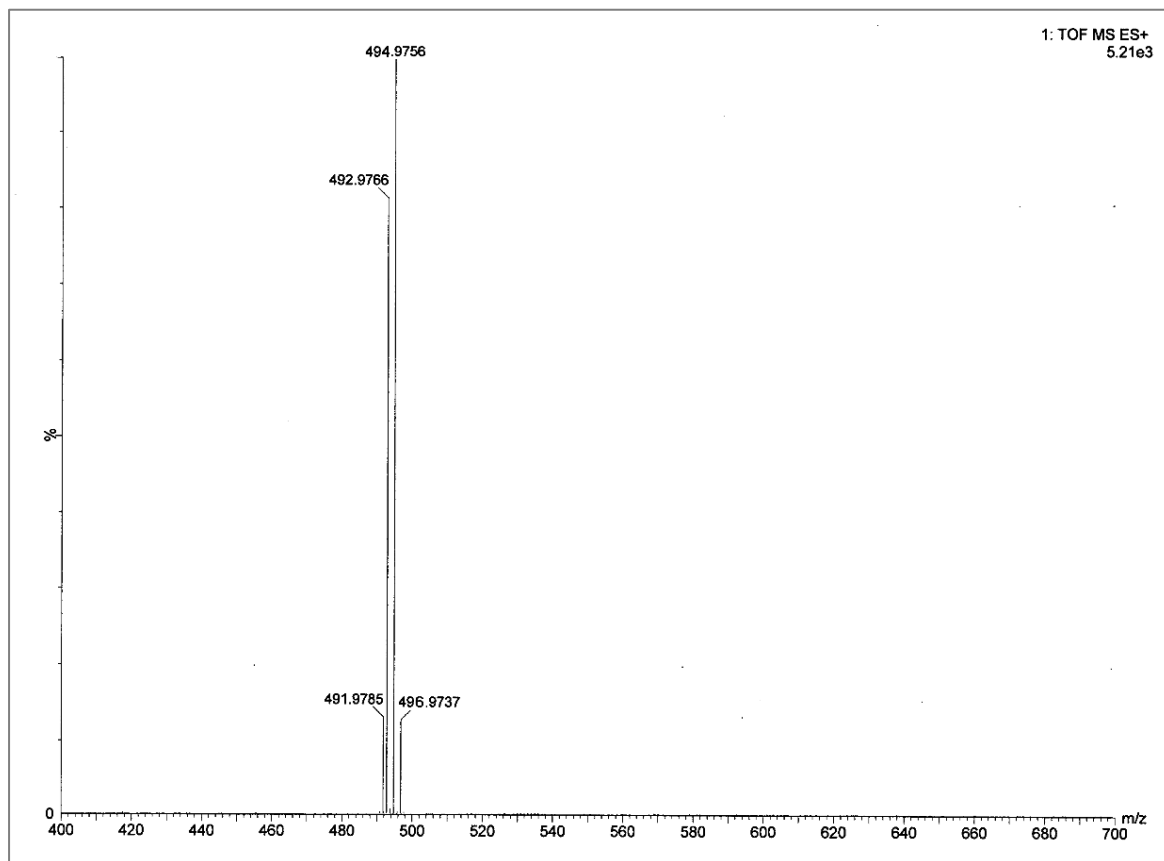


Fig.II.7. HRMS spectrum of [Pd(LS^{Et})Cl] in acetonitrile

II.2.3. Crystallography

Good quality single crystals of HLS^{Et} and its palladium complex (**C1**) suitable for X-ray diffraction were grown by slow evaporation of methanol and acetonitrile solutions, respectively. X-ray data were collected on Bruker AXS D8 Quest CMOS diffractometer using graphite monochromated Mo K α radiation ($\lambda = 0.71073 \text{ \AA}$) at 293 K. Reflection data were collected applying the ω scan technique. The collected frames were reduced using SAINT program. Absorption correction was done by multi-scan method using the SADABS absorption correction program. The structures were solved by direct method and refined using the SHELXTL program [33,34] by full-matrix least-squares based on F^2 . Refinement of non-hydrogen atoms were performed anisotropically and the riding model helps to locate all the hydrogen atoms.

Table II.1: Crystal data and details of the structure determination of **HLS^{Et}** and **C1**

	HLS ^{Et}	[Pd(LS ^{Et})Cl] (C1)
Formula	C ₂₂ H ₁₈ N ₂ OS ₂	C ₂₂ H ₁₇ ClN ₂ OPdS ₂
Formula Weight	390.50	531.34
Crystal System	<i>Orthorhombic</i>	<i>Monoclinic</i>
Space group	<i>P2₁2₁2₁</i>	<i>P2₁/n</i>
<i>a</i> (Å)	5.5339(2)	14.2991(7)
<i>b</i> (Å)	17.3619(7)	14.1025(9)
<i>c</i> (Å)	19.8744(8)	20.6517(10)
$\alpha/\beta/\gamma$ (°)	90/90/90	90/95.103(3)/90
<i>V</i> (Å ³)	1909.51(13)	4148.0(4)
<i>Z</i>	4	8
ρ (calc) (g/cm ³)	1.358	1.702
μ (Mo Ka) (mm ⁻¹)	0.293	1.242
<i>F</i> (000)	816	2128
Crystal Size (mm)	0.13 × 0.09 × 0.06	0.16 × 0.11 × 0.09
<i>T</i> (K)	296(2)	293(2)
Radiation wavelength (Å)	0.71073	0.71073
θ (Min-Max) (°)	1.557-27.501	1.67-27.31
<i>hkl</i> range	-7 to 7, -22 to 22 and - 25 to 25	-18 to 18; -17 to 17 and -25 to 26
Reflection No., <i>R</i> (int)	31196, 0.0339	8449, 0.0676
Observed data (<i>I</i> > 2 σ (<i>I</i>))	3688	5963
<i>N</i> ref, <i>N</i> par	4375, 248	8449, 524
<i>R</i> ^a , <i>wR</i> ₂ ^b , <i>S</i> ^c	0.0322, 0.0755, 1.028	0.0579, 0.1749, 1.095
Residual Density (e/Å ³)	-0.142 and 0.148	-0.982 and 0.891
CCDC	2128117	2128118

$$^a R_1 = \sum (|F_o| - |F_c|) / \sum |F_o|$$

$$^b wR_2 = \{ \sum [w (F_o^2 - F_c^2)^2] / \sum [w (F_o^2)^2] \}^{1/2}, w = 1/[\sigma^2(F_o^2) + (0.0424P)^2 + 0.1237P] \text{ for HLS}^{\text{Et}} \text{ and } w = 1/[\sigma^2(F_o^2) + (0.0727P)^2 + 12.3261P] \text{ for C1, where } P = (F_o^2 + 2 F_c^2)/3$$

$$^c \text{GOF (S)} = \{ \sum [w(F_o^2 - F_c^2)^2] / (n - p) \}^{1/2}, \text{ where } n = \text{number of measured data and } p = \text{number of parameters.}$$

II.2.4. Computational method

Complete geometry optimizations of HLS^{Et} and the complex C1 were done by DFT method exploiting B3LYP hybrid exchange correlation functional [35,36] in Gaussian09 program package [37]. For palladium atom LanL2DZ effective core potential basis set [38-40], while for other atoms all electron basis set 6-31+G(d) was employed. The percentage of contributions of different groups to the molecular orbital was calculated using the GaussSum program [41]. The UV-Vis spectral properties of the compounds in acetonitrile were computed by TDDFT method [42-44] using CPCM method [45-47].

II.2.5. DNA-binding studies

II.2.5.1. UV-Vis absorption studies

A stock solution of complex (1.0×10^{-4} M) was prepared in 1:10 acetonitrile/buffer mixture (Tris-HCl/ NaCl buffer of pH 7.4). A stock solution of CT-DNA (2.19×10^{-3} M) was prepared in buffer solution. The absorption spectrum of the complex was measured between 300 and 600 nm. CT-DNA solution was gradually added to it, stirred properly, and equilibrated for 4 min before collecting the spectra. Addition continued until saturation occurred. These spectral-titration results are essential for determining the binding constant (K_b) with CT-DNA. Eq. (1) was used to determine K_b (in M^{-1}) [48].

$$[\text{DNA}]/(\varepsilon_a - \varepsilon_f) = [\text{DNA}]/(\varepsilon_b - \varepsilon_f) + 1/K_b(\varepsilon_b - \varepsilon_f) \dots\dots\dots (1)$$

Where [DNA] is the concentration of CT DNA in base pairs, the extinction coefficients $\varepsilon_a, \varepsilon_f$ and ε_b correspond to $A_{\text{obs}}/[\text{complex}]$, free Pd(II) complex, and the extinction coefficient of the Pd(II) complex when it is in totally bound form, respectively. The plot of $[\text{DNA}]/(\varepsilon_a - \varepsilon_f)$ against [DNA] will produce slope $1/(\varepsilon_b - \varepsilon_f)$ and intercept $1/K_b(\varepsilon_b - \varepsilon_f)$; K_b is the ratio of slope to intercept.

II.2.5.2. Competitive binding study with EB by fluorescence method

The ability of the synthesized palladium complex (**C1**) to dislocate EB from its EB-CTDNA complex was studied by the fluorescence method. 10 μM EB and 10 μM CT-DNA were mixed homogeneously to prepare the CTDNA–EB adduct in Tris-HCl/NaCl buffer solution (pH 7.4). Upon excitation at 540 nm of the resulting mixture an emission maxima observed at 608 nm. Quenching of that emission was monitored with the subsequent addition of **C1**.

II.2.6. BSA binding studies

The binding interaction between BSA and Pd(II) complex (**C1**) was examined by UV-Vis and fluorescence methods. A stock solution of BSA was prepared using 500 mM phosphate buffer saline (PBS) at pH 7.4. Concentration of BSA solution was measured by taking the absorbance at 280 nm (molar extinction coefficient $66,400 \text{ dm}^3 \text{ mol}^{-1} \text{ cm}^{-1}$) [49]. Stock solution of **C1** was prepared in DMSO medium and was suitably diluted with PBS whenever necessary. UV-Vis spectra of BSA solution (10 μM) were taken with the variation of complex concentration. The changes in tryptophan-based fluorescence of BSA in the presence of **C1** were studied with the excitation wavelength at 280 nm. Quenching of emission intensity at $\sim 336 \text{ nm}$ for BSA was monitored with subsequent addition of **C1**.

II.2.7. Cell viability and proliferation assays

II.2.7.1. MTT Assay

Viability of human gastric cancer cells (AGS) and normal liver cells (WRL 68) was carried out by MTT assay [50]. The cultured cell lines were treated with different concentrations of HLS^{Et} and palladium complex **C1** (1, 100, 200, 300, 400 and 500 μM) in 96 well plates. After 24 hours of treatment, 100 μL DMSO was mixed to each well of 96 well plate and absorbance at 570 nm was measured using Microtiter plate reader. The results were plotted in graph pad prism as percentage of viable cells in each well and 100% viable cells was characterized as a control. IC_{50} values were computed by nonlinear regression fit using log

(inhibition) vs. response plot. The log of drug concentration and the optical density was represented on x-axis and y-axis respectively.

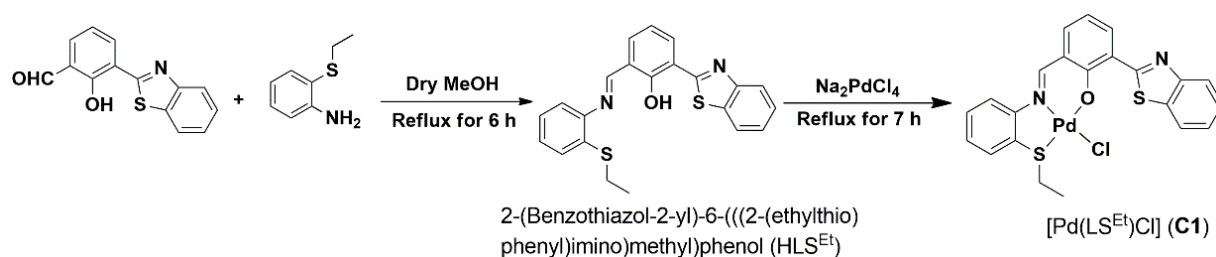
II.2.7.2. Colony Formation Assay

Each well of a 6 well plate, having approximately 500 AGS cells, was treated with HLS^{Et} (72.15 μ M) and palladium complex **C1** (9.55 μ M) and incubated for 24 h. After that cell were cultured in clean cell media till the colonies developed from the single cells. Formed colonies were washed and fixed using 1X PBS and 10% methanol respectively. Cells colonies were then stained using haematoxylin observed under Bright Field Microscope (Leica DM1000, Germany). Using the graph pad prism software, we plotted a graph of colony percentages relative to the control on the x-axis and IC₅₀ concentration of HLS^{Et} and palladium complex **C1** in the y-axis.

II.3. Results and discussion:

II.3.1. Synthesis and spectral characterization

The palladium(II) complex, [Pd(LS^{Et})Cl] (**C1**) with benzothiazole based pincer ligand (HLS^{Et}) is synthesized by the reaction of Na₂PdCl₄ with HLS^{Et} ligand in 1:1 molar ratio in acetonitrile under refluxing condition (**Scheme II.1**). Both HLS^{Et} and its Pd(II) complex, **C1** are thoroughly characterized by spectroscopic techniques. IR spectrum of free ligand HL showed $\nu(\text{C}=\text{N})$ at 1608 cm^{-1} , which upon complexation with Pd(II) shifted to 1596 cm^{-1} , confirming the probable complex formation. In ¹H NMR spectra, the HC=N proton of the palladium complex (**C1**) shows a singlet peak at 9.33 ppm, whereas HC=N proton of free HLS^{Et} appears at 8.72 ppm. Aromatic proton signals for **C1** appear at 7.01-8.79 ppm in CDCl₃. UV-Vis spectrum of HLS^{Et} exhibits high energy intense bands at 363 nm and 288 nm associated with a shoulder peak at 312 nm. For Pd(II) complex (**C1**) two strong and sharp bands appear at 465 nm and 321 nm in acetonitrile. In addition, two shoulder peaks appear at 438 nm and 355 nm (Fig.II.5).



Scheme II.1. Synthesis of ligand (HLS^{Et}) and its palladium(II) complex, [Pd(LS^{Et})Cl] (C1)

II.3.2. Crystal structures of HL¹, [Pd(L¹)₂] (1) and [Pd(L²)₂] (2)

Geometries of HLS^{Et} and C1 were further confirmed by single-crystal X-ray diffraction method. HLS^{Et} crystallizes in the orthorhombic crystal system with $P2_12_12_1$ space group, whereas complex C1 crystallizes in the monoclinic system containing $P2_1/n$ space group (Table II.1). Fig. II.8 and Fig. II.9 represent the ORTEP plots for HLS^{Et} and C1, respectively. Some selected bond distances and bond angles of the complex are presented in Table II.2. The distortion from square planar geometry for palladium complex (C1) is evident from bond parameters. Chelation of HLS^{Et} with palladium metal is done by thioether S, imino N and phenolic O atom in the complex. The imine bond distance, N1-C7 (1.282(3) Å) in HLS^{Et} is significantly elongated in the complex, C1 (1.301(10) Å) due to the coordination of imine-N to Pd and $d\pi(\text{Pd}) \rightarrow \pi^*(\text{CH}=\text{N})$ back donation in the complex. The Pd-N bond (Pd1-N1) distance 1.983(6) Å in C1 is in good agreement with the reported Pd-N(imine) bond distances [51,52]. Pd-O(phenolate) bond distance (Pd1-O1, 1.997(5) Å) in C1 is also well correlated with the reported Pd-O bond distances [53,54]. Likewise, the Pd-S(thioether) bond distance, 2.224(2) Å in the complex is also well corroborated with the reported bond distances [51-54]. Moreover, the DFT optimized bond parameters of C1 are also well correlated with the X-ray bond distances and angles with the maximum deviation in Pd-S bond distance by ~ 0.071 Å (Table II.2).

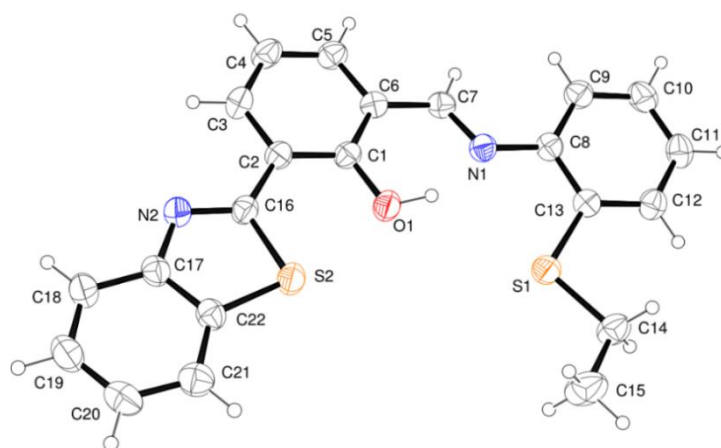


Fig.II.8. ORTEP plot of HLS^{Et} with 35% ellipsoidal probability

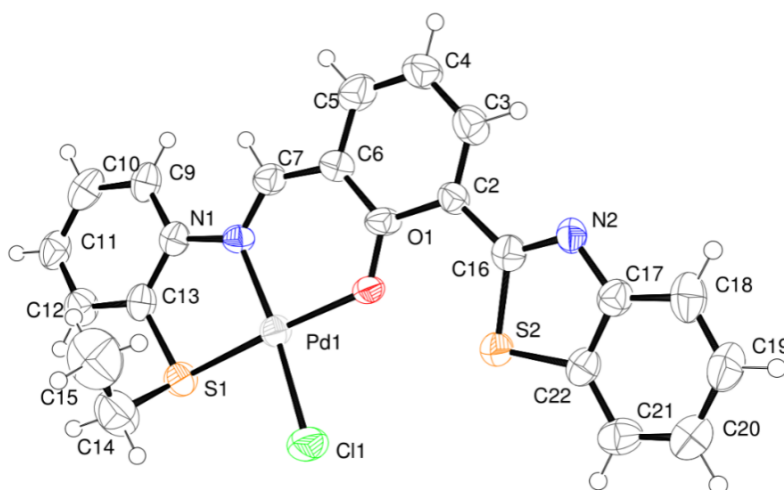


Fig.II.9. ORTEP plot of C1 with 35% ellipsoidal probability

Table II.2: X-ray and calculated (DFT/B3LYP) bond distances (Å) and angles (°) of **C1**

Bonds(Å)	X-ray	Calc.
Pd1 - N1	1.983(6)	2.039
Pd1 - O1	1.997(5)	2.025
Pd1 - S1	2.224(2)	2.295
Pd1 - Cl1	2.311(2)	2.336
S1- C13	1.772(8)	1.799
S1 - C14	1.821(11)	1.857
O1 - C1	1.298(9)	1.292
N1 - C7	1.301(10)	1.314
N1 - C8	1.439(9)	1.423
Angles (°)		
N1 - Pd1 - O1	94.2(2)	93.017
N1 - Pd1 - S1	87.28(18)	86.426
N1 - Pd1 - Cl1	173.55(19)	175.612
O1 - Pd1 - S1	175.12(17)	177.498
O1 - Pd1 - Cl1	90.00(16)	91.237
S1 - Pd1 - Cl1	88.88(8)	89.369

II.3.3. DFT calculations

To understand the electronic structures, geometries of HLS^{Et} and **C1** are optimized by DFT/B3LYP method. Contour plots of some selected molecular orbitals obtained from DFT calculations are given in Fig.II.10 and Fig.II.11 for HLS^{Et} and **C1**, respectively. Energy and % of composition of some selected MOs for **C1** are tabulated in Table II.3. HOMO of **C1** has 97% contribution of ligand fragments with a significant contribution of phenolate moiety.

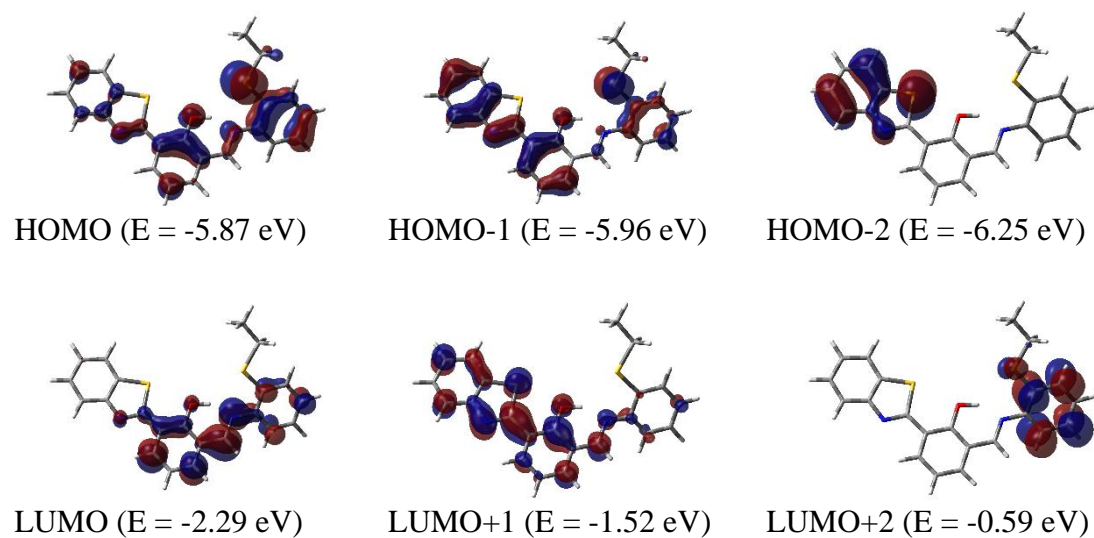


Fig.II.10. Contour plots of some selected molecular orbital of HLS^{Et}

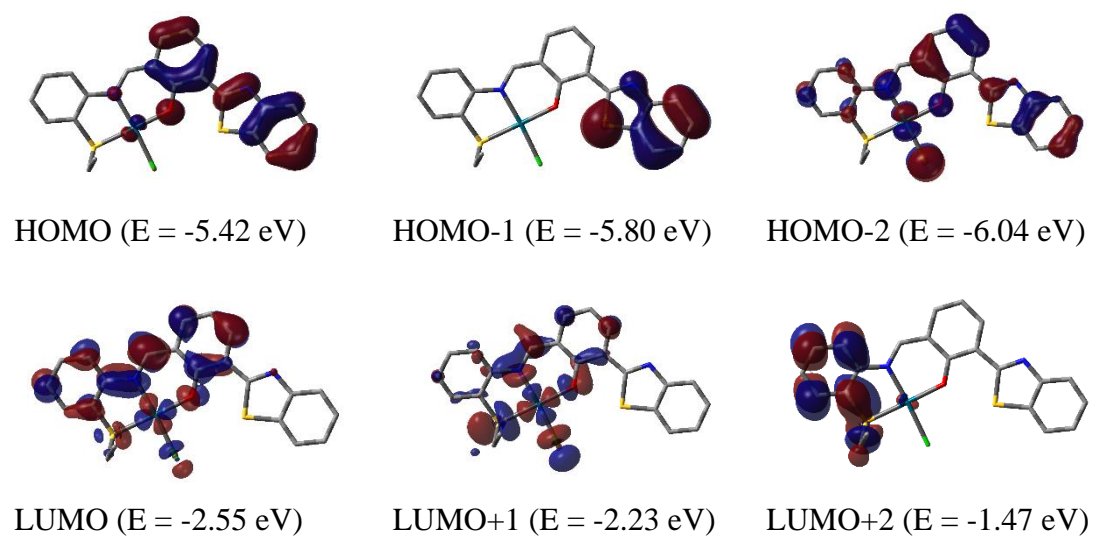


Fig.II.11. Contour plots of selected molecular orbitals of complex C1

Table II.3. Energy and compositions (%) of selected molecular orbitals of **C1**

MO	C1			
	E (eV)	% of composition		
		Pd	LS ^{Et}	Cl
LUMO+5	-0.05	90	10	0
LUMO+4	-0.44	02	98	0
LUMO+3	-1.11	0	100	0
LUMO+2	-1.47	02	97	0
LUMO+1	-2.23	38	51	11
LUMO	-2.55	12	85	03
HOMO	-5.42	02	97	01
HOMO-1	-5.80	0	100	0
HOMO-2	-6.04	14	69	17
HOMO-3	-6.50	16	11	73
HOMO-4	-6.55	18	36	47
HOMO-5	-6.86	71	20	09
HOMO-6	-6.97	03	96	01
HOMO-7	-7.03	10	81	09
HOMO-8	-7.43	14	77	09
HOMO-9	-7.59	07	91	02
HOMO-10	-7.64	37	52	11

The HOMO-1 has 100% ligand contribution, whereas HOMO-2 has 69% ligand contribution along with a reduced contribution (17%) of $p\pi(\text{Cl})$ and $d\pi(\text{Pd})$ (14%) orbitals. HOMO-3 has 73% $p\pi(\text{Cl})$ and 16% $d\pi(\text{Pd})$ character. LUMO of **C1** has 85% $\pi^*(\text{LS}^{\text{Et}})$ character, and LUMO+1 has mixed $\pi^*(\text{LS}^{\text{Et}})$ (51%) and $d\pi(\text{Pd})$ (38%) character. The energy gap between HOMO and LUMO for **C1** is obtained to be 2.87 eV is reduced compared to the free ligand HOMO-LUMO energy gap (3.58 eV).

II.3.4. TDDFT calculation and electronic spectra

To elucidate the electronic transitions in HLS^{Et} and **C1**, TDDFT calculation was carried out in acetonitrile employing TDDFT/CPCM method. Calculated electronic transitions for HLS^{Et} and **C1** are summarized in Table II.4.

Table II.4. Vertical electronic transitions of HLS^{Et} and **C1** calculated by TDDFT/CPCM method

Comps.	λ (nm)	E (eV)	Osc. Strength (f)	Key excitations	Character ^a	$\lambda_{\text{expt.}}$ (nm) (ϵ , $\text{M}^{-1}\text{cm}^{-1}$)
HLS^{Et}	409.2	3.0300	0.1967	(98%)HOMO→LUMO	$\text{p}\pi(\text{S})/\pi\rightarrow\pi^*$	
	371.2	3.3401	0.2992	(88%)HOMO-1→LUMO	$\pi\rightarrow\pi^*$	363 (11174)
	327.8	3.7819	0.2558	(77%)HOMO-2→LUMO	$\pi\rightarrow\pi^*$	312 (15567)
	307.0	4.0386	0.5199	(83%)HOMO-1→LUMO+1	$\pi\rightarrow\pi^*$	288 (23251)
	286.8	4.3224	0.1669	(82%)HOMO-2→LUMO+1	$\pi\rightarrow\pi^*$	
C1	527.5	2.3505	0.0207	(73%)HOMO→LUMO	$\pi(\text{L})\rightarrow\pi^*(\text{L})$ (ILCT)	
	455.0	2.7252	0.1331	(47%)HOMO→LUMO+1 (23%)HOMO→LUMO	$\pi(\text{L})\rightarrow\pi^*(\text{L})/\text{d}\pi(\text{Pd})$ (ILCT/LMCT)	465 (10371)
	431.4	2.8741	0.1041	(41%)HOMO→LUMO+1 (25%)HOMO-3→LUMO	$\pi(\text{L})\rightarrow\pi^*(\text{L})/\text{d}\pi(\text{Pd})$ $\text{p}\pi(\text{Cl})\rightarrow\pi^*(\text{L})$ (XLCT)	438 (sh.)
	397.6	3.1183	0.0461	(43%)HOMO-5→LUMO (31%)HOMO-5→LUMO+1	$\text{d}\pi(\text{Pd})\rightarrow\pi^*(\text{L})$ (MLCT)	
	372.9	3.3250	0.1921	(77%)HOMO-1→LUMO	$\pi(\text{L})\rightarrow\pi^*(\text{L})$ (ILCT)	355 (sh.)
	323.1	3.8378	0.4111	(91%)HOMO→LUMO+2	$\pi(\text{L})\rightarrow\pi^*(\text{L})$ (ILCT)	321 (19156)
	294.1	4.2160	0.1967	(39%)HOMO-6→LUMO+1 (32%)HOMO-9→LUMO	$\pi(\text{L})\rightarrow\pi^*(\text{L})$ (ILCT)	298 (16064)
	289.7	4.2803	0.1835	(67%)HOMO-1→LUMO+2	$\pi(\text{L})\rightarrow\pi^*(\text{L})$ (ILCT)	

^a ILCT: Intra-ligand charge transfer; XLCT: halogen to ligand charge transfer; MLCT: metal to ligand charge transfer; LMCT: ligand to metal charge transfer.

The calculated band at 455 nm ($f = 0.133$) for **C1** is in good agreement with the experimental band at 465 nm ($\epsilon = 10371 \text{ M}^{-1}\text{cm}^{-1}$) corresponds to the mixed HOMO \rightarrow LUMO/LUMO+1 transitions having mixed ILCT and LMCT character. The experimental shoulder peak at 438 nm resembles with the calculated band at 431 nm ($f = 0.104$) with mixed HOMO \rightarrow LUMO+1 and HOMO-3 \rightarrow LUMO transitions with combined ILCT and LMCT character along with a reduced contribution of halogen to ligand charge transfer (XLCT). The high energy band that appeared at 321 nm corresponds to the ILCT character (Table II.4).

II.3.5. DNA binding studies

II.3.5.1. UV-Vis method

To understand the mode of interactions with DNA is very crucial for the development of new anti-cancer drugs. At present, the spectroscopic methods are widely used to study the mode of interactions. These studies show that the drugs can interact with DNA covalently or by non-covalent interaction, groove binding or by electrostatic interactions [55,56]. Absorption and emission spectroscopies are widely used to interpret the mode of interactions of drug molecules with DNA [57]. UV-Vis is a powerful tool to assess how well palladium the complexes bind to CT DNA [58]. The absorption spectra of complex **C1** were taken in the presence and absence of CT DNA. **C1** exhibits a broad peak at 470 nm, but in the presence of CT DNA, a hypochromic shift in the absorption spectra is observed (Fig.II.12). The intrinsic binding constant (K_b) was evaluated to understand the affinity of the complex towards CT DNA. The K_b value of the Pd(II) complex (**C1**) is $4.01 \times 10^5 \text{ M}^{-1}$ which is comparable to the reported literature values [59,60].

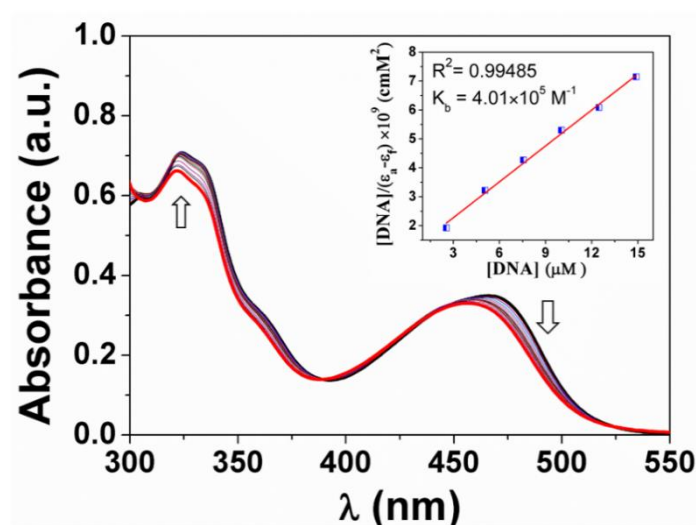


Fig.II.12. Absorption spectra of complex **C1** in Tris-HCl/NaCl buffer upon increasing CT DNA concentrations. Inset: Plot of $[DNA]/(\epsilon_a - \epsilon_f)$ vs. $[DNA]$

II.3.5.2. Fluorescence method

The present palladium complex, **C1** is non-fluorescent in solution with or without CT DNA. But when ethidium bromide (EB), a typical intercalator, forms EB-CT DNA intercalating complex, there is a mammoth increase in fluorescence intensity of EB at 605 nm upon excitation at 540 nm [61]. Upon steady addition of Pd(II) complex, the fluorescence intensity is successively decreased due to the replacement of EB from its EB-CT DNA system (Fig.II.13) [62]. The titration curves clearly demonstrate the competition between the complex and EB for DNA binding sites. A linear Stern-Volmer equation (Eq. (1)) [63] accords well with the fluorescence quenching curve of the EB-CT DNA system for the complex.

$$I_0/I = 1 + K_{sv}[Q] \dots \dots \dots (1)$$

Where I and I_0 signify the fluorescence intensities of the EB-CT DNA system with and without the complex, respectively, K_{sv} is the Stern-Volmer quenching constant, and $[Q]$ is the molar concentration of the complex (quencher). K_{sv} value is obtained from the slope of the plot and is found to be $4.3 \times 10^5 \text{ M}^{-1}$ for **C1**.

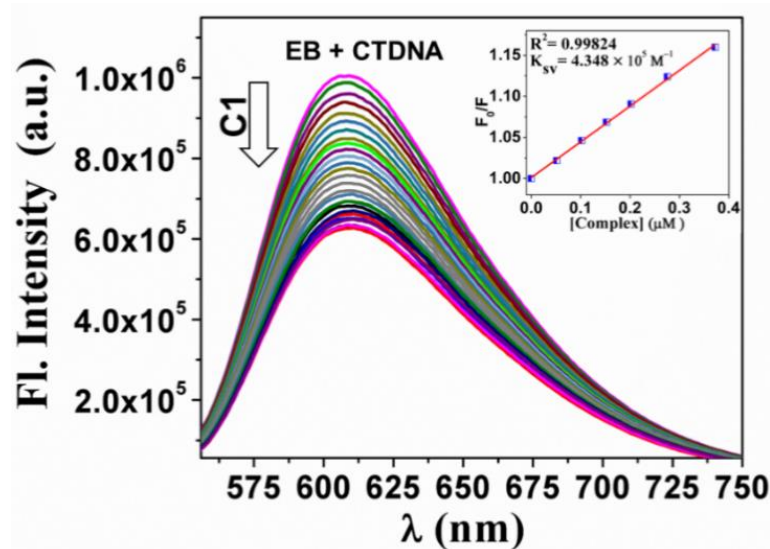


Fig.II.13. Emission spectra of EB–CT DNA ($\lambda_{\text{ex}}=540$ nm) in presence of increasing concentrations of **C1**. Inset: Plots of emission intensity F_0/F vs. [complex]

II.3.6.BSA binding studies

II.3.6.1. UV-Vis method

The interaction of palladium(II) complexes with bovine serum albumin (BSA) provides the information about the intrinsic fluorescence property of BSA. UV-Vis spectra of BSA solution (10 μM in PBS at pH 7.4) were recorded in the range of 200-500 nm in presence of variable concentration of the complex (**C1**), shown in Fig.II.14 BSA has a characteristic band at 280 nm. Gradual addition of **C1** (100 μL) to the BSA solution causes a steady increase in absorption intensity at 280 nm along with a bit of blue shift. This hypsochromic shift attributes to the ground-state alliance between the complex and protein [64,65]. The apparent association constant (K_a) was calculated from the plot of $1/(A_{\text{obs}}-A_0)$ vs. $1/[\text{complex}]$ (Fig.II.14 inset) adopting the following equation [66,67].

$$\frac{1}{A_{\text{obs}} - A_0} = \frac{1}{A_c - A_0} + \frac{1}{K_a(A_c - A_0)[\text{complex}]}$$

Where A_{obs} indicates the observed absorbance (at 280 nm) of the solution having various concentrations of **C1**, A_0 and A_c denote BSA absorbance in the absence and presence of **C1**. The calculated value of an apparent association constant (K_a) for the complex (**C1**) is $2.8 \times 10^4 \text{ M}^{-1}$ which matches well with the literature values for Pd(II) complexes [68-71].

II.3.6.2. Fluorescence method

The BSA-complex interactions were also studied by fluorescence spectral titration method. The complex is non-fluorescent in DMSO solution. But upon excitation at 280 nm, BSA exhibits a strong fluorescence at 336 nm. With the subsequent addition of 100 μL complex (**C1**) to the BSA solution, the fluorescence intensity of BSA at ~ 336 nm was dramatically quenched (58.26 % quenching) (Fig.II.15). This hypochromicity in the spectra is mainly attributed to the interaction of **C1** with BSA. The Stern-Volmer quenching constant value (K_{sv}) was calculated [72] and depicted in Fig.II.16 The high K_{sv} ($5.5 \times 10^4 \text{ M}^{-1}$) value indicates that the complex exhibits a good fluorescence quenching ability. To learn more about the quenching effect, the equilibrium binding constant (K_b) and number of binding sites (n) available for the complex were also calculated from the graph of $\log [(F_0 - F)/F]$ versus $\log [\text{complex}]$ (Fig.II.15 inset) applying the Scatchard equation [73,74] below:

$$\log \frac{(F_0 - F)}{F} = \log K_b + n \log [\text{complex}]$$

Based on the plot, calculated values of n and K_b for the complex are 0.947 and $2.92 \times 10^4 \text{ M}^{-1}$ respectively, which reflects the strong affinity of the complex with the serum albumins.

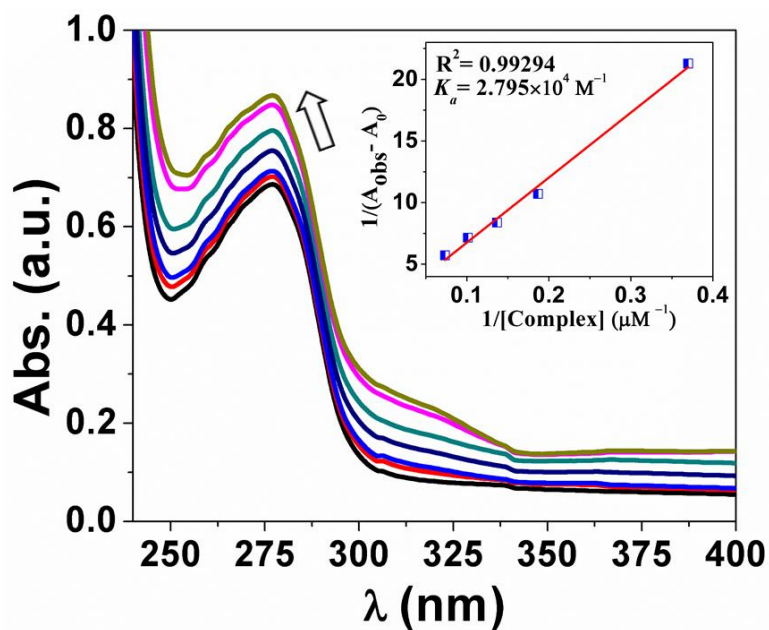


Fig.II.14. Absorption spectra of BSA (10 μM aqueous solution) upon increasing concentrations of C1 at 300 K. Insets: $1/(A_{\text{obs}} - A_0)$ vs. $1/[\text{Complex}]$ plots of BSA absorption titration

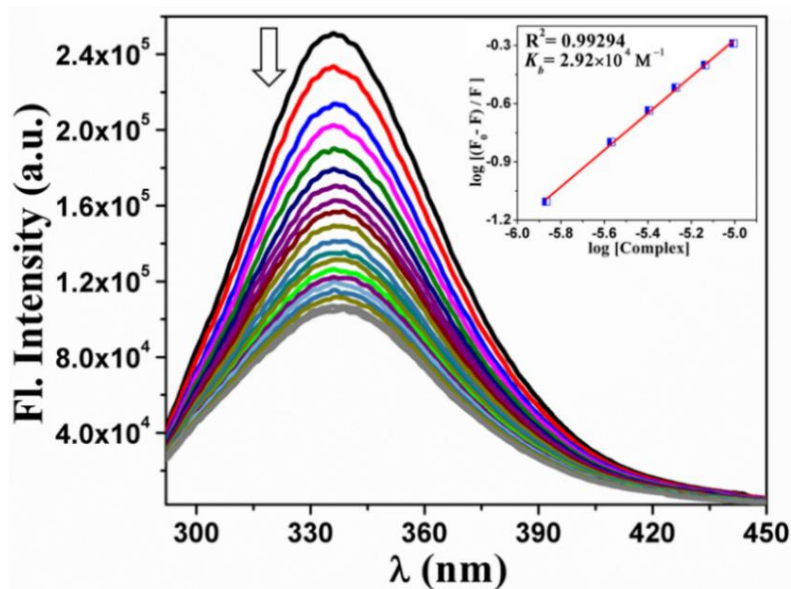


Fig.II.15. Change in emission spectra of BSA (10 μM) upon gradual addition of C1 at 300 K ($\lambda_{\text{ex}}=280$ nm, $\lambda_{\text{em}}=336$ nm). Insets: Scatchard plots of the BSA fluorescence titration

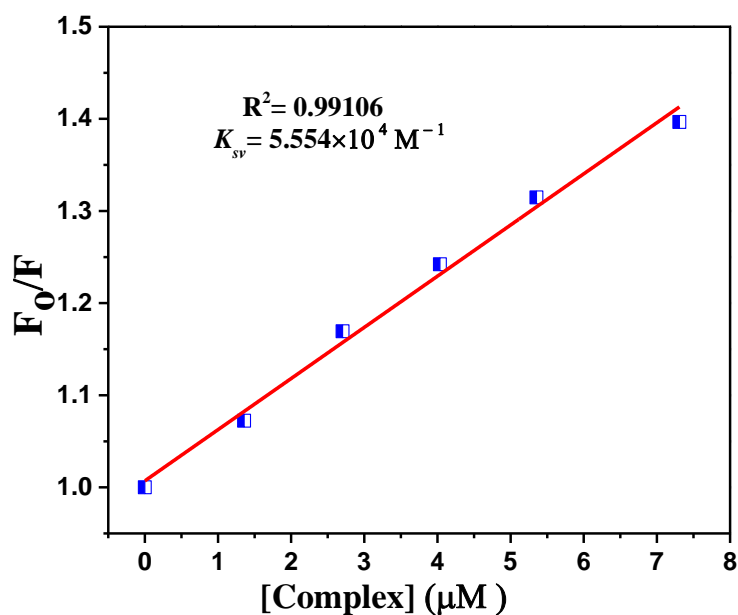


Fig.II.16. Stern-Volmer fluorescence quenching plot obtained by titration of BSA solution with the complex (C1)

II.3.7. *In vitro* antiproliferative studies

II.3.7.1. MTT Assay

The effect of ligand (HLS^{Et}) and palladium (II) complex **C1** on the proliferation of gastric cancer cells was evaluated by MTT assay method. The percentage of viable cell against various concentrations frame is shown in Fig.II.17. Results unveiled a dose-dependent antiproliferative effect of HLS^{Et} and **C1** as compared to the control. The highest concentration of palladium complex (500 $\mu\text{g/ml}$) significantly decreases the viability of gastric cancer cells up to 3.1% in contrast to the free ligand (HLS^{Et}). IC_{50} values of treated AGS cells were determined by nonlinear plot. IC_{50} values against AGS cell line were calculated as $72.15 \pm 1.87 \mu\text{M}$ and $9.55 \pm 1.23 \mu\text{M}$ for HLS^{Et} and **C1** respectively (Table II.5). Moreover, the IC_{50} value of the present palladium(II) complex is found to be less compared to the cisplatin against AGS cell lines ($\text{IC}_{50} = 23.13 \pm 1.03$) (Fig.II.18). We have also investigated the effect of palladium(II) complex (**C1**) on a normal cell line, WRL 68, by

MTT assay (Fig.II.19). The result showed that **C1** has no significant cytotoxicity on WRL68 up to 200 μM concentration.

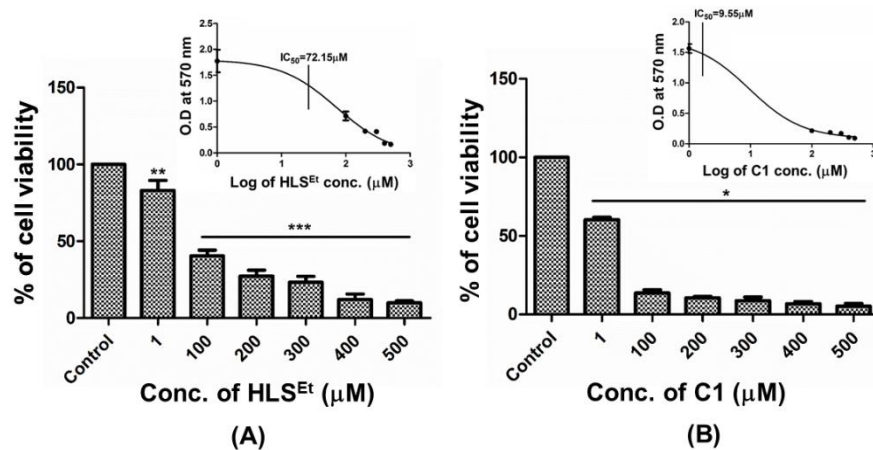


Fig.II.17. Viability of AGS cell lines upon increasing concentrations of (A) HLS^{Et} (B) C1 (In set: IC₅₀ values of AGS cell lines for HLS^{Et} and C1)

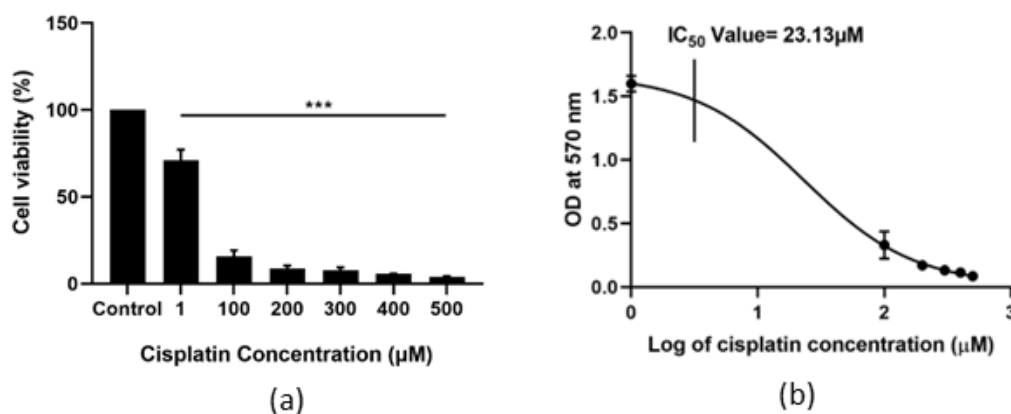


Fig.II.18.a. % of cell viability of cisplatin towards AGS cancer cell lines **b.** IC₅₀ of cisplatin towards AGS cell lines

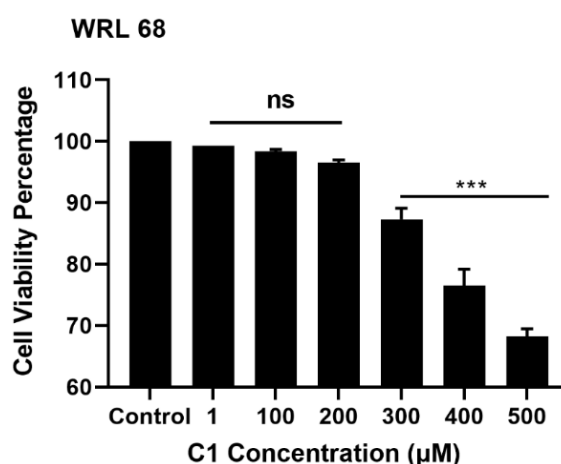


Fig.II.19. % of cell viability of **C1** towards WRL 68 cell lines

Table II.5. IC₅₀ value of free ligand (HLS^{Et}) and its Pd(II) complex (**C1**) determined by MTT assay on AGS cell line

Compounds	IC ₅₀ (µM ± SD)
HLS ^{Et}	72.15 ± 1.87
C1	9.55 ± 1.23
Cisplatin	23.13 ± 1.03

II.3.7.2. Colony Formation Assay

The Colony formation assay was done to evaluate the antiproliferative effect of palladium complex (**C1**) in gastric cancer cells. Cells were treated with HLS^{Et} (72.15 µM) and **C1** (9.55 µM) for 24 h. We plotted a graph showing the colony percentages relative to the control with respective to the IC₅₀ concentrations of HLS^{Et} and **C1** (Fig.II.21). Comparing control to both palladium complex (**C1**) and HLS^{Et}, fewer colonies were observed for the complex **C1** (Fig.II.20). Results show that palladium complex, **C1** diminished 50% of the colonies at low

concentration compared to HLS^{Et} . The results of this study confirmed that complex, **C1** reduced the cell viability (AGS cells) at a low dose when compared to HLS^{Et} .

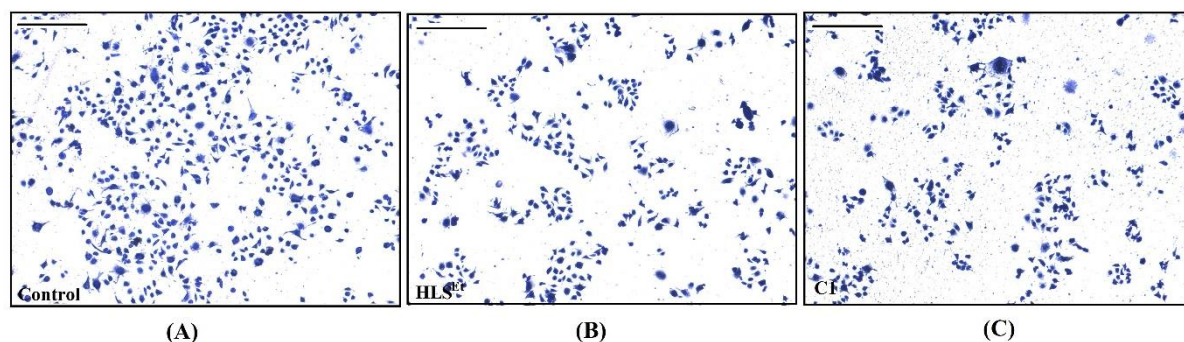


Fig.II.20. Colony formation of AGS cell lines (A) control and upon treatment of (B) HLS^{Et} (72.15 μM) and (C) **C1** (9.55 μM) for 24 h.

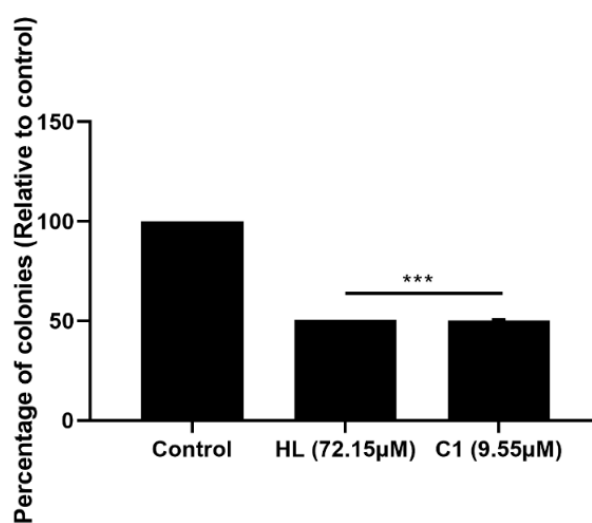


Fig.II.21. % of colonies of AGS cell lines relative to the control

II.4. Conclusions

New palladium(II) complex, $[\text{Pd}(\text{LS}^{\text{Et}})\text{Cl}]$ (**C1**) with benzothiazole based ONS donor pincer ligand (HLS^{Et}) is synthesized. Structures of both HLS^{Et} and **C1** are confirmed by crystallographic method. Interaction of **C1** with CT DNA and BSA proteins is investigated by absorption and fluorescence methods. The complex effectively displaces ethidium

bromide (EB) from its EB-DNA complex and Stern-Volmer quenching constant, K_{sv} is found to be $5.5 \times 10^4 \text{ M}^{-1}$. Cytotoxicity of the Pd(II) complex assessed by MTT assay method revealed that the half-maximal inhibitory concentration (IC_{50}) of the palladium(II) complex (C1) ($9.55 \pm 1.23 \mu\text{M}$) is less compared to cisplatin ($23.13 \pm 1.03 \mu\text{M}$) towards AGS cancer lines.

II.5. References

1. M. Naghavi, A. A. Abajobir, C. Abbafati, K. M. Abbas, F. Abd-Allah, S. F. Abera, V. Aboyans, O. Adetokunboh, A. Afshin, A. Agrawal and A. Ahmadi, *Lancet*, 2017, **390**, 1151.
2. T. Helleday, E. Petermann, C. Lundin, B. Hodgson and R. A. Sharma, *Nat. Rev. Cancer*, 2008, **8**, 193.
3. M. Fojta, A. Daňhel, L. Havran and V. Vyskočil, *Trends Anal. Chem.*, 2016, **79**, 160.
4. B. B. Zmejkovski, A. Savić, J. Poljarević, N. Pantelić, S. Arandžević, S. Radulović, S. Grgurić-Šipka, G. N. Kaluđerović and T. J. Sabo, *Polyhedron*, 2014, **80**, 106.
5. A. P. Koley, R. Nirmala, L. S. Prasad, S. Ghosh and P. T. Manoharan, *Inorg. Chem.*, 1992, **31**, 1764.
6. M. S. Jana, A. K. Pramanik, S. Kundu, D. Sarkar, S. Jana and T. K. Mondal, *Inorg. Chim. Acta*, 2013, **394**, 583.
7. A. P. Koley, S. Purohit, L. S. Prasad, S. Ghosh and P. T. Manoharan, *Inorg. Chem.*, 1992, **31**, 305.
8. S. Sinha, M. Chakraborty, N. R. Pramanik, T. K. Raychaudhuri, T. K. Mondal, D. Sarkar, M. G. Drew, S. Ghosh and S. S. Mandal, *Polyhedron*, 2013, **55**, 192.
9. J. K. Barton, *Science*, 1986, **233**, 727.
10. L. Zhou, D. Powell and K. M. Nicholas, *Inorg. Chem.*, 2007, **46**, 7789.
11. L. M. Berreau, *Eur. J. Inorg. Chem.*, 2006, 273.
12. K. Akdi, R. A. Vilaplana, S. Kamah and F. González-Vílchez, *J. Inorg. Biochem.*, 2005, **99**, 1360.
13. R. Prabhakaran, S. V. Renukadevi, R. Karvembu, R. Huang, J. Mautz, G. Huttner, R. Subashkumar and K. Natarajan, *Eur. J. Med. Chem.*, 2008, **43**, 268.

14. K. P. Balasubramanian, R. Karvembu, R. Prabhakaran, V. Chinnusamy and K. Natarajan, *Spectrochim. Acta A*, 2007, **68**, 50.
15. K. M. Vyas, R. G. Joshi, R. N. Jadeja, C. R. Prabha and V. K. Gupta, *Spectrochim. Acta A*, 2011, **84**, 256.
16. T. Rosu, E. Pahontu, C. Maxim, R. Georgescu, N. Stanica and A. Gulea, *Polyhedron*, 2011, **30**, 154.
17. F. Thomas, *Eur. J. Inorg. Chem.*, 2007, 2379.
18. N. J. Wheate, S. Walker, G. E. Craig and R. Oun, *Dalton Trans.*, 2010, **39**, 8113.
19. C. Monneret, *Ann. Pharm. Fr.*, 2011, **69**, 286.
20. S. E. Sherman, D. Gibson, A. H. Wang and S. J. Lippard, *J. Am. Chem. Soc.*, 1988, **110**, 7368.
21. R. E. Windsor, S. J. Strauss, C. Kallis, N. E. Wood and J. S. Whelan, *Cancer*, 2012, **118**, 1856.
22. M. N. Alam and F. Huq, *Coord. Chem. Rev.*, 2016, **316**, 36.
23. A. C. Caires, *Med. Chem.*, 2007, **7**, 484.
24. B. X. Huang, H. Y. Kim and C. Dass, *J. Am. Soc. Mass Spectrom.*, 2004, **15**, 1237.
25. N. Shahabadi, M. Maghsudi, Z. Kiani and M. Pourfoulad, *Food Chem.*, 2011, **124**, 1063.
26. Y. J. Hu, Y. Liu, X. S. Shen, X. Y. Fang and S.S. Qu, *J. Mol. Struct.*, 2007, **738**, 143.
27. S. Kundu, A. K. Pramanik, A. S. Mondal and T. K. Mondal, *J. Mol. Struct.*, 2016, **1116**, 1.
28. S. Kundu, S. Biswas, A. S. Mondal, P. Roy and T. K. Mondal, *J. Mol. Struct.*, 2015, **1100**, 27.
29. A. S. Mondal, M. S. Jana, C. K. Manna, R. Naskar and T. K. Mondal, *J. Mol. Struct.*, 2018, **1164**, 94.

30. S. Mondal, T. K. Mondal, Y. Rajesh, M. Mandal and C. R. Sinha, *Polyhedron*, 2018, **151**, 344.
31. M. S. Jana, A. K. Pramanik, D. Sarkar, S. Biswas and T. K. Mondal, *Polyhedron*, 2014, **81**, 66.
32. A. A. Bhosle, M. Banerjee, N. Barooah, A. C. Bhasikuttan, K. Kadu, S. R. Ramanan and A. Chatterjee, *J. Photochem. Photobiol. A: Chem.*, 2022, **426**, 113770.
33. G. M. Sheldrick, *Acta Cryst.*, 2008, **A64**, 112.
34. G. M. Sheldrick, *Acta Cryst.*, 2015, **C71**, 3.
35. A. D. Becke, *J. Chem. Phys.*, 1993, **98**, 5648.
36. C. Lee, W. Yang and R. G. Parr, *Phys. Rev. B*, 1998, **37**, 785.
37. M. J. Frisch, G. W. Trucks, H. B. Schlegel, G. E. Scuseria, M. A. Robb, J. R. Cheeseman, G. Scalmani, V. Barone, B. Mennucci, G. A. Petersson, H. Nakatsuji, M. Caricato, X. Li, H. P. Hratchian, A. F. Izmaylov, J. Bloino, G. Zheng, J. L. Sonnenberg, M. Hada, M. Ehara, K. Toyota, R. Fukuda, J. Hasegawa, M. Ishida, T. Nakajima, Y. Honda, O. Kitao, H. Nakai, T. Vreven, J. A. Montgomery, J. E. Peralta, F. Ogliaro, M. Bearpark, J. J. Heyd, E. Brothers, K. N. Kudin, V. N. Staroverov, R. Kobayashi, J. Normand, K. Raghavachari, A. Rendell, J. C. Burant, S. S. Iyengar, J. Tomasi, M. Cossi, N. Rega, J. M. Millam, M. Klene, J. E. Knox, J. B. Cross, V. Bakken, C. Adamo, J. Jaramillo, R. Gomperts, R. E. Stratmann, O. Yazyev, A. J. Austin, R. Cammi, C. Pomelli, J. W. Ochterski, R. L. Martin, K. Morokuma, V. G. Zakrzewski, G. A. Voth, P. Salvador, J. J. Dannenberg, S. Dapprich, A. D. Daniels, O. Farkas, J. B. Foresman, J. V. Ortiz, J. Cioslowski, J. D. Fox, 2009 Gaussian 09, revision D. 01. Gaussian Inc., C. T. Wallingford
38. J. Hay and W. R. Wadt, *J. Chem. Phys.*, 1985, **82**, 270.
39. W. R. Wadt and J. Hay, *J. Chem. Phys.*, 1985, **82**, 284.

40. P. J. Hay and W. R. Wadt, *J. Chem. Phys.*, 1985, **82**, 299.
41. N. M. O'Boyle, A. L. Tenderholt and K. M. Langner, *J. Comput. Chem.*, 2008, **29**, 839.
42. R. Bauernschmitt and R. Ahlrichs, *Chem. Phys. Lett.*, 1996, **256**, 454.
43. R. E. Stratmann, G. E. Scuseria and M. J. Frisch, *J. Chem. Phys.*, 1998, **109**, 8218.
44. M. E. Casida, C. Jamorski, K. C. Casida and D. R. Salahub, *J. Chem. Phys.*, 1998, **108**, 4439.
45. V. Barone and M. Cossi, *J. Phys. Chem. A*, 1998, **102**, 1995.
46. M. Cossi and V. Barone, *J. Chem. Phys.*, 2001, **115**, 4708.
47. M. Cossi, N. Rega, G. Scalmani and V. Barone, *J. Comput. Chem.*, 2003, **24**, 669.
48. M. Anjomshoa, H. Hadadzadeh, M. Torkzadeh-Mahani, S. J. Fatemi, M. Adeli-Sardou, H. A. Rudbari and V. M. Nardo, *Eur. J. Med. Chem.*, 2015, **96**, 66.
49. N. S. Quiming, R. B. Vergel, M. G. Nicolas and J. A. Villanueva, *J. Health Sci.*, 2005, **51**, 8.
50. T. L. Riss, R. A. Moravec, A. L. Niles, S. Duellman, H. A. Benink, T. J. Worzella and L. Minor 2013 Cell viability assays. Assay Guidelines manuals
51. P. Pattanayak, S. P. Parua, D. Patra, C. K. Lai, P. Brandao, V. Felix and S. Chattopadhyay, *Inorg. Chim. Acta*, 2015, **429**, 122.
52. C. K. Manna, R. Naskar, B. Bera, A. Das and T. K. Mondal, *J. Mol. Struct.*, 2021, **1237**, 130322.
53. M. M. Tamizh, B. F. T. Cooper, C. L. B. Macdonald and R. Karvembu, *Inorg. Chim. Acta*, 2013, **394**, 391.
54. P. Kalaivani, R. Prabhakaran, M. V. Kaveri, R. Huang, R. J. Staple and K. Natarajan, *Inorg. Chim. Acta*, 2013, **405**, 415.
55. C. X. Zhang and S. J. Lippard, *Curr. Opin. Chem. Biol.*, 2003, **7**, 481.

56. Q. L. Zhang, J. G. Liu, H. Chao, G. Q. Xue and L. N. Ji, *J. Inorg. Biochem.*, 2001, **83**, 49.
57. F. A. Tanious, D. Ding, D. A. Patrick, C. Bailly, R. R. Tidwell and W. D. Wilson, *Biochemistry*, 2000, **39**, 12091.
58. K. Akdi, R. A. Vilaplana, S. Kamah and F. Gonzalez-Vilchez, *J. Inorg. Biochem.*, 2005, **99**, 1360.
59. N. Bandyopadhyay, P. Basu, G. S. Kumar, B. Guhathakurta, P. Singh and J. P. Naskar, *J. Photochem. Photobiol. B*, 2017, **173**, 560.
60. C. V. Barra, F. V. Rocha, L. Morel, A. Gautier, S. S. Garrido, A. E. Mauro, R. C. G. Frem and A. V. G. Netto, *Inorg. Chim. Acta*, 2017, **446**, 54.
61. E. Nyarko, N. Hanada, A. Habib and M. Tabata, *Inorg. Chim. Acta*, 2004, **357**, 739.
62. J. B. Lepecq and C. Paoletti, *J. Mol. Biol.*, 1967, **27**, 87.
63. Y. Zhao, J. Zhu, W. He, Z. Yang, Y. Zhu, Y. Li, J. Zhang and Z. Guo, *Chem. Eur. J.*, 2006, **12**, 6621.
64. E. Ramachandran, D. S. Raja, N. P. Rath and K. Natarajan, *Inorg. Chem.*, 2013, **52**, 1504.
65. D. S. Raja, N. S. P. Bhuvanesh and K. Natarajan, *Inorg. Chem.*, 2011, **50**, 12852.
66. A. Wolfe, G. H. Shimer and T. Mehan, *Biochemistry*, 1987, **26**, 6392.
67. A. Paul, S. Mistri, A. Bhunia, S. Manna, H. Puschmann and S. C. Manna, *RSC Adv.*, 2016, **6**, 60487.
68. A. Shanmugapriya, G. Kalaiarasi, P. Kalaivani, F. Dallemer and R. Prabhakaran, *Inorg. Chim. Acta*, 2016, **449**, 107.
69. A. A. Franich, M. D. Živković, J. Milovanović, D. Arsenijević, A. Arsenijević, M. Milovanović, M. I. Djuran and S. Rajković, *J. Inorg. Biochem.*, 2020, **210**, 111158.

70. A. Ramezanpour, K. Karami, M. Kharaziha, M. Zakariazadeh, J. Lipkowski, A. Shahpiri, N. Azizi and M. Namazian, *Polyhedron*, 2021, **206**, 115333.
71. G. Ayyannan, M. Mohanraj, M. Gopiraman, R. Uthayamalar, G. Raja, N. Bhuvanesh, R. Nandhakumar and C. Jayabalakrishnan, *Inorg. Chim. Acta*, 2020, **512**, 119868.
72. J. R. Lakowicz, *Principles of Fluorescence Spectroscopy*, Third Edition., Springer, New York, USA, 2006.
73. J. R. Lakowicz, *Fluorescence Quenching: Theory and applications*, Principles of Fluorescence Spectroscopy, Kluwer Academic/Plenum Publishers, New York, 1999, p. 53.
74. X. Z. Feng, Z. Lin, L. J. Yang, C. Wang and C. L. Bai, *Talanta*, 1998, **47**, 1223.

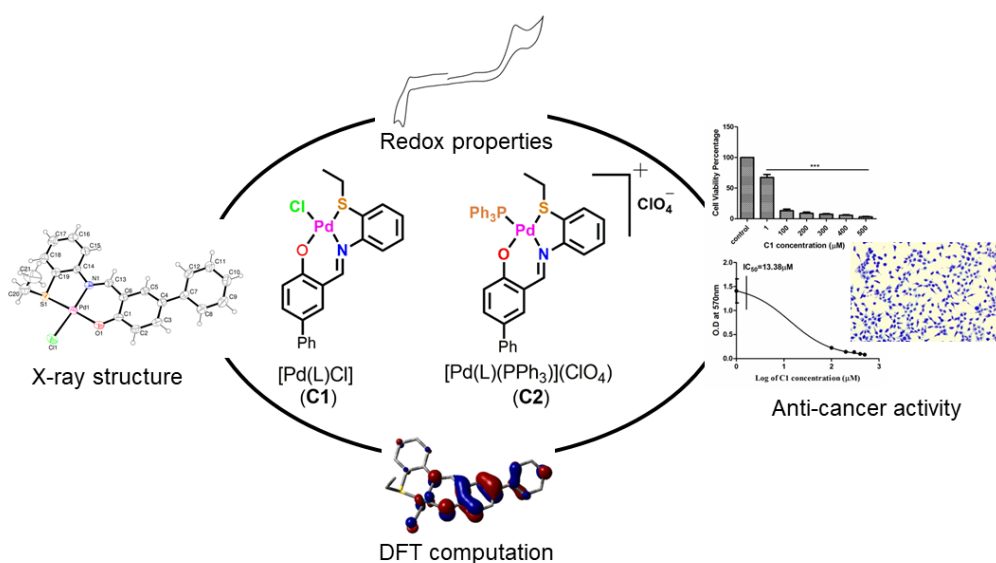
CHAPTER-III

Palladium(II) complexes with thioether based ONS donor ligand: Synthesis, characterization, X-ray structure, DFT study and anti-cancer activity

Palladium(II) complexes with thioether based ONS donor ligand: Synthesis, characterization, X-ray structure, DFT study and anti-cancer activity

Abstract

Synthesis of new palladium(II) complexes, $[\text{Pd}(\text{L})\text{Cl}]$ (**C1**) and $[\text{Pd}(\text{L})\text{PPh}_3](\text{ClO}_4)$ (**C2**), with ONS donor thioether ligand (HL) is reported. All the complexes were thoroughly characterized by using numerous spectroscopic techniques like FT-IR, NMR and UV-visible spectroscopy and so forth. Distorted square planar geometries of the complexes were confirmed unambiguously by means of single crystal X-ray diffraction analysis. Moreover, DFT and TDDFT calculations were performed to interpret the electronic structure, redox and spectral properties of the complexes. Cytotoxicity of the complexes was evaluated in vitro using MTT assay on human gastric cancer cell lines (AGS). The anti-cancer effects of HL and palladium(II) complexes (**C1/C2**) on AGS cell lines were determined by comparing the half maximal inhibitory concentration (IC_{50}) values. The results revealed that synthesized palladium(II) complexes (**C1/C2**) showed higher anti-cancer activity ($\text{IC}_{50} = 13.4 \mu\text{M}$ for **C1** and $16.0 \mu\text{M}$ for **C2**) compare to HL against AGS cell lines ($67.1 \mu\text{M}$).



III.1. Introduction

In recent years, transition metal complexes incorporated with ONS donor ligands are considerably studied because of their mode of coordination, structural diversity, spectral features and extensive biological applications for instance antitumor, antifungal, antibacterial, antiviral, anti-tuberculosis and anti-inflammatory activities [1-5]. Furthermore, thioether ligands can stabilize unusual oxidation states of the transition metals within the complexes and participated in a variety of engrossing electrochemical reactions [6-8]. Schiff base ligand with transition metal complexes showcase pivotal inhibition of DNA synthesis via binding through intercalation mode [9]. Again, transition metal complexes with S and N donor chelating ligands are of great interest because of their significant antifungal, antibacterial and anticancer activities [10-14]. Sulfur atom of thioether ligand coordinated to metal centre can also mimic the active sites of numerous metalloproteins [15-17]. Moreover, transition metal complexes with polydentate ligands are important due to the fact that they are capable to binding and cleaving of DNA under physiological conditions [18, 19].

In general, metal-based drugs like cisplatin ($\text{cis-Pt}(\text{NH}_3)_2\text{Cl}_2$), an antitumor drug, exhibits its cytotoxic activity by targeting DNA and forming covalent bonds between the platinum metal and the close by purine bases through their N7 positions [20]. But cisplatin suffers severe consequences like nephrotoxicity and ototoxicity [21, 22], which stimulate researchers to discover alternative chemotherapeutic strategies. In this context, palladium can also be a better alternative for platinum as anticancer drug because of their coordination capability, thermodynamical, structural and chemical similarities [23]. But ligand exchange activities of the palladium complexes display almost 10^4 - 10^5 times more than their platinum counterparts [24] and leads to the formation of undesired chemical species before reaching to the target biomolecules [25]. This problem can be addressed by using suitable chelating agents to form stable complexes. In addition, ligands like pyridine and its derivatives,

quinoline, pyrazole and 1,10-phenanthroline coordinated with Pd(II) ions have proven promising antitumor activities [26-28]. Consequently, new derivatives of palladium(II) complexes may be designed to enhance anticancer activity and reduce toxicity.

In recent years, the coordination chemistry of transition metal complexes with thioether ligands are extensively studied by our group [29-35], herein we have synthesized two palladium(II) complexes, [Pd(L)Cl] (**C1**) and [Pd(L)PPh₃](ClO₄) (**C2**) with ONS donor thioether ligand (HL). The complexes were thoroughly characterized by numerous spectroscopic techniques. The geometries of the complexes were confirmed by single crystal X-ray diffraction study. Theoretical calculations with the aid of DFT/B3LYP approach were executed to interpret the electronic structure, redox and spectral properties of the complexes.

III.2. Experimental

III.2.1. Materials and methods

All the reagents and solvents were commercially available grade and were used as received. 2-Aminothiophenol, PdCl₂ and [n-Bu₄N][ClO₄] (TBAP) were purchased from Sigma Aldrich. 4-Hydroxy-[1,1'-biphenyl]-3-carbaldehyde was prepared following the published procedure [35].

Microanalyses (C, H, N) were carried out using PerkinElmer Series-II CHN-2400 CHNS/O elemental analyzer. UV-Visible and IR spectra were recorded on a PerkinElmer UV/VIS spectrophotometer (model: Lambda 25) and PerkinElmer Spectrum RX1 FT-IR spectrometer respectively. NMR spectra were recorded in CDCl₃ on a Bruker (AC) 300 MHz FT-NMR spectrometer in the presence of TMS as internal standard. HRMS mass spectra were taken on a Waters (XevoG2 Q-TOF) mass spectrometer. Cyclic voltammetric experiments were performed using a CHI Electrochemical workstation. A platinum wire working electrode, a platinum wire auxiliary electrode and Ag/AgCl reference electrode were

used in a standard three-electrode configuration using [n-Bu₄N][ClO₄] as supporting electrolyte with solute concentration $\sim 10^{-3}$ M and scan rate of 50 mV s⁻¹.

III.2.2. Synthesis

III.2.2.1. Synthesis of HL

In a 50 mL round bottom flask, 0.198 g (1 mmol) of 4-hydroxy-[1,1'-biphenyl]-3-carbaldehyde and 0.153 g (1 mmol) of 2-(ethylthio)aniline were dissolved in 25 mL of dry methanol and refluxed for ca. 6 h and cool down to room temperature. The solvent was then removed by slow evaporation to yield yellow crystalline product of HL. Yield: 0.254 g (76%).

Anal. Calcd. for C₂₁H₁₉NOS: C, 75.64; H, 5.74; N, 4.20. Found: C, 75.47; H, 5.64; N, 4.12.

IR (KBr, cm⁻¹): 2971 ν (CH), 1652 ν (C=N), 753 ν (C-S). ¹H NMR (300 MHz, CDCl₃): δ , 1.36 (3H, t, J=7.3), 2.96 (2H, q, J=7.2), 7.12-7.56 (12H, ArH, m), 8.68 (1H, s), 13.27 (1H, s).

UV-Vis in acetonitrile (λ_{\max} , nm) (ϵ , M⁻¹cm⁻¹): 262 (19617); 368 (4059). HRMS, m/z: Calculated, 334.1266; found, 334.1160 [M + H]⁺.

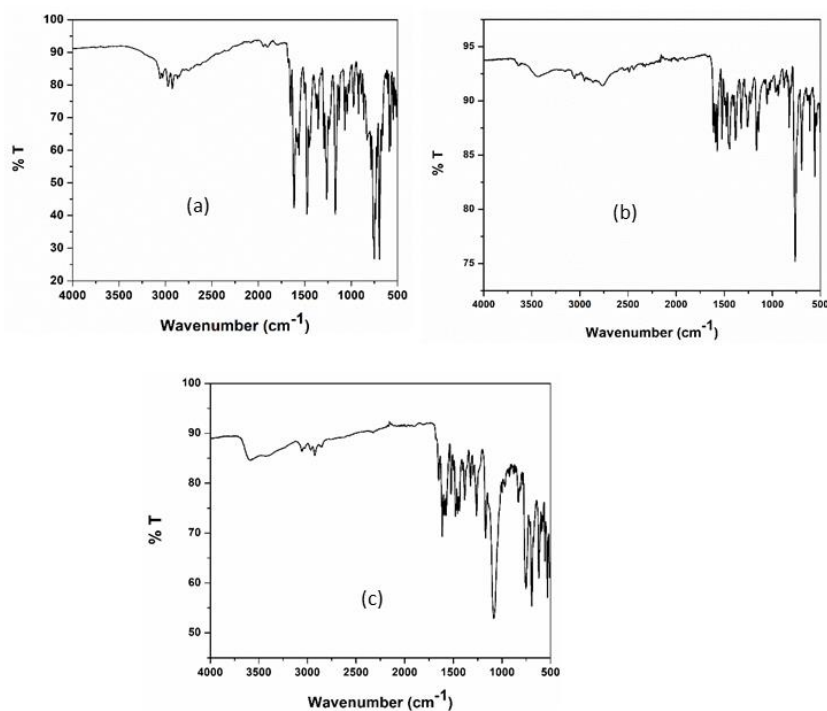


Fig.III.1. IR spectrum of (a)HL¹ (b)C1 and (c)C2

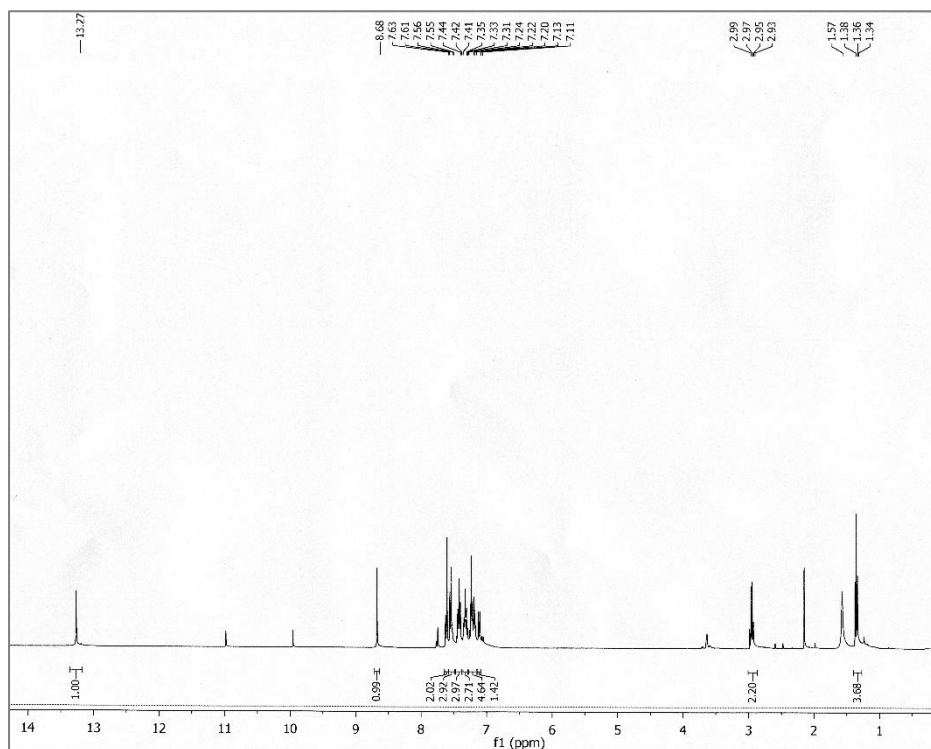


Fig.III.2. ^1H NMR spectrum of HL¹ in CDCl_3

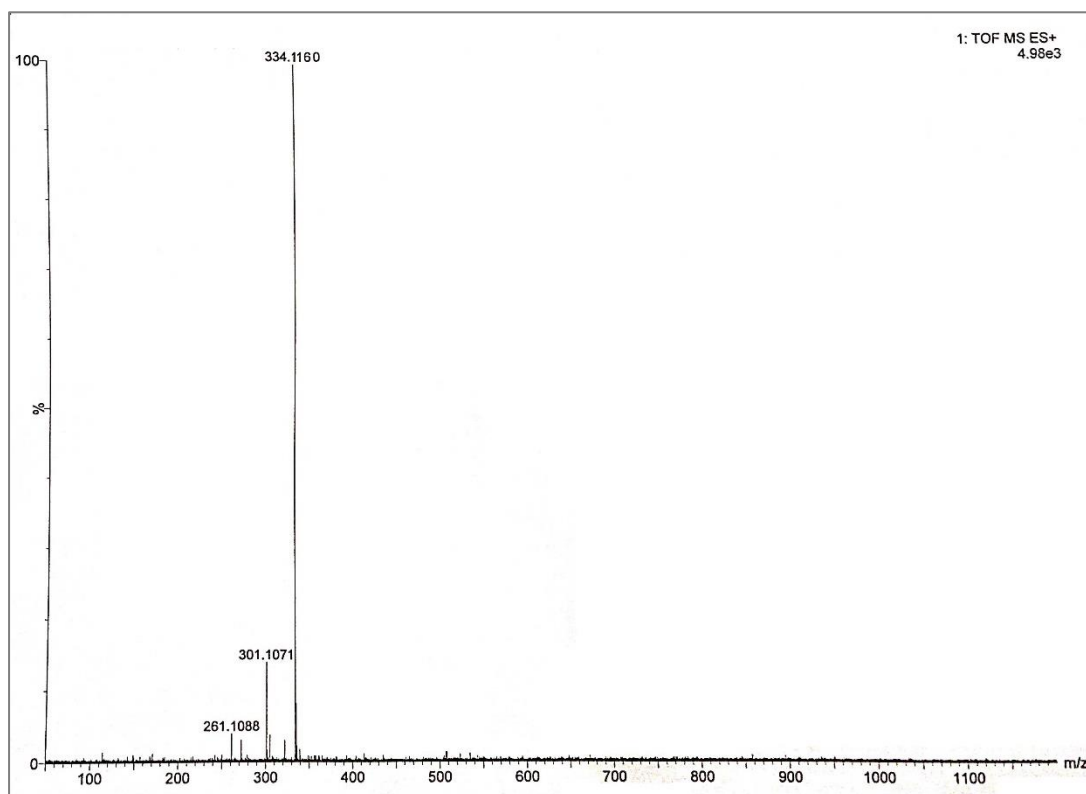


Fig.III.3. HRMS spectrum of HL¹ in acetonitrile

III.2.2.2. Synthesis of [Pd(L)Cl] (C1)

In a 100 mL round bottom flask, 0.037g (0.209 mmol) palladium chloride (PdCl₂) was dissolved in 20 mL acetonitrile under refluxing condition. To it, 0.070 g (0.209 mmol) of HL in 10 mL acetonitrile was added. The reaction mixture was refluxed for ca. 7 h to yield a red solution and cooled to room temperature. The solvent was then allowed to evaporate slowly in air, a red coloured crystals of [Pd(L)Cl] (C1) were deposited on the wall of beaker. The crystals were collected and the purity of the product was checked by TLC; Yield was 0.081 g (82 %).

Microanalytical data for C₂₁H₁₈CINOPdS (C1): Anal. Calc. (%):C, 53.18; H, 3.83; N, 2.95. Found (%):C, 53.05; H, 3.78; N, 2.91. IR data (KBr disc) (cm⁻¹): 2931 ν (CH), 1611 ν (C=N), 751 ν (C-S). ¹H NMR data in CDCl₃ (δ , ppm): 8.72 (s, 1H, HC=N); 7.23-7.95 (12H, ArH, m); 3.10 (q, J = 6.8 Hz, 2H); 1.51 (t, J= 7.5 Hz, 3H) . λ_{max} (ϵ , M⁻¹ cm⁻¹) in acetonitrile: 461(1502), 344 (2939), 327 (4775), 274 (18350). HRMS, m/z: Calc., 438.0144; found, 438.0172 [M]⁺. E_{pa}: 0.96 V; E_{pc}: -1.48.

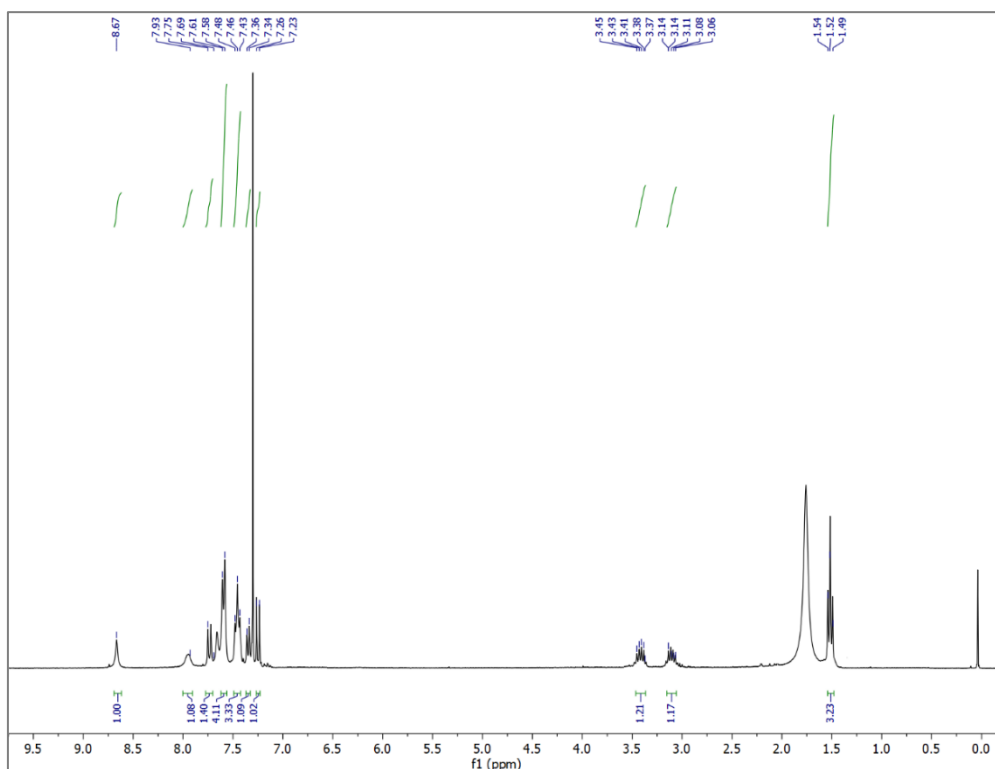


Fig.III.4. ¹H NMR spectrum of C1 in CDCl₃

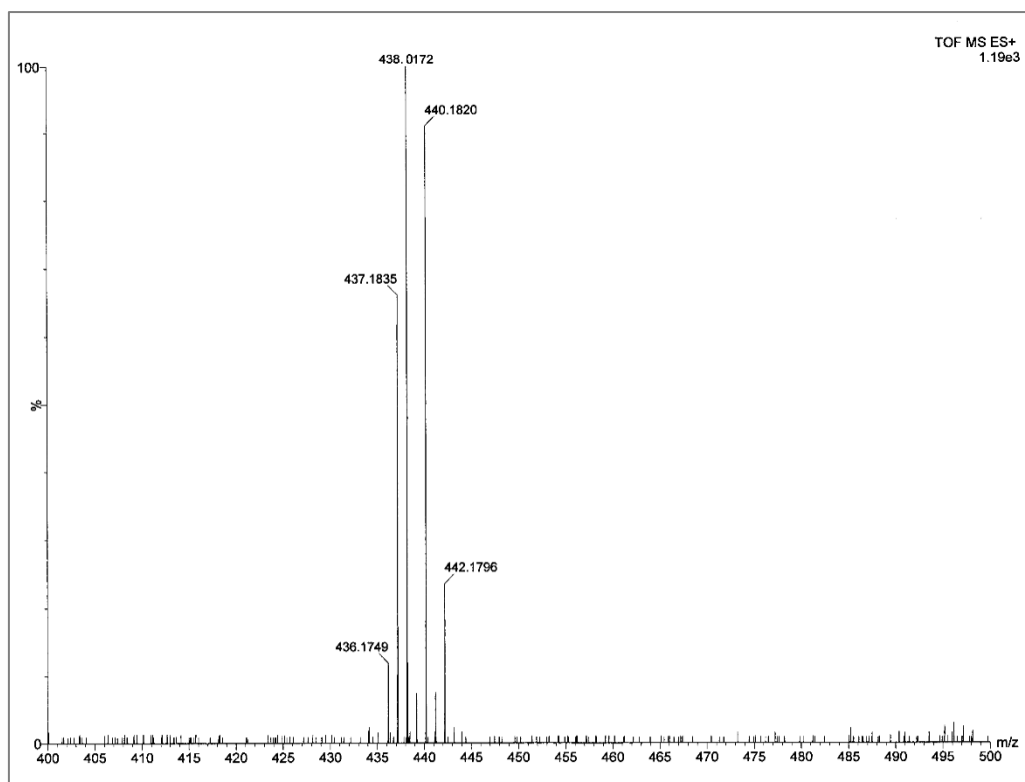


Fig.III.5. HRMS spectrum of C1 in acetonitrile

III.2.2.3. Synthesis of $[\text{Pd}(\text{L})\text{PPh}_3][\text{ClO}_4]$ (C2)

In a 50 mL round bottom flask, 0.037 g (0.209 mmol) of palladium chloride (PdCl_2) was dissolved in 20 mL acetonitrile under refluxing condition. To it 0.070 g (0.209 mmol) of HL and 0.108 g (0.418 mmol) of triphenylphosphine (PPh_3) were added and refluxed for ca. 6 h to yield a deep orange solution. The reaction mixture was cooled and solvent was removed under reduced pressure to yield brown gummy mass. It was then dissolved in minimum volume of methanol and aqueous solution of sodium perchlorate was added under stirring condition to get brown precipitate. It was then filtered, washed with cold water and dried in CaCl_2 desiccator. The product was then dissolved in acetonitrile and allowed to evaporate slowly in air; a red coloured crystals of $[\text{Pd}(\text{L})\text{PPh}_3](\text{ClO}_4)(\text{C2})$ were deposited on the wall of beaker. The crystals were collected and the purity of the product was checked by TLC; Yield was 0.098 g (67 %).

Microanalytical data for C₃₉H₃₃NOPSPd (**C2**): Anal. Calc. (%): C, 66.81; H, 4.74; N, 2.00. Found (%): C, 66.7; H, 4.69; N, 1.9. IR data (KBr disc) (cm⁻¹): 2925 ν (CH), 1614 ν (C=N), 750 ν (C-S). ¹H NMR data in CDCl₃ (δ , ppm): 8.20 (s, 1H, HC=N), 7.31-7.88 (27H, ArH, m), 3.14 (q, J = 6.4 Hz, 2H), 1.55 (t, J= 6.8 Hz, 3H). λ_{\max} (ϵ , M⁻¹ cm⁻¹) in acetonitrile: 465 (1005), 377 (2939), 343 (4447), 262 (19224). HRMS, m/z: Calc., 700.1055; found, 700.1301 [M]⁺. E_{pa}: 1.30 V; E_{pc}: -1.18 V.

Safety note: Perchlorate salts are potentially explosive and should be used in small quantities with care

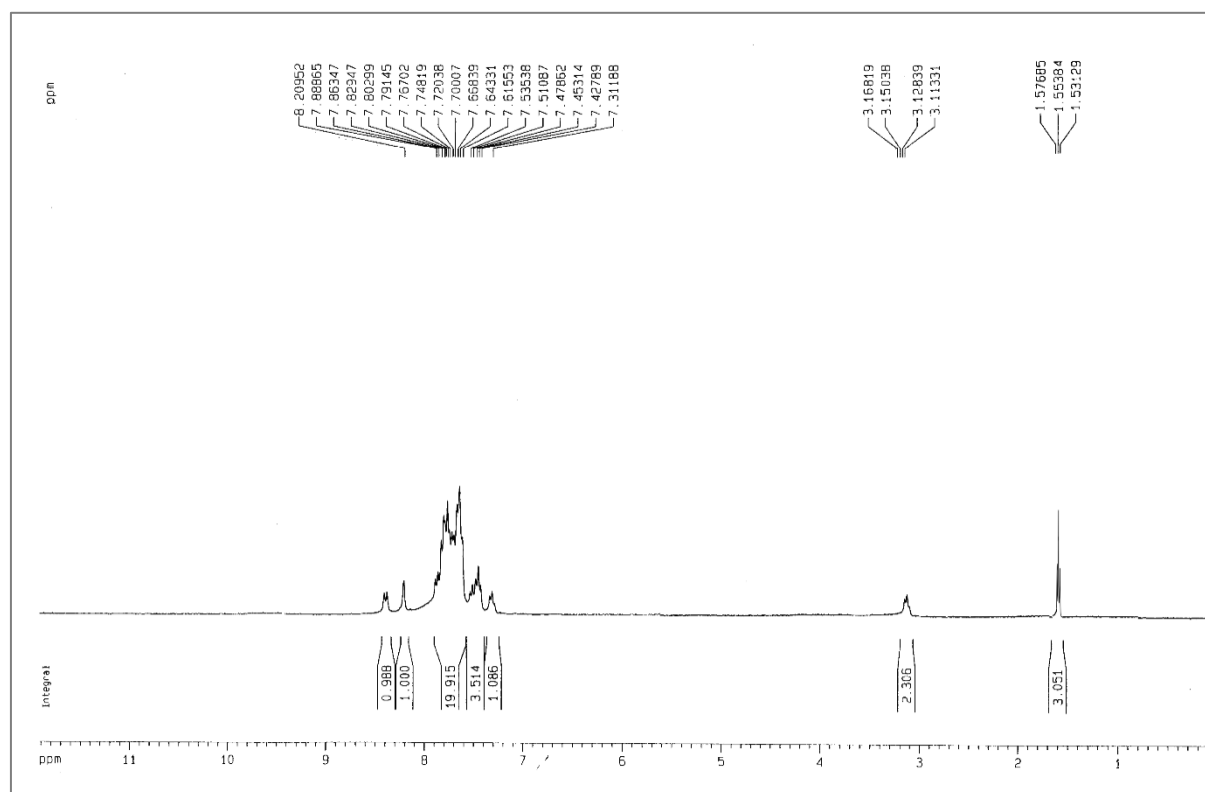


Fig.III.6. ¹H NMR spectrum of **C2** in CDCl₃

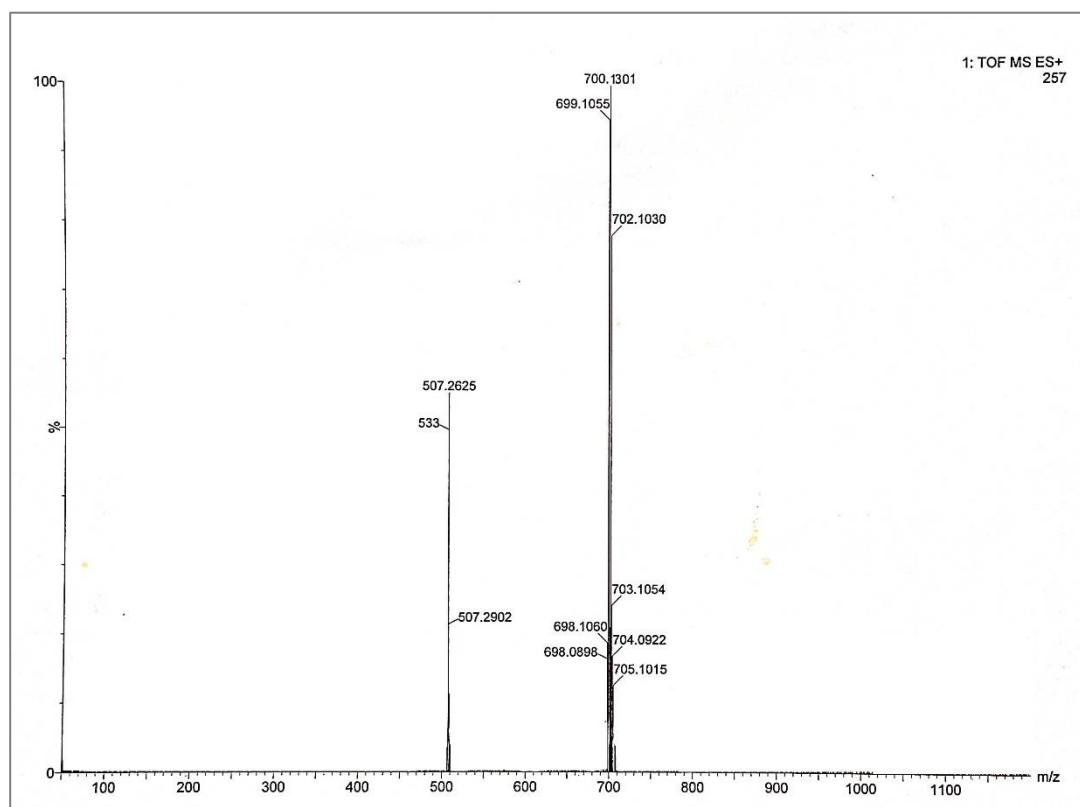


Fig.III.7. HRMS of complex C2

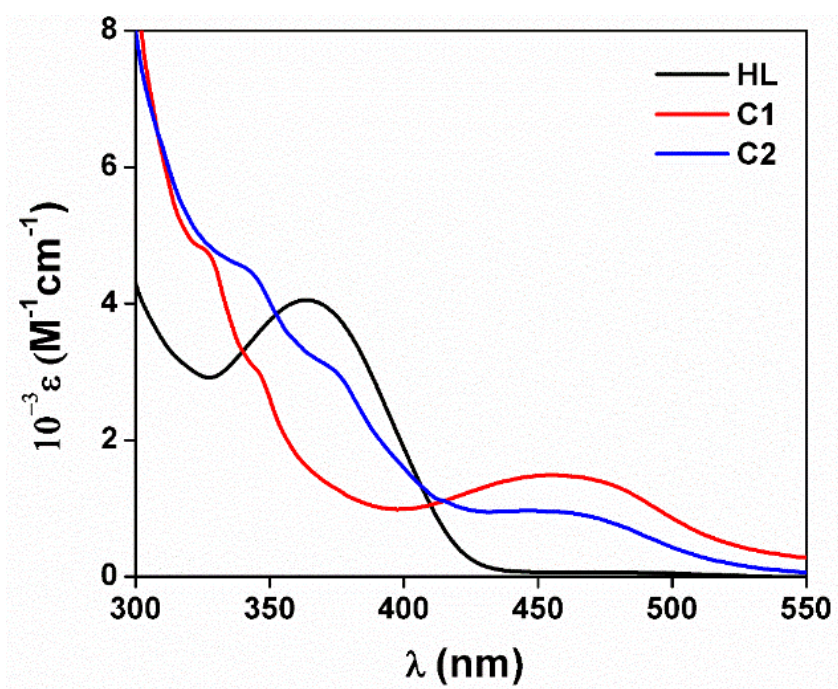


Fig.III.8. UV-Vis spectra of HL, C1 and C2

III.2.3. Crystal structure determination and refinement

Single crystals of palladium complexes **C1** and **C2** grown by layering dichloromethane solutions of the complexes with three times excess volume of *n*-hexane. X-ray data were collected in a Bruker AXS D8 Quest CMOS diffractometer equipped with PHOTON III detector using graphite monochromated Mo K α radiation ($\lambda = 0.71073 \text{ \AA}$) and the ω scan technique at 293 K. The collected frames were processed with the SAINT [36] and corrected for absorption using SADABS program [37]. Crystallographic data and experimental information are summarized in Table III.1. The structures were solved by direct method and refined by full-matrix least-squares on F^2 using the SHELXTL program package [38, 39]. All non-hydrogen atoms were refined anisotropically. The positions of all hydrogen atoms were generated geometrically (Csp³-H = 0.96 and Csp²-H = 0.93 \AA), assigned isotropic thermal parameters, and allowed to ride on their respective parent carbon atoms in the final cycle of refinement.

III.2.4. Computational method

Full geometry optimizations were performed by density functional theory (DFT) method using B3LYP hybrid exchange correlation functional for the complexes [40, 41] with Gaussian09 program package [42] with the aid of the GaussView, Version 5 visualization program. All elements besides palladium were assigned the 6-31G(d) basis set, while the LanL2DZ basis set with effective core potential was used for palladium atom [43-45]. Vibrational frequency was calculated to ensure that each configuration is indeed a local minimum on the potential energy surface. Time-dependent density functional theory (TDDFT) formalism [46-48] using conductor-like polarizable continuum model (CPCM) [49-51] was used to compute the vertical electronic transitions of the complexes in acetonitrile. GaussSum [52] was used to calculate the fractional contributions of various groups to each molecular orbital.

Table III.1. Crystallographic data and refinement parameters of C1 and C2

	[Pd(L)Cl] (C1)	[Pd(L)PPh ₃](ClO ₄) (C2)
Formula	C ₂₁ H ₁₈ ClNOPdS	C ₃₉ H ₃₃ NOPSPd
Formula Weight	474.31	700.10
Crystal System	<i>Orthorhombic</i>	<i>Monoclinic</i>
Space group	<i>P 21 21 21</i>	<i>P 21/n</i>
<i>a</i> (Å)	5.5437(8)	12.5049(11)
<i>b</i> (Å)	17.975(3)	19.2040(16)
<i>c</i> (Å)	19.754(3)	15.4364(12)
β (°)	90	112.688(2)
<i>V</i> (Å ³)	1968.5(5)	3420.1(5)
<i>Z</i>	4	4
ρ (calc) (g/cm ³)	1.661	1.555
μ (Mo Ka) (mm ⁻¹)	1.201	0.776
<i>F</i> (000)	992	1632
Crystal Size (mm)	0.17 × 0.12 × 0.09	0.18 × 0.13 × 0.10
<i>T</i> (K)	293(2)	293(2)
Radiation wavelength (Å)	0.71073	0.71073
θ (Min-Max) (°)	2.266-27.161	1.780-27.184
<i>Hkl</i> range	-7 to 7, -23 to 23 and -25 to 25	-16 to 16; -24 to 24 and -19 to 19
Total, Unique Data, <i>R</i> (int)	121592, 4309, 0.0552	48068, 7528, 0.0789
Observed data (<i>I</i> > 2 σ (<i>I</i>))	4020	5387
<i>N</i> ref, <i>N</i> par	4309, 250	7528, 442
<i>R</i> ^a , <i>wR</i> ₂ ^b , <i>S</i> ^c	0.0326, 0.0674, 1.167	0.0590, 0.1041, 1.069
Residual Density (e/Å ³)	-0.382 and 0.452	-0.388 and 0.495

$$^a R_1 = \sum (|F_o| - |F_c|) / \sum |F_o|$$

$$^b wR_2 = \{ \sum [w (F_o^2 - F_c^2)^2] / \sum [w (F_o^2)^2] \}^{1/2}, w = 1/[\sigma^2(F_o^2) + (0.0185P)^2 + 2.1291 P] \text{ for}$$

$$\mathbf{C1} \text{ and } w = 1/[\sigma^2(F_o^2) + (0.0276P)^2 + 5.7480 P] \text{ for } \mathbf{C2}, \text{ where } P = (F_o^2 + 2 F_c^2)/3$$

$$^c \text{GOF (S)} = \{ \sum [w(F_o^2 - F_c^2)^2] / (n - p) \}^{1/2}, \text{ where } n = \text{number of measured data and } p = \text{number of parameters.}$$

III.2.5. Cell culture and treatment

Gastric cancer cell lines AGS was obtained from National centre for cell science, Pune, India and maintained in RPMI-1640 medium (Gibco, life technologies) supplemented with 10% Fetal Bovine Serum (FBS) (Gibco, life technologies, USA). All cell lines were stored at 37°C in a humidified incubator under 5% CO₂ atmosphere and experiments were performed after 3rd passage of cell line.

III.2.6. Cell proliferation assay

III.2.6.1. MTT Assay

Cell viability assay with AGS cells was carried out as described by Riss et.al [53]. Briefly 0.1×10⁴ cells per well in 96 well plate was exposed to increasing concentrations of HL, palladium complexes **C1** and **C2**(1, 100, 200, 300, 400 and 500 μM) for 24 h at 37°C. After incubation, 100 μL DMSO was added to each well and the absorbance was measured at 570 nm using microtitre plate reader (Tecan, infinite M200). Results were expressed as percentage of viable cells, with 100% representing control cells and IC₅₀ value was calculated using nonlinear regression (curve fit) followed by log (inhibition) vs. response equation in graph pad prism software. The amount of drug was plotted on the X axis as the log of drug concentration and OD was plotted on the Y axis. Statistical significance of each group with untreated control is analyzed by One Way ANOVA test (P ANOVA < 0.0001) followed by a post hoc Tukey's test. Data is represented as mean ± S.D of triplicates determinations from their independent experiments with **P value < 0.01 and ***P value < 0.0001 versus untreated control.

III.2.6.2. Colony Formation Assay

Approximately 500 cells per well of AGS cells were cultured in 6 well plates. Cells were treated with HL (67.1 μM), palladium complex **C1** (13.4 μM) and palladium complex **C2** (16

μM). After 24 hours of treatment, cells were grown in fresh media for 3 days at 37°C until colonies were formed. Formed cell colonies were washed with 1X PBS and fixed in 10% methanol for 15 minutes followed by Harry's haematoxylin staining. Colonies, defined as >50 cells, were counted under Bright Field Microscope (Leica DM1000, Germany) at 4X magnification and graph was plotted as percentage of colonies relative to the control with various concentration of HL, palladium complexes **C1** and **C2** in Graph pad prism software.

III.2.6.3. Statistical analysis

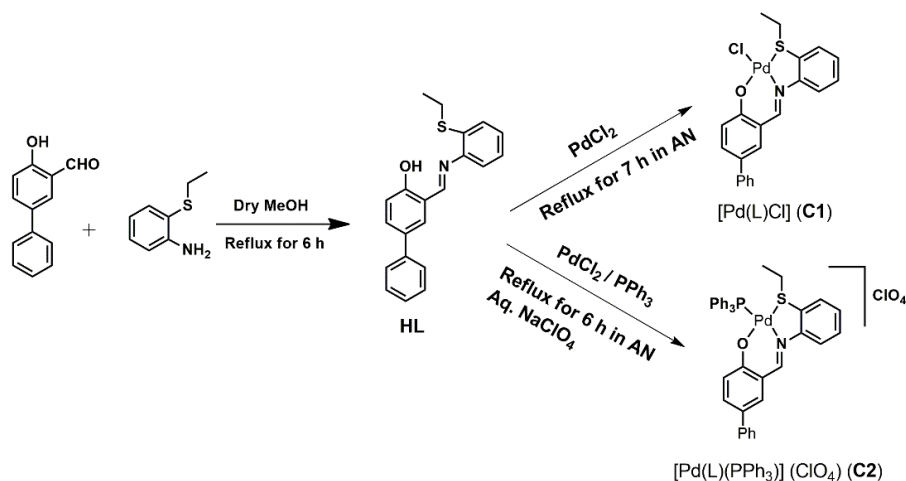
Representative data from three independent experiments are shown as mean value \pm S.D. One-way Analysis Variance (ANOVA) with post hoc comparisons by Tukey test was carried out to assess the significant difference between each treated group and control. The value $P < 0.05$ was considered statistically significant. Statistical data analyses were performed with Graph pad prism 5 software.

III.3. Results and discussion

III.3.1. Synthesis and spectral characterization

The palladium(II) complexes, $[\text{Pd}(\text{L})\text{Cl}]$ (**C1**) with thioether containing ONS donor ligand (HL) was synthesized by the reaction of PdCl_2 and HL in 1:1 mole ratio in acetonitrile under reflux. Similarly, complex, $[\text{Pd}(\text{L})\text{PPh}_3](\text{ClO}_4)$ (**C2**) was synthesized by the reaction of PdCl_2 , HL and PPh_3 in 1:1:2 mole ratio under reflux followed by precipitation with NaClO_4 (Scheme III.1). Elemental analyses of the final products are consistent with the proposed formula of the complexes. IR spectra of the complexes exhibit peak at $1611\text{-}1614\text{ cm}^{-1}$ correspond to $\nu(\text{C}=\text{N})$ and it appeared in lower frequency region compare to free ligand value (1652 cm^{-1}). ^1H NMR spectra of the complexes exhibit a sharp singlet peak at 8.67 ppm and 8.20 ppm for complex **C1** and **C2** respectively corresponds to $\text{HC}=\text{N}$ protons of the ligands. The $-\text{SCH}_2$ proton signals appeared as quartet in 3.10-3.14 ppm in the complexes. Aromatic

proton signals appeared in the range 7.23-7.95 ppm in CDCl_3 . UV-Visible spectra of the complexes in acetonitrile exhibit weak broad peak at 459-465 nm and two close by shoulder peaks at 344-346 nm and 324-327 nm. In addition, a ligand centered high energy intense peak appeared at 262-274 nm in the complexes (Fig.III.8)



Scheme III.1. Synthesis of HL and its palladium(II) complexes, **C1** and **C2**

III.3.2. Crystal structure

In order to authenticate the coordination mode of the ligand (HL), the molecular structures of palladium(II) complexes **C1** and **C2** were confirmed by single crystal X-ray diffraction method. ORTEP plots of the complexes along with atom numbering scheme are shown in Fig.III.9.a and Fig.III.9.b for **C1** and **C2** respectively. Selected bond distances and bond angles of the complexes are summarized in TableIII.2. The bond parameters of the complexes are suggesting slightly distorted square planar geometry around palladium atom. HL is coordinated to the palladium metal through phenolic O, imino N and thioether S atoms in the complexes. The imino bond distances (N1-C13) are found to be 1.298(7) and 1.288(6) Å in **C1** and **C2** respectively. The Pd-N bond (Pd1-N1) distances 1.997(4) Å in **C1** and 2.047(3) Å in **C2** are comparable to the reported Pd-N(imino) bond distances [54, 55]. The Pd-O bond distances (Pd1-O1, 1.995(4) Å in **C1** and 1.999(3) Å in **C2**) in the complexes are also well

correlated with the Pd-O distances in reported palladium complexes [56, 57]. Similarly, the Pd-S(thioether) bond distances appeared in the range 2.2397(16)-2.2636(13) Å are well-corroborated with the literature value [54-57].

Table III.2. Selected bond distances (Å) and angles (°) of **C1** and **C2**

Bonds(Å)	[Pd(L)Cl] (C1)		[Pd(L)PPh ₃](ClO ₄) (C2)	
	X-ray	Calc.	X-ray	Calc.
Pd1 - N1	1.997(4)	2.044	2.047(3)	2.074
Pd1 - O1	1.995(4)	2.015	1.999(3)	2.015
Pd1 - S1	2.2397(16)	2.297	2.2636(13)	2.330
Pd1 - Cl1	2.3246(14)	2.336	-	-
Pd1 - P1	-	-	2.2899(12)	2.354
S1- C19	1.770(6)	1.798	1.773(4)	1.796
O1 - C1	1.306(6)	1.291	1.308(5)	1.310
Angles (°)				
N1 - Pd1 - O1	94.67(16)	93.739	93.56(14)	92.719
N1 - Pd1 - S1	87.09(13)	86.348	85.86(11)	84.872
N1 - Pd1 - Cl1	174.77(13)	175.891	-	-
N1 - Pd1 - P1	-	-	177.24(11)	177.504
O1 - Pd1 - S1	175.78(13)	177.180	177.45(11)	177.385
O1 - Pd1 - Cl1	87.70(11)	90.092	-	-
O1- Pd1- P1	-	-	85.28(9)	85.051
S1- Pd1- P1	-	-	95.41(5)	97.336
S1 - Pd1 - Cl1	90.86(6)	89.8975	-	-

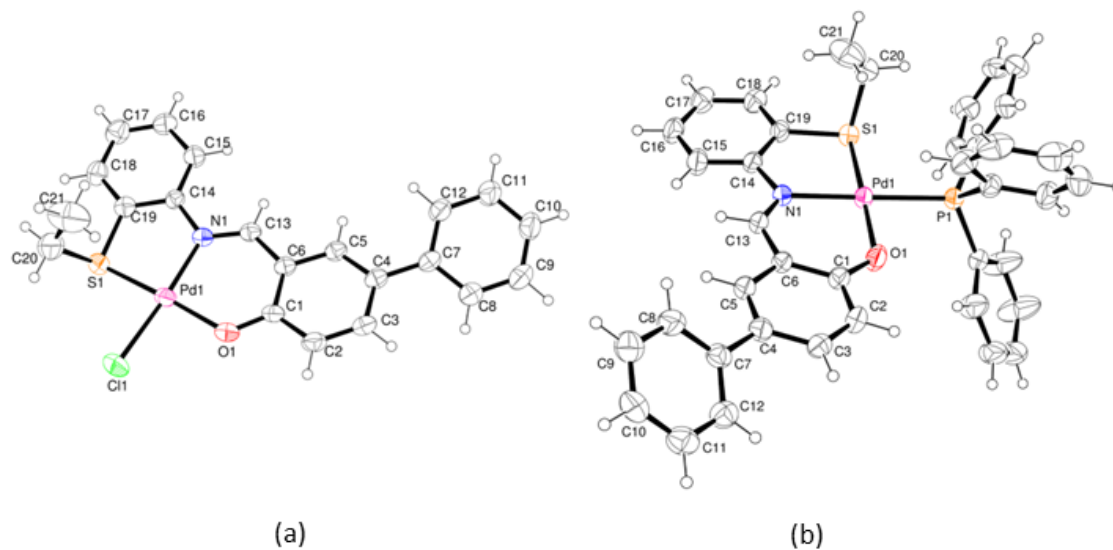


Fig.III.9. ORTEP plots with 35% ellipsoidal probability of (a) [Pd(L)Cl] (**C1**) (b) [Pd(L)PPh₃](ClO₄) (**C2**)

III.3.3. DFT and TDDFT calculations

Geometries of [Pd(L)Cl] (**C1**) and [Pd(L)PPh₃](ClO₄) (**C2**) were optimized by DFT/B3LYP method to understand the electronic structure of the complexes. Calculated bond distances and bond angles of the complexes are summarized in Table III.2. Calculated geometric parameters clearly show that it is in good agreement with the experimental data. The maximum deviations in bond distances are observed for Pd-S bond by ~ 0.05 Å and ~ 0.07 Å respectively for complex **C1** and **C2** respectively and for Pd-P bond by ~ 0.06 Å for complex **C2**.

Contour plots of selected molecular orbitals of the complexes are shown in Fig.III.10 and Fig.III.11 for **C1** and **C2** respectively. The highest energy occupied molecular orbitals (HOMOs) of the complexes have 90-98% ligand contribution with maximum population on the phenolate moiety. HOMO-1 and HOMO-2 for **C1** have 51-78% contribution of $p\pi(\text{C1})$ orbitals along with reduced contribution (16-25%) of $d\pi(\text{Pd})$ orbitals, while HOMO-3 has 72% $d\pi(\text{Pd})$ character. LUMO of **C1** has 88% $\pi^*(\text{L})$ character and LUMO+1 has mixed

$d\pi(\text{Pd})$ and $\pi^*(\text{L})$ character (Table.III.3). For complex **C2**, HOMO-1 to HOMO-3 have 95-99% $\pi(\text{L})$ character. LUMO has mixed $d\pi(\text{Pd})$ (35%) and $\pi^*(\text{L})$ (43%) character, while LUMO+1 has 90% $\pi^*(\text{L})$ character. The HOMO-LUMO energy gaps in the complexes are found to be 3.05 eV and 2.73 eV for complexes **C1** and **C2** respectively.

Table III.3. Energy and % of composition of some selected molecular orbitals of **C1** and **C2**

MO	C1				C2			
	E (eV)	% of composition			E (eV)	% of composition		
		Pd	L	Cl		Pd	L	PPh ₃
LUMO+5	-0.07	02	98	0	-3.02	06	05	89
LUMO+4	-0.45	02	98	0	-3.29	03	03	95
LUMO+3	-0.57	01	99	0	-3.38	05	07	88
LUMO+2	-1.34	02	98	0	-3.64	08	87	05
LUMO+1	-2.04	40	48	12	-4.59	06	90	04
LUMO	-2.37	09	88	03	-4.95	35	43	22
HOMO	-5.42	06	90	03	-7.68	02	98	0
HOMO-1	-6.21	25	24	51	-8.48	0	100	0
HOMO-2	-6.39	16	06	78	-8.78	04	95	01
HOMO-3	-6.69	72	18	10	-8.96	04	96	01
HOMO-4	-6.78	09	76	15	-9.14	14	08	78
HOMO-5	-6.84	0	100	0	-9.34	01	0	99
HOMO-6	-6.87	12	84	04	-9.39	01	01	99
HOMO-7	-7.28	13	79	09	-9.49	04	06	90
HOMO-8	-7.54	42	46	12	-9.63	04	31	65
HOMO-9	-7.78	31	64	05	-9.72	06	04	89
HOMO-10	-7.94	05	93	02	-9.79	05	58	37

UV-Vis absorption bands of the complexes are interpreted by TDDFT calculations using B3LYP/CPCM method in acetonitrile. For complex **C1**, the calculated band at 449 nm ($f = 0.127$) corresponds to the mixed HOMO \rightarrow LUMO and HOMO-1 \rightarrow LUMO transitions ($\lambda_{\text{expt.}} = 461$ nm, $\varepsilon = 1502$ M⁻¹cm⁻¹) having intra-ligand charge transfer (ILCT) and halogen to ligand charge transfer (XLCT) character along with reduced contribution of metal to ligand charge transfer (MLCT) character. The moderately intense transition at 331 nm (HOMO-2 \rightarrow LUMO transition, $f = 0.177$) corresponds to the experimentally observed shoulder peak at 327 nm, have mixed XLCT and MLCT character. The high energy strong transition at 281 nm ($f = 0.539$) ($\lambda_{\text{expt.}} = 274$ nm, $\varepsilon = 18350$ M⁻¹cm⁻¹) corresponds to ILCT character (Table III.4). TDDFT calculation on the optimized geometry of complex **C2** predicts the low energy transition at 455 nm ($f = 0.112$) corresponds to the experimental band at 465 nm ($\varepsilon = 1005$ M⁻¹cm⁻¹) having mixed ligand to metal charge transfer (LMCT) and ILCT character. Again, the experimental bands at 377 and 343 nm correspond to ILCT transitions along with partial contribution of MLCT transition. The high energy transition at 272 nm ($f = 0.241$) due to HOMO-3 \rightarrow LUMO+1 transition corresponds to the intense band at 262 nm for the complex **C2**.

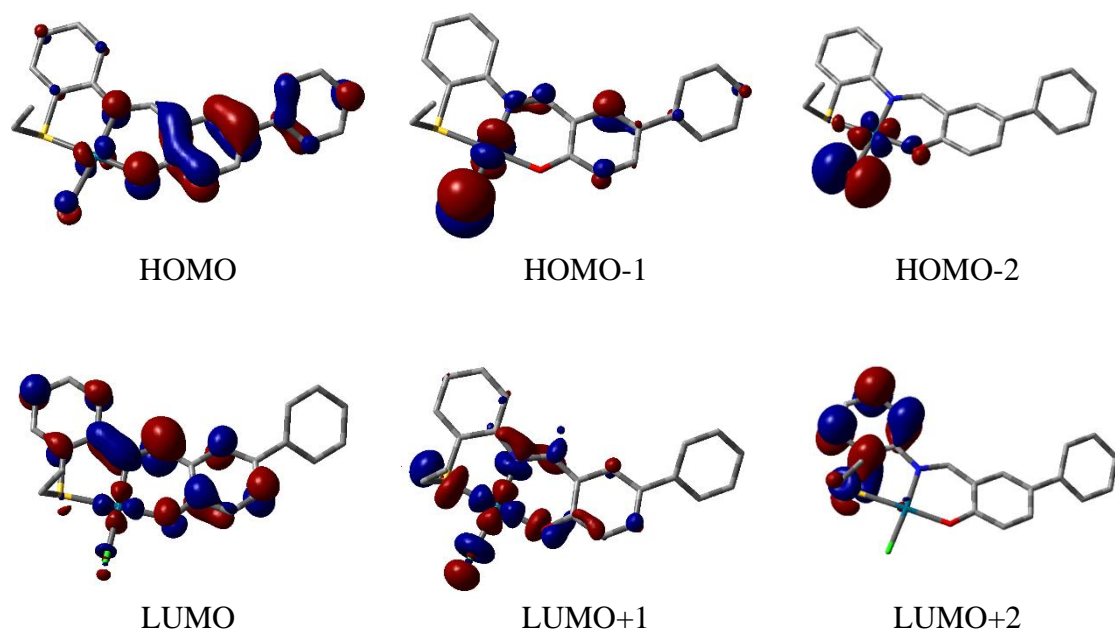


Fig.III.10. Contour plots of selected molecular orbital of C1

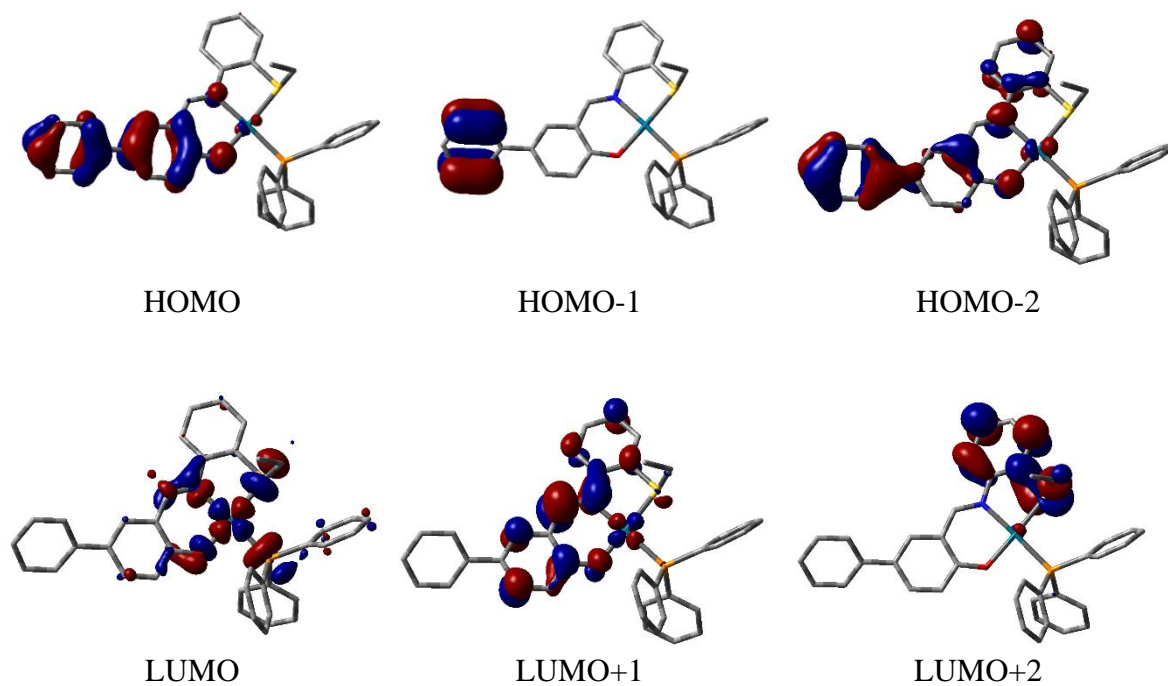


Fig.III.11. Contour plots of selected molecular orbital of C2

Table III.4. Vertical electronic transition calculated by TDDFT/CPCM method of **C1** and **C2**

Compds.	λ (nm)	E (eV)	Osc. Strength (f)	Key excitations	Character ^a	$\lambda_{\text{expt.}}$ (nm) (ϵ , M ⁻¹ cm ⁻¹)
C1	485.0	2.5562	0.0074	(77%)HOMO→LUMO+1	$\pi(\text{L}) \rightarrow d\pi(\text{Pd})/\pi^*(\text{L})$ (LMCT/ILCT)	
	449.3	2.7596	0.1273	(62%)HOMO→LUMO (31%)HOMO-1→LUMO	$\pi(\text{L}) \rightarrow \pi^*(\text{L})$ (ILCT) $d\pi(\text{Pd})/p\pi(\text{Cl}) \rightarrow \pi^*(\text{L})$ (MLCT/XLCT)	461(1502)
	331.0	3.7455	0.1774	(75%)HOMO-2→LUMO	$d\pi(\text{Pd})/p\pi(\text{Cl}) \rightarrow \pi^*(\text{L})$ (MLCT/XLCT)	327 (4775)
	281.3	4.4075	0.5389	(78%)HOMO-6→LUMO	$\pi(\text{L}) \rightarrow \pi^*(\text{L})$ (ILCT)	274(18350)
	272.5	4.5493	0.2007	(50%)HOMO-7→LUMO (24%)HOMO→LUMO+3	$\pi(\text{L}) \rightarrow \pi^*(\text{L})$ (ILCT)	
	607.4	2.0414	0.0000	(87%)HOMO→LUMO	$\pi(\text{L}) \rightarrow d\pi(\text{Pd})/\pi^*(\text{L})$ (LMCT/ILCT)	
	454.9	2.7253	0.1125	(68%)HOMO-1→LUMO	$\pi(\text{L}) \rightarrow d\pi(\text{Pd})/\pi^*(\text{L})$ (LMCT/ILCT)	465(1005)
C2	410.1	3.0229	0.0408	(65%)HOMO-2→LUMO	$\pi(\text{L}) \rightarrow d\pi(\text{Pd})/\pi^*(\text{L})$ (LMCT/ILCT)	
	374.0	3.3151	0.0511	(72%)HOMO-1→LUMO	$\pi(\text{L}) \rightarrow d\pi(\text{Pd})/\pi^*(\text{L})$ (LMCT/ILCT)	377(2939)
	331.5	3.7397	0.0722	(51%)HOMO-2→LUMO+1 (27%)HOMO-2→LUMO	$\pi(\text{L}) \rightarrow \pi^*(\text{L})$ (ILCT) $\pi(\text{L}) \rightarrow d\pi(\text{Pd})/\pi^*(\text{L})$ (LMCT/ILCT)	343 (4447)
	272.23	4.5544	0.2412	(73%)HOMO-3→LUMO+1	$\pi(\text{L}) \rightarrow \pi^*(\text{L})$ (ILCT)	262(19224)

^a ILCT: Intra-ligand charge transfer transition; MLCT: Metal to ligand charge transfer transition; LMCT: Ligand to metal charge transfer transition; XLCT: Halogen to ligand charge transfer transition.

III.3.4. Electrochemistry

The complexes (**C1/C2**) exhibit one irreversible anodic peak and one irreversible cathodic peak within the experimental potential range of ± 2.0 V *versus* Ag/AgCl reference electrode

in CH₃CN (Fig.III.12). For complex **C1**, the anodic peak corresponds to the oxidation was found to be at 0.96 V, which was significantly shifted to higher potential for complex **C2** and observed at 1.30 V. The irreversible reduction peak was observed at -1.18 for **C2** and -1.48 V for **C1**. The irreversible oxidation for the complexes may be assigned as Pd(II) to Pd(IV) oxidation or oxidation of phenolate moiety to form phenoxy radical. DFT calculation clearly shows that the HOMOs of the complexes have >90% ligand character with predominant contribution of phenolate moiety and negligible contribution of $d\pi(\text{Pd})$ orbitals. So, the oxidation of the complexes corresponds to the oxidation of phenolate moiety to form phenoxy radical [55]. Moreover, the oxidation potential is well correlated with the energies of HOMOs of the complexes. The lower oxidation potential of **C1** (0.96 V) compare to complex **C2** (1.30 V) is well corroborated with the greater stability of HOMO of **C2** ($E = -5.42$ eV) compare to complex **C1** ($E = -7.68$ eV). LUMO of **C1** has 88% ligand character with major contribution of $\pi^*(\text{C}=\text{N})$ orbitals. Thus, the irreversible reduction for **C1** corresponds to the reduction of imine bond. But for complex **C2**, LUMO has mixed contribution of $d\pi(\text{Pd})$ (35%) and $\pi^*(\text{L})$ (43%). So, the irreversible reduction for **C2** may be because of Pd(II) to Pd(I) reduction or reduction of Schiff base ligand.

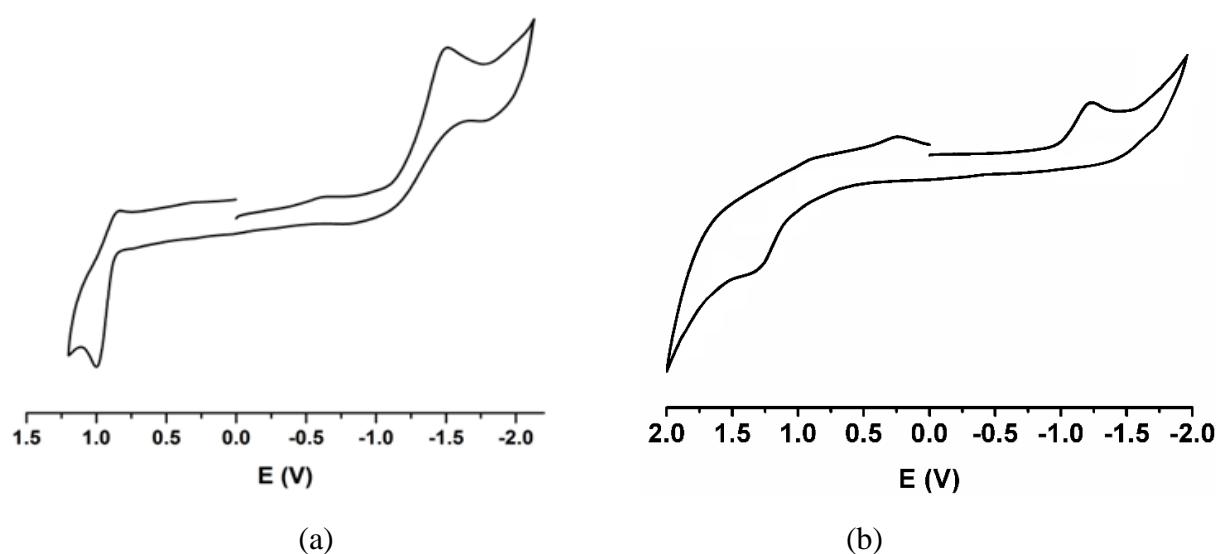


Fig.III.12. Cyclic voltammogram of **C1**(a) and **C2** (b) in acetonitrile

III.3.5. In vitro antiproliferative studies**III.3.5.1. MTT Assay**

The in vitro antiproliferative activities of ligand (HL) and palladium(II) complexes (**C1** and **C2**) were evaluated by MTT assay against AGS cell line. The percentage of cell viability versus concentration graphs are shown in Fig.III.15. Results revealed that both ligand HL and its palladium(II) complexes inhibit the viability of AGS cells in a dose dependent manner at 24 hours as compared to the control. Palladium complexes (**C1** and **C2**) significantly decrease the viability of AGS cells up to 3.1% and 3.9% at its highest concentration, i.e., 500 µg/ml as compared to HL treatments and control. For better understanding the cytotoxic activities of the compounds, IC₅₀ value was calculated using nonlinear regression (curve fit) followed by log (inhibition) vs. response equation in graph pad prism software. The amount of drug was plotted on the X axis as the log of drug concentration and OD was plotted on the Y axis. IC₅₀ values of the palladium(II) complexes (**C1**, 13.38±1.05 µM and **C2**, 16.01±1.22 µM) are found to very low as compared to the free ligand HL (67.13±1.97 µM) towards AGS cell lines (Table III.5). Moreover, the reported palladium(II) complexes (**C1** and **C2**) are found to be more effective in comparison to the antiproliferative activity of cisplatin with AGS tumor cell lines (IC₅₀ = 22.80 ± 1.48 µM)(Fig.III.13).

Table III.5. IC₅₀* value of the ligand (HL) and its palladium(II) complexes (**C1** and **C2**) against AGS cell line.*IC₅₀ is the concentration required to inhibit 50% of cellular growth. The values are the mean of triplicate determinations.

Compounds	IC ₅₀ (µM ± SD)
HL	67.1 ± 1.97
C1	13.4 ± 1.05
C2	16.0 ± 1.22
Cisplatin	22.8± 1.48

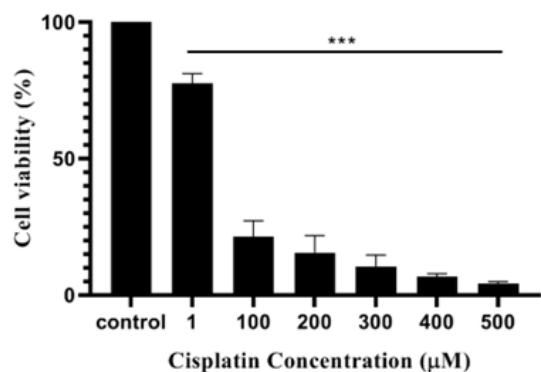


Fig. III.13. % of cell viability of cisplatin towards AGS cancer cell lines

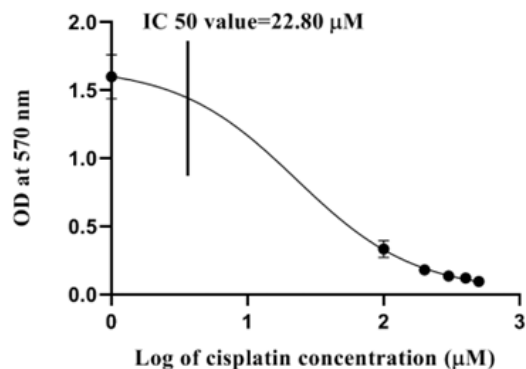
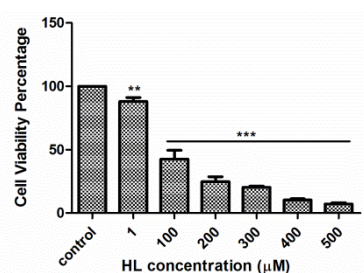
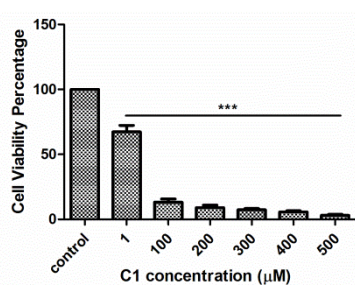


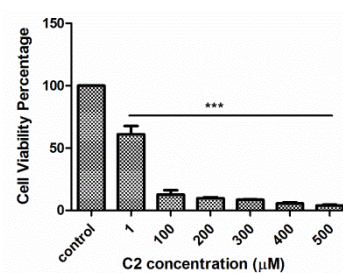
Fig. III.14. IC50 of cisplatin towards AGS cell lines.



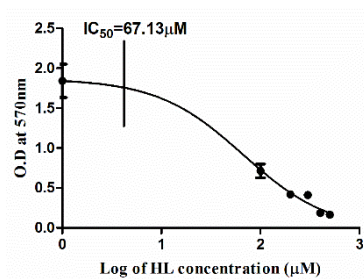
(a)



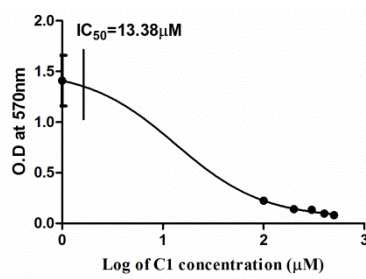
(b)



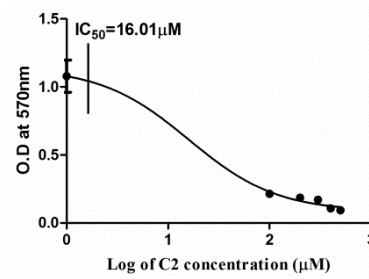
(c)



(d)



(e)



(f)

Fig.III.15. % of cell viability of HL (a), C1 (b) and C2 (c) towards AGS cell lines. IC50 (half maximum inhibitory concentration) of HL (d), C1 (e) and C2 (f) calculated using nonlinear regression (curve fit) followed by log (inhibition) vs response equation in graph pad prism software, the amount of drug was plotted on the X axis as the log of drug concentration and OD was plotted on the Y axis.

III.3.5.2. Colony Formation Assay

To further confirm the effect of palladium complexes on AGS cell lines colony formation assay was performed. Cells were treated with HL (67.1 μM), palladium complex **C1** (13.4 μM) and palladium complex **C2** (16 μM) for 24 h. Graph was plotted as percentage of colonies relative to the control with chosen concentrations of HL and its palladium complexes in Graph pad prism software (Fig.III.16). Decrease in colonies were observed in both palladium complexes and HL as compared to control. Palladium complexes **C1** and **C2** reduced the colonies to 16% and 9% at its lowest concentration compared to the control. These result all showed that palladium complexes inhibit the cell viability of AGS cells at its low dose as compared to HL.

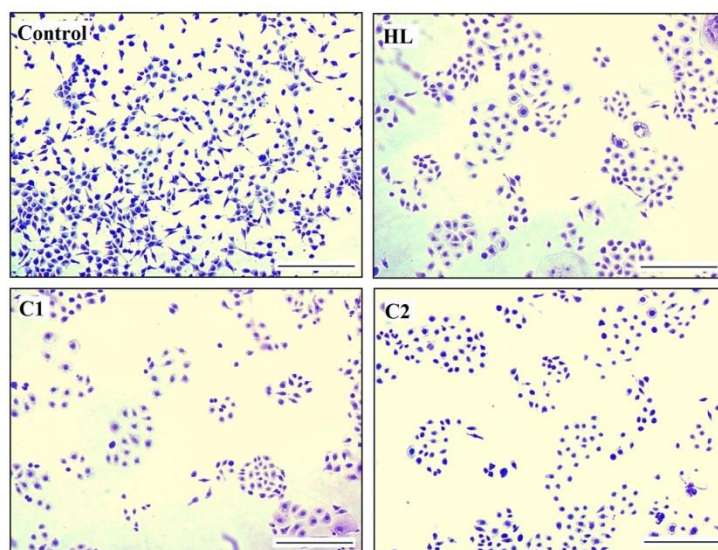


Fig.III.16. Colony formation of AGS cell lines after treatment of HL (67.1 μM), **C1** (13.4 μM) and **C2** (16 μM) for 24 h.

III.4. Conclusion

Herein, two new palladium(II) complexes, $[\text{Pd}(\text{L})\text{Cl}]$ (**C1**) and $[\text{Pd}(\text{L})\text{PPh}_3](\text{ClO}_4)$ (**C2**) with ONS donor thioether ligands (HL) were synthesized and successfully characterized by various spectroscopic techniques. The geometries of the complexes exhibit distorted square

planar geometry around palladium as confirmed by single crystal X-ray analysis. Electronic structure, redox and spectral properties of the complexes were interpreted by DFT and TDDFT calculations. The palladium(II) complexes exhibit potential anti-cancer activity towards AGS cancer cell lines with IC₅₀ values of 13.38±1.05 μM and 16.01±1.22 μM for **C1** and **C2** respectively. To further confirm the effect of palladium complexes on gastric cancer cells colony formation assay was carried out and results showed that palladium complexes inhibit the cell viability of AGS cells at its low dose as compared to HL.

III.5. References

1. M. Kalita, P. Gogoi, P. Barman, B. Sarma, A.K. Buragohain and R.D. Kalita, *Polyhedron*, 2014, **74**, 93-98.
2. A.M. Fayed, S.A. Elsayed, A.M. El-Hendawy and M.R. Mostafa, *Spectrochim. Acta A*, 2014, **129**, 293-302.
3. M. Ulaganatha Raja, N. Gowri and R. Ramesh, *Polyhedron*, 2010, **29**, 1175-1181.
4. N. R. Pramanik, M. Chakraborty, D. Biswal, S. S. Mandal, S. Ghosh, S. Chakrabarti, W. S. Sheldrick, M. G. B. Drew, T. K. Mondal and D. Sarkar, *Polyhedron*, 2015, **85**, 196-207.
5. S. Sinha, M. Chakraborty, N. R. Pramanik, T. K. Raychaudhuri, T. K. Mondal, D. Sarkar, M. G. B. Drew, S. Ghosh and S. S. Mandal, *Polyhedron*, 2013, **55**, 192-200.
6. A. P. Koley, S. Purohit, S. Ghosh, L. S. Prasad and P. T. Manoharan, *Inorg. Chem.*, 1992, **31**, 305-311.
7. A. P. Koley, R. Nirmala, S. Ghosh, L. S. Prasad and P. T. Manoharan, *Inorg. Chem.*, 1992, **31**, 1764-1769.
8. M. S. Jana, A. K. Pramanik, S. Kundu, D. Sarkar, S. Jana and T. K. Mondal, *Inorg. Chim. Acta*, 2013, **394**, 583-590.
9. M. Mishra, K. Tiwari, S. Shukla, R. Mishra and V.P. Singh, *Spectrochim. Acta A*, 2014, **132**, 452-464.
10. R. Karvembu, S. Hemalatha, R. Prabhakaran and K. Natarajan, *Inorg. Chem. Commun.*, 2003, **6**, 486-490.
11. K. P. Balasubramanian, R. Karvembu, R. Prabhakaran, V. Chinnusamy and K. Natarajan, *Spectrochim. Acta A*, 2007, **68**, 50-54.
12. K. M. Vyas, R. G. Joshi, R. N. Jadeja, C. R. Prabha and V. K. Gupta, *Spectrochim. Acta A*, 2011, **84**, 256-268.

13. T. Rosu, E. Pahontu, C. Maxim, R. Georgescu, N. Stanica and A. Gulea, *Polyhedron*, 2011, **30**, 154-162.
14. F. Thomas, *Eur. J. Inorg. Chem.*, 2007, 2379-2404.
15. L. Zhou, D. Powell and K. M. Nicholas, *Inorg. Chem.*, 2007, **46**, 7789-7799.
16. L. M. Berreau, *Eur. J. Inorg. Chem.*, 2006, 273-283.
17. K. Akdi, R. A. Vilaplana, S. Kamah and F. Gonzalez-Vilchez, *J. Inorg. Biochem.*, 2005, **99**, 1360-1368.
18. M. Laine, F. Richards, E. Tarnaud, C. Bied-Charreton and C. Verchere-Beaur, *J. Biol. Inorg. Chem.*, 2004, **9**, 550-562.
19. P. Tsiveriotis and N. Hadjiliadis, *Coord. Chem. Rev.*, 1999, **190**, 171-184.
20. S. E. Sherman, D. Gibson, A. H. J. Wang and S. J. Lippard, *J. Am. Chem. Soc.*, 1988, **110**, 7368-7381.
21. M. K. Amir, S. Z. Khan, F. Hayat, A. Hassan and I. S. Butler, *Inorg. Chim. Acta*, 2016, **451**, 31-40.
22. Y. Gou, G. Huang, J. Li, F. Yang and H. Liang, *Coord. Chem. Rev.*, 2021, **441**, 213975.
23. J. Zhang, L. Li, L. Wang, F. Zhang and X. Li, *Eur. J. Med. Chem.*, 2010, **45**, 5337-5344.
24. A. Shoukry, T. Rau, M. Shoukry and R. Van Eldik, *J. Chem. Soc. Dalton Trans.*, 1998, **18**, 3105-3112.
25. M. Saeidifar, H. Mirzaei, N. A. Nasab and H. Mansouri-Torshizi, *J. Mol. Struct.*, 2017, **1148**, 339-346.
26. Md N. Alam and F. Huq, *Coord. Chem. Rev.*, 2016, **316**, 36-67.
27. T. Thirunavukkarasu, H. A. Sparkes and K. Natarajan, *Inorg. Chim. Acta*, 2018, **482**, 229-239.

28. M. C. Zhu, X. Cui, S. Zhang, L. Liu, Z. Han and E. Gao, *J. Inorg. Biochem.*, 2016, **157**, 34-45.
29. M. K. Paira, T. K. Mondal, E. López-Torres, J. Ribas, C. Sinha, *Polyhedron*, 2010, **29**, 3147-3156.
30. A. S. Mondal, M. S. Jana, C. K. Manna, R. Naskar and T. K. Mondal, *J. Mol. Struct.*, 2018, **1164**, 94-99.
31. S. Kundu, S. Biswas, A. S. Mondal, P. Roy and T. K. Mondal, *J. Mol. Struct.*, 2015, **1100**, 27-33.
32. S. Mondal, T. K. Mondal, Y. Rajesh, M. Mandal and C. R. Sinha, *Polyhedron*, 2018, **151**, 344-354.
33. S. Biswas, P. Roy, S. Jana and T. K. Mondal, *J. Organomet. Chem.*, 2017, **846**, 201-207.
34. M. S. Jana, A. K. Pramanik, D. Sarkar, S. Biswas and T. K. Mondal, *Polyhedron*, 2014, **81**, 66-73.
35. S. Kundu, A. K. Pramanik, A.S. Mondal and T. K. Mondal, *J. Mol. Struct.*, 2016, **1116**, 1-8.
36. Bruker. SAINT v8.38A. Bruker AXS Inc., Madison, Wisconsin, USA.
37. L. Krause, R. Herbst-Irmer, G. M. Sheldrick and D. Stalke, *J. Appl. Cryst.*, 2015, **48**, 3-10.
38. G. M. Sheldrick, A short history of SHELX, *Acta Cryst.*, A64, 2008, **A64**, 112-122.
39. G. M. Sheldrick, Crystal structure refinement with SHELXL, *Acta Cryst.*, 2015, **C71**, 3-8.
40. A. D. Becke, *J. Chem. Phys.*, 1993, **98**, 5648-5652.
41. C. Lee, W. Yang and R. G. Parr, *Phys. Rev.*, 1988, **B37**, 785-789.
42. P. J. Hay and W. R. Wadt, *J. Chem. Phys.*, 1985, **82**, 270-283.

43. W. R. Wadt and P. J. Hay, *J. Chem. Phys.*, 1985, **82**, 284-298.
44. P. J. Hay and W. R. Wadt, *J. Chem. Phys.*, 1985, **82**, 299-310.
45. Gaussian 09, Revision D.01, M. J. Frisch, G. W. Trucks, H. B. Schlegel, G. E. Scuseria, M. A. Robb, J. R. Cheeseman, G. Scalmani, V. Barone, B. Mennucci, G. A. Petersson, H. Nakatsuji, M. Caricato, X. Li, H. P. Hratchian, A. F. Izmaylov, J. Bloino, G. Zheng, J. L. Sonnenberg, M. Hada, M. Ehara, K. Toyota, R. Fukuda, J. Hasegawa, M. Ishida, T. Nakajima, Y. Honda, O. Kitao, H. Nakai, T. Vreven, J. A. Montgomery, Jr., J. E. Peralta, F. Ogliaro, M. Bearpark, J. J. Heyd, E. Brothers, K. N. Kudin, V. N. Staroverov, R. Kobayashi, J. Normand, K. Raghavachari, A. Rendell, J. C. Burant, S. S. Iyengar, J. Tomasi, M. Cossi, N. Rega, J. M. Millam, M. Klene, J. E. Knox, J. B. Cross, V. Bakken, C. Adamo, J. Jaramillo, R. Gomperts, R. E. Stratmann, O. Yazyev, A. J. Austin, R. Cammi, C. Pomelli, J. W. Ochterski, R. L. Martin, K. Morokuma, V. G. Zakrzewski, G. A. Voth, P. Salvador, J. J. Dannenberg, S. Dapprich, A. D. Daniels, Ö. Farkas, J. B. Foresman, J. V. Ortiz, J. Cioslowski, and D. J. Fox, Gaussian, Inc., Wallingford CT, 2009.
46. R. Bauernschmitt and R. Ahlrichs, *Chem. Phys. Lett.*, 1996, **256**, 454-464.
47. R. E. Stratmann, G. E. Scuseria and M. J. Frisch, *J. Chem. Phys.*, 1998, **109**, 8218-8224.
48. M. E. Casida, C. Jamorski, K. C. Casida and D. R. Salahub, *J. Chem. Phys.*, 1998, **108**, 4439-4449.
49. V. Barone and M. Cossi, *J. Phys. Chem. A*, 1998, **102**, 1995-2001.
50. M. Cossi and V. Barone, *J. Chem. Phys.*, 2001, **115**, 4708-4717.
51. M. Cossi, N. Rega, G. Scalmani and V. Barone, *J. Comput. Chem.*, 2003, **24**, 669-681.

52. N. M. O'Boyle, A. L. Tenderholt and K. M. Langner, *J. Comput. Chem.*, 2008, **29**, 839-845.
53. T. L. Riss, R. A. Moravec, A. L. Niles, S. Duellman, H. A. Benink, T. J. Worzella and L. Minor, *Cell viability assays. Assay Guidelines manuals*, 2013.
54. P. Pattanayak, S. P. Parua, D. Patra, C.-K. Lai, P. Brandao, V. Felix and S. Chattopadhyay, *Inorg. Chim. Acta*, 2015, **429**, 122-131.
55. C. K. Manna, R. Naskar, B. Bera, A. Das and T. K. Mondal, *J. Mol. Struct.*, 2021, **1237**, 130322.
56. M. M. Tamizh, B. F. T. Cooper, C. L. B. Macdonald and R. Karvembu, *Inorg. Chim. Acta*, 2013, **394**, 391-400.
57. P. Kalaivani, R. Prabhakaran, M. V. Kaveri, R. Huang, R. J. Staples and K. Natarajan, *Inorg. Chim. Acta*, 2013, **405**, 415-426.

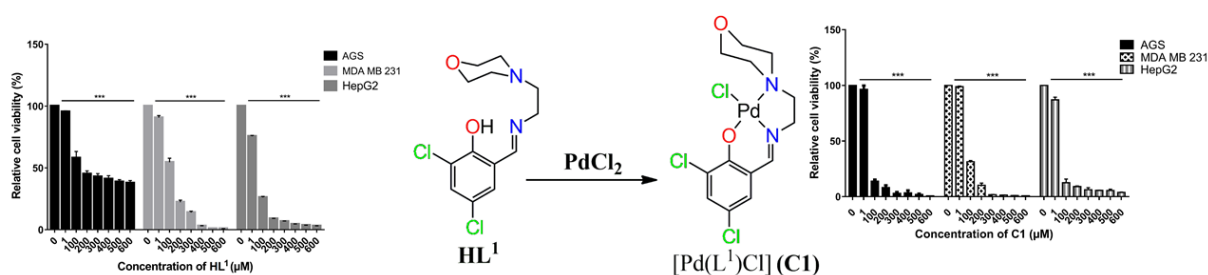
CHAPTER-IV

**Palladium(II) complexes with
morpholine based ONN pincers:
Synthesis, X-ray structure, protein
(CT-DNA/BSA) binding study and
in-vitro cytotoxicity**

Palladium(II) complexes with morpholine based ONN pincers: Synthesis, X-ray structure, protein (CT-DNA/BSA) binding study and in-vitro cytotoxicity

Abstract

New ONN donor pincer ligands, 2,4-dichloro-6-(((2-morpholinoethyl)imino)methyl)phenol (HL^1) and 4-dichloro-6-(((2-morpholinophenyl)imino)methyl)phenol (HL^2) and their palladium complexes $[Pd(L^1)Cl]$ (**C1**) and $[Pd(L^2)Cl]$ (**C2**) are synthesized and thoroughly characterized by spectroscopic techniques. X-ray structures of the complexes reveal that HL^1 and HL^2 act as tridentate O,N,N chelator in Pd(II) complexes forming distorted square planar geometry. The ability of the Pd(II) complexes to bind with CT DNA are investigated by UV–Vis method and the binding constant are found to be $3.52 \times 10^5 \text{ M}^{-1}$ and $1.87 \times 10^5 \text{ M}^{-1}$ for **C1** and **C2** respectively. Competitive binding study with ethidium bromide (EB) by fluorescence method suggests that the Pd(II) complexes efficiently displace EB from EB-DNA complex. The Calculated Stern-Volmer dynamic quenching constant, K_{sv} are found to be $1.50 \times 10^5 \text{ M}^{-1}$ and $1.87 \times 10^5 \text{ M}^{-1}$ for **C1** and **C2** respectively. Moreover, the interactions of Pd(II) complexes (**C1/C2**) with bovine serum albumin (BSA) are also studied. The antiproliferative activity of the complexes are investigated with gastric adenocarcinoma cell line (AGS), triple negative breast cancer cell line (MDA-MB 231) and hepatocellular carcinoma cell line (HepG2). Both the Pd(II) complexes exhibit substantial cytotoxicity towards HepG2 ($IC_{50} = 14.22\text{-}15.08 \text{ }\mu\text{M}$) and AGS ($IC_{50} = 8.47\text{-}10.73 \text{ }\mu\text{M}$) cell lines.



IV.1. Introduction

According to World Health Organization (WHO), cancer is treated as 2nd leading cause of death among noninfectious diseases accounting almost 72% death worldwide [1,2]. So, the development of a new potential anticancer drug with minimal side effects remains the focus of interest among the scientists [3]. Design of anticancer drugs with improved potency are utmost challenging [4]. Nowadays, metals fabricated with various ligands are considered in healing with various diseases. Recently Schiff bases with ONN and ONS donor ligand fabricated with 1st, 2nd and 3rd row transition metals are remarkably considered owing to several biological applications like anticancer, antiviral, antifungal, anti-tuberculosis and anti-inflammatory activity as well as their mode of coordination [5,6]. Because of modifying ability and significant lipophilicity ligands play crucial role to improve drug resistance [7,8]. Moreover, Schiff base ligands can stabilize the uncommon oxidation states. It has been reported that different heterocyclic aromatic ligands like pyridine, phenanthroline [9,10] and their derivatives act as DNA intercalators in Pd complexes. Since tumour cells grow rapidly compare to non-neoplastic cells, anticancer drugs mainly modify the DNA structure by forming irreversible covalent and also noncovalent bond which hampers DNA replication and transcription [11-18].

Discovery of cisplatin as an anti-cancer drug in 1979 is considered as remarkable innovation in the field of medicinal chemistry. Cisplatin has been used mainly in the treatment of testicular and ovarian cancer worldwide [19-26]. Platinum metal of cisplatin molecule interact with nearby purine bases via their N7 positions by forming irreversible covalent bond. However, cisplatin has a number of negative side effects such as nausea, vomiting, nephrotoxicity, ototoxicity, bone marrow suppression, and neurotoxicity [27]. Among all the transition metal ions, study of palladium(II) complexes as antitumor drugs have grown much more interest than Pt(II) complexes in the field of medicinal chemistry due to structural

similarity and chemical reactivity. Some notable points towards validation of Pd(II) complexes as better anticancer agent than Pt(II) complexes are that Pd(II) complexes have improved solubility compared to Pt(II) complexes and also the aquation rate and the rate of ligand exchange of Pd(II) complexes are about 10^5 times compared to their Pt(II) analogues [28-34].

Bovine serum albumin has considerably been studied in place of human serum albumin because of their structural similarity. In circulatory system, transportation of nutrients and drugs have been carried out by most abundant protein serum albumin through non-covalent interaction. Binding ability of serum proteins with therapeutic drugs are crucial for absorption, excretion and metabolism. Moreover, study of DNA interactions with these drugs fabricated with different chelating ligand has drawn considerable interests due to their potential applications [35-42].

Herein, new morpholine based ONN donor pincer ligands (HL^1 and HL^2) and their palladium complexes $[Pd(L^1)Cl]$ (**C1**) and $[Pd(L^2)Cl]$ (**C2**) are synthesized and thoroughly characterized by spectroscopic techniques. The ability of the Pd(II) complexes to bind with CT DNA and bovine serum albumin (BSA) are investigated. In-vitro cytotoxicity, colony formation assay and cell migration studies are performed to monitor the inhibitory action of the Pd(II) complexes. Theoretical calculations by DFT and TDDFT methods are performed to interpret the electronic structure and spectral properties of the compounds.

IV.2. Experimental

IV.2.1. Materials

3, 5-Dichloro phenol, palladium(II) chloride, 4-(2-aminoethyl)morpholine, 2-morpholino aniline were purchased from Sigma Aldrich. 3, 5-Dichloro-2-hydroxybenzaldehyde was prepared according to the published paper [43]. Gastric cancer cell line AGS, triple negative

breast cancer cell line MDA MB 231 and liver cancer cell line HepG2 were obtained from National centre for cell science (NCCS), Pune, India.

IV.2.2. Instrumentation

The elemental analyses (C, H, N) were performed by PerkinElmer 2400 series II analyser. ^1H NMR spectra were noted down by using Bruker 300 MHz instrument. For NMR spectra, CDCl_3 and DMSO-d_6 were used as solvent using TMS as an internal standard. HRMS mass spectra were recorded on Waters (Xevo G2 Q-TOF) mass spectrometer. Electronic spectra were taken on a Perkin Elmer Lambda 750 spectrophotometer. Fluorescence spectra were taken on a Shimadzu RF-6000 Spectro fluorophotometer. FTIR spectra were recorded on a RX-1 PerkinElmer spectrophotometer in the range of $4000\text{-}400\text{ cm}^{-1}$ equipped with a Golden Gate Diamond attenuated total reflectance (ATR) device.

IV.2.3. Synthesis

IV.2.3.1. Synthesis of HL¹

Synthesis of Schiff-base ligand HL¹ was carried out by a simple one-step reaction. To prepare the ligand HL¹, 0.191 g (1 mmol) of 3, 5-dichloro-2-hydroxybenzaldehyde and 0.129 g (1 mmol) of 4-(2-aminoethyl)morpholine were refluxed for 3 h at $50\text{-}60\text{ }^\circ\text{C}$ in dry methanol under continuous stirring condition. A straw-yellow precipitate HL¹ was formed. The precipitate was filtered and thoroughly washed with ethanol. Yield: 0.240 g (79.2%).

Anal. Calc. for $\text{C}_{13}\text{H}_{16}\text{N}_2\text{Cl}_2\text{O}_2$: C, 51.50; H, 5.32; N, 9.24. Found: C, 51.45; H, 5.30; N, 9.20. IR (KBr, cm^{-1}): 3453 $\nu(\text{OH})$ 2972 $\nu(\text{CH})$, 1635 $\nu(\text{C}=\text{N})$, 1103 $\nu(\text{C}-\text{N})$. ^1H NMR (300 MHz, DMSO-d_6): δ 2.49-2.52 ($-\text{CH}_2$, m, 4H), 2.69 ($-\text{CH}_2$, t, $J = 6\text{ Hz}$, 2H), 3.68-3.77 ($-\text{CH}_2$, m, 6H), 7.40 (ArH, s, 1H), 8.24 ($\text{CH}=\text{N}-$, s, 1H), 14.45 ($-\text{OH}$, s, 1H). UV-vis in acetonitrile (λ_{max} , nm) (ϵ , $\text{M}^{-1}\text{cm}^{-1}$): 280 (29868); 330 (18642). HRMS: calculated for $\text{C}_{13}\text{H}_{16}\text{Cl}_2\text{N}_2\text{O}_2\text{Na}$ $[\text{M}+\text{Na}]^+$ (m/z): 325.0487; found: 325.0135.

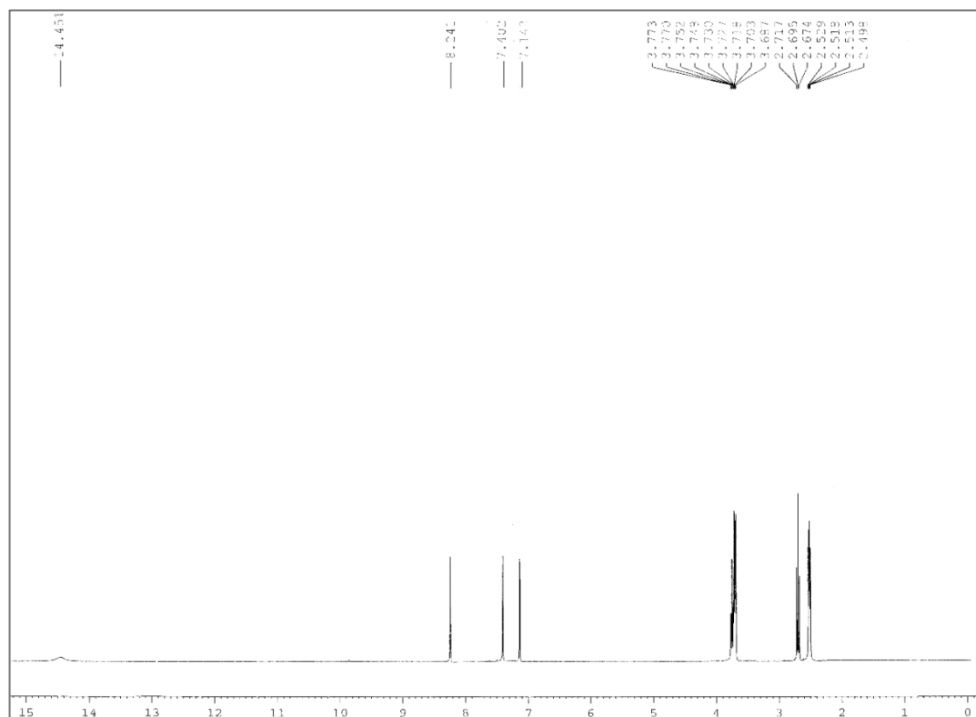


Fig.IV.1. ^1H NMR spectrum of HL¹ in CDCl_3

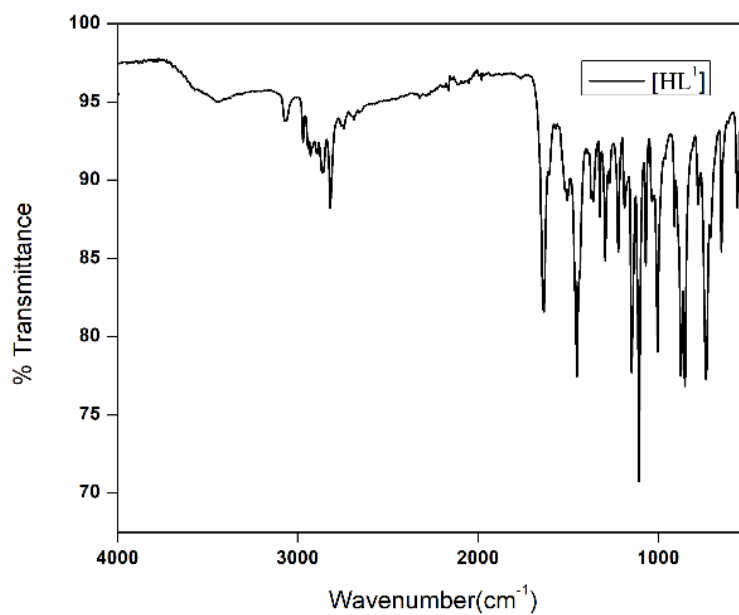


Fig.IV.2. IR spectrum of HL¹(KBr disk)

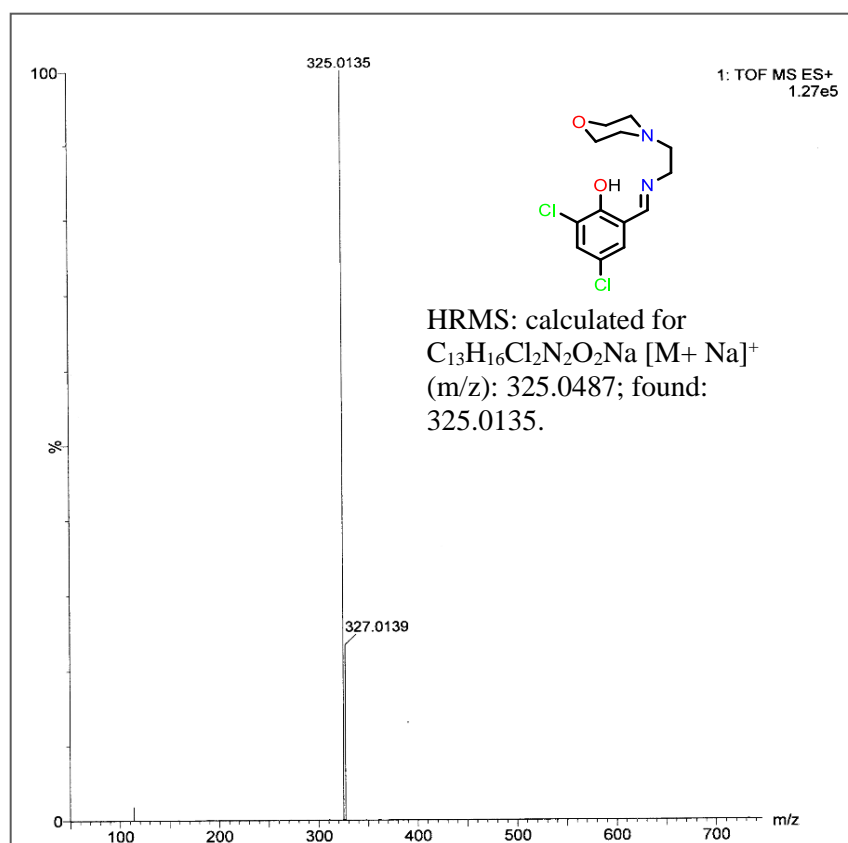


Fig.IV.3. HRMS spectrum of HL¹ in acetonitrile

IV.2.3.2. Synthesis HL²

HL² was prepared following the similar procedure of HL¹ by refluxing 0.191 g (1 mmol) of 3,5-dichloro-2-hydroxybenzaldehyde and 0.178 g (1 mmol) of 2-morpholinoaniline in dry methanol. Yield: 0.290 g (82.6%).

Anal. Calc. for $C_{17}H_{16}N_2Cl_2O_2$: C, 58.13; H, 4.59; N, 7.98. Found: C, 58.11; H, 4.56; N, 7.96. IR (KBr, cm^{-1}): 3478 ν (O-H), 2961 ν (C-H), 1612 ν (C=N), 1110 ν (C-N). ¹H NMR (300 MHz, DMSO-*d*₆): δ 3.02 (-CH₂, t, J = 6 Hz, 4H), 3.92 (-CH₂, t, J = 6 Hz, 4H), 7.15 (ArH, t, J = 15 Hz, 1H), 7.22 (ArH, d, J = 6 Hz, 1H), 7.28 (ArH, s, 2H), 7.33 (ArH, t, J = 6 Hz, 1H), 7.48 (ArH, d, J = 3 Hz, 1H), 8.65 (CH=N-, s, 1H), 14.69 (-OH, s, 1H). UV-Vis in acetonitrile (λ_{max} , nm) (ϵ , $M^{-1}cm^{-1}$): 270 (24249); 361 (15237). HRMS: calculated for $C_{17}H_{16}Cl_2N_2O_2Na [M+Na]^+$ (m/z): 373.0487; found: 373.0417.

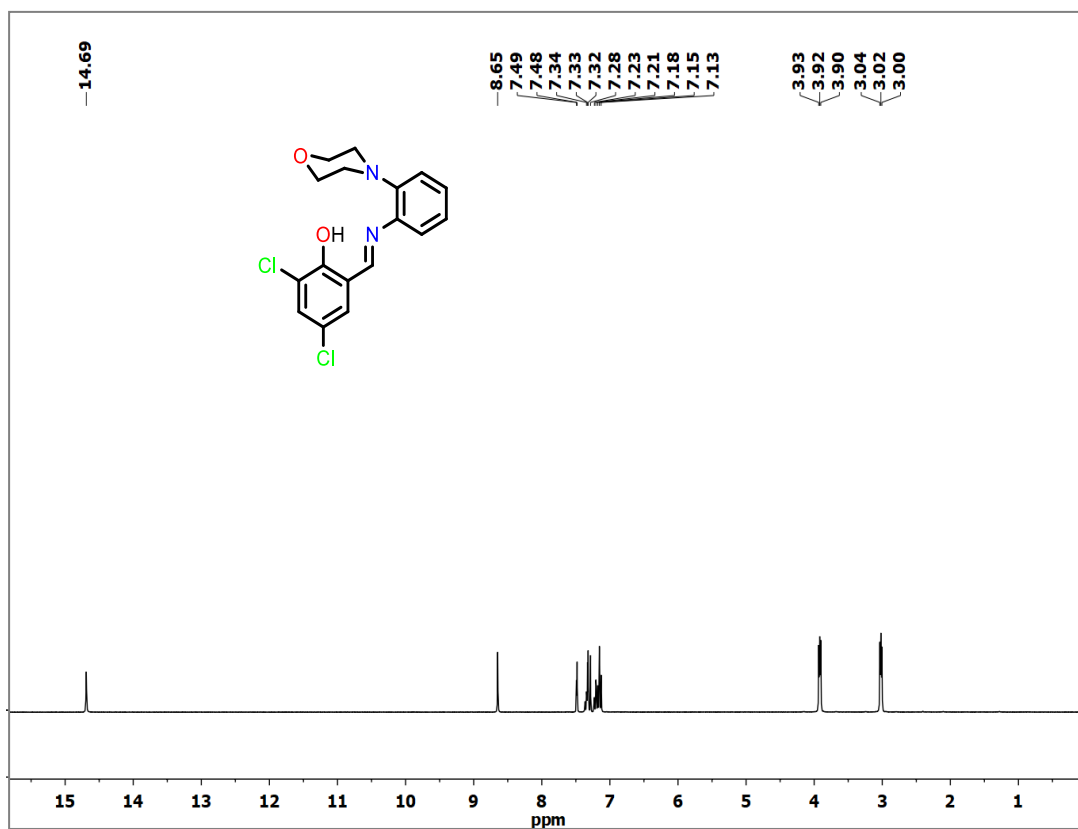


Fig.IV.4. 1H NMR spectrum of HL^1 in $CDCl_3$

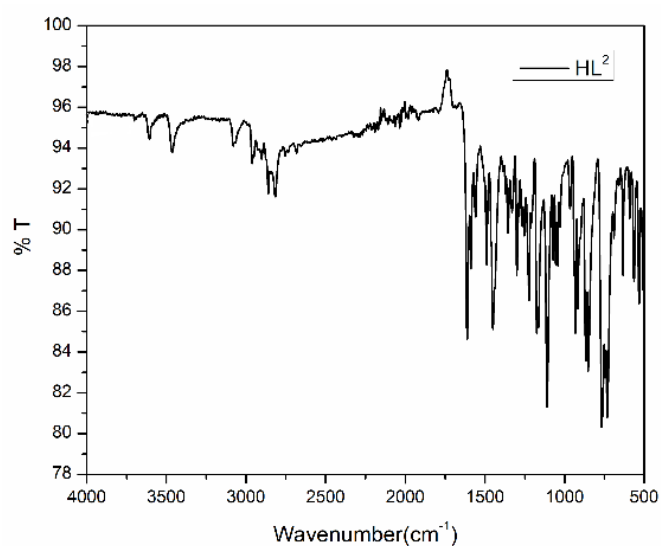


Fig.IV.5. IR spectrum of HL^1 (KBr disk)

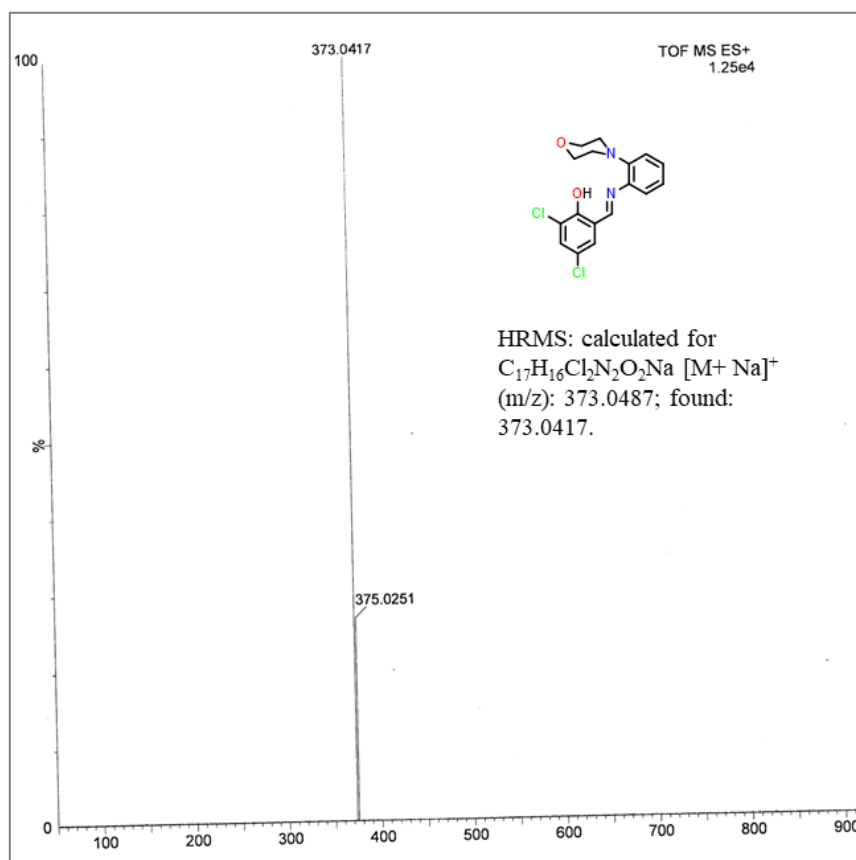


Fig.IV.6. HRMS spectrum of HL² in acetonitrile

IV.2.3.3. Synthesis of [Pd(L¹)Cl] (C1)

At first in a round bottom flask 0.037g (0.209 mmol) of PdCl₂ was dissolved in 15 mL acetonitrile under refluxing condition. To it 0.063 g (0.209 mmol) of HL¹ in 15 mL acetonitrile was mixed dropwise. The reaction mixture was then refluxed for 5 h to yield red coloured solution. The reaction mixture was then cooled to room temperature. Red coloured solid product of [Pd(L¹)Cl] (C1) was collected by slow evaporation of the solvent. Yield: 0.075 g (81.5%).

Microanalytical data for C₁₃H₁₅Cl₃N₂O₂Pd (C1): Anal. Calc. (%):C, 35.16; H, 3.40; N, 6.31. Found (%):C, 35.11; H, 3.22; N, 6.13. IR data (KBr disc) (cm⁻¹): 2955 ν (CH), 1590 ν (C=N).

¹H NMR (300 MHz, DMSO-d₆): δ 2.59 (-CH₂, t, J = 6 Hz, 2H), 2.96 (-CH₂, t, J = 6 Hz, 2H),

3.16 (-CH₂, t, J = 6 Hz, 2H), 3.45 (-CH₂, t, J = 9 Hz, 2H), 3.83-3.93 (-CH₂, m, 4H), 7.47 (ArH, s, 1H), 7.57 (ArH, s, 1H), 8.09 (CH=N-, s, 1H). λ_{\max} (ϵ , M⁻¹ cm⁻¹) in acetonitrile: 292 (16006), 374 (sh), 416 (7989). HRMS: calculated for C₁₃H₁₅Cl₂N₂O₂ [M-Cl]⁺ (m/z): 406.9545; found: 406.9540.

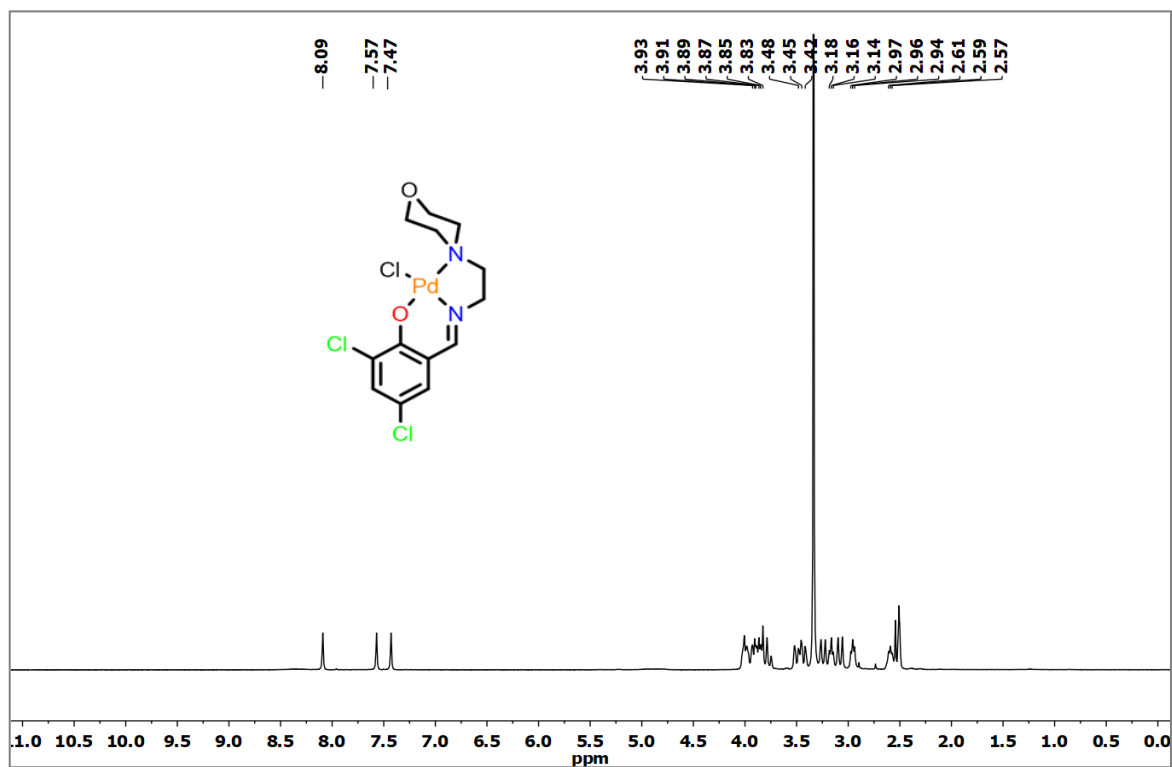


Fig.IV.7. ¹H NMR spectrum of [Pd(L¹)Cl] in CDCl₃

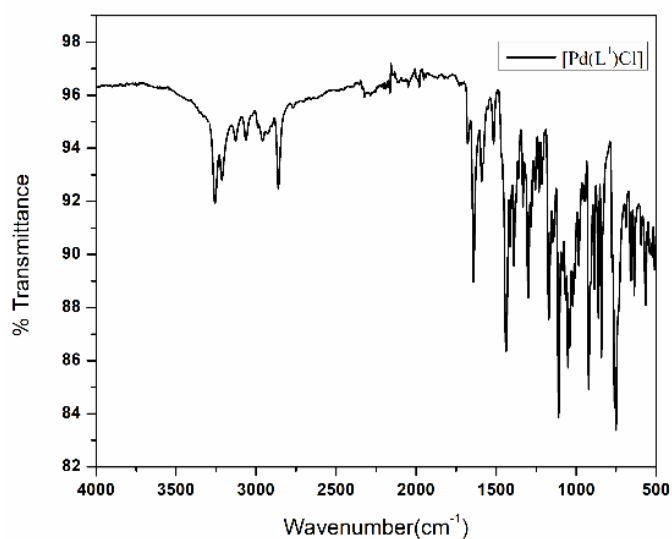


Fig.IV.8. IR spectrum of [Pd(L¹)Cl](KBr disk)

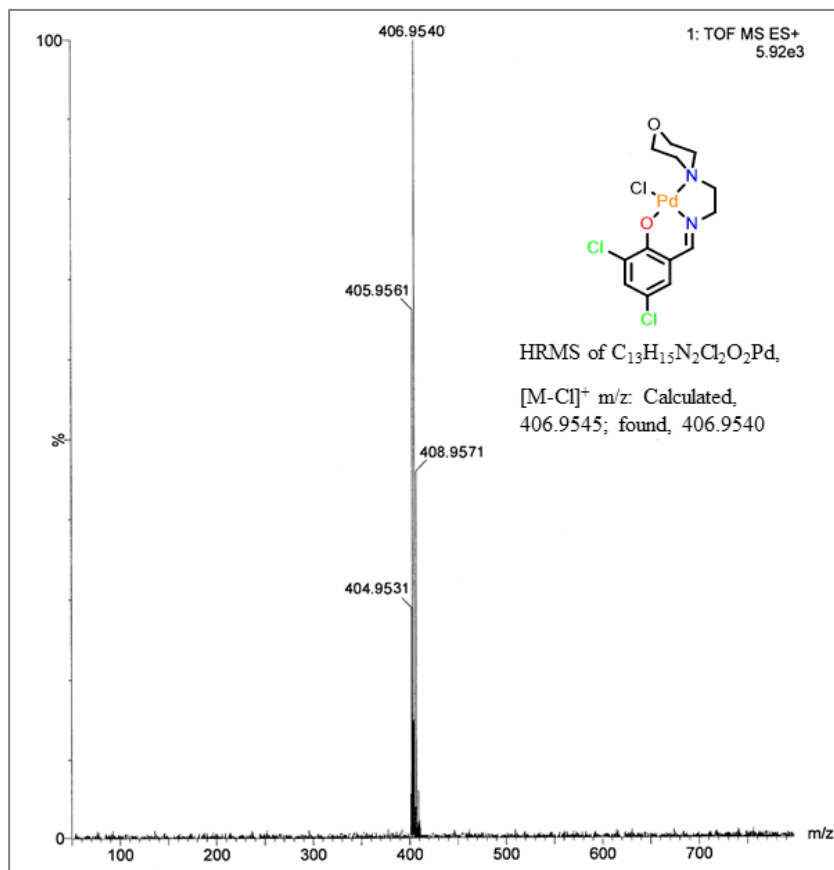


Fig.IV.9. HRMS spectrum of $[\text{Pd}(\text{L}^1)\text{Cl}]$ in acetonitrile

IV.2.3.4. Synthesis of $[\text{Pd}(\text{L}^2)\text{Cl}]$ (C2)

$[\text{Pd}(\text{L}^2)\text{Cl}]$ (C2) was synthesized following the similar procedure of C1. Yield: 0.08 g (78.4%).

Microanalytical data for $\text{C}_{17}\text{H}_{15}\text{Cl}_3\text{N}_2\text{O}_2\text{Pd}$ (C2): Anal. Calc. (%): C, 41.49; H, 3.07; N, 5.69.

Found (%): C, 41.35; H, 3.01; N, 5.53. IR data (KBr disc) (cm^{-1}): 2935 $\nu(\text{CH})$, 1596 $\nu(\text{C}=\text{N})$.

^1H NMR (300 MHz, DMSO-d_6): δ 4.3 ($-\text{CH}_2$, t, $J = 6$ Hz, 4H), 4.48 ($-\text{CH}_2$, t, $J = 6$ Hz, 4H), 7.56 (ArH, d, $J = 3$ Hz, 1H), 7.61 (ArH, d, $J = 3$ Hz, 1H), 7.68 (ArH, s, 2H), 7.88 (ArH, t, $J = 6$ Hz, 1H), 8.01 (ArH, t, $J = 6$ Hz, 1H), 8.99 ($\text{CH}=\text{N}-$, s, 1H). λ_{max} (ϵ , $\text{M}^{-1} \text{cm}^{-1}$) in acetonitrile: 295 (17553), 335 (9546), 433 (sh), 465 (7406). HRMS: calculated for $\text{C}_{17}\text{H}_{15}\text{Cl}_2\text{N}_2\text{O}_2$ $[\text{M}-\text{Cl}]^+$ (m/z): 454.9545; found: 454.9541.

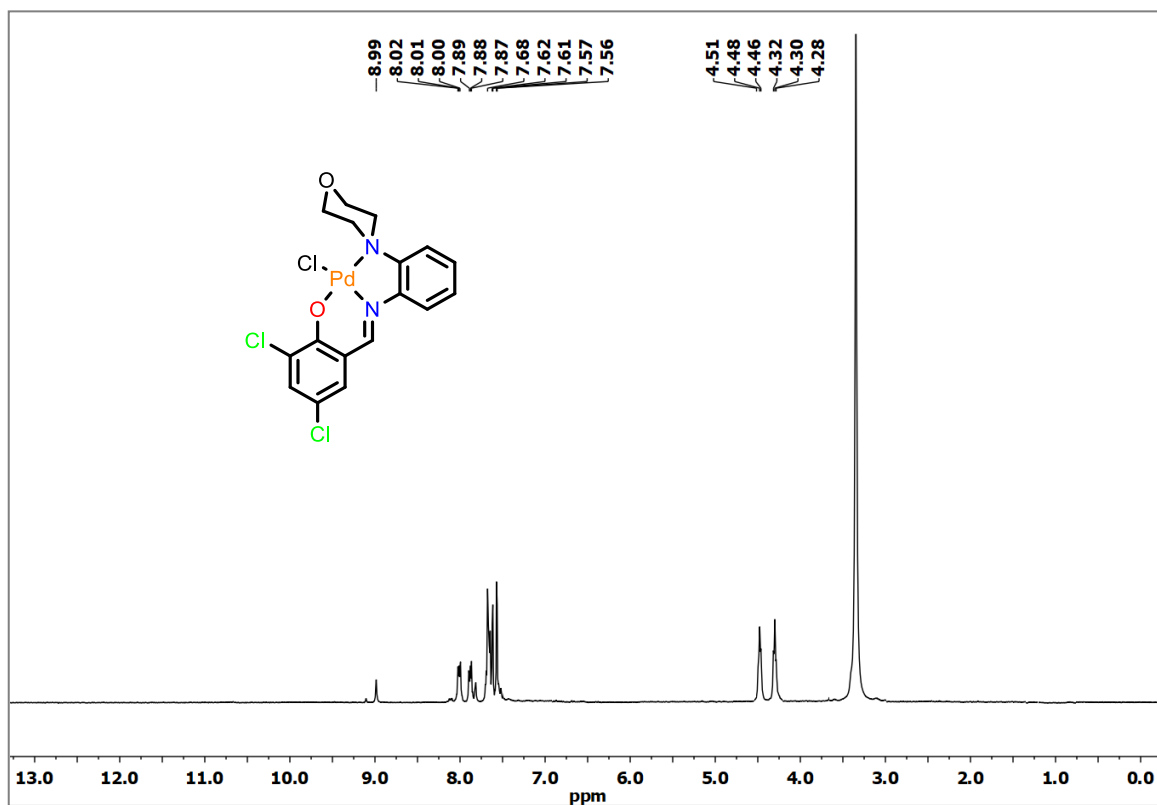


Fig.IV.10. ^1H NMR spectrum of $[\text{Pd}(\text{L}^2)\text{Cl}]$ in CDCl_3

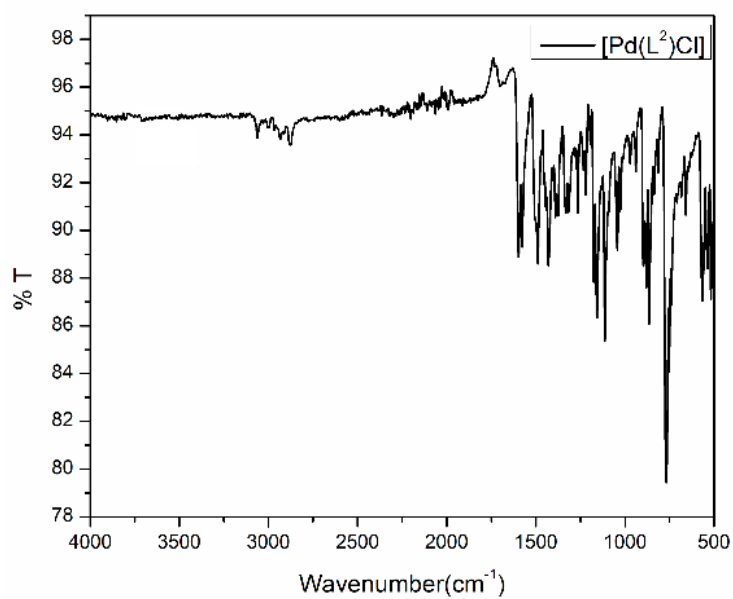


Fig.IV.11. IR spectrum of $[\text{Pd}(\text{L}^2)\text{Cl}]$ (KBr disk)

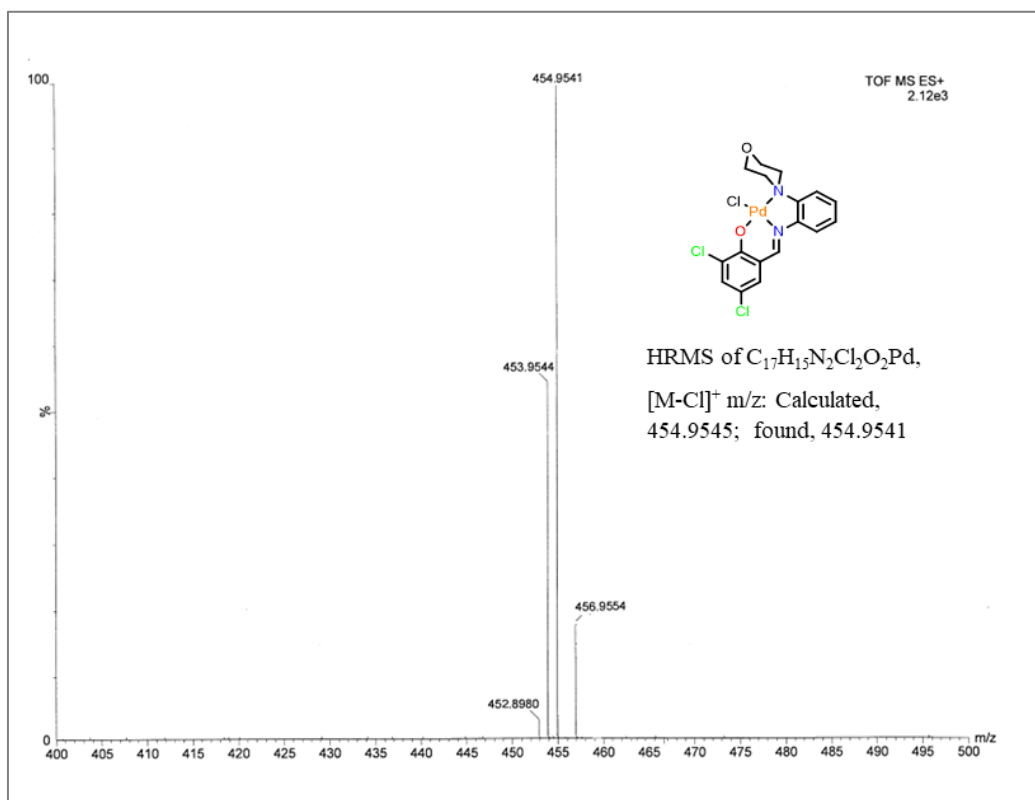


Fig.IV.12. HRMS spectrum of $[\text{Pd}(\text{L}^2)\text{Cl}]$ in acetonitrile

IV.2.4. DNA-binding interaction Studies

IV.2.4.1. UV-Vis titration

For UV-Vis titrations, a CT-DNA (2.19×10^{-3} M) solution in Tris-HCl/ NaCl buffer (at pH 7.4) and complex solution (1.0×10^{-4} M) in 1:10 acetonitrile/buffer were prepared. The UV-Vis spectra of the complexes were measured between 300 and 600 nm. CT-DNA solution was gradually added to it, stirred properly, and equilibrated for 4 min before collecting the spectra. Addition continued until saturation occurred. These spectral-titration results are important for determining the equilibrium binding constant (K_b) of the complex with CT-DNA. Eq. (1) was used to determine K_b (in M^{-1}) [44].

$$[\text{DNA}]/(\varepsilon_a - \varepsilon_f) = [\text{DNA}]/(\varepsilon_b - \varepsilon_f) + 1/K_b(\varepsilon_b - \varepsilon_f) \dots(1)$$

where [DNA] is the concentration of CT DNA in base pairs, the extinction coefficients ϵ_a , ϵ_f and ϵ_b correspond to $A_{\text{obs}}/[\text{complex}]$, free Pd(II) complex, and the extinction coefficient of the Pd(II) complex when it is in totally bound form, respectively. The plot of $[\text{DNA}]/(\epsilon_a - \epsilon_f)$ against [DNA] will produce slope $1/(\epsilon_b - \epsilon_f)$ and intercept $1/K_b(\epsilon_b - \epsilon_f)$; K_b is the ratio of slope to intercept.

IV.2.4.2. Competitive binding study with EB by fluorescence method

The ability of the synthesized palladium complexes (**C1/C2**) to dislocate EB from its EB-DNA complexes were studied by the fluorescence method. 10 μM EB and 10 μM CT DNA in Tris-HCl/NaCl buffer solution (pH 7.4) were mixed homogeneously to prepare the CT DNA-EB complexes which produced fluorescence emission at 608 nm when excited at 540 nm. Quenching of that emission was monitored with the subsequent addition of **C1** and **C2**.

IV.2.5. BSA interaction experiments

The binding interaction between BSA and Pd(II) complexes (**C1/C2**) were investigated by employing UV-Vis as well as fluorescence methods. A stock solution of BSA was prepared using 500 mM phosphate buffer saline (PBS) at pH 7.4 and stored in the dark at 4°C for further use. BSA concentration was measured by taking absorbance at 280 nm in UV-Vis spectra [45] (molar extinction coefficient $66,400 \text{ dm}^3 \text{ mol}^{-1} \text{ cm}^{-1}$). The stock solution of **C1** and **C2** were prepared in DMSO medium and were suitably diluted with PBS whenever necessary. For recording UV-Vis spectra, BSA-concentration was kept constant (10 μM) while varying the concentration of complex added to it. In fluorescence experiment, tryptophan fluorescence of BSA was recorded in the range 290–500 nm at an excitation wavelength of 280 nm using a slit width of 5 nm. Quenching of emission intensity at ~336 nm for BSA were monitored with subsequent addition of metal complexes.

IV.2.6. Anti-cancer activity

IV.2.6.1. Cell Culture

AGS cell line exhibiting gastric adenocarcinoma, MDA MB 231 of breast adenocarcinoma origin exhibiting triple negative subtype and hepatocellular carcinoma cell line HepG2 was purchased from National centre for cell science, Pune, India and maintained in DMEM high glucose medium (MDA MB 231 and HepG2) and RPMI-1640 medium (AGS) (Gibco) supplemented with 10% Fetal Bovine Serum (FBS) (Gibco). All the cell lines were maintained in a humidified incubator at 37°C, having an atmosphere comprised of 5% CO₂. All experiments were performed at early passage numbers.

IV.2.6.2. Cell Viability Assay

Cell viability assay was performed as described earlier by Riss T L et.al. [46]. Initially, 1×10^3 cells per well in 96 well plate were plated and treated with increasing concentrations of HL¹, HL², and their Pd(II) complexes **C1** and **C2**, and cisplatin (1, 100, 200, 300, 400, 500 and 600 μ M) for 24 hours at 37 °C. Subsequently, MTT solution (10 μ L) (5mg/ml in PBS) was added in each well. Post incubation for 3 hours, 100 μ L DMSO was added to each well and the absorbance was measured at 570 nm using a multi-mode plate reader (SpectraMax i3x, Molecular devices). Nonlinear regression (curve fit) followed by log (inhibition) vs. response equation in graph pad prism software was used to calculate IC₅₀ value.

IV.2.6.3. Colony Formation Assay

500 cells per well of all the three cell lines were plated in 6 well plates. Subsequently, the cells were exposed to C1 (56 μ M for MDA MB 231, 15 μ M for AGS, 11 μ M for HepG2), HL¹ (184 μ M for MDA MB 231, 88 μ M for AGS and 55 μ M for HepG2), C2 (41 μ M for MDA MB 231, 14 μ M for AGS and 8.5 μ M for HepG2) and HL² (175 μ M for MDA MB 231, 166 μ M for AGS and 30 μ M for HepG2) and incubated at 37°C until colonies formed in the untreated

control group. Then the formed colonies were thoroughly washed with 1X PBS and fixed using methanol, followed by Crystal violet staining for 15 minutes. Colonies, defined as >50 cells, were calculated under inverted Bright Field Microscope (Olympus CKX41, Japan) at 4X objective magnification.

IV.2.6.4. Statistical analysis

All experiments were performed in triplicates and the representative data are exhibited as mean value \pm S.D. With the help of Turkey test One-way Analysis Variance (ANOVA) with post hoc comparisons were performed in order to evaluate the major variation between control and each treated group. P value of less than 0.05 was considered to be statistically significant. All the analyses were performed with Graph pad prism 5 software.

IV.2.6.5. In Vitro Cell Migration Assay

In a 6-well plate, MDA MB231 breast cancer cells were cultured till 90% confluency. A straight scratch was made with the help of a 200 μ l sterile pipette tip on the confluent cells followed by washing with PBS. After that, the cells were treated with Pd(II) complexes in serum-free DMEM high glucose medium. The area of the wound closure was measured after incubating the cells for 0, 12 and 24 h, comparing with the initial wound size at 0 hours. The wound area was measured by ImageJ software and the wound area was quantified at each time point from the digital images.

IV.2.7. Computational method

Geometry optimization of the compounds were executed by DFT/B3LYP [47] method. All elements were assigned 6-31G(d) basis set except palladium. For palladium atom the LanL2DZ [48] basis set with effective core potential was employed. All calculations were carried out with Gaussian09 program [49] package via the GaussView, Version 5 visualization program. Simulation of the vertical electronic transitions in acetonitrile solvent

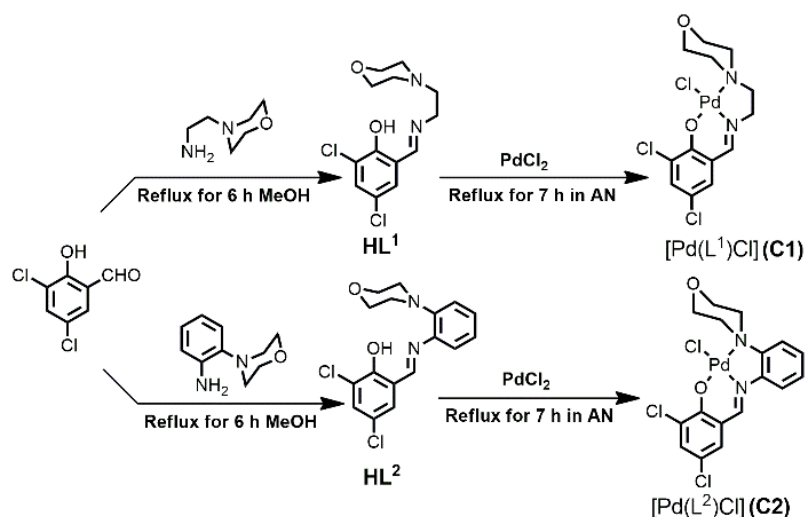
were successfully explored by Time-dependent density functional theory (TDDFT) [50] formalism using conductor-like polarizable continuum model (CPCM) [51]. Gauss Sum [52] was used to calculate the fractional contributions of various groups to each molecular orbital.

IV.2.8. Crystal structure determination and refinement

X-ray data for **C1** and **C2** were collected with the help of graphite monochromated Bruker AXS D8 Quest CMOS diffractometer (Mo K α radiation $\lambda = 0.71073 \text{ \AA}$) at 293 K. Reflection data were recorded using the ω scan technique. The collected frames were processed through the SAINT [53] reduction and SADABS [54] absorption correction program. The structures were solved by direct method using the SHELXL-2016/6 program [55] and refined by full-matrix least-squares based on F^2 . Hydrogen atoms were positioned at geometrically constrained positions and then refined as riding their pivot atoms. All atoms except hydrogen were refined anisotropically. Crystallographic data and experimental details are summarized in Table 1.

IV.3. Results and discussion

The Pd(II) complexes, [Pd(L¹)Cl] (**C1**) and [Pd(L²)Cl] (**C2**) were synthesized by the reaction of PdCl₂ with HL¹ and HL² in 1:1 mole ratio respectively under refluxing condition in acetonitrile (scheme IV.1). Ligands were synthesized following the reported method [56]. Both the ligands (HL¹/HL²) as well as complexes (**C1**/**C2**) were thoroughly characterized by several spectroscopic techniques. The geometries of the complexes were confirmed by single crystal X-ray crystallography method.



Scheme IV.1. Synthesis of palladium(II) complexes, $[\text{Pd}(\text{L}^1)\text{Cl}]$ (**C1**) and $[\text{Pd}(\text{L}^2)\text{Cl}]$ (**C2**)

Table IV.1. Crystal data and details of the structure determination of **C1** and **C2**

	$[\text{Pd}(\text{L}^1)\text{Cl}]$ (C1)	$[\text{Pd}(\text{L}^2)\text{Cl}]$ (C2)
Formula	$\text{C}_{13}\text{H}_{15}\text{Cl}_3\text{N}_2\text{O}_2\text{Pd}$	$\text{C}_{17}\text{H}_{15}\text{Cl}_3\text{N}_2\text{O}_2\text{Pd}$
Formula Weight	444.02	510.07
Crystal System	<i>Orthorhombic</i>	<i>Monoclinic</i>
Space group	<i>P 21 21 21</i>	<i>P 21/c</i>
<i>a</i> (Å)	6.430(2)	6.3309(9)
<i>b</i> (Å)	10.092(4)	8.5712(11)
<i>c</i> (Å)	24.111(9)	33.250(5)
β (°)	90	94.257(4)
<i>V</i> (Å ³)	1564.6(10)	1799.3(4)
<i>Z</i>	4	4
ρ (calc) (g/cm ³)	1.885	1.883
μ (Mo Ka) (mm ⁻¹)	1.702	1.498
<i>F</i> (000)	880	1016
Crystal Size (mm)	0.14 × 0.09 × 0.07	0.14 × 0.11 × 0.07
<i>T</i> (K)	293(2)	293(2)
Radiation wavelength (Å)	0.71073	0.71073
θ (Min-Max) (°)	2.188-27.100	2.454-25.242
<i>hkl</i> range	-8 to 8, -12 to 12 and -26 to 30	-7 to 7; -10 to 10 and -3 to 40
Total, Unique Data, <i>R</i> (int)	13886, 3401, 0.0200	3317, 2746, 0.0863
Observed data (<i>I</i> > 2σ(<i>I</i>))	3336	2746
<i>N</i> ref, <i>N</i> par	3401, 190	3317, 238
<i>R</i> ^a , <i>wR</i> ₂ ^b , <i>S</i> ^c	0.0175, 0.0418, 1.046	0.0863, 0.2313, 1.568
Residual Density (e/Å ³)	-0.361 and 0.422	-2.049 and 1.732
CCDC No.	2153401	2153402

IV.3.1. Spectral characterization

IR spectrum of HL¹ displays a broad peak at 3453 cm⁻¹ (Fig.IV.2) which corresponds to $\nu(\text{O-H})$ stretching. Intense sharp peak at 2972 cm⁻¹ corresponds to $\nu(\text{C-H})$ stretching. $\nu(\text{C=N})$ and $\nu(\text{C-N})$ appear at 1635 cm⁻¹ and 1103 cm⁻¹ respectively. Infrared spectrum of HL² displays a broad peak at 3478 cm⁻¹ and peak at 2961 cm⁻¹ corresponds to $\nu(\text{C-H})$ stretching. Imine stretching frequency of HL² appears at 1612 cm⁻¹ while sharp peak at 1110 cm⁻¹ corresponds to $\nu(\text{C-H})$ stretching (Fig.IV.5). C-H stretching frequency of [Pd(L¹)Cl] (**C1**) appears at 2955 cm⁻¹ while $\nu(\text{C=N})$ shifts from 1635 cm⁻¹ to 1590 cm⁻¹ due to complex formation (Fig.IV.8). C-H stretching frequency of [Pd(L²)Cl] (**C2**) appears at 2935 cm⁻¹ (Fig.IV.11). ¹HNMR spectra of HL¹ and HL² were recorded in CDCl₃ whereas for Pd(II) complexes **C1** and **C2** the spectra were recorded in DMSO-d₆ solvent. For HL¹ and HL², phenolic -OH peaks appear as singlet at 14.45 and 14.69 ppm respectively whereas imine hydrogen (CH=N-) peaks appear as singlet at 8.24 and 8.65 ppm respectively (Fig.IV.1 and 4). Aromatic protons of HL¹ and HL² appear at 7.15-7.48 ppm. Imine protons (CH=N-) of the complexes **C1** and **C2** appear as singlet at 8.09 and 8.99 ppm respectively (Fig.IV.7 and 10). Disappearance of imine proton peak from ligand to complex in both cases confirm the chelation of O atom to Pd atom. Mass spectra of HL¹ and HL² show m/z peak at 325.0135 and 373.0317 (Fig.IV.3 and 6) corresponding to [M+Na]⁺. For complexes **C1** and **C2**, the m/z peaks appear at 406.9540 and 454.9541 (Fig.IV.9 and 12) respectively corresponding to [M-Cl]⁺. Absorption spectra of ligands (HL¹ and HL²) and complexes (**C1** and **C2**) were taken in acetonitrile. HL¹ exhibits one sharp peak at 330 nm along with moderately intense high energy peak at 280 nm whereas its Pd(II) complex **C1** exhibits moderately intense low energy broad band at 416 nm and 374 nm along with a high energy band at 292 nm. For HL², broad moderately intense low energy peak appears at 361 nm along with high energy band appear at 270 nm. The complex **C2**

exhibits low energy broad band at 465 nm along with a shoulder band at 433 nm. A high energy peaks appear at 295 nm and 335 nm (Fig.IV.13).

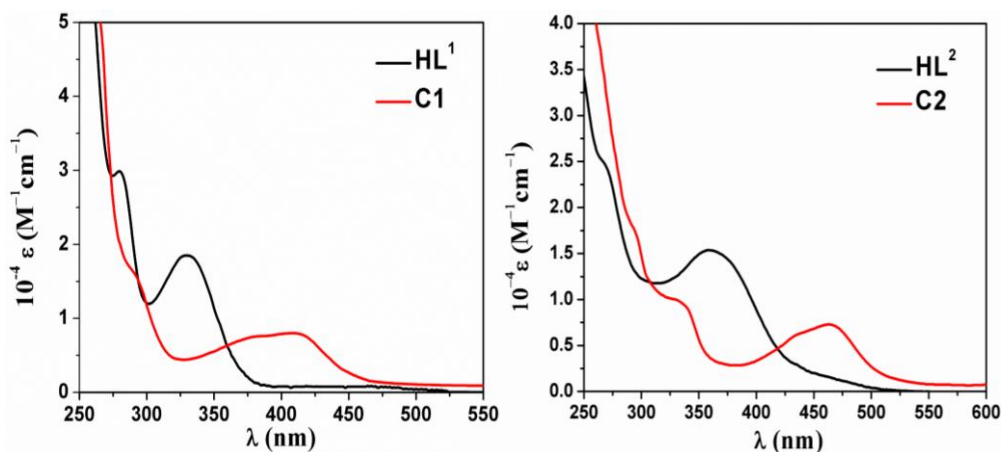


Fig.IV.13. UV-Vis spectra of $[Pd(L^1)Cl]$ and $[Pd(L^2)C]$ in acetonitrile

IV.3.2. Crystallographic study

To authenticate the coordination modes of HL^1 and HL^2 in the complexes, geometries of **C1** and **C2** were further confirmed by single crystal X-ray diffraction method. Complex **C1** crystallizes in orthorhombic crystal system with $P2_1 2_1 2_1$ space group and complex **C2** crystallizes in monoclinic crystal system with $P2_1/c$ space group. The ORTEP plots of the complexes along with atom numbering scheme are shown in Fig.IV.14. Ligands HL^1 and HL^2 act as tridentate O,N,N donor pincers in the complexes. In complex **C1**, Pd-metal is coordinated with HL^1 through phenolic oxygen atom (O1), imine nitrogen atom (N2) and morpholino nitrogen atom (N1) via formation one five-membered (Pd1-N2-C6-C5-N1) and one six-membered (Pd1-N2-C7-C8-C9-O1) chelate ring with chelate bite angles $\angle N2-Pd1-N1$ and $\angle N2-Pd1-O1$, $84.35(10)^\circ$ and $92.26(10)^\circ$ respectively. Similarly, in **C2** chelate bite angles $\angle N2-Pd1-N1$ and $\angle N2-Pd1-O1$, $84.5(3)^\circ$ and $94.0(3)^\circ$ respectively significantly deviate from 90° suggest the distorted square planar geometry. The selected bond distances and bond angles of the complexes are given in Table IV.2. Pd1-N2(imine) bond distances for the complexes are found to be $1.960(3) \text{ \AA}$ and $1.970(8) \text{ \AA}$ respectively for **C1** and **C2** and

comparable to the literature values [57]. Pd1-C11 bond distance of both the complexes **C1** and **C2** are found to be 2.318(9) Å and 2.329(3) Å respectively.

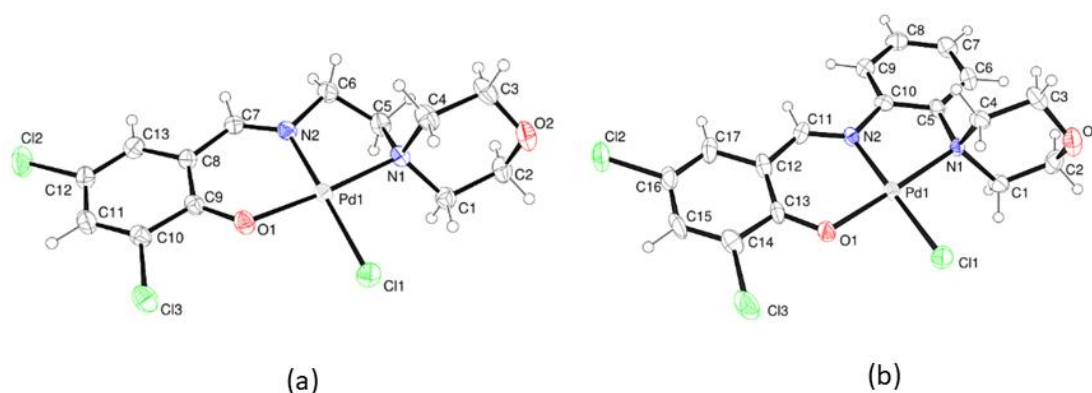


Fig.IV.14. ORTEP plot of [Pd(L¹)Cl](C1) and [Pd(L¹)Cl](C2) with 35% ellipsoidal probability

IV.3.3. Computational study

The geometries of HL¹ and HL² and their Pd(II) complexes **C1** and **C2** were optimized in singlet ground state by DFT/B3LYP method. The optimized bond parameters, bond angles and bond distances of the complexes are well corroborated with X-ray data which are given in Table IV.2. Energy and compositions of selected molecular orbitals are given in Table IV.3. Contour plots of selected molecular orbitals of HL¹ and HL² are given in Fig.IV.15-16 and whereas for the complexes the contour plots are given in Fig.IV.17-18. The higher energy occupied molecular orbital (HOMO) for both the complexes have 84-85% ligand contribution along with reduced contribution (9-10%) of Pd($d\pi$). HOMO-1 and HOMO-2 have mixed Pd($d\pi$) (15-24%) and Cl($p\pi$) (54-80%) character. HOMO-3 and HOMO-7 exclusively have Pd($d\pi$) (72-75%) character. The low-lying virtual orbital, LUMO has ligand character (94-98%) whereas LUMO+1 predominantly has Pd($d\pi$) (52-54%) and 34-37% ligand character.

TDDFT calculation was executed on the optimized geometries of the complexes to gain more knowledge about the electronic transitions. For **C1**, the low energy transition at 436 nm (HOMO-1→LUMO transition) corresponds to the experimental band at 416 nm having

mixed metal to ligand charge transfer (MLCT) and XLCT (halogen to ligand charge transfer) character. The experimentally observed shoulder band 375 nm is well supported with the

Table IV.2. Selected bond distances (Å) and angles (°) of **C1** and **C2**

Bonds(Å)	[Pd(L ¹)Cl] (C1)		[Pd(L ²)Cl](C2)	
	X-ray	Calc.	X-ray	Calc.
Pd1 – N1	2.079(2)	2.139	2.081(8)	2.136
Pd1 – O1	1.996(2)	2.010	1.994(7)	2.003
Pd1 – N2	1.960(3)	2.004	1.970(8)	2.003
Pd1 – Cl1	2.318(9)	2.338	2.329(3)	2.343
N1 – C4	1.498(4)	1.504	1.511(13)	1.519
O1 – C9	1.300(4)	1.292	-	-
O1 – C13	-	-	1.287(13)	1.287
Angles (°)				
N1 – Pd1 – O1	175.39(9)	176.014	177.3(3)	177.606
N1 – Pd1 – N2	84.35(10)	84.370	84.5(3)	83.864
N1 – Pd1 – Cl1	95.62(8)	93.446	95.9(2)	94.470
N2 – Pd1 – Cl1	176.36(8)	176.277	177.7(2)	178.335
O1 – Pd1 – N2	92.26(10)	91.852	94.0(3)	93.741
O1 – Pd1 – Cl1	87.96(7)	90.391	85.5(2)	87.923
C13- O1- Pd1	-	-	123.5(7)	125.374
C9 – O1 – Pd1	124.46(19)	125.577	-	-

calculated transition at 374 nm (HOMO→LUMO+1/HOMO-4→LUMO transitions) having mixed LMCT (ligand to metal charge transfer) and ILCT (Intra ligand charge transfer) character. High energy strong band at 294 nm correspond to ILCT transition. For **C2**, the low energy experimental band at 465 nm corresponds to the (HOMO-2→LUMO+1/HOMO→LUMO transitions) transition at 452 nm has mixed XMCT (halogen to metal charge transfer) and ILCT character. The band at 433 nm corresponds to mixed ILCT and XMCT character (Table IV.4). The band at 335 nm (HOMO-1→LUMO transition) corresponds to mixed XLCT and MLCT character, while the band at 295 nm corresponds to ILCT character.

Table IV.3. Energy and compositions (%) of selected molecular orbitals of **C1** and **C2**

MO	C1				C2			
	E (eV)	% of composition			E (eV)	% of composition		
		Pd	L ¹	Cl		Pd	L ²	Cl
LUMO+5	0.41	05	95	0	-0.18	97	03	0
LUMO+4	0.20	80	19	1	-0.20	01	99	0
LUMO+3	-0.15	01	99	0	-0.66	0	100	0
LUMO+2	-0.50	02	98	0	-1.25	01	99	0
LUMO+1	-2.08	52	37	12	-2.14	54	34	13
LUMO	-2.12	05	94	01	-2.61	02	98	0
HOMO	-5.68	10	84	06	-5.76	09	85	6
HOMO-1	-6.32	24	23	54	-6.38	23	23	54
HOMO-2	-6.45	17	05	78	-6.49	15	05	80
HOMO-3	-6.76	75	16	10	-6.77	72	17	10
HOMO-4	-7.04	03	83	14	-6.9	01	84	15
HOMO-5	-7.33	09	83	8	-7.34	13	83	4
HOMO-6	-7.56	73	27	0	-7.6	72	28	0
HOMO-7	-7.79	22	53	25	-7.79	04	95	1
HOMO-8	-8.01	38	47	16	-7.79	21	54	26
HOMO-9	-8.12	05	82	12	-7.93	01	98	1

Table IV.4. Vertical electronic transitions of, HL¹, HL², C1 and C2 calculated by TDDFT/B3LYP/CPCM method

Comps.	λ (nm)	E (eV)	Osc. Strength (f)	Key excitations	Character ^a	$\lambda_{\text{expt.}}$ (nm)
HL ¹	331.3	3.7429	0.1262	(98%)HOMO→LUMO	$\pi(\text{L}) \rightarrow \pi^*(\text{L})$	330
	315.3	3.9319	0.0177	(97%)HOMO-1→LUMO	$n(\text{L}) \rightarrow \pi^*(\text{L})$	
	268.4	4.6197	0.1512	(95%)HOMO-2→LUMO	$\pi(\text{L}) \rightarrow \pi^*(\text{L})$	280
HL ²	345.6	3.5876	0.2671	(97%)HOMO-1→LUMO	$\pi(\text{L}) \rightarrow \pi^*(\text{L})$	361
	275.0	4.5094	0.2242	(51%)HOMO-4→LUMO (23%)HOMO-3→LUMO	$\pi(\text{L}) \rightarrow \pi^*(\text{L})$	270
	255.6	4.8506	0.2518	(97%)HOMO→LUMO+3	$n(\text{L}) \rightarrow \pi^*(\text{L})$	
C1	480.2	2.5817	0.0006	(85%)HOMO→LUMO	$\pi(\text{L})/\text{d}\pi(\text{Pd}) \rightarrow \pi^*(\text{L})$ (ILCT/MLCT)	
	435.9	2.8444	0.0126	(72%)HOMO-1→LUMO	$\text{p}\pi(\text{Cl})/\text{d}\pi(\text{Pd}) \rightarrow \pi^*(\text{L})$ (XL CT/MLCT)	416
	378.8	3.2730	0.0726	(56%)HOMO→LUMO+1 (32%)HOMO-4→LUMO	$\pi(\text{L}) \rightarrow \text{d}\pi(\text{Pd})$ (LMCT) $\pi(\text{L}) \rightarrow \pi^*(\text{L})$ (ILCT)	374
	287.8	4.3075	0.1335	(73%)HOMO-5→LUMO	$\pi(\text{L}) \rightarrow \pi^*(\text{L})$ (ILCT)	292
C2	451.8	2.7441	0.0988	(49%)HOMO-2→LUMO+1 (46%)HOMO→LUMO	$\text{p}\pi(\text{Cl}) \rightarrow \text{d}\pi(\text{Pd})$ (XMCT) $\pi(\text{L}) \rightarrow \pi^*(\text{L})$ (ILCT)	465
	423.6	2.9268	0.0880	(52%)HOMO→LUMO (42%)HOMO-2→LUMO+1	$\pi(\text{L}) \rightarrow \pi^*(\text{L})$ (ILCT) $\text{p}\pi(\text{Cl}) \rightarrow \text{d}\pi(\text{Pd})$ (XMCT)	433
	337.0	3.6793	0.1773	(90%)HOMO-1→LUMO	$\text{p}\pi(\text{Cl})/\text{d}\pi(\text{Pd}) \rightarrow \pi^*(\text{L})$ (XL CT/MLCT)	335
	293.4	4.2259	0.2426	(88%)HOMO-5→LUMO	$\pi(\text{L}) \rightarrow \pi^*(\text{L})$ (ILCT)	295

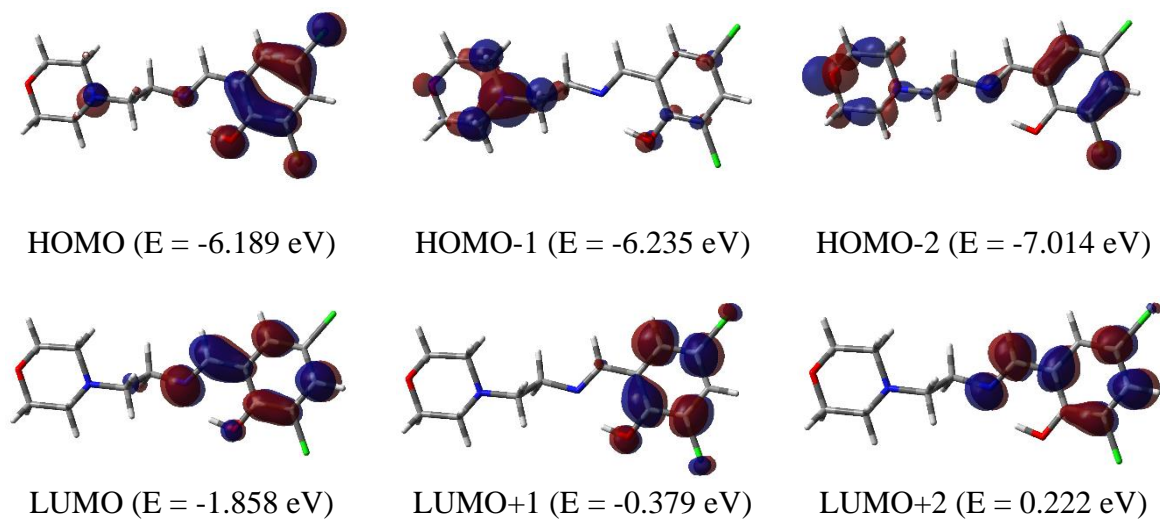


Fig.IV.15. Contour plots of some selected molecular orbital of HL¹

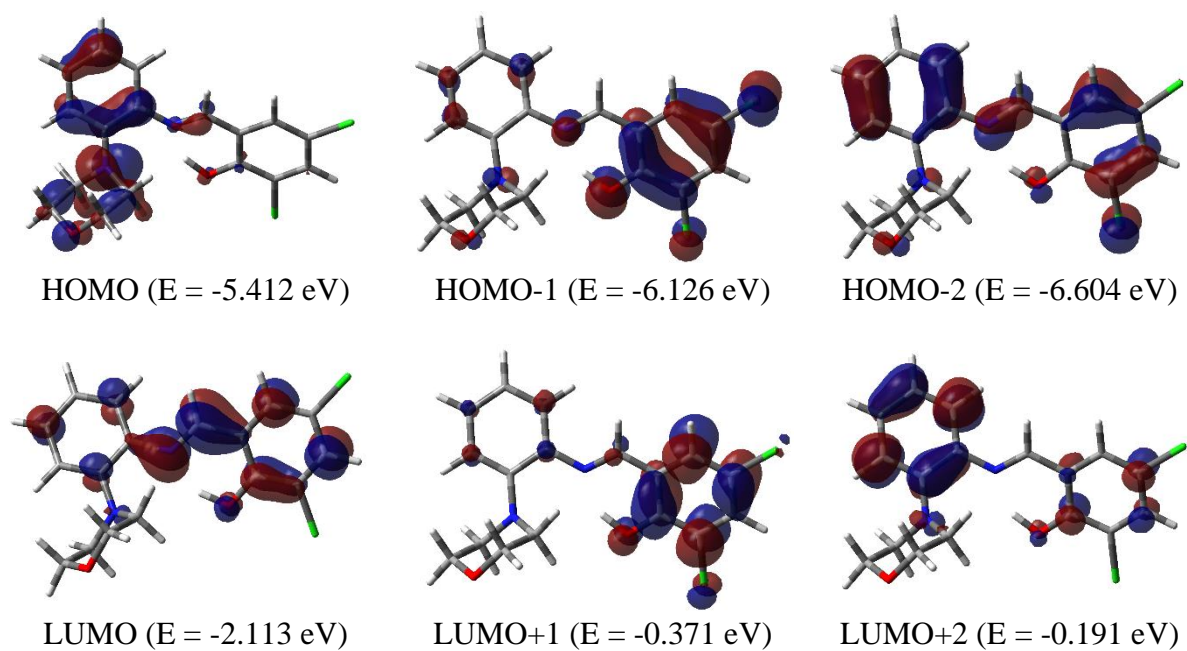


Fig.IV.16. Contour plots of some selected molecular orbital of HL²

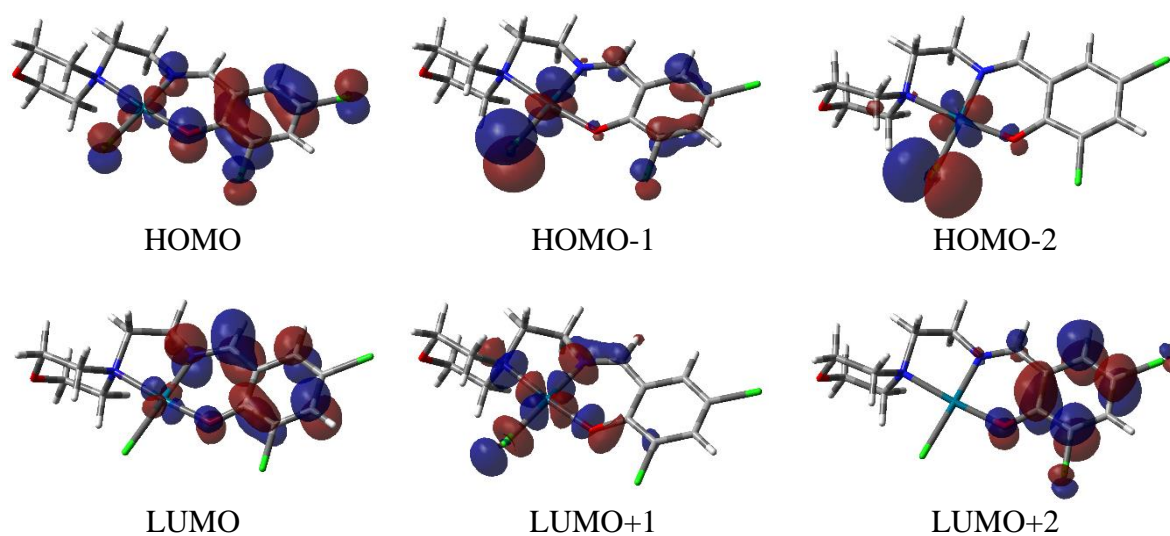


Fig.IV.17. Contour plots of some selected molecular orbital of $[\text{Pd}(\text{L}^1)\text{Cl}]$ (C1)

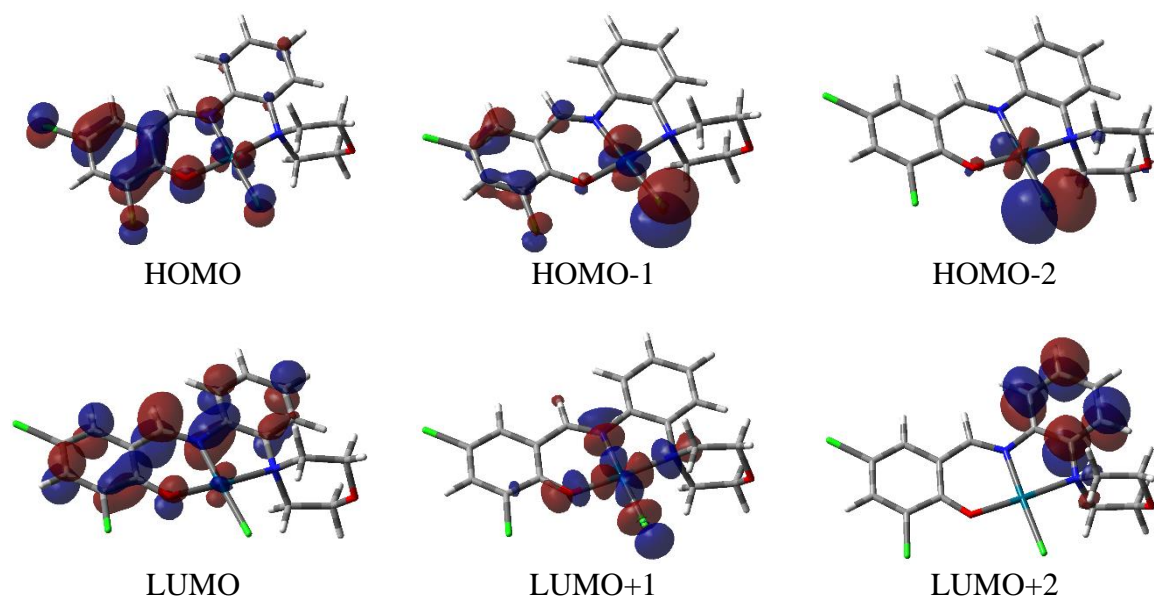


Fig.IV.18. Contour plots of some selected molecular orbital of $[\text{Pd}(\text{L}^2)\text{Cl}]$ (C2)

IV.3.4. DNA binding studies

The understanding of the mode of interactions with DNA is very crucial for developing of new anti-cancer drugs. At present, the spectroscopic methods are widely used to study the mode of interactions. These studies show that the drugs can interact to DNA covalently or by non-covalent interaction, groove binding or by electrostatic interactions [58,59]. Absorption and emission spectroscopies are widely used to interpret the mode of interactions of drug molecules with DNA [60].

IV.3.4.1. UV-Vis method

UV-Vis titration is a powerful method to assess how well palladium complexes interact to CT DNA [61]. Absorption spectra of the complexes C1 and C2 were taken in absence and presence of CT DNA. C1 exhibits a broad peak with two absorption maxima at 411 nm and 358 nm and C2 exhibits a sharp maxima peak at 342 nm. But upon subsequent addition of CT DNA, a hypochromic shift is observed in the absorption spectra for both the complexes (Fig. IV.19.a-b). The intrinsic binding constant (K_b) was evaluated to understand the affinity of the complexes towards CT DNA. The K_b value of the C1 and C2 are found to be $3.52 \times 10^5 \text{ M}^{-1}$ and $2.27 \times 10^5 \text{ M}^{-1}$ respectively which are comparable to the reported literature values [62,63].

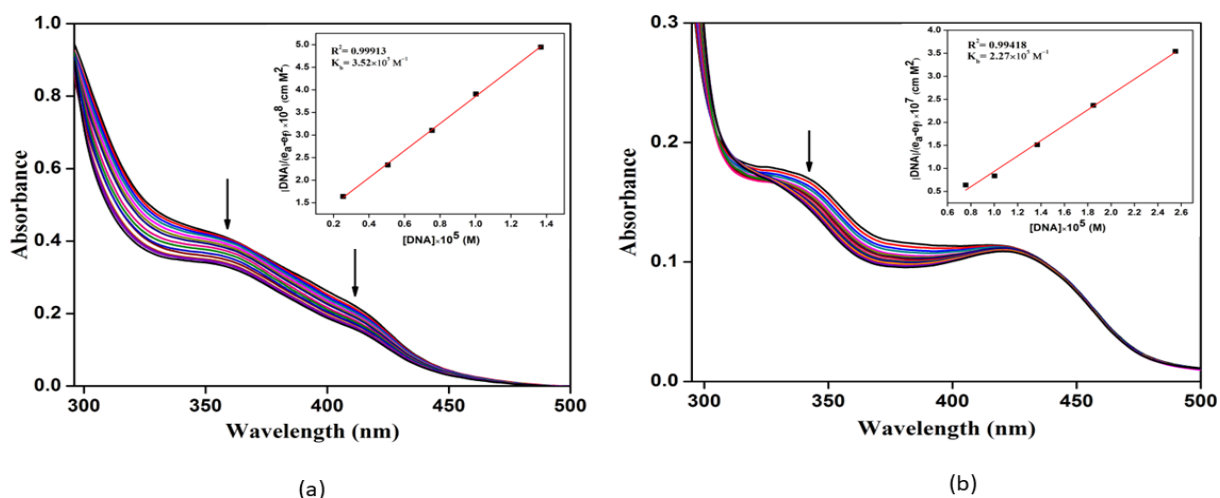


Fig.IV.19. Change in absorption spectra of complex **C1(a)** and **C2(b)** in Tris-HCl/NaCl buffer with the gradual addition of CT DNA. Inset: Plot of $[DNA]/(\epsilon_a - \epsilon_f)$ vs. $[DNA]$.

IV.3.4.2. Fluorescence method

There is no inherent fluorescence observed in CT DNA. The palladium complexes are also non-fluorescent in solution with or without CT DNA. But when ethidium bromide (EB), a typical intercalator, forms EB-CT DNA intercalating complex, there is a mammoth increase in fluorescence intensity of EB at 605 nm upon excitation at 540 nm [64]. Upon steady addition of Pd(II) complexes **C1** and **C2**, the fluorescence intensities are successively decreased due to the replacement of EB from its EB-CT DNA system (Fig.IV.20.a-b) [65]. The titration curves clearly demonstrate the competition between the complexes and EB for DNA binding sites. A linear Stern–Volmer equation (Eq. (2)) [66] accords well with the fluorescence quenching curve of the EB-CT DNA system for the complex.

$$I_0/I = 1 + K_{sv}[Q] \dots \dots \dots (2)$$

Where I and I_0 signify the fluorescence intensities of the EB-CT DNA system with and without the complex, respectively, K_{sv} is the Stern-Volmer quenching constant, and $[Q]$ is the molar concentration of the complex (quencher). K_{sv} values are obtained from the slopes of the plots and are determined to be $1.504 \times 10^5 \text{ M}^{-1}$ and $1.873 \times 10^5 \text{ M}^{-1}$ for the complex **C1** and **C2** respectively.

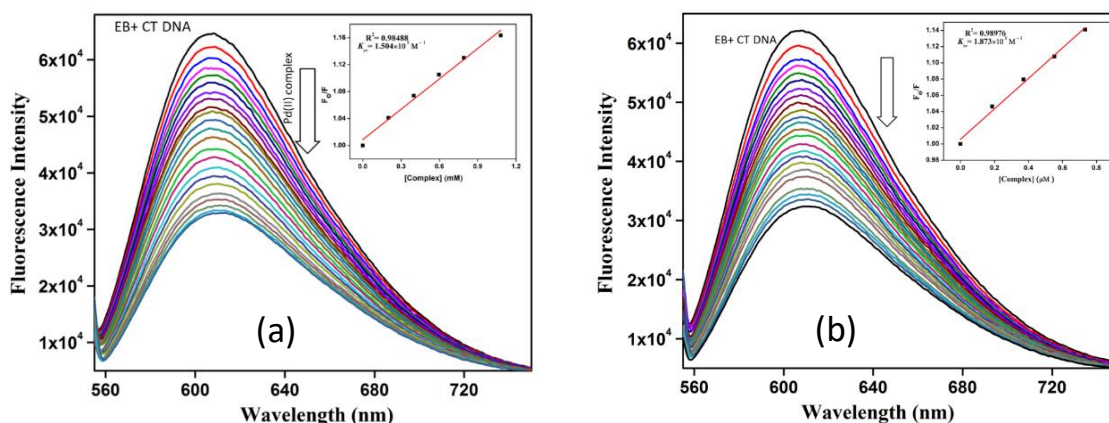


Fig.IV.20. Emission spectra ($\lambda_{ex} = 540 \text{ nm}$) of EB-CT DNA in presence of increasing concentrations of **C1** (a) and **C2**(b) Inset: Plots of emission intensity F_0/F vs. [complex].

IV.3.5. BSA binding studies

IV.3.5.1. UV-Vis method

Electronic absorption spectra of BSA (10 μM in PBS at pH 7.4) was recorded in the range of 200-500 nm in presence of different concentration of the complexes. BSA has a characteristic absorption peak at 280 nm. Repeated addition of 100 μL complex to the BSA solution causes a steady increase in 280 absorption intensity along with a bit of blue shift. This hypsochromic shift attributes to the ground-state alliance between the complexes and protein [67,68]. The apparent association constant (K_a) was calculated from the plot of $1/(A_{obs}-A_0)$ vs $1/[\text{complex}]$ (Fig.IV.21.a-b inset) adopting the following equation [69,70].

$$\frac{1}{A_{obs} - A_0} = \frac{1}{A_c - A_0} + \frac{1}{K_a(A_c - A_0)[\text{complex}]}$$

Where A_{obs} indicates the observed absorbance (at 280 nm) of the solution having various concentrations of the complex, A_0 and A_c denote BSA absorbance only and serum albumin with the complex. The calculated value of apparent association constant (K_a) for the complex C1 and C2 are $2.18 \times 10^5 \text{ M}^{-1}$ and $1.23 \times 10^5 \text{ M}^{-1}$ respectively which matches with the literature value of Pd-complexes [71-74].

Table IV.5. Stern-Volmer quenching constants (K_{sv}), apparent association constants (K_a), equilibrium binding constants (K_b), number of binding sites(n) in the interaction of C1 and C2 with BSA

System	UV Method	Fluorescence Method			
	$K_a \times 10^5 (\text{M}^{-1})$	Hypo(%)	$K_b \times 10^5 (\text{M}^{-1})$	$K_{sv} \times 10^5 (\text{M}^{-1})$	n
C1	2.18	44.94	3.01	2.52	1.028
C2	1.23	35.72	2.59	2.45	1.018

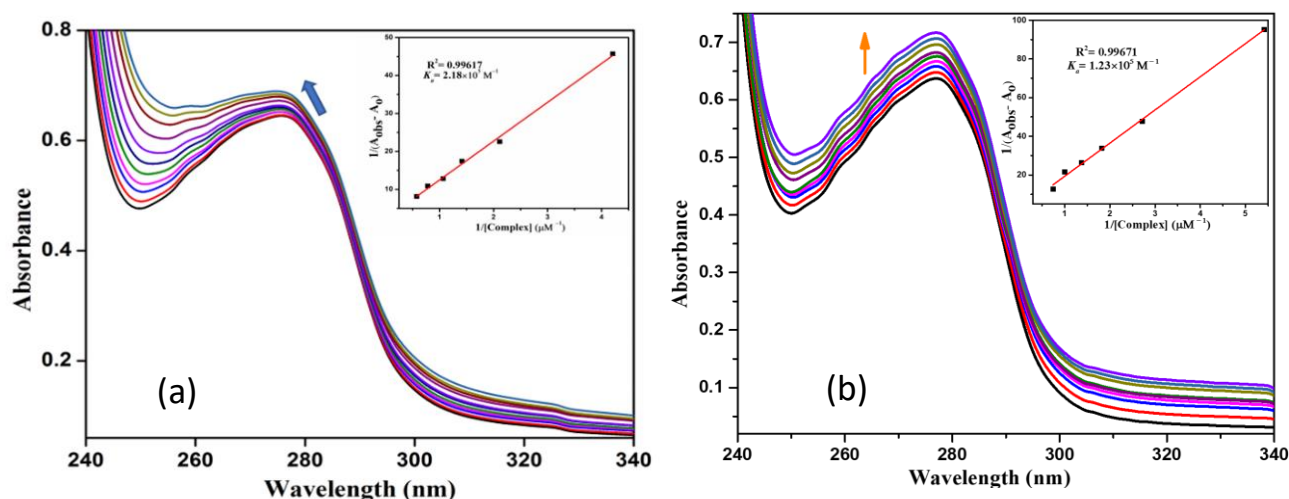


Fig.IV.21. Change of absorption spectra of BSA (10 μM aqueous solution) upon gradual addition of 100 μL complex [C1(a) and C2(b)] solution in DMSO at 300 K. Insets: $1/(A_{\text{obs}} - A_0)$ vs. $1/[\text{complex}]$ plots of BSA absorption titration.

IV.3.5.2. Fluorescence method

The BSA-complex interactions were also studied by fluorescence spectral titration technique. Complex is non-fluorescent in DMSO solution. But upon excitation at 280 nm, an aqueous solution (10 μM , pH 7.4 PBS buffer) of BSA demonstrates a strong fluorescence at 336 nm. Now with subsequent addition of 100 μL complex to the BSA solution, fluorescence intensity of BSA at ~ 336 nm dramatically quenched (44.94 % and 35.72 % quenching). This hypochromicity in the spectra is mainly attributed due to the interaction of complexes with the protein. The Stern-Volmer quenching constant values (K_{sv}) for the complexes were calculated [75] and depicted in Table IV.5. The high K_{sv} ($2.52 \times 10^5 \text{ M}^{-1}$ and 2.45×10^5) value indicates that complexes exhibit good fluorescence quenching ability. To learn more of the quenching effect, the equilibrium binding constants (K_b) and number of binding sites (n) available for the complexes were also estimated from the graph of $\log [(F_o - F)/F]$ versus $\log [\text{complex}]$ (Fig.IV.22. a-b inset) applying the Scatchard equation [76,77] below:

$$\log \frac{(F_0 - F)}{F} = \log K_b + n \log [\text{complex}]$$

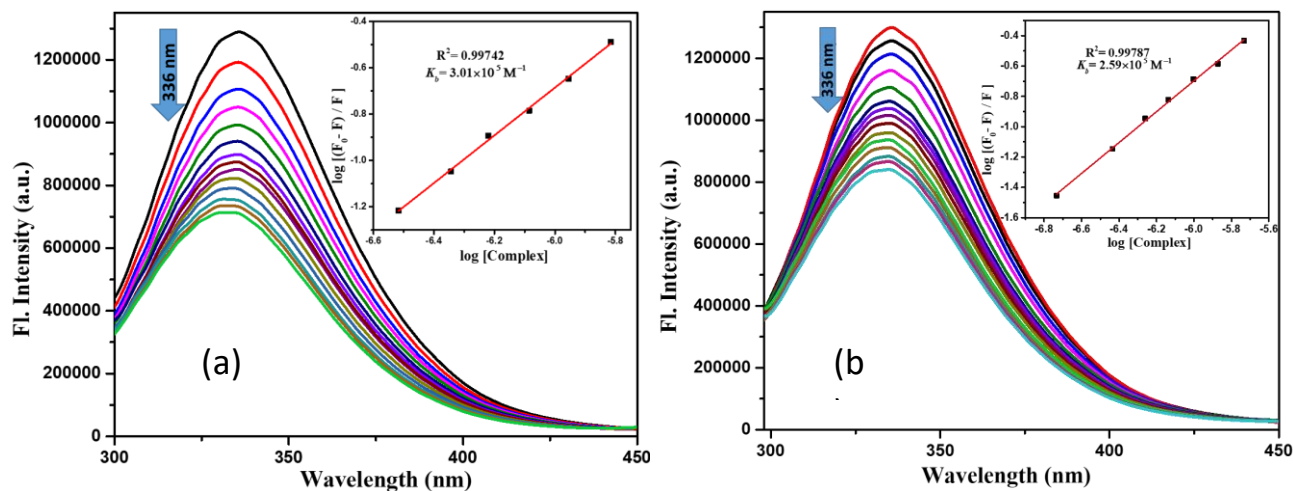


Fig.IV.22. Change of fluorescence spectra of BSA (10 μM) upon gradual addition of 100 μL complex [C1(a) and C2(b)] solution in DMSO at 300 K ($\lambda_{\text{ex}}=280$ nm, $\lambda_{\text{em}}=336$ nm). Insets: Scatchard plots of the BSA fluorescence titration.

Based on the plot, for the complex C1 and C2 calculated values of n for are 1.028 and 1.018 respectively and calculated values of K_b are $3.01 \times 10^5 \text{ M}^{-1}$ and $2.59 \times 10^5 \text{ M}^{-1}$ respectively which reflects the strong affinity of the complexes with the serum albumins.

IV.3.6. Biological study

IV.3.6.1. Cytotoxicity of [Pd(L¹)Cl] and [Pd(L²)Cl] in different cancer cells

In-vitro cytotoxicity study by MTT method revealed that both ligands HL¹ and HL² and their Pd(II) complexes C1 and C2 inhibit the viability of AGS, MDA-MB-231 and HepG2 cells in a dose dependent manner at 24 h as compared to the control (Fig.IV.23). However, the complexes were significantly more effective in decreasing the viability of all the three cell lines at lower concentrations as compared to their respective ligand and control. IC₅₀ value was determined with the help of nonlinear regression (curve fit) curve followed by log (inhibition) vs. response equation in graph pad prism software. IC₅₀ values for the suggest, the Pd(II) complexes are much more effective towards HepG2 cell lines ($10.73 \pm 1.26 \mu\text{M}$ for C1

and $8.47 \pm 1.17 \mu\text{M}$ for **C2**) compared to AGS ($15.08 \pm 2.08 \mu\text{M}$ for **C1** and $14.22 \pm 1.51 \mu\text{M}$ for **C2**) and MDA-MB-231 ($55.97 \pm 3.68 \mu\text{M}$ for **C1** and $41.25 \pm 3.45 \mu\text{M}$ for **C2**) cell lines. Moreover, the cell cytotoxicity is comparable and even better compared to cisplatin (Table IV.6).

	AGS	MDA-MB-231	HepG2
Compounds	IC₅₀ of compounds (μM)		
HL¹	87.72 ± 2.5	183.96 ± 4.01	55 ± 2.5
HL²	166.3 ± 3.04	174.56 ± 4.09	30.28 ± 3.02
C1	15.08 ± 2.08	55.97 ± 3.68	10.73 ± 1.26
C2	14.22 ± 1.51	41.25 ± 3.45	8.47 ± 1.17
cisplatin	24.43 ± 1.27	93.79 ± 3.45	10.99 ± 1.44

Table IV.6. IC₅₀ values of HL¹, HL² and their Pd(II) complexes **C1** and **C2** towards AGS, MDA-MB231 and HEPG2 cell lines

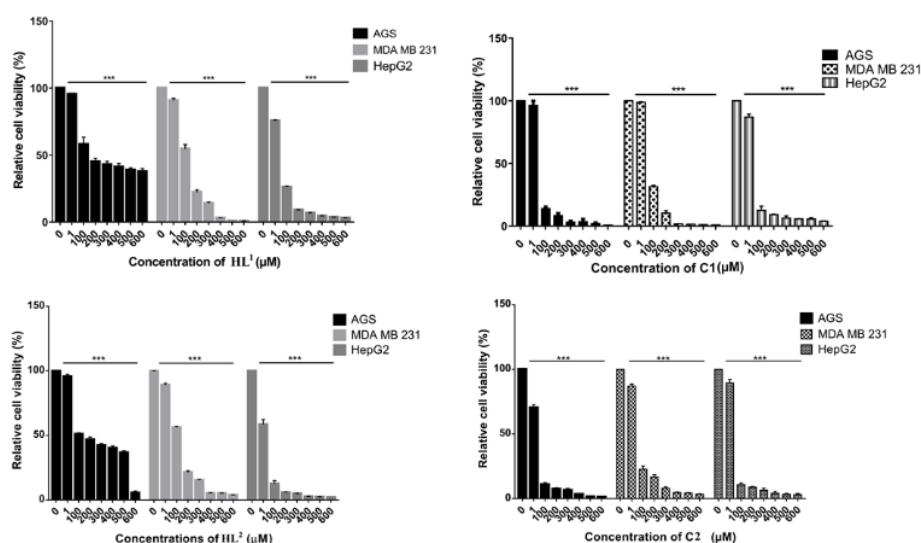


Fig.IV.23. % of cell viability of HL¹, C1, HL², C2 towards AGS, MDA-MB231 and HEPG2 cell lines. cells (1×10^6 cells/mL) were treated with different concentrations of HL¹, C1, HL², C2 ranging from 0 to 600 μM for 24 h.

IV.3.6.2. Colony Formation Assay

To further validate the consequence of complexes on different cancer cells colony formation assay was executed [78]. Cells were treated with HL¹ (184 μ M for MDA-MB-231, 88 μ M for AGS and 55 μ M for HepG2), HL² (175 μ M for MDA-MB-231, 166 μ M for AGS and 30 μ M for HepG2), C1 (56 μ M for MDA-MB-231, 15 μ M for AGS, 11 μ M for HepG2) and C2 (41 μ M for MDA-MB-231, 14 μ M for AGS and 8.5 μ M for HepG2) for 24 h. Noteworthy decrease in colonies were noticed in HL¹, HL², C1 and C2 as compared to control but the complexes had a much more significant effect in reducing the number of colonies as compared to their respective ligands (Fig.IV.24). Thus, these results confirm that complexes inhibit the cell viability of AGS, MDA-MB 231 and HepG2 cells at its low dose as compared to their ligands.

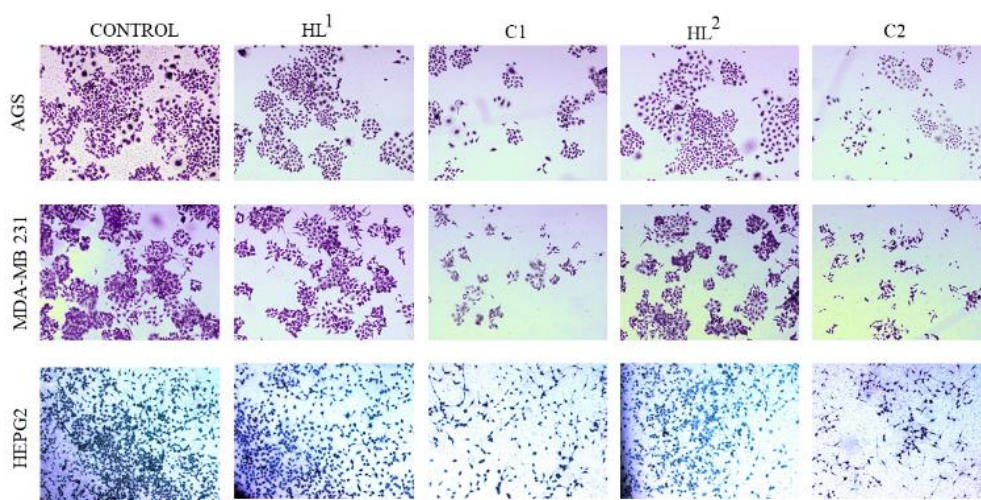


Fig.IV.24. Colony formation of AGS, MBA-MB231 and HEPG2 cell lines after treatment of HL¹(184 μ M for MDA MB 231, 88 μ M for AGS and 55 μ M for HepG2),HL²(175 μ M for MDA-MB 231, 166 μ M for AGS and 30 μ M for HepG2),C1(56 μ M for MDA-MB 231, 15 μ M for AGS, 11 μ M for HepG2) and C2(41 μ M for MDA MB 231, 14 μ M for AGS and 8.5 μ M for HepG2) for 24 h.

IV.3.6.3. In Vitro Cell Migration study

All normal living cells exhibit the property migration which is responsible for immune response, normal development and disease processes. However, tumor cells show uncontrolled cell migration. Wound healing assay was performed on MDA-MB-231 cells to find the inhibitory action of both the complexes [79-81]. Area of wound in MDA-MB-231 cells are gradually decreased in a time-dependent manner (0, 12, and 24 h) when treated with IC_{50} of **C1** and **C2** complexes [82]. The result also suggests that the number of cells is considerably decreased in the scratched area, suggesting that both the complexes **C1** and **C2** could reduce the site-specific cell migration (Fig.IV.25).

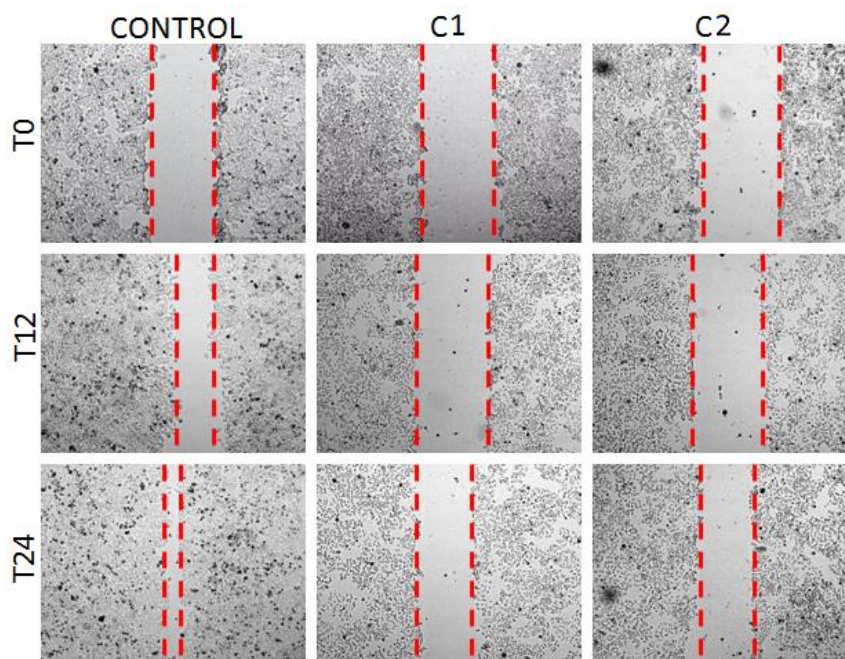


Fig.IV.25. MDA-MB231 cells (1×10^6 cells/mL) were treated with $-\mu\text{M}$ (IC_{50}) of **C1** and **C2** complexes for 12 and 24 h. Scratch assay (migration inhibition study) were monitored under microscope.

IV.4. Conclusions

New Pd(II) complexes with ONN donor ligands are fabricated and systematically characterized by several spectroscopic techniques. Single crystal X-ray study of the complexes confirmed that HL^1 and HL^2 act as tridentate O,N,N chelator in Pd(II) complexes.

Interaction of **C1** and **C2** with CT-DNA and BSA protein are investigated by UV-Vis as well as fluorescence methods. The complexes effectively displace ethidium bromide (EB) from EB-DNA complexes. The antiproliferative activity of the complexes displayed that Pd-complexes exhibit greater cytotoxicity than their respective ligands as well as cis-platin in AGS, MBA-MB231 and HEPG2 cell lines. Cytotoxicity of both Pd(II) complexes towards HepG2 (IC_{50} , 14.22-15.08 μ M) and AGS (IC_{50} , 8.47-10.73 μ M) cell lines are significant.

IV.5. References

1. R. L. Siegel, K. D. Miller and A. Jemal, *Cancer Statistics, 2019*, *Ca Cancer J. Clin.*, 2019, **69**, 7-34.
2. D. S. M. Chan, L. Abar, M. Cariolou, N. Nanu, D. C. Greenwood, E. V. Bandera, A. McTiernan and T. Norat, *Cancer Causes Control*, 2019, **30**, 1183-1200.
3. M. Hanif and C. G. Hartinger, *Future Med. Chem.*, 2018, **10**, 615-617.
4. M. De Rycker, B. Baragaña, S. L. Duce and I. H. Gilbert, *Nature*, 2018, **559**, 498-506.
5. S. G. Churusova, D. V. Aleksanyan, E. Y. Rybalkina, O. Y. Susova, A. S. Peregudov, V. V. Brunova, E. I. Gutsul, Z. S. Klemenkova, Y. V. Nelyubina and V. N. Glushko, *Inorg. Chem.*, 2021, **60**, 9880-9898.
6. A. I. Matesanz, E. Jimenez-Faraco, M. C. Ruiz, L. M. Balsa, C. Navarro-Ranninger, I. E. León and A. G. Quiroga, *Inorg. Chem. Front.*, 2018, **5**, 73-83.
7. A. Kumar, A. Naaz, A. Prakasham, M. K. Gangwar, R. J. Butcher, D. Panda and P. Ghosh, *ACS omega*, 2017, **2**, 4632-4646.
8. Z. D. Bugarc'ic', J. Bogojeski and R. van Eldik, *Coord. Chem. Rev.*, 2015, **292**, 91-106.
9. D. Hernández-Romero, S. Rosete-Luna, A. López-Monteon, A. Chávez-Pinã, N. Pérez-Hernández, J. Marroquín-Flores, A. Cruz-Navarro, G. Pesado-Gómez, D. Morales-Morales and R. Colorado-Peralta, *Coord. Chem. Rev.*, 2021, **439**, 213930.
10. R. Kant and S. Maji, *Dalton Trans.*, 2021, **50**, 785-800.
11. H. H. Repich, V. V. Orysyk, L. G. Palchykovska, S. I. Orysyk, Y. L. Zborovskii, O. V. Vasylchenko, O. V. Storozhuk, A. A. Biluk, V. V. Nikulina, L. V. Garmanchuk, V. I. Pekhnyo and M. V. Vovk, *J. Inorg. Biochem.*, 2017, **168**, 98-106.
12. S. Medici, M. Peana, V. M. Nurchi, J. I. Lachowicz, G. Crisponi and M. A. Zoroddu, *Coord. Chem. Rev.*, 2015, **284**, 329-350.

13. M. Fanelli, M. Formica, V. Fusi, L. Giorgi, M. Micheloni and P. Paoli, *Coord. Chem. Rev.*, 2016, **310**, 41-79.
14. M. N. Alam and F. Huq, *Coord. Chem. Rev.*, 2016, **316**, 36-67.
15. N. J. Wheate, S. Walker, G. E. Craig and R. Oun, *Dalt. Trans.*, 2010, **39**, 8113-8127.
16. J. Pranczk, D. Jacewicz, D. Wyrzykowski and L. Chmurzynski, *Curr. Pharmaceut. Anal.*, 2014, **10**, 2-9.
17. S. N. Mbugua, N. R. S. Sibuyi, L. W. Njenga, R. A. Odhiambo, S. O. Wandiga, M. Meyer, R. A. Lalancette and M. O. Onani, *ACS Omega*, 2020, **25**, 14942–14954.
18. Z. Breijyeh, B. Jubeh and R. Karaman, *Molecules*, 2020, **25**, 1340.
19. C. Orvig and M. J. Abrams, *Chem. Rev.*, 1999, **99**, 2201-2204.
20. C. S. Allardyce, A. Dorcier, C. Scolaro and P. J. Dyson, *App. Organomet. Chem.*, 2005, **19**, 1-10.
21. P. J. Dyson and G. Sava, *Dalton Trans.*, 2006, **16**, 1929-1933.
22. M. J. Hannon, *Pure Appl. Chem.*, 2007, **79**, 2243-2261.
23. K. B. Garbutcheon-Singh, M. P. Grant, B. W. Harper, A. M. Krause-Heuer, M. Manohar, N. Orkey and J. R. Aldrich Wright, *Current Topics in Med. Chem.*, 2011, **11**, 521-542.
24. M. Feizi-Dehnyebi, E. Dehghanian and H. Mansouri-Torshizi, *Spectrochim. Acta Part A*, 2021, **249**, 119215.
25. A. Shanmugapriya, G. Kalaiarasi, M. Ravi, H. A. Sparkes, P. Kalaivanid and R. Prabhakaran, *New J. Chem.*, 2021, **45**, 20227-20240.
26. M. Aminzadeh, H. Mansouri-Torshizi, R. Aleeshah, K. Abdi and M. Saeidifar, *Biometals*, 2021, **34**, 1173-1179.
27. R. Oun, Y. E. Moussa and N. J. Wheate, *Dalton Trans.*, 2018, **47**, 6645–6653.

28. J. Li, C. Zheng, M. Wang, A. D. Umamo, Q. Dai, C. Zhang, H. Huang, Q. Yang, X. Yang, J. Lu and W. Pan, *Oncogene*, 2022, **41**, 1114-1128.
29. N. Shahabadil, L. Ghaffari, Z. Mardani and F. Shiri, *Biological Trace Element Research*, 2022, **200**, 1988–2000.
30. Y. OuYang, J. Gao, L. Zhao, J. Lu, H. Zhong, H. Tang, S. Jin, L. Yue, Y. Li, W. Guo, Q. Xu and Y. Lai, *J. Med. Chem.*, 2021, **64**, 7646–7666.
31. N. F. Romashev, P. A. Abramov, I. V. Bakaev, I. S. Fomenko, D. G. Samsonenko, A. S. Novikov, K. K. Tong, D. Ahn, P. V. Dorovatovskii, Y. V. Zubavichus, A. A. Ryadun, O. A. Patutina, M. N. Sokolov, M. V. Babak and A. L. Gushchin, *Inorg. Chem.*, 2022, **61**, 2105–2118.
32. L. Bai, C. Gao, Q. Liu, C. Yu, Z. Zhang, L. Cai, B. Yang, Y. Qian, J. Yang and X. Liao, *Eur. J. Med. Chem.*, 2017, **140**, 349-382.
33. C. S. Allardyce and P. J. Dyson, *Dalton. Trans.*, 2016, **45**, 3201-3209.
34. R. G. Kenny, S. W. Chuah, A. Crawford and C. J. Marmion, *Eur. J. Inorg. Chem.*, 2017, **12**, 1596-1612.
35. K. Laws and K. Suntharalingam, *ChemBioChem*, 2018, **19**, 2246-2253.
36. B. S. Murray, M. V Babak, C. G. Hartinger and P. J. Dyson, *Coord. Chem. Rev.*, 2016, **306**, 86-114.
37. E. Alessio, *Eur. J. Inorg. Chem.*, 2017, **12**, 1549-1560.
38. J. Reedijk, *Eur. J. Inorg. Chem.*, 2009, **10**, 1303-1312.
39. D. Wang and S. J. Lippard, *Nat. Rev. Drug Discov.*, 2005, **4**, 307-320.
40. V. Brabec, O. Hrabina and J. Kasparikova, *Coord. Chem. Rev.*, 2017, **351**, 2-31.
41. S. Komeda, *Metallomics*, 2011, **3**, 650-655.
42. T. C. Johnstone, K. Suntharalingam and S. J. Lippard, *Chem. Rev.*, 2016, **116**, 3436-3486.

43. K. Skonieczny, G. Charalambidis, M. Tasiór, M. Krzeszewski, A. Kalkan-Burat, A. G. Coutsolelos and D. T. Gryko, *Org. Synth.*, 2012, **89**, 220-229.
44. M. Anjomshoa, H. Hadadzadeh, M. Torkzadeh-Mahani, S.J. Fatemi, M. AdeliSardou, H.A. Rudbari and V.M. Nardo, *Eur. J. Med. Chem.*, 2015, **96**, 66-82.
45. N. S. Quiming, R. B. Vergel, M. G. Nicolas and J. A. Villanueva, *J. Health Sci.*, 2005, **51**, 8-15.
46. T. L. Riss, R. A. Moravec, A. L. Niles, S. Duellman, H. A. Benink, T. J. Worzella and L. Minor, *Assay Guidelines manuals*, 2013.
47. (a) A. D. Becke, *J. Chem. Phys.*, 1993, **98**, 5648- 5652; (b) C. Lee, W. Yang and R. G. Parr, *Phys. Rev. B: Condens. Matter Mater. Phys.*, 1988, **37**, 785-789.
48. (a) P. J. Hay and W. R. Wadt, *J. Chem. Phys.*, 1985, **82**, 270-283; (b) W. R. Wadt and P. J. Hay, *J. Chem. Phys.*, 1985, **82**, 284-298; (c) P. J. Hay and W. R. Wadt, *J. Chem. Phys.*, 1985, **82**, 299-310.
49. M. J. Frisch, G. W. Trucks, H. B. Schlegel, G. E. Scuseria, M. A. Robb, J. R. Cheeseman, G. Scalmani, V. Barone, B. Mennucci, G. A. Petersson, H. Nakatsuji, M. Caricato, X. Li, H. P. Hratchian, A. F. Izmaylov, J. Bloino, G. Zheng, J. L. Sonnenberg, M. Hada, M. Ehara, K. Toyota, R. Fukuda, J. Hasegawa, M. Ishida, T. Nakajima, Y. Honda, O. Kitao, H. Nakai, T. Vreven, J. A. Montgomery, Jr., J. E. Peralta, F. Ogliaro, M. Bearpark, J. J. Heyd, E. Brothers, K. N. Kudin, V. N. Staroverov, R. Kobayashi, J. Normand, K. Raghavachari, A. Rendell, J. C. Burant, S. S. Iyengar, J. Tomasi, M. Cossi, N. Rega, J. M. Millam, M. Klene, J. E. Knox, J. B. Cross, V. Bakken, C. Adamo, J. Jaramillo, R. Gomperts, R. E. Stratmann, O. Yazyev, A. J. Austin, R. Cammi, C. Pomelli, J. W. Ochterski, R. L. Martin, K. Morokuma, V. G. Zakrzewski, G. A. Voth, P. Salvador, J. J. Dannenberg, S. Dapprich, A. D. Daniels, O. Farkas, J. B. Foresman, J. V. Ortiz, J.

- Cioslowski and D. J. Fox, Gaussian 09, Revision D.01, Gaussian, Inc., Wallingford CT, 2009.
50. (a) R. Bauernschmitt and R. Ahlrichs, *Chem. Phys. Lett.*, 1996, **256**, 454-464; (b) R. E. Stratmann, G. E. Scuseria and M. J. Frisch, *J. Chem. Phys.*, 1998, **109**, 8218; (c) M. E. Casida, C. Jamorski, K. C. Casida and D. R. Salahub, *J. Chem. Phys.*, 1998, **108**, 4439-4449.
51. (a) V. Barone and M. Cossi, *J. Phys. Chem. A*, 1998, **102**, 1995-2001; (b) M. Cossi and V. Barone, *J. Chem. Phys.*, 2001, **115**, 4708-4717; (c) M. Cossi, N. Rega, G. Scalmani and V. Barone, *J. Comput. Chem.*, 2003, **24**, 669-681.
52. N. M. O'Boyle, A. L. Tenderholt and K. M. Langner, *J. Comput. Chem.*, 2008, **29**, 839-845.
53. Bruker. SAINT v8.38A. Bruker AXS Inc., Madison, Wisconsin, USA.
54. L. Krause, R. Herbst-Irmer, G. M. Sheldrick and D. Stalke, *J. Appl. Cryst.*, 2015, **48**, 3-10.
55. (a) G. M. Sheldrick, *Acta Cryst.*, 2008, **A64**, 112-122; (b) G. M. Sheldrick, *Acta Cryst.*, 2015, **C71**, 3-8.
56. R. Naskar, P. Ghosh, C. K. Manna, N. Murmu and T. K. Mondal, *Inorganica Chim. Acta.*, 2022, **534**, 120802.
57. (a) S. Biswas, P. Roy and T. K. Mondal, *J. Mol. Struct.*, 2017, **1142**, 110-115; (b) J. – A. Alvarez-Hernández, N. Andrade-López, J. G. Alvarado-Rodríguez, S. González-Montiel, L. Á. Zárate-Hernández and J. Cruz-Borbolla, *Polyhedron*, 2022, **214**, 115635; (c) D. Qiu, Y. Guo, H. Wang, X. Bao, Y. Feng, Q. Huang, J. Zeng and G. Qiu, *Inorg. Chem. Commun.*, 2011, **14**, 1520-1524.
58. K. Akdi, R.A. Vilaplana, S. Kamah and F. Gonzalez-Vilchez, *J. Inorg. Biochem.*, 2005, **99**, 1360–1368.

59. N. Bandyopadhyay, P. Basu, G. S. Kumar, B. Guhathakurta, P. Singh and J. P. Naskar, *J. Photochem. Photobiol. B*, 2017, **173**, 560–570.
60. C.V. Barra, F.V. Rocha, L. Morel, A. Gautier, S. S. Garrido, A.E. Mauro, R. C. G. Frem and A. V. G. Netto, *Inorg. Chim. Acta*, 2017, **446**, 54–60.
61. E. Nyarko, N. Hanada, A. Habib and M. Tabata, *Inorg. Chim. Acta*, 2004, **357**, 739–745.
62. J. B. Lepecq and C. Paoletti, *J. Mol. Biol.*, 1967, **27**, 87–106.
63. Y. Zhao, J. Zhu, W. He, Z. Yang, Y. Zhu, Y. Li, J. Zhang and Z. Guo, *Chem. Eur. J.*, 2006, **12**, 6621–6629.
64. E. Ramachandran, D. S. Raja, N. P. Rath and K. Natarajan, *Inorg. Chem.*, 2013, **52**, 1504-1514.
65. D. Senthil Raja, N. S. P. Bhuvanesh and K. Natarajan, *Inorg. Chem.*, 2011, **50**, 12852-12866.
66. A. Wolfe, G. H. Shimer and T. Mehan, *Biochemistry*, 1987, **26**, 6392-6396.
67. A. Paul, S. Mistri, A. Bhunia, S. Manna, H. Puschmann and S. C. Manna, *RSC Adv.*, 2016, **6**, 60487-60501.
68. A. Paul, A. Figuerola, V. Bertolasi and S. C. Manna, *Polyhedron*, 2016, **119**, 460-470.
69. X.-Q. Zhou, Q. Sun, L. Jiang, S.-T. Li, W. Gu, J.-L. Tian, X. Liu and S.-P. Yan, *Dalton Trans.*, 2015, **44**, 9516-9527.
70. W.-J. Lian, X.-T. Wang, C.-Z. Xie, H. Tian, X.-Q. Song, H.-T. Pan, X. Qiao and J.Y. Xu, *Dalton Trans.*, 2016, **45**, 9073-9087.
71. A. S. D. Tabatabai, E. Dehghanian and H. Mansouri-Torshizi, *Biometals*, 2022, **35**, 245-266.

72. S. Abedanzadeh, K. Karami, M. Rahimi, M. Edalati, M. Abedanzadeh, A. Mohammad Tamaddon, M. DehdashtiJahromi, Z. Amirghofran, J. Lipkowskif and K. Lyczko, *Dalton Trans.*, 2020, **49**, 14891-14907.
73. R. O. Omondi, N. R. Sibuyi, A. O. Fadaka, M. Meyer, D. Jaganyi and S. O. Ojwach, *Dalton Trans.*, 2021, **50**, 8127-8143.
74. X. Wei, Y. Yang, J. Ge, X. Lin, D. Liu, S. Wang, J. Zhang, G. Zhou and S. Li, *Journal of Inorganic Biochemistry*, 2020, **202**, 110857.
75. J. R. Lakowicz, *Principles of Fluorescence Spectroscopy*, Third Edition., Springer, New York, USA, 2006.
76. J.R. Lakowicz, *Fluorescence Quenching: Theory and applications*, Principles of Fluorescence Spectroscopy, Kluwer Academic/Plenum Publishers, New York, 1999, p. 53.
77. X. Z. Feng, Z. Lin, L. J. Yang, C. Wang and C. L. Bai, *Talanta*, 1998, **47**, 1223-1229.
78. H. Li, X. Li, S. Liu, L. Guo, B. Zhang, J. Zhang and Q. Ye, *Hepatology*, 2017, **66**, 1920-1933.
79. W. Dai, F. Wang, L. He, C. Lin, S. Wu, P. Chen, Y. Zhang, M. Shen, D. Wu, C. Wang, J. Lu, Y. Zhou, X. Xu, L. Xu and C. Guo, *Mol. Carcinogenesis*, 2013, **54**, 301-311.
80. I. K. Sani, S. H. Marashi and F. Kalalinia, *Toxicology in Vitro*, 2015, **29**, 893-900.
81. Y. Chang, Y. Yuan, Q. Zhang, Y. Rong, Y. Yang, M. Chi, Z. Liu, Y. Zhang, P. Yu and Y. Teng, *RSC Adv.*, 2020, **10**, 1191-1197.
82. F. U Rahman, M. Z. Bhatti, A. Ali, H. Q. Duong, Y. Zhang, B. Yang, S. Koppireddi, Y. Lin, H. Wang, Z. T. Li and D. W. Zhang, *Euro. J. Med. Chem.*, 2018, **143**, 1039-1052.

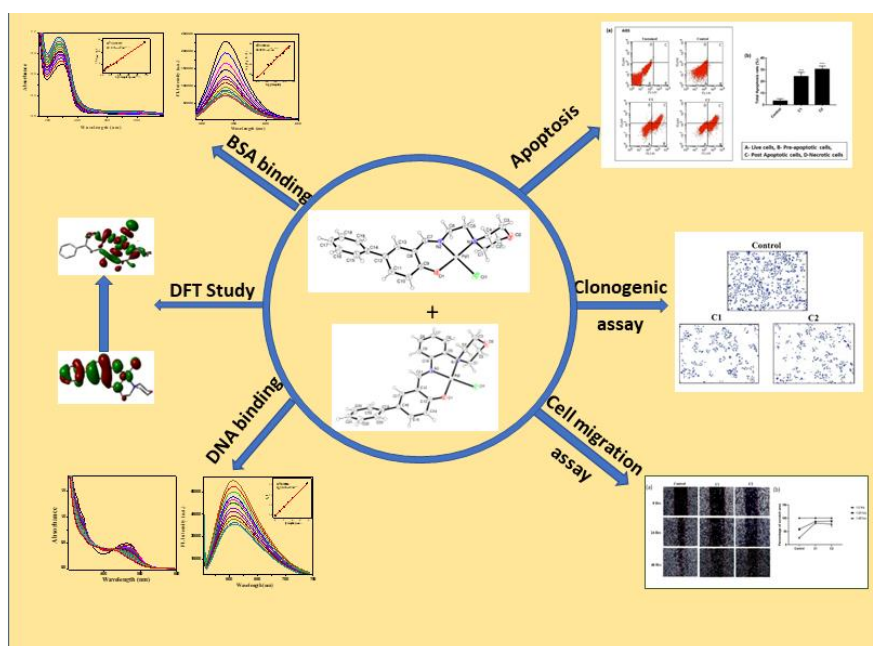
CHAPTER-V

**Synthesis, spectral characterization,
DFT investigation, and in vitro anti
proliferative activity of new ONN
donor morpholine-based ligands and
their Pd(II) complexes**

Synthesis, spectral characterization, DFT investigation, and in vitro anti proliferative activity of new ONN donor morpholine-based ligands and their Pd(II) complexes

Abstract

New ONN donor pincer ligands, 2,4-dichloro-6-(((2-morpholinoethyl)imino)methyl)phenol (HL^1) and 4-dichloro-6-(((2-morpholinophenyl)imino)methyl)phenol (HL^2) and their palladium complexes $[Pd(L^1)Cl]$ (**C1**) and $[Pd(L^2)Cl]$ (**C2**) are synthesized and thoroughly characterized by spectroscopic techniques. X-ray structures of the complexes reveal that HL^1 and HL^2 act as tridentate O,N,N chelator in Pd(II) complexes forming distorted square planar geometry. The ability of the Pd(II) complexes to bind with CT DNA are investigated by UV–Vis method and the binding constant are found to be $2.63 \times 10^5 \text{ M}^{-1}$ and $8.96 \times 10^4 \text{ M}^{-1}$ for **C1** and **C2** respectively. Competitive binding study with ethidium bromide (EB) by fluorescence method suggests that the Pd(II) complexes efficiently displace EB from EB-DNA complex. The Calculated Stern-Volmer dynamic quenching constant, K_{sv} are found to be $1.51 \times 10^5 \text{ M}^{-1}$ and $4.31 \times 10^4 \text{ M}^{-1}$ for **C1** and **C2** respectively. Moreover, the interactions of Pd(II) complexes (**C1/C2**) with bovine serum albumin (BSA) are also studied. The antiproliferative activity of the complexes are investigated with gastric adenocarcinoma cell line (AGS), triple negative breast cancer cell line (MDA-MB 231), lung cancer cell line (A549) and hepatocellular carcinoma cell line (HepG2). Both the Pd(II) complexes exhibit substantial cytotoxicity towards HepG2 ($IC_{50} = 29.2\text{-}32.3 \text{ }\mu\text{M}$) and AGS ($IC_{50} = 11.19\text{-}12.12 \text{ }\mu\text{M}$) cell lines.



V.1. Introduction

Cancer is ranked as the second most common cause of death worldwide among non-infectious diseases, accounting for over 72% of fatalities [1-2]. Therefore, scientists' primary focus continues to be on developing new, potentially effective anticancer medications with few side effects [3]. The development of anticancer medications with increased potency is extremely challenging [4]. Metals made with different ligands are now thought to be effective in treating a variety of ailments. A number of biological uses, including their mechanism of coordination and anticancer, antiviral, antifungal, anti-tuberculosis, and anti-inflammatory action, have recently drawn attention to Schiff bases with ONN and ONS donor ligands made using first, second, and third row transition metals [5-6]. Because of their powerful lipophilicity and ability to alter, ligands are essential for enhancing drug resistance [7-8]. Additionally, the unusual oxidation states can be stabilised by Schiff base ligands. Numerous heterocyclic aromatic ligands, including pyridine, phenanthroline [9-10], and their derivatives, have been found to function as DNA intercalators in Pd and Ru complexes. Anticancer medications primarily alter DNA structure by establishing irreversible covalent and noncovalent bonds that obstruct DNA replication and transcription because tumour cells proliferate more quickly than non-neoplastic cells [11-18].

The 1979 discovery of the anti-cancer medication cisplatin is regarded as a notable advancement in the field of medicinal chemistry. Throughout the world, cisplatin has mostly been used to treat ovarian and testicular cancer [19-26]. The platinum metal in the cisplatin molecule interacts with neighbouring purine bases via their N7 positions by forging an irreversible covalent link. just six platinum derivatives exist now. Only six platinum compounds are now being used for chemotherapy on a global scale. However, despite the fact that these platins have a lot of benefits in the treatment of cancer, they also have a lot of negative side effects, such as nausea, vomiting, nephrotoxicity, ototoxicity, bone marrow

suppression, neurotoxicity [27], etc. Palladium(II) complexes have garnered significantly greater interest in the field of medicinal chemistry than Pt(II) complexes among all the transition metal ions because of their structural similarities and chemical reactivity as potential anticancer medicines. The fact that Pd(II) complexes have better solubility than Pt(II) complexes, as well as the fact that their aquation rate and rate of ligand exchange are nearly 10^5 times higher compare to their Pt(II) analogues, are some notable factors supporting the claim that Pd(II) complexes are better anticancer agents than Pt(II) complexes [28-34]. Because of their structural closeness, bovine serum albumin has received much research instead of human serum albumin. The most prevalent protein, serum albumin, transports nutrients and medications through non-covalent interactions in the circulatory system. For absorption, excretion, and metabolism, serum proteins' capacity to bind with medicinal medicines is essential. Additionally, research on DNA interactions with these medications made with various chelating ligands has generated a lot of attention because of their prospective applications [35-42].

This paper describes the synthesis of two novel ONN donor ligands (HL^1 and HL^2) and their complexes (C1 and C2). By carefully examining several spectrometric techniques, such as NMR, IR, Mass, UV-Vis, as well as single crystal X-ray studies, $[Pd(L^1)Cl]$ and $[Pd(L^2)Cl]$ have been characterised. The MTT assay and colony formation assay were used to test the in-vitro cytotoxicity of the complexes and ligands on the human breast cancer cell line MCF 7, human lung cancer cell line A549, the hepatocellular carcinoma cell line HepG2, and the gastric adenocarcinoma cell line AGS. Additionally, a cell migration investigation was carried out on the AGS cell line to track the inhibitory effects of both Pd(II) complexes. With the aid of the DFT and TDDFT approach, theoretical calculations of the complexes were carried out to understand the experimental evidence of electronic structure.

V.2. Experimental

V.2.1. Materials

[1,1'-biphenyl]-4-ol, Palladium(II) Chloride, 2-morpholinoaniline, 4-(2-Aminoethyl)morpholine (Sigma Aldrich), Dulbecco's modified Eagle's medium (DMEM), Roswell Park Memorial Institute Medium (RPMI), Fetal Bovine Serum (FBS), ethylenediaminetetraacetic acid (EDTA), trypsin (Gibco BRL, Grand Island (4,5-Dimethylthiazol-2-yl)2,5-diphenyltetrazolium bromide (45989, MTT-CAS298-93-1-Calbiochem), DMSO (Merck-Millipore), Tissue culture plastic wares (Genetix Biotech Asia Pvt. Ltd.), highly polymerized calf thymus (CT) DNA (stored at 4 °C), bovine serum albumin (BSA) (stored at 4 °C), and Tris-HCl buffer (Sigma-Aldrich) were obtained. Merck supplied the solvents we bought, including dry methanol, acetonitrile, and acetone. To make all the solutions, double distilled water was used. The cited paper describes the preparation of 4-hydroxy-[1,1'-biphenyl]-3-carbaldehyde [43]. Four cancer cell lines- MCF 7 for human breast cancer, A549 for human lung cancer, HepG2 for liver cancer and AGS for stomach cancer were received from the National Centre for cell science (NCCS), Pune, India

V.2.2. Instrumentation

The PerkinElmer 2400 series II analyser carried out the elemental analyses (C, H, and N). The 300 MHz Bruker equipment was used to record the ^1H NMR spectra. CDCl_3 and DMSO-d_6 were utilised as solvents for NMR spectra, with TMS serving as an internal standard. Chemical shifts are reported in units, while the coupling constants for ^1H - ^1H and ^1H -C are measured in Hz. On a Waters (Xevo G2 Q-TOF) mass spectrometer, HRMS mass spectra were captured. Utilizing a PerkinElmer Lambda 750 spectrophotometer, electronic spectra were recorded.

V.2.3. Synthesis

V.2.3.1. Synthesis of HL¹

The Schiff-base ligand HL¹ was made via a straightforward one-step process. To synthesis the ligand HL¹, 198 mg of 4-hydroxy-[1,1'-biphenyl]-3-carbaldehyde and 130 mg of 4-(2-Aminoethyl)morpholine in 1:1 molar ratio were heated in dry methanol and refluxed at 50–60 °C while stirring continuously. This resulted in the formation of the straw-yellow Schiff-base product (E)-3-(((2-morpholinoethyl)imino)methyl)-[1,1'-biphenyl]-4-ol (HL¹). Ethanol was used to properly cleanse the yellow product before it was recrystallized.

Anal. Calc. for C₁₉H₂₂N₂O₂: C, 73.52; H, 7.14; N, 9.03. Found: C, 73.48; H, 7.08; N, 9.01. IR (KBr, cm⁻¹): 3551 υ(O-H), 2993 υ(C-H), 1630 υ(C=N), 1110 υ(C-N). ¹H NMR (300 MHz, DMSO-d₆): δ 2.45-2.51 (-CH₂, m, 4H), 2.62 (-CH₂, t, J = 6 Hz, 2H), 3.57 (-CH₂, t, J = 3 Hz, 4H), 3.74 (-CH₂, t, J = 6 Hz, 2H), 6.95 (ArH, d, J = 6 Hz, 1H), 7.31 (ArH, t, J = 6 Hz, 1H), 7.44 (ArH, t, J = 6 Hz, 2H), 7.64 (ArH, t, J = 6 Hz, 3H), 7.77 (ArH, s, 1H), 8.64 (CH=N-, s, 1H), 13.71 (-OH, s, 1H). UV-vis in acetonitrile (λ_{max}, nm) (ε, M⁻¹cm⁻¹): 245 (28920); 330 (2117). HRMS, m/z: Calculated, 333.1579; found, 333.1567 [M + Na]⁺. Yield: 0.251 g (81%).

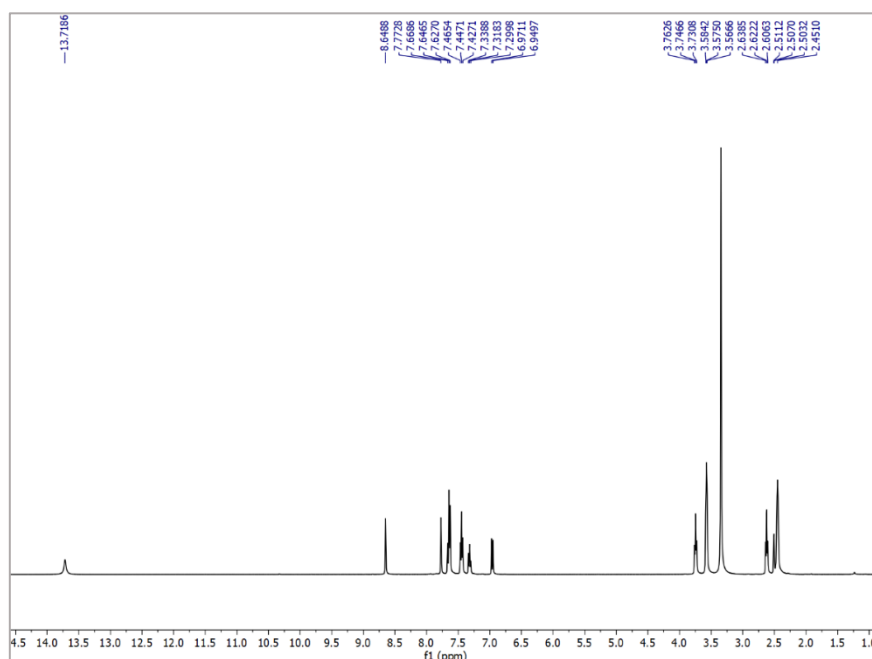


Fig.V.1. ¹H NMR spectrum of HL¹ in DMSO-d₆

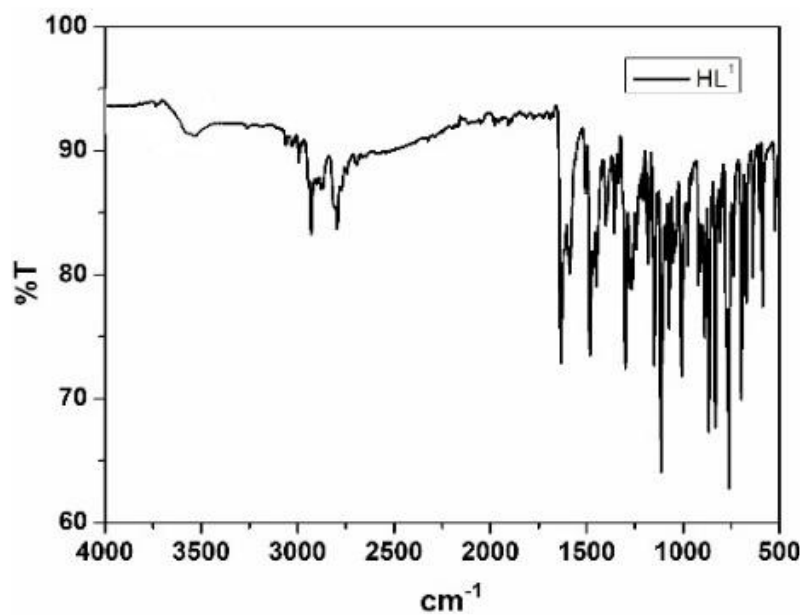


Fig.V.2. IR spectrum of HL¹ (KBr disk)

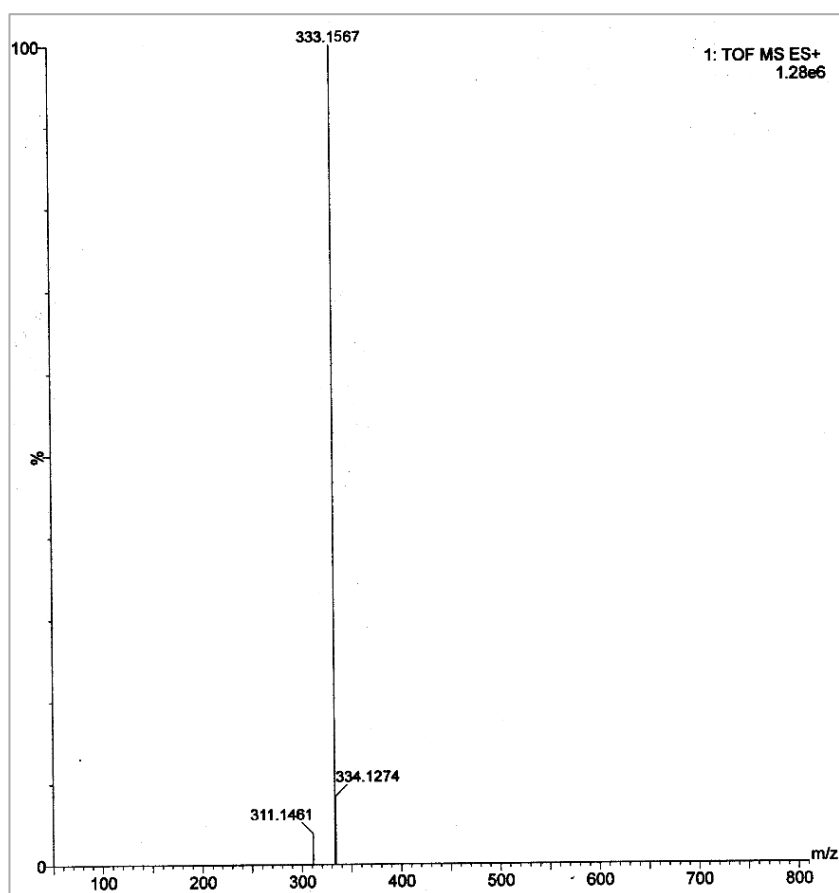


Fig.V.3. HRMS spectrum of HL¹ in acetonitrile

V.2.3.2. Synthesis HL²

The ligand HL² was made by dissolving 178 mg of 2-Morpholinoaniline and 198 mg of 4-hydroxy-[1,1'-biphenyl]-3-carbaldehyde in dry methanol under refluxing conditions at 50–60°C. After 3 hours, (E)-3-(((2-morpholinophenyl)imino)methyl)-[1,1'-biphenyl]-4-ol, a straw-yellow solid Schiff-base product, was produced. It was filtered and repeatedly washed with ethanol. In ethanol, the synthetic ligand was recrystallized. Yield: 0.283 g (79.2 %).

Anal. Calc. for C₂₃H₂₂N₂O₂: C, 77.07; H, 6.19; N, 7.82. Found: C, 77.03; H, 6.11; N, 7.78. IR (KBr, cm⁻¹): 3478 ν (O-H), 2953 ν (C-H), 1620 ν (C=N), 1113 ν (C-N). ¹H NMR (300 MHz, CDCl₃): δ 3.07 (-CH₂, t, J = 3.4 Hz, 4H), 3.94 (-CH₂, t, J = 3 Hz, 4H), 7.12-7.19 (ArH, m, 3H), 7.24 (ArH, d, J = 6 Hz, 1H), 7.31-7.40 (ArH, m, 2H), 7.49 (ArH, t, J = 6 Hz, 2H), 7.61-7.68 (ArH, m, 4H), 8.79 (CH=N-, s, 1H), 13.91 (-OH, s, 1H). UV-Vis in acetonitrile (λ_{\max} , nm) (ϵ , M⁻¹cm⁻¹): 260 (27460); 366 (6359). HRMS, m/z: Calculated, 381.1579; found, 381.1568 [M + Na]⁺.

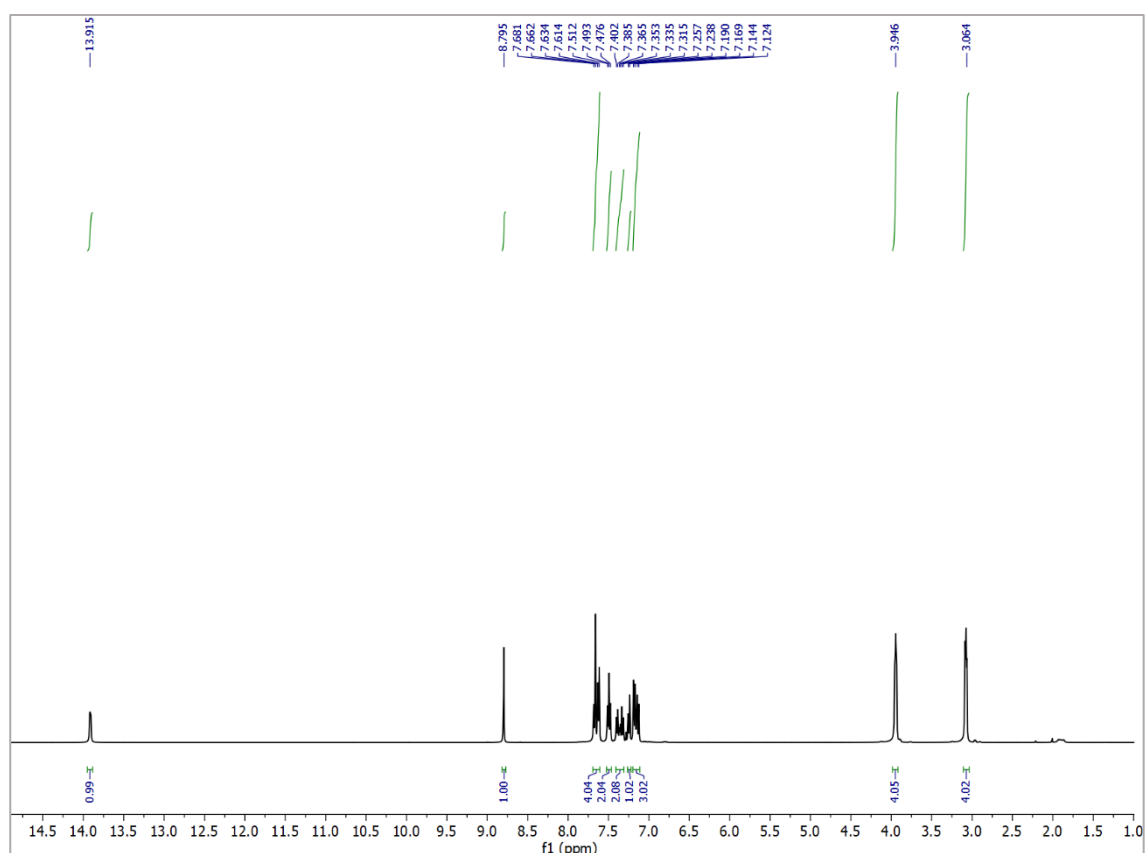


Fig.V.4. ¹H NMR spectrum of HL¹ in CDCl₃

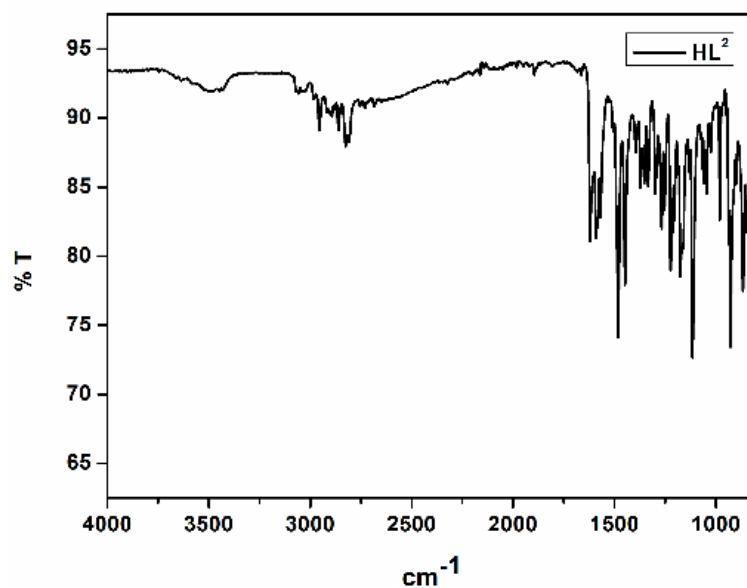


Fig.V.5. IR spectrum of HL¹ (KBr disk)

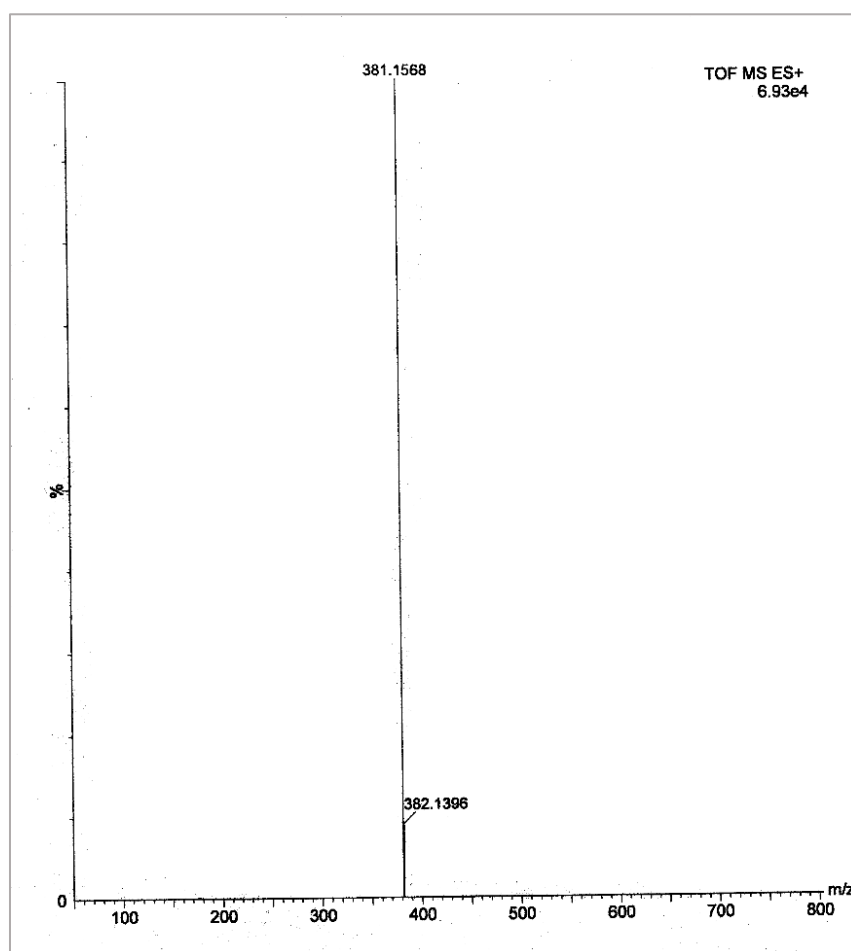


Fig.V.6. HRMS spectrum of HL² in acetonitrile

V.2.3.3. Synthesis of [Pd(L¹)Cl] (C1)

At first in a round bottom flask 0.037g (0.209 mmol) of PdCl₂ was dissolved in 15 mL acetonitrile under refluxing condition. To it, 0.064 g (0.209 mmol) of HL¹ in 15 mL acetonitrile was mixed dropwise. The reaction mixture was then refluxed for 5 h to yield red coloured solution. The reaction mixture was then cooled to room temperature. Red coloured solid product of [Pd(L¹)Cl] (C1) was collected by slow evaporation of the solvent. Yield: 0.070 g (75 %).

Microanalytical data for C₁₉H₂₁ClN₂O₂Pd (C1): Anal. Calc. (%): C, 50.57; H, 4.69; N, 6.21. Found (%): C, 50.48; H, 4.60; N, 6.15. IR data (KBr disc) (cm⁻¹): 2852 ν(CH), 1586 ν(C=N). ¹H NMR (300 MHz, DMSO-d₆): 3.14-3.24 (-CH₂, m, 4H), 3.45-3.51 (-CH₂, m, 2H), 3.84-4.00 (-CH₂, m, 6H), 6.86 (ArH, d, J = 6.6 Hz, 1H), 7.26 (ArH, t, J = 7.5 Hz, 1H), 7.41 (ArH, t, J = 6 Hz, 2H), 7.57-7.65 (ArH, m, 3H), 7.73 (ArH, s, 1H), 8.08 (CH=N-, s, 1H). λ_{max} (ε, M⁻¹ cm⁻¹) in acetonitrile: 402(1945), 352(1854), 270(24550), 250(sh.). HRMS, m/z: 415.0638 [M]⁺. found 415.0631

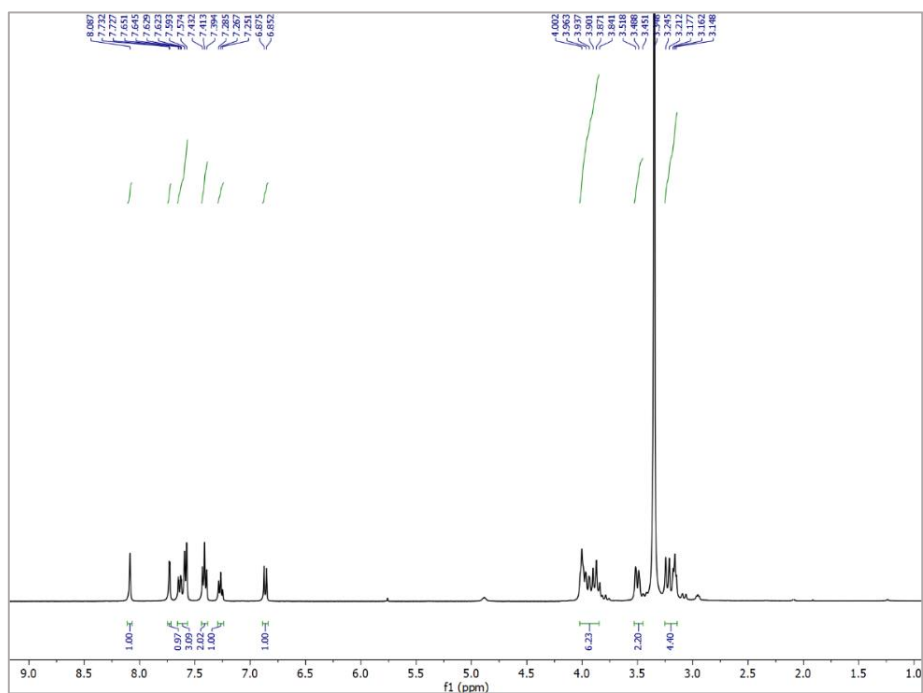


Fig.V.7. ¹H NMR spectrum of [Pd(L¹)Cl] in DMSO-d₆

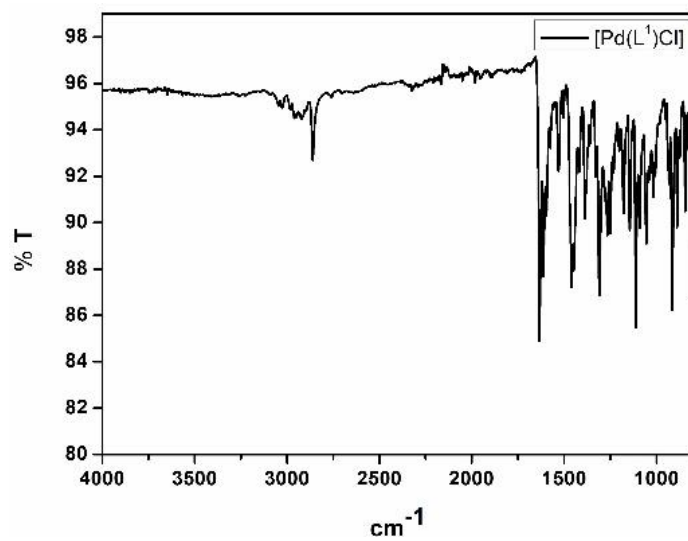


Fig.V.8. IR spectrum of [Pd(L¹)Cl] (KBr disk)

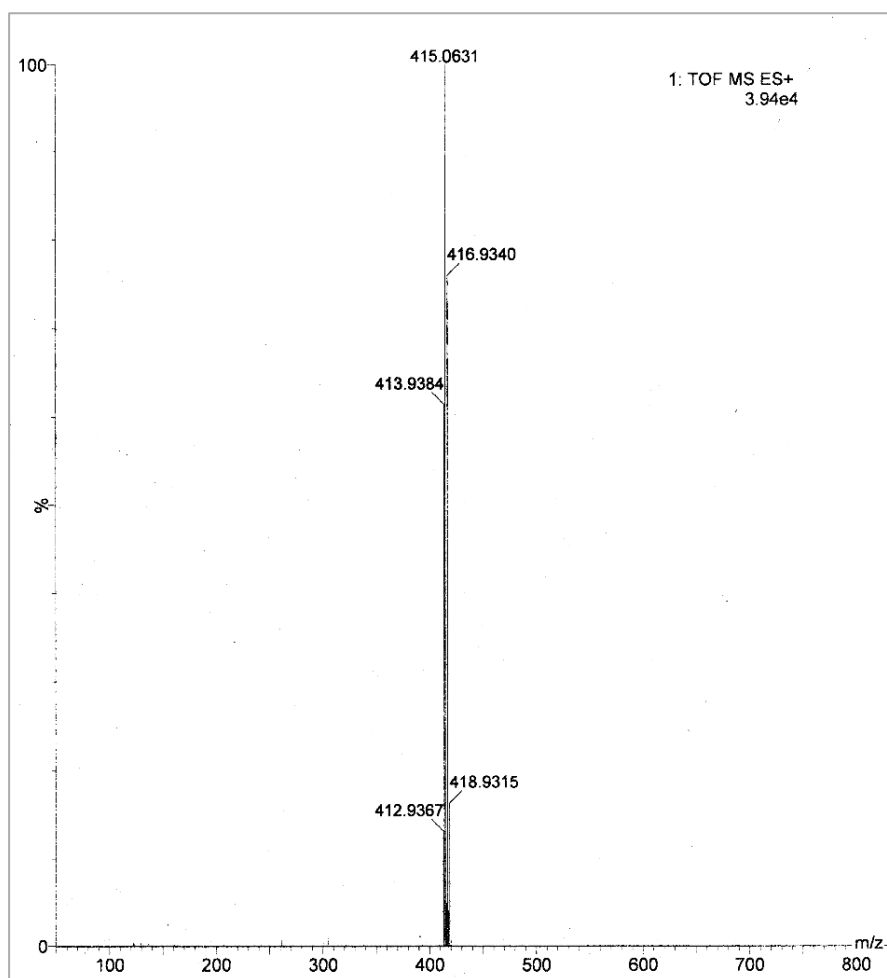


Fig.V.9. HRMS spectrum of [Pd(L¹)Cl] in acetonitrile

V.2.3.4. Synthesis of [Pd(L²)Cl] (C2)

[Pd(L²)Cl] (C2) was synthesized following the similar procedure of C1. Yield: 0.081 g (78 %).

Microanalytical data for C₂₃H₂₁ClN₂O₂Pd (C2): Anal. Calc. (%): C, 55.33; H, 4.24; N, 5.61.

Found (%): C, 55.30; H, 4.21; N, 5.65. IR data (KBr disc) (cm⁻¹): 2920 ν (CH), 1595 ν (C=N).

¹H NMR (300 MHz, CDCl₃): δ 3.35-3.43 (-CH₂, m, 2H), 3.99-4.07 (-CH₂, m, 2H), 4.37-4.45 (-CH₂, m, 2H), 4.76-4.84 (-CH₂, m, 2H), 7.22 (ArH, d, J = 8.9 Hz, 1H), 7.32 (ArH, d, J = 7.2 Hz, 1H), 7.42 (ArH, t, J = 7.8 Hz, 4H), 7.53-7.57 (ArH, m, 3H), 7.63-7.66 (ArH, m, 1H), 7.81 (ArH, t, d = 9 Hz, 1H), 7.96 (ArH, d, J = 9 Hz, 1H), 8.28 (CH=N-, s, 1H). $\lambda_{\max}(\epsilon, M^{-1} \text{ cm}^{-1})$ in acetonitrile: 465 (462), 346 (sh), 324 (sh), 262 (9620). HRMS, m/z: 463.0638 [M]⁺. found 463.0629.

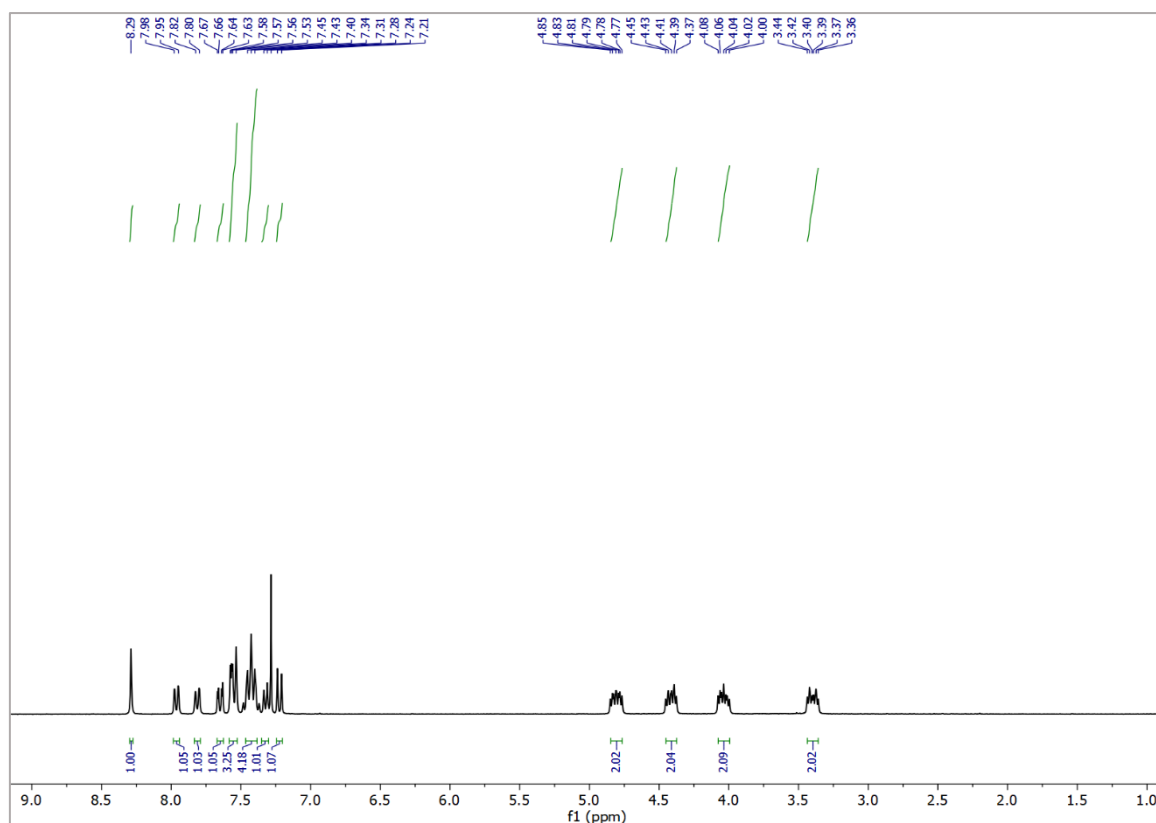


Fig.V.10. ¹H NMR spectrum of [Pd(L²)Cl] in CDCl₃

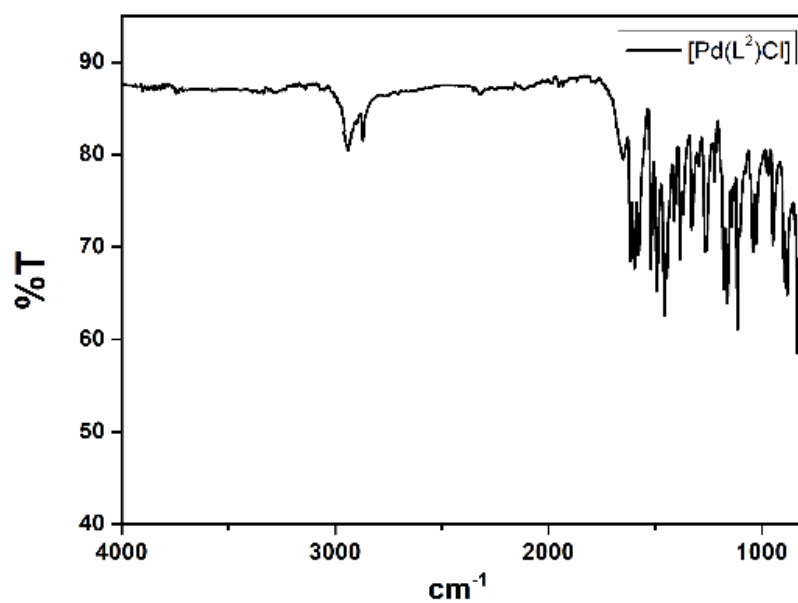


Fig.V.11. IR spectrum of [Pd(L²)Cl] (KBr disk)

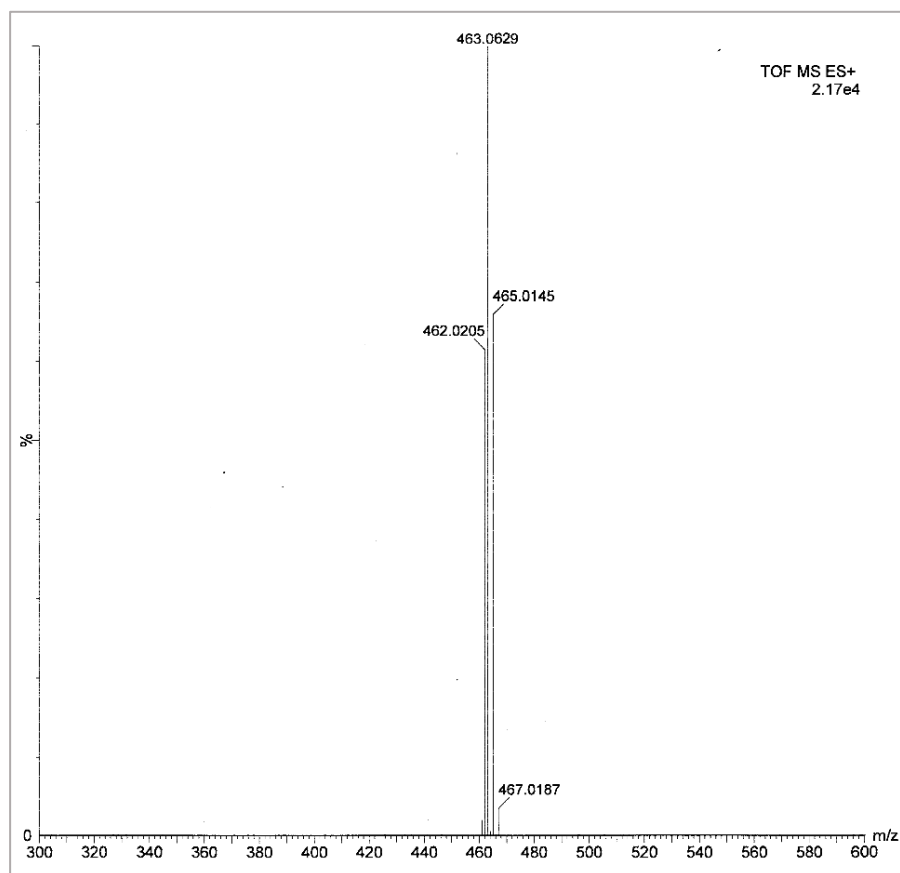


Fig.V.12. HRMS spectrum of [Pd(L²)Cl] in acetonitrile

V.2.4. DNA-binding interaction Studies

V.2.4.1. UV-Vis titration

A CT-DNA solution (2.19×10^{-3} M) in Tris-HCl/NaCl buffer (pH 7.4) and a complex solution (1.0×10^{-4} M) in a 1:10 acetonitrile/buffer solution were produced for UV-Vis titrations. The compounds' UV-Vis spectra were measured between 300 and 600 nm. The CT-DNA solution was now progressively added to it, properly mixed, and allowed to equilibrate for 4 min before the spectra were taken. When saturation was reached, addition was continued. It's crucial to know the equilibrium binding constant (K_b) of the complex with CT-DNA based on the findings of the spectral titration. K_b (in M^{-1}) was calculated using Eq. (1) [44].

$$[\text{DNA}]/(\varepsilon_a - \varepsilon_f) = [\text{DNA}]/(\varepsilon_b - \varepsilon_f) + 1/K_b(\varepsilon_b - \varepsilon_f) \dots(1)$$

The extinction coefficients a, f and b correspond to $A_{\text{obs}}/[\text{complex}]$, free Pd(II) complex, and the extinction coefficient of the Pd(II) complex when it is in fully bound state, respectively.

Where [DNA] is the concentration of CT DNA in base pairs. When $[\text{DNA}]/(\varepsilon_a - \varepsilon_f)$ is plotted against [DNA], the slope and intercept are given by $1/(\varepsilon_b - \varepsilon_f)$ and $1/K_b(\varepsilon_b - \varepsilon_f)$, respectively. K_b is the slope-to-intercept ratio was figured out using Eq. (1).

V.2.4.2. Competitive binding study with EB by fluorescence method

The fluorescence approach was used to investigate the ability of the produced palladium complexes (C1 and C2) to release EB from its EB-DNA complexes. To synthesise the CT DNA-EB complexes, 10 μM EB and 10 μM CT DNA were mixed uniformly in a Tris-HCl/NaCl buffer solution (pH 7.4). These complexes produced fluorescence emission at 608 nm when stimulated at 540 nm. Following the addition of C1 and C2, the quenching of that emission was seen.

V.2.5. BSA interaction experiments

Using UV-Vis and fluorescence techniques, the binding relationship between BSA and Pd(II) complexes (C1 and C2) was studied. A 500 mM phosphate buffer saline (PBS) stock solution of BSA was made and kept at 4°C in the dark for future use. By measuring the absorbance at 280 nm in UV-Vis spectra, BSA content was determined (molar extinction coefficient $66,400 \text{ dm}^3 \text{ mol}^{-1} \text{ cm}^{-1}$) [45]. When necessary, the DMSO medium in which the stock solutions of C1 and C2 were prepared was appropriately diluted with PBS. BSA concentration (10 M) was maintained while the complex added to it was varied in concentration in order to record UV-Vis spectra. Tryptophan fluorescence of BSA was observed during a fluorescence experiment at wavelengths between 290 and 500 nm at a slit width of 5 nm and an excitation wavelength of 280 nm. With the addition of metal complexes, the BSA emission intensity quenching at 336 nm was observed.

V.2.6. Anti-cancer activity

V.2.6.1. Cell Culture

Human breast cancer cell line MCF 7, human lung cancer cell line A549, gastric adenocarcinoma cell line AGS, and hepatocellular carcinoma cell line HepG2 was bought from the National Center for Cell Science in Pune, India, and kept in DMEM high glucose medium (for A549, HepG2 and MCF 7) and RPMI 1640 medium (for AGS) with 10% Fetal Bovine Serum (FBS) supplements (Gibco). All of the cell lines were maintained in a 37°C humidified incubator with a 5 % CO₂ environment. Early passage numbers were used for all tests.

V.2.6.2. Cell Viability Assay

The cell viability experiment was followed as previously elucidate by Riss T L et al [46]. A 96-well plate with 1×10^3 cells per well was initially treated for 24 hours at 37 °C with escalating concentrations of C1, HL¹, C2, HL² and cisplatin (1, 100, 200, 300, 400, and 600

μM). Each well was then filled with 10 μl of MTT solution (5 mg/ml in PBS). A multi-mode plate reader was used to measure the absorbance at 570 nm after each well had been incubated for 3 hours (SpectraMax i3x, Molecular devices). The IC_{50} value was determined using nonlinear regression (curve fit) and the graph pad prism software's log (inhibition) vs. response equation.

V.2.6.3. Colony Formation Assay

In six-well plates, approximately 500 AGS cells were plated. The cells were then exposed to C1 (12 μM) and C2 (11 μM), Following thorough washing with 1X PBS and fixing with methanol, the generated colonies were stained with crystal violet for 15 minutes. Colonies, defined as more than 50 cells, were counted using Olympus CKX41, an inverted bright field microscope with a 4X objective magnification.

V.2.6.4. Statistical analysis

Each experiment was carried out in triplicate, and the typical data are shown as mean values with standard deviations. To assess the main differences between the control and each treated group, one-way analysis of variance (ANOVA) and post hoc comparisons was done with the use of the Turkey test. P value of 0.05 or less was regarded as statistically significant. The software used for analysis of all the tests was Graph Pad Prism 5.

V.2.6.5. In Vitro Cell Migration Assay

AGS gastric cancer cells were grown in a 6-well plate until they were 90% confluent. On the confluent cells, a straight scratch was produced using a 200 μl sterile pipette tip. This was followed by a PBS wash. Following that, Pd(II) complexes were administered to the cells in serum-free RPMI media. After incubating the cells for 0, 12, and 24 hours, the area of the wound closure was measured and compared to the starting wound size at 0 hours. The wound

area was quantified from the digital photos at each time point using ImageJ software to measure the wound area.

V.2.6.6. Apoptosis Assay

To distinguish between apoptosis and necrosis, Annexin V Apoptosis Kit (Santa Cruz Biotechnology, INC.) was used, as described by the manufacturer's protocol. 1×10^6 cells were seeded in 6 well plates and treated with a chosen concentration of C1 and C2. After 24 hours, the treated cells were trypsinized and centrifuged at 1200 rpm for 5 minutes. The pellet was dissolved in 1X assay buffer of Annexin-PI assay kit and stained with Annexin V-FITC and propidium iodide (PI). Stained cells were then analysed by flow cytometry using BD FACSVerserTM. Total 5000 events were obtained for gating and dual parameter dot plot of FL1-H (X-axis; FITC-fluorescence) verse FL2-H (Yaxis; PI- fluorescence) was displayed in logarithmic fluorescence intensity.

V.2.7. Computational method

Density functional theory (DFT) was used to optimise the geometry of the complexes and their ligands while utilising the B3LYP hybrid exchange correlation function [47]. With the exception of palladium, all elements were assigned to the 6-31G(d) basis set. However, for the palladium atom, the LanL2DZ basis set with an effective core potential was used [48]. Every optimised configuration had to be in a local minima on the P.E. surface for the vibrational frequency calculations to be accurate, and only positive Eigen values were taken into account. The Gaussian09 program package was used to do all computations through the GaussView, Version 5 visualisation tool [49]. Conductor-like polarizable continuum model (CPCM) and Time-dependent density functional theory (TDDFT) formalism were successfully used to simulate the vertical electronic transitions in acetonitrile solvent [50-51]. The fractional contributions of various groups to each molecular orbital were calculated using Gauss Sum [52].

V.2.8. Crystal structure determination and refinement

A few good grade and well-shaped Complex crystals were chosen using a microscope from among the many crystals retrieved from the crystal tube. With the aid of a graphite monochromated Bruker AXS Kappa smart Apex-III diffractometer outfitted with an Apex-III CCD area detector (Mo Ka radiation = 0.71073 Å) at 293 K, X-ray data for palladium complexes were measured. The ω scan technique was used to record reflection data. The SAINT reduction software [53] and the SADABS absorption correction programme were used to process the obtained frames [54].

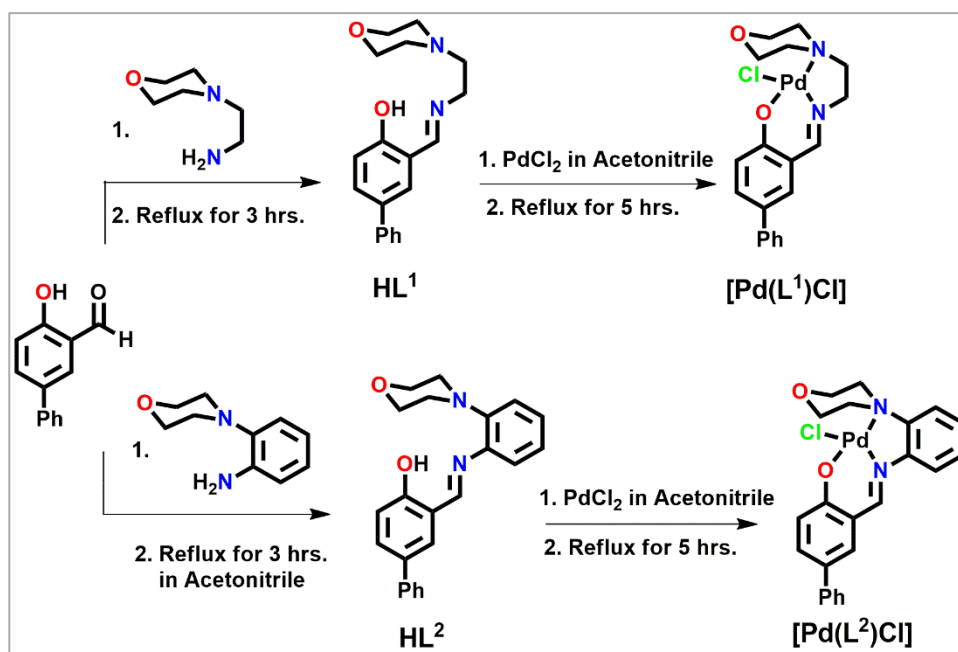
Table V.1. Crystal data and details of the structure determination of C1 and C2

	[Pd(L ¹)Cl] (C1)	[Pd(L ²)Cl] (C2)
Formula	C19 H21 Cl1 N2 O2 Pd1	C23 H21 Cl1 N2 O2 Pd
Formula Weight	451.25	499.27
Crystal System	<i>Orthorhombic</i>	<i>Monoclinic</i>
Space group	<i>P c a 21</i>	<i>P 21/n</i>
<i>a</i> (Å)	14.7343(12)	6.7343(7)
<i>b</i> (Å)	23.3349(17)	12.8594(12)
<i>c</i> (Å)	10.3970(7)	23.048(2)
β (°)	90	94.439(3)
<i>V</i> (Å ³)	3574.7(5)	1989.9(3)
<i>Z</i>	4	4
ρ (calc) (g/cm ³)	1.677	1.667
μ (Mo Ka) (mm ⁻¹)	1.203	1.089
<i>F</i> (000)	1824	1008
Crystal Size (mm)	0.09 × 0.07 × 0.05	0.13 × 0.10 × 0.08
<i>T</i> (K)	293(2)	293(2)
Radiation wavelength (Å)	0.71073	0.71073
θ (Min-Max) (°)	2.227-27.110	1.815-27.758
<i>hkl</i> range	-18 to 18, -24 to 29 and -12 to 13	-8 to 8, -16 to 16 and -30 to 29
Total, Unique Data, <i>R</i> (int)	30139, 7552, 0.0500	29350, 3868, 0.0396
Observed data (<i>I</i> > 2 σ (<i>I</i>))	6221	3868
<i>N</i> ref, <i>N</i> par	7552, 451	4631, 262
<i>R</i> ^a , <i>wR</i> ₂ ^b , <i>S</i> ^c	0.0332, 0.0603, 1.061	0.0538, 0.0712, 1.134
Residual Density (e/Å ³)	-0.617 and 0.771	-0.467 and 0.383

Using the SHELXL-2016/6 programme, the structures were directly solved, and they were then refined using full-matrix least-squares based on F^2 [55]. Geometrically restricted places for hydrogen atoms were first chosen, and they were afterwards refined as riding their pivot atoms. All atoms aside from hydrogen were anisotropically polished.

V.3. Results and discussion

PdCl_2 was used to react with HL^1 and HL^2 in a 1:1 mole ratio, respectively, under refluxing conditions in acetonitrile to synthesize the complexes $[\text{Pd}(\text{L}^1)\text{Cl}]$ and $[\text{Pd}(\text{L}^2)\text{Cl}]$ (scheme V.1). The reported procedure was followed to synthesis ligands [56]. Through the use of single crystal X-ray crystallography, the complexes' shape was verified. ^1H NMR spectroscopy and ESI mass spectrometry were used to fully analyse the ligands and complexes.



Scheme V.1. Synthesis of palladium(II) complexes, $[\text{Pd}(\text{L}^1)\text{Cl}]$ (C1) and $[\text{Pd}(\text{L}^2)\text{Cl}]$ (C2)

V.3.1. Spectral characterization

The $\nu(\text{O-H})$ stretching is represented by a large peak in the IR spectra of HL^1 at 3551 cm^{-1} (Fig.V.2). $\nu(\text{C-H})$ stretching is associated with the intense sharp peak at 2993 cm^{-1} . The positions of $\nu(\text{C=N})$ and $\nu(\text{C-N})$ are 1630 cm^{-1} and 1110 cm^{-1} , respectively. The HL^2 infrared spectrum has a large peak at 3478 cm^{-1} and a peak at 2953 cm^{-1} (Fig.V.5) that is associated with $\nu(\text{C-H})$ stretching. The HL^2 imine stretching frequency is at 1620 cm^{-1} , while the strong peak for $\nu(\text{C-H})$ stretching is at 1113 cm^{-1} . While $\nu(\text{C=N})$ moves from 1630 cm^{-1} (for HL^1) to 1586 cm^{-1} due to complex formation, the C-H stretching frequency of $[\text{Pd}(\text{L}^1)\text{Cl}]$ appears at 2852 cm^{-1} (Fig.V.8). C-H stretching frequency of $[\text{Pd}(\text{L}^2)\text{Cl}]$ appears at 2920 cm^{-1} (Fig.V.11). Due to complexation, the imine stretching frequency of $[\text{Pd}(\text{L}^2)\text{Cl}]$ decreases from 1620 cm^{-1} (for HL^2) to 1595 cm^{-1} . In contrast to HL^1 and $[\text{Pd}(\text{L}^1)\text{Cl}]$, whose $^1\text{HNMR}$ spectra were recorded in DMSO-d_6 , $^1\text{HNMR}$ spectra of HL^2 and $[\text{Pd}(\text{L}^2)\text{Cl}]$ were recorded in CDCl_3 . For HL^1 and HL^2 , phenolic -OH peaks show up as singlets at 13.71 and 13.91 ppm, respectively, whereas imine hydrogen (CH=N-) peaks show up as singlets at 8.64 and 8.79 ppm, respectively (Fig.V.1 and Fig.V.4). All of the aromatic protons in HL^1 and HL^2 are present between 6.95 and 7.77 ppm. Imine hydrogen (CH=N-) of $[\text{Pd}(\text{L}^1)\text{Cl}]$ and $[\text{Pd}(\text{L}^2)\text{Cl}]$ showed two singlets at respective concentrations of 8.08 and 8.28 ppm (Fig.V.7 and Fig.V.10). $\text{Pd}(\text{L}^1)\text{Cl}$ and $\text{Pd}(\text{L}^2)\text{Cl}$ both have aromatic protons that are present in the range of 7.22 to 7.96 ppm. Both instances confirm the chelation of the O atom to the Pd atom by the elimination of imine hydrogen peaks from the ligand to complex. The mass spectra of HL^1 and HL^2 have m/z peaks at 333.1567 (Fig.V.3) and 381.1568 (Fig.V.6), respectively, which correspond to $[\text{M}+\text{Na}]^+$. The m/z peaks for $[\text{Pd}(\text{L}^1)\text{Cl}]$ and $[\text{Pd}(\text{L}^2)\text{Cl}]$, which correspond to $[\text{M}-\text{Cl}]^+$, are seen at 415.0631 (Fig.V.9) and 463.0629 (Fig.V.12), respectively. Acetonitrile was used to collect the absorption spectra of the ligands (HL^1 and HL^2) and their complexes ($[\text{Pd}(\text{L}^1)\text{Cl}]$ and $[\text{Pd}(\text{L}^2)\text{Cl}]$). HL^1 has a single sharp peak at 330 nm and an intense high

energy peak at 245 nm along with shoulder band at 273 nm, while the analogous complex $[\text{Pd}(\text{L}^1)\text{Cl}]$ displays a moderately intense low energy broad band at 402 nm and 352 nm together with a high energy band at 270 nm. A large, somewhat low energy peak and high energy band are visible at 366 nm and 260 nm for HL^2 , respectively. At 465 nm, the red-shifted band for $[\text{Pd}(\text{L}^2)\text{Cl}]$ can be seen. At 280 nm, there is a significant energy peak (Fig.V.13).

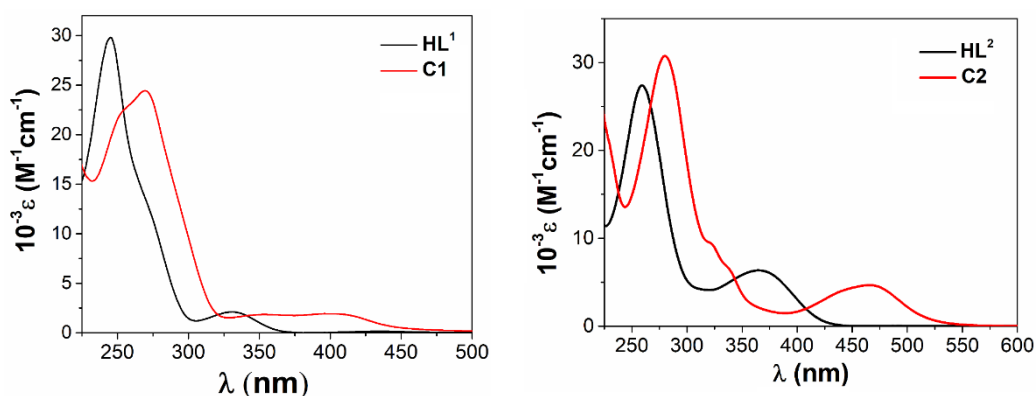


Fig.V.13. UV-Vis spectra of HL^1 , HL^2 , $[\text{Pd}(\text{L}^1)\text{Cl}](\text{C1})$ and $[\text{Pd}(\text{L}^2)\text{Cl}](\text{C2})$ in acetonitrile

V.3.2. Crystallographic study

A single crystal X-ray diffraction approach was used to further validate the genuine coordination mode of C1 and C2. In an orthorhombic crystal system with the $P_{c a 21}$ space group, complex C1 crystallises, whereas complex C2 crystallises in a monoclinic crystal system with the $P_{21/n}$ space group. The complexes' ORTEP plots and atom numbering scheme are shown in Fig.V.14. In the complexes, the ligands HL^1 and HL^2 function as tridentate O,N,N donor ligands. In complex C1, Pd-metal is coordinated with HL^1 through phenolic oxygen atom (O1), imine nitrogen atom (N2) and morpholino nitrogen atom (N1) via formation one five-membered (Pd1-N2-C6-C5-N1) and one six-membered (Pd1-N2-C7-C8-C9-O1) chelate ring with chelate bite angles $\angle\text{N2-Pd1-N1}$ and $\angle\text{N2-Pd1-O1}$, $84.55(18)^\circ$ and $92.17(18)^\circ$ respectively. Similarly, in C2 chelate bite angles $\angle\text{N2-Pd1-N1}$ and $\angle\text{N2-Pd1-O1}$, $84.11(10)^\circ$ and $94.58(10)^\circ$ respectively significantly deviate from 90° suggest the distorted

square planar geometry. The selected bond distances and bond angles of the complexes are given in Table V.2. Pd1-N2(imine) bond distances for the complexes are found to be 1.960(5) Å and 1.969(2) Å respectively for **C1** and **C2** and comparable to the literature values [57]. Pd1-Cl1 bond distance of both the complexes **C1** and **C2** are found to be 2.318(16) Å and 2.333(8) Å respectively.

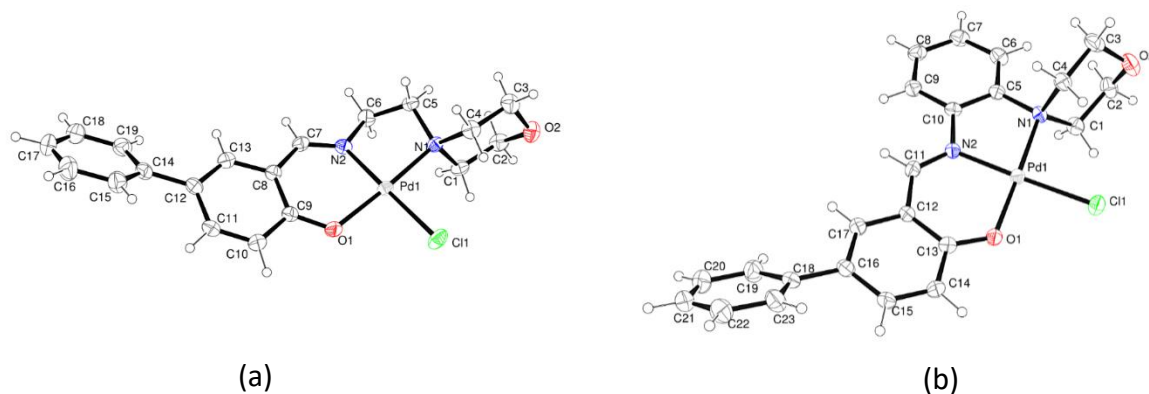


Fig.V.14. ORTEP plot of [Pd(L¹)Cl](a) and [Pd(L²)Cl](b) with 35% ellipsoidal probability

Table V.2. Selected bond distances (Å) and angles (°) of **1** and **2**

Bonds(Å)	[Pd(L ¹)Cl] (1)		[Pd(L ²)Cl] (2)	
	X-ray	Calc.	X-ray	Calc.
Pd1 – N1	2.076(5)	2.146	2.083(2)	2.140
Pd1 – O1	1.994(4)	2.004	1.978(2)	1.997
Pd1 – N2	1.960(5)	2.006	1.969(2)	2.005
Pd1 – Cl1	2.3186(16)	2.344	2.333(8)	2.350
N1 – C4	1.501(6)	1.502	1.516(4)	1.517
O1 – C9	1.325(6)	1.300	-	-
O1 – C13	-	-	1.307(4)	1.294
Angles (°)				
N1 – Pd1 – O1	176.72(17)	176.025	178.42(10)	177.744
N1 – Pd1 – N2	84.55(18)	84.160	84.11(10)	83.690
N1 – Pd1 – Cl1	94.79(13)	94.560	95.44(7)	94.560
N2 – Pd1 – Cl1	176.79(8)	93.552	176.79(8)	178.247
O1 – Pd1 – N2	92.17(18)	92.124	94.58(10)	94.057
O1 – Pd1 – Cl1	88.49(12)	90.230	85.83(7)	87.691
C13- O1- Pd1	-	-	124.0(2)	125.026
C9 – O1 – Pd1	122.5(4)	125.189	-	-

V.3.3. Computational study

By employing the DFT approach and the B3LYP exchange-correlation functional, the geometry of the two ligands and two complexes was optimised in the singlet ground state. The two complexes' optimised bond characteristics, such as bond angles and bond distances, are in good agreement with the X-ray crystal structure information provided in Table V.1. In Table V.3, specific molecular orbitals' energies and compositions are listed. For both ligands, contour plots of chosen molecular orbitals are provided in Fig.V.15 and Fig.V.16, respectively. For both complexes, contour plots of molecular orbitals are provided in Fig.V.17 and Fig.V.18 respectively. The higher energy occupied molecular orbital (HOMO) for both the complexes have 88-89% ligand contribution along with reduced contribution (7-8%) of Pd($d\pi$). HOMO-1 and HOMO-2 have mixed Pd($d\pi$) (17-26%) and Cl($p\pi$) (53-79%) character. To learn more about the electronic transition, the complexes' optimised geometries underwent TDDFT calculations. For [Pd(L1)Cl], the experimental band at 402 nm with XLCT (halogen to ligand charge transfer) characteristics correlates to the low energy transition at 431 nm (HOMO-2 \rightarrow LUMO transition). The estimated transition at 352 nm (HOMO-5 \rightarrow LUMO / HOMO-4 \rightarrow LUMO/ HOMO \rightarrow LUMO+1 transitions) exhibiting mixed LMCT (ligand to metal charge transfer) and ILCT (Intra ligand charge transfer) character provides strong support for the experimentally observed moderately bright band at 377.4 nm. An additional high energy band with an ILCT transition can be found at 270 nm. The transition at 456 nm for [Pd(L²)Cl] has mixed XMCT (halogen to metal charge transfer) and ILCT characteristics, and the low energy experimental band at 465 nm correlates to that transition. The band at 340 nm, on the other hand, corresponds to a mixed MLCT (metal to ligand charge transfer) and XLCT (halogen to ligand charge transfer) character (Table V.4). Mixed XLCT and MLCT character is associated with the band at 325 nm (HOMO-2 \rightarrow LUMO transition). The ILCT transition feature is corresponding to the band at 280 nm.

Table V.3. Energy and compositions (%) of selected molecular orbitals of **C1** and **C2**

MO	C1			C2				
	E (eV)	% of composition			E (eV)	% of composition		
		Pd	L	Cl		Pd	L	Cl
LUMO+5	0.37	14	85	1	-0.06	17	83	0
LUMO+3	-0.34	89	10	0	-0.55	01	99	0
LUMO+2	-0.47	02	98	0	-1.05	01	99	0
LUMO+1	-1.74	05	95	0	-1.87	53	34	12
LUMO	-1.82	52	36	12	-2.28	02	98	0
HOMO	-5.29	08	88	04	-5.39	07	89	3
HOMO-1	-6.1	26	20	54	-6.16	25	22	53
HOMO-2	-6.26	18	05	76	-6.32	17	05	79
HOMO-3	-6.51	76	14	11	-6.54	74	15	11
HOMO-4	-6.74	14	86	0	-6.72	01	82	17
HOMO-5	-6.76	02	98	0	-6.82	08	92	0
HOMO-6	-6.94	05	77	19	-6.83	10	90	0
HOMO-7	-7.08	09	81	10	-7.10	11	84	5
HOMO-8	-7.47	64	36	0	-7.53	61	39	0
HOMO-9	-7.58	20	57	23	-7.57	20	56	24
HOMO-10	-7.93	34	46	20	-7.73	97	02	01

Table V.4. Vertical electronic transitions of, HL¹, HL², C1 and C2 calculated by TDDFT/B3LYP/CPCM method

Comps.	λ (nm)	E (eV)	Osc. Strength (f)	Key excitations	Character ^a	$\lambda_{\text{expt.}}$ (nm) (ϵ (M ⁻¹ cm ⁻¹))
HL ¹	352.5	3.5175	0.0314	(98%)HOMO→LUMO	$\pi(\text{L}) \rightarrow \pi^*(\text{L})$	
	335.6	3.6947	0.0784	(92%)HOMO-1→LUMO	$n(\text{L}) \rightarrow \pi^*(\text{L})$	330 (2117)
	276.0	4.4918	0.1294	(92%)HOMO→LUMO+1	$\pi(\text{L}) \rightarrow \pi^*(\text{L})$	273 (sh.)
	255.2	4.8579	0.4425	(92%)HOMO-2→LUMO	$\pi(\text{L}) \rightarrow \pi^*(\text{L})$	245 (28920)
HL ²	438.7	2.8263	0.2573	(98%)HOMO→LUMO	$n/\pi(\text{L}) \rightarrow \pi^*(\text{L})$	
	371.7	3.3357	0.0963	(96%)HOMO-1→LUMO	$\pi(\text{L}) \rightarrow \pi^*(\text{L})$	366 (6359)
	324.7	3.8190	0.2293	(96%)HOMO-2→LUMO	$\pi(\text{L}) \rightarrow \pi^*(\text{L})$	
	270.9	4.5759	0.2785	(72%)HOMO→LUMO+1 (24%)HOMO-5→LUMO	$\pi(\text{L}) \rightarrow \pi^*(\text{L})$	260 (27460)
	264.1	4.6939	0.3497	(50%)HOMO-5→LUMO (32%)HOMO-1→LUMO+1	$\pi(\text{L}) \rightarrow \pi^*(\text{L})$	
C1	500.9	2.4753	0.0012	(84%)HOMO→LUMO	$\pi(\text{L}) \rightarrow d\pi(\text{Pd})$ (LMCT)	
	431.0	2.8765	0.0126	(77%)HOMO-2→LUMO	$p\pi(\text{Cl}) \rightarrow d\pi(\text{Pd})$ (XMCT)	402 (1945)
	388.2	3.1937	0.0189	(64%)HOMO→LUMO+1	$\pi(\text{L}) \rightarrow \pi^*(\text{L})$ (ILCT)	
	377.4	3.2854	0.0629	(39%)HOMO-5→LUMO (27%)HOMO-4→LUMO (21%)HOMO→LUMO+1	$\pi(\text{L}) \rightarrow d\pi(\text{Pd})$ (LMCT) $\pi(\text{L}) \rightarrow \pi^*(\text{L})$ (ILCT)	352 (1854)
	287.2	4.3172	0.6342	(50%)HOMO-4→LUMO+1 (31%)HOMO→LUMO+2	$\pi(\text{L}) \rightarrow \pi^*(\text{L})$ (ILCT)	270 (24550)
	250.8	4.9441	0.4344	(73%)HOMO-7→LUMO+1	$\pi(\text{L}) \rightarrow \pi^*(\text{L})$ (ILCT)	250 (sh.)
C2	508.8	2.4367	0.0001	(84%)HOMO→LUMO+1	$\pi(\text{L}) \rightarrow d\pi(\text{Pd})$ (LMCT)	
	455.8	2.7203	0.1359	(71%)HOMO→LUMO (25%)HOMO-2→LUMO+1	$\pi(\text{L}) \rightarrow \pi^*(\text{L})$ (ILCT) $p\pi(\text{Cl}) \rightarrow d\pi(\text{Pd})$ (XMCT)	465 (4690)
	424.7	2.9194	0.0422	(67%)HOMO-2→LUMO+1 (26%)HOMO→LUMO	$p\pi(\text{Cl}) \rightarrow d\pi(\text{Pd})$ (XMCT) $\pi(\text{L}) \rightarrow \pi^*(\text{L})$ (ILCT)	
	377.6	3.2836	0.1305	(81%)HOMO-1→LUMO	$p\pi(\text{Cl})/d\pi(\text{Pd}) \rightarrow \pi^*(\text{L})$ (XLCT/MLCT)	340 (6320)
	334.3	3.7086	0.2363	(94%)HOMO-2→LUMO	$p\pi(\text{Cl})/d\pi(\text{Pd}) \rightarrow \pi^*(\text{L})$ (XLCT/MLCT)	325 (9350)
	291.1	4.2587	0.4992	(88%)HOMO-6→LUMO	$\pi(\text{L}) \rightarrow \pi^*(\text{L})$ (ILCT)	280 (30850)

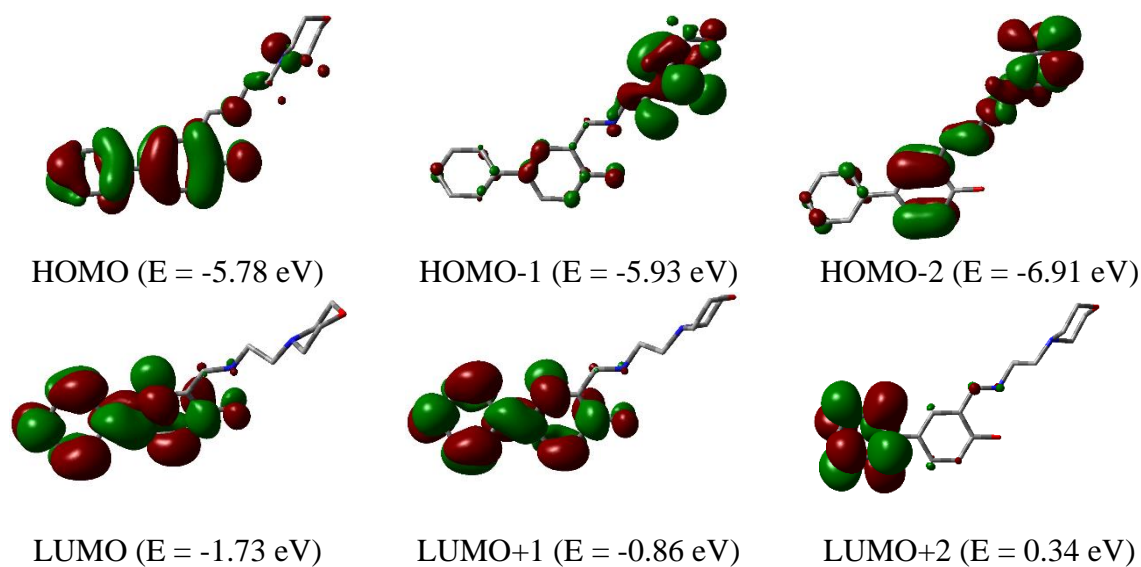


Fig.V.15. Contour plots of some selected molecular orbital of HL¹

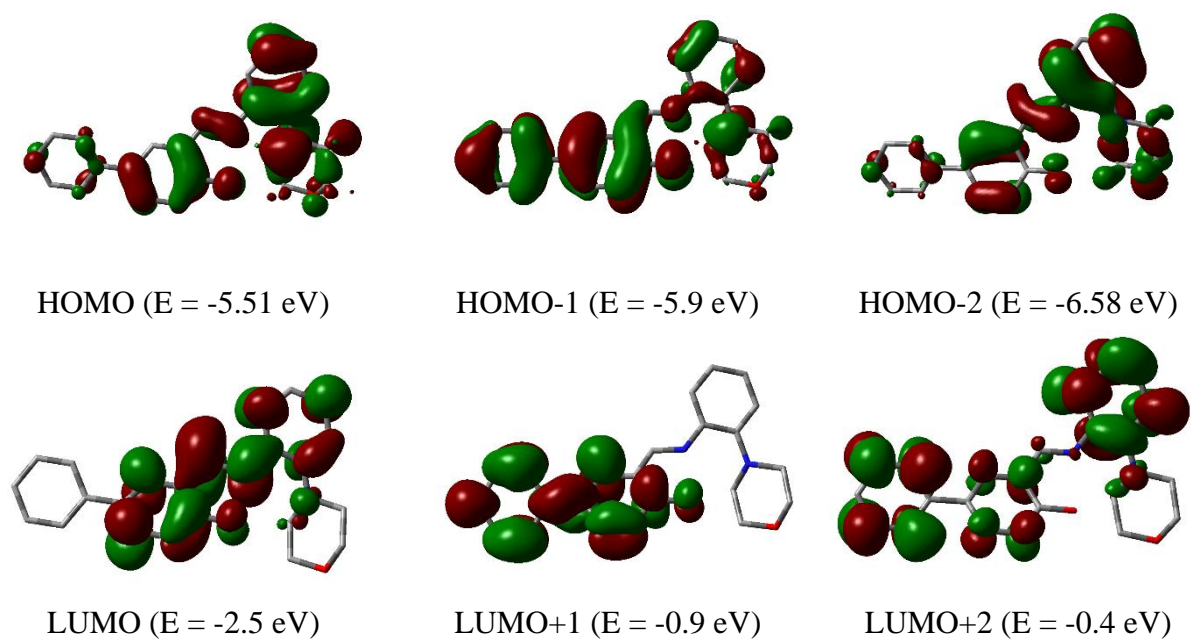


Fig.V.16. Contour plots of some selected molecular orbital of HL²

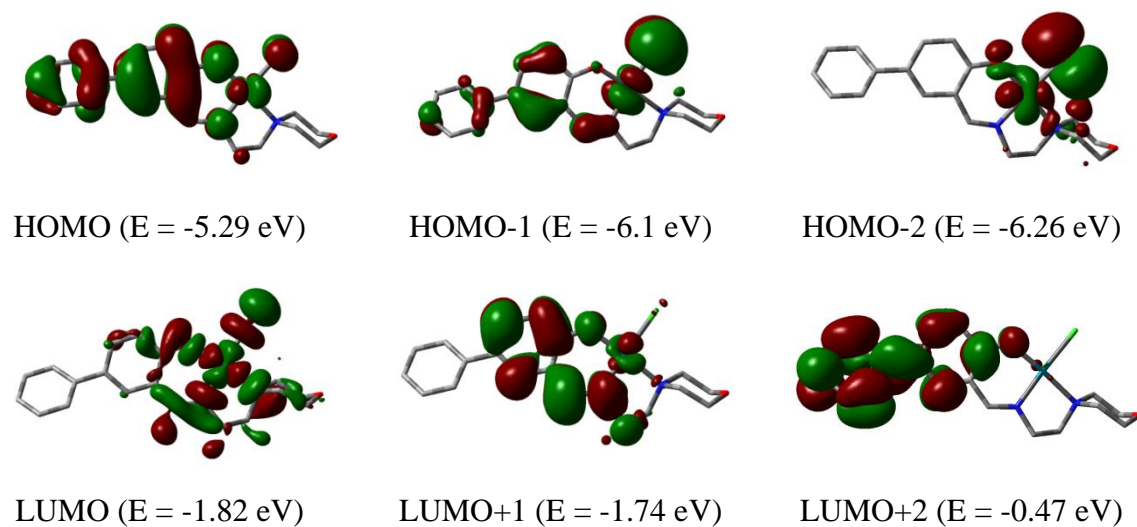


Fig.V.17. Contour plots of some selected molecular orbital of [Pd(L¹)Cl] (C1)

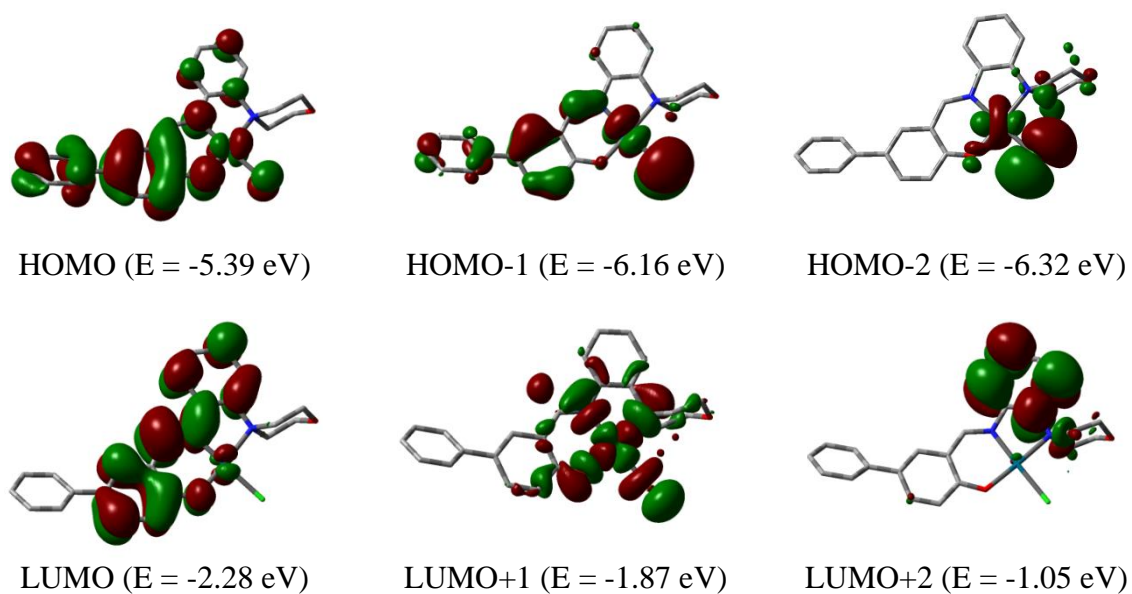


Fig.V.18. Contour plots of some selected molecular orbital of [Pd(L²)Cl] (C2)

V.3.4. DNA binding studies

For the creation of new anti-cancer medications, it is essential to comprehend the method of interactions with DNA. Spectroscopic approaches are currently employed extensively to analyse the manner of interactions. These studies demonstrate that medicines can interact with DNA covalently, non-covalently, groove-bound, or electrostatically [58-59]. It is common practise to analyse the manner of interactions between pharmacological molecules and DNA using absorption and emission spectroscopies [60].

V.3.4.1. UV-Vis method

A potent technique to evaluate how well palladium complexes interact with CT DNA is UV-Vis titration [61]. Complex C1 and C2 absorption spectra were recorded both with and without CT DNA. The complex C2 displays a sharp peak at 465 nm, while the complex C1 displays a wide peak with two absorption maxima at 406 nm and 355 nm. However, a hypochromic shift in the absorption spectra is seen with the addition of CT DNA. To comprehend the complexes' affinity for CT DNA, the intrinsic binding constant (K_b) was assessed. According to published literature [62,63], the K_b values for the C1 and C2 are $2.63 \times 10^5 \text{ M}^{-1}$ and $8.96 \times 10^4 \text{ M}^{-1}$, respectively.

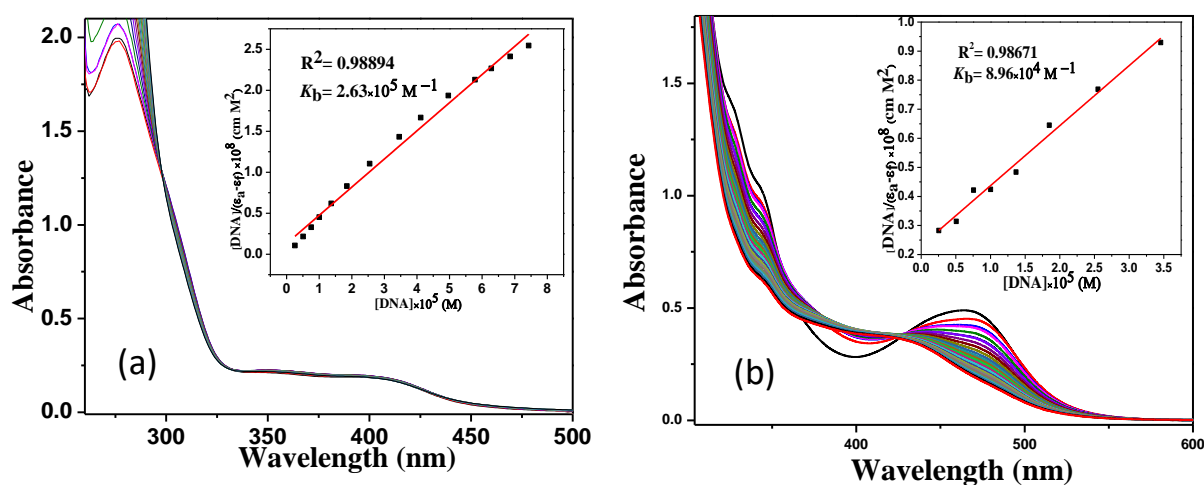


Fig. V.19. Change in absorption spectra of complex C1(a) and C2(b) in Tris-HCl/NaCl buffer with the gradual addition of CT DNA. Inset: Plot of $[DNA]/(\epsilon_a - \epsilon_f)$ vs. $[DNA]$.

V.3.4.2. Fluorescence method

Inherent fluorescence is not seen in CT DNA. Both with and without CT DNA, the palladium complexes are non-fluorescent in solution. However, the fluorescence intensity of ethidium bromide (EB), a common intercalator, is greatly increased upon excitation at 540 nm when it forms the EB-CT DNA intercalating complex [64]. The replacement of EB from its EB-CT DNA system causes the fluorescence intensities to gradually drop with steady addition of Pd(II) complexes C1 and C2 (Fig.V.20) [65]. The rivalry between the complexes and EB for DNA binding sites is readily seen in the titration curves. The fluorescence quenching curve of the EB-CT DNA system for the complex is well matched by a linear Stern-Volmer equation (Eq. (2)) [66].

$$I_0/I = 1 + K_{sv}[Q] \dots \dots \dots (2)$$

Where K_{sv} is the Stern-Volmer quenching constant, $[Q]$ is the molar concentration of the complex, and I and I_0 represent the fluorescence intensities of the EB-CT DNA system with and without the complex, respectively (quencher). The slopes of the plots were used to calculate the K_{sv} values, which were $1.51 \times 10^5 \text{ M}^{-1}$ for complex C1 and $4.31 \times 10^4 \text{ M}^{-1}$ for complex C2, respectively.

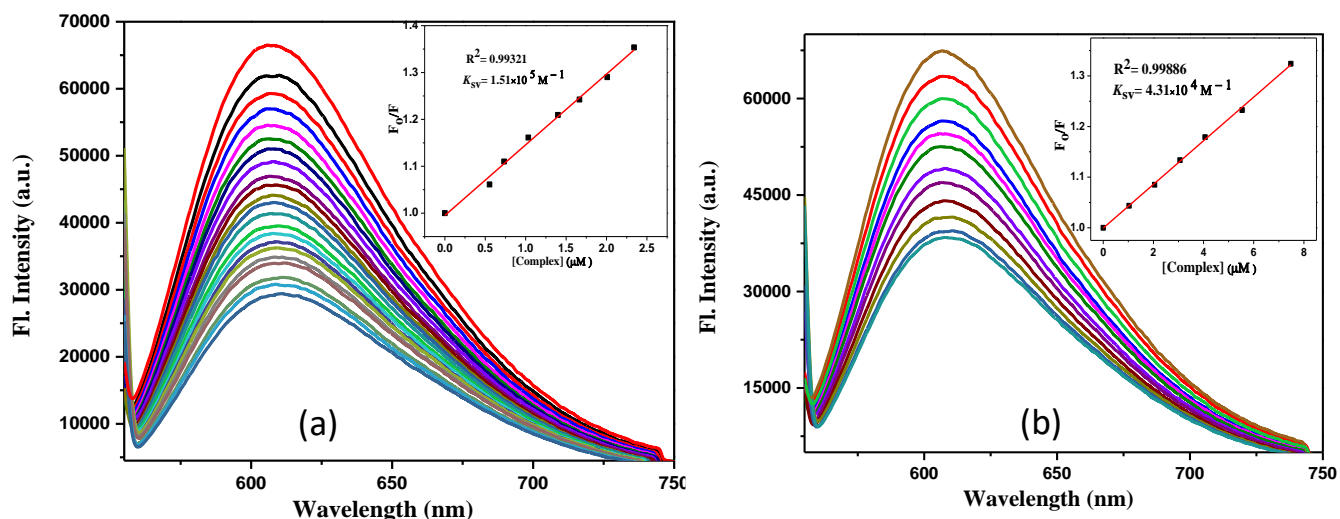


Fig.V.20. Emission spectra ($\lambda_{\text{ex}} = 540 \text{ nm}$) of EB-CT DNA in presence of increasing concentrations of C1 (a) and C2 (b) Inset: Plots of emission intensity F_0/F vs. [complex]

V.3.5. BSA binding studies

V.3.5.1. UV-Vis method

When varied concentrations of the complexes were present, the electronic absorption spectra of BSA (10 μM in PBS at pH 7.4) were recorded in the 200–500 nm region. At 280 nm, BSA has a distinctive absorption peak. The strength of the 280 nm absorption increases steadily when 100 μL of the complex is repeatedly added to the BSA solution, coupled with a small amount of blue shift. The protein and complex ground-state alliance is responsible for this hypsochromic change [67-68]. Using the following equation, the apparent association constant (K_a) was determined from the plot of $1/(A_{\text{obs}} - A_0)$ vs $1/[\text{complex}]$ (Fig.V.21) [69-70].

$$\frac{1}{A_{\text{obs}} - A_0} = \frac{1}{A_c - A_0} + \frac{1}{K_a(A_c - A_0)[\text{complex}]}$$

A_0 and A_c denote serum albumin alone and BSA absorbance, respectively, whereas A_{obs} is the observed absorbance (at 280 nm) of the solution bearing varying concentrations of the complex. According to calculations, the apparent association constants (K_a) for complexes

C1 and C2 are $1.76 \times 10^5 \text{ M}^{-1}$ and $6.58 \times 10^4 \text{ M}^{-1}$, respectively. These values are consistent with those in the literature for Pd-complexes [71-74].

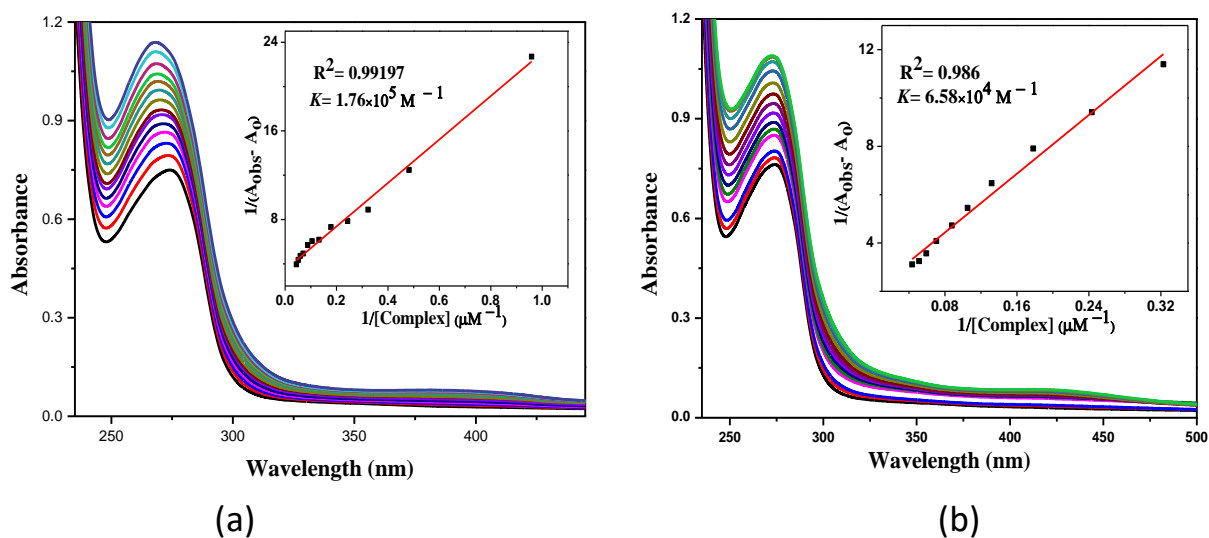


Fig.V.21. Change of absorption spectra of BSA ($10 \mu\text{M}$ aqueous solution) upon gradual addition of $100 \mu\text{L}$ complex [C1(a) and C2(b)] solution in DMSO at 300 K . Insets: $1/(A_{\text{obs}} - A_0)$ vs. $1/[\text{complex}]$ plots of BSA absorption titration.

V.3.5.2. Fluorescence method

Using the fluorescence spectral titration method, the interactions between the BSA-complex were investigated. When dissolved in DMSO, the complex is not luminous. However, a $10 \mu\text{M}$, pH 7.4 PBS buffer solution of BSA exhibits a potent 336 nm fluorescence upon 280 nm excitation. BSA's fluorescence intensity at 336 nm was now considerably reduced after the addition of $100 \mu\text{L}$ of the complex to the BSA solution (44.94% and 35.72% quenching). The interaction between complexes and proteins is largely responsible for the hypochromicity in the spectra [75]. Table V.5 shows the computed values of the complexes' Stern-Volmer quenching constants (K_{sv}). The complexes display strong fluorescence quenching capacity, as evidenced by the high K_{sv} value ($2.39 \times 10^5 \text{ M}^{-1}$ and 8.52×10^4). The following Scatchard equation was used to estimate the equilibrium binding constants (K_{b}) and number of binding

sites (n) available for the complexes from the graph of $\log [(F_0-F)/F]$ vs $\log [\text{complex}]$ (Fig. V.22) in order to learn more about the quenching effect [76, 77]:

$$\log \frac{(F_0 - F)}{F} = \log K_b + n \log [\text{complex}]$$

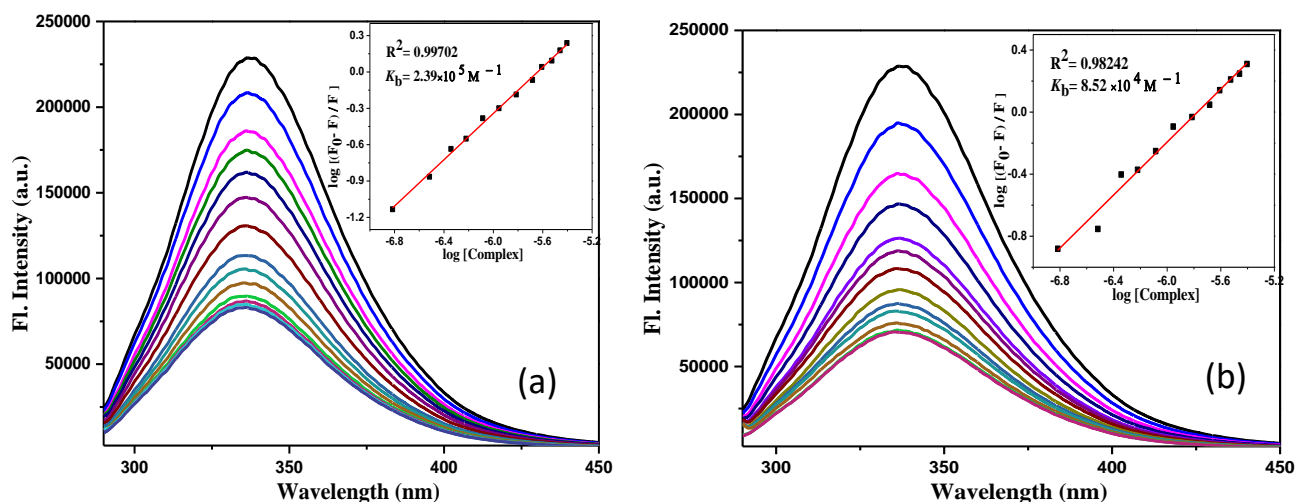


Fig.V.22. Change of fluorescence spectra of BSA (10 μM) upon gradual addition of 100 μL complex [C1(a) and C2(b)] solution in DMSO at 300 K ($\lambda_{\text{ex}}=280$ nm, $\lambda_{\text{em}}=336$ nm). Insets: Scatchard plots of the BSA fluorescence titration.

Based on the plot, for the complex C1 and C2 calculated values of n for are 0.954 and 0.854 respectively and calculated values of K_b are $2.39 \times 10^5 \text{ M}^{-1}$ and $8.52 \times 10^4 \text{ M}^{-1}$ respectively which reflects the strong affinity of the complexes with the serum albumins.

Table V.5. Stern-Volmer quenching constants (K_{sv}), apparent association constants (K_a), equilibrium binding constants (K_b), number of binding sites(n) in the interaction of C1 and C2 with BSA

System	UV method	Fluorescence method			
	K_a (M^{-1})	Hypo(%)	K_b (M^{-1})	K_{sv} (M^{-1})	n
C1	1.76×10^5	63.86	2.39×10^5	2.96×10^5	0.954
C2	6.58×10^4	67.11	8.52×10^4	7.34×10^4	0.854

V.3.6. Biological study

V.3.6.1. Cytotoxicity of $[Pd(L^1)Cl]$ and $[Pd(L^2)Cl]$ in different cancer cells

Results showed that AGS, A549, MCF7 and HepG2 cells were less likely to survive for 24 hours when exposed to both ligands, HL¹ and HL², as well as their complexes C1 and C2 (Table V.6). This effect was dosage dependent. However, compared to their respective ligand treatments and controls, the complexes were noticeably more effective at reducing the viability of all three cell lines at lower doses. Using the graph pad prism software's nonlinear regression (curve fit) curve and log (inhibition) vs. response equation, the IC₅₀ value was calculated.

Table V.6. IC₅₀ values of HL¹, HL² and their Pd(II) complexes **C1** and **C2** towards AGS, MDA-MB231 and HEPG2 cell lines

Compounds	MCF-7	A549	HepG2	AGS	WRL68
HL¹	>200	>200	>200	>200	>200
HL²	>200	>200	>200	>200	>200
C1	35.5±1.2	44.2±1.5	32.3±1.2	12.12±3.1	>200
C2	32.8±3.1	41.3±3.2	29.2±1.3	11.19±1.4	>200
Cisplatin	15.2±1.6	16.2±2.8	9.8±2.1	22.1±2.3	>200

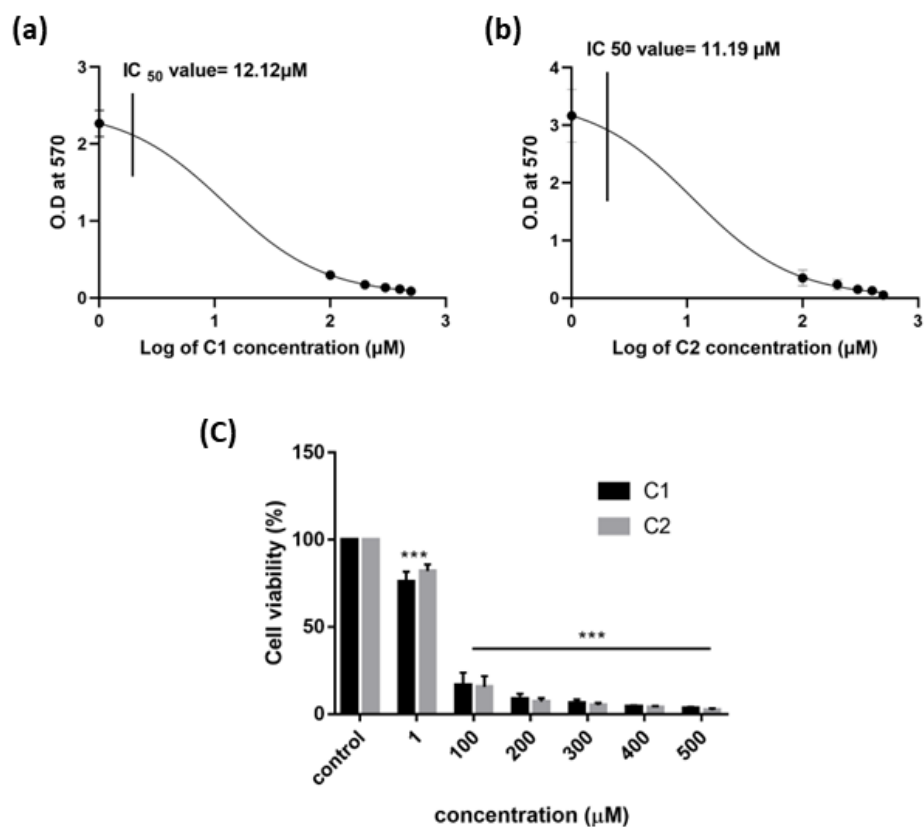


Fig.V.23. IC₅₀ values of AGS cell lines in presence of (a) C1 and (b) C2. (c) Viability of AGS cell lines upon increasing concentrations of C1 and C2

V.3.6.2. Colony Formation Assay

Colony formation assay was used to further validate the impact of complexes on gastric cancer AGS cell line [78]. For 24 hours, Cells received treatments with C1 (12 μM) and C2 (11 μM). Significantly fewer colonies were observed in C1 and C2 when compared to the control (Fig.V.24).

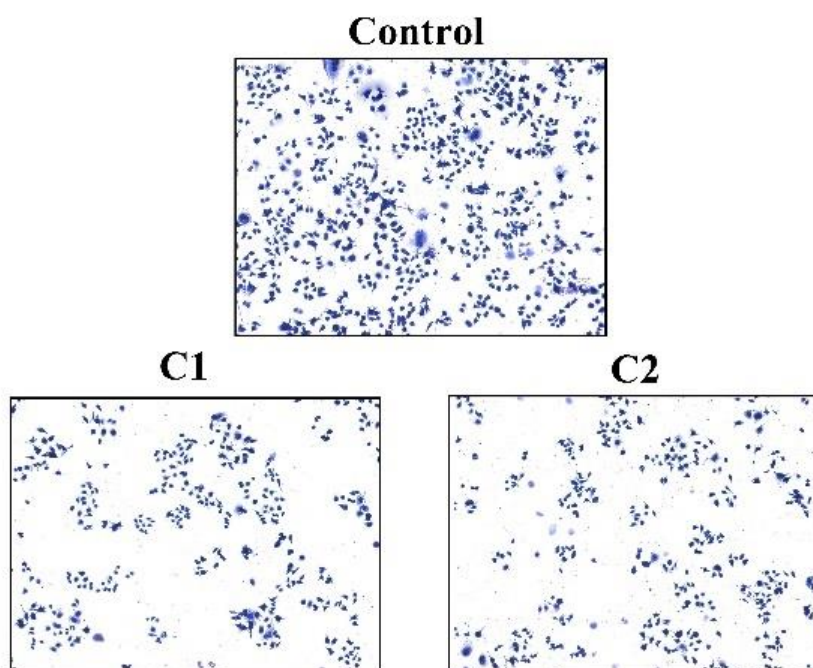


Fig.V.24. Colony formation of AGS cell lines upon treatment of C1 (12 μ M) and C1 (11 μ M) for 24 h.

V.3.6.3. In Vitro Cell Migration study

The characteristic of migration, which is responsible for immunological response, typical development, and disease processes, is present in all healthy living cells. Tumor cells, however, exhibit unchecked cell migration. AGS cells were used in a wound healing test to determine the inhibitory effects of both complexes [79, 81]. When AGS cells are exposed to the IC_{50} of C1 and C2 complexes, the area of the wound gradually decreases in a time-dependent manner (0, 24, and 48 h) [82]. The outcome also indicates that there are significantly less cells in the scratched area, indicating that both complexes C1 and C2 may lessen site-specific cell migration (Fig.V.25).

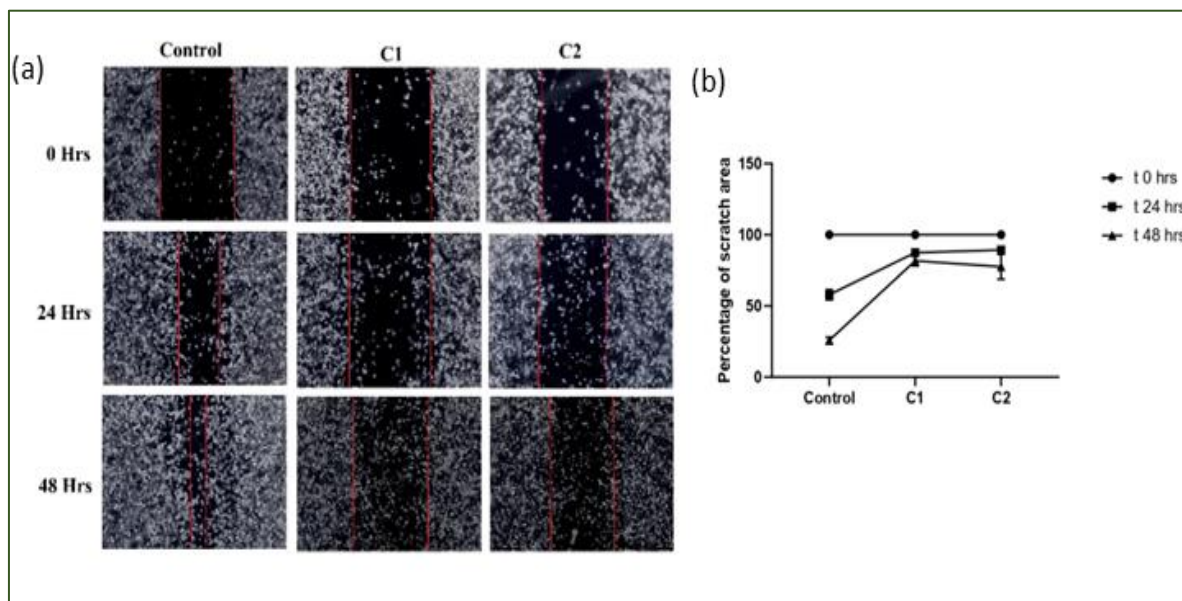


Fig.V.25. AGS cells (1×10^6 cells/mL) were treated with 12 μ M and 11 μ M (IC_{50}) of C1 and C2 complexes respectively for 0, 24 and 48 h. Scratch assay (migration inhibition study) were monitored under microscope.

V.3.6.4. C1 and C2 Induces Breast Cancer Cell Death by Apoptosis not Necrosis

To determine the percentage of apoptotic cells upon treatment with C1 and C2, we utilized double labelling technique using Annexin V-FITC and PI binding, exploiting flowcytometry [83-84]. Our data revealed that in comparison to control, treatment with C1 and C2 produced significant percentages of cells in early and late apoptosis. The total apoptotic rates in breast cancer cell including both early and late apoptosis was calculated as 24.55 % and 29.14% for C1 and C2 respectively (Fig.V.26).

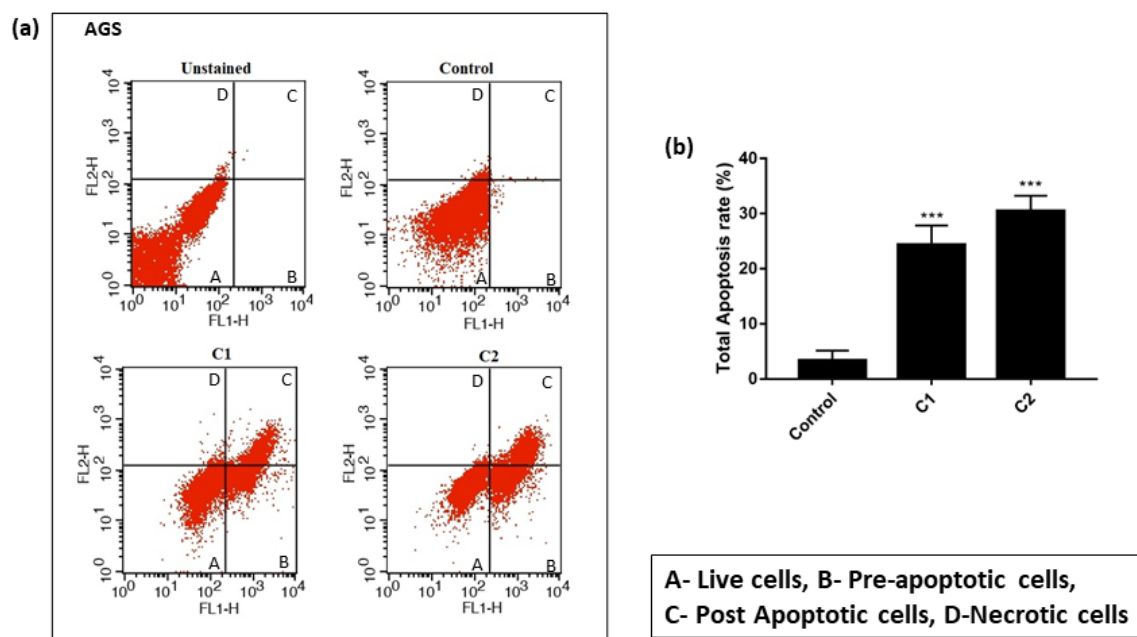


Fig.V.26. C1 and C2 induce apoptosis in AGS. Cells were treated with indicated concentration of C1 and C2 for 24 hours and analysed for apoptosis by flow cytometry (fig-a). Total apoptosis rate was calculated as the sum of early apoptosis and late apoptosis. There was an increase in apoptotic rate in both cell lines after C1 and C2 treatment (fig-b). Statistical significance of each group with untreated control is analysed by One Way ANOVA test ($P_{ANOVA} < 0.0001$). ANOVA test was followed by post hoc Tukey's test to analyse the significant difference between each group. Data is represented as mean \pm S.D of triplicates determinations from their independent experiments with *P value

V.4. Conclusions

A variety of spectroscopic methods are used to construct and systematically analyse new Pd(II) complexes with ONN donor ligands. The complexes' single crystal X-ray analysis revealed that HL¹ and HL² can function as tridentate O,N,N chelators in Pd(II) complexes. UV-Vis and fluorescence techniques are used to examine how C1 and C2 interact with CT-DNA and BSA protein. Ethidium bromide (EB) from EB-DNA complexes is successfully displaced by the complexes. In AGS, A549, MCF 7, HEPG2 and WRL68 cell lines, the antiproliferative activity of the complexes demonstrated that Pd-complexes exhibit greater

cytotoxicity than their respective ligands and cisplatin. Both Pd(II) complexes exhibit considerable cytotoxicity against the AGS (IC₅₀, 11.19-12.12μM) cell lines. To further understand, the nature of cell death in chosen gastric cancer cell line by treatment with C1 and C2, we performed apoptosis assay by flowcytometry. Apoptosis is a mode of programmed cell death that is coordinated and regulated by members of caspase family of cysteine proteases and defect in which is a major causative factor in the growth, development and progression of cancer. We found that treatment with C1 and C2 significantly increases the percentage of apoptotic cells.

V.5. References

1. B. S. Chhikara and K. Parang, *Chem. Biol.*, 2023, **10**, 451-451.
2. D. S. M. Chan, L. Abar, M. Cariolou, N. Nanu, D. C. Greenwood, E. V. Bandera, A. McTiernan and T. Norat, *Cancer Causes Control*, 2019, **30**, 1183-1200.
3. M. Jiang, J. Zhang, S. Xu, Y. Li, W. Li, H. Liang and F. Yang, *Dalton Trans.*, 2023, **52**, 269-280.
4. M. De Rycker, B. Baragaña, S. L. Duce and I. H. Gilbert, *Nature*, 2018, **559**, 498-506.
5. A. I. Matesanz, E. Jimenez-Faraco, M. C. Ruiz, L. M. Balsa, C. Navarro-Ranninger, I. E. León and A. G. Quiroga, *Inorg. Chem. Front.*, 2018, **5**, 73-83.
6. S. G. Churusova, D. V. Aleksanyan, E. Y. Rybalkina, O. Y. Susova, A. S. Peregudov, V. V. Brunova, E. I. Gutsul, Z. S. Klemenkova, Y. V. Nelyubina and V. N. Glushko, *Inorg. Chem.*, 2021, **60**, 9880-9898.
7. Z. D. Bugarčić, J. Bogojeski and R. van Eldik, *Coord. Chem. Rev.*, 2015, **292**, 91-106.
8. A. Kumar, A. Naaz, A. Prakasham, M. K. Gangwar, R. J. Butcher, D. Panda and P. Ghosh, *ACS omega*, 2017, **2**, 4632-4646.
9. D. Hernández-Romero, S. Rosete-Luna, A. López-Monteon, A. Chávez-Pinã, N. Pérez-Hernández, J. Marroquín-Flores, A. Cruz-Navarro, G. Pesado-Gómez, D. Morales-Morales and R. Colorado-Peralta, *Coord. Chem. Rev.*, 2021, **439**, 213930.
10. R. Kant and S. Maji, *Dalton Trans.*, 2021, **50**, 785-800.
11. H. H. Repich, V. V. Orysyk, L. G. Palchykovska, S. I. Orysyk, Y. L. Zborovskii, O. V. Vasylchenko, O. V. Storozhuk, A. A. Biluk, V. V. Nikulina, L. V. Garmanchuk, V. I. Pekhnyo and M. V. Vovk, *J. Inorg. Biochem.*, 2017, **168**, 98-106.
12. M. Fanelli, M. Formica, V. Fusi, L. Giorgi, M. Micheloni and P. Paoli, *Coord. Chem. Rev.*, 2016, **310**, 41-79.

13. S. Medici, M. Peana, V. M. Nurchi, J. I. Lachowicz, G. Crisponi and M. A. Zoroddu, *Coord. Chem. Rev.*, 2015, **284**, 329-350.
14. J. Pranczk, D. Jacewicz, D. Wyrzykowski and L. Chmurzynski, *Curr. Pharmaceut. Anal.*, 2014, **10**, 2-9.
15. Z. Breijyeh , B. Jubeh and R. Karaman, *Molecules*, 2020, **25**, 1340.
16. M. N. Alam and F. Huq, *Coord. Chem. Rev.*, 2016, **316**, 36-67.
17. N. J. Wheate, S. Walker, G. E. Craig and R. Oun, *Dalt. Trans.*, 2010, **39**, 8113-8127.
18. S. N. Mbugua, N. R. S. Sibuyi, L. W. Njenga, R. A. Odhiambo, S. O. Wandiga , M. Meyer , R. A. Lalancette and M. O. Onani, *ACS Omega*, 2020, **25**, 14942–14954.
19. C. Orvig and M. J. Abrams, *Chem. Rev.*, 1999, **99**, 2201-2204.
20. C. S. Allardyce, A. Dorcier, C. Scolaro and P. J. Dyson, *App. Organomet. Chem.*, 2005, **19**, 1-10.
21. K. B. Garbutcheon-Singh, M. P. Grant, B. W. Harper, A. M. Krause-Heuer, M. Manohar, N. Orkey and J. R. Aldrich Wright, *Current Topics in Med. Chem.*, 2011, **11**, 521-542.
22. P. J. Dyson and G. Sava, *Dalton Trans.*, 2006, **16**, 1929-1933.
23. M. J. Hannon, *Pure Appl. Chem.*, 2007, **79**, 2243-2261.
24. M. Aminzadeh, H. Mansouri-Torshizi, R. Aleeshah, K. Abdi and M. Saeidifar, *Biometals*, 2021, **34**, 1173-1179.
25. M. Feizi-Dehnayebi , E. Dehghanian and H. Mansouri-Torshizi, *Spectrochim. Acta Part A*, 2021, **249**, 119215.
26. A. Shanmugapriya, G. Kalaiarasi, M. Ravi, H. A. Sparkes, P. Kalaivanid and R. Prabhakaran, *New J. Chem.*, 2021, **45**, 20227-20240.
27. R. Oun, Y. E. Moussa and N. J. Wheate, *Dalton Trans.*, 2018, **47**, 6645–6653.

28. Y. OuYang, J. Gao, L. Zhao, J. Lu, H. Zhong, H. Tang, S. Jin, L. Yue, Y. Li, W. Guo, Q. Xu and Y. Lai, *J. Med. Chem.*, 2021, **64**, 7646–7666.
29. J. Li, C. Zheng, M. Wang, A. D. Umamo, Q. Dai, C. Zhang, H. Huang, Q. Yang, X. Yang, J. Lu and W. Pan, *Oncogene*, 2022, **41**, 1114-1128.
30. R. G. Kenny, S. W. Chuah, A. Crawford and C. J. Marmion, *Eur. J. Inorg. Chem.*, 2017, **12**, 1596-1612.
31. N. Shahabadil, L. Ghaffari, Z. Mardani and F. Shiri, *Biological Trace Element Research*, 2022, **200**, 1988–2000.
32. N. F. Romashev, P. A. Abramov, I. V. Bakaev, I. S. Fomenko, D. G. Samsonenko, A. S. Novikov, K. K. Tong, D. Ahn, P. V. Dorovatovskii, Y. V. Zubavichus, A. A. Ryadun, O. A. Patutina, M. N. Sokolov, M. V. Babak and A. L. Gushchin, *Inorg. Chem.*, 2022, **61**, 2105–2118.
33. L. Bai, C. Gao, Q. Liu, C. Yu, Z. Zhang, L. Cai, B. Yang, Y. Qian, J. Yang and X. Liao, *Eur. J. Med. Chem.*, 2017, **140**, 349-382.
34. C. S. Allardyce and P. J. Dyson, *Dalton. Trans.*, 2016, **45**, 3201-3209.
35. K. Laws and K. Suntharalingam, *ChemBioChem*, 2018, **19**, 2246-2253.
36. B. S. Murray, M. V Babak, C. G. Hartinger and P. J. Dyson, *Coord. Chem. Rev.*, 2016, **306**, 86-114.
37. E. Alessio, *Eur. J. Inorg. Chem.*, 2017, **12**, 1549-1560.
38. S. K. Tarai, S. Mandal, R. Bhaduri, A. Pan, P. Biswas, A. Bhattacharjee and S. C. Moi, *Spectrochim. Acta A Mol. Biomol.*, 2023, **287**, 122059.
39. D. Wang and S. J. Lippard, *Nat. Rev. Drug Discov.*, 2005, **4**, 307-320.
40. V. Brabec, O. Hrabina and J. Kasparkova, *Coord. Chem. Rev.*, 2017, **351**, 2-31.
41. S. Komeda, *Metallomics*, 2011, **3**, 650-655.

42. T. C. Johnstone, K. Suntharalingam and S. J. Lippard, *Chem. Rev.*, 2016, **116**, 3436-3486.
43. K. Skonieczny, G. Charalambidis, M. Tasior, M. Krzeszewski, A. Kalkan-Burat, A. G. Coutsolelos and D. T. Gryko, *Org. Synth.*, 2012, **89**, 220-229.
44. M. Anjomshoa, H. Hadadzadeh, M. Torkzadeh-Mahani, S. J. Fatemi, M. AdeliSardou, H. A. Rudbari and V. M. Nardo, *Eur. J. Med. Chem.*, 2015, **96**, 66-82.
45. N. S. Quiming, R. B. Vergel, M. G. Nicolas and J. A. Villanueva, *J. Health Sci.*, 2005, **51**, 8-15.
46. T. L. Riss, R. A. Moravec, A. L. Niles, S. Duellman, H. A. Benink, T. J. Worzella and L. Minor, *Assay Guidelines manuals*, 2013.
47. (a) C. Lee, W. Yang and R. G. Parr, *Phys. Rev. B: Condens. Matter Mater. Phys.*, 1988, **37**, 785-789; (b) A. D. Becke, *J. Chem. Phys.*, 1993, **98**, 5648-5652.
48. (a) P. J. Hay and W. R. Wadt, *J. Chem. Phys.*, 1985, **82**, 270-283; (b) W. R. Wadt and P. J. Hay, *J. Chem. Phys.*, 1985, **82**, 284-298; (c) P. J. Hay and W. R. Wadt, *J. Chem. Phys.*, 1985, **82**, 299-310.
49. M. J. Frisch, G. W. Trucks, H. B. Schlegel, G. E. Scuseria, M. A. Robb, J. R. Cheeseman, G. Scalmani, V. Barone, B. Mennucci, G. A. Petersson, H. Nakatsuji, M. Caricato, X. Li, H. P. Hratchian, A. F. Izmaylov, J. Bloino, G. Zheng, J. L. Sonnenberg, M. Hada, M. Ehara, K. Toyota, R. Fukuda, J. Hasegawa, M. Ishida, T. Nakajima, Y. Honda, O. Kitao, H. Nakai, T. Vreven, J. A. Montgomery, Jr., J. E. Peralta, F. Ogliaro, M. Bearpark, J. J. Heyd, E. Brothers, K. N. Kudin, V. N. Staroverov, R. Kobayashi, J. Normand, K. Raghavachari, A. Rendell, J. C. Burant, S. S. Iyengar, J. Tomasi, M. Cossi, N. Rega, J. M. Millam, M. Klene, J. E. Knox, J. B. Cross, V. Bakken, C. Adamo, J. Jaramillo, R. Gomperts, R. E. Stratmann, O. Yazyev, A. J. Austin, R. Cammi, C. Pomelli, J. W. Ochterski, R. L. Martin, K. Morokuma, V. G. Zakrzewski, G. A. Voth, P. Salvador,

- J. J. Dannenberg, S. Dapprich, A. D. Daniels, O. Farkas, J. B. Foresman, J. V. Ortiz, J. Cioslowski and D. J. Fox, Gaussian 09, Revision D.01, Gaussian, Inc., Wallingford CT, 2009.
50. (a) R. E. Stratmann, G. E. Scuseria and M. J. Frisch, *J. Chem. Phys.*, 1998, **109**, 8218; (b) R. Bauernschmitt and R. Ahlrichs, *Chem. Phys. Lett.*, 1996, **256**, 454-464; (c) M. E. Casida, C. Jamorski, K. C. Casida and D. R. Salahub, *J. Chem. Phys.*, 1998, **108**, 4439-4449.
51. (a) V. Barone and M. Cossi, *J. Phys. Chem. A*, 1998, **102**, 1995-2001; (b) M. Cossi and V. Barone, *J. Chem. Phys.*, 2001, **115**, 4708-4717; (c) M. Cossi, N. Rega, G. Scalmani and V. Barone, *J. Comput. Chem.*, 2003, **24**, 669-681.
52. N. M. O'Boyle, A. L. Tenderholt and K. M. Langner, *J. Comput. Chem.*, 2008, **29**, 839-845.
53. Bruker. SAINT v8.38A. Bruker AXS Inc., Madison, Wisconsin, USA.
54. L. Krause, R. Herbst-Irmer, G.M. Sheldrick and D. Stalke, *J. Appl. Cryst.*, 2015, **48**, 3-10.
55. (a) G. M. Sheldrick, *Acta Cryst.*, 2008, **A64**, 112-122; (b) G. M. Sheldrick, *Acta Cryst.*, 2015, **C71**, 3-8.
56. S. Biswas, P. Roy and T. K. Mondal, *J. Mol. Struct.*, 2017, **1142**, 110-115
57. (a) J. -A. Alvarez-Hernández, N. Andrade-López, J. G. Alvarado-Rodríguez, S. González-Montiel, L. Á. Zárate-Hernández and J. Cruz-Borbolla, *Polyhedron*, 2022, **214**, 115635; (b) D. Qiu, Y. Guo, H. Wang, X. Bao, Y. Feng, Q. Huang, J. Zeng and G. Qiu, *Inorg. Chem. Commun.*, 2011, **14**, 1520-1524.
58. C. V. Barra, F. V. Rocha, L. Morel, A. Gautier, S. S. Garrido, A. E. Mauro, R. C. G. Frem and A. V. G. Netto, *Inorg. Chim. Acta*, 2017, **446**, 54-60.

59. K. Akdi, R. A. Vilaplana, S. Kamah and F. Gonzalez-Vilchez, *J. Inorg. Biochem.*, 2005, **99**, 1360–1368.
60. N. Bandyopadhyay, P. Basu, G. S. Kumar, B. Guhathakurta, P. Singh and J. P. Naskar, *J. Photochem. Photobiol. B*, 2017, **173**, 560–570.
61. P. Krishnamoorthy, P. Sathyadevi, A. H. Cowley, R. R. Butorac, and N. Dharmaraj, *Eur. J. Med. Chem.*, 2011, **46**, 3376-3387.
62. J. Albert, B. Al Janabi, J. Granell, M. S. Hashemi, D. Sainz, M. K. Khosa, C. Calvis, R. Messeguer, L. Baldomà, J. Badia, and M. Font-Bardia, *J. Organomet. Chem.*, 2023, **983**, 122555.
63. Y. Zhao, J. Zhu, W. He, Z. Yang, Y. Zhu, Y. Li, J. Zhang and Z. Guo, *Chem. Eur. J.*, 2006, **12**, 6621–6629.
64. E. Ramachandran, D. S. Raja, N. P. Rath and K. Natarajan, *Inorg. Chem.*, 2013, **52**, 1504-1514.
65. D. Senthil Raja, N. S. P. Bhuvanesh and K. Natarajan, *Inorg. Chem.*, 2011, **50**, 12852-12866.
66. S. U. Parsekar, K. Paliwal, P. Haldar, P. K. S. Antharjanam and M. Kumar, *ACS Omega*, 2022, **7**, 2881-2896.
67. Y. J. Hu, Y. Liu, J. B. Wang, X. H. Xiao and S. S. Qu, *J. Pharm. Biomed. Anal.*, 2004, **36**, 915.
68. J. Lu, Q. Sun, J. L. Li, L. Jiang, W. Gu, X. Liu, J. L. Tian and S. P. Yan, *J. Inorg. Biochem.*, 2014, **137**, 46.
69. A. Wolfe, G. H. Shimer and T. Mechan, *Biochemistry*, 1987, **26**, 6392-6396.
70. A. Paul, S. Mistri, A. Bhunia, S. Manna, H. Puschmann, S. C. Manna, *RSC Adv.*, 2016, **6**, 60487.

71. S. Abedanzadeh, K. Karami, M. Rahimi, M. Edalati, M. Abedanzadeh, A. Mohammad Tamaddon, M. Dehdashti Jahromi, Z. Amirghofran, J. Lipkowskif and K. Lyczko, *Dalton Trans.*, 2020, **49**, 14891-14907.
72. A. S. D. Tabatabai, E. Dehghanian and H. Mansouri-Torshizi, *Biometals*, 2022, **35**, 245-266.
73. X. Wei, Y. Yang, J. Ge, X. Lin, D. Liu, S. Wang, J. Zhang, G. Zhou and S. Li, *Journal of Inorganic Biochemistry*, 2020, **202**, 110857.
74. R. O. Omondi, N. R. Sibuyi, A. O. Fadaka, M. Meyer, D. Jaganyi and S. O. Ojwach, *Dalton Trans.*, 2021, **50**, 8127-8143.
75. J. R. Lakowicz, *Principles of Fluorescence Spectroscopy*, Third Edition., Springer, New York, USA, 2006.
76. X. Z. Feng, Z. Lin, L. J. Yang, C. Wang and C. L. Bai, *Talanta*, 1998, **47**, 1223-1229.
77. J. R. Lakowicz, *Fluorescence Quenching: Theory and applications*, Principles of Fluorescence Spectroscopy, Kluwer Academic/Plenum Publishers, New York, 1999, p. 53.
78. H. Li, X. Li, S. Liu, L. Guo, B. Zhang, J. Zhang and Q. Ye, *Hepatology*, 2017, **66**, 1920-1933.
79. Y. Chang, Y. Yuan, Q. Zhang, Y. Rong, Y. Yang, M. Chi, Z. Liu, Y. Zhang, P. Yu and Y. Teng, *RSC Adv.*, 2020, **10**, 1191-1197.
80. W. Dai, F. Wang, L. He, C. Lin, S. Wu, P. Chen, Y. Zhang, M. Shen, D. Wu, C. Wang, J. Lu, Y. Zhou, X. Xu, L. Xu and C. Guo, *Mol. Carcinogenesis*, 2013, **54**, 301-311.
81. I. K. Sani, S. H. Marashi and F. Kalalinia, *Toxicology in Vitro*, 2015, **29**, 893-900.
82. F. U Rahman, M. Z. Bhatti, A. Ali, H. Q. Duong, Y. Zhang, B. Yang, S. Koppireddi, Y. Lin, H. Wang, Z. T. Li and D. W. Zhang, *Euro. J. Med. Chem.*, 2018, **143**, 1039-1052.
83. Y. Pang, G. Qin, L. Wu, X. Wang and T. Chen, *Exp. Cell Res.*, 2016, **347**, 251-260.

84. Y. Jiang, X. Zhou, X. Chen, G. Yang, Q. Wang, K. Rao, W. Xiong and J. Yuan, *Mutat. Res.*, 2011, **726**, 75-83.

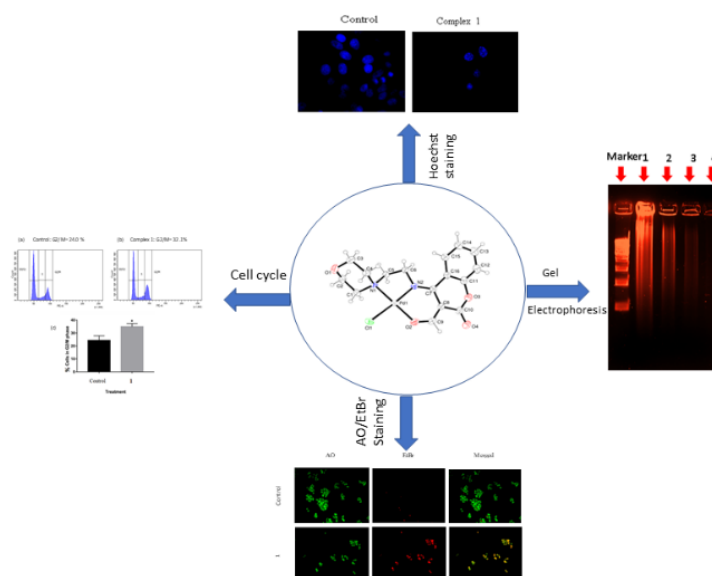
CHAPTER-VI

**New coumarin-morpholine O,N,N
donor pincer ligand appended
Palladium(II) complex : in-situ
Synthesis, spectral characterization,
in-vitro anti-cancer activity and
interaction with protein**

New coumarin-morpholine O,N,N donor pincer ligand appended Palladium(II) complex : in-situ Synthesis, spectral characterization, in-vitro anti-cancer activity and interaction with protein

Abstract

A new coumarin-morpholine O,N,N donor pincer ligand appended palladium(II) complex, [Pd(HMC)Cl] (**1**) was synthesized (where HMC=(3E,4E)-3-(hydroxymethylene)-4-((2-morpholinoethyl)imino)chroman-2-one). Interaction of complex **1** with CT DNA was investigated and its binding constant was found to be $1.43 \times 10^5 \text{ M}^{-1}$. The proficiency of displacement of ethidium bromide (EB) from its EB-CTDNA complex by **1** was performed by fluorescence quenching method and Stern-Volmer quenching constant (K_{sv}) was found to be $1.43 \times 10^5 \text{ M}^{-1}$. Similarly, the interaction of **1** with BSA protein was investigated by UV-Vis and fluorescence methods. The apparent association constant (K_a) and K_{sv} were determined ($K_a = 4.39 \times 10^4 \text{ M}^{-1}$ and $K_{sv} = 1.16 \times 10^5 \text{ M}^{-1}$). In vitro cytotoxicity of complex **1** towards gastric cancer cell lines (AGS) and breast cancer cell lines (MDA MB 231 and MCF-7) were performed by MTT assay, colony formation assay, cell cycle analysis and Hoechst and AO/EtBr staining. Intercalation of the complex with DNA was evaluated by performing agarose gel electrophoresis of various concentrations of the complex.



VI.1. Introduction

One of the chronic diseases that has led to higher mortality rates worldwide and shorter life expectancies in every other nation is cancer. Lung and colorectal cancer are the next most often diagnosed and fatal cancers in females, respectively [1]. Breast cancer alone is responsible for 30% of all new instances of female cancer in 2018, according to statistics on cancer worldwide. According to statistical projections, the US could see 62,930 new instances of breast cancer in 2018. Additionally, it has been noted that death rates in developing nations were greater than in the richest nations [2]. According to data from the Indian Council of Medical Research (ICMR), the number of cancer cases has nearly doubled over the past several years. Breast, Lung, cervical, and oral cancer are considered to be India's top priority cancers [3]. Covalent and non-covalent interactions between metal complexes and DNA are possible. Both intercalation and major/minor groove binding are examples of non-covalent interactions. In DNA, the guanine N7 position [4] is known to be the most electron-rich and oxidizable location, making it a good candidate for covalent coordination to a metal centre. Improving the design of metallodrugs requires a deeper understanding of the coordination behaviour of a metal ion under biologically relevant conditions, as well as their kinetic and thermodynamic stabilities and redox behaviour [5,6]. However, one should keep in mind that in the biological systems they often operate far from thermodynamic equilibrium. For this reason, it is of the utmost importance to have an understanding of the nature of the interactions that metallodrugs have with cell membranes, proteins, enzymes, and DNA in order to create effective drugs for the treatment of diseases [7,8].

Though *cis*-platin and related platinum complexes are successful anticancer drugs, platinum being a heavy metal their use is limited by their severe dose-limiting side effects like nephrotoxicity, myelosuppression, and neurotoxicity. Other common side effects include

anaphylaxis, cytopenia's etc. So, developing other transition metal complexes as active anticancer agents with better efficiency and new mechanisms of action has become a central research theme in bioinorganic chemistry [9-13].

One of the most extensively utilized heterocyclic secondary amines, morpholine, contains nitrogen and oxygen and is employed as a building block of physiologically active chemicals [14]. Morpholine's presence in organic molecules has frequently resulted in major changes in their chemical, physical, and biological properties over the previous several decades. Morpholine is an important pharmacophoric unit, and its derivatives have attracted significant attention, with anti-oxidant [15], anti-tumor [16], antimalarial [17], anti-bacterial [18], anti-fungal [19] and other properties documented. Most morpholine-containing substances are well-known agrochemicals and pharmaceuticals, such as levofloxacin, linezolid, sulphonamides, BM212, and others. They are also effective anti-bacterial agents. Sulphonamides and BM212 are pharmacophoric units found in over 200 medications on the market. These compounds have promising applications in current drug discovery and medical chemistry.

In this context, the synthesis, characterization, and structural elucidation of Coumarin-morpholine appended Palladium **Complex 1** has been performed by single crystal X-ray crystallography. The ability of the Pd(II) complex to bind with CT DNA is investigated by UV-Vis method and the binding constant is found to be $1.43 \times 10^5 \text{ M}^{-1}$. Competitive binding study with ethidium bromide (EB) by fluorescence method suggests that the Pd(II) complex efficiently displace EB from EB-DNA complex. The Calculated Stern-Volmer dynamic quenching constant, K_{sv} is found to be $1.16 \times 10^5 \text{ M}^{-1}$. Moreover, the interactions of Pd(II) complex (**1**) with bovine serum albumin (BSA) are also studied. The antiproliferative activity of the complexes are investigated with gastric adenocarcinoma cell line (AGS), breast cancer cell line (MDA-MB 231 and MCF-7). The Pd(II) complex exhibit substantial cytotoxicity

towards MDA MB 231 ($IC_{50} = 23.01 \mu M$), AGS ($IC_{50} = 35.48 \mu M$) and ($IC_{50} = 51.01 \mu M$) cell lines.

VI.2. Experimental section

VI.2.1. Materials and reagents

The analytical grade starting materials such as 4-Chloro-3-formylcoumarin, 4-(2-Aminoethyl)morpholine and Na_2PdCl_4 (Merck, India) were used for the preparation of **Complex 1**. All other chemicals were of reagent grade, obtained from Merck (India) and used without further purification. Calf thymus DNA (CT-DNA) and bovine serum albumin (BSA) (stored at $4 \text{ }^\circ C$) were procured from Sigma Aldrich, USA. DNA solutions were prepared afresh in Tris-HCL buffer at pH 6.8 for every set of experiments. Millipore water was used throughout the investigation. *Bis*(benzimidazole) (Hoechst 33258, $\geq 98\%$ purity) was procured from Sigma-Aldrich, whereas, ethidium bromide was procured from Avra synthesis Pvt. Ltd, India. MeOH, DMSO (Cell culture Grade) and agarose were purchased from Sigma. 3-(4, 5-dimethylthiazol-2-yl)-2, 5-diphenyl- tetrazolium bromide (MTT) and Crystal violet solution (Gram's crystal violet) were purchased from Merck. Dulbecco's modified Eagle's medium (DMEM), Roswell Park Memorial Institute Medium (RPMI) and FBS were obtained from Gibco. 1% penicillin/streptomycin and Trypsin-EDTA were purchased from Invitrogen. All compounds were used subsequently without further purification. Cisplatin was obtained from calbiochem (sigma Aldrich, 232120-50MG) and dissolved in sodium chloride solution in water (154 mM NaCl) for culture treatment.

VI.2.2. Preparation of Palladium complex 1

Coumarin-morpholine-based Palladium Complex 1 was prepared by the following procedure (Scheme VI.1). The mixture of 4-chloro-2-oxo-2H-chromene-3-carbaldehyde (0.058 g, 1 mmol) and 2-morpholinoethanamine (0.036 g, 1 mmol) in dry methanol (40 mL) was refluxed at $80 \text{ }^\circ C$ for 3 h to form the ligand, and then, directly Na_2PdCl_4 (0.081 g, 1 mmol)

was added to the clear yellowish solution and refluxed for 6 h at 80 °C. The solution turned a reddish-brown colour during this time. The resultant solution was filtered and kept undisturbed, permitting slow evaporation for a few days. The block-shaped, brownish single crystals were collected by filtration within 1 week, with a Yield of ~65–70%.

Anal. Calc. for $C_{16}H_{17}ClN_2O_4Pd$ (1): C, 43.36; H, 3.87; N, 6.32. Found: C, 43.31; H, 3.85; N, 6.29. IR (KBr, cm^{-1}): 2864 $\nu(C-H)$, 1707 $\nu(C=N)$. 1H NMR (300 MHz, DMSO- d_6): δ , 10.54(1H, s), 8.41 (1H, s), 7.29-8.03 (4H, ArH, m), 4.28 (2H, t, $J=5.07$), 3.86-4.01(4H,m), 3.16 (2H, t, $J=5.8$). λ_{max} , (nm) in acetonitrile (ϵ , $M^{-1}cm^{-1}$): 245 (32740); 288 (11457); 307 (9646); 322 (9465); 340 (6515). HRMS (ESI, positive): calcd. for $C_{16}H_{17}N_2O_4Pd [M]^+$ (m/z): 407.0223; found: 407.0221.

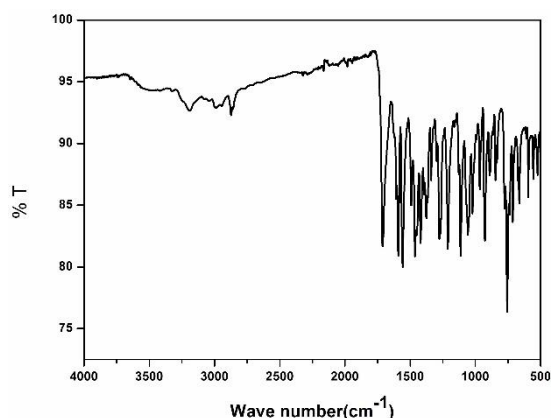


Fig. VI.1. IR spectrum of 1 (KBr disk)

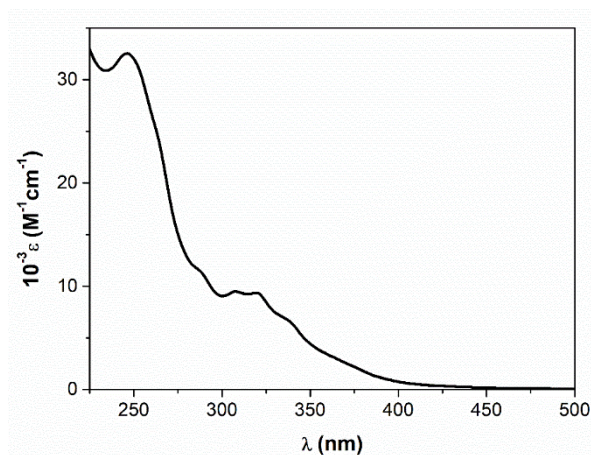


Fig. VI.2. UV-Vis spectrum of 1 in acetonitrile

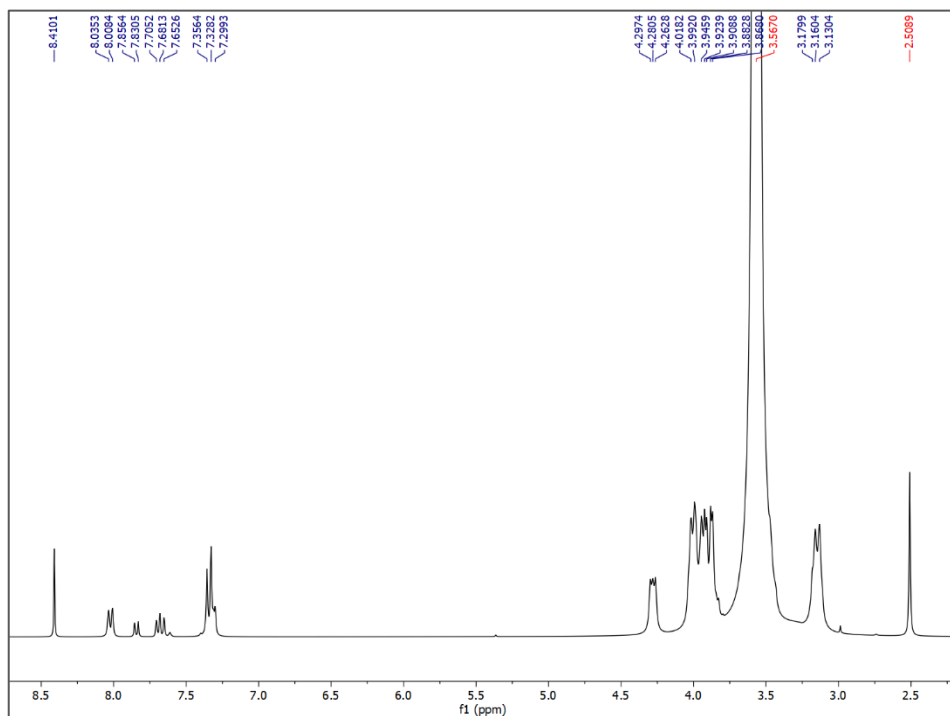


Fig. VI.3. ^1H NMR spectrum of **1** in DMSO-d_6

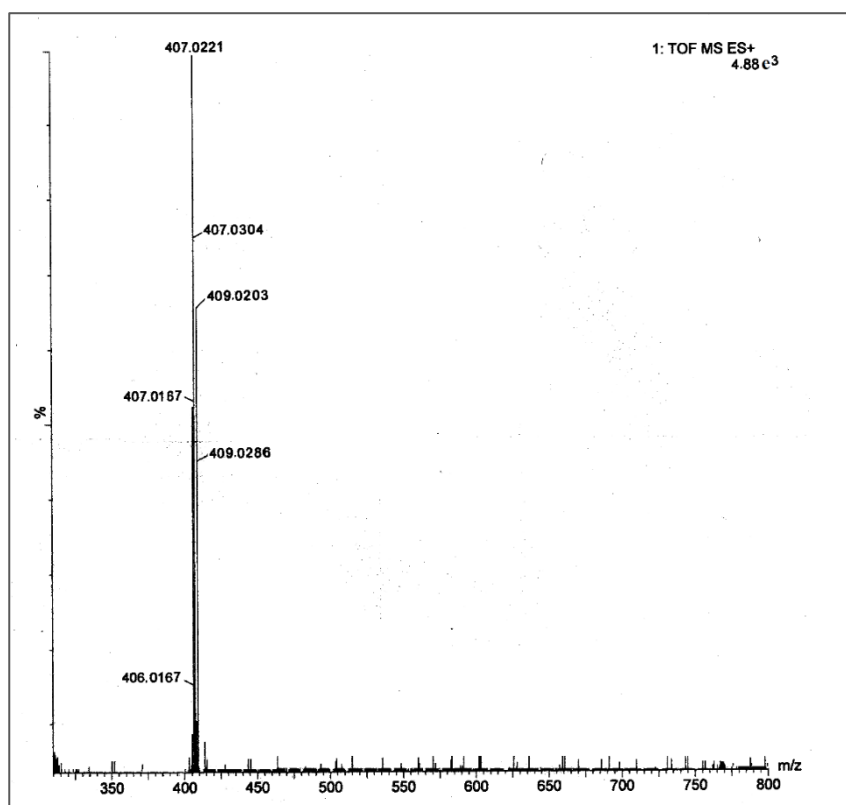


Fig. VI.4. HRMS spectrum of **1** in acetonitrile

VI.2.3. Physical measurements

Infrared spectra in the range 500–4000 cm^{-1} (Fig.VI.1) were traced from KBr pellets on Nicolet Magna IR 750 series-II FTIR spectrophotometer. Elemental analyses (C, H and N) were performed using a PerkinElmer Series-II CHN-2400 CHNS/O elemental analyzer. UV-Vis spectra were taken on Shimadzu UV-1900i spectrophotometer. Emission spectra were taken on a Shimadzu spectrofluorometer (Model: RF 6000). NMR spectra were recorded on a Bruker (300 MHz) NMR spectrometer. A Single crystal X-ray diffraction data were collected using a Bruker AXS D8 Quest CMOS diffractometer using graphite monochromated Mo $K\alpha$ radiation ($\lambda = 0.71073 \text{ \AA}$) at 293 K. The mass spectral analyses were performed in a Waters Mass Spectrometer (model: XEVOG2QTOF# YCA351)

VI.2.4. Crystallography

Good quality single crystals of palladium complex (**1**) suitable for X-ray diffraction were grown by slow evaporation of methanol solution. X-ray data were collected on Bruker AXS D8 Quest CMOS diffractometer using graphite monochromated Mo $K\alpha$ radiation ($\lambda = 0.71073 \text{ \AA}$) at 293 K. Reflection data were collected applying the ω scan technique. The collected frames were reduced using SAINT program. Absorption correction was done by multi-scan method using the SADABS absorption correction program. The structures were solved by direct method and refined using the SHELXTL program [20,21] by full-matrix least-squares based on F^2 . All the hydrogen atoms belonging to carbon atoms were fixed in their geometrically idealized positions.

Table VI.1: Crystal data and details of the structure determination of **1**

	[Pd(L)Cl] (1)
Formula	C ₁₆ H ₁₇ ClN ₂ O ₄ Pd
Formula Weight	443.16
Crystal System	<i>Triclinic</i>
Space group	<i>P-1</i>
<i>a</i> (Å)	7.8464(6)
<i>b</i> (Å)	9.6409(8)
<i>c</i> (Å)	12.2746(10)
$\alpha/\beta/\gamma$ (°)	67.639(2)/72.235(2)/80.670(2)
<i>V</i> (Å ³)	816.64(11)
<i>Z</i>	2
ρ (calc) (g/cm ³)	1.802
μ (Mo Ka) (mm ⁻¹)	1.323
<i>F</i> (000)	444
Crystal Size (mm)	0.15 × 0.10 × 0.08
<i>T</i> (K)	293(2)
Radiation wavelength (Å)	0.71073
θ (Min-Max) (°)	2.287- 27.187
<i>hkl</i> range	-10 to 10; -12 to 12 and -15 to 15
Reflection No., <i>R</i> (int)	6433, 0.0252
Observed data (<i>I</i> > 2 σ (<i>I</i>))	3460
<i>N</i> _{ref} , <i>N</i> _{par}	3565, 221
<i>R</i> ^a , <i>wR</i> ₂ ^b , <i>S</i> ^c	0.0171, 0.0450, 1.084
Residual Density (e/Å ³)	-0.333 and 0.252

$$^a R_1 = \sum (|F_o| - |F_c|) / \sum |F_o|$$

$$^b wR_2 = \{ \sum [w (F_o^2 - F_c^2)^2] / \sum [w (F_o^2)^2] \}^{1/2}, w = 1/[\sigma^2(F_o^2) + (0.0424P)^2 + 0.1237P] \text{ for HLS}^{\text{Et}} \text{ and } w = 1/[\sigma^2(F_o^2) + (0.0727P)^2 + 12.3261P] \text{ for } \mathbf{C1}, \text{ where } P = (F_o^2 + 2 F_c^2)/3$$

$$^c \text{GOF (S)} = \{ \sum [w(F_o^2 - F_c^2)^2] / (n - p) \}^{1/2}, \text{ where } n = \text{number of measured data and } p = \text{number of parameters.}$$

VI.2.5. Computational method

For a theoretical explanation, we have performed the computational data analysis adopting DFT method, which is incorporated with the conductor-like polarizable continuum model (CPCM). In this study, "Becke, 3-parameter, Lee–Yang–Parr" the hybrid correlation function [22,23] are also utilized. To get the fully optimized geometry of **Complex 1**, we have taken 6-31+G(d) basis set for C, H, N, O and Cl atom, and for Pd atom, we used LanL2DZ basis set [25-27]. The absorption spectrum of **Complex 1** was also calculated in acetonitrile medium using the time-dependent DFT (TD-DFT) method [29-31] associated with the CPCM [32-34] using the same basis set. All the related calculations were made applying Gaussian 09 package [24]. The percentage of contributions of different groups to the molecular orbital was calculated using the GaussSum program [28].

VI.2.6. DNA-binding studies

VI.2.6.1. UV–Vis absorption studies

A stock solution of complex (1.0×10^{-4} M) was prepared in 1:10 acetonitrile/buffer mixture (Tris–HCl/ NaCl buffer of pH 7.4). A stock solution of CT-DNA (2.19×10^{-3} M) was prepared in buffer solution. The absorption spectrum of the complex was measured between 300 and 600 nm. CT-DNA solution was gradually added to it, stirred properly, and equilibrated for 4 min before collecting the spectra. Addition continued until saturation occurred. These spectral-titration results are essential for determining the binding constant (K_b) with CT-DNA. Eq. (1) was used to determine K_b (in M^{-1}) [35].

$$[\text{DNA}]/(\varepsilon_a - \varepsilon_f) = [\text{DNA}]/(\varepsilon_b - \varepsilon_f) + 1/K_b(\varepsilon_b - \varepsilon_f) \dots\dots\dots (1)$$

Where [DNA] is the concentration of CT DNA in base pairs, the extinction coefficients ε_a , ε_f and ε_b correspond to $A_{\text{obs}}/[\text{complex}]$, free Pd(II) complex, and the extinction coefficient of the Pd(II) complex when it is in totally bound form, respectively. The plot of $[\text{DNA}]/(\varepsilon_a - \varepsilon_f)$

against [DNA] will produce slope $1/(\epsilon_b - \epsilon_f)$ and intercept $1/K_b(\epsilon_b - \epsilon_f)$; K_b is the ratio of slope to intercept.

VI.2.6.2. Competitive binding study with EB by fluorescence method

The ability of the synthesized palladium complex (**1**) to dislocate EB from its EB-CTDNA complex was studied by the fluorescence method. 10 μM EB and 10 μM CT-DNA were mixed homogeneously to prepare the CTDNA–EB adduct in Tris– HCl/NaCl buffer solution (pH 7.4). Upon excitation at 540 nm of the resulting mixture an emission maxima observed at 608 nm. Quenching of that emission was monitored with the subsequent addition of **1**.

VI.2.7. BSA binding studies

The binding interaction between BSA and Pd(II) complex (**1**) was examined by UV-Vis and fluorescence methods. A stock solution of BSA was prepared using 500 mM phosphate buffer saline (PBS) at pH 7.4. Concentration of BSA solution was measured by taking the absorbance at 280 nm (molar extinction coefficient $66,400 \text{ dm}^3 \text{ mol}^{-1} \text{ cm}^{-1}$) [36]. Stock solution of **1** was prepared in DMSO medium and was suitably diluted with PBS whenever necessary. UV-Vis spectra of BSA solution (10 μM) were taken with the variation of complex concentration. The changes in tryptophan-based fluorescence of BSA in the presence of **1** were studied with the excitation wavelength at 280 nm. Quenching of emission intensity at $\sim 336 \text{ nm}$ for BSA was monitored with subsequent addition of **1**.

VI.2.8. Cell viability and proliferation assays

VI.2.8.1. Mammalian cell culture

The cell lines MDA MB 231, MCF7 and AGS were procured from NCCS, Pune, India. MDA MB 231 cells were culture in DMEM high glucose media, MCF7 and WRL68 cells were cultured in MEM media containing Earle's salts and AGS was cultured in RPMI 1640 media. Foetal bovine serum (final concentration of 10%) was added to the respective media to prepare the complete growth media, along with 1X Anti- Anti solution (Invitrogen). All the

cells were maintained at 37°C with 5% CO₂ atmosphere and were passaged at 70-80% confluency.

VI.2.8.2. MTT Assay

1x10³ MDA MB 231, AGS, MCF7 and WRL68 cells were seeded in each well of 96 well plates and allowed to adhere overnight [37]. Then, the complete media was discarded and fresh complete media containing various doses of 1 (0-600 μM) and Cisplatin were added to the cells. Post 24 hours incubation, MTT (2mg/ml), 10 μl of it was added to each well. Subsequently, the cells were incubated for 4 hours at 37°C. Then, the formed formazan crystals were solubilised in DMSO. The optical density was measured on a multi-mode plate reader (SpectraMax i3x, Molecular devices) at 570 nm. GraphPad Prism 5.0 was utilised for the calculation of the IC₅₀ and this data was further utilised to construct the cell viability graph of different cell line.

VI.2.8.3. Colony Formation Assay

Low density plating (500 cells per well) of MDA MB 231 cells was done and incubated at 37°C and 5% CO₂ environment, overnight. The cells were then subjected to treatment with 1 and incubated further for 24 hours. Subsequently, the media was changed and the cells were further cultured for 5 days. The colonies that formed (>50 cells) were subjected to fixation in 100% cold Methanol and then in order to visualise the cells, they were stained with 0.5% crystal violet solution for 15 mins, followed by washing with distilled water. The colonies were observed and imaged under an inverted light microscope (Olympus).

VI.2.8.4. Detection of DNA fragmentation by Hoechst staining

MDA MB 231 cells were treated with complex 1 for 24 hours and then Hoechst 33258 (Sigma) (final concentration 2.5 μg/ml) was added to the cells and incubated at RT under dark conditions for 30 minutes. Then the cells were visualised using a fluorescence microscope and imaged using CellSens software.

VI.2.8.5. CT-DNA gel electrophoresis

The highly popular agarose gel electrophoresis was performed for observing the effect of complex 1 on the CT-DNA structure. Initially, four solutions were prepared and they were as follows: Tube 1 (50 µl of CT DNA stock solution and 50 µl Tris-HCl buffer); Tube 2 (50 µl of CT DNA, 20 µl of complex 1 and 30 µl Tris-HCl buffer); Tube 3 (50 µl of CT DNA, 30 µl of complex 1 and 20 µl Tris-HCl buffer) and Tube 4 (50 µl of CT DNA, 40 µl of complex 1 and 10 µl Tris-HCl buffer). All the tubes were then incubated at RT overnight and on the next day all the tubes were incubated at 37°C for 60 minutes prior to sample preparation for gel electrophoresis. Samples were prepared by mixing 2 µl loading dye and 8 µl of each sample and then were loaded and electrophoresed on a 1% agarose gel. The gel electrophoresis was performed in TAE buffer at 50V for 2 hours. After the dye front in all the lanes reached about 3/4th of the total gel length, electrophoresis was stopped, the gel was taken out of the buffer tank, stained in Ethidium bromide solution for 45 minutes and was visualised in ChemiDoc XRS+ instrument with Image Lab software (Bio-Rad).

VI.2.8.6. Detection of apoptosis by AO/EtBr staining

MDA MB 231 cells were cultured in a six well plate (3×10^4 cells/well) and treated with complex 1 for 24 hours. Subsequently, the cells were washed with PBS and fixed in a methanol: glacial acetic acid (3:1) solution for 30 mins at 4°C. The cells were washed again in PBS and subjected to 1:1 AO/EtBr solution for 30 minutes at RT. After another wash with PBS, the cells were viewed and imaged under a fluorescence microscope (Olympus).

VI.2.8.7. Cell cycle analysis

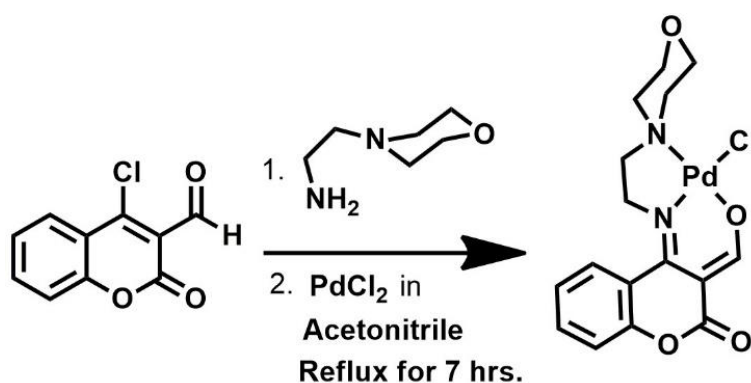
MDA MB 231 cells were harvested by trypsinisation and resuspended in PBS post 24 hours treatment with complex 1. Then, in a drop-wise manner, cold ethanol was added to it, to a final concentration of 70%. The cells were then fixed on ice for 2 hours and subsequently

washed. The fixed cells were pelleted down in a centrifuge and resuspended in staining buffer (PBS containing 100 $\mu\text{g/ml}$ RNase A and 50 $\mu\text{g/ml}$ Propidium Iodide) and incubated in dark conditions at 4°C overnight. Next, the cells were acquired using the BD LSRFortessa flow cytometry instrument and the data was analysed using FlowJo software.

VI.3. Results and discussion

VI.3.1. Synthesis and spectral characterization

Coumarin-morpholine-based Palladium complex **1** was synthesized by reacting with 4-chloro-2-oxo-2H-chromene-3-carbaldehyde, 2-morpholinoethanamine and Na_2PdCl_4 in 1:1:1 molar ratio via in-situ method (Scheme VI.1). Pd(II) complex, **1** are thoroughly characterized by several spectroscopic techniques. IR spectrum of **1** showed $\nu(\text{C-H})$ at 2864 cm^{-1} and $\nu(\text{C=N})$ at 1707 cm^{-1} . In ^1H NMR spectra (Fig.VI.3), the singlet peak appeared at 8.41 ppm, which indicates the aldehyde proton peak of the complex **1**. Aromatic proton signals for **1** appear at 7.29-8.03 ppm in DMSO-d_6 . UV-Vis spectrum of **1** in acetonitrile exhibits moderately low energy intense bands at 322 nm and 307 nm. One sharp high energy band appear at 245 nm. In addition, two shoulder peaks appear at 340 nm and 288 nm (Fig.VI.2).



Scheme VI.1. Synthesis of palladium(II) complex, $[\text{Pd}(\text{L})\text{Cl}]$ (**1**)

Table VI.2: X-ray and calculated (DFT/B3LYP) bond distances (Å) and angles (°) of **1**

Bonds(Å)	X-ray	Calc.
Pd(1)-N(1)	2.106(7)	2.12251
Pd(1)- N(2)	2.032(7)	2.04295
Pd(1)- O(2)	1.950(8)	2.01094
Pd(1)- Cl(1)	2.334(2)	2.33994
N(1)- C(5)	1.463(11)	1.49876
C(5)- C(6)	1.580(12)	1.52219
N(2)- C(6)	1.413(11)	1.46368
N(2)- C(7)	1.289(11)	1.32088
O(2)- C(16)	1.248(12)	1.26772
C(15)- C(16)	1.438(11)	1.40804
C(7)- C(15)	1.473(13)	1.44356
Angles (°)		
O(2)- Pd(1)- N(2)	94.9(3)	92.90840
O(2)- Pd(1)- N(1)	177.8(4)	176.51150
N(2)- Pd(1)- N(1)	84.0(3)	85.40663
O(2)- Pd(1)- Cl(1)	87.1(3)	89.02397
N(2)- Pd(1)- Cl(1)	171.0(2)	174.79912
N(1)- Pd(1)- Cl(1)	94.3(2)	92.91491
C(1)- N(1)- Pd(1)	107.2(5)	109.19786
C(4)- N(1)- Pd(1)	110.7(5)	112.59031
C(5)- N(1)- Pd(1)	102.9(5)	103.33399
N(2)- C(6)- C(5)	106.6(7)	111.61495
N(2)- C(7)- C(8)	127.5(9)	124.42584

VI.3.3. DFT calculations

To understand the electronic structure, geometry of **1** are optimized by DFT/B3LYP method. Contour plots of some selected molecular orbitals obtained from DFT calculations are given in Fig.VI.6 for **1**. Energy and % of composition of some selected MOs for complex **1** are tabulated in Table VI.3. HOMO of complex **1** has 43% ligand contribution along with 25% contribution of $d\pi(\text{Pd})$ (14%) orbitals. HOMO-1 has 77% $p\pi(\text{Cl})$ character with a reduced contribution (17%) of $d\pi(\text{Pd})$ orbitals, whereas HOMO-2 has 61% ligand contribution along with a reduced contribution (24%) of $p\pi(\text{Cl})$ and $d\pi(\text{Pd})$ (15%) orbitals. HOMO-3 has 67% $d\pi(\text{Pd})$ character along with 25% ligand character. LUMO of **1** has 70% $\pi^*(\text{L})$ character, and LUMO+1 has mixed $\pi^*(\text{L})$ (61%) and $d\pi(\text{Pd})$ (32%) character. The energy gap between HOMO and LUMO for **1** is found to be 3.89 eV.

Table VI.3. Energy and compositions (%) of selected molecular orbitals of **C1**

MO	E (eV)	% of composition		
		Pd	L	Cl
LUMO+5	-0.01	9	91	0
LUMO+4	-0.35	6	94	0
LUMO+3	-0.49	80	20	0
LUMO+2	-0.8	3	97	0
LUMO+1	-2.09	32	61	7
LUMO	-2.22	24	70	6
HOMO	-6.11	25	43	32
HOMO-1	-6.55	17	7	77
HOMO-2	-6.61	15	61	24
HOMO-3	-6.77	67	25	8
HOMO-4	-6.94	7	79	14
HOMO-5	-7.28	4	91	5
HOMO-6	-7.54	12	77	11
HOMO-7	-7.63	9	90	1
HOMO-8	-7.73	74	26	0
HOMO-9	-7.88	16	43	40
HOMO-10	-8.37	43	43	14

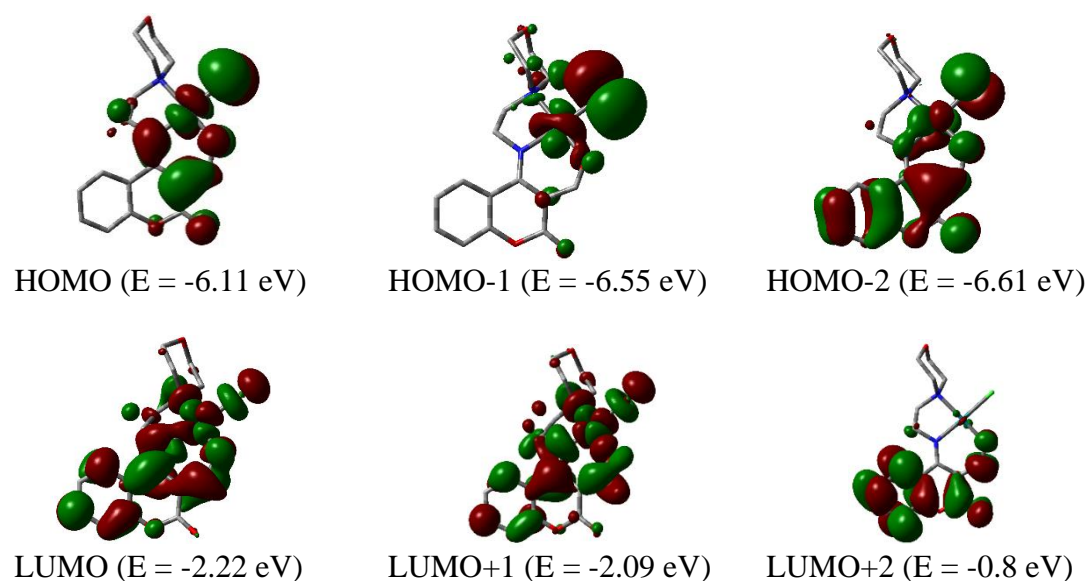


Fig.VI.6. Contour plots of some selected molecular orbital of **1**

VI.3.4. TDDFT calculation and electronic spectra

To elucidate the electronic transitions in **1**, TDDFT calculation was carried out in acetonitrile employing TDDFT/CPCM method. Calculated electronic transitions for **1** are summarized in Table VI.4. The calculated band at 346 nm ($f = 0.0227$) for **1** is in good agreement with the experimental band at 340 nm ($\epsilon = 6515 \text{ M}^{-1}\text{cm}^{-1}$) corresponds to the mixed HOMO \rightarrow LUMO+1 transitions having mixed MLCT, XLCT, XMCT and ILCT character. The experimental peak at 322 nm resembles with the calculated band at 319 nm ($f = 0.0855$) with mixed HOMO-2 \rightarrow LUMO, HOMO-1 \rightarrow LUMO and HOMO-1 \rightarrow LUMO+1 transitions with combined MLCT, XLCT, XMCT and ILCT character. The calculated band at 309 nm ($f = 0.0326$) for **1** is in good agreement with the experimental band at 307 nm ($\epsilon = 9646 \text{ M}^{-1}\text{cm}^{-1}$) corresponds to the mixed HOMO-3 \rightarrow LUMO, HOMO-2 \rightarrow LUMO+1 and HOMO-2 \rightarrow LUMO transitions having mixed MLCT, XLCT, XMCT and ILCT character. The high energy band and shoulder peak that appeared at 245 nm and 288 nm corresponds to the ILCT character (Table VI.4).

Table VI.4. Vertical electronic transitions of **1** calculated by TDDFT/CPCM method

λ (nm)	E (eV)	Osc. Strength (f)	Key excitations	Character	$\lambda_{\text{expt.}}$ (nm) (ϵ ($\text{M}^{-1}\text{cm}^{-1}$))
345.7	3.5865	0.0227	(77%)HOMO \rightarrow LUMO+1	Pd(d π) \rightarrow L(π^*), MLCT Cl(p π) \rightarrow L(π^*), XLCT Cl(p π) \rightarrow Pd(d π) XMCT L(π) \rightarrow L(π^*), ILCT	340 (6515)
318.9	3.8872	0.0855	(27%)HOMO-2 \rightarrow LUMO (25%)HOMO-1 \rightarrow LUMO (25%)HOMO-1 \rightarrow LUMO+1	Pd(d π) \rightarrow L(π^*), MLCT Cl(p π) \rightarrow L(π^*), XLCT Cl(p π) \rightarrow Pd(d π) XMCT L(π) \rightarrow L(π^*), ILCT	322 (9465)
308.5	4.0183	0.0326	(31%)HOMO-3 \rightarrow LUMO (27%)HOMO-2 \rightarrow LUMO+1 (22%)HOMO-2 \rightarrow LUMO	Pd(d π) \rightarrow L(π^*), MLCT Cl(p π) \rightarrow L(π^*), XLCT Cl(p π) \rightarrow Pd(d π) XMCT L(π) \rightarrow L(π^*), ILCT	307 (9646)
292.9	4.2323	0.1348	(79%)HOMO-5 \rightarrow LUMO	L(π) \rightarrow L(π^*), ILCT	288 (11457)
253.0	4.9003	0.1505	(69%)HOMO-6 \rightarrow LUMO	L(π) \rightarrow L(π^*), ILCT	245 (32740)
250.1	4.9569	0.2409	(74%)HOMO-7 \rightarrow LUMO	L(π) \rightarrow L(π^*), ILCT	

^a ILCT: Intra-ligand charge transfer; XLCT: halogen to ligand charge transfer; MLCT: metal to ligand charge transfer.

VI.3.5. DNA binding studies

VI.3.5.1. UV-Vis method

To understand the mode of interactions with DNA is very crucial for the development of new anti-cancer drugs. At present, the spectroscopic methods are widely used to study the mode of interactions. These studies show that the drugs can interact with DNA covalently or by non-covalent interaction, groove binding or by electrostatic interactions [39,40]. Absorption and emission spectroscopies are widely used to interpret the mode of interactions of drug molecules with DNA. UV-Vis is a powerful tool to assess how well palladium complexes bind to CT DNA [41,42]. The absorption spectra of complex **1** were taken in the presence and absence of CT DNA. **1** exhibits a broad peak at 319 nm, but in the presence of CT DNA, a hypochromic shift in the absorption spectra is observed (Fig.VI.7). The intrinsic binding constant (K_b) was evaluated to understand the affinity of the complex towards CT DNA. The K_b value of the Pd(II) complex (**1**) is $1.43 \times 10^5 \text{ M}^{-1}$ which is comparable to the reported literature values [43,44].

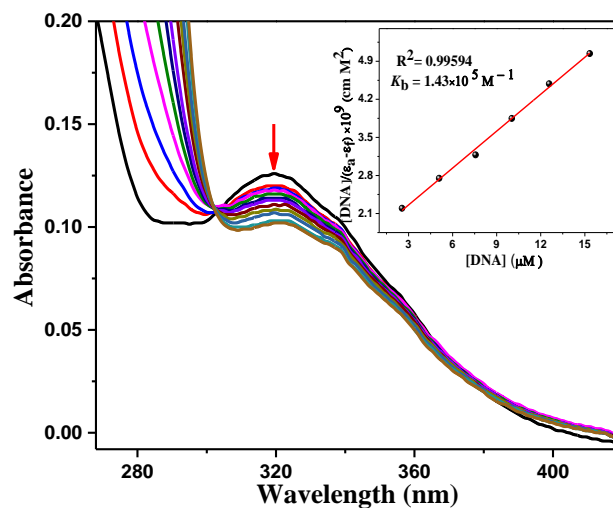


Fig.VI.7. Absorption spectra of complex **1** in Tris-HCl/NaCl buffer upon increasing CT DNA concentrations. Inset: Plot of $[\text{DNA}]/(\epsilon_a - \epsilon_f)$ vs. $[\text{DNA}]$

VI.3.5.2. Fluorescence method

The present palladium complex, **1** is non-fluorescent in solution with or without CT DNA. But when ethidium bromide (EB), a typical intercalator, forms EB-CT DNA intercalating complex, there is a mammoth increase in fluorescence intensity of EB at 608 nm upon excitation at 540 nm [45]. Upon steady addition of Pd(II) complex, the fluorescence intensity is successively decreased due to the replacement of EB from its EB-CT DNA system (Fig.VI.8) [46]. The titration curves clearly demonstrate the competition between the complex and EB for DNA binding sites. A linear Stern–Volmer equation (Eq. (1))[47] accords well with the fluorescence quenching curve of the EB-CT DNA system for the complex.

$$I_0/I = 1 + K_{sv}[Q] \dots \dots \dots (1)$$

Where I and I_0 signify the fluorescence intensities of the EB-CT DNA system with and without the complex, respectively, K_{sv} is the Stern–Volmer quenching constant, and $[Q]$ is the molar concentration of the complex (quencher). K_{sv} value is obtained from the slope of the plot and is found to be $1.16 \times 10^5 \text{ M}^{-1}$ for **1**.

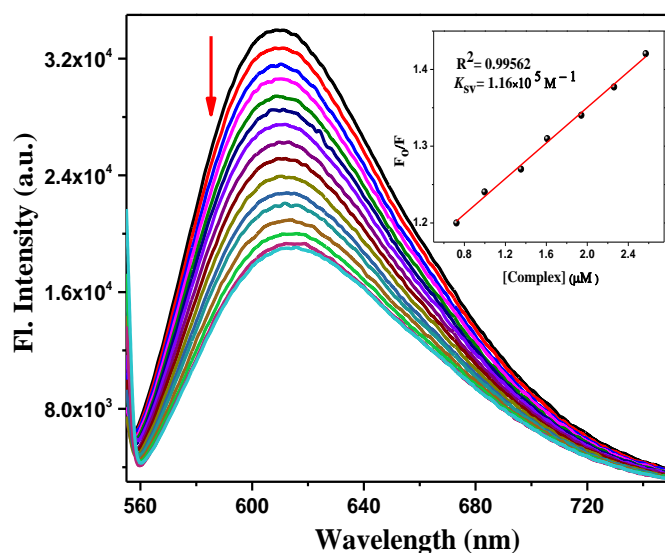


Fig.VI.8. Emission spectra of EB-CT DNA ($\lambda_{ex}=540 \text{ nm}$) in presence of increasing concentrations of **1**. Inset: Plots of emission intensity F_0/F vs. [complex]

VI.3.6. BSA binding studies

VI.3.6.1. UV-Vis method

The interaction of palladium(II) complexes with bovine serum albumin (BSA) provides the information about the intrinsic fluorescence property of BSA [48]. UV-Vis spectra of BSA solution (10 μM in PBS at pH 7.4) were recorded in the range of 200-500 nm in presence of variable concentration of the complex (**1**), shown in Fig.VI.9. BSA has a characteristic band at 280 nm. Gradual addition of **1** (100 μL) to the BSA solution causes a steady increase in absorption intensity at 280 nm along with a bit of blue shift [49,50]. This hypsochromic shift attributes to the ground-state alliance between the complex and protein. The apparent association constant (K_a) was calculated from the plot of $1/(A_{obs}-A_0)$ vs. $1/[\text{complex}]$ (Fig.VI.9 inset) adopting the following equation [51].

$$\frac{1}{A_{obs} - A_0} = \frac{1}{A_c - A_0} + \frac{1}{K_a(A_c - A_0)[\text{complex}]}$$

Where A_{obs} indicates the observed absorbance (at 280 nm) of the solution having various concentrations of **1**, A_0 and A_c denote BSA absorbance in the absence and presence of **1**. The calculated value of an apparent association constant (K_a) for the complex (**1**) is $4.93 \times 10^4 \text{ M}^{-1}$ which matches well with the literature values for Pd(II) complexes [52-55].

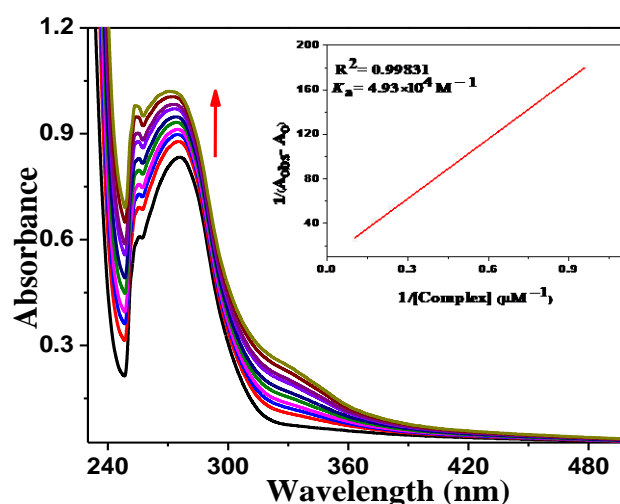


Fig.VI.9. Absorption spectra of BSA (10 μM aqueous solution) upon increasing concentrations of **1** at 300 K. Insets: $1/(A_{obs} - A_0)$ vs. $1/[\text{complex}]$ plots of BSA absorption titration.

VI.3.6.2. Fluorescence method

The BSA-complex interactions were also studied by fluorescence spectral titration method. The complex is non-fluorescent in DMSO solution. But upon excitation at 280 nm, BSA exhibits a strong fluorescence at 336 nm. With the subsequent addition of 100 μL complex (**1**) to the BSA solution, the fluorescence intensity of BSA at ~ 336 nm was dramatically quenched (53.72 % quenching) (Fig.VI.10). This hypochromicity in the spectra is mainly attributed to the interaction of **1** with BSA. The Stern-Volmer quenching constant value (K_{sv}) was calculated [56] and depicted in Fig.VI.10. The high K_{sv} ($7.39 \times 10^4 \text{ M}^{-1}$) value indicates that the complex exhibits a good fluorescence quenching ability. To learn more about the quenching effect, the equilibrium binding constant (K_b) and number of binding sites (n) available for the complex were also calculated from the graph of $\log [(F_0-F)/F]$ versus $\log [\text{complex}]$ (Fig.VI.10 inset) applying the Scatchard equation [57, 58] below:

$$\log \frac{(F_0 - F)}{F} = \log K_b + n \log [\text{complex}]$$

Based on the plot, calculated values of n and K_b for the complex are 1.066 and $7.29 \times 10^4 \text{ M}^{-1}$ respectively, which reflects the strong affinity of the complex with the serum albumins.

Table VI.5. DNA and BSA binding data for complex 1

System	DNA binding		BSA binding				
	UV method	Fluorescence method	UV method	Fluorescence method			
	K_b (M^{-1})	K_{sv} (M^{-1})	K_a (M^{-1})	Hypo(%)	K_b (M^{-1})	K_{sv} (M^{-1})	n
Complex 1	1.43×10^5	1.16×10^5	4.39×10^4	53.72	7.29×10^4	7.39×10^4	1.066

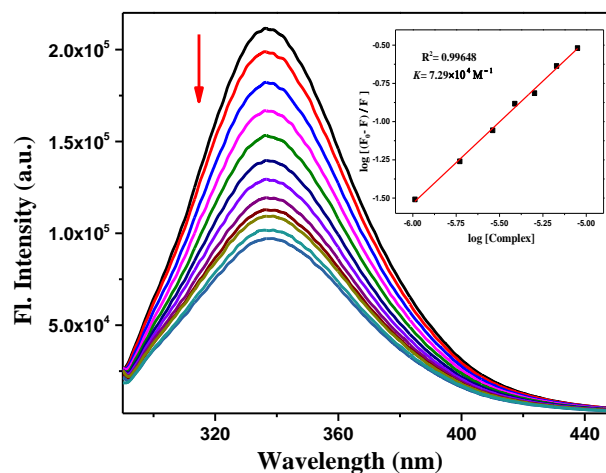


Fig.VI.10. Change in emission spectra of BSA (10 μM) upon gradual addition of **1** at 300 K ($\lambda_{\text{ex}}=280$ nm, $\lambda_{\text{em}}=336$ nm). Inset: Scatchard plots of the BSA fluorescence titration

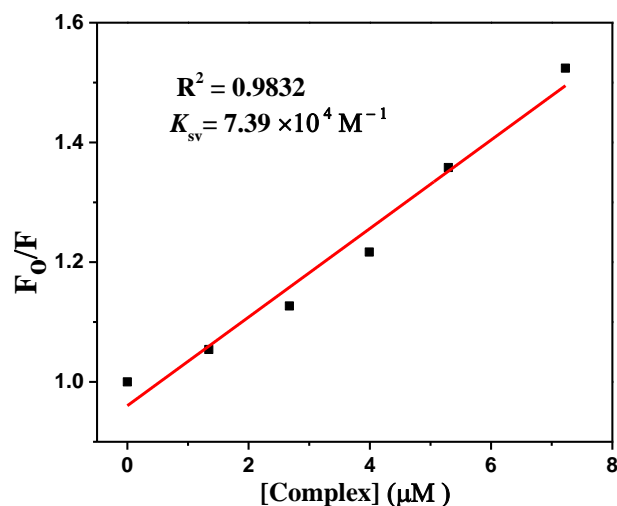


Fig.VI.11. Stern-Volmer fluorescence quenching plot obtained by titration of BSA solution with the complex (**1**)

VI.3.7. *In vitro* antiproliferative studies

VI.3.7.1. MTT Assay

The various IC_{50} values of the different cell lines for the different compounds are shown in the table VI.6. It was observed that the compound **1** was the most effective in inhibiting the growth and proliferation of MDA MB 231 cells as compared to the other cell lines. Thus, for further experiments, MDA MB 231 cells were used. Notably, **1** has a very high IC_{50} value

(>200 μM) when WRL68 cells (normal hepatic cell line) are treated with it. From this we can conclude that **1** has selective toxicity towards cancer cells and has negligible to no toxicity on normal cell lines.

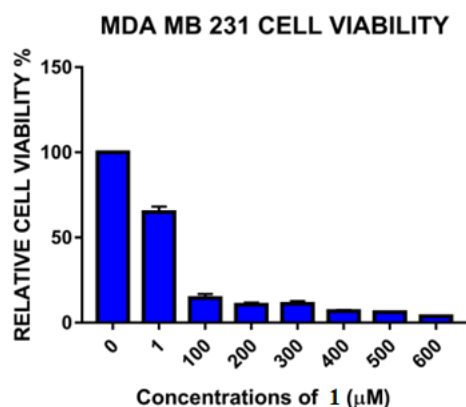


Fig.VI.12. Viability of MDA MB 231 cell lines upon increasing concentrations of **1**

Table VI.6. IC₅₀ value of complex (**1**) determined by MTT assay on AGS cell line

	MDA MB 231	AGS	MCF7	WRL68
Compounds	IC ₅₀ of compounds (μM)			
1	23.01 \pm 1.8	35.48 \pm 2.4	51.01 \pm 2.5	>200
CISPLATIN	90.31 \pm 2.2	27.79 \pm 2.6	12.27 \pm 1.3	>200

VI.3.7.2. Colony Formation Assay

The Clonogenic assay revealed that complex **1** significantly inhibited the colony formation and proliferative potential of MDA MB 231 cells when compared to control (Fig.VI.13) [59]. After 24 hours of treatment, the colony size as well as their numbers were visibly diminished in the concentration which proved the anticancer property of **Complex 1**.

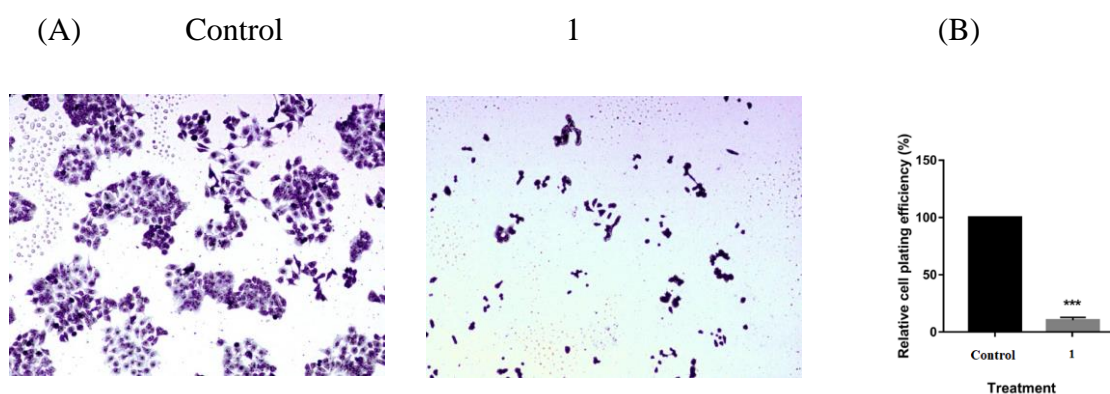


Fig.VI.13. Colony formation of MDA MB 231 cell lines (A) control and upon treatment of **1** (9.55 μ M) for 24 h. (B) % of colonies of MDA MB 231 cell lines relative to the control

VI.3.7.3. Detection of DNA fragmentation by Hoechst staining:

Treatment of MDA MB 231 cells with complex 1 lead to nuclear DNA fragmentation as evident from the Hoechst-stained cells (Fig.VI.14) as compared to control [60]. This indicates that complex 1 interacts with nuclear DNA and leads to its fragmentation, ultimately resulting in the death/apoptosis of cancer cells.

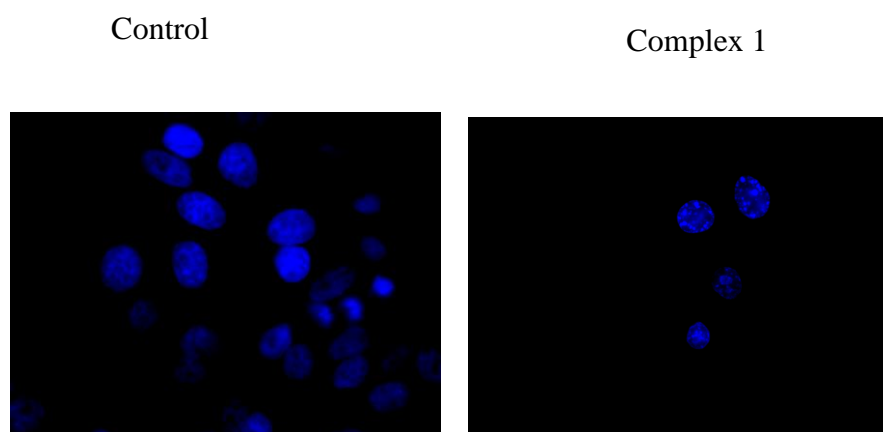


Fig.VI.14. DNA fragmentation assay using Hoechst 33,258 dye on MDA MB231 cells after treatment with 2.5 μ M of complex 1. The cell nuclei in the control are mostly unlike the treatment groups where the nucleus has undergone fragmentation and shrinkage with the

increase in the dose of treatment. The images have been captured in the DAPI channel at 40X magnification Scale bar corresponds to 20 μm .

VI.3.7.4. CT-DNA gel electrophoresis:

The possible intercalation of complex 1 with DNA was evaluated by performing agarose gel electrophoresis of various concentrations of complex 1 with CT-DNA. From the result in Fig.VI.15 it is evident that the intensity of the electrophoresed CT-DNA decreased with increasing concentration of complex 1 as compared to the free CT-DNA band. This may be attributed to the interaction between the complex 1 and the CT-DNA [61,62]. Also, the aggregation of the complex 1 on the double helix and its subsequent damage of CT-DNA may cause this decrease in intensity and mobility.

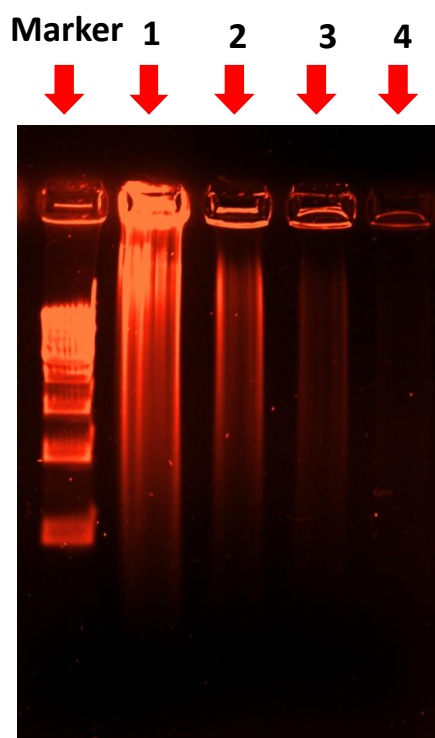


Fig.VI.15. Agarose gel electrophoresis pattern of: Marker (marker is circular DNA for checking the instrument); lane 1(50 μl of CT DNA stock solution and 50 μl Tris-HCl buffer); lane 2(50 μl of CT DNA, 20 μl 1 and 30 μl Tris-HCl buffer); lane 3 (50 μl of CT DNA, 30 μl

1 and 20 μ l Tris-HCl buffer) and lane 4 (50 μ l of CT DNA, 40 μ l 1 and 10 μ l Tris-HCl buffer)

VI.3.7.5. Detection of apoptosis by AO/EtBr staining:

From Fig.VI.16 it is evident that complex 1 induces apoptosis in MDA MB 231 cells as compared to control.

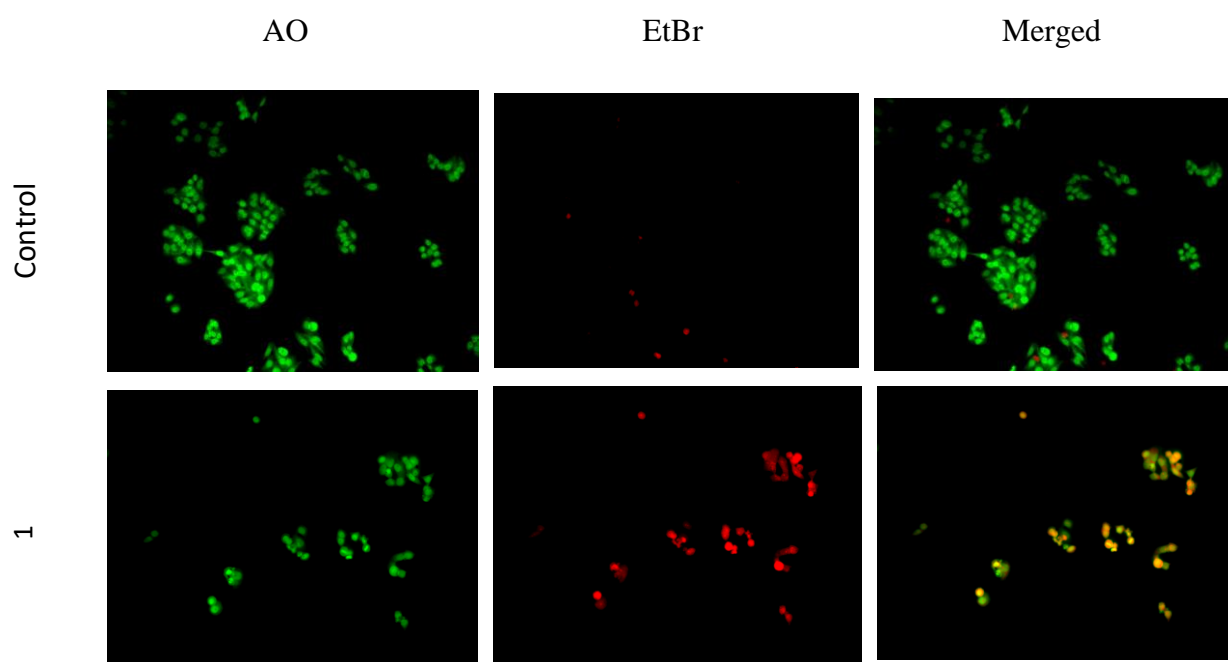


Fig.VI.16. Acridine Orange/Ethidium Bromide (AO/EB) dual staining. Fluorescence microscopy images of MDA MB 231 cells after treating with 1(23.01 μ M; 24 h) followed by staining with acridine orange (4 μ g/ml) and ethidium bromide (4 μ g/ml) as observed under Olympus microscope at 200X magnification.

VI.3.7.6. Cell cycle analysis:

MDA MB 231 cells were significantly arrested in the G2/M phase of cell cycle as compared to control when treated with complex 1 (Fig.VI.17).

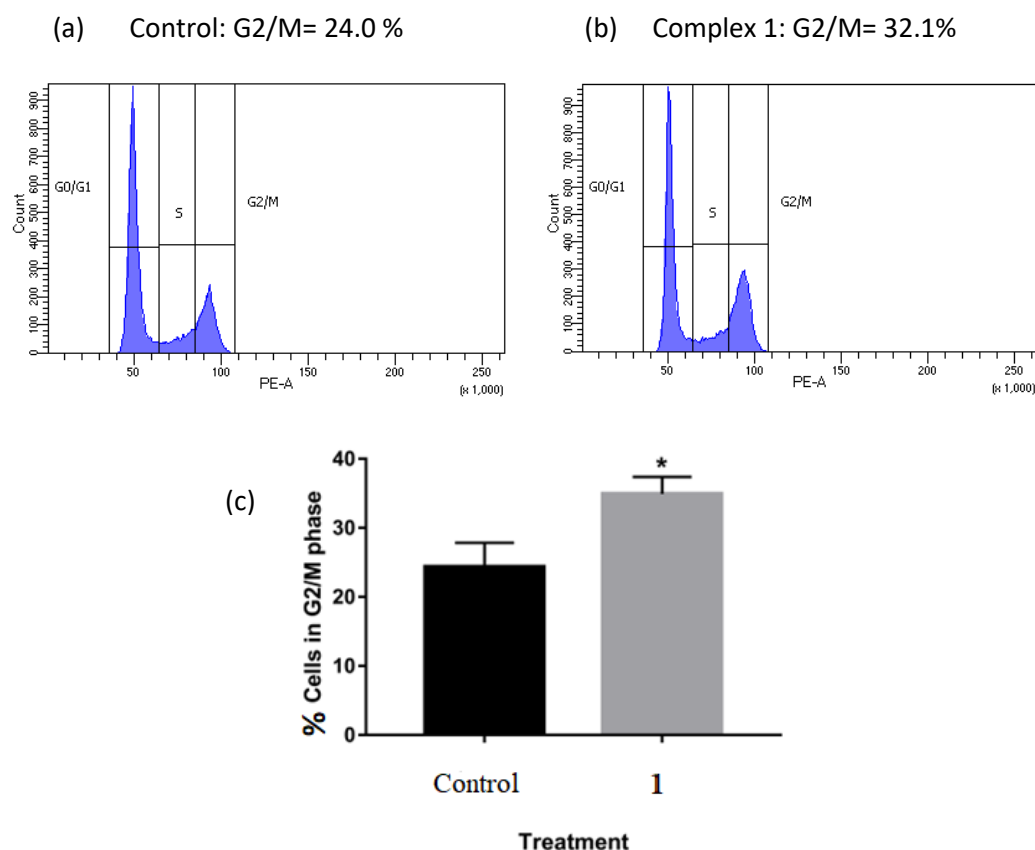


Fig.VI.17. Cell cycle analysis of complex 1 on cell cycle distribution in MDA-MB-231 cell line for 24 h. Flow cytometry assay of (a) Control (b) treatment with complex 1 for 24 h. (c) % cell in G2/M phase Vs. Treatment.

VI.4. Conclusions

New coumarin-morpholine ONN donor pincer ligand appended palladium(II) complex **1** is synthesized. Distorted square planar Structure of complex **1** is confirmed by crystallographic method. Interaction of **1** with CT DNA and BSA proteins is investigated by absorption and fluorescence methods. The complex effectively displaces ethidium bromide (EB) from its EB-DNA complex and Stern-Volmer quenching constant, K_{SV} is found to be $1.16 \times 10^5 \text{ M}^{-1}$. In vitro cytotoxicity of complex **1** towards gastric cancer cell lines (AGS) and

breast cancer cell lines (MDA MB 231 and MCF-7) were performed by MTT assay, colony formation assay, cell cycle analysis and Hoechst and AO/EtBr staining. Intercalation of the complex with DNA was evaluated by performing agarose gel electrophoresis of various concentrations of the complex.

VI.5. References

1. F. Bray, J. Ferlay, I. Soerjomataram, R. L. Siegel, L. A. Torre and A. Jemal, *Cancer J. Clin.*, 2018, **68**, 394–424.
2. R. L. Siegel, K. D. Miller and A. Jemal, *Ca-Cancer J. Clin.*, 2019, **69**, 7–34.
3. Cancer statistics–India against cancer. <http://cancerindia.org.in/cancer-statistics/>. Accessed February 5, 2019.
4. S. E. Sherman, D. Gibson, A. H. J. Wang and S. J. Lippard, *J. Am. Chem. Soc.*, 1988, **110**, 7368–7381.
5. F. Yu, V. M. Cangelosi, M. L. Zastrow, M. Tegoni, J. S. Plegaria, A. G. Tebo, C. S. Mocny, L. Ruckthong, H. Qayyum and V. L. Pecoraro, *Chem. Rev.*, 2014, **114**, 3495–3578.
6. Z. Zhao, J. Zhang, S. Zhi, W. Song and J. Zhao, *J. Inorg. Biochem.*, 2019, **197**, 110696–110705.
7. Q. Que, and J. D. Helmann, *Mol. Microbiol.*, 2000, **35**, 1454–1468.
8. E. Guedon, C. M. Moore, Q. Que, T. Wang, R. W. Ye and J. D. Helmann, *Mol. Microbiol.*, 2003, **49**, 1477–1491.
9. a) Y. Jung and S. J. Lippard, *Chem. Rev.*, 2007, **107**, 1387–1407. (b) P. C. A. Bruijninx and P. J. Sadler, *Curr. Opin. Chem. Biol.*, 2008, **12**, 197–206. (c) C. G. Hartinger, A. A. Nazarov, S. M. Ashraf, P. J. Dyson and B. K. Keppler, *Curr. Med. Chem.*, 2008, **15**, 2574–2591. (d) I. Kostova., *Curr. Med. Chem.*, 2006, **13**, 1085–1107. (e) K. S. Lovejoy, R. C. Todd, S. Zhang, M. S. McCormick, J. A. D’Aquino, J. T. Reardon, A. Sancar, K. M. Giacomini and S. J. Lippard, *Proc. Natl. Acad. Sci. U.S.A.*, 2008, **105**, 8902–8907.
10. E. R. Jamieson, S. J. Lippard, *Chem. Rev.*, 1999, **99**, 2467–2498.

11. (a) N. J. Farrer, L. Salassa, P. J. Sadler, *Dalton Trans.*, 2009, 10690–10701. (b) R. W.-Y. Sun, M. F.-Y. Ng, E. L.-M. Wong, J. Zhang, S. S.-Y. Chui, L. Shek, T.-C. Lau and C.-M. Che, *Dalton Trans.*, 2009, 10712–10716.
12. P. J. Dyson and G. Sava, *Dalton Trans.*, 2006, 1929–1933.
13. D. R. Richardson, D. S. Kalinowski, V. Richardson, P. C. Sharpe, D. B. Lovejoy, M. Isalam and P. V. Bernhardt, *J. Med. Chem.*, 2009, **52**, 1459–1470.
14. V. A. Pal'chikov, *Russ. J. Org. Chem.*, 2013, **49**, 787–814.
15. A. N. Matralis, A. P. Kourounakis, *ACS Med. Chem. Lett.*, 2019, **10**, 98–104.
16. Z. Li, Z.-C. Wang, X. Li, et al., *Eur. J. Med. Chem.*, 2019, **169**, 168–184.
17. A. Jarrahpour, R. Heiran, V. Sinou, et al., *Iran J. Pharm. Res.*, 2019, **18**, 34–48.
18. K. Ohui, E. Afanasenko, F. Bacher, et al., *J. Med. Chem.*, 2019, **62**, 512–530.
19. G. R. Jachak, R. Ramesh, D. G. Sant, S. U. Jorwekar, M. R. Jadhav, S. G. Tupe, M. V. Deshpande, D. S. Reddy, *ACS Med. Chem. Lett.*, 2015, **6**, 1111–1116.
20. G. M. Sheldrick, *Acta Cryst.*, 2008, **A64**, 112.
21. G. M. Sheldrick, *Acta Cryst.*, 2015, **C71**, 3.
22. A. D. Becke, *J. Chem. Phys.*, 1993, **98**, 5648.
23. C. Lee, W. Yang, R. G. Parr, *Phys. Rev. B*, 1998, **37**, 785.
24. M. J. Frisch, G. W. Trucks, H. B. Schlegel, G. E. Scuseria, M. A. Robb, J. R. Cheeseman, G. Scalmani, V. Barone, B. Mennucci, G. A. Petersson, H. Nakatsuji, M. Caricato, X. Li, H. P. Hratchian, A. F. Izmaylov, J. Bloino, G. Zheng, J. L. Sonnenberg, M. Hada, M. Ehara, K. Toyota, R. Fukuda, J. Hasegawa, M. Ishida, T. Nakajima, Y. Honda, O. Kitao, H. Nakai, T. Vreven, J. A. Montgomery, J. E. Peralta, F. Ogliaro, M. Bearpark, J. J. Heyd, E. Brothers, K. N. Kudin, V. N. Staroverov, R. Kobayashi, J. Normand, K. Raghavachari, A. Rendell, J. C. Burant, S. S. Iyengar, J. Tomasi, M. Cossi, N. Rega, J. M. Millam, M. Klene, J. E. Knox, J. B. Cross, V.

- Bakken, C. Adamo, J. Jaramillo, R. Gomperts, R. E. Stratmann, O. Yazyev, A. J. Austin, R. Cammi, C. Pomelli, J. W. Ochterski, R. L. Martin, K. Morokuma, V. G. Zakrzewski, G. A. Voth, P. Salvador, J. J. Dannenberg, S. Dapprich, A. D. Daniels, O. Farkas, J. B. Foresman, J. V. Ortiz, J. Cioslowski, J. D. Fox, 2009 Gaussian 09, revision D. 01. Gaussian Inc., C. T. Wallingford
25. J. Hay and W. R. Wadt, *J. Chem. Phys.*, 1985, **82**, 270.
26. W. R. Wadt and J. Hay, *J. Chem. Phys.*, 1985, **82**, 284.
27. P. J. Hay and W. R. Wadt, *J. Chem. Phys.*, 1985, **82**, 299.
28. N. M. O'Boyle, A. L. Tenderholt, K. M. Langner, *J. Comput. Chem.*, 2008, **29**, 839.
29. R. Bauernschmitt and R. Ahlrichs, *Chem. Phys. Lett.*, 1996, **256**, 454.
30. R. E. Stratmann, G. E. Scuseria and M. J. Frisch, *J. Chem. Phys.*, 1998, **109**, 8218.
31. M. E. Casida, C. Jamorski, K. C. Casida and D. R. Salahub, *J. Chem. Phys.*, 1998, **108**, 4439.
32. V. Barone and M. Cossi, *J. Phys. Chem. A*, 1998, **102**, 1995.
33. M. Cossi and V. Barone, *J. Chem. Phys.*, 2001, **115**, 4708.
34. M. Cossi, N. Rega, G. Scalmani and V. Barone, *J. Comput. Chem.*, 2003, **24**, 669.
35. M. Anjomshoa, H. Hadadzadeh, M. Torkzadeh-Mahani, S. J. Fatemi, M. Adeli-Sardou, H. A. Rudbari and V. M. Nardo, *Eur. J. Med. Chem.*, 2015, **96**, 66.
36. N. S. Quiming, R. B. Vergel, M. G. Nicolas and J. A. Villanueva, *J. Health Sci.*, 2005, **51**, 8.
37. T. L. Riss, R. A. Moravec, A. L. Niles, S. Duellman, H. A. Benink, T. J. Worzella and L. Minor, 2013 Cell viability assays. Assay Guidelines manuals.
38. (a) S. Biswas, P. Roy and T. K. Mondal, *J. Mol. Struct.*, 2017, **1142**, 110-115; (b) J. – A. Alvarez-Hernández, N. Andrade-López, J. G. Alvarado-Rodríguez, S. González-Montiel, L. Á. Zárate-Hernández and J. Cruz-Borbolla, *Polyhedron*, 2022, **214**,

- 115635; (c) D. Qiu, Y. Guo, H. Wang, X. Bao, Y. Feng, Q. Huang, J. Zeng and G. Qiu, *Inorg. Chem. Commun.*, 2011, **14**, 1520-1524.
39. K. Akdi, R. A. Vilaplana, S. Kamah and F. Gonzalez-Vilchez, *J. Inorg. Biochem.*, 2005, **99**, 1360–1368.
40. N. Bandyopadhyay, P. Basu, G. S. Kumar, B. Guhathakurta, P. Singh and J. P. Naskar, *J. Photochem. Photobiol. B*, 2017, **173**, 560–570.
41. C. V. Barra, F. V. Rocha, L. Morel, A. Gautier, S. S. Garrido, A. E. Mauro, R. C. G. Frem and A. V. G. Netto, *Inorg. Chim. Acta*, 2017, **446**, 54–60.
42. E. Nyarko, N. Hanada, A. Habib and M. Tabata, *Inorg. Chim. Acta*, 2004, **357**, 739-745.
43. J. B. Lepecq and C. Paoletti, *J. Mol. Biol.*, 1967, **27**, 87–106.
44. Y. Zhao, J. Zhu, W. He, Z. Yang, Y. Zhu, Y. Li, J. Zhang and Z. Guo, *Chem. Eur. J.*, 2006, **12**, 6621–6629.
45. E. Ramachandran, D. S. Raja, N. P. Rath and K. Natarajan, *Inorg. Chem.*, 2013, **52**, 1504-1514.
46. D. Senthil Raja, N. S. P. Bhuvanesh and K. Natarajan, *Inorg. Chem.*, 2011, **50**, 12852-12866.
47. A. Wolfe, G. H. Shimer and T. Mechan, *Biochemistry*, 1987, **26**, 6392-6396.
48. A. Paul, S. Mistri, A. Bhunia, S. Manna, H. Puschmann and S. C. Manna, *RSC Adv.*, 2016, **6**, 60487-60501.
49. A. Paul, A. Figuerola, V. Bertolasi and S. C. Manna, *Polyhedron*, 2016, **119**, 460-470.
50. X.-Q. Zhou, Q. Sun, L. Jiang, S.-T. Li, W. Gu, J.-L. Tian, X. Liu and S.-P. Yan, *Dalton Trans.*, 2015, **44**, 9516-9527.
51. W.-J. Lian, X.-T. Wang, C.-Z. Xie, H. Tian, X.-Q. Song, H.-T. Pan, X. Qiao and J.Y. Xu, *Dalton Trans.*, 2016, **45**, 9073-9087.

52. A. S. D. Tabatabai, E. Dehghanian and H. Mansouri-Torshizi, *Biometals*, 2022, **35**, 245-266.
53. S. Abedanzadeh, K. Karami, M. Rahimi, M. Edalati, M. Abedanzadeh, A. Mohammad Tamaddon, M. Dehdashti Jahromi, Z. Amirghofran, J. Lipkowskif and K. Lyczko, *Dalton Trans.*, 2020, **49**, 14891-14907.
54. R. O. Omondi, N. R. Sibuyi, A. O. Fadaka, M. Meyer, D. Jaganyi and S. O. Ojwach, *Dalton Trans.*, 2021, **50**, 8127-8143.
55. X. Wei, Y. Yang, J. Ge, X. Lin, D. Liu, S. Wang, J. Zhang, G. Zhou and S. Li, *Journal of Inorganic Biochemistry*, 2020, **202**, 110857.
56. J. R. Lakowicz, *Principles of Fluorescence Spectroscopy*, Third Edition., Springer, New York, USA, 2006.
57. J. R. Lakowicz, *Fluorescence Quenching: Theory and applications*, Principles of Fluorescence Spectroscopy, Kluwer Academic/Plenum Publishers, New York, 1999, p. 53.
58. X. Z. Feng, Z. Lin, L. J. Yang, C. Wang and C. L. Bai, *Talanta*, 1998, **47**, 1223-1229.
59. H. Li, X. Li, S. Liu, L. Guo, B. Zhang, J. Zhang and Q. Ye, *Hepatology*, 2017, **66**, 1920-1933.
60. E. Ulukaya, F. Ari, K. Dimas, M. Sarimahmut, E. Guney, N. Sakellaridis, and V. T. Yilmaz, *J. Cancer Res. Clin. Oncol.*, 2011, **137**, 1425-1434.
61. K. Umemura, F. Nagami, T. Okada and R. Kuroda, *Nucleic Acids Res.*, 2000, **9**, 28.
62. L. M. Davis, J. D. Harvey and B. C. Baguley, *Chem Biol Interact.*, 1987, **62**, 45-58.

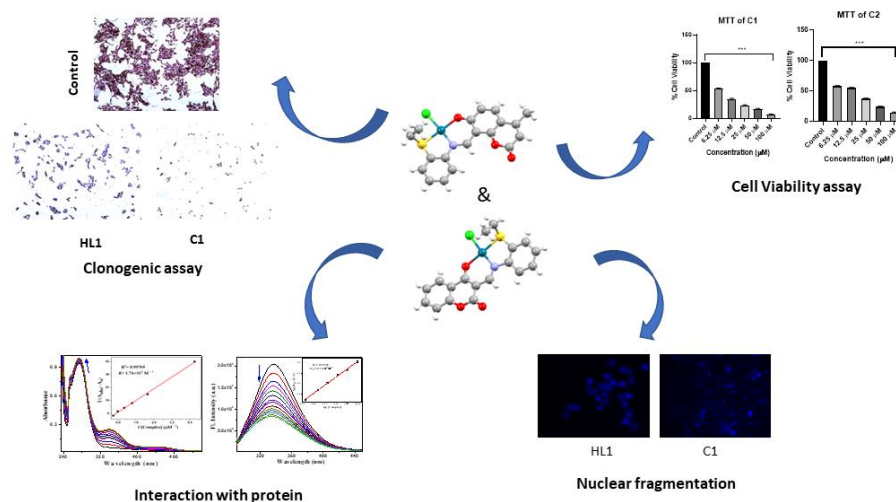
CHAPTER-VII

**New Palladium(II) complexes
appended with coumarin based Schiff
base O,N,S pincers: X-ray structure,
protein binding study, DFT study
and anti-cancer activity in breast
cancer cell lines**

New Palladium(II) complexes appended with coumarin based Schiff base O,N,S pincers: X-ray structure, protein binding study, DFT study and anti-cancer activity in breast cancer cell lines

Abstract

New ONS donor pincer ligands, (E)-8-(((2-(ethylthio)phenyl)imino)methyl)-7-hydroxy-4-methyl-2H-chromen-2-one (HL¹) and (E)-3-(((2-(ethylthio)phenyl)imino)methyl)-4-hydroxy-2H-chromen-2-one (HL²) and their palladium complexes [Pd(L¹)Cl] (**C1**) and [Pd(L²)Cl] (**C2**) are synthesized and thoroughly characterized by spectroscopic techniques. X-ray structures of the complexes reveal that HL¹ and HL² act as tridentate O,N,S chelator in Pd(II) complexes forming distorted square planar geometry. The ability of the Pd(II) complexes to bind with CT DNA are investigated by UV–Vis method and the binding constant are found to be $3.50 \times 10^5 \text{ M}^{-1}$ and $1.99 \times 10^5 \text{ M}^{-1}$ for **C1** and **C2** respectively. Competitive binding study with ethidium bromide (EB) by fluorescence method suggests that the Pd(II) complexes efficiently displace EB from EB-DNA complex. The Calculated Stern-Volmer dynamic quenching constant, K_{sv} are found to be $2.62 \times 10^5 \text{ M}^{-1}$ and $1.59 \times 10^5 \text{ M}^{-1}$ for **C1** and **C2** respectively. Moreover, the interactions of Pd(II) complexes (**C1/C2**) with bovine serum albumin (BSA) are also studied. The antiproliferative activity of the complexes are investigated with human breast cancer cell line MCF 7 and triple negative breast cancer cell line (MDA-MB 231). Both the Pd(II) complexes exhibit substantial cytotoxicity towards MCF 7 cell lines ($IC_{50} = 7.13 - 11.88 \mu\text{M}$).



VII.1. Introduction

Cancer is one of the chronic diseases that has resulted in higher mortality rates and shorter life expectancies in every other country. Lung and colorectal cancer are the next most often diagnosed and deadly malignancies in women [1,2]. According to cancer data from throughout the world, breast cancer alone was responsible for 30% of all new cases of female cancer in 2018. According to statistics, the United States could experience 62,930 new cases of breast cancer in 2018. Also, death rates in underdeveloped countries were higher than in the richest countries [3,4]. Cancer diagnoses have substantially risen in the last several years, according to data from the Indian Council of Medical Research (ICMR). Breast, lung, cervical, and oral cancer are among India's top priorities [5]. Metal complexes and DNA can interact in both covalent and non-covalent ways. Non-covalent interactions include intercalation and major/minor groove binding. The guanine N7 position in DNA is known to be the most electron-rich and oxidizable, making it an excellent candidate for covalent coordination to a metal centre [6]. Enhancing metallodrug design necessitates a better understanding of a metal ion's coordination behaviour under biologically relevant conditions, as well as their kinetic and thermodynamic stabilities and redox behaviour. Nonetheless, it is important to remember that biological systems frequently operate outside of thermodynamic equilibrium. As a result, it is critical to understand the nature of the interactions that metallodrugs have with cell membranes, proteins, enzymes, and DNA in order to develop effective drugs for disease treatment [7-9].

Whereas cis-platin and related platinum complexes are effective anticancer medications, their use is limited due to significant dose-limiting side effects such as nephrotoxicity, myelosuppression, and neurotoxicity. Anaphylaxis, cytopenia, and other frequent side effects are listed below. As a result, developing additional transition metal complexes as active

anticancer drugs with improved efficacy and novel modes of action has emerged as a major research focus in bioinorganic chemistry [10-14].

Coumarins are an interesting class of naturally occurring chemicals that are extensively dispersed [15,16]. After being discovered in various plants from the Rutaceae, Umbelliferae (Apiaceae), Compositae (Asteraceae), Leguminosae, and Moraceae families, coumarin was originally isolated in the seeds of *D. odorata*. Physiological properties of coumarins, which are naturally occurring bioactive compounds, include anticoagulant, anticancer, antiviral, anti-inflammatory, antioxidant, antibacterial, and enzyme inhibition [17,18].

In light of their structural similarities, bovine serum albumin has been extensively explored in substitution of human serum albumin. Serum albumin, the most abundant protein in the circulatory system, transports nutrients and medicines via non-covalent interaction. Therapeutic drug absorption, excretion, and metabolism rely on serum proteins' binding capabilities with the medicines. Also, due to their potential utility, research into DNA interactions with these medicines produced with various chelating ligands has attracted significant attention [19-22].

Herein, new coumarin based ONS donor pincer ligands (HL^1 and HL^2) and their palladium complexes $[Pd(L^1)Cl]$ (**C1**) and $[Pd(L^2)Cl]$ (**C2**) are synthesized and thoroughly characterized by spectroscopic techniques. The ability of the Pd(II) complexes to bind with CT DNA and bovine serum albumin (BSA) are investigated. In-vitro cytotoxicity and colony formation assay are performed on breast cancer cell lines (MCF 7 and MDA MB 231) to monitor the inhibitory action of the Pd(II) complexes. Hoechst and AO/EB staining of the complexes also performed for nuclear fragmentation. Theoretical calculations by DFT and TDDFT methods are performed to interpret the electronic structure and spectral properties of the compounds.

VII.2. Experimental

VII.2.1. Materials

The analytical grade starting materials such as 2-Aminothiophenol, 4-Methylumbelliferone, 4-Hydroxycoumarin, PdCl₂ were obtained from Sigma Aldrich. All other chemicals were of reagent grade, obtained from Merck (India) and used without further purification. Calf thymus DNA (CT-DNA) and bovine serum albumin (BSA) (stored at 4 °C) were procured from Sigma Aldrich, USA. DNA solutions were prepared afresh in Tris-HCL buffer at pH 6.8 for every set of experiments. Millipore water was used throughout the investigation. *Bis*(benzimidazole) (Hoechst 33258, ≥98% purity) was procured from Sigma-Aldrich, whereas, ethidium bromide was procured from Avra synthesis Pvt. Ltd, India. MeOH, DMSO (Cell culture Grade) and agarose were purchased from Sigma. 3-(4, 5-dimethylthiazol-2-yl)-2, 5-diphenyl- tetrazolium bromide (MTT) and Crystal violet solution (Gram's crystal violet) were purchased from Merck. Dulbecco's modified Eagle's medium (DMEM) and FBS were obtained from Gibco. 1% penicillin/streptomycin and Trypsin-EDTA were purchased from Invitrogen. All compounds were used subsequently without further purification. Cisplatin was obtained from calbiochem (sigma Aldrich, 232120-50MG) and dissolved in sodium chloride solution in water (154 mM NaCl) for culture treatment. 4-hydroxy-2-oxo-2H-chromene-3-carbaldehyde and 7-hydroxy-4-methyl-2-oxo-2H-chromene-8-carbaldehyde were prepared according to the published procedure [23].

VII.2.2. Instrumentation

The elemental analyses (C, H, N) were executed with the help of PerkinElmer 2400 series II analyser. ¹H NMR spectra were noted down by using Bruker 300 MHz instrument. For NMR spectra, CDCl₃ was used as solvent using TMS as an internal standard. The mass spectral analyses were performed in a Waters Mass Spectrometer (model: XEVOG2QTOF# YCA351). Electronic spectra were taken on a PerkinElmer Lambda 750 spectrophotometer. Fluorescence spectra were taken on a Shimadzu RF-6000 Spectro fluorophotometer. FTIR spectra were recorded on a RX-1 PerkinElmer spectrophotometer in the range of 4000–400 cm⁻¹ equipped with a Golden Gate Diamond attenuated total reflectance (ATR) device.

VII.2.3. Synthesis

VII.2.3.1. Synthesis of HL¹

The mixture of 7-hydroxy-4-methyl-2-oxo-2H-chromene-8-carbaldehyde (0.15 g, 0.73 mmol) and 2-(ethylthio)aniline (0.11 g, 0.73 mmol) was dissolved in a Round bottom flask in dry methanol and refluxed under stirring condition for 3 h to form the yellow Schiff-base product HL¹. The product was collected in a beaker and purity of the product was checked by TLC; yield, 0.196 g (79%).

Anal. Calc. for C₁₉H₁₇NO₃S: C, 67.24; H, 5.05; N, 4.13. Found: C, 67.21; H, 5.04; N, 4.09. IR (KBr, cm⁻¹): 2919 ν (CH), 1710 ν (C=N). ¹H NMR (300 MHz, CDCl₃): δ 1.36 (-CH₃, t, J = 7.3 Hz, 3H), 2.42 (-CH₃, s, 3H), 2.98 (-CH₂, q, J = 7.3 Hz, 2H), 6.19 (=C-H, s, 1H), 6.94-7.60 (ArH, 6H), 9.33 (CH=N-, s, 1H), 14.93 (-OH, s, 1H). UV-vis in acetonitrile (λ_{\max} , nm) (ϵ , M⁻¹cm⁻¹): 212 (19055), 240 (10394), 312 (14894), 365 (6475). HRMS: calculated for C₁₉H₁₈NO₃S [M+H]⁺ (m/z): 340.1002; found: 340.1003.

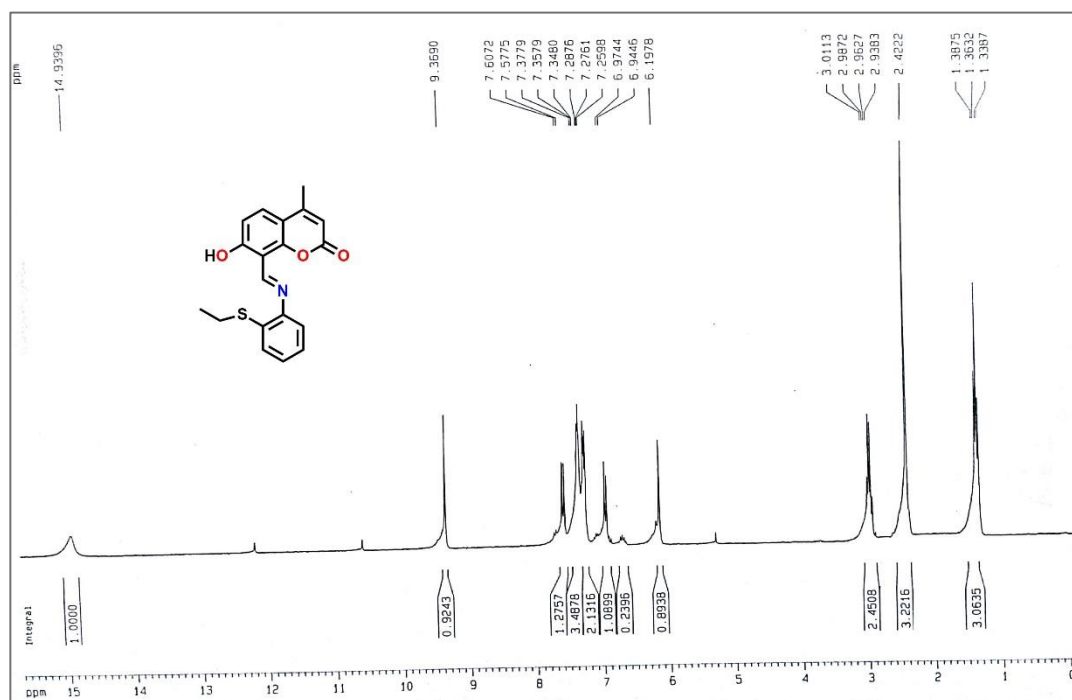


Fig. VII.1. ¹H NMR spectrum of HL¹ in CDCl₃

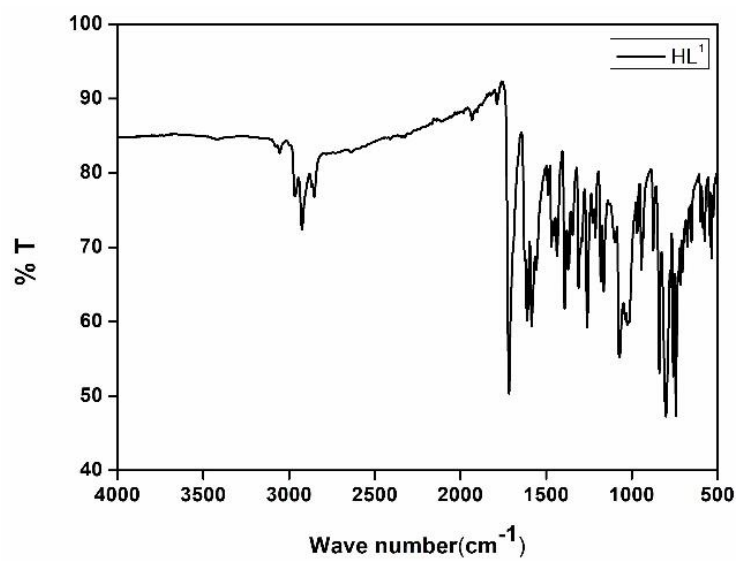


Fig.VII.2. IR spectrum of HL¹ (KBr disk)

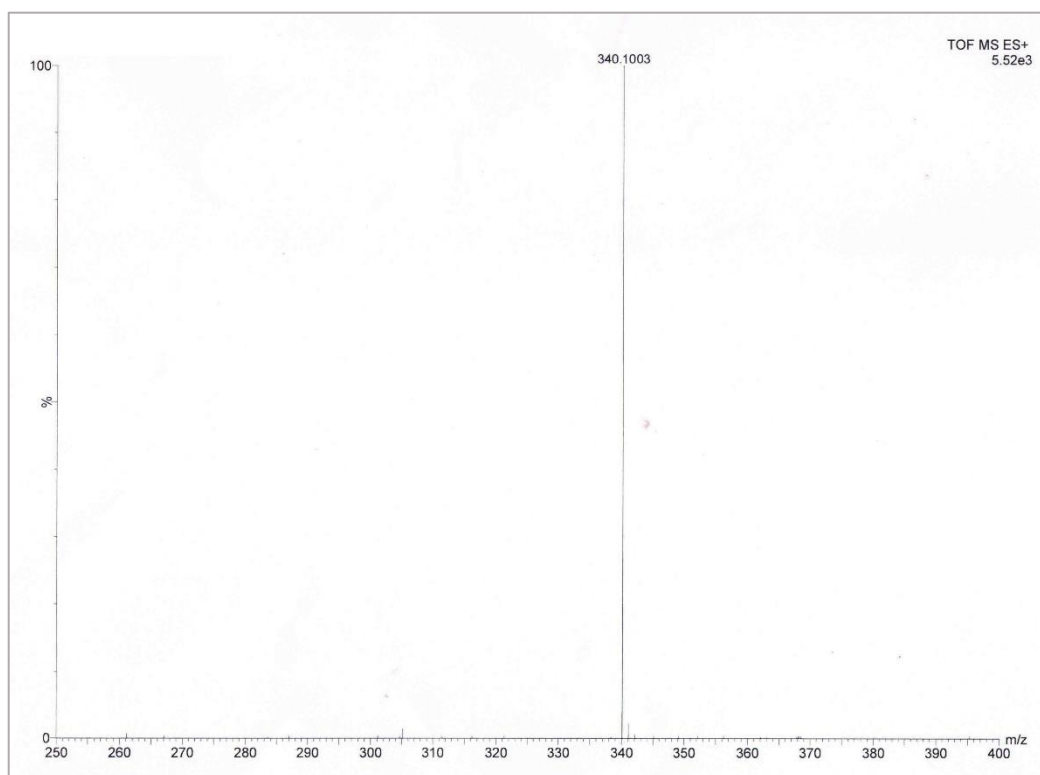


Fig.VII.3. HRMS spectrum of HL¹ in acetonitrile

VII.2.3.2. Synthesis of HL²

HL² was prepared following the similar procedure of HL¹ by refluxing 0.190 g (1 mmol) of 4-hydroxy-2-oxo-2H-chromene-3-carbaldehyde and 0.153 g (1 mmol) of 2-(ethylthio)aniline in dry methanol. Yield: 0.263 g (81%).

Anal. Calc. for C₁₈H₁₅NO₃S: C, 66.44; H, 4.65; N, 4.30. Found: C, 66.42; H, 4.64; N, 4.27. IR (KBr, cm⁻¹): 2929 ν (C-H), 1708 ν (C=N). ¹H NMR (300 MHz, CDCl₃): δ 1.22 (-CH₃, t, J = 6 Hz, 3H), 2.63 (-CH₂, t, J = 4 Hz, 2H), 7.15-7.61 (ArH, 8H), 8.14 (CH=N-, s, 1H), 15.77 (-OH, s, 1H). UV-vis in acetonitrile (λ_{max} , nm) (ϵ , M⁻¹cm⁻¹): 222 (11271), 253 (11641), 340 (9311). HRMS: calculated for C₁₈H₁₆NO₃S [M+H]⁺ (m/z): 326.0845; found: 326.0847.

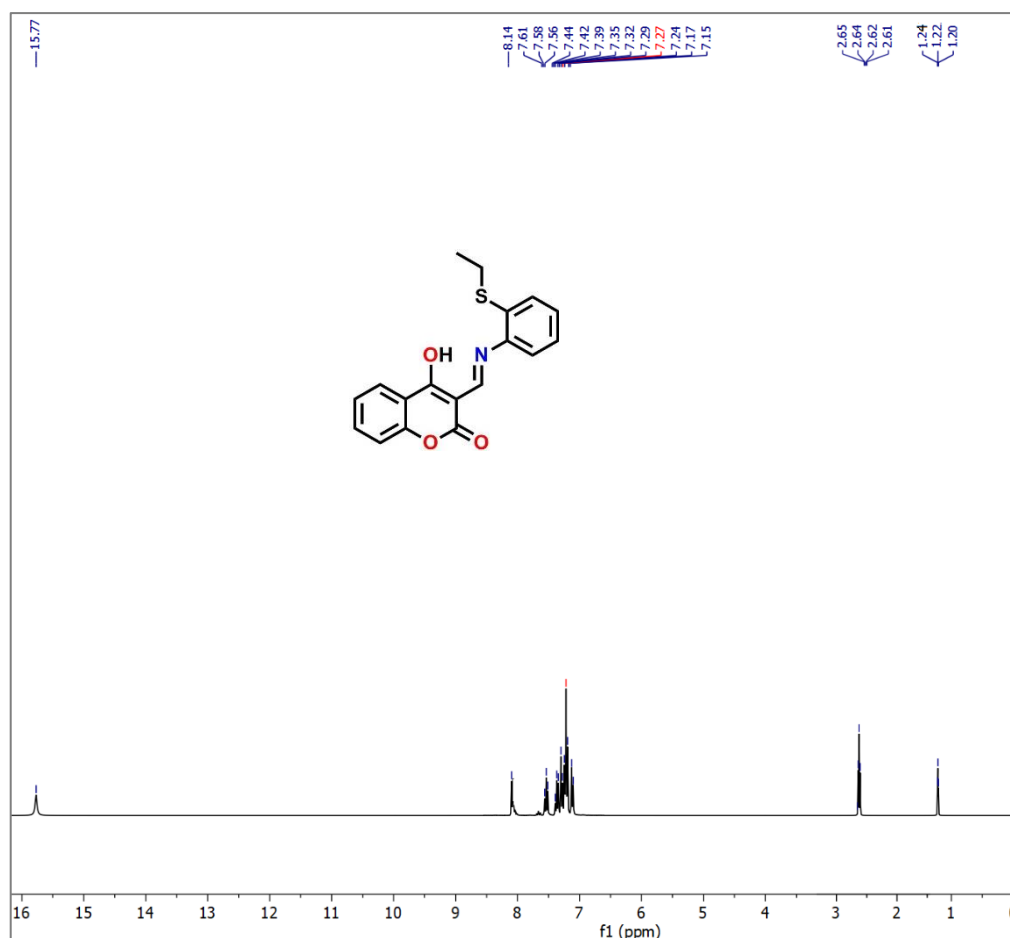


Fig. VII.4. ¹H NMR spectrum of HL¹ in CDCl₃

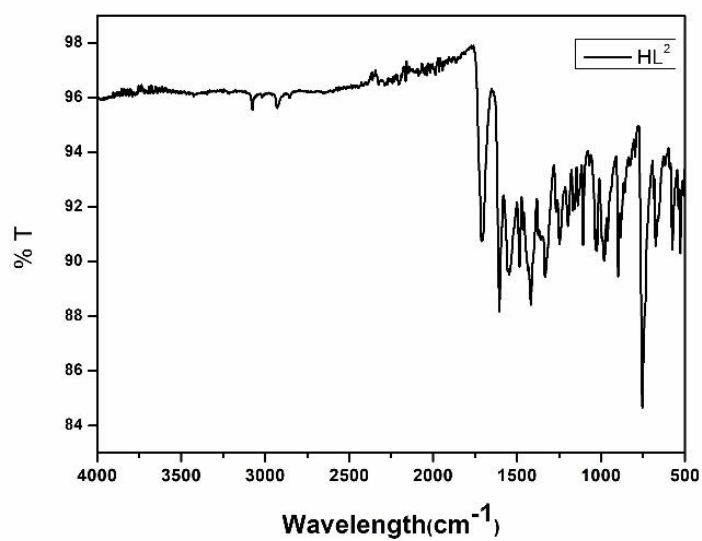


Fig.VII.5. IR spectrum of HL² (KBr disk)

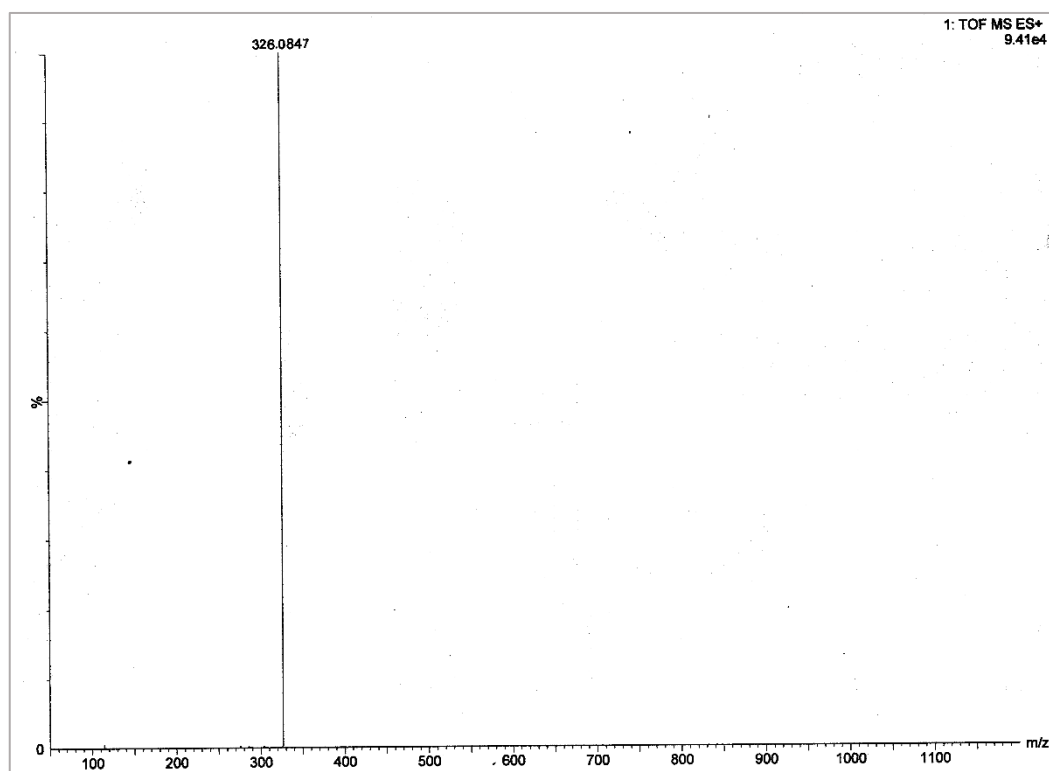


Fig.VII.6. HRMS spectrum of HL² in acetonitrile

VII.2.3.3. Synthesis of [Pd(L¹)Cl] (C1)

In a round bottom flask, 0.07 g (0.39 mmol) PdCl₂ was dissolved in 40 ml acetonitrile. To it, 0.133 g (0.39 mmol) of HL¹ was added and the resulting mixture was refluxed for 4 h to yield a red coloured solution. The resulting mixture was filtered and kept undisturbed in a beaker for few days. After two weeks, the solvent was evaporated and few red coloured block-shaped crystals were deposited on the wall of the beaker. Yield: 0.122 g (65%).

Microanalytical data for C₁₉H₁₆ClNO₃PdS (C1): Anal. Calc. (%):C, 47.52; H, 3.36; N, 2.92.

Found (%):C, 47.51; H, 3.31; N, 2.89. IR data (KBr disc) (cm⁻¹): 2922 ν(CH), 1716 ν(C=N).

¹H NMR (300 MHz, CDCl₃): δ 1.49 (-CH₃, t, J = 6 Hz, 2H), 2.40 (-CH₃, s, 3H), 3.05-3.44 (-CH₂, m, 2H), 6.06 (=C-H, s, 1H), 7.08-7.60 (ArH, 6H), 9.48 (CH=N-, s, 1H). λ_{max} (ε, M⁻¹ cm⁻¹) in acetonitrile: 224 (15616), 272 (5578), 336 (11995), 355 (sh.), 430 (sh.), 460 (2225).

HRMS: calculated for C₁₉H₁₆NO₃PdS [M-Cl]⁺ (m/z): 443.9886; found: 443.9882.

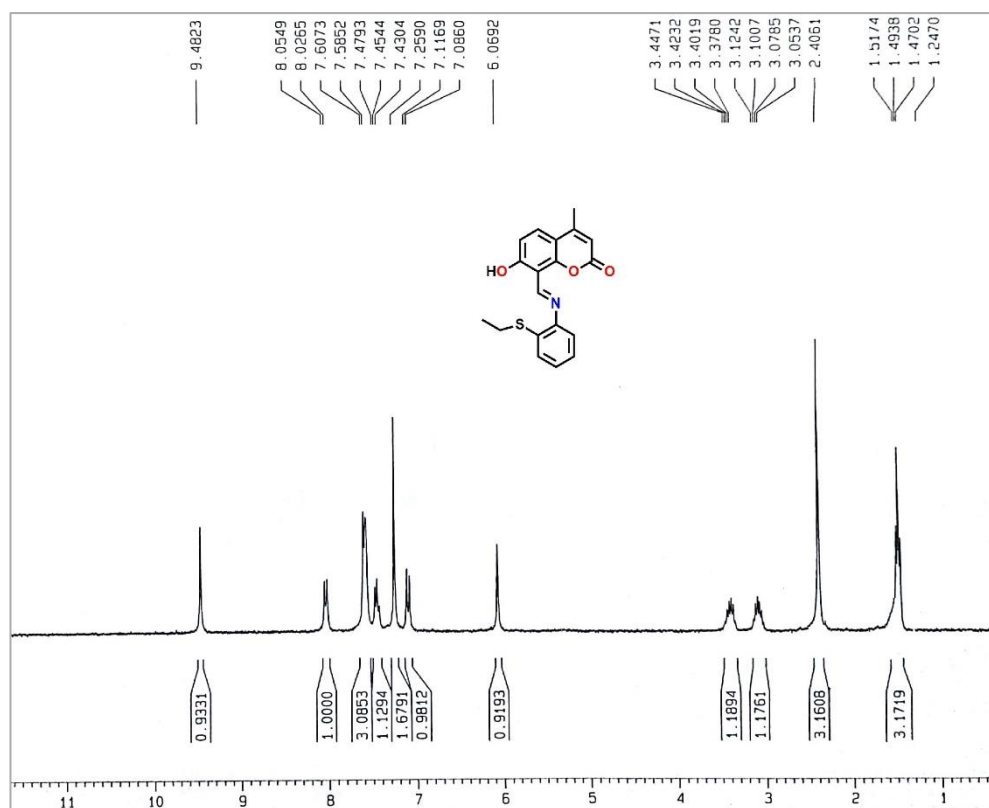


Fig.VII.7. ¹H NMR spectrum of [Pd(L¹)Cl] in CDCl₃

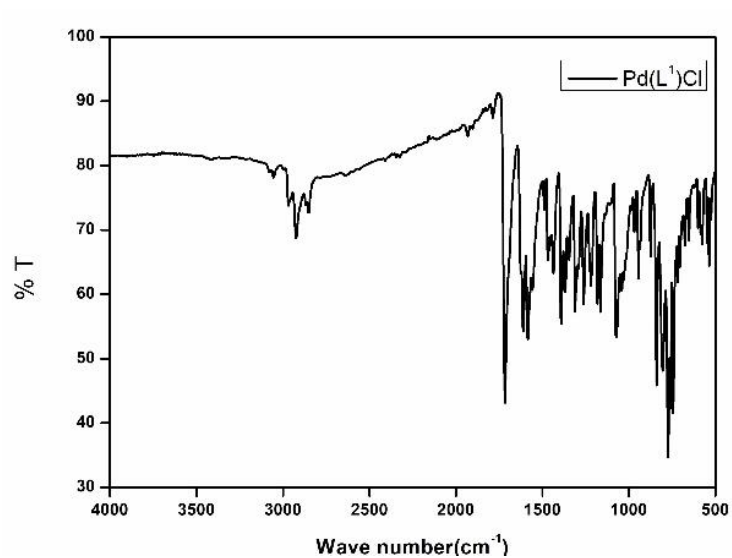


Fig.VII.8. IR spectrum of [Pd(L¹)Cl] (KBr disk)

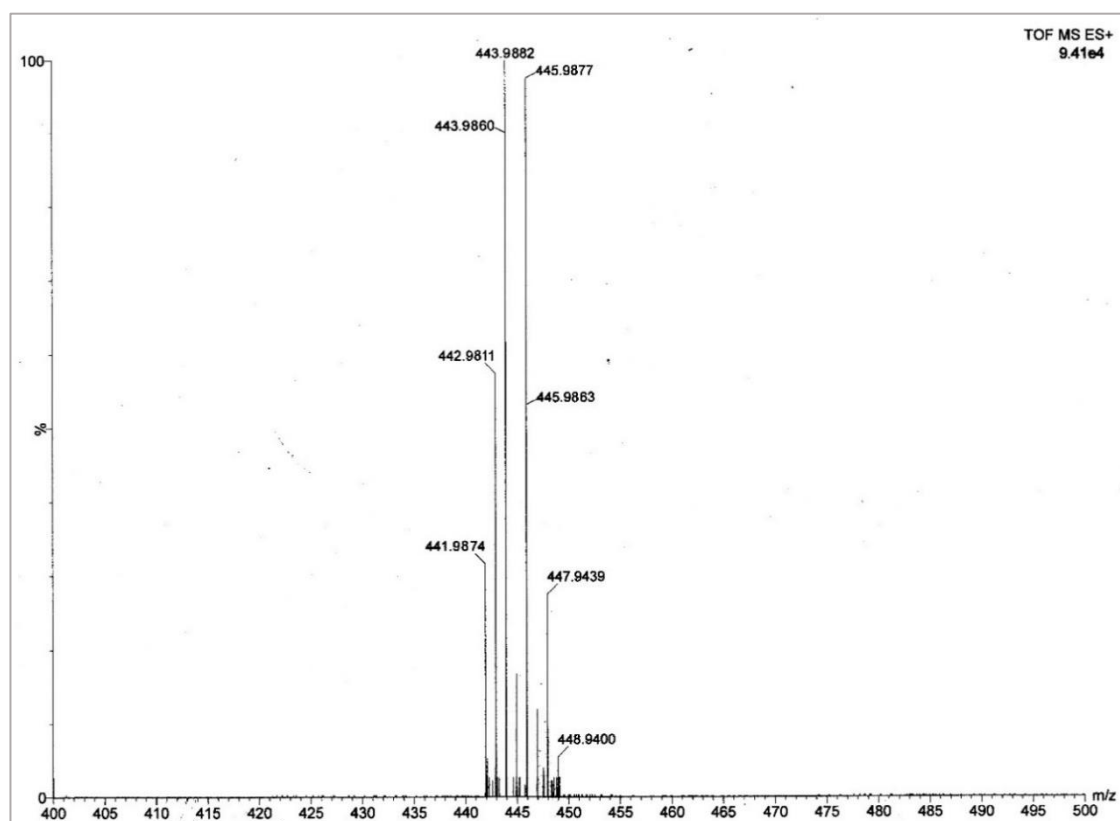


Fig.VII.9. HRMS spectrum of [Pd(L¹)Cl] in acetonitrile

VII.2.3.4. Synthesis of [Pd(L²)Cl] (C2)

The synthesis of palladium compound C2 followed the same steps as that of complex C1.

Yield: 0.126 g (69%).

Microanalytical data for C₁₈H₁₄ClNO₃PdS (C2): Anal. Calc. (%): C, 46.37; H, 3.03; N, 3.00.

Found (%): C, 46.35; H, 3.01; N, 3.01. IR data (KBr disc) (cm⁻¹): 3039 ν(CH), 1712 ν(C=N).

¹H NMR (300 MHz, CDCl₃): δ 1.54 (-CH₃, t, J = 6 Hz, 3H), 3.04-3.44 (-CH₂, m, 2H), 6.91-

8.34(ArH, 8H), 9.20 (CH=N-, s, 1H). λ_{max}(ε, M⁻¹ cm⁻¹) in acetonitrile: 212 (12073), 278

(4790), 346 (1872), 401 (sh.), 427 (4527), 452 (sh.). HRMS: calculated for C₁₈H₁₄NO₃PdS

[M-Cl]⁺ (m/z): 429.9729; found: 429.9726.

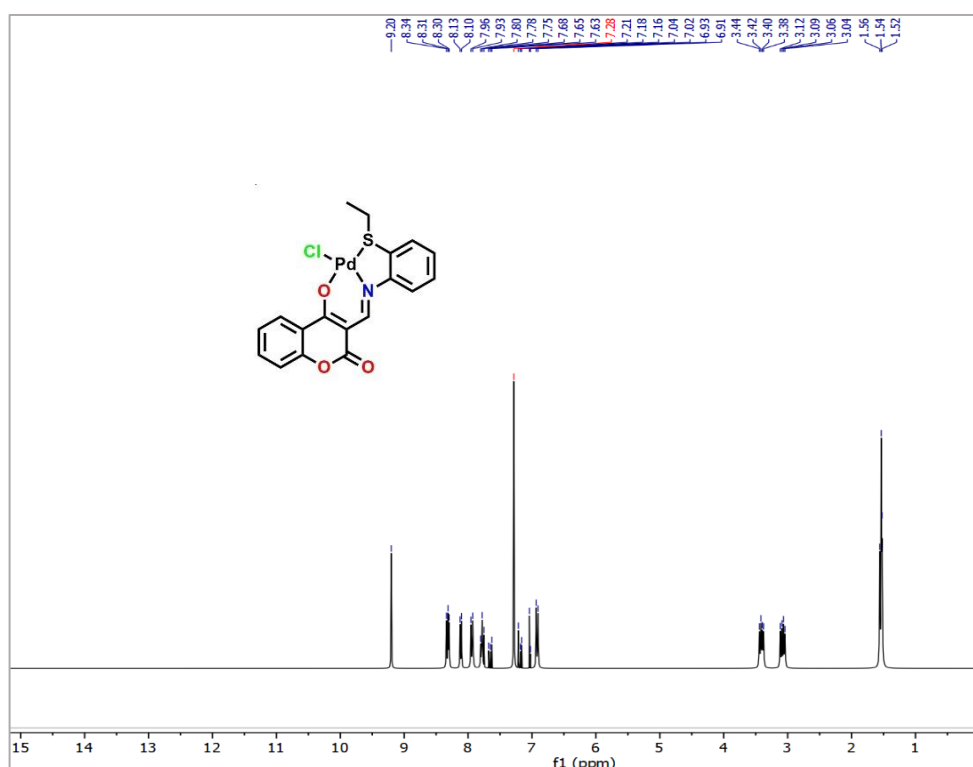


Fig.VII.10. ¹H NMR spectrum of [Pd(L²)Cl] in CDCl₃

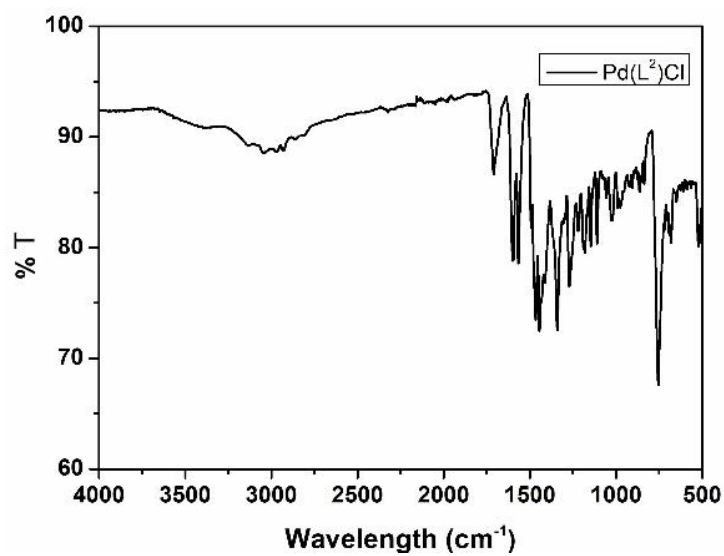


Fig.VII.11. IR spectrum of [Pd(L²)Cl] (KBr disk)

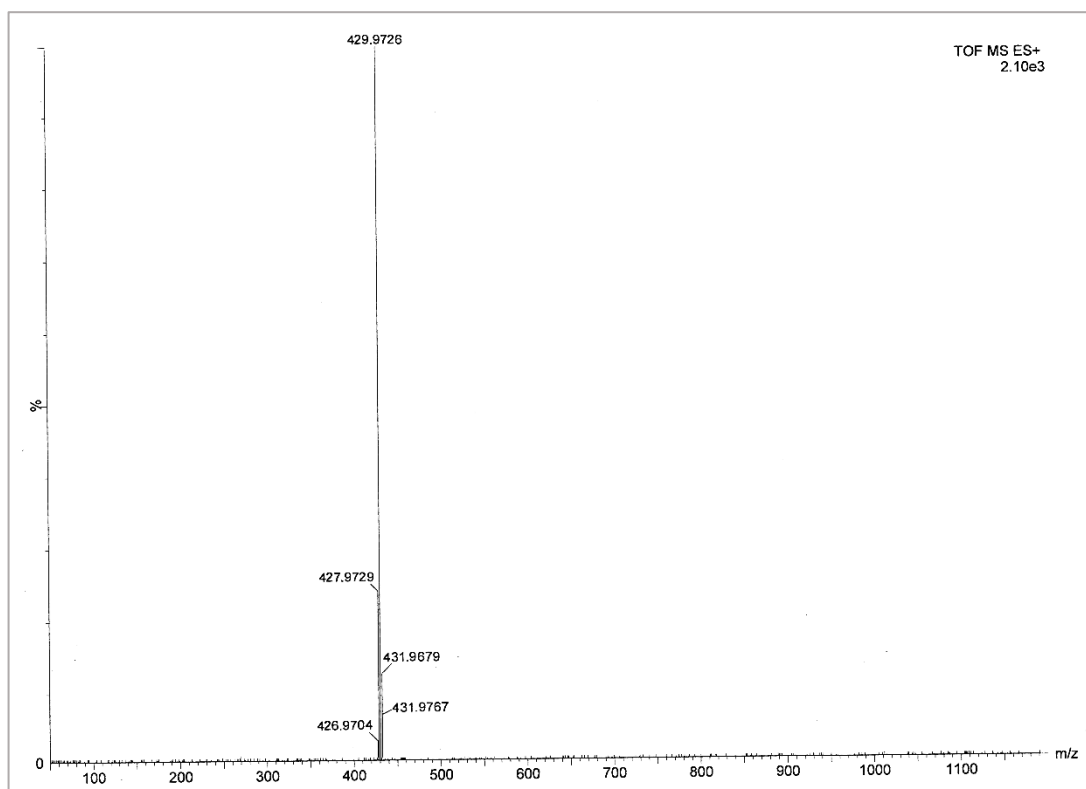


Fig.VII.12. HRMS spectrum of [Pd(L²)Cl] in acetonitrile

VII.2.4. DNA-binding interaction Studies

VII.2.4.1. UV-Vis titration

For UV-Vis titrations, a CT-DNA (2.19×10^{-3} M) solution in Tris-HCl/ NaCl buffer (at pH 7.4) and complex solution (1.0×10^{-4} M) in 1:10 acetonitrile/buffer were prepared. The UV-Vis spectra of the complexes were measured between 300 and 600 nm. CT-DNA solution was gradually added to it, stirred properly, and equilibrated for 4 min before collecting the spectra. Addition continued until saturation occurred. These spectral-titration results are important for determining the equilibrium binding constant (K_b) of the complex with CT-DNA. Eq. (1) was used to determine K_b (in M^{-1}) [24].

$$[\text{DNA}]/(\varepsilon_a - \varepsilon_f) = [\text{DNA}]/(\varepsilon_b - \varepsilon_f) + 1/K_b(\varepsilon_b - \varepsilon_f) \dots(1)$$

where [DNA] is the concentration of CT DNA in base pairs, the extinction coefficients ε_a , ε_f and ε_b correspond to $A_{\text{obs}}/[\text{complex}]$, free Pd(II) complex, and the extinction coefficient of the Pd(II) complex when it is in totally bound form, respectively. The plot of $[\text{DNA}]/(\varepsilon_a - \varepsilon_f)$ against [DNA] will produce slope $1/(\varepsilon_b - \varepsilon_f)$ and intercept $1/K_b(\varepsilon_b - \varepsilon_f)$; K_b is the ratio of slope to intercept.

VII.2.4.2. Competitive binding study with EB by fluorescence method

The ability of the synthesized palladium complexes (**C1/C2**) to dislocate EB from its EB-DNA complexes were studied by the fluorescence method. 10 μM EB and 10 μM CT DNA in Tris-HCl/NaCl buffer solution (pH 7.4) were mixed homogeneously to prepare the CT DNA-EB complexes which produced fluorescence emission at 608 nm when excited at 540 nm. Quenching of that emission was monitored with the subsequent addition of **C1** and **C2**.

VII.2.5. BSA interaction experiments

The binding interaction between BSA and Pd(II) complexes (**C1/C2**) were investigated by employing UV-Vis as well as fluorescence methods. A stock solution of BSA was prepared

using 500 mM phosphate buffer saline (PBS) at pH 7.4 and stored in the dark at 4°C for further use. BSA concentration was measured by taking absorbance at 280 nm in UV-Vis spectra [25] (molar extinction coefficient $66,400 \text{ dm}^3 \text{ mol}^{-1} \text{ cm}^{-1}$). The stock solution of **C1** and **C2** were prepared in DMSO medium and were suitably diluted with PBS whenever necessary. For recording UV-Vis spectra, BSA-concentration was kept constant ($10 \mu\text{M}$) while varying the concentration of complex added to it. In fluorescence experiment, tryptophan fluorescence of BSA was recorded in the range 290–450 nm at an excitation wavelength of 280 nm using a slit width of 5 nm. Quenching of emission intensity at ~ 336 nm for BSA were monitored with subsequent addition of metal complexes.

VII.2.6. Anti-cancer activity

VII.2.6.1. Cell Culture

Human breast cancer cell line MCF 7, triple negative breast cancer cell line MDA-MB-231 and WRL68 were bought from the National Center for Cell Science in Pune, India, and kept in MEM media containing Earle's salts (for MCF 7 and WRL68) and DMEM high glucose medium (for MDAMB231) with 10 % Fetal Bovine Serum (FBS) supplements (Gibco). All the cell lines were maintained in a 37°C humidified incubator with a 5 % CO₂ environment. Early passage numbers were used for all tests.

VII.2.6.2. Cell Viability Assay

3-(4, 5-Dimethylthiazol-2-yl)-2, 5-diphenyl tetrazolium bromide (MTT) was used to test the viability of HL¹, HL², C1, C2 and cis-platin in different cell lines [26]. A 96-well plate with 1×10^3 cells per well was initially treated for 24 hours at 37 °C with escalating concentrations of HL¹, HL², cisplatin ($12.5 \mu\text{M}$ to $200 \mu\text{M}$) and complex 1, complex 2 ($6.25 \mu\text{M}$ to $100 \mu\text{M}$). Each well was then filled with 25 μl of MTT solution (5 mg/ml in PBS) and incubated for 3 hours at 37°C. 100 μl of DMSO: Methanol was added to each well and the absorbance was

measured at 570 nm in a Spectramax i3X microtitre plate reader. The IC₅₀ value was determined using CompuSyn software.

VII.2.6.3. Colony Formation Assay

In six-well plates, approximately 500 cells of MCF 7 cell line were plated and then they were incubated at 37°C for 24 hours [27]. The cells were then exposed to HL¹, HL², C1 and C2. This was followed by washing with 1X PBS and fixing with methanol. The generated colonies were stained with crystal violet for 15 minutes. Colonies, defined as more than 50 cells, were counted using Olympus CKX41, an inverted bright field microscope with a 4X objective magnification.

VI.2.6.4. Detection of DNA fragmentation by Hoechst staining

MCF 7 cells were treated with HL¹, HL², C1 and C2 for 24 hours and then Hoechst 33258 (Sigma) (final concentration 2.5 µg/ml) was added to the cells and incubated at RT under dark conditions for 30 minutes [28]. Then the cells were visualised using a fluorescence microscope and imaged using CellSens software.

VI.2.6.5. Detection of apoptosis by AO/EtBr staining

MCF 7 cells were cultured in a six well plate (3 x 10⁴ cells/well) and treated with HL¹, HL², C1 and C2 for 24 hours. Subsequently, the cells were washed with PBS and fixed in a methanol: glacial acetic acid (3:1) solution for 30 mins at 4°C. The cells were washed again in PBS and subjected to 1:1 AO/EtBr solution for 30 minutes at RT [29]. After another wash with PBS, the cells were viewed and imaged under a fluorescence microscope (Olympus).

VII.2.6.6. Statistical analysis

Each experiment was carried out in triplicate, and the typical data are shown as mean values with standard deviations. To assess the main differences between the control and each treated group, one-way analysis of variance (ANOVA) and post hoc comparisons was done with the

use of the Turkey test. P value of 0.05 or less was regarded as statistically significant. The software used for analysis of all the tests was Graph Pad Prism 8.0.1.

VII.2.7. Computational method

For a theoretical explanation, we have performed the computational data analysis adopting DFT method, which is incorporated with the conductor-like polarizable continuum model (CPCM). In this study, "Becke, 3-parameter, Lee–Yang–Parr" the hybrid correlation function [30,31] are also utilized. To get the fully optimized geometry of **C1** and **C2**, we have taken 6-31+G(d) basis set for C, H, N, O, S and Cl atom, and for Pd atom, we used LanL2DZ basis set [33-35]. The absorption spectrum of **C1** and **C2** were also calculated in acetonitrile medium using the time-dependent DFT (TD-DFT) method [37-39] associated with the CPCM [40-42] using the same basis set. All the related calculations were made applying Gaussian 09 package [32]. The percentage of contributions of different groups to the molecular orbital was calculated using the Gauss Sum program [36].

VII.2.8. Crystal structure determination and refinement

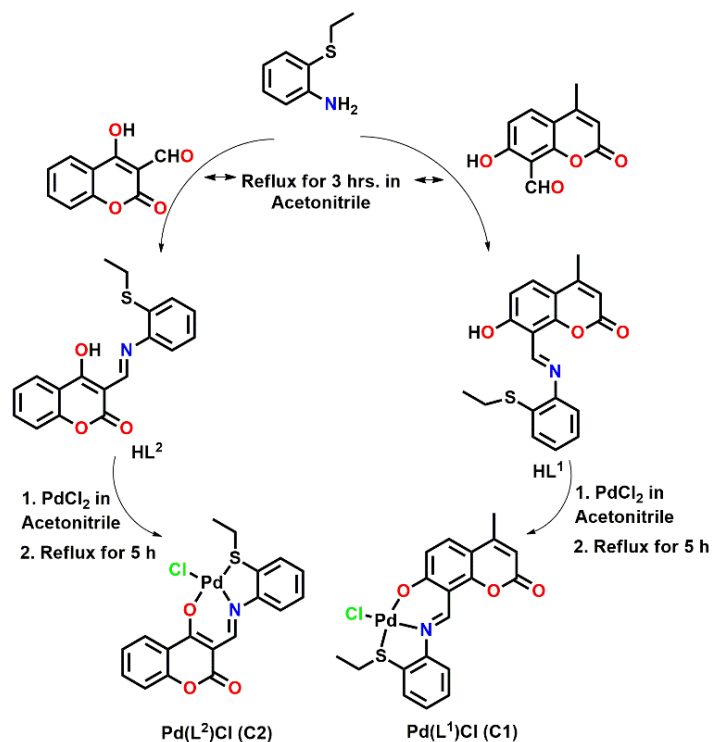
Best quality single crystals of the complexes were collected from the beaker and sorted under microscope for measurement of single crystal XRD. X-ray data were collected on Bruker AXS D8 Quest CMOS diffractometer using graphite monochromated Mo K α radiation ($\lambda = 0.71073 \text{ \AA}$) at 293 K. Reflection data were collected applying the ω scan technique. The collected frames were reduced using SAINT program. Absorption correction was done by multi-scan method using the SADABS absorption correction program. The structures were solved by direct method and refined using the SHELXTL program [43,44] by full-matrix least-squares based on F^2 . All the hydrogen atoms belonging to carbon atoms were fixed in their geometrically idealized positions. In Table VII.1, Crystallographic data and experimental details are summarized.

Table VII.1. Crystal data and details of the structure determination of **C1** and **C2**

	[Pd(L ¹)Cl] (C1)	[Pd(L ²)Cl] (C2)
Formula	C ₁₉ H ₁₆ ClNO ₃ PdS	C ₁₈ H ₁₄ ClNO ₃ PdS
Formula Weight	480.23	466.21
Crystal System	<i>Monoclinic</i>	<i>Triclinic</i>
Space group	<i>C 2/c</i>	<i>P -1</i>
<i>a</i> (Å)	22.9426(8)	9.9343(7)
<i>b</i> (Å)	10.5289(3)	10.2432(7)
<i>c</i> (Å)	17.5266(5)	10.3563(7)
α, β, γ (°)	90, 113.621(2), 90	83.302(2), 68.686(2), 62.332(2)
<i>V</i> (Å ³)	3879.0(2)	867.77(11)
<i>Z</i>	4	2
ρ (calc) (g/cm ³)	1.645	1.784
μ (Mo Ka) (mm ⁻¹)	1.220	1.360
<i>F</i> (000)	1920	464
Crystal Size (mm)	0.09 × 0.08 × 0.06	0.12 × 0.11 × 0.09
<i>T</i> (K)	293(2)	293(2)
Radiation wavelength (Å)	0.71073	0.71073
θ (Min-Max) (°)	2.163- 27.000	2.989- 27.522
<i>hkl</i> range	-29 to 27, -12 to 13 and -19 to 22	-12 to 12; -13 to 13 and -13 to 13
Total, Unique Data, <i>R</i> (int)	16288, 3141, 0.0303	30183, 3977, 0.0246
Observed data (<i>I</i> > 2 σ (<i>I</i>))	4199	3675
<i>N</i> ref, <i>N</i> par	4199, 235	3977, 226
<i>R</i> ^a , <i>wR</i> ₂ ^b , <i>S</i> ^c	0.0451, 0.1038, 0.988	0.0239, 0.0589, 1.062
Residual Density (e/Å ³)	-0.876 and 0.881	-0.451 and 0.624

VII.3. Results and discussion

The Pd(II) complexes, [Pd(L¹)Cl] (**C1**) and [Pd(L²)Cl] (**C2**) were synthesized by the reaction of PdCl₂ with HL¹ and HL² in 1:1 mole ratio respectively under refluxing condition in acetonitrile (scheme VII.1). Ligands were synthesized following the reported method [45]. Both the ligands (HL¹/HL²) as well as complexes (**C1**/**C2**) were thoroughly characterized by several spectroscopic techniques. The geometries of the complexes were confirmed by single crystal X-ray crystallography method.



Scheme VII.1: Synthesis of palladium(II) complexes, $[\text{Pd(L}^1\text{)Cl}]$ (**C1**) and $[\text{Pd(L}^2\text{)Cl}]$ (**C2**)

VII.3.1. Spectral characterization

IR spectrum of HL^1 displays intense sharp peak at 2919 cm^{-1} and 1710 cm^{-1} corresponds to $\nu(\text{C-H})$ stretching and $\nu(\text{C=N})$ stretching respectively (Fig.VII.2). Whereas in case of HL^2 , sharp peak at 2929 cm^{-1} and 1708 cm^{-1} are responsible for $\nu(\text{C-H})$ stretching and $\nu(\text{C=N})$ stretching respectively (Fig.VII.4). The C-H stretching frequencies appear at 2922 cm^{-1} and 3039 cm^{-1} for **C1** and **C2**, respectively (Fig.VII.6). The imine stretching frequencies appear at 1716 cm^{-1} and 1712 cm^{-1} due to complex formation for **C1** and **C2**, respectively (Fig.VII.8). $^1\text{HNMR}$ spectra of HL^1 , HL^2 , **C1** and **C2** were recorded in CDCl_3 solvent. For HL^1 and HL^2 , phenolic $-\text{OH}$ peaks appear as singlet at 14.93 and 15.77 ppm respectively whereas imine hydrogen (CH=N-) peaks appear as singlet at 9.33 and 8.14 ppm respectively (Fig.VII.1 and 4). Aromatic protons of HL^1 and HL^2 appear in between 6.94 to 7.61 ppm. Imine protons (CH=N-) of the complexes **C1** and **C2** appear as singlet at 9.48 and 9.20 ppm respectively (Fig.VII.7 and 10). The disappearance of the phenolic $-\text{OH}$ proton signal from ligands to

complexes confirms the chelation of O atom to Pd atom in both cases. Mass spectra of HL¹ and HL² show m/z peak at 340.1003 and 326.0847 (Fig.VII.3 and 6) corresponding to [M+H]⁺. For complexes C1 and C2, the m/z peaks appear at 443.9882 and 429.9726 (Fig.VII.9 and 12) respectively corresponding to [M-Cl]⁺. The absorption spectra of ligands (HL¹ and HL²) and complexes (C1 and C2) were taken in acetonitrile. HL¹ exhibits one low energy peak at 365 nm and one intense peak at 312 along with intense high energy peak at 212 nm whereas its Pd(II) complex C1 exhibits moderately intense low energy broad band at 460 nm and and intense low energy band at 336 nm along with a high energy band at 224 nm. For HL², a broad moderately intense low energy peak appears at 340 nm, along with high energy bands appear at 253 nm and 222 nm. The complex C2 exhibits low-energy broad bands at 427 nm and 346 nm along with two shoulder bands at 452 nm and 401 nm. High energy peaks appear at 278 nm and 212 nm (Fig. VII.13).

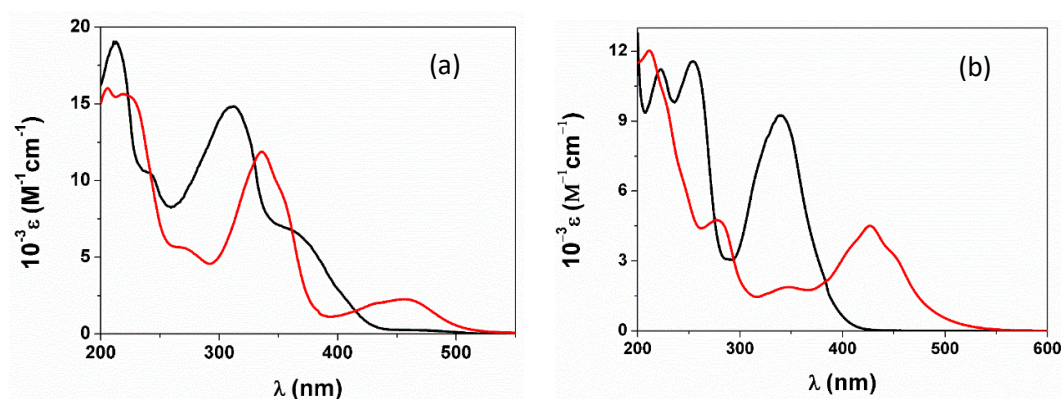


Fig.VII.13. UV-Vis spectra of (a) HL¹ (-) and [Pd(L¹)Cl](-) (b) HL² (-) and [Pd(L²)Cl](-) in acetonitrile

VII.3.2. Crystallographic study

Actual chelating mode of ligands with their respective complexes were confirmed by single crystal X-ray diffraction method. Complex C1 crystallizes in monoclinic crystal system with C 2/c space group whereas complex C2 crystallizes in triclinic crystal system with P21/c space group. In the complexes both the Ligands HL¹ and HL² act as tridentate chelators

containing O,N,S donor atoms. In complex **C1**, Pd-metal is coordinated with HL¹ through phenolic oxygen atom (O1), imine nitrogen atom (N1) and thioether sulfur atom (S1) via formation one five-membered (Pd1-N2-C12-C17-S1) and one six-membered (Pd1-N1-C11-C2-C1-O1) chelate ring with chelate bite angles \angle N1-Pd1-S1 and \angle N1-Pd1-O1, 87.95(14)° and 94.17(17)° respectively. Similarly, in **C2** chelate bite angles \angle N1-Pd1-S1 and \angle N1-Pd1-O1, 87.47(5)° and 93.83(7)° respectively significantly deviates from 90° suggest the distorted square planar geometry. The selected bond distances and bond angles of the complexes are given in Table VII.2. Pd1-N1(imine) bond distances for the complexes are found to be 1.993(4) Å and 1.993(18) Å respectively for **C1** and **C2** and comparable to the literature values [46]. Pd1-C11 bond distance of both the complexes **C1** and **C2** are found to be 2.291(12) Å and 2.298(7) Å respectively. The ORTEP plots of the complexes along with atom numbering scheme are shown in Fig.VII.14.

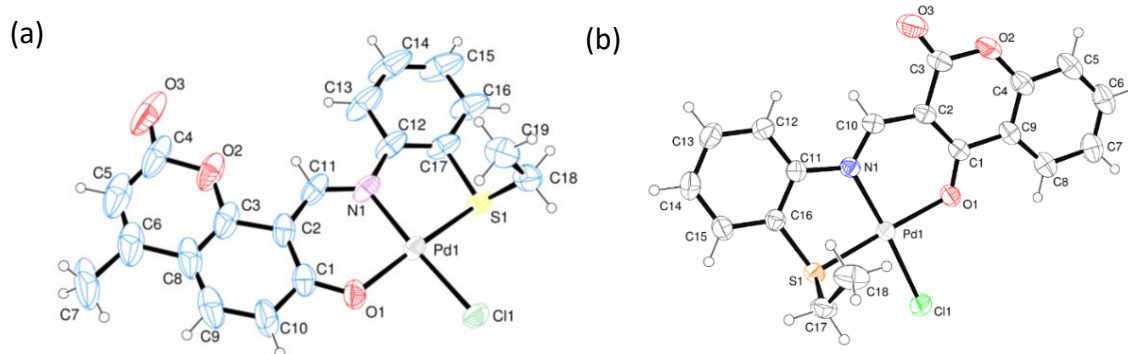


Fig.VII.14. ORTEP plot of (a) [Pd(L¹)Cl](C1) and (b) [Pd(L¹)Cl](C2) with 35% ellipsoidal probability

VII.3.3. Computational study

Geometries of both the ligands as well as complexes were optimized by DFT/B3LYP method. The optimized bond parameters, bond angles and bond distances of the complexes are well corroborated with X-ray data which are given in Table VII.2. Energy and compositions of selected molecular orbitals are given in Table VII.3. Contour plots of

selected molecular orbitals of HL¹ and HL² are given in Fig.VII.15-16 and whereas for the complexes the contour plots are given in Fig.VII.17-18. The higher energy occupied molecular orbital (HOMO) for both the complexes have 88-66% ligand contribution along with reduced contribution (5-19%) of Pd(dπ). HOMO-2 has mixed Pd(dπ) (16%) and Cl(pπ) (79-80%) character. HOMO-3 and HOMO-7 exclusively have ligand (64-94%) character. The low-lying virtual orbital, LUMO has ligand character (90-72%) whereas LUMO+1 predominantly has Pd(dπ) (41-28%) and 46-64 % ligand character for C1 and C2 respectively.

TDDFT calculation was executed on the optimized geometries of the complexes to gain more knowledge about the electronic transitions. For **C1**, the low energy transition at 442 nm (HOMO-1→LUMO transition) corresponds to the experimental band at 460 nm having mixed ILCT (Intra ligand charge transfer), metal to ligand charge transfer (MLCT) and XLCT (halogen to ligand charge transfer) character. The experimentally observed shoulder band 430 nm is well supported with the calculated transition at 418 nm (HOMO-2→LUMO transition) having mixed metal to ligand charge transfer (MLCT) and XLCT (halogen to ligand charge transfer) character. An experimentally observed shoulder peak at 355 nm corresponds to XMCT (halogen to metal charge transfer). High-energy strong bands at 336 nm, 272 nm, and 224 nm correspond to the ILCT transition. For **C2**, the low energy experimental band at 427 nm corresponds to the (HOMO-2→LUMO) transition at 440 nm has mixed XLCT and MLCT character. The shoulder peak at 452 nm correspond to HOMO→LUMO transition having mixed ILCT and MLCT character. The band at 346 nm corresponds to mixed ILCT and MLCT character (Table VII.4). The bands at 278 nm (HOMO-7→LUMO transition) and 212 nm (HOMO-5→LUMO+2 transition) correspond to ILCT character.

Table VII.2. Selected bond distances (Å) and angles (°) of **C1** and **C2**

Bonds(Å)	[Pd(L ¹)Cl] (C1)		[Pd(L ²)Cl](C2)	
	X-ray	Calc.	X-ray	Calc.
Pd1 – N1	1.993(4)	2.040	1.993(18)	2.039
Pd1 – O1	2.000(3)	2.020	2.013(16)	2.036
Pd1 – S1	2.221(13)	2.293	2.222(6)	2.287
Pd1 – Cl1	2.291(12)	2.334	2.298(7)	2.335
O1 – C1	1.283(6)	1.286	1.272(3)	1.273
S1- C16	-	-	1.771(2)	1.798
S1- C17	1.775(5)	1.798	1.816(3)	1.857
Angles (°)				
N1 – Pd1 – O1	94.17(17)	93.311	93.83(7)	93.238
N1 – Pd1 – S1	87.95(14)	86.577	87.47(5)	86.557
O1 – Pd1 – S1	176.86(12)	177.496	177.44(5)	177.425
N1- Pd1- Cl1	176.69(15)	176.195	176.04(5)	176.394
O1- Pd1- Cl1	89.03(10)	90.182	90.08(5)	89.996
S1- Pd1- Cl1	88.89(5)	89.997	88.64(3)	90.281
C(1)-O(1)-Pd(1)	125.9(4)	125.787	124.20(15)	125.398
C(11)- N(1)- Pd(1)	121.8(4)	121.944	117.09(14)	117.744

Table VII.3. Energy and compositions (%) of selected molecular orbitals of **C1** and **C2**

MO	C1				C2			
	E (eV)	% of composition			E (eV)	% of composition		
		Pd	L ¹	Cl		Pd	L ²	Cl
LUMO+5	0	91	9	0	-0.03	93	7	0
LUMO+4	-0.51	1	99	0	-0.34	2	98	0
LUMO+3	-1.37	2	97	0	-1.08	1	99	0
LUMO+2	-1.59	1	99	0	-1.38	3	97	0
LUMO+1	-2.19	41	46	12	-2.3	28	64	8
LUMO	-2.49	8	90	2	-2.46	22	72	6
HOMO	-5.76	7	88	5	-6.1	16	66	19
HOMO-1	-6.3	22	37	41	-6.63	8	68	25
HOMO-2	-6.53	16	5	79	-6.67	16	5	80
HOMO-3	-6.81	8	66	26	-6.79	8	64	28
HOMO-4	-6.86	73	17	9	-6.98	77	16	6
HOMO-5	-7.27	34	63	3	-7.18	29	70	1
HOMO-6	-7.5	10	88	3	-7.48	4	94	3
HOMO-7	-7.58	8	87	5	-7.59	3	94	2
HOMO-8	-7.77	16	65	18	-7.79	9	89	1
HOMO-9	-7.88	12	87	0	-7.9	22	48	30

Table VII.4. Vertical electronic transitions of HL¹, HL², C1 and C2 calculated by TDDFT/B3LYP/CPCM method

Comps.	λ (nm)	E (eV)	Osc. Strength (f)	Key excitations	Character ^a	$\lambda_{\text{expt.}}$ (nm) (ϵ , M ⁻¹ cm ⁻¹)
HL ¹	382.6	3.2408	0.1580	(82%)HOMO→LUMO	$\pi/n \rightarrow \pi^*$	365 (6475)
	358.8	3.4556	0.1139	(72%)HOMO-1→LUMO	$\pi/n \rightarrow \pi^*$	
	328.1	3.7795	0.4242	(75%)HOMO-2→LUMO	$\pi \rightarrow \pi^*$	312 (14894)
	245.7	5.0468	0.0794	(75%)HOMO-4→LUMO+1	$\pi \rightarrow \pi^*$	240 (10394)
	210.7	5.8851	0.2911	(50%)HOMO-3→LUMO+2 (27%)HOMO-2→LUMO+4	$\pi \rightarrow \pi^*$	212 (19055)
HL ²	433.8	2.8579	0.0411	(98%)HOMO→LUMO	$\pi/n \rightarrow \pi^*$	
	351.6	3.5259	0.4353	(97%)HOMO-1→LUMO	$\pi \rightarrow \pi^*$	340 (9311)
	306.4	4.0465	0.1292	(64%)HOMO-1→LUMO+1 (24%)HOMO-3→LUMO	$\pi \rightarrow \pi^*$	
	271.2	4.5714	0.1940	(77%)HOMO-4→LUMO	$\pi \rightarrow \pi^*$	253 (11641)
	268.8	4.6128	0.0996	(44%)HOMO→LUMO+2 (34%)HOMO-1→LUMO+1	$\pi \rightarrow \pi^*$	
	238.0	5.2084	0.1442	(72%)HOMO-2→LUMO+1	$\pi \rightarrow \pi^*$	222 (11271)
	232.4	5.3340	0.1493	(42%)HOMO-3→LUMO+1 (31%)HOMO-1→LUMO+3	$\pi \rightarrow \pi^*$	
C1	504.0	2.4599	0.0080	(75%)HOMO→LUMO	$\pi(L) \rightarrow \pi^*(L)$ (ILCT)	
	442.6	2.8011	0.0459	(77%)HOMO-1→LUMO	$\pi(L)/p\pi(Cl)/d\pi(Pd) \rightarrow \pi^*(L)$ (ILCT/XLCT/MLCT)	460 (2225)
	418.3	2.9637	0.0412	(72%)HOMO-2→LUMO	$p\pi(Cl)/d\pi(Pd) \rightarrow \pi^*(L)$ (XLCT/MLCT)	430 (sh.)
	351.4	3.5280	0.2268	(66%)HOMO-2→LUMO+1	$p\pi(Cl) \rightarrow d\pi(Pd)$ (XMCT)	355 (sh.)
	324.5	3.8210	0.5785	(91%)HOMO→LUMO+2	$\pi(L) \rightarrow \pi^*(L)$ (ILCT)	336 (11995)
	275.1	4.5060	0.0602	(42%)HOMO-7→LUMO (37%)HOMO-6→LUMO	$\pi(L) \rightarrow \pi^*(L)$ (ILCT)	272 (5578)
	234.6	5.2861	0.1344	(66%)HOMO-6→LUMO+2	$\pi(L) \rightarrow \pi^*(L)$ (ILCT)	224 (15616)
C2	486.9	2.5466	0.0041	(77%)HOMO→LUMO	$\pi(L)/d\pi(Pd) \rightarrow \pi^*(L)$ (ILCT/MLCT)	452 (sh.)
	440.2	2.8167	0.0165	(77%)HOMO-2→LUMO	$p\pi(Cl)/d\pi(Pd) \rightarrow \pi^*(L)$ (XLCT/MLCT)	427 (4527)
	393.4	3.1516	0.0416	(37%)HOMO-3→LUMO (32%)HOMO→LUMO+1	$\pi(L)/p\pi(Cl) \rightarrow \pi^*(L)$ (ILCT/XLCT)	401 (sh.)
	377.8	3.2813	0.1024	(78%)HOMO-5→LUMO	$\pi(L)/d\pi(Pd) \rightarrow \pi^*(L)$ (ILCT/MLCT)	346 (1872)
	301.9	4.1073	0.1114	(70%)HOMO-6→LUMO	$\pi(L) \rightarrow \pi^*(L)$ (ILCT)	
	270.5	4.5840	0.0786	(70%)HOMO-7→LUMO	$\pi(L) \rightarrow \pi^*(L)$ (ILCT)	278 (4790)
	221.7	5.5909	0.1957	(73%)HOMO-5→LUMO+2	$\pi(L) \rightarrow \pi^*(L)$ (ILCT)	212 (12073)

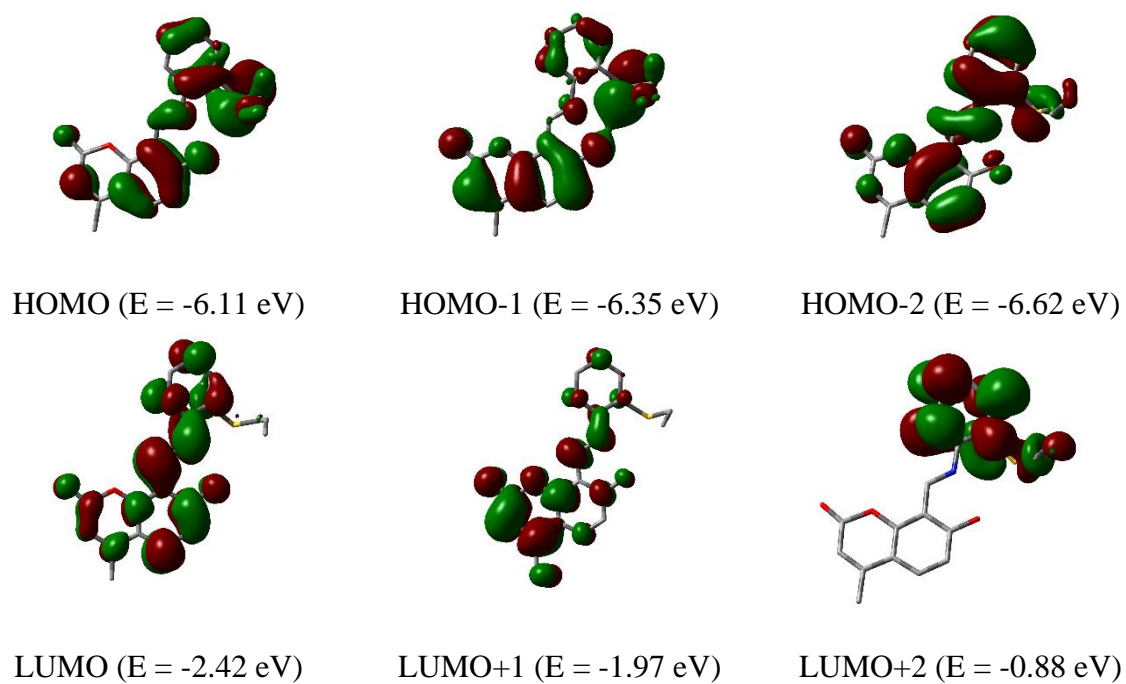


Fig.VII.15. Contour plots of some selected molecular orbital of HL¹

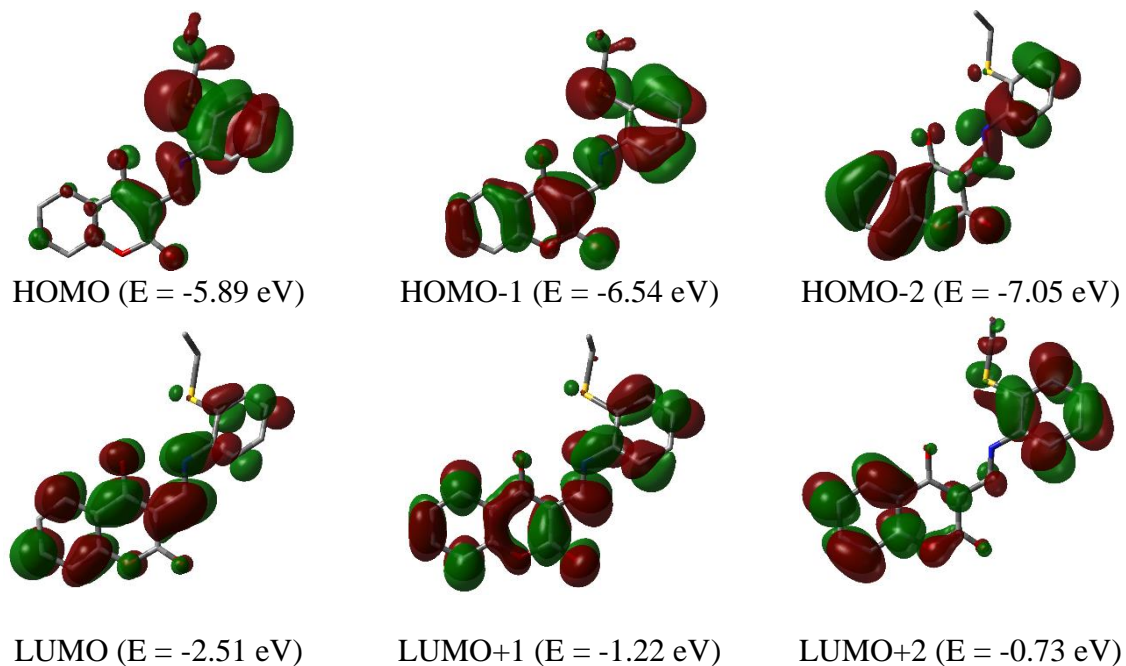


Fig.VII.16. Contour plots of some selected molecular orbital of HL²

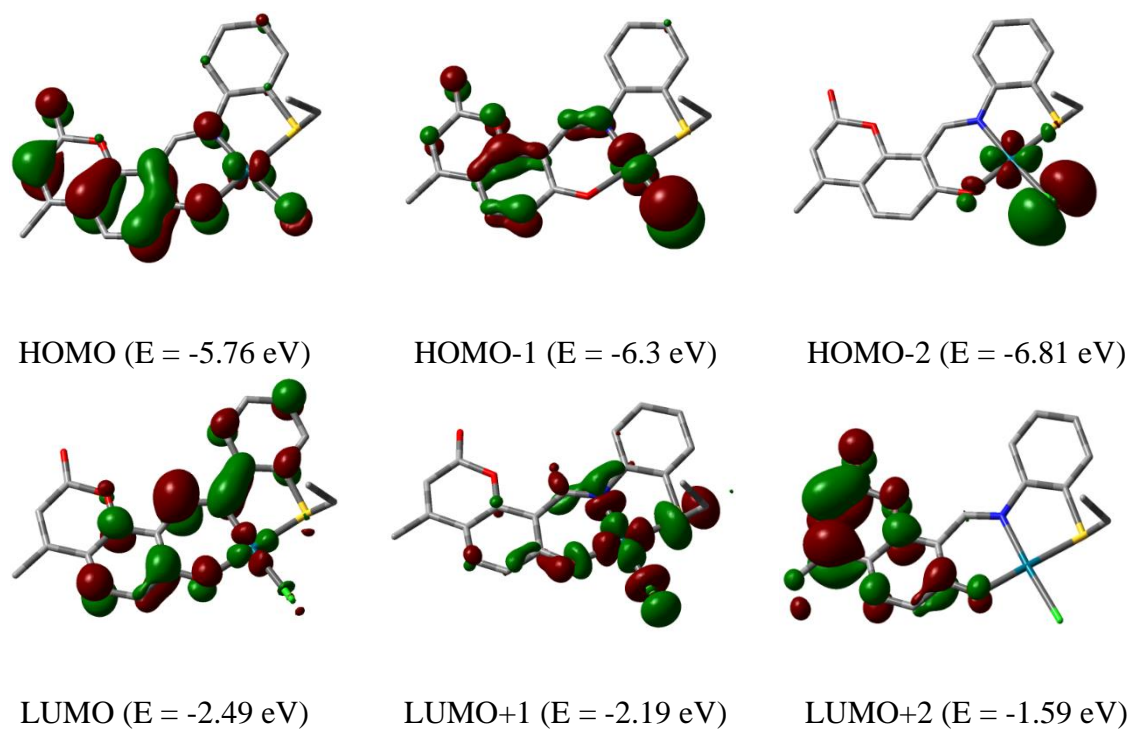


Fig.VII.17. Contour plots of some selected molecular orbital of $[\text{Pd}(\text{L}^1)\text{Cl}]$ (C1)

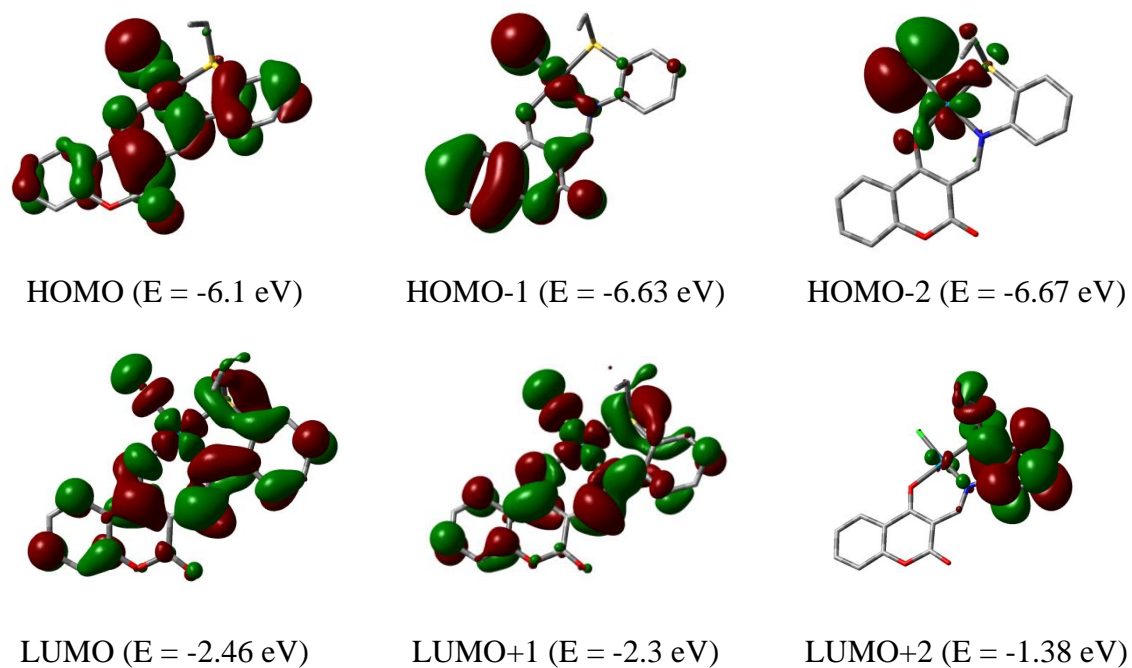


Fig.VII.18. Contour plots of some selected molecular orbital of $[\text{Pd}(\text{L}^2)\text{Cl}]$ (C2)

VII.3.4. DNA binding studies

The understanding of the mode of interactions with DNA is very crucial for developing of new anti-cancer drugs. At present, the spectroscopic methods are widely used to study the mode of interactions. These studies show that the drugs can interact to DNA covalently or by non-covalent interaction, groove binding or by electrostatic interactions [47,48]. Absorption and emission spectroscopies are widely used to interpret the mode of interactions of drug molecules with DNA [49].

VII.3.4.1. UV-Vis method

UV-Vis titration is a powerful method to assess how well palladium complexes interact to CT DNA [50]. Absorption spectra of the complexes C1 and C2 were taken in absence and presence of CT DNA. C1 exhibits a broad peak with two absorption maxima at 340 nm and 458 nm and C2 exhibits a sharp maxima peak at 430 nm. But upon subsequent addition of CT DNA, a hypochromic shift is observed in the absorption spectra for both the complexes (Fig. VII.19.a-b). The intrinsic binding constant (K_b) was evaluated to understand the affinity of the complexes towards CT DNA. The K_b value of the C1 and C2 are found to be $3.50 \times 10^5 \text{ M}^{-1}$ and $1.99 \times 10^5 \text{ M}^{-1}$ respectively which are comparable to the reported literature values [51,52].

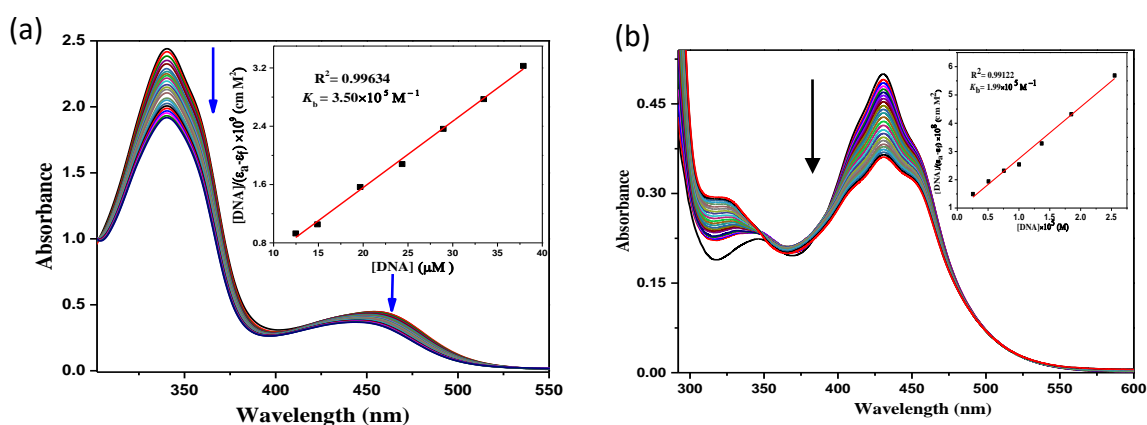


Fig.VII.19. Change in absorption spectra of complex **C1(a)** and **C2(b)** in Tris-HCl/NaCl buffer with the gradual addition of CT DNA. Inset: Plot of $[\text{DNA}]/(\epsilon_a - \epsilon_f)$ vs. $[\text{DNA}]$.

VII.3.4.2. Fluorescence method

There is no inherent fluorescence observed in CT DNA. The palladium complexes are also non-fluorescent in solution with or without CT DNA. But when ethidium bromide (EB), a typical intercalator, forms EB-CT DNA intercalating complex, there is a mammoth increase in fluorescence intensity of EB at 606 nm upon excitation at 540 nm [53]. Upon steady addition of Pd(II) complexes **C1** and **C2**, the fluorescence intensities are successively decreased due to the replacement of EB from its EB-CT DNA system (Fig. VII.20.a-b) [54]. The titration curves clearly demonstrate the competition between the complexes and EB for DNA binding sites. A linear Stern-Volmer equation (Eq. (2)) [55] accords well with the fluorescence quenching curve of the EB-CT DNA system for the complex.

$$I_0/I = 1 + K_{sv}[Q] \dots \dots \dots (2)$$

Where I and I_0 signify the fluorescence intensities of the EB-CT DNA system with and without the complex, respectively, K_{sv} is the Stern-Volmer quenching constant, and $[Q]$ is the molar concentration of the complex (quencher). K_{sv} values are obtained from the slopes of the plots and are determined to be $2.62 \times 10^5 \text{ M}^{-1}$ and $1.59 \times 10^5 \text{ M}^{-1}$ for the complex **C1** and **C2** respectively.

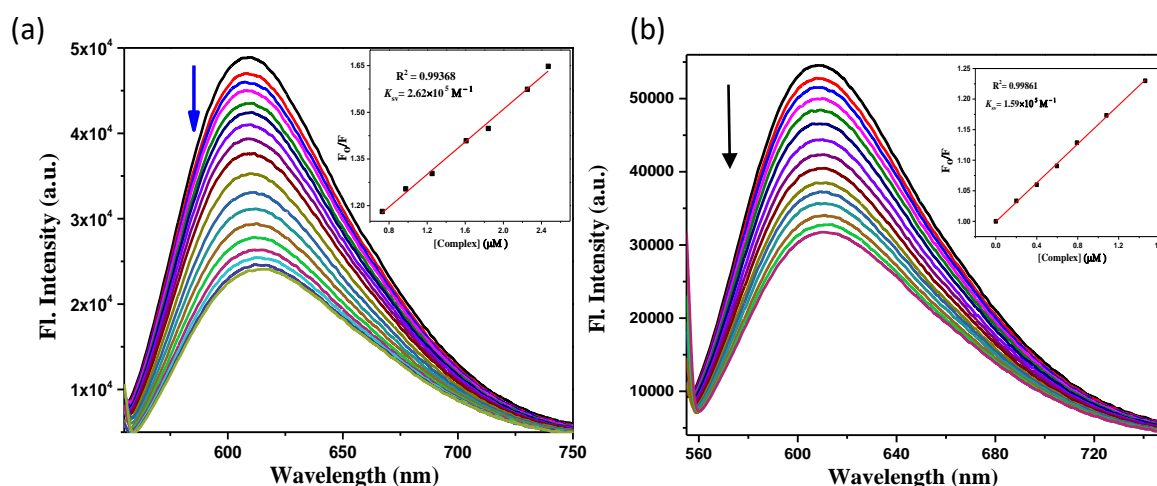


Fig.VII.20. Emission spectra ($\lambda_{ex} = 540 \text{ nm}$) of EB-CT DNA in presence of increasing concentrations of **C1** (a) and **C2** (b) Inset: Plots of emission intensity F_0/F vs. [complex].

VII.3.5. BSA binding studies

VII.3.5.1. UV-Vis method

Electronic absorption spectra of BSA (10 μM in PBS at pH 7.4) was recorded in the range of 200-500 nm in presence of different concentration of the complexes. BSA has a characteristic absorption peak at 280 nm. Repeated addition of 100 μL complex to the BSA solution causes a steady increase in 280 absorption intensity along with a bit of blue shift. This hypsochromic shift attributes to the ground-state alliance between the complexes and protein [56,57]. The apparent association constant (K_a) was calculated from the plot of $1/(A_{obs}-A_0)$ vs $1/[\text{complex}]$ (Fig.VII.21.a-b inset) adopting the following equation [58,59].

$$\frac{1}{A_{obs} - A_0} = \frac{1}{A_c - A_0} + \frac{1}{K_a(A_c - A_0)[\text{complex}]}$$

Where A_{obs} indicates the observed absorbance (at 280 nm) of the solution having various concentrations of the complex, A_0 and A_c denote BSA absorbance only and serum albumin with the complex. The calculated value of apparent association constant (K_a) for the complex C1 and C2 are $1.74 \times 10^5 \text{ M}^{-1}$ and $4.81 \times 10^5 \text{ M}^{-1}$ respectively which matches with the literature value of Pd-complexes [60-63].

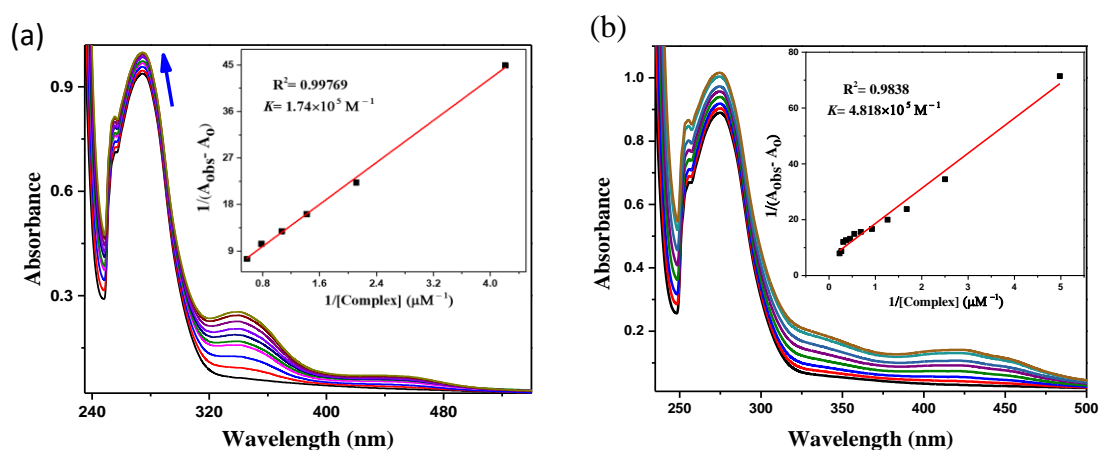


Fig.VII.21. Change of absorption spectra of BSA (10 μM aqueous solution) upon gradual addition of 100 μL complex [C1(a) and C2(b)] solution in DMSO at 300 K. Insets: $1/(A_{obs} - A_0)$ vs. $1/[\text{complex}]$ plots of BSA absorption titration.

VII. 3.5.2. Fluorescence method

The BSA-complex interactions were also studied by fluorescence spectral titration technique. Complex is non-fluorescent in DMSO solution. But upon excitation at 280 nm, an aqueous solution (10 μM , pH 7.4 PBS buffer) of BSA demonstrates a strong fluorescence at 336 nm. Now with subsequent addition of 100 μL complex to the BSA solution, fluorescence intensity of BSA at ~ 336 nm dramatically quenched (59.41 % and 58.83 % quenching). This hypochromicity in the spectra is mainly attributed due to the interaction of complexes with the protein. The Stern-Volmer quenching constant values (K_{sv}) for the complexes were calculated [64] and depicted in Table VII.5. The high K_{sv} ($1.54 \times 10^5 \text{ M}^{-1}$ and 3.89×10^5) value indicates that complexes exhibit good fluorescence quenching ability. To learn more of the quenching effect, the equilibrium binding constants (K_b) and number of binding sites (n) available for the complexes were also estimated from the graph of $\log [(F_0 - F)/F]$ versus $\log [\text{complex}]$ (Fig.VII.22.a-b inset) applying the Scatchard equation [65,66] below:

$$\log \frac{(F_0 - F)}{F} = \log K_b + n \log [\text{complex}]$$

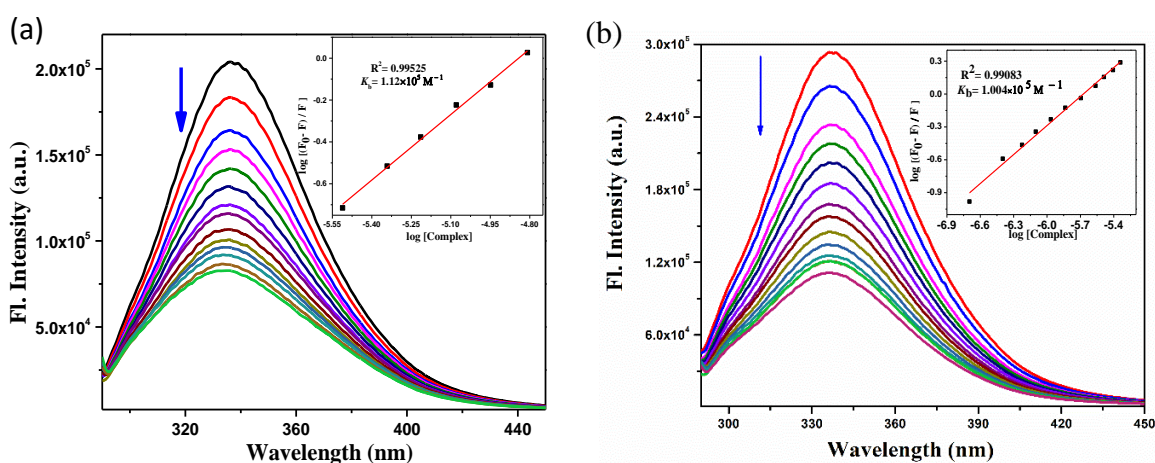


Fig.VII.22. Change of fluorescence spectra of BSA (10 μM) upon gradual addition of 100 μL complex [C1(a) and C2(b)] solution in DMSO at 300 K ($\lambda_{\text{ex}}=280$ nm, $\lambda_{\text{em}}=336$ nm). Insets: Scatchard plots of the BSA fluorescence titration.

Based on the plot, for the complex C1 and C2 calculated values of n for are 1.043 and 0.88 respectively and calculated values of K_b are $1.12 \times 10^5 \text{ M}^{-1}$ and $1.00 \times 10^5 \text{ M}^{-1}$ respectively which reflects the strong affinity of the complexes with the serum albumins.

Table VII.5. Stern-Volmer quenching constants (K_{sv}), apparent association constants (K_a), equilibrium binding constants (K_b), number of binding sites(n) in the interaction of C1 and C2 with DNA and BSA

System	DNA binding			BSA binding				
	UV method	Fluorescence method		UV method	Fluorescence method			
	$K_b (\text{M}^{-1})$	Hypo(%)	$K_{sv} (\text{M}^{-1})$	$K_a (\text{M}^{-1})$	Hypo(%)	$K_b (\text{M}^{-1})$	$K_{sv} (\text{M}^{-1})$	n
C1	3.50×10^5	51.18	2.62×10^5	1.74×10^5	59.41	1.12×10^5	1.54×10^5	1.043
C2	1.99×10^5	42.09	1.59×10^5	4.81×10^5	58.83	1.00×10^5	3.89×10^5	0.88

VII.3.6. Biological study

VII.3.6.1. Cytotoxicity of $[\text{Pd}(\text{L}^1)\text{Cl}]$ and $[\text{Pd}(\text{L}^2)\text{Cl}]$ in different cancer cells

The table below displays the IC_{50} values for ligands as well as complexes across all cell lines tested. After 24 hours, it was shown that complex C1 ($\text{IC}_{50} = 7.13 \mu\text{M}$) and complex C2 ($\text{IC}_{50} = 11.88 \mu\text{M}$) were the most potent inhibitors of MCF-7 cell growth and proliferation compared to other cell lines. Therefore, MCF-7 cells were utilized in subsequent investigations. When tested on the normal hepatic cell line WRL68, complex C1 and C2 showed an extremely high IC_{50} value ($>200 \text{ M}$). This suggests that complex C1 and complex C2 are very toxic to cancer cells while having little effect on normal cells.

Table VII.6. IC₅₀ values of HL¹, HL², C1 and C2 towards MCF 7, MDA MB 231 and WRL 68 cell lines

	MCF 7	MDA-MB-231	WRL 68
Compounds	IC₅₀ of compounds (μM)		
HL¹	162.36±2.5	>200	>200
HL²	171.15±3.04	>200	>200
C1	7.13±2.08	56.97±3.48	>200
C2	11.88±1.51	43.25±3.65	>200
cisplatin	15.15±2.5	92.21±2.2	>200

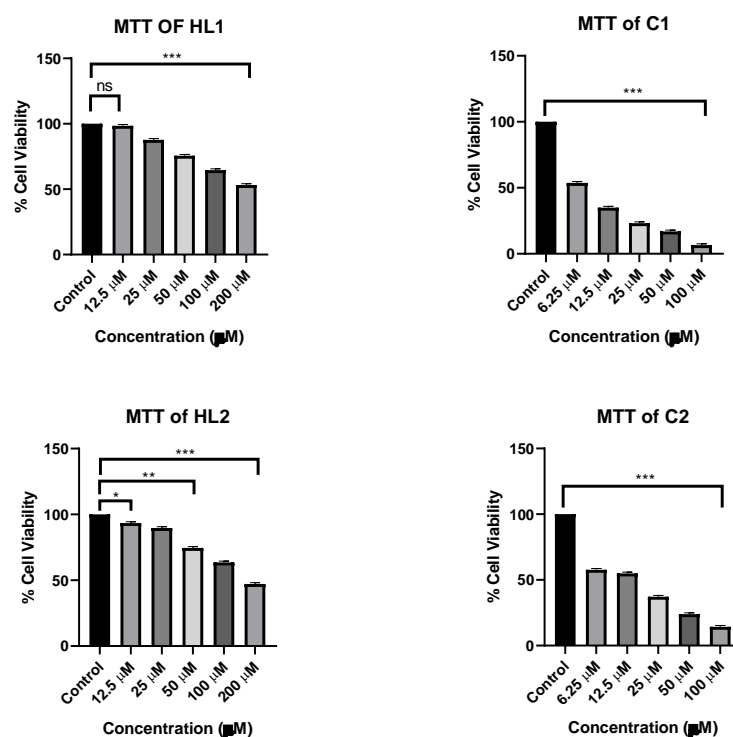


Fig.VII.23. % of cell viability of HL¹, C1, HL² and C2 towards MCF-7 cell lines. cells (1x10⁶ cells/mL) were treated with different concentrations of HL¹, C1, HL², C2 ranging from 6.25 to 200 μM for 24 h. Data is represented as mean ± S.D of triplicates determinations from their independent experiments with *** indicates P<0.001 versus untreated control.

VII.3.6.2. Colony Formation Assay

For 24 hours, MCF-7 was treated with various concentrations of ligands as well as their respective complexes. At 4X magnification, the cells were observed in a bright field. The numbers and sizes of the colony were examined [67], and a significant decrease was found for both complexes compared to ligands and controls (Fig.VII.24).

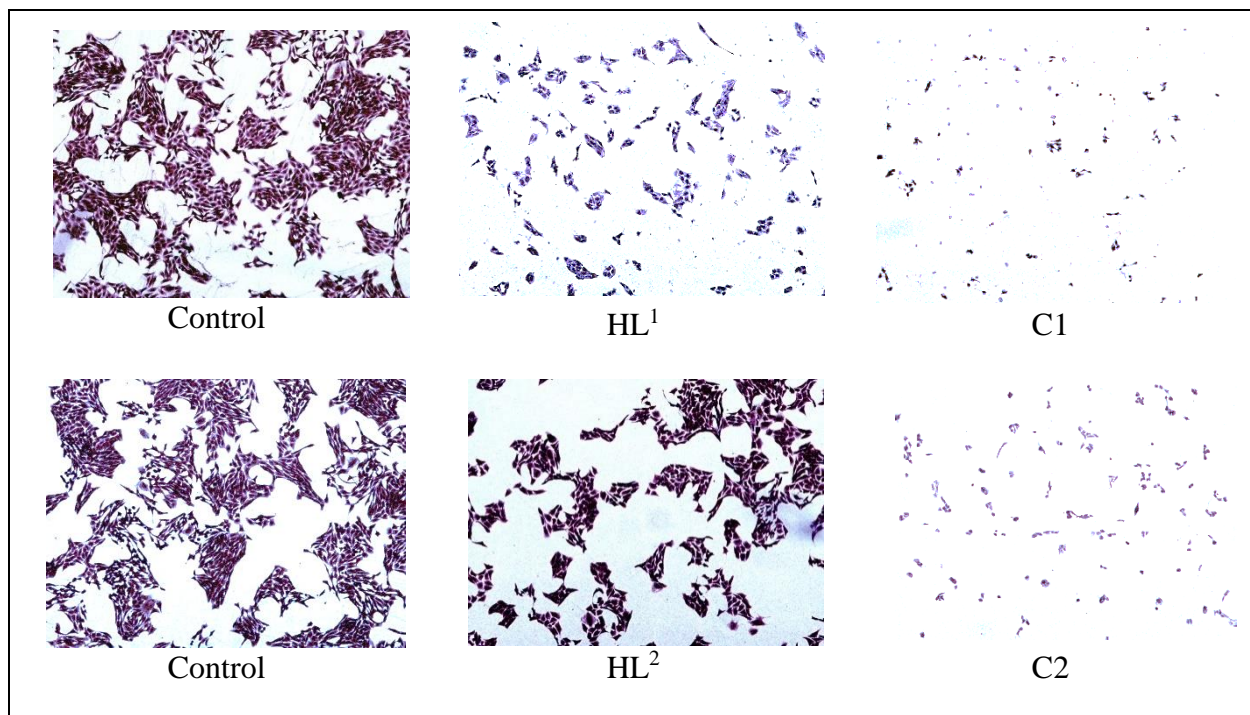


Fig.VII.24. Colony formation of MCF 7 cell lines with control and upon treatment of C1 (7.13 μ M) and C2 (11.88 μ M) for 24 h.

VII.3.6.3. Hoechst Assay

Hoechst Staining Assay, which is sensitive to DNA, was used to investigate the anti-cancer effect of the C1 and C2 on breast cancer cells in more detail. After 24 hours of exposure to both Palladium complexes, MCF-7 cells showed changes in their nucleus morphology (Fig.VII.25). In the treated cells, there were blatant signs of nuclear fragmentation, which indicated the occurrence of cellular apoptosis along with nucleus shrinkage, cytoplasmic vacuolation, blebbing, and chromatin condensation. In contrast, in the untreated control, the

nucleus had a distinct shape, appeared blue, and had no morphological alterations. These findings demonstrated the substantial apoptosis-inducing potential of C1 and C2 [68].

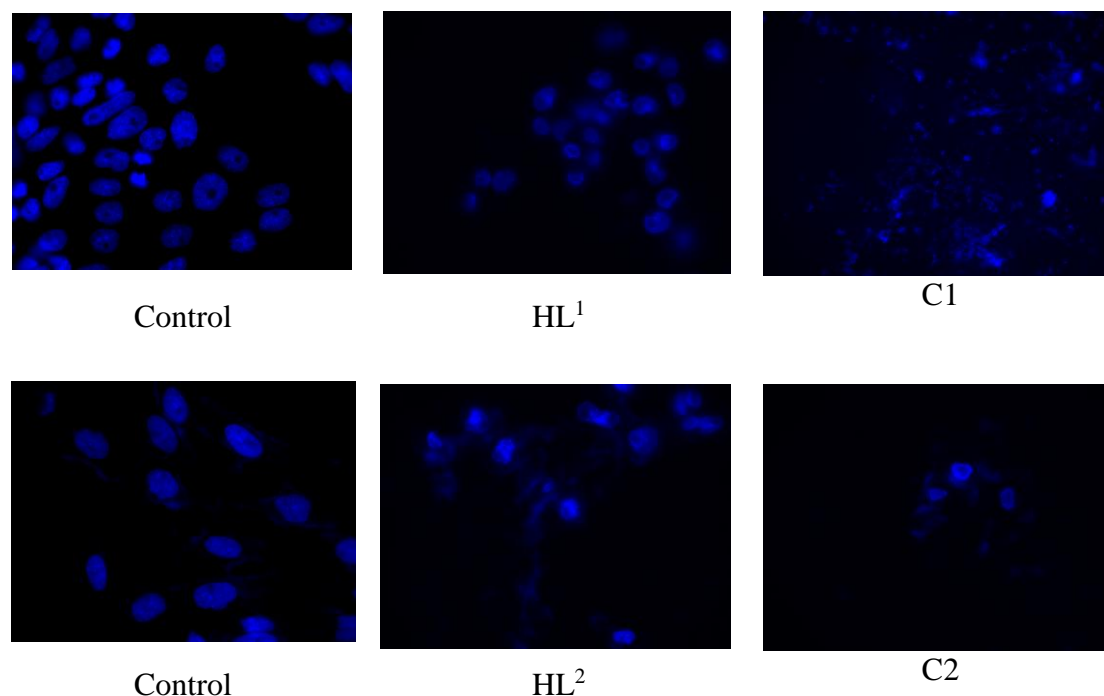


Fig.VII.25. DNA fragmentation assay using Hoechst 33,258 dye on MCF 7 cells after treatment with of HL¹, HL², C1 and C2. The cell nuclei in the control are mostly unlike the treatment groups where the nucleus has undergone fragmentation and shrinkage with the increase in the dose of treatment. The images have been captured in the DAPI channel at 40X magnification Scale bar corresponds to 20 μm .

VII.3.6.3. AO/EB Staining

An established method for determining the frequency of cellular apoptosis, which is distinguished by different alterations in cellular morphology and DNA fragmentation, is AO/EB staining. Green staining of viable cells with ordered cellular structure shows no evidence of apoptosis. While cells that stain red suggest cellular death combined with chromatin condensation or fragmentation, cells that retain a yellow stain are indicative of early apoptosis where the cell membrane is intact but there is clear commencement of DNA fragmentation. MCF-7 cells displayed an increase in red/orange staining after being exposed

to selective dose of the C1 and C2, which is a clear sign of apoptosis and is characterised by nuclear morphological distortion, membrane blebbing, fragmentation, and shrinkage (Fig.VII.26).

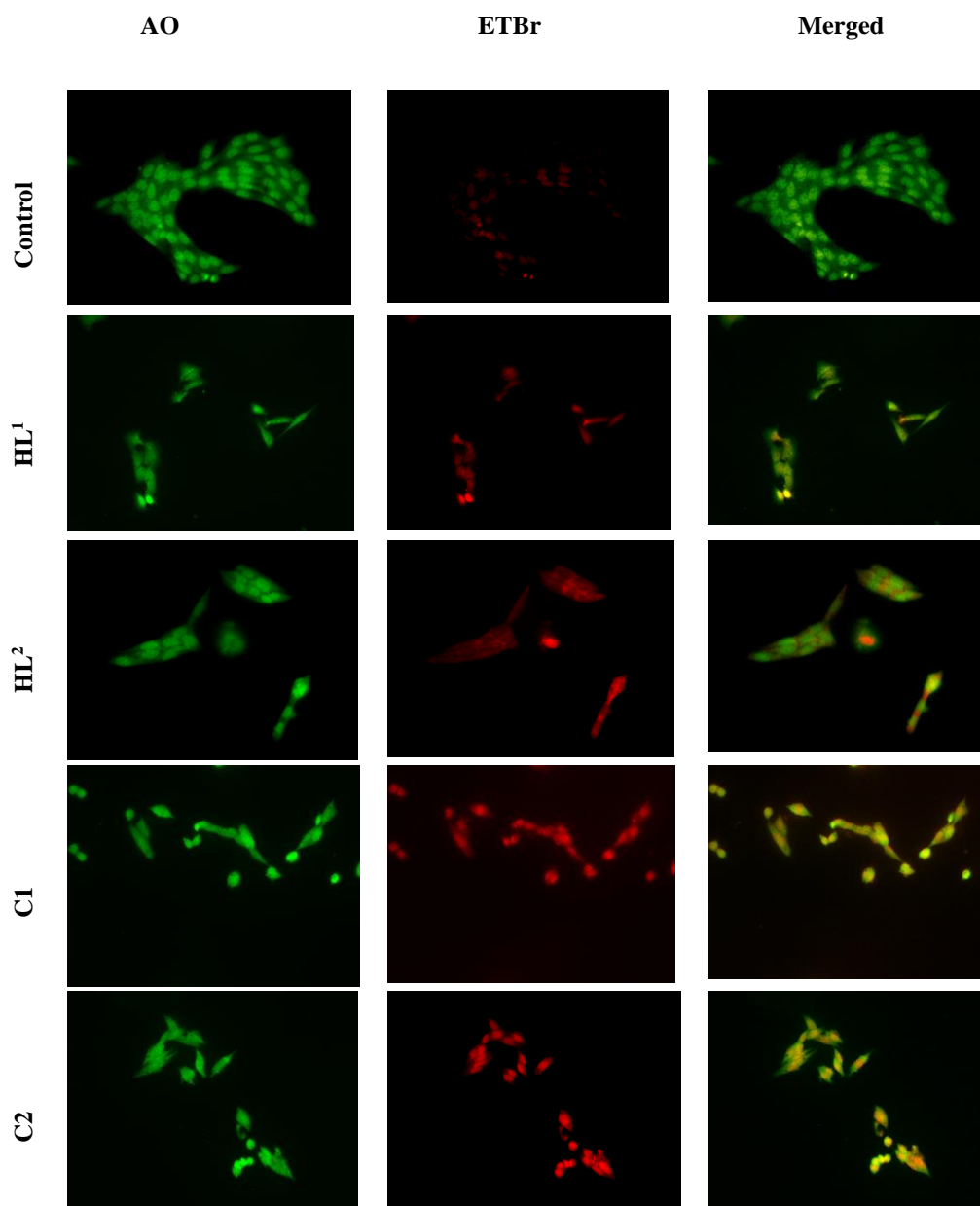


Fig.VII.26. Acridine Orange/Ethidium Bromide dual staining with the MCF 7 cells. Fluorescence microscopy images of MCF 7 cells after treating with HL¹, HL², C1 and C2 for 24 h followed by staining with acridine orange (4 µg/ml) and ethidium bromide (4 µg/ml) as observed under Olympus microscope at 200X magnification. Cells treated with HL¹ and HL² show early apoptosis with nucleus stained with Acridine orange whereas cells upon 24 h

exposure to both C1 and C2 showed orange/red fluorescence due to the uptake of EtBr stain. This nucleus is a typical representation of a late apoptotic cell.

VII.4. Conclusions

New Pd(II) complexes with coumarin based ONS donor ligands are fabricated and thoroughly characterized by several spectroscopic techniques. Single crystal X-ray study of the complexes revealed that HL¹ and HL² act as tridentate O,N,S chelator in Pd(II) complexes. Interaction of C1 and C2 with CT-DNA and BSA protein are investigated by UV-Vis as well as fluorescence methods. The complexes effectively displace ethidium bromide (EB) from EB-DNA complexes. The antiproliferative activity of the complexes displayed that Pd-complexes exhibit greater cytotoxicity than their respective ligands as well as cis-platin in both breast cancer cell lines. Cytotoxicity of both Pd(II) complexes towards MCF 7 (IC₅₀, 7.13 – 11.88 μM) cell lines are significant.

VII.5. References

1. R. L. Siegel, K. D. Miller and A. Jemal, *Cancer Statistics, 2019*, *Ca Cancer J. Clin.*, 2019, **69**, 7.
2. F. Bray, J. Ferlay, I. Soerjomataram, R. L. Siegel, L. A. Torre and A. Jemal, *Ca-Cancer J. Clin.*, 2018, **68**, 394.
3. M. Naghavi, A. A. Abajobir, C. Abbafati, K. M. Abbas, F. Abd-Allah, S. F. Abera, V. Aboyans, O. Adetokunboh, A. Afshin, A. Agrawal and A. Ahmadi, *Lancet*, 2017, **390**, 1151.
4. D. S. M. Chan, L. Abar, M. Cariolou, N. Nanu, D. C. Greenwood, E. V. Bandera, A. McTiernan and T. Norat, *Cancer Causes Control*, 2019, **30**, 1183.
5. Cancer statistics—India against cancer. <http://cancerindia.org.in/cancer-statistics/>. Accessed February 5, 2019.
6. R. Oun, Y. E. Moussa and N. J. Wheate, *Dalton Trans.*, 2018, **47**, 6645.
7. S. Medici, M. Peana, V. M. Nurchi, J. I. Lachowicz, G. Crisponi and M. A. Zoroddu, *Coord. Chem. Rev.*, 2015, **284**, 329.
8. S. N. Mbugua, N. R. S. Sibuyi, L. W. Njenga, R. A. Odhiambo, S. O. Wandiga, M. Meyer, R. A. Lalancette and M. O. Onani, *ACS Omega*, 2020, **25**, 14942.
9. Z. Breijyeh, B. Jubeh and R. Karaman, *Molecules*, 2020, **25**, 1340.
10. a) C. G. Hartinger, A. A. Nazarov, S. M. Ashraf, P. J. Dyson and B. K. Keppler, *Curr. Med. Chem.*, 2008, **15**, 2574. (b) I. Kostova., *Curr. Med. Chem.*, 2006, **13**, 1085. (c) K. S. Lovejoy, R. C. Todd, S. Zhang, M. S. McCormick, J. A. D'Aquino, J. T. Reardon, A. Sancar, K. M. Giacomini and S. J. Lippard, *Proc. Natl. Acad. Sci. U.S.A.*, 2008, **105**, 8902–8907.
11. E. R. Jamieson and S. J. Lippard, *Chem. Rev.*, 1999, **99**, 2467.

12. (a) N. J. Farrer, L. Salassa and P. J. Sadler, *Dalton Trans.*, 2009, 10690. (b) R. W.-Y. Sun, M. F.-Y. Ng, E. L.-M. Wong, J. Zhang, S. S.-Y. Chui, L. Shek, T.-C. Lau and C.-M. Che, *Dalton Trans.*, 2009, 10712.
13. P. J. Dyson and G. Sava, *Dalton Trans.*, 2006, 1929.
14. D. R. Richardson, D. S. Kalinowski, V. Richardson, P. C. Sharpe, D. B. Lovejoy, M. Isalam and P. V. Bernhardt, *J. Med. Chem.*, 2009, **52**, 1459.
15. Y. Chen, H. R. Liu, H. S. Liu, M. Cheng, P. Xia, K. Qian, P. C. Wu, C. Y. Lai, Y. Xia, Z. Y. Yang and S. L. Morris-Natschke, *Eur. J. Med. Chem.*, 2012, **49**, 74.
16. A. Thakur, R. Singla and V. Jaitak, *Eur. J. Med. Chem.*, 2015, **101**, 476.
17. X. Zhou, X. B. Wang, T. Wang and L. Y. Kong, *Bioorg. Med. Chem.*, 2008, **16**, 8011.
18. C. A. Kontogiorgis and D. J. Hadjipavlou-Litina, *J. Med. Chem.*, 2005, **48**, 6400.
19. K. Laws and K. Suntharalingam, *ChemBioChem*, 2018, **19**, 2246.
20. E. Alessio, *Eur. J. Inorg. Chem.*, 2017, **12**, 1549.
21. T. C. Johnstone, K. Suntharalingam and S. J. Lippard, *Chem. Rev.*, 2016, **116**, 3436.
22. V. Brabec, O. Hrabina and J. Kasparkova, *Coord. Chem. Rev.*, 2017, **351**, 2.
23. K. Skonieczny, G. Charalambidis, M. Tasiar, M. Krzeszewski, A. Kalkan-Burat, A. G. Coutsolelos and D. T. Gryko, *Org. Synth.*, 2012, **89**, 220.
24. M. Anjomshoa, H. Hadadzadeh, M. Torkzadeh-Mahani, S. J. Fatemi, M. AdeliSardou, H. A. Rudbari and V. M. Nardo, *Eur. J. Med. Chem.*, 2015, **96**, 66.
25. N. S. Quiming, R. B. Vergel, M. G. Nicolas and J. A. Villanueva, *J. Health Sci.*, 2005, **51**, 8-15.
26. T. L. Riss, R. A. Moravec, A. L. Niles, S. Duellman, H. A. Benink, T. J. Worzella and L. Minor, *Assay Guidelines manuals*, 2013.

27. N. Dastmalchi, R. Safaralizadeh, S. M. B. Khojasteh, M. A. Shadbad, M. A. Hosseinpourfeizi, S. Azarbarzin, A. Rajabi and B. Baradaran, *Mol. Biol. Rep.*, 2022, **49**, 8325.
28. L. C. Crowley, B. J. Marfell and N. J. Waterhouse, *Cold Spring Harbor Protocols*, 2016(9), 087205.
29. P. Elumalai, D. N. Gunadharini, K. Senthilkumar, S. Banudevi, R. Arunkumar, C. S. Benson, G. Sharmila and J. Arunakaran, *Toxicology letters*, 2012, **215**, 131.
30. A. D. Becke, *J. Chem. Phys.*, 1993, **98**, 5648.
31. C. Lee, W. Yang and R. G. Parr, *Phys. Rev. B*, 1998, **37**, 785.
32. M. J. Frisch, G. W. Trucks, H. B. Schlegel, G. E. Scuseria, M. A. Robb, J. R. Cheeseman, G. Scalmani, V. Barone, B. Mennucci, G. A. Petersson, H. Nakatsuji, M. Caricato, X. Li, H. P. Hratchian, A. F. Izmaylov, J. Bloino, G. Zheng, J. L. Sonnenberg, M. Hada, M. Ehara, K. Toyota, R. Fukuda, J. Hasegawa, M. Ishida, T. Nakajima, Y. Honda, O. Kitao, H. Nakai, T. Vreven, J. A. Montgomery, J. E. Peralta, F. Ogliaro, M. Bearpark, J. J. Heyd, E. Brothers, K. N. Kudin, V. N. Staroverov, R. Kobayashi, J. Normand, K. Raghavachari, A. Rendell, J. C. Burant, S. S. Iyengar, J. Tomasi, M. Cossi, N. Rega, J. M. Millam, M. Klene, J. E. Knox, J. B. Cross, V. Bakken, C. Adamo, J. Jaramillo, R. Gomperts, R. E. Stratmann, O. Yazyev, A. J. Austin, R. Cammi, C. Pomelli, J. W. Ochterski, R. L. Martin, K. Morokuma, V. G. Zakrzewski, G. A. Voth, P. Salvador, J. J. Dannenberg, S. Dapprich, A. D. Daniels, O. Farkas, J. B. Foresman, J. V. Ortiz, J. Cioslowski, J. D. Fox, 2009 Gaussian 09, revision D. 01. Gaussian Inc., C. T. Wallingford
33. J. Hay and W. R. Wadt, *J. Chem. Phys.*, 1985, **82**, 270.
34. W. R. Wadt and J. Hay, *J. Chem. Phys.*, 1985, **82**, 284.
35. P. J. Hay and W. R. Wadt, *J. Chem. Phys.*, 1985, **82**, 299.

36. N. M. O'Boyle, A. L. Tenderholt and K. M. Langner, *J. Comput. Chem.*, 2008, **29**, 839.
37. R. Bauernschmitt and R. Ahlrichs, *Chem. Phys. Lett.*, 1996, **256**, 454.
38. R. E. Stratmann, G. E. Scuseria and M. J. Frisch, *J. Chem. Phys.*, 1998, **109**, 8218.
39. M. E. Casida, C. Jamorski, K. C. Casida and D. R. Salahub, *J. Chem. Phys.*, 1998, **108**, 4439.
40. V. Barone and M. Cossi, *J. Phys. Chem. A*, 1998, **102**, 1995.
41. M. Cossi and V. Barone, *J. Chem. Phys.*, 2001, **115**, 4708.
42. M. Cossi, N. Rega, G. Scalmani and V. Barone, *J. Comput. Chem.*, 2003, **24**, 669.
43. G. M. Sheldrick, *Acta Cryst.*, 2008, **A64**, 112.
44. G. M. Sheldrick, *Acta Cryst.*, 2015, **C71**, 3.
45. R. Naskar, P. Ghosh, C. K. Manna, N. Murmu and T. K. Mondal, *Inorganica Chim. Acta.*, 2022, **534**, 120802.
46. (a) S. Biswas, P. Roy and T. K. Mondal, *J. Mol. Struct.*, 2017, **1142**, 110; (b) J. –A. Alvarez-Hernández, N. Andrade-López, J. G. Alvarado-Rodríguez, S. González-Montiel, L. Á. Zárate-Hernández and J. Cruz-Borbolla, *Polyhedron*, 2022, **214**, 115635; (c) D. Qiu, Y. Guo, H. Wang, X. Bao, Y. Feng, Q. Huang, J. Zeng and G. Qiu, *Inorg. Chem. Commun.*, 2011, **14**, 1520.
47. K. Akdi, R.A. Vilaplana, S. Kamah and F. Gonzalez-Vilchez, *J. Inorg. Biochem.*, 2005, **99**, 1360.
48. N. Bandyopadhyay, P. Basu, G. S. Kumar, B. Guhathakurta, P. Singh and J. P. Naskar, *J. Photochem. Photobiol. B*, 2017, **173**, 560.
49. C.V. Barra, F.V. Rocha, L. Morel, A. Gautier, S. S. Garrido, A.E. Mauro, R. C. G. Frem and A. V. G. Netto, *Inorg. Chim. Acta*, 2017, **446**, 54.
50. E. Nyarko, N. Hanada, A. Habib and M. Tabata, *Inorg. Chim. Acta*, 2004, **357**, 739-745.
51. J. B. Lepecq and C. Paoletti, *J. Mol. Biol.*, 1967, **27**, 87.

52. Y. Zhao, J. Zhu, W. He, Z. Yang, Y. Zhu, Y. Li, J. Zhang and Z. Guo, *Chem. Eur. J.*, 2006, **12**, 6621.
53. E. Ramachandran, D. S. Raja, N. P. Rath and K. Natarajan, *Inorg. Chem.*, 2013, **52**, 1504.
54. D. Senthil Raja, N. S. P. Bhuvanesh and K. Natarajan, *Inorg. Chem.*, 2011, **50**, 12852.
55. A. Wolfe, G. H. Shimer and T. Mehan, *Biochemistry*, 1987, **26**, 6392.
56. A. Paul, S. Mistri, A. Bhunia, S. Manna, H. Puschmann and S. C. Manna, *RSC Adv.*, 2016, **6**, 60487-60501.
57. A. Paul, A. Figuerola, V. Bertolasi and S. C. Manna, *Polyhedron*, 2016, **119**, 460-470.
58. X.-Q. Zhou, Q. Sun, L. Jiang, S.-T. Li, W. Gu, J.-L. Tian, X. Liu and S.-P. Yan, *Dalton Trans.*, 2015, **44**, 9516-9527.
59. W.-J. Lian, X.-T. Wang, C.-Z. Xie, H. Tian, X.-Q. Song, H.-T. Pan, X. Qiao and J.Y. Xu, *Dalton Trans.*, 2016, **45**, 9073-9087.
60. A. S. D. Tabatabai, E. Dehghanian and H. Mansouri-Torshizi, *Biometals*, 2022, **35**, 245-266.
61. S. Abedanzadeh, K. Karami, M. Rahimi, M. Edalati, M. Abedanzadeh, A. Mohammad Tamaddon, M. Dehdashti Jahromi, Z. Amirghofran, J. Lipkowskif and K. Lyczko, *Dalton Trans.*, 2020, **49**, 14891-14907.
62. R. O. Omondi, N. R. Sibuyi, A. O. Fadaka, M. Meyer, D. Jaganyi and S. O. Ojwach, *Dalton Trans.*, 2021, **50**, 8127-8143.
63. X. Wei, Y. Yang, J. Ge, X. Lin, D. Liu, S. Wang, J. Zhang, G. Zhou and S. Li, *Journal of Inorganic Biochemistry*, 2020, **202**, 110857.
64. J. R. Lakowicz, *Principles of Fluorescence Spectroscopy*, Third Edition., Springer, New York, USA, 2006.

65. J. R. Lakowicz, *Fluorescence Quenching: Theory and applications*, Principles of Fluorescence Spectroscopy, Kluwer Academic/Plenum Publishers, New York, 1999, p. 53.
66. X. Z. Feng, Z. Lin, L. J. Yang, C. Wang and C. L. Bai, *Talanta*, 1998, **47**, 1223.
67. H. Li, X. Li, S. Liu, L. Guo, B. Zhang, J. Zhang and Q. Ye, *Hepatology*, 2017, **66**, 1920.
68. E. Ulukaya, F. Ari, K. Dimas, M. Sarimahmut, E. Guney, N. Sakellaridis and V. T. Yilmaz, *J. Cancer Res. Clin. Oncol.*, 2011, **137**, 1425.

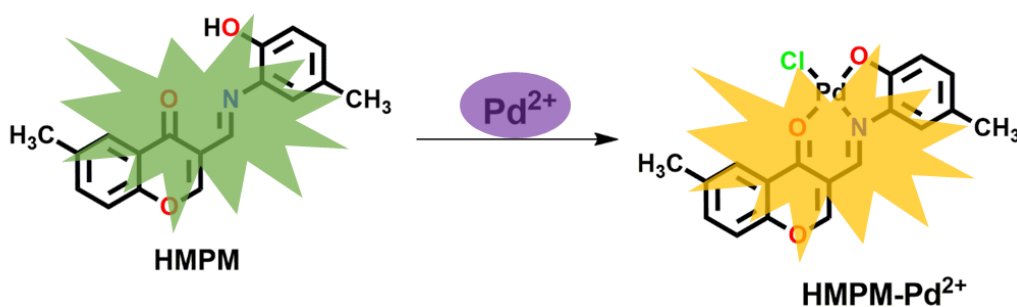
CHAPTER-VIII

A new chromone based fluorescence probe for ratiometric detection of Pd²⁺

A new chromone based fluorescence probe for ratiometric detection of Pd²⁺

Abstract

A new chromone based fluorescent probe (HMPM) is introduced for selective detection of Pd²⁺. The designed probe exhibits a ratiometric fluorescence enhancement which can be attributed to the ESIPT and/or chelation enhancement fluorescence (CHEF) processes. HMPM is efficient enough to detect Pd²⁺ solely in presence of other metal ions in DMSO/H₂O solution (1:1, v/v, pH=7.2) with a limit of detection as low as 2.9 nM. Furthermore, the complex formation of HMPM with Pd²⁺ is confirmed by single crystal X-ray diffraction method. The changes in electronic structure and absorption spectrum of HMPM upon complexation with Pd²⁺ are supported by DFT and TDDFT calculations. Moreover, the probe (HMPM) could be effectively used for the detection of Pd²⁺ by dip-stick method.



VIII.1. Introduction

Palladium is one of the rare and valuable transition metal of platinum group elements (PGEs). It is widely used in an array of applications such as the jewelry industry, coating materials, dental crowns and chemical catalysts and also broadly used as a significant component in a range of materials such as fuel cells [1-7]. It has a crucial role to play in chemical transformations by acting as a catalyst in reactions like the Suzuki–Miyaura, Sonogashira, Heck, Pd-catalyzed depropargylation reactions that are extensively used to create complex molecules in the pharmaceuticals industries [8-11]. Palladium is also an essential material in highly technological fields such as navigation, aviation and also in the automotive industry [12]. The non-biodegradable nature of palladium along with its enhanced emission in the environment can result in severe health hazards via accumulating in the food chain. Due to their high nucleophilicity, palladium can bind to thiol-containing proteins such as casein and silk fibroin, DNA or other biomolecules which eventually result in the degradation of DNA and cell mitochondria and also in enzyme inhibition [13-14]. Owing to its thiophilic nature, palladium can bind with DNA, proteins and other macromolecules and perturb a range of cellular processes [15-17]. Environmental pollution emissions to water and soil may be the result of palladium residues in pharmaceutical compounds or in the environment [18-20] thereby making the proposed maximum dietary intake for this ubiquitous and lethal heavy metal less than 1.5-15 g per person per day and its threshold in drugs is 5-10 ppm [21]. Furthermore, palladium also hampers the activity of many enzymatic reactions such as alkaline phosphatase, creatine kinase and prolyl hydroxylase [22-23]. Although a large number of carbon-carbon bond formation reactions are facilitated by palladium catalysts, the extensive use of palladium has led into an elevated level of residual palladium in water systems and soil, which is destructive to public health [24-26]. Hence designing and fabricating a selective and distinctly responsive analytical method for the identification of

palladium in the environment is crucial to evaluate potential unpleasant health effects caused by this particular metal residue.

The usual techniques used for quantification of palladium species, such as atomic absorption spectroscopy(AAS), inductively coupled plasma atomic emission spectroscopy, solid-phase micro extraction high-performance liquid chromatography etc., offer a fast and exceptionally sensitive analysis, although often proved to be more time-consuming and sometimes needed intricate sample-pretreatment methods, refined instrumentation and meticulous and thorough experimental and thus are not so suitable for real-time and in-situ analysis [27-29]. In recent years fluorescent sensors are widely used for the detection of Pd²⁺ because of their high selectivity, high sensitivity, cost effective and real time detection [30-33]. So far different strategies are adopted to develop fluorescent sensors for effective detection of Pd²⁺. Palladium catalyzed chemical transformation is one of the popular strategy used to develop fluorescent sensor for selective detection of Pd²⁺ [34-36]. As an efficient fluorescence quencher, Pd²⁺ could also be detected by using strong fluorescence probes by fluorescence quenching mechanism [37-39]. However, fluorescence “turn-on” chemosensor is considered to be more efficient. Recently, several fluorescence enhanced probes are reported for the detection of Pd²⁺ [40-42]. Nevertheless, the use of ratiometric fluorescent probes is advantageous compared to either fluorescence “turn-off” or “turn-on” probes because ratiometric fluorescent probes possess effective intrinsic correction and may greatly increase the sensitivity and accuracy of the detection [12,43,44]. Herein, we have developed a ratiometric fluorescence probe (HMPM) for the detection of Pd²⁺ based on excited state intramolecular proton transfer (ESIPT) process. So far, many ratiometric fluorescent sensors are developed for palladium based on ESIPT process to get the ratiometric fluorescence changes [31,36,45,46]. The probe shows a sharp “turn-on” increase in the emission spectra

upon addition of Pd²⁺ with a detection limit of 2.9 nM in DMSO/H₂O solution (1:1, v/v, pH=7.2).

VIII.2. Experimental

VIII.2.1. Materials and methods

3-Formyl-6-methylchromone and 2-amino-4-methyl phenol were purchased from Sigma-Aldrich. HRMS were recorded on Waters (Xevo G2 Q-TOF) mass spectrometer. ¹H and ¹³C NMR spectra were recorded on a Bruker 300 MHz instrument in DMSO-d₆ solvent using TMS as an internal standard. UV-Vis studies were executed through a PerkinElmer Lambda 750 spectrophotometer while the fluorescence property was measured using Shimadzu RF-6000 fluorescence spectrophotometer at room temperature (298 K). Fluorescence lifetimes were measured using a time-resolved spectrofluorometer from IBH, UK.

VIII.2.2. Synthesis

VIII.2.2.1. Synthesis of (E)-3-(((2-hydroxy-5-methylphenyl)imino)methyl)-6-methyl_4H-chromen-4-one (HMPM)

To the suspension of 3-formyl-6-methylchromone (0.05 g, 0.265 mmol) in acetonitrile, 2-amino-4-methyl phenol (0.032 g, 0.265 mmol) was added with continuous stirring. The reaction mixture was then refluxed for 5 h. The reaction mixture was cooled to room temperature and solvent was removed by slow evaporation method. After that the yellow Schiff base product was purified by column chromatography using dichloromethane as eluent. Yield was 0.065 g; 85%.

¹H NMR (300 MHz, DMSO-d₆): δ 2.24 (s, 3H), 2.51 (s, 3H), 6.71-6.82 (m, 2H), 6.89 (d, *J*=6.2 Hz, 1H), 7.12 (d, *J*=4.0 Hz, 1H), 7.30 (s, 1H), 7.62 (s, 1H), 7.99 (d, *J*=9.6 Hz, 1H), 9.97 (s, 1H), 11.94 (s, 1H).

¹³C NMR (75 MHz, DMSO-d₆): δ 25.43, 104.25, 114.15, 117.23, 120.25, 122.05, 125.73, 131.18, 132.16, 133.64, 136.03, 137.20, 148.49, 153.10, 154.99, 161.13, 190.03.

HRMS (ESI, positive): calcd. for $C_{18}H_{16}NO_3$ [HMPM + H]⁺ (m/z): 294.1130; found: 294.1063.

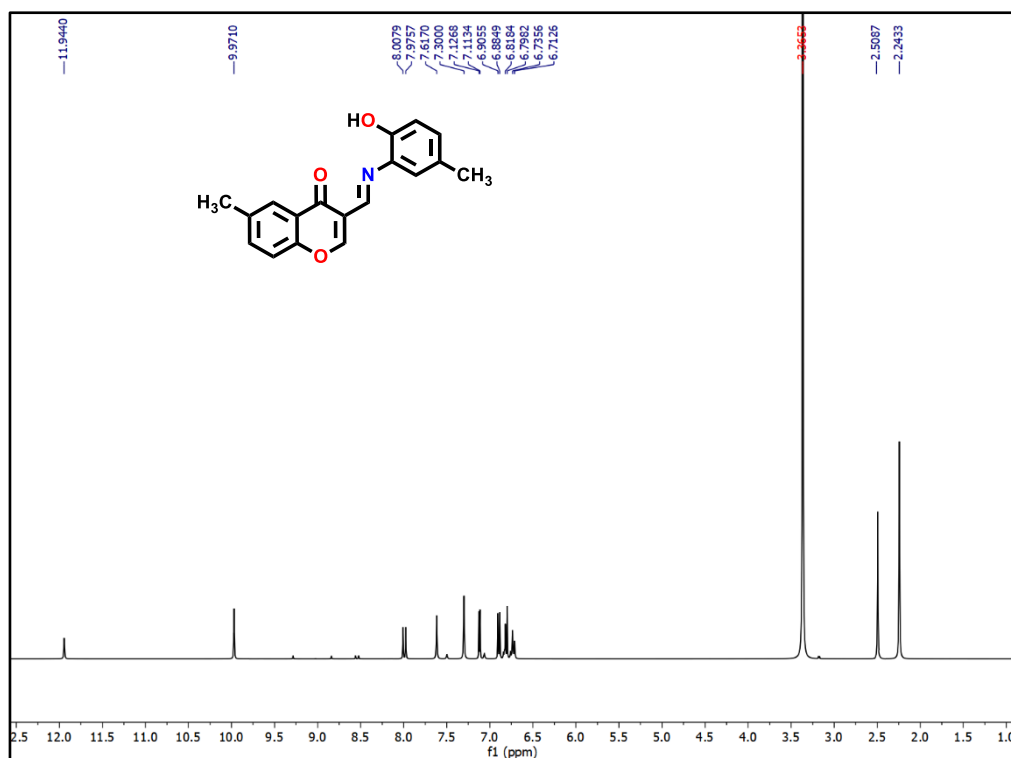


Fig.VIII.1. ¹H NMR (300 MHz) spectra of HMPM in DMSO-d₆

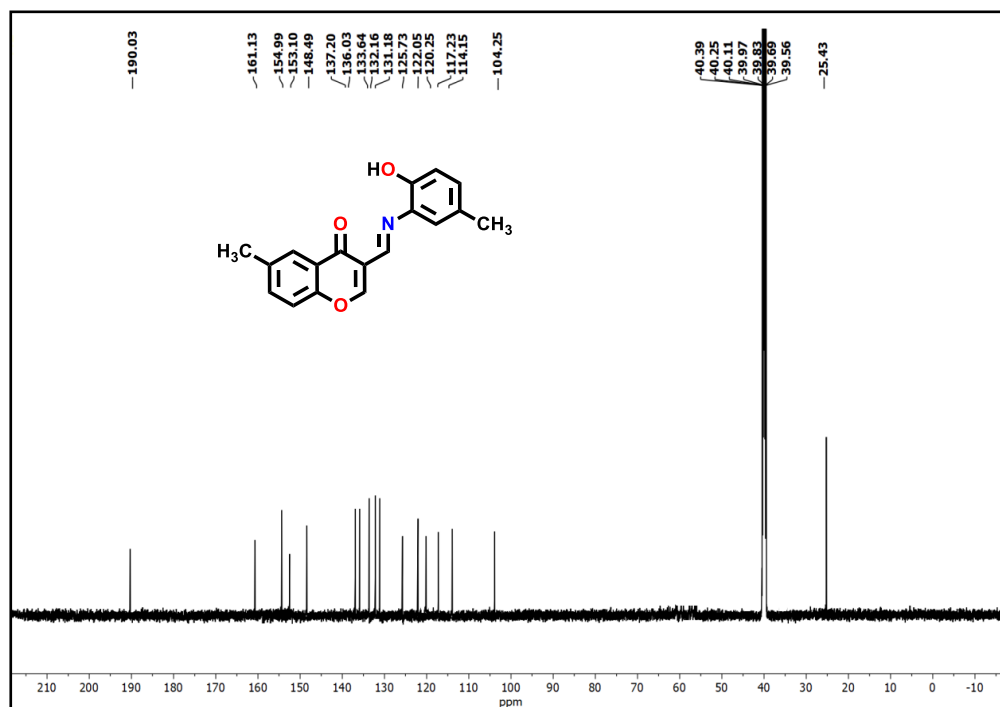


Fig.VIII.2. ¹³C NMR (75 MHz) spectra of the probe (HMPM) in DMSO-d₆

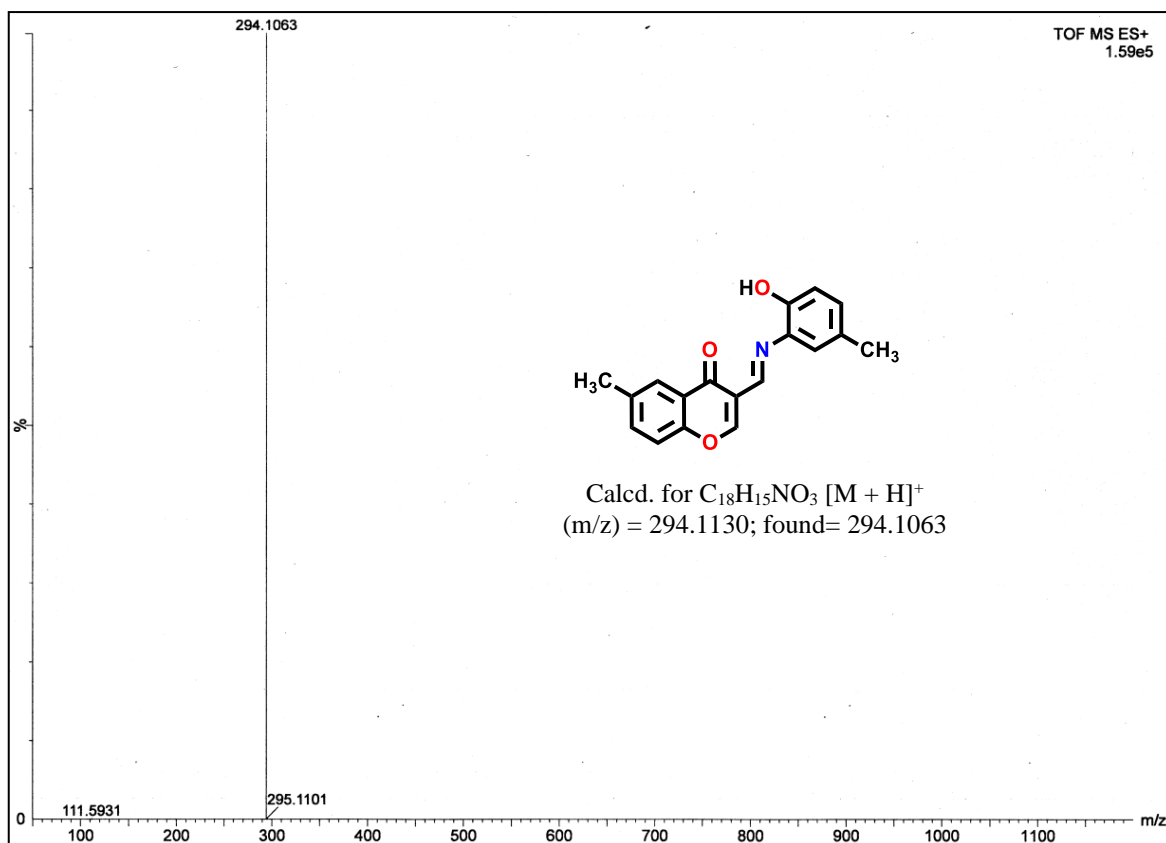


Fig.VIII.3. HRMS of the probe (HMPM)

VIII.2.2.2. Synthesis of Pd^{2+} complex (HMPM- Pd^{2+}) of the probe

$PdCl_2$ (0.039 g) was dissolved in 10 mL under refluxing condition. To it acetonitrile solution of HMPM (0.065g) and refluxed for 12 h. The reaction mixture was cooled to room temperature and then filtered. Single crystal of the complex was formed into the side-wall of the beaker by slow evaporation of the solvent.

HRMS (ESI, Positive): calcd. for $C_{18}H_{14}NO_3Pd$ $[HMPM+Pd^{2+}]^+$ (m/z): 398.0009; found: 398.0194.

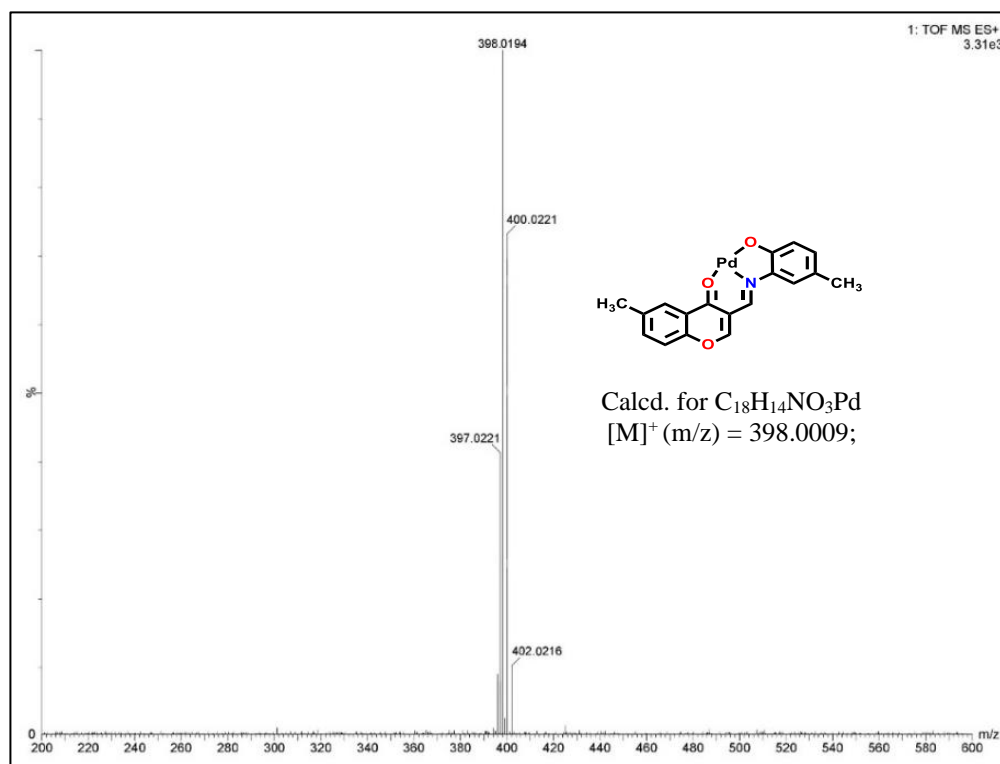


Fig.VIII.4. HRMS spectrum of HMPM -Pd²⁺

VIII.2.3. General method of UV-Vis and fluorescence titration

VIII.2.3.1. UV-Vis method

For UV-vis titrations, stock solution of the probe (HMPM) was prepared in DMSO/H₂O (1/1, v/v) (at 25°C) solution using HEPES buffer (pH = 7.2). The solutions of the guest cations were prepared using their chloride salts in deionized water using HEPES buffer at pH=7.2 in the order of 1×10^{-5} M. Solutions of a range of concentrations containing the probe and increasing concentrations of the cations were prepared independently. The spectra of these solutions were recorded by means of UV-vis method.

VIII.2.3.2. Fluorescence method

For fluorescence titrations, stock solution of HMPM (10 μM) was used similar to that of UV-vis titration. The solutions of the guest cations using their chloride salts in the order of 1×10^{-5} M, were prepared in deionised water similarly. Solutions of different concentrations containing the probe and increasing concentrations of cations were prepared separately then and the spectra of these solutions were recorded by means of fluorescence method.

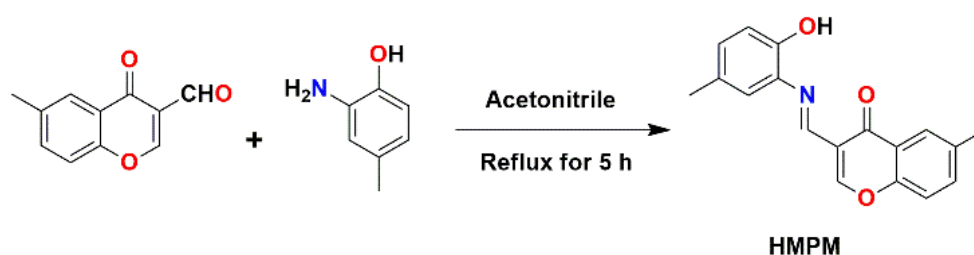
VIII.2.4. Computational method

All calculations were performed with Gaussian 09 program package [47] with the aid of the Gauss View visualization program. Full geometry optimizations were executed using the density functional theory (DFT) method at the B3LYP [48,49] level for the compounds. All elements except palladium was assigned 6-31+G(d) basis set. The LanL2DZ basis set with effective core potential (ECP) set of Hay and Wadt [50-52] was used for Pd. The vibrational frequency calculations were carried out to ensure that the optimized geometries signify the local minima and there were only positive eigen values. Vertical electronic excitations based on B3LYP optimized geometries were computed using the time-dependent density functional theory (TDDFT) formalism [53-55] in DMSO using conductor-like polarizable continuum model (CPCM) [56-58].

VIII.3. Results and discussion

VIII.3.1. Design and synthesis

The synthetic procedures of the probe (HMPM) are shown in scheme 1. Condensation of 3-formyl-6-methylchromone and 2-amino-4-methyl phenol in acetonitrile under refluxing condition for 5 h affords the desired probe (HMPM) with a high yield (0.065 g, 85 %). The geometry of the probe was confirmed by IR, NMR and HRMS spectra.



Scheme VIII.1: synthesis of the probe (HMPM)

VIII.3.2. Cation sensing studies

VIII.3.2.1. UV-Vis study

In UV-Vis, the probe, HMPM exhibits sharp absorbance bands at 295 nm and 395 nm in DMSO/H₂O (1/1, v/v, 10 mM HEPES buffer, pH = 7.2). Upon gradual addition of Pd²⁺ (40 μM) to the probe solution the band at 295 nm disappears and moderately intense new bands appear at 458 nm and 355 nm with the formation of isosbestic points at 378 nm and 416 nm respectively (Fig. VIII.5.a.). UV-Vis spectra of HMPM are also taken in presence of other metal ions i.e., Na⁺, Bi³⁺, Ca²⁺, Mg²⁺, Mn²⁺, Fe³⁺, Cr³⁺, Al³⁺, Co²⁺, Ni²⁺, Cu²⁺, Cd²⁺ and Hg²⁺ and it is noticed that the appearance low energy absorption band at 458 nm is very much specific for Pd²⁺ and there are no interferences for other metal ions (Fig.VIII.5.b.).

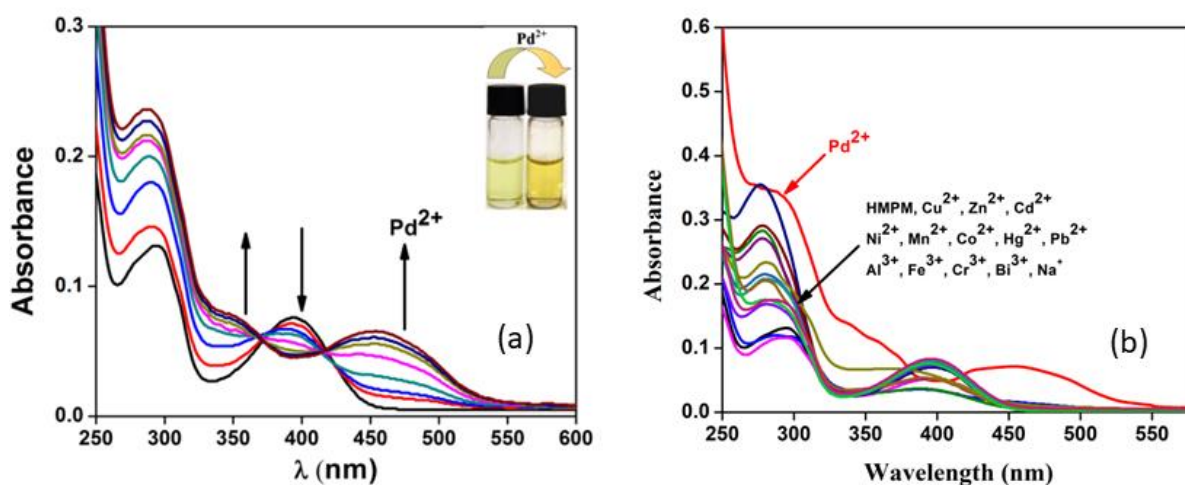


Fig.VIII.5. Change of absorption spectra of HMPM (10 μM) upon gradual addition of (a) Pd²⁺ (0 to 40 μM). Inset: Photograph showing the visible color change of HMPM before and after addition of Pd²⁺(40 μM). (b) different metal ions i.e., Na⁺, Bi³⁺, Mn²⁺, Fe³⁺, Al³⁺, Cr³⁺, Co²⁺, Ni²⁺, Hg²⁺, Zn²⁺, Cu²⁺, Pb²⁺ and Cd²⁺(40 μM) in CH₃CN/H₂O (4/1, v/v) using HEPES buffered solution at pH=7.2.

VIII.3.2.2. Fluorescence study

The emission spectra of HMPM and its fluorescence titration with Pd^{2+} were also recorded in DMSO/ H_2O (1/1, v/v, 10 mM HEPES buffer, pH = 7.2) solution. HMPM itself exhibits a moderately intense emission band at 509 nm upon excitation at 410 nm. Gradual addition of Pd^{2+} to HMPM solution shows emission enhancement at 548 nm with red shift of 41 nm (Fig. VIII.6.a). This change may be attributed to the inhibition of ESIPT of HMPM and chelation enhancement fluorescence in the HMPM- Pd^{2+} complex. The emission spectra of HMPM (10 μM) were also recorded in presence of other metal ions i.e., Na^+ , K^+ , Ca^{2+} , Mg^{2+} , Mn^{2+} , Cu^{2+} , Fe^{3+} , Cr^{3+} , Co^{2+} , Ni^{2+} , Al^{3+} , Bi^{3+} , Cd^{2+} and Hg^{2+} (10 μM) in DMSO: H_2O (1/1, v/v, 10 mM HEPES buffer, pH=7.2) but there is hardly any change in emission intensity of HMPM except for Cu^{2+} (Fig.VIII.6.b).

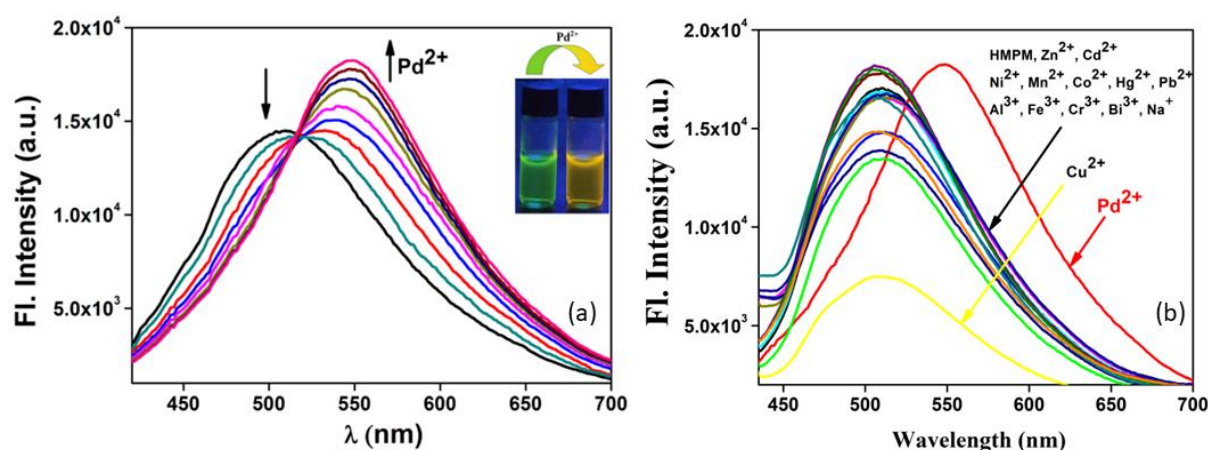


Fig.VIII.6. Change of emission spectra of HMPM (10 μM) upon gradual addition of (a) Pd^{2+} (0 to 20 μM). Inset: visible emission observed from HMPM in absence and presence of 40 μM of Pd^{2+} , taken under UV light. (b) different metal ions i.e., Pd^{2+} , Cu^{2+} , Na^+ , K^+ , Ca^{2+} , Mg^{2+} , Mn^{2+} , Cu^{2+} , Fe^{3+} , Cr^{3+} , Co^{2+} , Ni^{2+} , Al^{3+} , Bi^{3+} , Cd^{2+} and Hg^{2+} in $\text{CH}_3\text{CN}/\text{H}_2\text{O}$ (4/1, v/v) using HEPES buffered solution at pH=7.2.

In order to study the selectivity of HMPM for Pd^{2+} , interference experiment was carried out by measuring the emission intensity of HMPM (10 μM) in presence of other cations. It is

noticed from the experiment that the other metal ions do not cause any noteworthy interference for Pd²⁺ except for Cu²⁺ and Hg²⁺ (Fig.VIII.7).

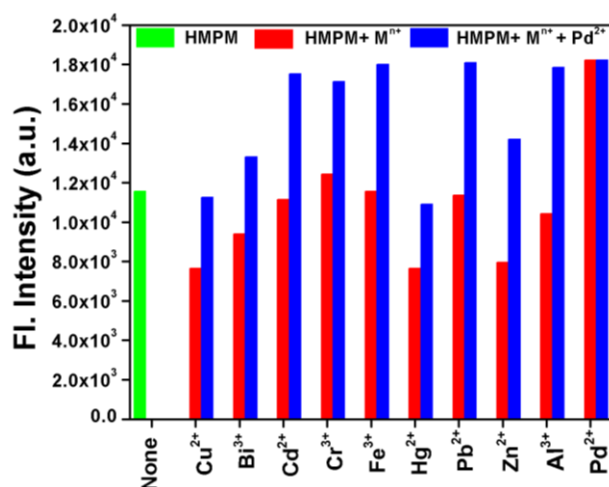


Fig.VIII.7. Competition study using fluorescence method after addition of different analytes (40 μ M) in the solution of HMPM (10 μ M) in presence of Pd²⁺ (40 μ M).

VIII.3.2.3. Binding studies of HMPM with Pd²⁺

The Mole ratio plot attained from fluorescence titration signifies that the probe shows an enhancement in emission intensity till the ratio of HMPM: Pd²⁺ reach at \sim 1, after that there is barely any increase in emission intensity (Fig. VIII.8.C). From emission spectral change, limit of detection of the probe HMPM with Pd²⁺ was calculated using the equation $LOD = K \times SD/S$ where 'SD' is the standard deviation of the blank solution and 'S' in the slope of the calibration curve (Fig. VIII.8.b). The limit of detection is found to be $(2.88 \pm 0.155) \times 10^{-9}$ M for Pd²⁺. This result evidently exhibits that this probe is greatly proficient in sensing Pd²⁺ even in very minute level. So as to quantify the stoichiometry of the complex of HMPM with Pd²⁺, job's plot analysis was executed. The maxima of the plot is appeared at a mole fraction of \sim 0.5 for HMPM-Pd²⁺ complex which corresponds to the 1:1 complex formation of HMPM with Pd²⁺ (Fig.VIII.8.a).

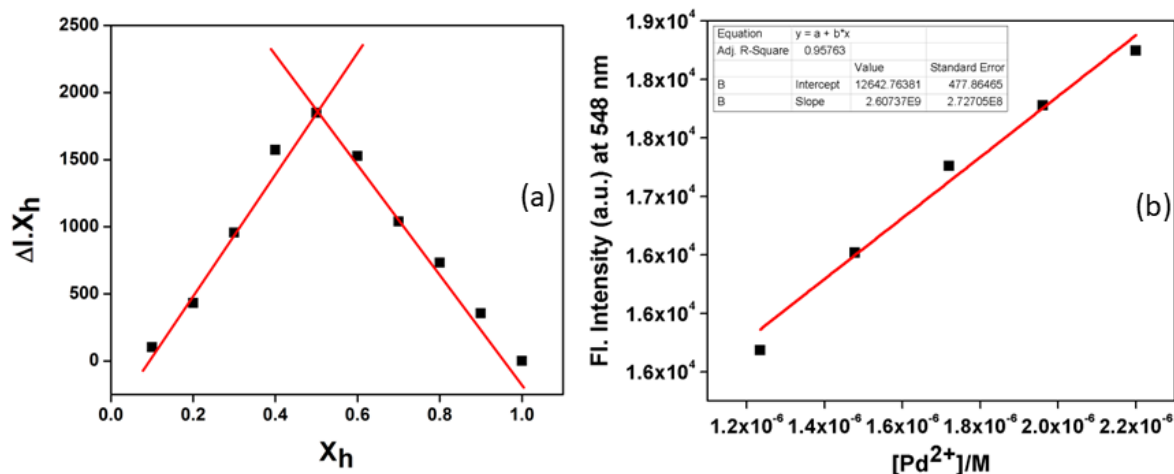


Fig.VIII.8: (a) Job's plot of HMPM for Pd^{2+} (b) Linear response curve of HMPM at 548 nm depending on the Pd^{2+} concentration

From the fluorescence titration, the association constant of HMPM with Pd^{2+} is calculated from Benesi-Hildebrand equation and it is found to be $(3.18 \pm 0.114) \times 10^5 M^{-1}$ (Fig.VIII.8.d), which points out the fact that the HMPM- Pd^{2+} complex is sufficiently stable. Moreover, the present probe is efficient enough for the detection of Pd^{2+} in comparison to the other reported fluorescence “turn-on” sensors (Table VIII.1).

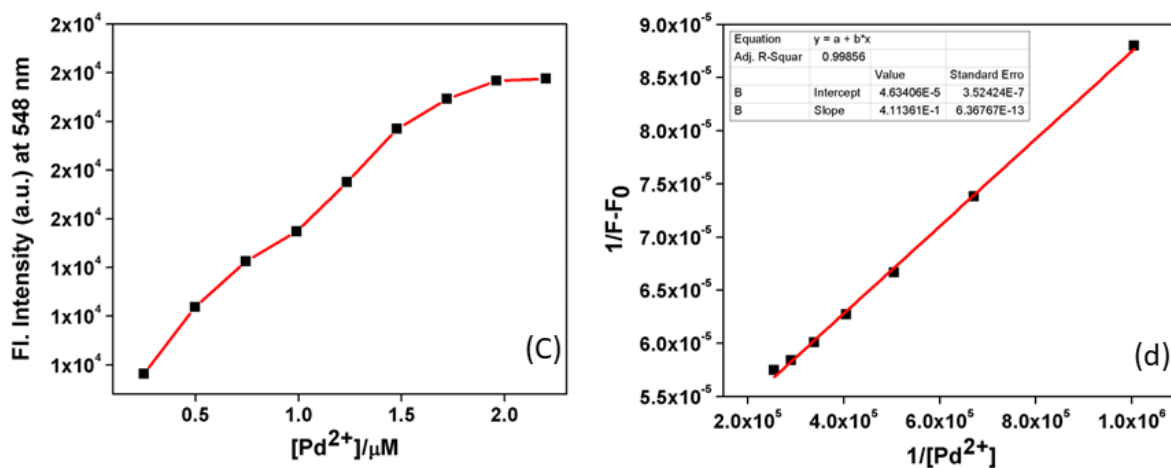


Fig.VIII.8: (c) Mole ratio plot of HMPM for Pd^{2+} (d) Determination of association constant of HMPM at 548 nm depending on the Pd^{2+} concentration using Benesi-Hildebrand equation

VIII.3.3. Fluorescence lifetime decay studies of HMPM with Pd²⁺

To comprehend the excited state stability, the fluorescence lifetime measurements were also executed. The lifetime decays of the free probe (HMPM) and HMPM-Pd²⁺ complex fit well with mono-exponential decay curve and the lifetime of HMPM (0.52 ns) is significantly increased in presence of Pd²⁺ (0.96 ns) (Fig. VIII.9).

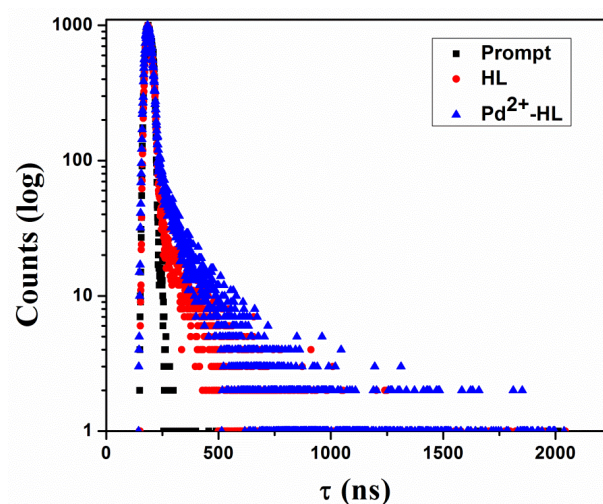
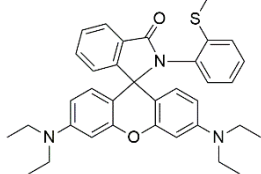
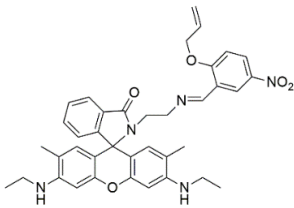
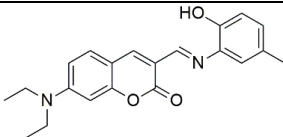
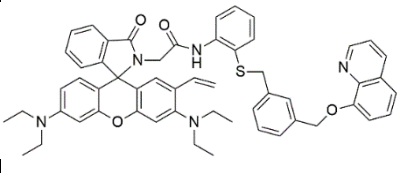
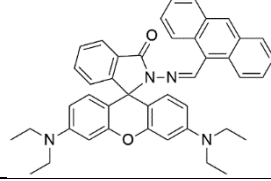
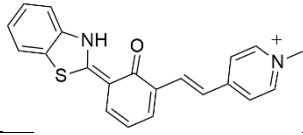
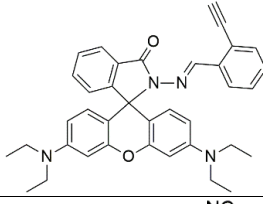
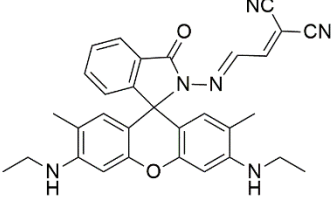
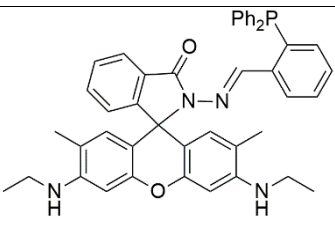
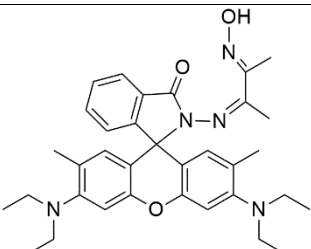
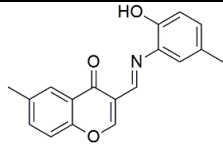


Fig. VIII.9: Lifetime decay profile of HMPM ($\tau_{av} = 0.52$ ns) and HMPM-Pd²⁺ ($\tau_{av} = 0.96$ ns)

Table VIII.1: Comparison between limit of detection (LOD) and solvent used for some reported fluorescence turn-on sensor for Pd(II) ion

Sl. No.	Probe	Solvent	LOD	Ref.
1.		CH ₃ CN/H ₂ O	2.4×10 ⁻⁹ M	[4]
2.		CH ₃ CN/H ₂ O	5×10 ⁻⁸ M	[5]
3.		CH ₃ CN/H ₂ O	7.4×10 ⁻⁸ M	[6]

4.		CH ₃ CN/H ₂ O	7.0×10 ⁻⁸ M	[7]
5.		H ₂ O	3.0×10 ⁻⁸ M	[8]
6.		H ₂ O	5.7×10 ⁻⁸ M	[9]
7.		EtOH/H ₂ O	1.9×10 ⁻⁷ M	[10]
8.		EtOH/H ₂ O	1.7×10 ⁻⁶ M	[11]
9.		EtOH/H ₂ O	5.0×10 ⁻⁹ M	[12]
10.		H ₂ O	1.5×10 ⁻⁸ M	[13]
11.		DMSO/H ₂ O	2.9×10 ⁻⁹ M	Present study

VIII.3.4. Effect of pH on complexation

The acid-base titration study revealed that HMPM does not experience any noteworthy alteration in the emission profile at 548 nm within the pH range from 2-10. So it can be said from this investigation that the probe is stable in this pH range. In presence of Pd^{2+} the emission intensity significantly increased at the pH range of 5-9, the emission intensity increases as expected thereby confirming that in this range HMPM is efficient in detecting Pd^{2+} whereas at higher pH range (pH = 10-12) the emission intensity sharply decreases (Fig. VIII.10). So it can be said from the pH study that HMPM can successfully detect Pd^{2+} in the neutral pH range (pH = 7).

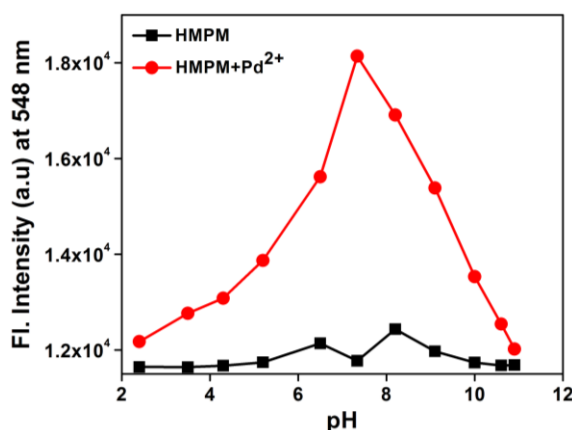
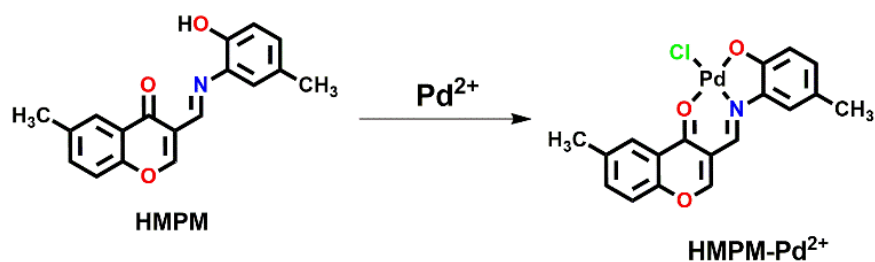


Fig. VIII.10. Fluorescence response of HMPM- Pd^{2+} as a function of pH in DMSO/ H_2O (1/ 1, v/v), pH is adjusted by using aqueous solutions of 1 M HCl or 1 M NaOH

VIII.3.5. Mechanism of Pd^{2+} sensing

The red shift of emission wavelength by 41 nm of HMPM in presence of Pd^{2+} addition may be attributed to one of the recognized sensing mechanism, ICT (Internal Charge Transfer) [59-61] process and/or the inhibition of ESIPT (excited state intramolecular proton transfer) [45,46] process due to the deprotonation of $-\text{OH}$ proton during complexation with Pd^{2+} . The enhancement of fluorescent intensity at 548 nm may also be attributed as chelation enhancement fluorescence (CHEF) [62,63] in HMPM- Pd^{2+} complex. A feasible binding mode of HMPM with Pd^{2+} is presented in the diagram below (Scheme 2).



Scheme VIII.2: Formation of HMPM-Pd²⁺ complex

IR spectrum of the free probe (HMPM) exhibits stretching bands at 1638 cm⁻¹ and 1614 cm⁻¹ correspond to $\nu(\text{C}=\text{O})$ and $\nu(\text{C}=\text{N})$ stretching. The broad stretching at ~3445 cm⁻¹ and 3202 cm⁻¹ corresponds to the free -OH moieties present in the probe (Fig.VIII.12.a) while in case of HMPM-Pd²⁺, no distinct -OH stretch is observed due to the coordination of HMPM with Pd²⁺ (Fig.VIII.12.b). The HRMS spectrum of HMPM exhibits a peak at m/z 294.1063 corresponds to [HMPM+H]⁺ (Fig. VIII.3), whereas for HMPM-Pd²⁺ complex m/z peak appears at 398.0194 corresponds to [HMPM-Pd]⁺ species, supporting the formation HMPM-Pd²⁺ complex (Fig.VIII.4). ¹H NMR spectrum of HMPM-Pd²⁺ complex, the peak at δ 11.9 ppm corresponds to -OH proton for free HMPM vanishes due to the deprotonation of -OH proton and coordination O atom to Pd²⁺ (Fig.VIII.1-2).

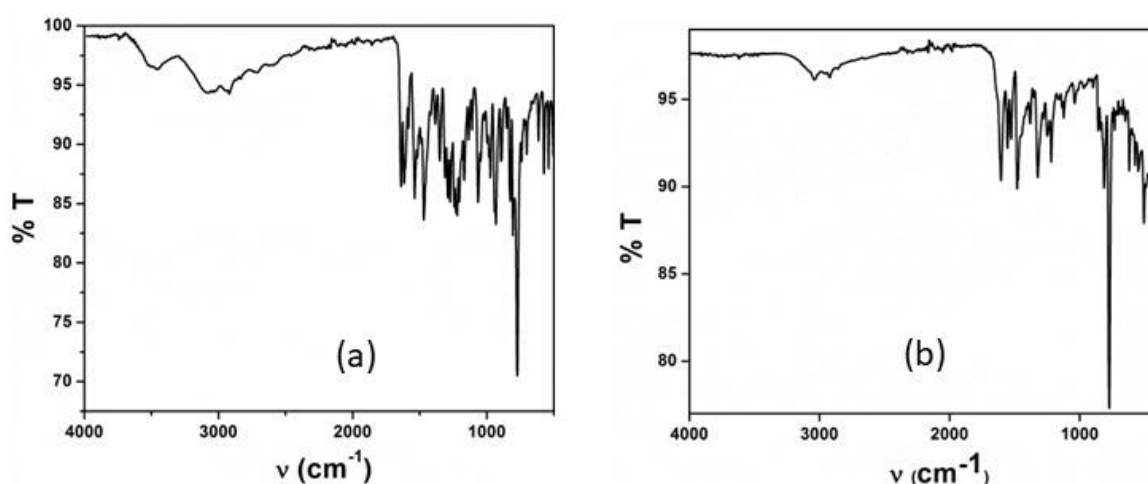


Fig.VIII.12. IR spectrum of (a) HMPM and (b) HMPM-Pd²⁺

VIII.3.6. Crystallographic study

The structure of HMPM-Pd²⁺ was further determined by single crystal X-ray diffraction method. The ORTEP plot with atom numbering scheme of the complex, HMPM-Pd²⁺ is shown in Fig.VIII.13.

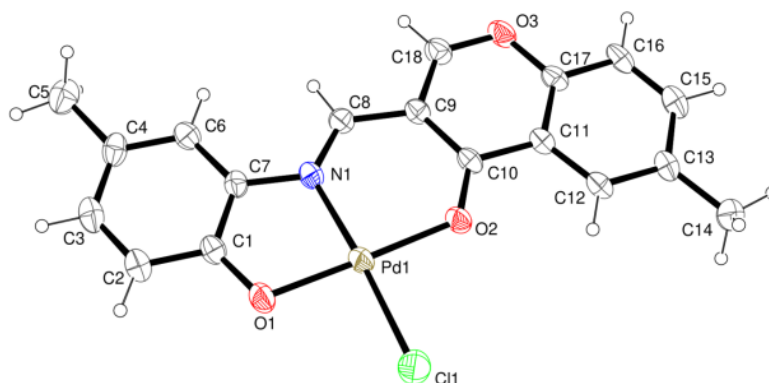


Fig.VIII.13. ORTEP plot of HMPM-Pd²⁺ complex with 35% ellipsoidal probability

HMPM acts as tridentate O, N, O donor ligand in the complex. The metal is coordinated with HMPM through phenolic oxygen (O1), imine nitrogen atom (N1), ester oxygen atom (O2) via formation of one five-membered (Pd1-O1-C1-C7-N1) and one six-membered (Pd1-N1-C8-C9-C10-O2) chelate rings with chelate bite angles, \angle N1-Pd1-O1 and \angle N1-Pd1-O2, 84.31(16) ° and 94.06(15)° respectively. The selected bond distances and bond angles of HMPM-Pd²⁺ are given in Table VIII.3. The bond distance, Pd1-O1 (1.961(3) Å) is notably shorter compare to the M-N(imine) bond distance, Pd1-N1 (1.972(4) Å) in the complex. The Pd-O(ester) bond distance is found to be longer, Pd1-O2 (1.988(3) Å) as expected.

Table VIII.2: Crystallographic data and refinement parameters of HMPM-Pd²⁺

Formula	C ₁₈ H ₁₄ ClNO ₃ Pd
Formula Weight	434.15
Crystal System	triclinic
Space group	$\bar{P}1$
a, b, c [Å]	6.9450(7), 11.0309(10), 12.2212(12)
α	92.607(3)
β	105.097(3)
γ	90.210(3)
V [Å ³]	902.89(15)
Z	2
D(calc) [g/cm ³]	1.597
Mu(MoKa) [/mm]	1.190
F(000)	432
Crystal Size [mm]	0.14 × 0.12 × 0.08
Temperature (K)	293(2)
Radiation Wavelength [Å]	0.71073
θ (Min-Max) [°]	1.728-26.496
Dataset (h; k; l)	-8 and 8; -13 and 13; -15 and 15
Data / restraints / parameters	3726/0 / 217
R1, wR2 [I > 2 σ (I)]	0.0553; 0.1065
GOF	1.060
Largest diff. Peak/hole, (e Å ⁻³)	0.794 and -0.667
CCDC No.	2067540

Table VIII.3: Selected bond distances (Å) and angles (°) of HMPM-Pd²⁺ complex

Bonds(Å)	X-ray	Calc.
Pd1 – N1	1.972(4)	2.037
Pd1 – O1	1.961(3)	1.990
Pd1 – O2	1.988(3)	2.050
Pd1 – Cl1	2.2921(18)	2.310
O1 – C1	1.335(6)	1.313
O2 – C10	1.255(6)	1.254
O3 – C18	1.307(6)	1.332
O3 – C17	1.376(6)	1.373
N1 – C8	1.287(6)	1.299
N1 – C7	1.414(6)	1.405
Angles(°)		
N1 – Pd1 – O1	84.31(16)	83.244
N1 – Pd1 – S2	94.06(15)	93.115
O1 – Pd1 – O2	178.36(15)	176.359
N1 – Pd1 – Cl1	176.08(12)	177.00710
O1 – Pd1 – Cl1	91.89(12)	93.763
O2 – Pd1 – Cl1	89.75(11)	89.878
C18 – O3 – C17	118.6(4)	119.293
C10 – O2 – Pd1	125.4(3)	125.797
C1 – O1 – Pd1	110.8(3)	111.214
C8 – N1 – Pd1	125.5(3)	124.442
C7 – N1 – Pd1	110.9(3)	110.479

VIII.3.7. Computational study

In order to explore the structural changes of HMPM and its complex with Pd²⁺ further, we executed density functional theory (DFT) and time dependent density functional theory (TDDFT) calculations with the B3LYP/6-31+G(d) method using the Gaussian 09 program.

The optimized geometries of HMPM and its Pd²⁺ complex are presented in Fig. VIII.14(a) and Fig.VIII.14(b) respectively.

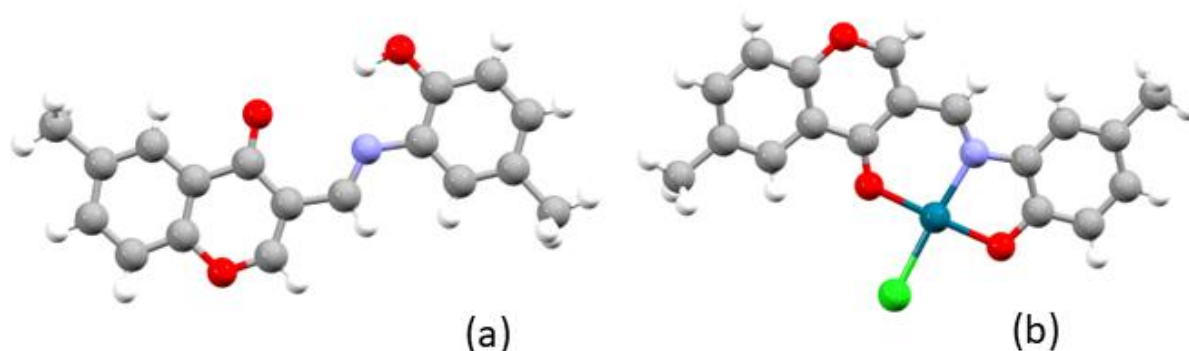


Fig.VIII.14: Optimized structure of (a) HMPM (b) HMPM-Pd²⁺ calculated by DFT/B3LYP/6-31+G(d) method

Contour plots of some selected molecular orbitals of HMPM and HMPM-Pd²⁺ are shown in Fig. VIII.15 and Fig. VIII.16 respectively. HOMO-LUMO energy gap for HMPM is found to be 3.42 eV which is significantly reduced to 2.50 eV in HMPM-Pd²⁺ complex. The reduced HOMO-LUMO energy gap clearly explains the formation of a new band at longer wavelength for HMPM-Pd²⁺ complex. Further, to interpret the changes in electronic transitions in HMPM and HMPM-Pd²⁺ complex, TDDFT calculations were carried out. Vertical electronic transitions calculated by TDDFT/CPCM method are summarized in table VIII.4. The newly developed band at 458 nm for HMPM-Pd²⁺ complex corresponds to HOMO→LUMO+1 transition having ILCT character. Again the new band at 355 nm corresponds to mixed HOMO/HOMO-1→LUMO/LUMO+1 transitions with mixed MLCT and halogen to ligand charge transfer (XLCT) character.

Table VIII.4. Vertical electronic transitions calculated by TDDFT/B3LYP/CPCM method for HMPM and HMPM-Pd²⁺ in DMSO

Compds.	Energy (eV)	Wavelength (nm)	Osc. strength (f)	Transition	Character	$\lambda_{\text{expt.}}$ (nm)
HMPM	3.2408	382.6	0.1580	(92%) HOMO→LUMO	$\pi \rightarrow \pi^*$	395
	3.4556	358.8	0.1139	(77%) HOMO-1→LUMO+1	$n \rightarrow \pi^*$	
	4.0151	308.8	0.4242	(91%) HOMO-2→LUMO+1	$\pi \rightarrow \pi^*$	295
	4.0953	302.8	0.1426	(94%) HOMO-3→LUMO	$\pi \rightarrow \pi^*$	
HMPM- Pd ²⁺	2.5270	490.6	0.0230	(98%) HOMO→LUMO	$\pi(\text{L}) \rightarrow \pi^*(\text{L})$ (ILCT)	
	2.6103	475.0	0.1766	(79%) HOMO→LUMO+1	$\pi(\text{L}) \rightarrow \pi^*(\text{L})$ (ILCT)	458
	3.5340	350.8	0.3449	(63%) HOMO-1→LUMO	$d\pi(\text{Pd})/p\pi(\text{Cl}) \rightarrow \pi^*(\text{L})$ (MLCT/XLCT)	355
				(29%) HOMO→LUMO+1	$\pi(\text{L}) \rightarrow \pi^*(\text{L})$ (ILCT)	
	3.8773	319.8	0.1232	(93%) HOMO-3→LUMO+1	$d\pi(\text{Pd}) \rightarrow \pi^*(\text{L})$ (MLCT)	
	4.1953	295.5	0.2103	(47%) HOMO-5→LUMO+1 (42%) HOMO-6→LUMO	$d\pi(\text{Pd})/\pi(\text{L}) \rightarrow \pi^*(\text{L})$ (MLCT/ILXT)	289
	4.9154	252.2	0.2538	(77%) HOMO-7→LUMO+1	$\pi(\text{L}) \rightarrow \pi^*(\text{L})$ (ILCT)	

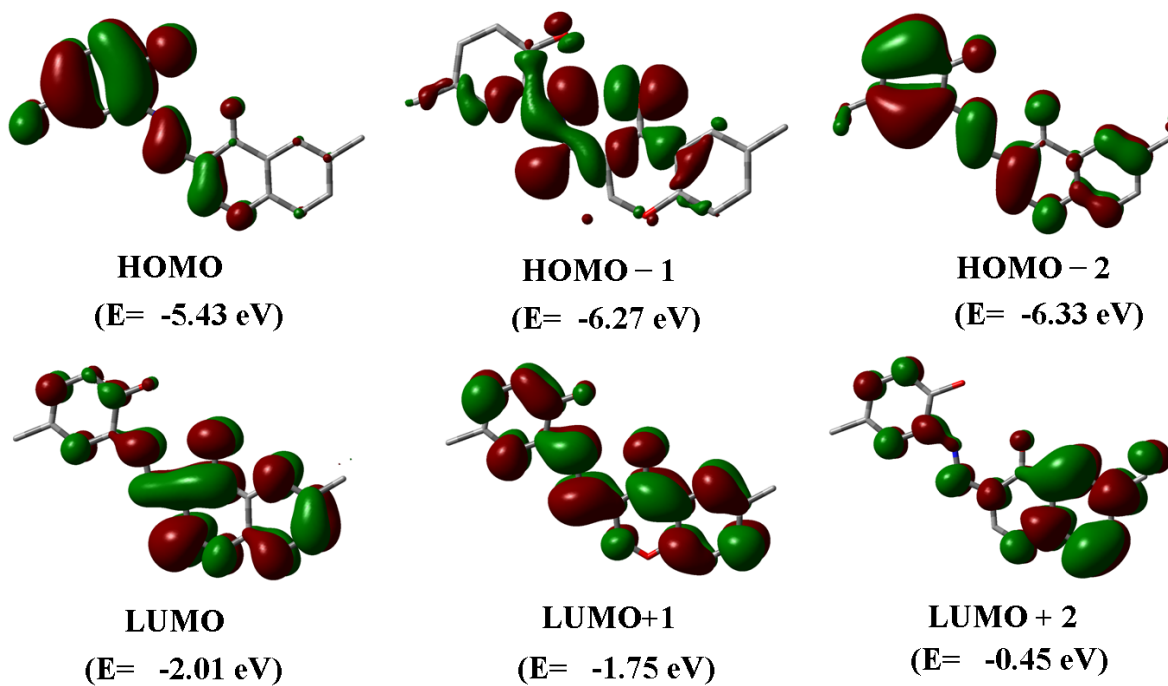


Fig.VIII.15. Contour plots of some selected molecular orbitals of HMPM

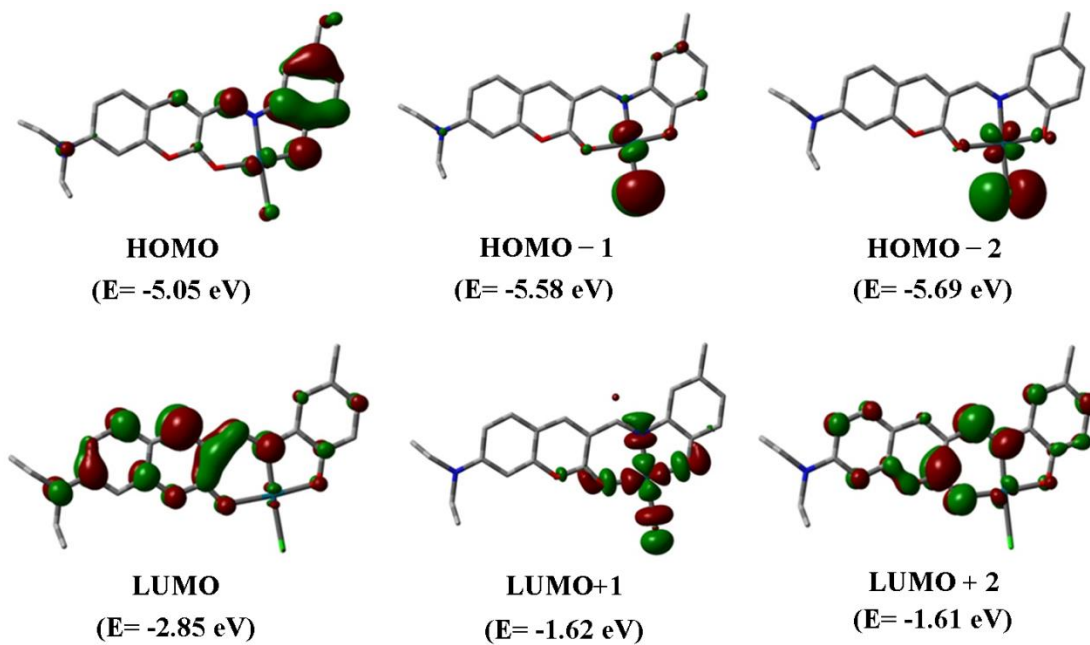


Fig.VIII.16. Contour plots of some selected molecular orbitals of HMPM-Pd²⁺ complex

Table VIII.4. Energy and compositions of some selected molecular orbitals of HMPM-Pd²⁺

MO	E, eV	% of composition		
		Pd	HMPM	Cl
LUMO+7	0.62	02	98	0
LUMO+6	0.45	03	97	0
LUMO+5	0.10	100	0	0
LUMO+4	-0.73	0	100	0
LUMO+3	-0.96	01	99	0
LUMO+2	-1.76	55	30	15
LUMO+1	-2.50	04	96	0
LUMO	-2.80	02	98	0
HOMO	-5.30	04	94	02
HOMO-1	-5.82	25	07	68
HOMO-2	-5.92	16	03	82
HOMO-3	-6.39	79	11	11
HOMO-4	-6.52	15	81	04
HOMO-5	-7.06	49	51	0
HOMO-6	-7.42	29	59	12
HOMO-7	-7.54	08	90	02
HOMO-8	-7.66	20	24	56
HOMO-9	-7.75	57	25	19
HOMO-10	-8.16	05	94	01
HOMO-11	-8.58	12	88	01
HOMO-12	-8.68	50	46	03

VIII.3.8. Dip-stick experiment: Sensing of Pd²⁺ using TLC plate

Enthused by the discrete and sharp detection of HMPM towards Pd²⁺, some potential application was brought out by using the single probe as a usable and portable tool for the sole detection of the metal cation. Without the support of any other instruments, it can provide with some crucial qualitative study on binding of Pd²⁺ with the probe HMPM in the solid state. To facilitate the fulfilment of this experiment, two thin-layer chromatography (TLC) plates were prepared and dipped into HMPM solution (2×10^{-4} M) in DMSO and then kept for few minutes for the evaporation of the solvent, followed by immersing the TLC plates to Pd²⁺ (2×10^{-3} M) solution and then again dried to evaporate the solvent.

The colour of the TLC plates changes from yellow to orange in ambient light while under UV light the colour changes from fern green to yellow in presence of Pd²⁺ (Fig. VIII.17). This experiment brings forth a real time monitoring and it is an analysis which is executed just via naked-eye detection and so using TLC plates we can easily explore a qualitative instantaneous detection of Pd²⁺.

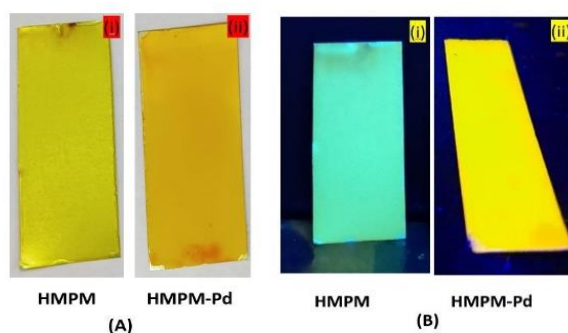


Fig.VIII.17: Changes in colour of HMPM coated TLC plates in presence of Pd²⁺, images taken in (A) ambient light and (B) under hand-held UV light

VIII.4. Conclusions

A new chromone based fluorescent probe, HMPM is synthesized and characterized by spectroscopic techniques. HMPM exhibits selective ratiometric fluorescence enhancement in presence of Pd²⁺ which can be attributed to the ESIPT and/or ICT process. Moreover, HMPM is efficient enough to detect Pd²⁺ in presence of other metal ions in nM range. The interaction HMPM with Pd²⁺ is established by various spectroscopic techniques. Further, the square planar geometry of HMPM-Pd²⁺ complex is confirmed by single crystal X-ray diffraction method in solid state. Electronic structures of HMPM and HMPM-Pd²⁺ are studied by Density Functional Theory (DFT) method. Most importantly the probe is efficient to detect Pd²⁺ by dip-stick method.

VIII.5. References

1. K. E. Jarvis, S. J. Parry and J. M. Piper, *Environ. Sci. Technol.*, 2001, **35**, 1031-1036.
2. Aarzo, Nidhi and M. Samim, *Sci. Total Environ.*, 2022, **823**, 153787.
3. E. Antolini, *Energy Environ. Sci.*, 2009, **2**, 915-931.
4. T. Iwasawa, M. Tokunaga, Y. Obora and Y. Tsuji, *J. Am. Chem. Soc.*, 2004, **126**, 6554-6555.
5. X.-F. Wu, H. Neumann and M. Beller, *Chem. Soc. Rev.*, 2011, **40**, 4986-5009.
6. R. Jana, T. P. Pathak and M. S. Sigman, *Chem. Rev.*, 2011, **111**, 1417-1492.
7. T. Jiang, Y. Yuan, S. Liu, J. Hunt and G. Tan, *ACS Omega*, 2020, **5**, 16021-16029.
8. P. Destito, A. Sousa-Castillo, J. R. Couceiro, F. López, M. A. Correa-Duarte and J. L. Mascareñas, *Chem. Sci.*, 2019, **10**, 2598-2603.
9. J. M. Chalker, C. S. C. Wood and B. G. Davis, *J. Am. Chem. Soc.*, 2009, **131**, 16346-16347.
10. C. D. Spicer and B. G. Davis, *Chem. Commun.*, 2011, **47**, 1698-1700.
11. Z. Gao, V. Gouverneur and B. G. Davis, *J. Am. Chem. Soc.*, 2013, **135**, 13612-13615.
12. F. Alt and F. Zereini, *Palladium Emissions in the Environment Analytical Methods, Environmental Assessment and Health Effects*, Springer: Berlin, Germany, 2006.
13. J. Kielhorn, C. Melber, D. Keller and I. Mangelsdorf, *Int. J. Hyg. Environ. Health*, 2002, **205**, 417-432.
14. T. R. de Moura, R. D. Zanetti, D. E. S. Silva, R. L. de Farias, A. E. Mauro, J. C. M. Pereira, A. A. de Souza, F. da Silva Siqueira, W. A. de Souza Júdice, M. A. Lima, F. V. Rocha, V. M. Deflon and A. V. de Godoy Netto, *New J. Chem.*, 2020, **44**, 19891-19901.
15. C. D. Spicer, T. Triemer and B. G. Davis, *J. Am. Chem. Soc.*, 2012, **134**, 800-803.
16. P. Kumar, V. Kumar and R. Gupta, *RSC Adv.*, 2017, **7**, 7734-7741.
17. J. -wu Yan, X. -lin Wang, L. -fu Zhou and L. Zhang, *RSC Adv.*, 2017, **7**, 20369-20372.

18. C. L. Wiseman and F. Zereini, *Sci. Total Environ.*, 2009, **407**, 2493-500.
19. X. Bu, K. Koide, E. J. Carder and C. J. Welch, *Org. Process Res. Dev.*, 2013, **17**, 108-113.
20. M. Chatzopoulou, K. S. Madden, L. J. Bromhead, C. Greaves, T. J. Cogswell, S. Da Silva Pinto, S. R. G. Galan, I. Georgiou, M. S. Kennedy, A. Kennett, G. Apps, A. J. Russell and G. M. Wynne, *ACS Med. Chem. Lett.*, 2022, **13**, 262-270.
21. J. Wang, F. Song, J. Wang and A. Peng, *Analyst*, 2013, **138**, 3667-3672.
22. A. Brammertz and M. Augthun, *The Annals of Occupational Hygiene*, 1997, **41**, 615-620.
23. K. Leopold, M. Maier, S. Weber and M. Schuster, *Environ Pollut.*, 2008, **156**, 341-347.
24. F. Zereini, C. Wiseman and W. Püttmann, *Environ. Sci. Technol.*, 2007, **41**, 451-456.
25. J. C. Ely, C. R. Neal, C. F. Kulpa, M. A. Schneegurt, J. A. Seidler and J. C. Jain, *Environ. Sci. Technol.*, 2001, **35**, 3816-3822.
26. F. Zereini, C. L. Wiseman and W. Püttmann, *Environ. Sci. Technol.*, 2012, **46**, 10326-10333.
27. B. Dimitrova, K. Benkhedda, E. Ivanova and F. Adams, *J. Anal. At. Spectrom.*, 2004, **19**, 1394-1396.
28. C. Locatelli, D. Melucci and G. Torsi, *Anal. Bioanal. Chem.*, 2005, **382**, 1567-1573.
29. K. Van Meel, A. Smekens, M. Behets, P. Kazandjian and R. Van Grieken, *Anal. Chem.*, 2007, **79**, 6383-6389.
30. K. P. Carter, A. M. Young and A. E. Palmer, *Chem. Rev.*, 2014, **114**, 4564-4601.
31. T. Gao, P. Xu, M. Liu, A. Bi, P. Hu, B. Ye, W. Wang and W. Zeng, *Chem. Asian J.*, 2015, **10**, 1142-1145.
32. A. K. Bhanja, S. Mishra, K. Das Saha and C. Sinha, *Dalton Trans.*, 2017, **46**, 9245-9252.
33. F. K. Tang, S. M. Chan, T. Wang, C. S. Kwan, R. Huang, Z. Cai, K. C. F. Leung, *Talanta*, 2020, **210**, 120634.

34. F. Song, A. L. Garner and K. Koide, *J. Am. Chem. Soc.*, 2007, **129**, 12354-12355.
35. M. Santra, S. K. Ko, I. Shin and K. H. Ahn, *Chem. Commun.*, 2010, **46**, 3964-3966.
36. B. Liu, H. wang, T. Wang, Y. Bao, F. Du, J. Tian, Q. Li and R. Bai, *Chem. Commun.*, 2012, **48**, 2867-2869.
37. S. Farshbaf and P. Anzenbacher, *Chem. Commun.*, 2019, **55**, 1770-1773.
38. S. Mahata, A. Bhattacharya, J. P. Kumar, B. B. Mandal and V. Manivannan, *J. Photochem. Photobiol. A*, 2020, **394**, 112441.
39. P. Kumar, V. Kumar and R. Gupta, *RSC Adv.*, 2017, **7**, 7734-7741.
40. H. Li, J. Fan, M. Hu, G. Cheng, D. Zhou, T. Wu, F. Song, S. Sun, C. Duan and X. Peng, *Chem. Eur. J.*, 2012, **18**, 12242-12250.
41. H. Li, J. Fan, F. Song, H. Zhu, J. Du, S. Sun and X. Peng, *Chem. Eur. J.*, 2010, **16**, 12349-12356.
42. S. Cai, Y. Lu, S. He, F. Wei, L. Zhao and X. Zeng, *Chem. Commun.*, 2013, **49**, 822-824.
43. M. H. Lee, J. S. Kim and J. L. Sessler, *Chem. Soc. Rev.*, 2015, **44**, 4185-4191.
44. B. Wang, X. -Q. Zhou, L. Li, Y. -X. Li, L. -P. Yu and Y. Chen, *Sens. Actuators B: Chem.*, 2022, **369**, 132392.
45. W. Luo, and W. Liu, *J. Mater. Chem.*, 2016, **4**, 3911-3915.
46. L. Cui, W. Zhu, Y. Xu and X. Qian, *Anal. Chim. Acta.*, 2013, **786**, 139-145.
47. Gaussian 09, Revision D.01, M. J. Frisch, G. W. Trucks, H. B. Schlegel, G. E. Scuseria, M. A. Robb, J. R. Cheeseman, G. Scalmani, V. Barone, B. Mennucci, G. A. Petersson, H. Nakatsuji, M. Caricato, X. Li, H. P. Hratchian, A. F. Izmaylov, J. Bloino, G. Zheng, J. L. Sonnenberg, M. Hada, M. Ehara, K. Toyota, R. Fukuda, J. Hasegawa, M. Ishida, T. Nakajima, Y. Honda, O. Kitao, H. Nakai, T. Vreven, J. A. Montgomery, Jr., J. E. Peralta, F. Ogliaro, M. Bearpark, J. J. Heyd, E. Brothers, K. N. Kudin, V. N. Staroverov, R. Kobayashi, J. Normand, K. Raghavachari, A. Rendell, J. C. Burant, S. S. Iyengar, J.

- Tomasi, M. Cossi, N. Rega, J. M. Millam, M. Klene, J. E. Knox, J. B. Cross, V. Bakken, C. Adamo, J. Jaramillo, R. Gomperts, R. E. Stratmann, O. Yazyev, A. J. Austin, R. Cammi, C. Pomelli, J. W. Ochterski, R. L. Martin, K. Morokuma, V. G. Zakrzewski, G. A. Voth, P. Salvador, J. J. Dannenberg, S. Dapprich, A. D. Daniels, Ö. Farkas, J. B. Foresman, J. V. Ortiz, J. Cioslowski and D. J. Fox, Gaussian, Inc., Wallingford CT, 2009.
48. A. D. Becke, *J. Chem. Phys.*, 1993, **98**, 5648-5652.
49. C. Lee, W. Yang and R. G. Parr, *Phys. Rev. B*, 1988, **37**, 785-789.
50. P. J. Hay and W. R. Wadt, *J. Chem. Phys.*, 1985, **82**, 270-283.
51. W. R. Wadt, P. J. Hay, *J. Chem. Phys.*, 1985, **82**, 284-298.
52. P. J. Hay and W. R. Wadt, *J. Chem. Phys.*, 1985, **82**, 299-310.
53. R. Bauernschmitt and R. Ahlrichs, *Chem. Phys. Lett.*, 1996, **256**, 454-464.
54. R. E. Stratmann, G. E. Scuseria and M. J. Frisch, *J. Chem. Phys.*, 1998, **109**, 8218-8224.
55. M. E. Casida, C. Jamorski, K. C. Casida and D. R. Salahub, *J. Chem. Phys.*, 1998, **108**, 4439-4449.
56. V. Barone and M. Cossi, *J. Phys. Chem. A*, 1998, **102**, 1995-2001.
57. M. Cossi and V. Barone, *J. Chem. Phys.*, 2001, **115**, 4708-4717.
58. M. Cossi, N. Rega, G. Scalmani and V. Barone, *J. Comput. Chem.*, 2003, **24**, 669-681.
59. K. Xiang, Y. Liu, C. Li, B. Tian and J. Zhang, *RSC Adv.*, 2015, **5**, 52516-52521.
60. W. Liu, J. Jiang, C. Chen, X. Tang, J. Shi, P. Zhang, K. Zhang, Z. Li, W. Dou, L. Yang and W. Liu, *Inorg. Chem.*, 2014, **53**, 12590-12594.
61. J. Jiang, H. Jiang, W. Liu, X. Tang, X. Zhou, W. Liu and R. Liu, *Org. Lett.*, 2011, **13**, 4922-4925.
62. J. J. Celestina, P. Tharmaraj, C. D. Sheela, L. Alphonse and J. Shakina, *Opt. Mater.*, 2020, **109**, 110444.

63. P. Naksen, S. Boonruang, N. Yuenyong, H. L. Lee, P. Ramachandran, W. Anutrasakda, M. Amatatongchai, S. Pencharee and P. Jarujamrus, *Talanta*, 2022, **242**, 123305.

List of Publication

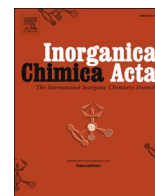
1. Palladium(II) complexes with thioether based ONS donor ligand: Synthesis, characterization, X-ray structure, DFT study and anti-cancer activity;
Rahul Naskar, Paramita Ghosh, Chandan Kumar Manna, Nabendu Murmu, Tapan Kumar Mondal,* *Inorganica Chim. Acta.* 534 (2022) 120802.
2. Palladium(II) complex bearing benzothiazole based O,N,S donor pincer ligand: Study of in-vitro cytotoxicity, interaction with CT-DNA and BSA protein;
Rahul Naskar, Paramita Ghosh, Subrata Mandal, Nabendu Murmu,* and Tapan Kumar Mondal,* *J. Chem. Sci.* 103 (2022) 134.
3. A new chromone based fluorescence probe for ratiometric detection of Pd²⁺;
Rahul Naskar, Saswati Gharami, Subrata Mandal, and Tapan Kumar Mondal,* *New J. Chem.* 46 (2022) 17912.
4. Palladium(II) and platinum(II) complexes with ONN donor pincer ligand: synthesis, characterization and in vitro cytotoxicity study;
Biswajit Bera, Sanchaita Mondal, Saswati Gharami, **Rahul Naskar**, Krishna Das Saha,* and Tapan K. Mondal,* *New J. Chem.* 46 (2022) 11277-11285.
5. A new “turn-on” molecular switch for idiosyncratic detection of Al³⁺ ion along with its application in live cell imaging;
Amitav Biswas, **Rahul Naskar**, Debarpan Mitra, Akash Das, Saswati Gharami, Nabendu Murmu and Tapan Kumar Mondal,* *New J. Chem.* 46 (2022) 21968-21975.
6. Manganese(II) complex with ONS donor redox non-innocent azothioether pincer ligand: synthesis, X-ray structure, electrochemistry and DFT computation;
Apurba Sau Mondal, **Rahul Naskar**, Chandan Kumar Manna and Tapan Kumar Mondal* *J. Chem. Sci.* 82 (2022) 134.
7. A new palladium(II) phosphino complex with ONS donor Schiff baseligand: Synthesis, characterization and catalytic activity towards Suzuki-Miyaura cross-coupling reaction;

- Chandan Kumar Manna, **Rahul Naskar**, Biswajit Bera, Akash Das, Tapan Kumar Mondal*,
J. Mol. Struct. 1237 (2021) 130322.
8. Synthesis of new rhodium(III) complex by benzylic C-S bond cleavage of thioether containing NNS donor Schiff base ligand: Investigation of catalytic activity towards transfer hydrogenation of Ketones;
Sujan Biswas, Chandan Kumar Manna, **Rahul Naskar**, Akash Das, Tapan Kumar Mondal*,
Inorg. Chim Acta, 115 (2021) 120096.
9. Synthesis, characterization, X-ray structure and DNA binding study of palladium(II) complex with new thioether containing ONS donor ligand;
Subrata Jana, **Rahul Naskar**, Chandan Kumar Manna and Tapan Kumar Mondal*, *J. Chem. Sci.* 64 (2020) 132.
10. Palladium(II) complex with 1-(2-pyridylazo)-2-naphthol (PAN): Synthesis, X-ray structure, electrochemistry, DFT computation and DNA binding study;
Chandan Kumar Manna, **Rahul Naskar** and Tapan Kumar Mondal*, *J. Indian Chem. Soc.* 96 (2019) 599.
11. Luminescent rhenium(I) carbonyl complex with redox noninnocent ONS donor azo-phenol ligand: Synthesis, X-ray structure, photophysical properties and live cell imaging;
Puspendu Roy, Deblina Sarkar, Paramita Ghosh, **Rahul Naskar**, Nabendu Murmu and Tapan Kumar Mondal*, *Polyhedron* 161 (2019) 154-160.
12. Synthesis of a rhodium(III) triphenylphosphine complex via C-S bond cleavage of an azo-thioether ligand: X-ray structure, electrochemistry and catalysis towards transfer hydrogenation of ketones;
Puspendu Roy, Chandan Kumar Manna, **Rahul Naskar** and Tapan Kumar Mondal*,
Polyhedron 158 (2019) 208.
13. Synthesis of thiolato bridged dimeric rhodium(III) triphenylphosphine complex via C-S bond cleavage: X-ray structure, DFT computation and catalytic evaluation towards transfer hydrogenation of ketones;

Puspendu Roy, **Rahul Naskar**, Chandan Kumar Manna and Tapan Kumar Mondal*, *J. Mol. Struct.* 1198 (2019) 126932.

14. Synthesis of a zinc(II) complex with hexadentate N₄S₂ donor thioether ligand: X-ray structure, DNA binding study and DFT computation;

Apurba Sau Mondal, Mahendra Sekhar Jana, Chandan Kumar Manna, **Rahul Naskar** and Tapan Kumar Mondal*, *J. Mol. Struct.* 1164 (2018) 94.



Palladium(II) complexes with thioether based ONS donor ligand: Synthesis, characterization, X-ray structure, DFT study and anti-cancer activity

Rahul Naskar^a, Paramita Ghosh^b, Chandan Kumar Manna^a, Nabendu Murmu^b,
Tapan Kumar Mondal^{a,*}

^a Inorganic Chemistry Section, Department of Chemistry, Jadavpur University, Kolkata 700032, India

^b Department of Signal Transduction and Biogenic Amines (STBA), Chittaranjan National Cancer Institute, Kolkata 700026, India

ARTICLE INFO

Keywords:

Palladium(II) complex
ONS donor thioether ligand
X-ray structure
Electrochemistry
DFT computation
Anti-cancer activity

ABSTRACT

Synthesis of new palladium(II) complexes, [Pd(L)Cl] (**C1**) and [Pd(L)PPh₃](ClO₄) (**C2**), with ONS donor thioether ligand (HL) is reported. All the complexes were thoroughly characterized by using numerous spectroscopic techniques like FT-IR, NMR and UV–visible spectroscopy and so forth. Distorted square planar geometries of the complexes were confirmed unambiguously by means of single crystal X–ray diffraction analysis. Moreover, DFT and TDDFT calculations were performed to interpret the electronic structure, redox and spectral properties of the complexes. Cytotoxicity of the complexes was evaluated in vitro using MTT assay on human gastric cancer cell lines (AGS). The anti-cancer effects of HL and palladium(II) complexes (**C1/C2**) on AGS cell lines were determined by comparing the half maximal inhibitory concentration (IC₅₀) values. The results revealed that synthesized palladium(II) complexes (**C1/C2**) showed higher anti-cancer activity (IC₅₀ = 13.4 μM for **C1** and 16.0 μM for **C2**) compare to HL against AGS cell lines (67.1 μM).

1. Introduction

In recent years, transition metal complexes incorporated with ONS donor ligands are considerably studied because of their mode of coordination, structural diversity, spectral features and extensive biological applications for instance antitumor, antifungal, anti-bacterial, antiviral, anti-tuberculosis and anti-inflammatory activities [1–5]. Furthermore, thioether ligands can stabilize unusual oxidation states of the transition metals within the complexes and participated in a variety of engrossing electrochemical reactions [6–8]. Schiff base ligand with transition metal complexes showcase pivotal inhibition of DNA synthesis via binding through intercalation mode [9]. Again, transition metal complexes with S and N donor chelating ligands are of great interest because of their significant antifungal, antibacterial and anticancer activities [10–14]. Sulfur atom of thioether ligand coordinated to metal centre can also mimic the active sites of numerous metalloproteins [15–17]. Moreover, transition metal complexes with polydentate ligands are important due to the fact that they are capable to binding and cleaving of DNA under physiological conditions [18,19].

In general, metal-based drugs like cisplatin (*cis*-Pt(NH₃)₂Cl₂), an antitumor drug, exhibits its cytotoxic activity by targeting DNA and

forming covalent bonds between the platinum metal and the close by purine bases through their N7 positions [20]. But cisplatin suffers severe consequences like nephrotoxicity and ototoxicity [21,22], which stimulate researchers to discover alternative chemotherapeutic strategies. In this context, palladium can also be a better alternative for platinum as anticancer drug because of their coordination capability, thermodynamical, structural and chemical similarities [23]. But ligand exchange activities of the palladium complexes display almost 10⁴–10⁵ times more than their platinum counterparts [24] and leads to the formation of undesired chemical species before reaching to the target biomolecules [25]. This problem can be addressed by using suitable chelating agents to form stable complexes. In addition, ligands like pyridine and its derivatives, quinoline, pyrazole and 1,10-phenanthroline coordinated with Pd(II) ions have proven promising antitumor activities [26–28]. Consequently, new derivatives of palladium(II) complexes may be designed to enhance anticancer activity and reduce toxicity.

In recent years, the coordination chemistry of transition metal complexes with thioether ligands are extensively studied by our group [29–35], herein we have synthesized two palladium(II) complexes, [Pd(L)Cl] (**C1**) and [Pd(L)PPh₃](ClO₄) (**C2**) with ONS donor thioether ligand (HL). The complexes were thoroughly characterized by numerous

* Corresponding author.

E-mail address: tapank.mondal@jadavpuruniversity.in (T.K. Mondal).

<https://doi.org/10.1016/j.ica.2022.120802>


Received 25 September 2021; Received in revised form 15 December 2021; Accepted 6 January 2022

Available online 15 January 2022

0020-1693/© 2022 Elsevier B.V. All rights reserved.



Palladium(II) complex bearing benzothiazole based O,N,S donor pincer ligand: Study of in-vitro cytotoxicity, interaction with CT-DNA and BSA protein

RAHUL NASKAR^a, PARAMITA GHOSH^b, SUBRATA MANDAL^a, SUBRATA JANA^a,
NABENDU MURMU^{b,*} and TAPAN KUMAR MONDAL^{a,*} 

^aInorganic Chemistry Section, Department of Chemistry, Jadavpur University, Kolkata 700032, India

^bDepartment of Signal Transduction and Biogenic Amines (STBA), Chittaranjan National Cancer Institute, Kolkata 700026, India

E-mail: nabendu.murmu@cnci.org.in; tapank.mondal@jadavpuruniversity.in

MS received 28 June 2022; revised 19 August 2022; accepted 23 August 2022

Abstract. A new palladium(II) complex, [Pd(LS^{Et})Cl] (**C1**) with benzothiazole based ONS donor pincer ligand (HLS^{Et}) was synthesized (where, HLS^{Et} = 2-(benzothiazol-2-yl)-6-(((2-(ethylthio)phenyl)imino)methyl)phenol). Interaction of **C1** with CT DNA was investigated, and its binding constant was found to be $4.0 \times 10^5 \text{ M}^{-1}$. The proficiency of ethidium bromide (EB) displacement from its EB-CTDNA complex by **C1** was performed by the fluorescence quenching method, and Stern-Volmer quenching constant (K_{sv}) was found to be $4.3 \times 10^5 \text{ M}^{-1}$. Similarly, the interaction of **C1** with BSA protein was investigated by UV-Vis and fluorescence methods. The apparent association constant (K_a) and K_{sv} were determined ($K_a = 2.8 \times 10^4 \text{ M}^{-1}$ and $K_{sv} = 5.5 \times 10^4 \text{ M}^{-1}$). In vitro cytotoxicity of the complex, [Pd(LS^{Et})Cl] (**C1**), towards human gastric cancer cell lines (AGS) was assessed by the MTT assay method. The half maximal inhibitory concentration (IC₅₀) of **C1** ($9.55 \pm 1.23 \text{ }\mu\text{M}$) towards AGS cancer lines was found to be lower than cisplatin ($23.13 \pm 1.03 \text{ }\mu\text{M}$).

Keywords. Palladium(II) complex; Benzothiazole; X-ray structure; DNA binding; DFT calculation; Cytotoxicity.

1. Introduction

Among noninfectious diseases causing 72% of death worldwide, cancer is considered the second leading according to mortality.¹ Most anticancer drugs target DNA molecules and modify the DNA structure by forming an irreversible covalent bond and the non-covalent bond, which ultimately affects DNA replication and transcription because cancer cells proliferate more than non-neoplastic cells.^{2,3} The ligands around the metal-based anticancer drugs play a pivotal role in showing anticancer activity because of their modifying ability and lipophilicity.⁴ There is considerable interest in Schiff bases containing ONS donor ligand chelated with different 3d- or 4d- metals owing to their chelation mode, structural, spectral features, and several biological aspects such as anticancer,

antibacterial, antiviral, antifungal, and anti-inflammatory activity.^{5,6} Schiff base ligands are also important because they can stabilize the uncommon oxidation states of transition metals.^{7,8}

Heterocyclic aromatic ligands such as pyridine, phenanthroline, and their derivatives are reported to be DNA intercalators in palladium and ruthenium complexes.⁹ Moreover, a thioether ligand containing an S atom chelated to metal may replicate the active site structures of several metalloproteins.^{10–12} N and S containing metal complexes show promising anticancer, antifungal, and antibacterial activities.^{13–17} After the remarkable discovery in medicinal chemistry, cisplatin is used as a chemotherapeutic drug worldwide. Only six platinum-based drugs have been approved so far, including three globally (cisplatin,

*For correspondence

Supplementary Information: The online version contains supplementary material available at <https://doi.org/10.1007/s12039-022-02101-w>.



Cite this: *New J. Chem.*, 2022, **46**, 17912

Received 11th May 2022,
 Accepted 17th August 2022

DOI: 10.1039/d2nj02310e

rsc.li/njc

A new chromone-based fluorescent probe for ratiometric detection of Pd²⁺†

Rahul Naskar, Saswati Gharami, Subrata Mandal and Tapan Kumar Mondal *

A new chromone-based fluorescent probe (HMPM) is introduced for the selective detection of Pd²⁺. The designed probe exhibits a ratiometric fluorescence enhancement, which can be attributed to the ESIPT and/or chelation enhancement fluorescence (CHEF) processes. HMPM is efficient enough to detect Pd²⁺ solely in the presence of other metal ions in DMSO/H₂O solution (1 : 1, v/v, pH = 7.2) with a limit of detection as low as 2.9 nM. Furthermore, the complex formation of HMPM with Pd²⁺ is confirmed by the single crystal X-ray diffraction method. The changes in electronic structure and absorption spectrum of HMPM upon complexation with Pd²⁺ are supported by DFT and TDDFT calculations. Moreover, the probe (HMPM) could be effectively used for the detection of Pd²⁺ by a dipstick method.

Introduction

Palladium is one of the rare and valuable transition metals of platinum group elements (PGEs). It is widely used in an array of applications such as the jewellery industry, coating materials, dental crowns and chemical catalysts and also broadly used as a significant component in a range of materials such as fuel cells.^{1–7} It has a crucial role to play in chemical transformations by acting as a catalyst in reactions like the Suzuki–Miyaura, Sonogashira, Heck, and Pd-catalyzed depropargylation reactions that are extensively used to create complex molecules in the pharmaceutical industries.^{8–11} Palladium is also an essential material in highly technological fields such as navigation, aviation and also in the automotive industry.¹² The non-biodegradable nature of palladium along with its enhanced emission in the environment can result in severe health hazards *via* accumulating in the food chain. Due to their high nucleophilicity, palladium can bind to thiol-containing proteins such as casein and silk fibroin, DNA or other biomolecules, which eventually results in the degradation of DNA and cell mitochondria and also in enzyme inhibition.^{13,14} Owing to its thiophilic nature, palladium can bind with DNA, proteins and other macromolecules and perturb a range of cellular processes.^{15–17} Environmental pollution emissions to water and soil may be the result of palladium residues in pharmaceutical compounds or in the environment,^{18–20} thereby making the proposed maximum dietary intake for this ubiquitous

and lethal heavy metal less than 1.5–15 g per person per day and its threshold in drugs is 5–10 ppm.²¹ Furthermore, palladium also hampers the activity of many enzymatic reactions such as alkaline phosphatase, creatine kinase and prolyl hydroxylase.^{22,23} Although a large number of carbon–carbon bond formation reactions are facilitated by palladium catalysts, the extensive use of palladium has led to an elevated level of residual palladium in water systems and soil, which is destructive to public health.^{24–26} Hence designing and fabricating a selective and distinctly responsive analytical method for the identification of palladium in the environment is crucial to evaluate potential unpleasant health effects caused by this particular metal residue.

The usual techniques used for the quantification of palladium species, such as atomic absorption spectroscopy (AAS), inductively coupled plasma atomic emission spectroscopy, solid-phase microextraction high-performance liquid chromatography, *etc.*, offer a fast and exceptionally sensitive analysis, although often prove to be more time-consuming and sometimes need intricate sample-pretreatment methods, refined instrumentation and meticulous and thorough experimental procedures and thus are not so suitable for real-time and *in situ* analysis.^{27–29} In recent years, fluorescent sensors are widely used for the detection of Pd²⁺ because of their high selectivity, high sensitivity, cost effectiveness and real time detection.^{30–33} So far, different strategies are adopted to develop fluorescent sensors for effective detection of Pd²⁺. Palladium-catalyzed chemical transformation is one of the popular strategies used to develop fluorescent sensors for the selective detection of Pd²⁺.^{34–36} As an efficient fluorescence quencher, Pd²⁺ could also be detected by using strong fluorescence probes by a fluorescence quenching mechanism.^{37–39} However, fluorescence “turn-on” chemosensors are considered to be more efficient. Recently,

Department of Chemistry, Jadavpur University, Kolkata-70003, India.

E-mail: tapank.mondal@jadavpuruniversity.in

† Electronic supplementary information (ESI) available. CCDC 2067540. For ESI and crystallographic data in CIF or other electronic format see DOI: <https://doi.org/10.1039/d2nj02310e>



Cite this: DOI: 10.1039/d2nj03481f

A new “turn-on” molecular switch for idiosyncratic detection of Al³⁺ ion along with its application in live cell imaging†

 Amitav Biswas,^a Rahul Naskar,^a Debarpan Mitra,^b Akash Das,^a Saswati Gharami,^a Nabendu Murmu^b and Tapan Kumar Mondal *^a

A highly sensitive, reversible, reusable and fluorogenic “turn-on” probe (HBTC) is fabricated for the sole detection of Al³⁺. On incremental addition of Al³⁺ in a solution of HBTC in ACN:H₂O (4:1), a sharp “turn-on” emission enhancement is observed at 480 nm. The reversibility of the probe (HBTC) was displayed on the addition of F⁻ solution. The detection limit is found to be of the order of 10⁻⁹ M which suggests that HBTC can detect Al³⁺ at a very minute level. The mechanism for Al³⁺ detection in ACN:H₂O (4:1) is attributed to forbidding C=N isomerization and ESIPT process simultaneously turning on the chelation-enhanced fluorescence process. The reusability and real-time application of the probe are also studied. Bioimaging study reveals that HBTC can detect Al³⁺ in human breast cancer cells (MDA-MB-231). Electronic structure of the probe is explained by density functional theory.

 Received 14th July 2022,
 Accepted 21st October 2022

DOI: 10.1039/d2nj03481f

rsc.li/njc

Introduction

Nowadays undue use of ionic pollutants in industry and the farming sector has become a menace to the environment.^{1,2} Hence rapid and accurate detection of those ions has become a promising part in the research field in modern times. It is well known that aluminium is the most abundant metallic element in earth's crust. And it has become an integrated part of daily lifestyle such as in drinking water supplies, utensils, packaging of foods, powder, cosmetic products, processed dairy products, cookware, bleached flour, component of medicine, medicine storage containers and manufacturing of cars.³⁻⁷ The WHO (World Health Organization) stated that the average consumption of Al³⁺ in the human body through several ways is about 3–10 mg per kg per day and the maximum recommended limit Al-contaminated water is 7.42 μM.⁸⁻¹⁰ Although it has negative effects on both biological and environment systems, it is extensively used on a daily basis. The central nervous system is deeply affected by overexposure of Al.¹¹ Abnormal concentration of Al in the human body is related to many neurological disorders including Alzheimer's disease, Parkinson's disease and dementia.¹²⁻¹⁴ On the other hand, regular intake of Al

beyond permissible limits causes bone disease, damage in the gastrointestinal tract, encephalopathy, microcytic hypochromic anaemia, myopathy, bone softening, impaired lung function, fibrosis and chronic renal failure.¹⁵⁻¹⁸ Therefore, it is imperative to develop probes that can detect and track aluminium ions with high sensitivity using minimal resources and under biological conditions. Among different sensing tools for detection of such kinds of environmental hazardous metal, fluorescence-based chemosensors are considered to be efficient for specifically detecting target analytes.¹⁹ Different mechanisms like excited-state intra-/intermolecular proton transfer (ESIPT), chelation-enhanced fluorescence (CHEF), metal–ligand charge transfer, photoinduced electron/energy transfer, fluorescence resonance energy transfer, intramolecular charge transfer, and –C=N– isomerisation are considered to be the reason for chemosensing processes.^{20,21} A strong oxidising site is preferred for the CHEF process, through which a radiative process gets turn on.²² Comparing with different transition metal ions, chemosensors detecting solely Al³⁺ are limited, due to poor coordination power, strong hydration enthalpy and lack of spectroscopic characteristics.^{23,24} Being a hard acid, Al³⁺ always prefers to bind hard centres like N and O donor sites. Schiff bases possess excellent coordinating capabilities, showing different biological activities and have potential analytical application.^{25,26} Hence, development of probes with such binding sites causing metal–ligand CHEF is an interesting approach due to a fluorescence “turn-on” mechanism on interaction with a guest.

Recently in 2021, Singh *et al.* reported a silatrane-based Schiff base-functionalized probe which can detect Al³⁺ ions

^a Department of Chemistry, Jadavpur University, Kolkata, 700032, India.

 E-mail: tapank.mondal@jadavpuruniversity.in
^b Department of Signal Transduction and Biogenic Amines (STBA), Chittaranjan National Cancer Institute, Kolkata, 700026, India

 † Electronic supplementary information (ESI) available. See DOI: <https://doi.org/10.1039/d2nj03481f>



REGULAR ARTICLE

Manganese(II) complex with ONS donor redox non-innocent azo-thioether pincer ligand: synthesis, X-ray structure, electrochemistry and DFT computation

APURBA SAU MONDAL, RAHUL NASKAR, CHANDAN KUMAR MANNA and TAPAN KUMAR MONDAL*

Department of Chemistry, Jadavpur University, Kolkata 700032, India
E-mail: tapank.mondal@jadavpuruniversity.in

MS received 18 January 2022; revised 28 May 2022; accepted 22 June 2022

Abstract. An octahedral Mn(II) complex, [Mn(L)₂] is synthesized with redox active ONS donor azo-thioether pincer ligand, 3-(2-(2-(methylthio)phenyl)hydrazono)pentane-2,4-dione (HL). The complex is thoroughly characterized by means of several spectroscopic methods. The geometry of the complex is authenticated by the single-crystal X-ray diffraction technique. X-ray structure of [Mn(L)₂] revealed that HL is coordinated to three adjacent sites of Mn through thioether-S, azo-N, and enoloic-O atoms in meridional configuration. Theoretical calculation by DFT/B3LYP is carried out to interpret the electronic structure of [Mn(L)₂]. Cyclic voltammogram of [Mn(L)₂] in acetonitrile exhibit Mn(II)/Mn(III) oxidation and ligand-based reduction couples with reference to Ag/AgCl reference electrode.

Keywords. Manganese(II) complex; Redox non-innocent; Azo-thioether ligand; X-ray structure; DFT calculation; Electrochemistry.

1. Introduction

Manganese is the 12th most naturally occurring trace element found in the living systems, and it is required for the normal functioning of the brain and nervous system and the metabolism of amino acids, lipid, protein, and carbohydrates.¹⁻⁴ The biological activity of manganese complexes is significantly studied because it is an essential element in many biological systems⁵⁻⁷ and plays an important role in bioinorganic chemistry.^{8,9} Manganese exhibits a variety of oxidation states which plays a significant role in several important catalytic reactions like disproportionation of H₂O₂ and in several redox-based biochemical processes like water oxidation in Photosystem II and superoxide dismutases.¹⁰⁻¹³

Polydentate ligands with N and S donor atoms are widely used in coordination chemistry because they are crucial in biomedicine, catalysis, and dye-sensitized solar cells.¹⁴⁻¹⁶ Compounds containing N and S atoms have repeatedly attracted the interest of chemists owing to



their significant antifungal, antibacterial, antiviral and anticancer activities.¹⁷⁻¹⁹ Since nitrogen is a borderline Pearson donor and sulfur is a soft donor, the coordination chemistry of transition metals with N and S donor ligands is widely studied because of their variable coordination sites and flexibility in binding.²⁰⁻²² In recent years, the coordination chemistry of thioether ligands with transition metals has been of interest for their chemical, electrochemical and biological activities.²³⁻²⁷ Moreover, the -acidity of azo-thioether ligands can be tuned, and by regulating the redox properties, metal ions are stabilized in their lower oxidation states in transition metal complexes.^{23,28-30} So far, the coordination chemistry of transition metals with azo-thioether ligands of acetylacetonone is significantly explored.³¹⁻³³ In continuation of our recent studies on the coordination chemistry transition metals with azo-thioether ligands,³⁴⁻³⁸ herein we have synthesized and characterized a new octahedral manganese(II) complex, [Mn(L)₂] with O,N,S donor azo-thioether pincer ligand, 3-(2-(2-(methylthio)phenyl)hydrazono)pentane-2,4-dione (HL).

*For correspondence

Supplementary Information: The online version contains supplementary material available at <https://doi.org/10.1007/s12039-022-02080-y>.


 Cite this: *New J. Chem.*, 2022, **46**, 11277

Palladium(II) and platinum(II) complexes with ONN donor pincer ligand: synthesis, characterization and *in vitro* cytotoxicity study†

 Biswajit Bera,^a Sanchaita Mondal,^b Saswati Gharami,^a Rahul Naskar,^a Krishna Das Saha ^{*b} and Tapan K. Mondal ^{*a}

New Pd(II) and Pt(II) complexes, [Pd(HL)Cl₂] (**C1**) and [Pt(L)Cl] (**C2**) with ONN donor pincer ligand, 5-(diethylamino)-2-((Z)-((E)-(phenyl(pyridin-2-yl)methylene)hydrazono)methyl)phenol (HL) were synthesized and thoroughly characterized using spectroscopic techniques. X-ray structures of the complexes revealed that HL acts as bidentate *N,N* and tridentate *O,N,N* chelator in Pd(II) and Pt(II) complexes, respectively. The antiproliferative activity of the complexes was explored against four different human cancer (MCF-7, HCT116, A549, HepG2) cell lines. However, the maximum cytotoxicity was seen in the HepG2 cell line [IC₅₀ = 6–12 μM] for both the complexes. IC₅₀ for both complexes, **C1** and **C2**, toward human peripheral blood mononuclear cells (hPBMC) cells were found to be >200 μM. The cytotoxicity of platinum complex (**C2**) was comparable to that of the cisplatin in HepG2 cell lines.

 Received 17th April 2022,
 Accepted 11th May 2022

DOI: 10.1039/d2nj01894b

rsc.li/njc

Introduction

According to the WHO, cancer is the second major reason for death worldwide.¹ Therefore any new effective anticancer agents with nominal side effects remain of crucial significance to the world research society.^{2–4} The advancement of drug resistance and disease relapse are the foremost challenges in anticancer drug design.⁵ Metals have always been handy in dealing with a variety of illnesses found globally.⁶ Owing to their exclusive nature, metal complexes, particularly those consisting of transition metals have achieved remarkable consideration as anticancer agents.⁷ Transition metal complexes as antitumor agents have been broadly utilized after *cis*-platin proved to be as successful as an anti-cancer drug. Lately, *cis*-platin has been recognized as one of the most extensively used antitumor drugs in the world due to its high effectiveness for testicular and ovarian cancers and in the treatment of cervical, bladder and many other varieties of carcinoma.⁸ Nevertheless, regardless of the positive outcomes of platinum compounds in destroying cancer cells, they also have lethal side effects which include nausea, vomiting, lessening of blood cell

and platelet production in bone marrow thereby affecting response to infection.⁹ Hence to prevail over these drawbacks, numerous platinum complexes were designed and fabricated and examined for their anticancer activities.^{10–12} The cytotoxic properties of these Pt(II) complexes were evaluated with respect to cell growth inhibition against different types of human cancer cell lines.

On the other hand, other than the platinum compounds, the palladium(II) compounds are the ones that are being used for cancer treatment as palladium(II) derivatives have antitumor activity similar to the *cis*-platin drug and they also show a lesser amount of kidney toxicity.^{13–15} Thus, the development of new palladium-based anti-cancer drugs is very crucial for effective and efficient use as chemotherapeutic agents. Thus far, significant importance has been given to studying Pd(II) complexes as anticancer drugs,^{16–20} among all other metal ions owing to their much resemblance with Pt(II). Although one obstacle to these Pd-based anticancer drugs is that the ligand exchange and aquation rates of Pd(II) complexes are about 105 times faster than that of the Pt(II) analogues.²¹ Thus, palladium could prevent the interaction with the target DNA by associating with the other donor groups present in the bloodstream, thereby enhancing their toxicity and diminishing their beneficial potential. Hence, an appropriate choice of ligands is vital in order to fabricate better and more competitive palladium, complex-based anticancer agents.¹⁵ Additionally, the palladium compounds have improved solubilities compared to Pt(II) analogues generally. Recent studies revealed that numerous Pd(II) compounds demonstrated a vastly proficient biological

^a Department of Chemistry, Jadavpur University, Kolkata-700032, India.
 E-mail: tapank.mondal@jadavpuruniversity.in

^b Cancer Biology & Inflammatory Disorder Division, CSIR-Indian Institute of Chemical Biology, Kolkata-700 032, India. E-mail: krishna@iicb.res.in

† Electronic supplementary information (ESI) available: NMR, IR and MS of all new compounds, X-ray structure analysis, DFT calculation *etc.* CCDC 2123838 and 2123839. For ESI and crystallographic data in CIF or other electronic format see DOI: <https://doi.org/10.1039/d2nj01894b>



A new palladium(II) phosphino complex with ONS donor Schiff base ligand: Synthesis, characterization and catalytic activity towards Suzuki-Miyaura cross-coupling reaction

Chandan Kumar Manna, **Rahul Naskar**, Biswajit Bera, Akash Das, Tapan Kumar Mondal*

Department of Chemistry, Inorganic Chemistry Section, Jadavpur University, Kolkata, 700032, India

ARTICLE INFO

Article history:

Received 14 December 2020

Revised 5 March 2021

Accepted 15 March 2021

Available online 26 March 2021

Keywords:

Palladium(II) phosphino complex

ONS donor Schiff base ligand

X-ray structure

DFT computation

Suzuki-Miyaura cross coupling

ABSTRACT

New palladium(II) phosphino complex, $[\text{Pd}(\text{PPh}_3)(\text{L})](\text{ClO}_4)$ (**1**) with thioether containing ONS donor Schiff base ligand (HL) is synthesized by the reaction of HL with sodium tetrachloropalladate (Na_2PdCl_4) and PPh_3 . The complex is thoroughly characterized by several spectroscopic techniques. The square planar geometry of the complex is confirmed by single crystal X-ray crystallography. Cyclic voltammetric study in acetonitrile exhibits ligand based irreversible oxidation and reduction peaks at +1.18 V and -1.25 V respectively versus Ag/AgCl reference electrode. Electronic structure and UV-vis spectrum of the complex are interpreted by DFT and TDDFT calculations. Catalytic property of the complex towards Suzuki-Miyaura cross coupling reactions is explored and excellent catalytic conversions (86-97%) are observed with various substituted aryl halides and phenylboronic acid at 100 °C.

© 2021 Elsevier B.V. All rights reserved.

1. Introduction

Since the first report of palladium-catalyzed Suzuki-Miyaura C-C cross-coupling reaction in 1979 [1,2], it is used as the most efficient and effective method for the synthesis of a wide variety of biaryl compounds, used in pharmaceutical applications and various chemical industries [3-6]. The efficiency of catalytic cross-coupling reactions is significantly varied with the ligand environment around the palladium center [7-10]. Moreover, palladium(0/II) phosphine complexes are known to be the most efficient catalysts for C-C cross coupling reactions [11-17]. Several palladium(II) triphenylphosphine-Schiff base complexes are also reported to be effective catalysts towards Suzuki-Miyaura cross-coupling reaction [18-20]. Again, the chemistry of transition metal complexes with ONS donor ligand are extensively studied because of their potential use in industrial and synthetic processes such as catalysis, photochemistry, and biological systems [21-25]. So far, several palladium(II) complexes with tridentate ONS donor ligands are synthesized, characterized and explored their catalytic and biological activities [26-28]. Palladium(II) complexes with ONS donor Schiff base ligands are successfully utilized as effective catalyst towards Suzuki-Miyaura cross-coupling reactions [29-33]. Herein,

we report the synthesis of a new palladium(II) triphenylphosphine complex, $[\text{Pd}(\text{PPh}_3)(\text{L})](\text{ClO}_4)$ (**1**) with ONS based thioether containing Schiff base ligand (HL). Structure of the complex is confirmed by single crystal X-ray diffraction method. Electronic structure and redox properties are interpreted by DFT studies. The complex is proved to be an efficient catalyst in Suzuki-Miyaura cross-coupling reactions of phenyl boronic acid with various aryl halides.

2. Experimental

2.1. Material and methods

All the reagents and solvents were purchased from commercial sources and were used as received. 3,5-Dichlorosalicylaldehyde, 2-aminothiophenol, triphenyl phosphine and Na_2PdCl_4 were purchased from Sigma Aldrich. 2-(Ethylthio)aniline was synthesized following the reported method [34].

Microanalyses (C, H, N) data were obtained using a PerkinElmer Series-II CHN-2400 CHNS/O elemental analyzer. Electronic spectra were measured on a Lambda 750 PerkinElmer spectrophotometer in dichloromethane. IR spectra were recorded on a RX-1 PerkinElmer spectrometer in the range of 4000–400 cm^{-1} with the samples in the form of KBr pellets. HRMS mass spectra were recorded on a Waters (Xevo G2 Q-TOF) mass spectrometer. $^1\text{H-NMR}$ spectra were recorded in CDCl_3 on a Bruker (AC) 300 MHz

* Corresponding author.

E-mail address: tapank.mondal@jadavpuruniversity.in (T.K. Mondal).



Synthesis of new rhodium(III) complex by benzylic C—S bond cleavage of thioether containing NNS donor Schiff base ligand: Investigation of catalytic activity towards transfer hydrogenation of ketones

Sujan Biswas, Chandan Kumar Manna, **Rahul Naskar**, Akash Das, Tapan Kumar Mondal*

Inorganic Chemistry Section, Department of Chemistry, Jadavpur University, Kolkata 700032, India

ARTICLE INFO

Keywords:

Rhodium(III) complex
C—S bond cleavage
Electrochemistry
Transfer hydrogenation of ketones
DFT computation

ABSTRACT

A new rhodium(III)-triphenylphosphine mixed ligand complex, $[\text{Rh}(\text{PPh}_3)(\text{L})\text{Cl}_2]$ (**1**) is synthesized by benzylic C—S bond cleavage of L-CH₂Ph ligand (where, L-CH₂Ph = 2-(benzylthio)-N-(pyridin-2-ylmethylene)aniline). The complex is thoroughly characterized by several spectroscopic techniques. Geometry of the complex is confirmed by single crystal X-ray crystallography. Electronic structure, redox properties, absorption and emission properties of the complex were studied. DFT and TDDFT calculations were carried out to interpret the electronic structure and absorption properties of the complex respectively. The synthesized Rh(III) complex was tested as catalyst towards transfer hydrogenation reaction of ketones in ^tPrOH and an excellent catalytic conversion was observed under mild conditions.

1. Introduction

It is well-known that C—S bonds can be activated by transition metals to form novel sulfur compounds or sulfide complexes [1–3] and this process is extensively studied for the last few decades due to its importance in industry [4–6]. Recently, transition-metal mediated C—S bond activation and cleavage is applied in diverse bioorganic and synthetic chemistry [7,8]. Moreover, transition metals mediated C—S bond activation along with the transformation processes are of stimulating interest from the perspective of synthetic, mechanistic as well as catalytic aspects [9–11]. Transition metal mediated cleavage of both C(aryl)-S and C(alkyl)-S bonds are extensively studied. Hanton et al. reported Cl⁻ triggered facile C(alkyl)-S cleavage of thioether moiety in platinum(II) complex [12]. Goswami et al. reported the effect of reaction temperature and $d\pi(\text{M}) \rightarrow \pi(\text{N}=\text{N})$ on C(alkyl)-S cleavage in platinum(II)-thioether complex [13]. Pramanik et al. explored the C(alkyl)-S cleavage in Rh(III) and Ir(III) complexes in presence of excess PPh₃ [14,15]. In recent years, Biswas et al. reported the activation of both C(aryl)-S and C(alkyl)-S bonds to form cyclometalates and metal-thiolato complexes respectively of group 9 metals [16]. In our previous works, we have reported the synthesis of Pd(II), Ru(II) and Rh(III) complexes by metal induced C(alkyl)-S and C(aryl)-S bond scission of thioether containing ligand systems [17–20]. Herein, we have synthesized a new Rh(III)-

triphenylphosphine complex supported by a tridentate pyridine-imine-thiolato ligand backbone via benzylic C—S bond cleavage of the thioether ligand, L-CH₂Ph (where, L-CH₂Ph = 2-(benzylthio)-N-(pyridin-2-ylmethylene)aniline). It's worth to mention here that the benzylic group plays an important role to cleavage of the C—S bond for the present case. In our previous work, no C—S bond scission was observed and a S(Me)-Rh coordination mode was found under the similar reaction conditions [21].


On the other hand, transfer hydrogenation of ketone to the corresponding alcohol is one of the most important fundamental subjects in modern synthetic chemistry [22,23] and is a convenient method to reduce carbonyl compounds without the use of hazardous hydrogen gas or moisture-sensitive hydride reagents [24–27]. Moreover, the transfer hydrogenation of ketones is widely accepted in industry as a cost-effective way for the production of a number of hydroxylated organic products [28]. Over the last few decades, significant effort on hydrogenation is given on the use of ruthenium, rhodium and iridium catalysts [29–31]. In view of the significant contribution of rhodium complexes towards catalysis, herein we have also explored the catalytic efficiency of the synthesized Rh(III) complex, $[\text{Rh}(\text{PPh}_3)(\text{L})\text{Cl}_2]$ (**1**) towards transfer hydrogenation of ketones in ^tPrOH.

* Corresponding author.

E-mail address: tapank.mondal@jadavpuruniversity.in (T. Kumar Mondal).



Synthesis, characterization, X-ray structure and DNA binding study of palladium(II) complex with new thioether containing ONS donor ligand

SUBRATA JANA, RAHUL NASKAR, CHANDAN KUMAR MANNA and TAPAN KUMAR MONDAL* 

Department of Chemistry, Jadavpur University, Kolkata, West Bengal 700 032, India
E-mail: tapank.mondal@jadavpuruniversity.in

MS received 6 November 2019; revised 14 December 2019; accepted 17 December 2019

Abstract. A palladium(II) complex, [Pd(L)Cl] (**1**) with a new ONS donor azo–thioether ligand (L) (where L = 2,4-dihydroxy-5-((2-(methylthio)phenyl)diazanyl)(phenyl)(phenyl)methanone) is successfully synthesized. The ligand and complex are thoroughly characterized by several spectroscopic techniques. The geometry of the complex is confirmed by single-crystal X-ray analysis. Electronic structure and spectral properties are interpreted by DFT and TDDFT calculations. The interaction of the complex with CT DNA was investigated by UV-vis method and binding constant is found to be $5.42 \times 10^4 \text{ M}^{-1}$. Competitive binding titration with ethidium bromide (EB) by fluorescence titration method was carried out to understand the efficiency of the complex to displace EB from EB-DNA complex. From fluorescence titration Stern-Volmer dynamic quenching constants, K_{sv} was calculated and is found to be $4.15 \times 10^4 \text{ M}^{-1}$. Cyclic voltammogram of the complex exhibits significant shifting of the reduction couple to the negative potential region and decrease in current height in the presence of CT DNA.

Keywords. Palladium(II) complex; ONS donor azo–thioether ligand; X-ray structure; DNA binding study; DFT computation.

1. Introduction

In the past few decades, the chemistry of transition metal complexes with ONS donor ligand are extensively studied because of their plausible applications in fundamental, applied sciences and coordination chemistry beneficial in industrial and synthetic processes such as catalysis, photochemistry, and biological systems.^{1–5} Due to the presence of both hard and soft donors, the chemistry of transition metals with ONS donor ligands is drawing unabated interest to gain the information about their mode of coordination, structural and spectral features.^{6–9} Moreover, because of redox non-innocent nature of azo-thioether ligands, the transition metal complexes have gained augmented research interest in recent years owing to the participation in a variety of interesting redox reactions.^{5,10,11} The complexes encompassing azo functional ligands

have acknowledged escalated consideration owing to their interesting physical, chemical, photophysical and photochemical properties.^{12–14} Besides, the study of compounds containing S and N atoms has engendered copious research interest in recent years due to their significant antifungal, antibacterial and anticancer activities.^{15,16} Moreover, thioether ligands are of fascinating and more important to the coordination chemists to develop effective model complexes to mimic the active sites of several metallo proteins.^{17–19}

Since the discovery of *cis*-platin as an antitumor drug, various closely related platinum and palladium complexes have designed and synthesized to improve the therapeutic activity of the antitumour drugs.²⁰ Because of the similarity in structure and coordination chemistry of these two metals, palladium-based complexes are also investigated significantly in the field of pharmaceutical chemistry.^{21,22} Palladium(II) complexes

*For correspondence

Electronic supplementary material: The online version of this article (<https://doi.org/10.1007/s12039-020-01763-8>) contains supplementary material, which is available to authorized users.

Palladium(II) complex with 1-(2-pyridylazo)-2-naphthol (PAN): Synthesis, X-ray structure, electrochemistry, DFT computation and DNA binding study

Chandan Kumar Manna, Rahul Naskar and Tapan Kumar Mondal*

Department of Chemistry, Jadavpur University, Kolkata-700 032, India

E-mail: tapank.mondal@jadavpuruniversity.in

Manuscript received online 01 April 2019, revised 16 April 2019, accepted 28 April 2019

Herein, we reports a simple approach for the synthesis of a palladium(II) complex with 1-(2-pyridylazo)-2-naphthol (PAN). The complex is characterized by several spectroscopic techniques. The structure is confirmed by single crystal X-ray diffraction method. The interaction of the complex with CT-DNA is investigated by UV-Vis method and binding constant is found to be $3.9 \times 10^4 \text{ M}^{-1}$. Competitive binding titration with ethidium bromide (EB) by fluorescence titration method reveals that the complex efficiently displaces EB from EB-DNA system and the Stern-Volmer dynamic quenching constant, K_{sv} is found to be $1.55 \times 10^4 \text{ M}^{-1}$. Electronic structure and UV-Vis spectrum of the complex are well interpreted by DFT and TDDFT calculations.

Keywords: Palladium(II) complex, X-ray structure, electrochemistry, DNA binding study, DFT calculation.

Introduction

Metal-based antitumor drugs like cisplatin, fulvestrant, goserelin, stilboestro, carboplatin and oxaliplatin are widely used in clinics¹⁻⁴, but there are some limitations due to the drug resistance over a period of time and adverse side effects⁵⁻⁸. These problems have stimulated a far-reaching search and encouraged chemists to develop alternative strategies based on different metals for more efficient, less toxic, and target-specific noncovalent DNA binding anticancer drugs^{9,10}. Therefore, attempts are being made to replace cisplatin with suitable alternatives and hence numerous transition metal complexes were tested for their anticancer activity¹¹⁻¹⁷. Among the transition metals, palladium(II) complexes which can efficiently bind and cleave DNA under physiological conditions are considered as potential candidates for antitumor drugs due to their structural and thermodynamic similarities to platinum(II) complexes. A number of palladium(II) complexes are developed and examined their potential antitumor activity¹⁸. Antiproliferative property in breast cancer and normal cells along with the cytotoxic activity and DNA binding property of several palladium(II) complexes are already been reported in literatures^{19,20}. DNA and protein are considered as the main targets for anticancer agents, since they are involved in many important mechanisms in cells. The interaction between protein and drugs provides valuable information about the structural features

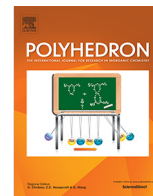
that determine the therapeutic effectiveness and the pharmacological response of drugs^{21,22}.

Azo compounds are widely used in optical recording devices, molecular switches and photovoltaic devices because of their excellent thermal and optical properties²³⁻³⁰. Azo dyes exhibit remarkable biological activities and because of their antibiotic, antifungal and anti-HIV activities they have immense importance in medicinal chemistry³¹⁻³³. Herein, we have used 1-(2-pyridylazo)-2-naphthol (PAN) as ligand which is commonly used as a photometric reagent for wide variety of metal ions and as a metal ion indicator in the complexometric titration. The palladium(II) complex with PAN is synthesized and characterized by several spectroscopic techniques. The structure is confirmed by single crystal X-ray diffraction method and electronic structure is interpreted by DFT calculation. Binding ability of the synthesized palladium(II) complex with CT-DNA has also been explored by UV-Vis and fluorescence method.

Experimental

Materials and methods:

Na_2PdCl_4 , $n\text{-Bu}_4\text{NPF}_6$ and 1-(2-pyridylazo)-2-naphthol (PAN) were purchased from Sigma Aldrich. All other chemicals and solvents were reagent grade commercial materials and were used without further purification.



Luminescent rhenium(I) carbonyl complex with redox noninnocent ONS donor azo-phenol ligand: Synthesis, X-ray structure, photophysical properties and live cell imaging

Puspendu Roy^{a,1}, Deblina Sarkar^b, Paramita Ghosh^c, Rahul Naskar^a, Nabendu Murmu^c, Tapan Kumar Mondal^{a,*}

^aDepartment of Chemistry, Jadavpur University, Kolkata 700032, India

^bDepartment of Chemistry, Bagnan College, Howrah, W.B. 711303, India

^cDepartment of Signal Transduction and Biogenis Amines (STBA), Chittaranjan National Cancer Institute, Kolkata 700026, India

ARTICLE INFO

Article history:

Received 21 September 2018

Accepted 3 January 2019

Available online 14 January 2019

Keywords:

Rhenium(I) carbonyl complex

ONS donor ligand

Electrochemistry

MTT assay

Live cell imaging

ABSTRACT

Herein, we have synthesized a new fluorescent rhenium(I) carbonyl complex **1**, bearing $\{\text{Re}(\text{CO})_3\}^+$ core with ONS donor thioether containing azo-phenol redox noninnocent ligand. The distorted octahedral geometry of the complex is confirmed by single crystal X-ray diffraction method. Cyclic voltammogram in acetonitrile exhibits irreversible oxidation peak ($E_{\text{pa}} = 1.36 \text{ V}$) along with quasi-reversible reduction peak at $E_{1/2} = -0.92 \text{ V}$ ($\Delta E = 210 \text{ mV}$). The complex exhibits low energy emission band at 525 nm with high emission quantum yield ($\phi = 0.115$). Cytotoxicity of the complex is studied by MTT method with human breast cancer cell lines (MCF-7) and IC_{50} value is found to be 23.6 μM . In presence of the complex (10 μM) a bright green fluorescence image of MCF-7 cell lines is observed under fluorescence microscope.

© 2019 Published by Elsevier Ltd.

1. Introduction

The chemistry of rhenium(I) carbonyl complexes with kinetically inert $\{\text{Re}(\text{CO})_3\}^+$ core is extensively studied because their rich photophysics, photochemistry [1–6] and catalytic properties [7–9]. The greater stability of $\{\text{Re}(\text{CO})_3\}^+$ core makes it a suitable candidate to metal node in molecular architecture [10–12]. Moreover, the complexes with this fragment are widely used for labeling of target biomolecules [13,14]. They are used for medical purposes like gene therapy [15] and therapeutic radiopharmaceuticals for cell imaging applications [16–19]. Moreover, the luminescent rhenium(I) compounds with $\{\text{Re}(\text{CO})_3\}^+$ core have become a new promising anticancer drug in comparison to cisplatin [20,21]. The rhenium(I) complexes are also extensively used in photocatalysis [22], organic light emitting diodes (OLEDs) devices [23–27] and electron transfer processes [28,29].

Tricarbonyl rhenium(I) complexes are extensively studied since the pioneer works by Wrighton et al. [30–34] owing to their distinctive luminescence properties [35,36]. These complexes exhibit

good thermal and photochemical stability, and there is still growing interest towards the photochemical and photophysical properties of these complexes, owing to their valuable applications, which include photo-redox chemistry [37,38], electrochemiluminescence [39], chemical and biological sensing [40–43].

The above state of development has encourage us to synthesize and characterize new rhenium(I) carbonyl complex bearing $\{\text{Re}(\text{CO})_3\}^+$ core with ONS donor thioether containing redox noninnocent azo-phenol ligand, 2-(2-(ethylthiophenyl)diazanyl)-4-methylphenol (HL). The structure of *fac*- $[\text{Re}(\text{CO})_3(\text{L})]$ (**1**) is confirmed by single crystal X-ray diffraction method. The photophysical and electrochemical properties of the complex are studied. The electronic structure and redox properties of the complex are interpreted by DFT calculation. In addition, the biocompatibility of the complex is checked with human breast cancer cell lines (MCF-7) by in vitro cytotoxicity assay using MTT. The complex is also used in cell bioimaging study in MCF-7 cell lines.

2. Experimental

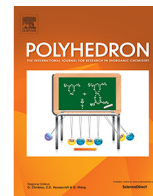
2.1. Material and methods

$\text{Re}(\text{CO})_5\text{Br}$ and 2-aminothiophenol were purchased from Sigma Aldrich. 2-(Ethylthio)benzenamine was synthesized by published

* Corresponding author.

E-mail address: tapank.mondal@jadavpuruniversity.in (T.K. Mondal).

¹ Present address: Department of Chemistry, Netaji Nagar Day College, University of Calcutta, Kolkata 700092, India.



Synthesis of a rhodium(III) triphenylphosphine complex via C–S bond cleavage of an azo-thioether ligand: X-ray structure, electrochemistry and catalysis towards transfer hydrogenation of ketones

Puspendu Roy^{a,b}, Chandan Kumar Manna^a, **Rahul Naskar^a**, Tapan Kumar Mondal^{a,*}

^a Department of Chemistry, Jadavpur University, Kolkata 700032, India

^b Department of Chemistry, Netaji Nagar Day College, University of Calcutta, Kolkata 700092, India

ARTICLE INFO

Article history:

Received 12 July 2018

Accepted 13 October 2018

Available online 1 November 2018

Keywords:

Rhodium(III) complex

C–S bond cleavage

Electrochemistry

Transfer hydrogenation

DFT calculation

ABSTRACT

A new rhodium(III) triphenylphosphine complex having the general formula $[\text{Rh}(\text{PPh}_3)_2(\text{L})\text{Cl}]$ (**1**) was synthesized by C–S bond cleavage of an ONS donor azo-thioether ligand ($\text{L}-\text{CH}_2\text{Ph}$). The complex was thoroughly characterized by various spectroscopic techniques. Its single crystal X-ray structure exhibits an octahedral geometry around the rhodium(III) center. A cyclic voltammogram of the complex exhibits ligand based quasi-irreversible oxidative and reductive responses. The electronic structure, redox properties and electronic excitations in the complex were interpreted by DFT and TDDFT calculations. The complex effectively catalyzed the transfer hydrogenation reaction of ketones with high yields in *i*-PrOH in the presence of a base.

© 2018 Elsevier Ltd. All rights reserved.

1. Introduction

There has been growing interest in transition metal mediated activation of carbon–sulfur bonds due to its importance in the fuel and coal industry for decades [1–4]. Transition metal mediated C–S bond activation and cleavage also play a vital role in the field of bioorganic and synthetic chemistry [5,6]. In order to improve the desired reactivities of metal catalyzed C–S bond activation, the design of ligand systems are important. By the adjustment of the binding affinity and the size of the ligand, both the electron density and steric factors at the metal center can be tuned in the complexes. The phosphine group PR_3 (R = alkyl, aryl, alkoxy etc.) is one of the important ligands used in organometallic chemistry for C–H and C–S activations. The effects on M–L bonds with the variation of the electronic and steric natures of the R group of PR_3 ligands are well quantified by Tolman [7,8]. Moreover, transition metal mediated C–S bond activation along with the transformation processes are of stimulating interest from the perspective of synthetic, mechanistic as well as catalytic aspects [9–12].

In recent years, catalytic transfer hydrogenation has received considerable attention because of its capacity to hydrogenate substrates under mild conditions and it avoids the use of high pressure

vessels and compressed H_2 or moisture-sensitive hydride reagents [13,14]. Continuous research is going on to develop new technologies for future industrial applications in terms of selectivity, efficiency, scope, simplicity and economic viability [15,16]. So, the development of new catalysts for the transfer hydrogenation of ketones is still of considerable interest. Currently, we are working on the design and development of ruthenium, rhodium and osmium metal complexes as catalysts in the transfer hydrogenation of ketones [17–19]. In the present contribution, we have synthesized a new rhodium(III) triphenylphosphine complex, $[\text{Rh}(\text{PPh}_3)_2(\text{L})\text{Cl}]$ (**1**), via C–S bond cleavage of a thioether containing ligand, 3-(2-(2-((pyridin-2-ylmethyl)thio)phenyl)hydrazono)pentane-2,4-dione ($\text{L}-\text{CH}_3$). The complex effectively catalyzes the transfer hydrogenation reaction of ketones in *i*-PrOH. The structure of the complex was confirmed by the single crystal X-ray diffraction method. The electronic structure and redox properties of the complex are interpreted by DFT calculations.

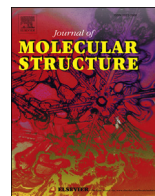
2. Experimental

2.1. Material and methods

All the reagents and solvents were purchased from commercial sources and used as received. Acetylacetone and the inorganic metal salts were obtained from E. Merck, India. 2-Aminothiophe-

* Corresponding author.

E-mail address: tapank.mondal@jadavpuruniversity.in (T.K. Mondal).



Synthesis of thiolato bridged dimeric rhodium(III) triphenylphosphine complex via C–S bond cleavage: X-ray structure, DFT computation and catalytic evaluation towards transfer hydrogenation of ketones

Puspendu Roy^{a, b}, **Rahul Naskar**^a, Chandan Kumar Manna^a, Tapan Kumar Mondal^{a, *}

^a Department of Chemistry, Jadavpur University, Kolkata, 700032, India

^b Department of Chemistry, Netaji Nagar Day College, University of Calcutta, Kolkata, 700092, India

ARTICLE INFO

Article history:

Received 16 April 2019

Received in revised form

31 July 2019

Accepted 14 August 2019

Available online 16 August 2019

Keywords:

Dimeric rhodium(III) complex

C–S bond cleavage

Transfer hydrogenation of ketones

DFT calculation

ABSTRACT

Herein, we have synthesized a new dimeric rhodium(III) triphenylphosphine complex, $[\text{Rh}_2(\text{PPh}_3)_2(\text{L})_2\text{Cl}_2]$ (**1**) via $\text{sp}^3(\text{C})$ –S bond cleavage of a thioether containing ligand, 1-(((2-(ethylthio)phenyl)diazanyl)methyl)naphthalen-2-ol (L- CH_2CH_3). The complex was thoroughly characterized by using various spectroscopic techniques. Dimeric structure with distorted octahedral geometry of each of the rhodium center is confirmed by single crystal X-ray diffraction method. Catalytic efficiency of the complex towards transfer hydrogenation of ketones is studied in *i*-PrOH. Electronic structure and UV–vis spectrum of the complex are interpreted by DFT and TDDFT computations.

© 2019 Elsevier B.V. All rights reserved.

1. Introduction

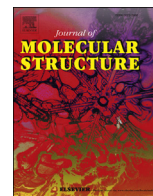
Transition metal mediated C–S bond activation, cleavage and transformation reactions are extensively studied for the last few decades owing to their importance in petroleum industry [1–3], synthetic chemistry [4–6], biorganic and bioinorganic chemistry [7–10]. The ligand systems played a crucial role in the metal catalyzed C–S bond activation. For desired reactivity, the binding affinity and the size of the ligands, electron density and steric factors of the ligands are tuned in the complexes [11,12]. More and more attentions are given to this research topic to explore convenient and efficient strategy. Recently, Majumdar et al. are extensively studied the iron and cobalt mediated C–S bond activation reactions and explored their chemical reactivity [13–15]. Hosoya et al. are reported the metal catalyzed selective aromatic C–S bond cleavage triggered transformations of thioarenes [16]. Shi et al. have successfully utilized rhodium catalyzed C–S bond activation to construct C–C bond [17]. Liebeskind and co-workers have reported the palladium and copper catalyzed cross coupling reactions via C–S bond cleavage reactions [18–20].

The transfer hydrogenation of ketones to the corresponding

alcohols has received considerable attention in chemical research because of its capacity to hydrogenate substrates in mild conditions [21–23] and avoids the use of high pressure vessels and compressed H_2 or moisture-sensitive hydride reagents [24–27]. People are deeply engaged to develop new catalysts for future industrial applications in terms of selectivity, efficiency, scope, simplicity and economic viability [28–31]. In our continued efforts to design and synthesis of platinum group metal complexes and to explore their catalytic activity towards transfer hydrogenation of ketones [32–35] herein, we have synthesized a new dimeric rhodium(III) triphenylphosphine complex, $[\text{Rh}_2(\text{PPh}_3)_2(\text{L})_2\text{Cl}_2]$ (**1**) via C–S bond cleavage of a thioether containing ligand, 1-(((2-(ethylthio)phenyl)diazanyl)methyl)naphthalen-2-ol (L- CH_2CH_3). The coordination chemistry of Pd(II) and Pt(II) with L- CH_2CH_3 was explored previously [36,37]. Recently, rhodium and iridium assisted $\text{sp}^2(\text{C})$ –S bond cleavage and formation of cyclometalated complexes were reported by S. Acharya et al. [38]. In the present work we have synthesized the dimeric Rh(III) complex by $\text{sp}^3(\text{C})$ –S bond cleavage of L- CH_2CH_3 . Moreover, the catalytic efficiency of the complex towards transfer hydrogenation of ketones is studied in *i*-PrOH. Structure of the complex is confirmed by single crystal X-ray diffraction method. Electronic structure of the complex is interpreted by DFT computations.

* Corresponding author.

E-mail address: tapank.mondal@jadavpuruniversity.in (T.K. Mondal).



Synthesis of a zinc(II) complex with hexadentate N_4S_2 donor thioether ligand: X-ray structure, DNA binding study and DFT computation

Apurba Sau Mondal, Mahendra Sekhar Jana, Chandan Kumar Manna, **Rahul Naskar**, Tapan Kumar Mondal*

Inorganic Chemistry Section, Department of Chemistry, Jadavpur University, Kolkata 700032, India



ARTICLE INFO

Article history:
Available online 13 March 2018

Keywords:
Zinc(II) complex
Azo-thioether ligand
X-ray and electronic structure
DNA binding study
DFT and TDDFT calculations

ABSTRACT

A new zinc(II) complex, $[Zn(L)](ClO_4)$ with hexadentate N_4S_2 donor azo-thioether ligand (HL) was synthesized and characterized by several spectroscopic techniques. The structure was confirmed by single crystal X-ray analysis. The interaction of the complex with CT DNA was investigated by UV–vis method and binding constant is found to be $6.6 \times 10^4 M^{-1}$. Competitive binding titration with ethidium bromide (EB) by fluorescence titration method reveals that the complex efficiently displaces EB from EB–DNA system and the Stern–Volmer dynamic quenching constant, K_{SV} is found to be $2.6 \times 10^4 M^{-1}$. DFT and TDDFT calculations were carried out to interpret the electronic structure and electronic spectra of the complex.

© 2018 Elsevier B.V. All rights reserved.

1. Introduction

For the last few decades azo compounds have received significant attention in scientific research and they are widely used as dyes and pigments for a long time [1,2]. The chemistry of the azo compounds is extensively studied because of their excellent thermal and optical properties and is extensively used in optical recording devices, molecular switches, toner and ink-jet printing [3–8]. In addition, azo dyes exhibit a variety of interesting biological activities and because of their antibiotic, antifungal and anti-HIV activities they have immense importance in medicinal chemistry [9–14]. In spite of its wide applications azo dyes exhibit carcinogenicity when interact with DNA and causes mutations [15,16].

The coordination chemistry of transition metals with N and S donor chelating ligands are widely studied because of their stability, chemical and electrochemical activities and diversity in binding mode of the ligand to metal centre [17–19]. Moreover, the coordination of the azo dyes with metal ions enhances their significance and used in colouring of fibres, printing technologies and textile dyeing [20–22]. Thioether ligands are also used for the synthesis of model complexes to mimic the active sites of several

metallo proteins [23–25]. Because of moderately hard and soft donor centers, multidentate ligands containing N and S donor atoms bind to a wide range of transition metals with diversity in binding mode [26–28]. Transition metal complexes with polydentate ligands are also important because of their capacity for binding and cleaving of DNA under physiological conditions [29,30]. Zinc is an important biometal essential for life, it is the second most abundant metal after iron present in biological systems and is present in more than 300 enzymes of living organisms [31]. The regulation of zinc also has various effects on the nervous system [32]. Zinc complexes are also found to be various applications as drugs because of their antimicrobial, anti-inflammatory, antidiabetic and antitumor activities [33–35].

As part of our continuing research on transition metal complexes with azo-thioether ligands [36–41], herein we have synthesized an octahedral zinc(II) complex, $[Zn(L)](ClO_4)$ with hexadentate azo-thioether ligand, 3-acetyl-1,5-bis(2-(pyridin-2-ylmethyl)thio)phenyl)formazan (HL) (Scheme 1). The complex was thoroughly characterized by several spectroscopic techniques. The geometry of the complex was confirmed by single crystal X-ray diffraction study. The ability of the complex to bind with CT DNA was investigated by UV–Vis method, while the competitive binding with ethidium bromide (EB) was carried out by fluorescence method in order to assess the ability of the complex to displace EB from EB–DNA system.

* Corresponding author.

E-mail address: tapank.mondal@jadavpuruniversity.in (T.K. Mondal).